

IEEE Benelux Photonics  
Chapter

# Annual Symposium 2022

24-25 November 2022

Eindhoven University of Technology  
The Netherlands



# Gamma radiation response of FBG inscribed in 20- $\mu\text{m}$ core graded-index polymer CYTOP fiber

I. Chapalo<sup>1</sup>, A. Gusarov<sup>2</sup>, A. Ioannou<sup>3</sup>, K. Chah<sup>1</sup>, A. Pospori<sup>3</sup>, Y.-G. Nan<sup>1</sup>, K. Kalli<sup>3</sup>, and P. Mégret<sup>1</sup>

<sup>1</sup> University of Mons, Electromagnetism and Telecom Department, Boulevard Dolez 31, 7000 Mons, Belgium

<sup>2</sup> SCK-CEN, Boeretang 200, 2400 Mol, Belgium

<sup>3</sup> Cyprus University of Technology, Photonics and Optical Sensors Research Laboratory, Saripolou 33, 3036, Limassol, Cyprus.

*We investigate online response of a fiber Bragg grating (FBG) inscribed in a polymer optical fiber on gamma radiation. The fiber had a 20- $\mu\text{m}$  graded-index CYTOP core and 250- $\mu\text{m}$  XYLEX overclad. The FBG was inscribed by fs laser using the plane-by-plane technique. We irradiated the grating by <sup>60</sup>Co sources at the dose rate of 5.3 kGy/h. The reflection peak (RP) of the grating was monitored before, during and after irradiation (online) using a commercial interrogator placed outside of the irradiation field. The FBG was connected with the interrogator by 10-m single-mode silica patchcord. We firstly applied a 40-kGy dose and then, after  $\approx 90$  hours of recovery, we applied the second dose of 80 kGy. The FBG demonstrated a blue shift of the RP during both sessions of irradiation. The speed of the RP change increased during receiving  $\approx 15$  kGy of the first irradiation, and then, the RP changed linearly with -3.5 pm/kGy speed. During the second irradiation, the RP changed linearly during the entire irradiation session with -4.13 pm/kGy speed. The linear FBG response to the received dose can be prospective for gamma radiation dosimetry.*

## Introduction

Changes of physical properties of optical fiber under ionizing irradiation can be applied for fiber optic dosimetry. Indeed, this aspect of development has been intensively investigated over the past decades [1,2]. The interest to optical fiber dosimetry is due to the possibility of online and distributed sensing, remote interrogation and small size of sensitive elements. Recently, increased attention from researchers has been focused on using polymer optical fibers (POFs) as a sensitive element for gamma- and X-rays dosimetry. Sensors based on the radiation induced attenuation (RIA) effect in the visible range in polymethylmethacrylate (PMMA) POF demonstrated an advantage of strong sensitivity compared to silica fiber [3,4]. Another POF type investigated for dosimetric applications is perfluorinated fiber based on CYTOP material. It demonstrated significantly stronger RIA in UV-VIS range comparing to PMMA [5]. FBGs inscribed in CYTOP fiber have been investigated under gamma radiation as well. They show blue wavelength shift of their reflection peaks as a result of gamma irradiation in standard 120- $\mu\text{m}$  core graded-index PF-POF [6].

In this work, we investigate the gamma radiation effect on the Bragg wavelength (BW) of the FBG inscribed in a few-mode graded-index POF with 20- $\mu\text{m}$  CYTOP core and 250- $\mu\text{m}$  XYLEX overclad. The BW was monitored online before, during and after irradiation. We show the BW evolution over time for two irradiation sessions with received doses of 40 and 80 kGy. We compare the obtained dependences with earlier published results for FBGs inscribed in standard CYTOP fiber of 120- $\mu\text{m}$  core.

## Experimental setup

Experiments were conducted at a Brigitte irradiation facility (SCK-CEN, Belgium). The irradiation setup consists of  $^{60}\text{Co}$  gamma radiation sources forming a cylindrical volume at a depth of seven meters in a water pool and providing the dose rate of 5.3 kGy/h (Fig. 1). For irradiation, the FBG was placed inside a stainless steel container, which can be sealed for under-water operation. The container was placed down to irradiation zone for a specified time according to the required irradiation dose using an industrial hoist. Before and after irradiation, the container was stored under water at a depth of  $\approx 2$  meters for pre irradiation stabilization and post irradiation monitoring of the BW. Temperature inside the contained was stabilized at  $42^\circ\text{C}$  by the oven controlled by the Eurotherm 2408 controller. A 9-m long tube of 5-cm diameter was hermetically connected to the container, so that the optical cables can be passed from the equipment setup towards the investigated samples. The FBG was connected to the standard commercial interrogator (FiberSensing FS2200) using 10-m SMF-28 patchcord threaded through the tube.

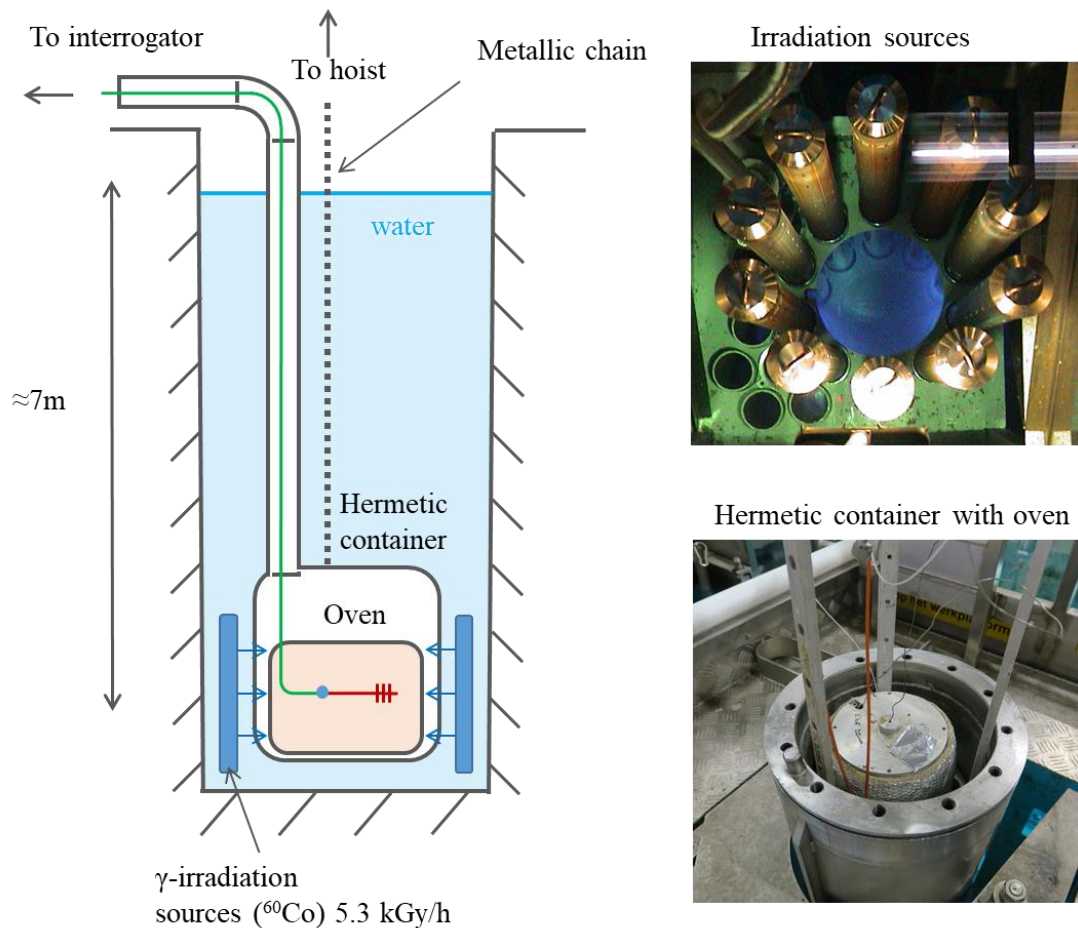


Fig. 1 Schematic of the experimental setup and photographs of irradiation sources and the container.

For the FBG inscription, we used the POF designed and produced by Chromis Technologies. It has a few-mode graded-index CYTOP core of 20- $\mu\text{m}$  diameter and an effective refractive index of 1.34. Reduced core diameter allows to decrease a possible number of excited mode groups in the POF by 3-4. Accurately adjusted launching conditions provide stable single-peak reflection spectrum of the FBG [7]. A protective overlaid of a 250- $\mu\text{m}$  diameter is made of a XYLEX material, which is a blend of

polycarbonate and an amorphous polyester. The FBG of 1 mm length was inscribed by femtosecond pulses generated by a HighQ laser femtoREGEN source at  $\lambda=517$  nm (220 fs pulse duration and 1 kHz repetition rate) using a plane-by-plane direct inscription method [8]. The POF sample containing the FBG was centered and connectorized with a standard silica SMF pigtail using two manual translation stages and the UV-curing glue. The FBG was annealed at 65°C during 3 hours before the experiment.

We performed two irradiation sessions with doses of 40 and 80 kGy. Between the sessions, we lifted the container with the FBG out of the irradiation zone and we stored it at underwater position during  $\approx 90$  hours for monitoring the BW evolution after irradiation. The BW was monitored with the same procedure after the second irradiation session as well.

## Experimental results

Fig. 2 (a) shows the evolution of the BW over time. After underwater stabilization, the FBG demonstrates the BW blue shift during the first (40-kGy) irradiation. After the first irradiation, a weak recovery of the BW ( $\approx 20\%$  of the first irradiation BW shift) is seen during up to 10 hours and then, a slow decrease of the BW at a rate of  $\approx 0.7$  pm/h is observed. The second irradiation (80 kGy) again caused the blue shift of the BW, however, the recovery is significantly stronger than after the first irradiation.

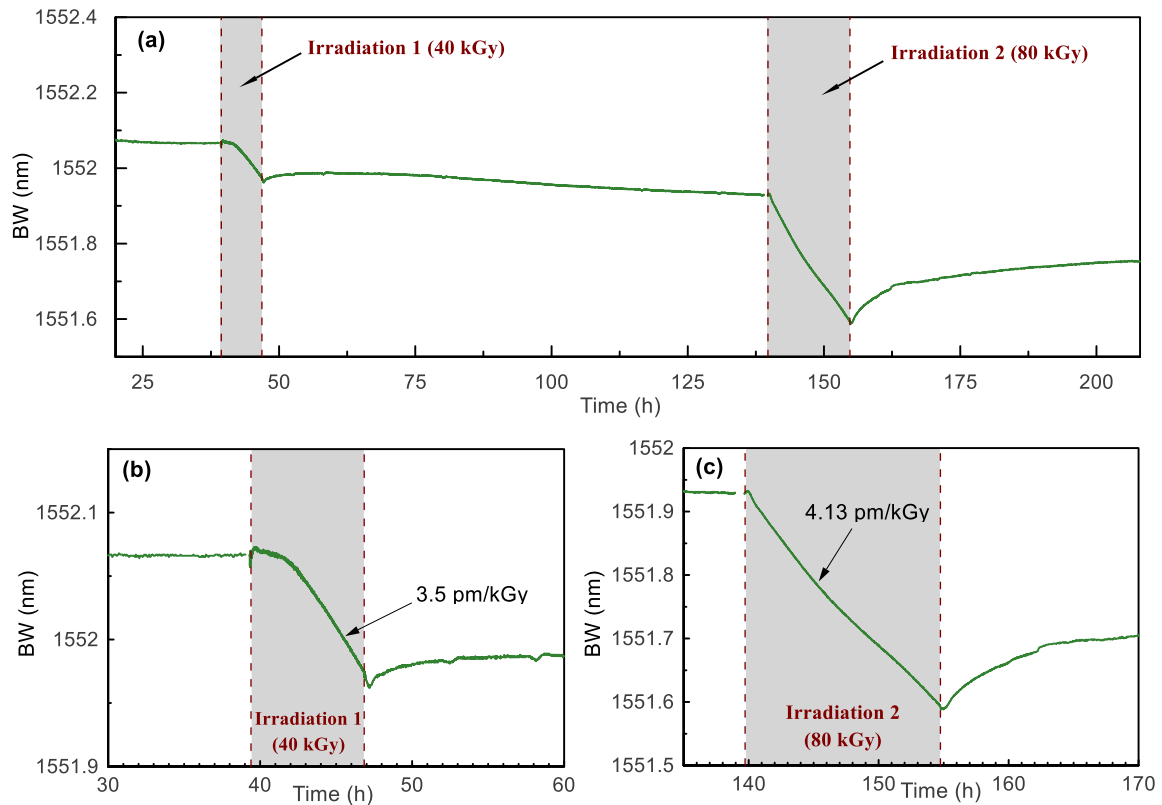


Fig. 2 Bragg wavelength evolution over time during two sessions of gamma radiation: general view (a), detailed graph of the first irradiation session of 40 kGy (b), and detailed graph of second irradiation session of 80 kGy (c).

Fig. 2(b) shows the first irradiation in more detail. A slight BW rise of  $\approx 10$  pm during 20 min is seen after the start of irradiation. Then, the BW turned to a slow decrease during another 1.5-2 hours, and finally, it reached stronger, linear decreasing part of the

graph with a slope of  $-3.5$  pm/kGy. The total BW shift during irradiation is  $-95$  pm. It should be mentioned that the BW experienced another 10-pm decrease immediately after irradiation. After that, the BW recovery process was observed.

The BW evolution during the second (80-kGy) irradiation (Fig. 2(c)) demonstrates very weak initial BW rise of  $\approx 5$  pm. Then, the BW decreased linearly with the slope of  $-4.13$  pm/kGy. The total BW change during the second irradiation is  $-340$  pm. The recovery BW shift is 130 pm at the end of the experiment (53 hours after the end of irradiation 2), i.e. 38% of the second irradiation BW shift.

The possible reason of the non-linear response during the beginning part of the first irradiation could be not ideally stabilized temperature. It changed by  $\approx 3^\circ\text{C}$  in the beginning of the first irradiation. Therefore, the BW could react simultaneously to the temperature and radiation. Before and during the second irradiation, the temperature was well stabilized, and the FBG demonstrated linear response to the irradiation dose.

Reference [6] presents the investigation the gamma radiation response of FBGs inscribed in a standard POF with 120- $\mu\text{m}$  CYTOP core and 490- $\mu\text{m}$  polycarbonate overclad. The blue shift of the BW was also demonstrated, however significantly higher sensitivity of  $-29.9$  pm/kGy was obtained. There could be several possible reasons that could affect sensitivity: temperature during irradiation, different fiber lateral dimensions, and even the history of the fiber's climatic conditions (especially the absence of temperature annealing). The latter can result in the additional shrinkage effect (and therefore additional blue shift of the BW) due to increased temperature during irradiation. However, the most significant reason, in our opinion, is different dose rates: 5.3 kGy/h in our experiment versus 635 Gy/h in [6].

## Conclusion

In this work we investigated the BW evolution under gamma radiation of the FBG inscribed in a few-mode CYTOP fiber. The CYTOP FBG seems prospective for gamma radiation dosimetry since it demonstrated a linear response to the received dose with a sensitivity of  $-4.13$  pm/kGy at  $42^\circ\text{C}$ . Future research should be focused on the effect of dose rate, temperature and total received dose on the FBG response to gamma radiation.

## References

- [1] A. Faustov, A. Gusarov, M. Wuilpart, A. Fotiadi, L. Liokumovich, I. Zolotovskiy, A. Tomashuk, T. de Schoutheete, and P. Mégret, "Comparison of Gamma-Radiation Induced Attenuation in Al-Doped, P-Doped and Ge-Doped Fibres for Dosimetry," *IEEE Transactions on Nuclear Science*, vol. 60 no. 4, 2511-2517, 2013.
- [2] S. Girard, et al. "Overview of radiation induced point defects in silica-based optical fibers," *Reviews in Physics*, vol. 4, 100032, 2019.
- [3] S. O'Keeffe and E. Lewis, "Polymer optical fibre for in situ monitoring of gamma radiation processes," *International Journal on Smart Sensing and Intelligent Systems*, vol. 2, no. 3, 490-502, 2009.
- [4] V. Prajzler, K. Masopoustova, and Z. Sarsounova, "Gamma radiation effects on plastic optical fibers," *Optical Fiber Technology*, vol. 72, 102995, 2022.
- [5] P. Stajanka, L. Mihai, D. Sporea, D. Negut, H. Sturm, M. Schukar, and K. Krebber, "Effects of gamma radiation on perfluorinated polymer optical fibers," *Optical Materials*, vol. 58, 226-233, 2016.
- [6] C. Broadway, D. Kinet, A. Theodosiou, K. Kalli, A. Gusarov, C. Caucheteur, and P. Mégret, "CYTOP Fibre Bragg Grating Sensors for Harsh Radiation Environments," *Sensors*, vol. 19, 2853, 2019.
- [7] A. Pospori, A. Ioannou, and K. Kalli, "Pre-strain effects on CYTOP fibre Bragg grating temperature sensors," *Proceedings of SPIE*, vol. 12140, 121400J, 2022.  
A. Theodosiou *et al.*, "Plane-by-Plane Femtosecond Laser Inscription Method for Single-Peak Bragg Gratings in Multimode CYTOP Polymer Optical Fiber," *Journal of Lightwave Technology*, vol. 35, no. 24, 5404-5410, 2017.

# A monolithically integrated tunable low-linewidth laser source

H. O. Çirkinoglu, K. Williams, and X. Leijtens

Eindhoven University of Technology, Eindhoven, The Netherlands

*Single mode tunable lasers are essential components for applications such as classical/quantum communications, sensing and metrology. We report on a monolithically integrated single mode tunable laser with 53 kHz linewidth operating around 1550nm, designed and fabricated in a generic InP integration platform. The laser cavity consists of two ring filters and an asymmetric Mach-Zehnder (MZ) filter, connected via two 1×3 MMI couplers. The laser LIV characteristics, optical output spectra, power spectral density of the phase noise and the tunability map of the laser are presented.*

## Introduction

Low linewidth and tunable lasers are key components in various applications. Coherent communications rely on low linewidth, frequency stabilized lasers to modulate and de-modulate phase encoded optical signals [1], where the requirement of the spectral stability gets more stringent as the modulation order increases [2, 3]. The laser linewidth affects the transmission rate in both continuous-variable (CV-QKD) [4] and discrete-variable quantum key distribution (DV-QKD) [5]. Low-linewidth and accurate tuning of the wavelength are crucial features for lasers to be used in technologies such as OCT [6], frequency modulated continuous wave LiDAR [7], or quantum sensing, where the lasers are required to precisely match the energy of atomic transitions [8,9].

Improving the spectral output of a monolithically integrated DBR laser using an intra-cavity ring resonator is studied in [10], resulting in a minimum intrinsic linewidth of 63kHz and a side-mode-suppression ratio (SMSR) of more than 60dB. Another example of a monolithically integrated low-linewidth integrated semiconductor DBR laser is demonstrated in [11], reducing the linewidth down to 10kHz by coupling with an extended passive Fabry-Perot resonator, while having a SMSR of 54dB. Further reducing the linewidth of tunable semiconductor lasers through hybrid [12] and heterogeneous [13] integration has been shown, resulting in linewidths on the order of 100Hz. Additionally, lasers with increased wavelength tuning range have been shown using intra-cavity Mach-Zehnder interferometers (MZI) [14], and through selective area growth [15], which are promising components for applications such as optical gas sensing.

Using the vernier effect of multiple cavities with long optical lengths has been shown to result in low linewidth, while increasing the required complexity in accurate and continuous wavelength tuning. Asymmetric MZI filters provide less complexity in wavelength tuning, while compromising the linewidth due to the lower quality factor of the filters. In this work, we report on a novel laser cavity design, which combines two rings and a MZI filter to provide low-linewidth and wide tunability across the C-band. The laser is monolithically integrated in the generic InP platform of Smart Photonics [16], and is able to achieve 53kHz linewidth and 58dB SMSR.

## Laser Design

Figure 1(a) shows the schematic of the laser, which consists of a 500 $\mu$ m long semiconductor optical amplifier (SOA) section, connected to two ring/racetrack resonators via 1×3 multi-mode interference (MMI) couplers on both sides. Since each coupler in the cavity is expected to result in additional unwanted reflections and losses,

the choice of using  $1 \times 3$  MMIs is made to minimize the number of couplers, while ensuring proper connectivity to each filter. One of the rings have an additional coarse-wavelength filter based on an asymmetric MZI, connected through  $2 \times 2$  MMI couplers. The laser cavity is designed with a goal of maximizing the photon lifetime, while having sufficient spectral filtering with a high quality-factor to provide single mode output with low linewidth [17]. The ratio between the length of the two ring filters are designed based on their respective comb spectra, and how the peaks of these spectra overlap. The resulting response of the combined filters is simulated and shown in Figure 1 (b). Around the most prominent peak, the two highest neighboring peaks are at a distance of 0.84nm and 1.31nm, each having 5% lower power. The distance between two resonant modes allows the use of an asymmetric MZI filter to provide enough suppression for the neighboring modes around the desired wavelength.

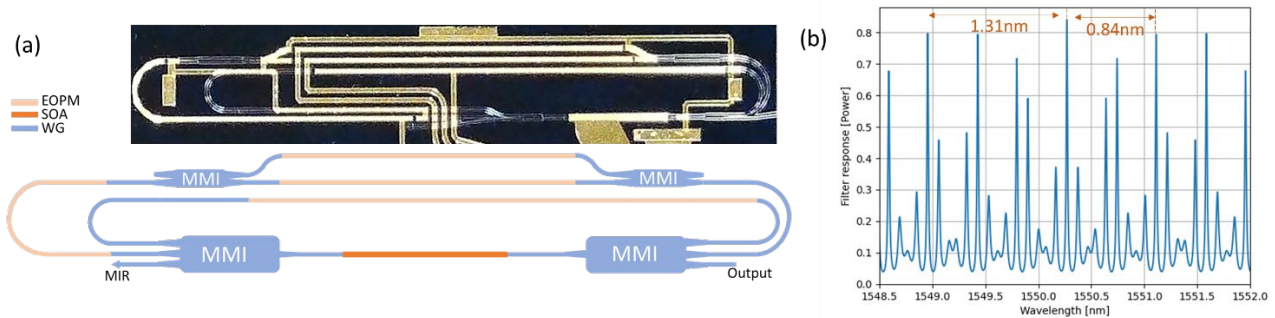


Figure 1- (a) Schematic of the laser (inset: the microscope image of the fabricated chip)  
 (b) Simulated spectral response of the laser cavity

The two rings, and the asymmetric MZI include electro-optic phase modulator (EOPM) sections in order to control the spectral location of their respective modes. The two ring EOPMs are designed to provide precise control and continuous tuning for the laser emission wavelength across smaller regions, where the asymmetric MZI filter is designed to provide wide tunability across the full emission spectrum of SOA. Fine-tuning of the wavelength through the control of only two voltage signals promises to offer low complexity in the characterization and modeling of the laser wavelength. The third output of the  $1 \times 3$  MMI on the left-hand side has a multi-mode interference mirror (MIR) to ensure uni-directionality, and the third output of the right-hand side  $1 \times 3$  MMI is the output of the laser. The laser is fabricated in the generic platform of Smart Photonics and have a  $1.2\text{mm}^2$  footprint. Inset in figure 1(a) shows a microscope image of the fabricated chip including the laser.

## Characterization Results

Figure 2(a) shows the LIV characteristics of the fabricated laser, measured at  $17^\circ\text{C}$ . The threshold current is at 38mA. The output power from the laser, coupled out using a lensed fiber is measured as 0.4mW for a pump current of 120mA.

The figure 2(b) shows the output spectrum of the laser, operated at  $17^\circ\text{C}$  with a 92mA SOA current. The cavity side-modes are 0.84nm and 1.32nm away from the main emission peak, in agreement with the cavity simulations. The side-mode-suppression ratio of both peaks are more than 58dB. There are two additional peaks around the center wavelength, resulting from relaxation oscillations at a frequency of 3.6GHz.

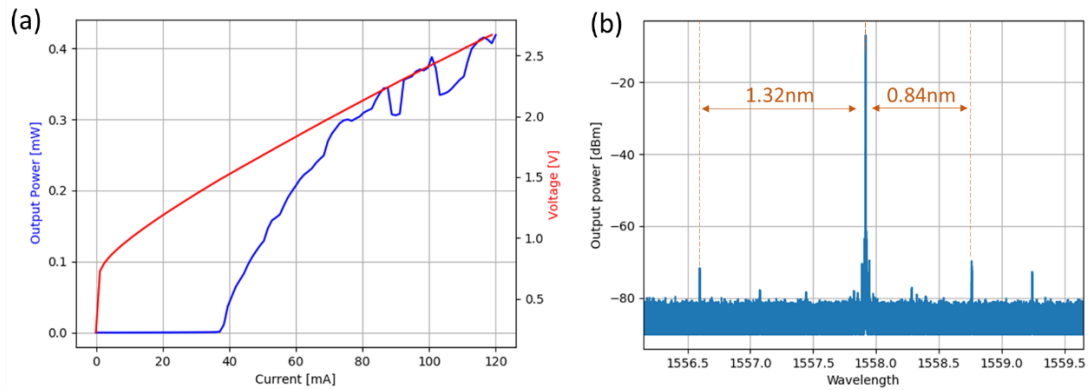


Figure 2 – (a) LIV characteristics and (b) the output spectrum of the laser

The figure 3(a) shows the frequency noise power spectral density of the laser operating at 79mA SOA current. The white noise level is measured by averaging the region of the spectrum shown in green between 20MHz-80MHz, indicating to a 53kHz intrinsic linewidth. The  $\beta$ -separation line shown in orange is defined as  $\beta_{sep}(f) = 8 \ln(2) f / \pi^2$  [18]. The effective linewidth starts to increase for observation times more than  $8\mu s$ , determined by the where the frequency noise crosses the  $\beta$ -separation line, which is around 125 KHz.

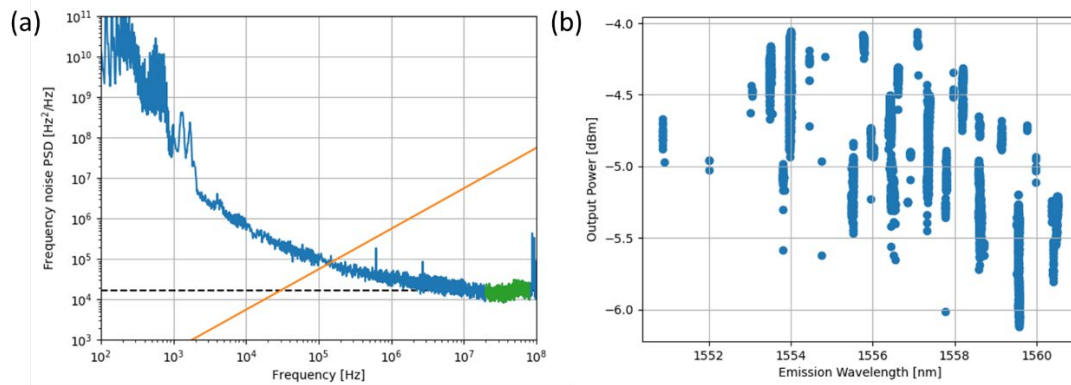


Figure 3- (a) Frequency noise power spectral density of the laser. (b) Various operating wavelengths with the corresponding fiber-coupled optical powers

The figure 3(b) shows the measured single mode emission wavelength and output power of the laser while the bias voltages on the EOPMs of both rings are scanned between 0V and -6V with a resolution of 0.1V. The SOA current and the bias voltage on the MZI filter are kept constant at 79mA and 0V respectively. By controlling the bias of the two ring EOPMs, the laser wavelength can be shifted over a range of 10nm, while the output power staying within a range of 2dB around -5dBm. Changing the bias voltage on the MZI arms is expected to provide larger wavelength tuning range.

## Conclusion & Outlook

A monolithically integrated low-linewidth and tunable laser with a novel cavity design is presented. The initial results show 53kHz linewidth with 58dB SMSR, and around 10nm of tuning range with a power stability of  $\sim 2$ dB. Complete investigation of the tuning range requires simultaneous tuning of the MZI filter and the ring cavities and is planned in future experiments.

## References

- [1] K. Kikuchi, "Fundamentals of coherent optical fiber communications." *Journal of Lightwave Technology* 34.1, 157-179, 2015.
- [2] M. Seimetz, "Laser linewidth limitations for optical systems with high-order modulation employing feed forward digital carrier phase estimation." In *Optical Fiber Communication Conference*, p. OTuM2. Optical Society of America, 2008.
- [3] S. Andreou, K. A. Williams, and E. Bente, "Electro-optic tuning of a monolithically integrated widely tuneable InP laser with free-running and stabilized operation." *Journal of Lightwave Technology* 38, no. 7, 1887-1894, 2019.
- [4] F. Laudenbach, C. Pacher, C.F. Fung, A. Poppe, M. Peev, B. Schrenk, M. Hentschel, P. Walther, and H. Hübel, "Continuous-variable quantum key distribution with Gaussian modulation—the theory of practical implementations." *Advanced Quantum Technologies* 1, no. 1, 1800011, 2018.
- [5] T. Honjo, T. Inoue, and K. Inoue, "Influence of light source linewidth in differential-phase-shift quantum key distribution systems." *Optics Communications* 284, no. 24, 5856-5859, 2011.
- [6] Y. Gao, J. Lo, S. Lee, R. Patel, L. Zhu, J. Nee, D. Tsou, R. Carney, and J. Sun, "High-power, narrow-linewidth, miniaturized silicon photonic tunable laser with accurate frequency control." *Journal of Lightwave Technology* 38, no. 2, 265-271, 2020.
- [7] B. J. Isaac, B. Song, S. Pinna, L. A. Coldren, and J. Klamkin, "Indium phosphide photonic integrated circuit transceiver for FMCW LiDAR." *IEEE Journal of Selected Topics in Quantum Electronics* 25, no. 6, 1-7, 2019.
- [8] F. Theron, O. Carraz, G. Renon, N. Zahzam, Y. Bidet, M. Cadoret, and A. Bresson, "Narrow linewidth single laser source system for onboard atom interferometry." *Applied Physics B* 118, no. 1, 1-5, 2015.
- [9] A. Wicht, A. Bawamia, M. Krüger, C. Kürbis, M. Schiemangk, R. Smol, A. Peters, and G. Tränkle, "Narrow linewidth diode laser modules for quantum optical sensor applications in the field and in space." In *Components and packaging for laser systems III*, vol. 10085, pp. 103-118, SPIE, 2017.
- [10] S. Andreou, K. A. Williams, and E. Bente, "Monolithically integrated InP-based DBR lasers with an intra-cavity ring resonator." *Optics Express* 27, no. 19, 26281-26294, 2019.
- [11] R. R. Kumar, A. Hänsel, M. F. Brusatori, L. Nielsen, L. M. Augustin, N. Volet, and M. Heck, "A 10-kHz intrinsic linewidth coupled extended-cavity DBR laser monolithically integrated on an InP platform." *Optics Letters* 47, no. 9, 2346-2349, 2022.
- [12] M. F. Brusatori, D. N. Duplat, I. Degli-Eredi, L. Nielsen, P. L. Tønning, P. Castera, N. Volet, and M. Heck, "Ultralow-linewidth ring laser using hybrid integration and generic foundry platforms." *Optics Letters* 47, no. 11, 2686-2689, 2022.
- [13] P. A. Morton, C. Xiang, J. B. Khurgin, C. D. Morton, M. Tran, J. Peters, J. Guo, M. J. Morton, and J. E. Bowers, "Integrated coherent tunable laser (ICTL) with ultra-wideband wavelength tuning and sub-100 Hz Lorentzian linewidth." *Journal of Lightwave Technology* 40, no. 6, 1802-1809, 2022.
- [14] S. Latkowski, A. Hänsel, N. Bhattacharya, T. De Vries, L. Augustin, K. Williams, M. Smit, and E. Bente, "Novel widely tunable monolithically integrated laser source." *IEEE Photonics Journal* 7, no. 6, 1-9, 2015.
- [15] F. Lemaître, S. Latkowski, C. Fortin, N. Lagay, R. Pajković, E. Smalbrugge, J. Decobert, H. Ambrosius, and K. Williams, "96 nm extended range laser source using selective area growth." In *2018 European Conference on Optical Communication (ECOC)*, pp. 1-3. IEEE, 2018.
- [16] M. Smit, X. Leijtens, H. Ambrosius, E. Bente, J. Van der Tol, B. Smalbrugge, Tjibbe De Vries et al., "An introduction to InP-based generic integration technology." *Semiconductor Science and Technology* 29, no. 8, 083001, 2014.
- [17] C. Henry, "Theory of the linewidth of semiconductor lasers." *IEEE Journal of Quantum Electronics* 18, no. 2, 259-264, 1982.
- [18] G. D. Domenico, S. Schilt, and P. Thomann, "Simple approach to the relation between laser frequency noise and laser line shape," *Appl. Opt.* vol. 49, no. 25, pp. 4801-4807, 2010.

# RF-choke for on-chip bias circuit monolithically integrated with high speed UTC-PD

J.P. de Graaf, D. Konstantinou, S. Rommel, I. Tafur Monroy, K. Williams and Y. Jiao

Eindhoven Hendrik Casimir Institute, Eindhoven University of Technology, Eindhoven, The Netherlands  
j.p.d.graaf@tue.nl

## Abstract

*This work reports on the monolithic integration of a bias circuit together with a high speed UTC-PD. The bias circuit consists of a coplanar waveguide line with a DC connection that is decoupled from the RF signal through a quarter wavelength stub. Two RF chokes are designed, for  $K_a$ - and V-band respectively, which are directly integrated with high speed UTC-PDs on an InP-Membrane On Silicon platform. S-parameter simulations demonstrate RF transmission losses below 3dB, reflections below -14dB and RF to DC isolation of 15dB over a range of 10GHz around the center frequencies of the two respective frequency bands.*

## Introduction

Although various bias-free uni-travelling carrier photodetectors (UTC-PDs) have been demonstrated [1]–[3], UTC-PDs generally demonstrate improved performance when a DC bias voltage is applied across the detector due to the increased internal electric field, which results in increased bandwidths and responsivities. When considering an integrated device to be used in commercial applications such as beyond-5G communications or microwave photonics, the photodetector should preferably be biased without the need of an external bias-tee, which can be achieved by an on-chip bias circuit. Such a circuit allows for separate DC and RF connections to interface with the UTC-PD. Although discrete component integration of a DC bias-tee with a UTC-PD can be used to achieve this [4], RF losses and impedance mismatches caused by wirebonds between the RF connections of the photodetector and bias-tee, as well as high costs from device assembly, can be avoided by monolithic integration [5].

This work reports on the monolithic integration of a bias circuit together with a high speed UTC-PD [6] in the nanophotonic InP-Membrane On Silicon (IMOS) platform [7]. Two circuits have been designed based on co-planar waveguide (CPW) RF chokes suitable for  $K_a$ -band (26.5–40GHz) and V-band (40–75GHz). The designs are numerically optimized to limit insertion loss, RF reflections and leakage from the RF to the DC path.

## Design

To provide a DC bias to the UTC-PD, an additional electrical path to the CPW line of the photodetector is required. For this design, a T-shaped connection is used to apply the DC bias to the RF path and thus to the UTC-PD. To prevent leakage of the RF signal towards the DC path, an RF filter is placed in the DC path, as can be seen in Fig. 1. The RF filter, or RF choke, consists of a quarter wavelength transformer leading to a virtual RF open circuit, blocking the RF signal to be passed through the DC line on the bias circuit [8, 9]. Capacitive decoupling of the RF line as present in a conventional bias-tee is not present in this design, which can however be added as part of external circuitry [8, 9]. The DC

and RF CPW line parameters are optimized to have a  $50\Omega$  characteristic impedance and for compatibility with a commercial 110GHz RF probe with a  $100\mu\text{m}$  pitch.

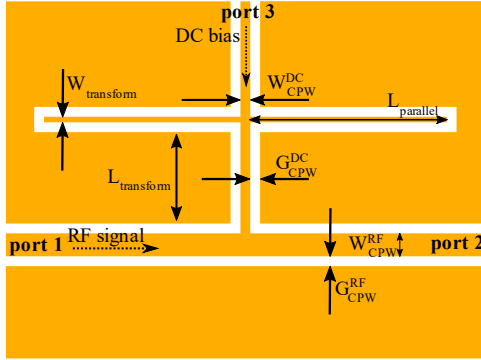


Figure 1: RF choke based bias circuit

Table 1: Used material parameters

Material	$\epsilon_r$	$h$ [ $\mu\text{m}$ ]
BCB (bonding)	2.5	1.8
BCB (planarization)	2.5	0.65
SiO <sub>2</sub> (cladding)	3.6	0.1
Si (substrate)	11.9	300
Gold (bias circuit)	-	0.4

All semiconductor layers used in the UTC-PD can be removed during the fabrication process. As a result, the bias circuit is designed based on a material stack consisting of a high resistivity  $300\mu\text{m}$  thick silicon substrate, followed by a combination of SiO<sub>2</sub> and BCB layers. All relevant material parameters are listed in Table 1.

The design relies on out of phase reflections on the quarter wavelength section, which is inherently frequency dependent, so the design is optimized for a frequency range of interest. Therefore, two devices have been designed, suitable for K<sub>a</sub>-band and V-band respectively. The length to the stub  $L_{\text{transform}}$  is designed to be match to the center frequency  $f_0$ , of the band of interest according to

$$L_{\text{transform}} = \frac{c}{4f_0\sqrt{\epsilon_{\text{eff}}}}. \quad (1)$$

The parameters  $W_{\text{transform}}$ ,  $L_{\text{parallel}}$  and  $L_{\text{transform}}$  (Fig. 1) have been numerically optimized to achieve the target performance specified in Table 2, where all goals have equal weight. CST Studio Suite was used for the numerical optimization and simulation of the devices.

Table 2: Optimization targets and simulated results

Parameter	Numerical optimization target performance	Ka band results (30-40GHz)	V band results (60-70GHz)
$S_{12}$ (transmission)	$> -1\text{dB}$	$> -3\text{dB}$	$> -3\text{dB}$
$S_{11}$ (reflection)	$< -12\text{dB}$	$< -14\text{dB}$	$< -18\text{dB}$
$S_{13}$ (RF to DC leakage)	$< -35\text{dB}$	$< -15\text{dB}$	$< -16\text{dB}$

## Simulation results

The obtained numerically optimized designs for both the K<sub>a</sub>- and V-band circuits are simulated with increased accuracy using CST Studio Suite to obtain the S-parameters that directly give the RF transmission, RF reflections and RF to DC leakage. The simulation results for K<sub>a</sub>- and V-band are provided as a solid line in Figures 2 and 3 respectively and show that not all target performance levels could be achieved simultaneously. The simulated transmission performance of both devices is limited to  $> -3\text{dB}$  and both the RF reflections and RF to DC isolation are limited to  $< -14\text{dB}$ . The results are also added to the overview in Table 2. In particular for the RF to DC isolation holds that there is an

optimum band around the designed center frequency, which follows from the frequency dependent design according to Eq. 1.

Although the numerical optimization of the RF choke designs is not performed including the UTC-PD, the CST simulation of the final V-band design was extended with the addition of the UTC-PD and connecting metal tapers from the detector contacts to the RF-choke CPW lines. The results are added in Fig. 3 as a dashed line, and demonstrate a slight increase in transmission losses ( $S_{12}$ ), as well as increased RF reflections across the full frequency range ( $S_{11}$ ). The RF to DC isolation is slightly improved, but is in line with results excluding the photodetector. The differences are caused by the presence of a slight impedance mismatch between the UTC-PD and the bias circuit.

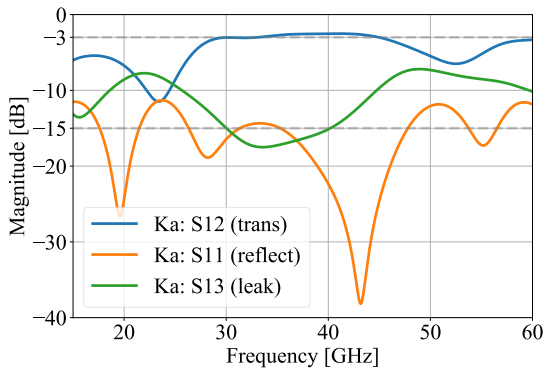


Figure 2: Simulated S-parameters for Ka band

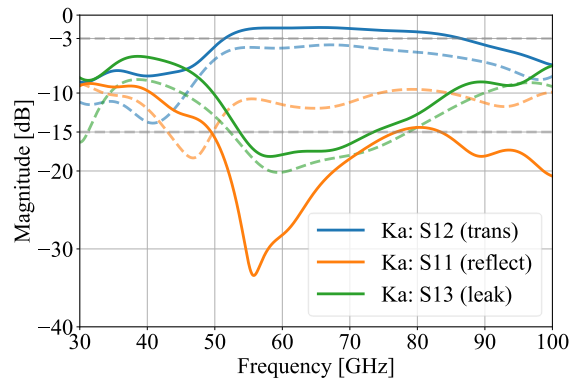


Figure 3: Simulated S-parameters for V band

## Fabrication

The final devices with a size of 1.5mm by 1.1mm for V band, and 2.5mm by 2.05mm for  $K_a$  band were realized in the final metallization layer which connects to the p- and n-contacts of previously patterned UTC-PDs as can be seen in Figures 5 and 6. The wafer was planarized using BCB followed by an  $\text{SiO}_2$  layer of 50nm to improve adhesion of the metal to the sample. The devices are fabricated by a metal lift-off step after patterning using electron beam lithography with PMMA resist. The metal stack consists of 50nm of titanium followed by 400nm of gold. Bias circuits are also fabricated without connections to a UTC-PD on the same wafer in order to characterize the devices individually.

Preliminary measurement results have confirmed electrical connection from the DC line to the UTC-PD enabling a DC bias to be applied. In future work, elaborate measurements using a vector network analyser will be carried out to determine the S-parameters of the devices.

## Conclusions

Monolithic integration of a bias circuit and UTC-PD can avoid losses, potential impedance mismatches caused by additional wirebonds as well as high costs from device fabrication and assembly, compared to discrete component integration. A bias circuit based on a CPW RF choke using a quarter wavelength RF filter in the DC line is designed based on first order approximations and numerical optimization for two frequency bands.

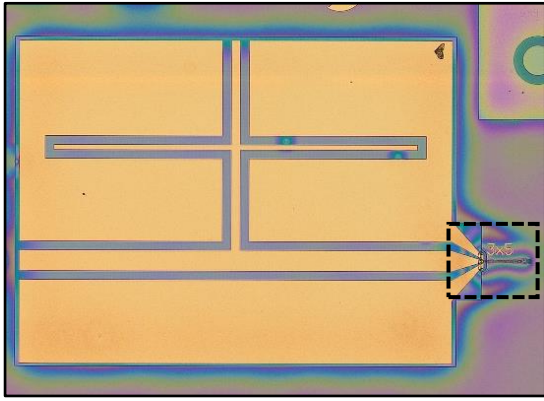


Figure 5: V-band bias T integrated with UTC-PD

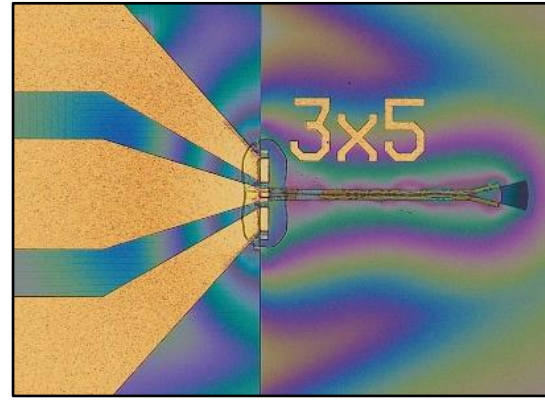


Figure 6: V-band bias T integrated with UTC-PD (close up)

Simulation results of two bias circuits designed for the IMOS platform for K<sub>a</sub>- and V-band demonstrate insertion loss below 3dB, RF reflections below -14dB and RF to DC isolation of at least 15dB for a frequency range of 10GHz around the center of the respective frequency band. The optimized designs are fabricated in the final metallization step in the nanophotonic IMOS platform, and are monolithically integrated with high speed UTC-PDs. Preliminary measurements have confirmed the device ability to provide a DC bias to the UTC-PD, and future measurements on a vector network analyser have to be carried out to determine specific device characteristics.

## Acknowledgement

This work was supported by the Institute of Design, Optoelectronics and Sensing (IDEAS) Project INTENSE and it is partially funded by 5G STEP FWD (grant no. 722429) project as part of the European Union's Horizon 2020 research and innovation programme.

## References

- [1] T. Umezawa, K. Akahane, N. Yamamoto, A. Kanno, K. Inagaki, and T. Kawanishi, "Zero-bias operational ultra-broadband UTC-PD above 110 GHz for high symbol rate PD-array in high-density photonic integration," *Opt. Fiber Commun. Conf. OFC 2015*, pp. 15–17, 2015.
- [2] J. Wun, Y. Zeng, and J. Shi, "for Zero-Bias Operation at Sub-THz Regime," *2016 Opt. Fiber Commun. Conf. Exhib.*, pp. 1–3, 2016.
- [3] T. Liu *et al.*, "Design of bias-free operational uni-traveling carrier photodiodes for terahertz wave generation," *Opt. Quantum Electron.*, vol. 50, no. 7, pp. 1–16, 2018.
- [4] I. Flammia, B. Khani, and A. Stohr, "A novel transition from grounded coplanar waveguide to substrate inte grated waveguide for 60 GHz Radio-over-Fiber photonic transmitters," *Proc. 13th Conf. Microw. Tech. Com. 2013 - MAREW 2013 Microw. Radio Electron. Week 2013*, pp. 73–76, 2013.
- [5] Y. G. Wey *et al.*, "108-GHz GaInAs/InP p-i-n photodiodes with integrated bias tees and matched resistors," *IEEE Photonics Technol. Lett.*, vol. 5, no. 11, pp. 1310–1312, 1993.
- [6] J. de Graaf *et al.*, "Beyond 110 GHz Uni-Traveling Carrier Photodiodes on an InP-Membrane-on-Silicon Platform," in *IEEE Journal of Selected Topics in Quantum Electronics*, vol. 28, no. 2: Optical Detectors, pp. 1-10, March-April 2022, Art no. 3802010.
- [7] Y. Jiao *et al.*, "Indium Phosphide Membrane Nanophotonic Integrated Circuits on Silicon," *Phys. Status Solidi Appl. Mater. Sci.*, vol. 217, no. 3, 2020.
- [8] I. Flammia, A. Stöhr, C. C. Leonhardt, J. Honecker, and A. G. Steffan, "71-76GHz grounded CPW to WR-12 transition for quasi-hermetic RoF wireless transmitter," *Electron. Lett.*, vol. 48, no. 9, pp. 506–508, Apr. 2012.
- [9] Y. Dong *et al.*, "System Integration and Packaging of a Terahertz Photodetector at W -Band," in *IEEE Transactions on Components, Packaging and Manufacturing Technology*, vol. 9, no. 8, pp. 1486-1494, Aug. 2019.

# Synthesis of an optical waveguide in bulk silica with a femtosecond laser inscription and wet etching treatment

<sup>1,2</sup> M. Tunon de Lara Ramos, <sup>2,3</sup> L. Amez Droz, <sup>1</sup> K. Chah, <sup>2</sup> P. Lambert, <sup>3,4</sup> C. Collette, <sup>1</sup> C. Caucheteur

<sup>1</sup> Electromagnetism and Telecommunication Department, Université de Mons, Belgium

<sup>2</sup> TIPs Department, CP 165/67, Université Libre de Bruxelles, 50 av FD Roosevelt, B-1050 Brussels

<sup>3</sup> Department of Aerospace and Mechanical Engineering, Université de Liège, Liège, Belgium

<sup>4</sup> BEAMS Department, CP 165/56, Université Libre de Bruxelles, 50 av FD Roosevelt, B-1050 Brussel

*Femtosecond laser pulses are more and more spread for the micro/nano-machining of various materials. The objective of our work is to create an optical structure within a bulk silica substrate thanks to the commercial device Femtoprint. This optical structure will be able to transmit a signal through silica glass and limit its loss so that it can further be used for sensing applications. In this article, we report our experimental achievements obtained with the machine for the creation of waveguides. We highlight the parameters that were optimized to produce them in planar substrates.*

## Introduction

During the last decades, femtosecond pulses lasers have been widely used for several applications [1]. The one we are focusing in our work is the creation of optical waveguides within planar silica substrates. The overall quality of the latter depends on the energy deposited by the femtosecond pulses laser on the surface of the material. The energy of deposition is described with the following equation [2]:

$$\Phi_d = \frac{4E_p}{\pi\omega_{nl}} \left(\frac{f}{v}\right) \quad (1)$$

where  $\Phi_d$  (in J/m<sup>2</sup>) represents the energy of deposition,  $E_p$  (in nJ) is the energy of the pulse,  $f$  (in Hz) is the repetition rate,  $v$  (in mm/s) is the speed of inscription and  $\omega_{nl}$  is the non-linear beam waste [3]. Depending on the value of the energy of deposition, three types of defaults can be generated [4,5]. For small  $\Phi_d$  values, a densification of the silica glass will be obtained, which induces a local modification of its refractive index. This is precisely what is required for the creation of optical waveguides. Another possible default is the creation of nano-gratings. They appear at higher deposition energy. Same energy levels as for the creation of nano-gratings are used for the creation of mechanical structures, provided that an etching process is conducted in KOH solution. The third type of defect is the direct ablation obtained at even higher energy values. The latter is not used in our work.

Our experimental work aims to create optical waveguides and optical fiber holders directly within a silica glass plate. The holder is very important for the alignment of the in-built optical waveguide with a connecting optical fiber. To create these two structures, we used the Femtoprint machine [6], which is fully automated on three different axes. The advantage of this process is that all the different parameters of the energy deposition

(cf. Eq. (1)) can be defined before the inscription. The next section will introduce the different experimental set-ups used for the inscription and characterization of the different optical structures.

## Experimental set-up

Figure 1a depicts the Femtoprint machine. Its operating principle is illustrated in the scheme of Fig. 1b while Fig. 1c shows the inside of the Femtoprint. It is important to note that the femtosecond pulses laser comes from the bottom to hit the surface of the silica glass plate placed on the 3-axis moving plate. This machine is used both for the synthesis of the optical waveguide and the holder to connect optical fiber on silica glass.

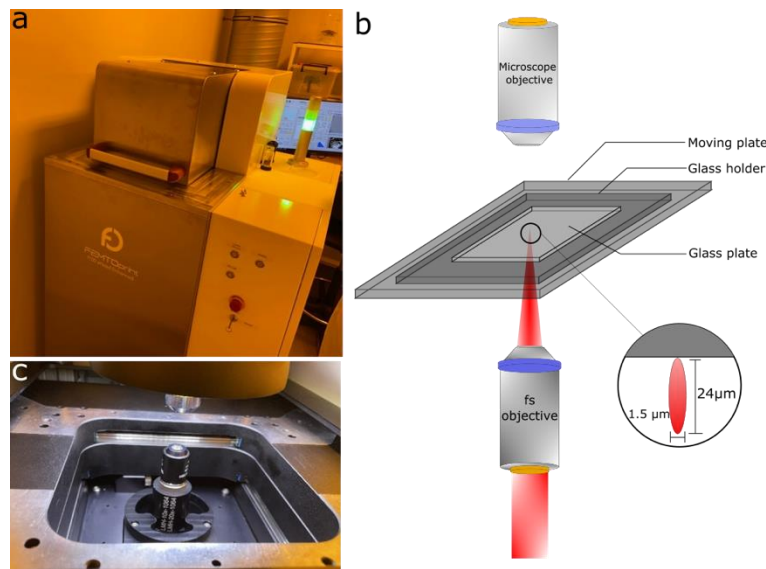


Figure 1. Picture of the Femtoprint machine from the outside (a), Sketch of the operating principle showing the glass substrate placed on a holder fixed on the moving stage and located above the laser objective (b), Picture showing laser objective located at the bottom and the microscope objective at the top used to calibrate the position and orientation of the glass substrate (c).

The optical characterization set-up is represented in Fig. 2. The input part, located on the left, comprises the InfraRed or the red beam that is used for injection within the manufactured optical waveguide. The latter is put on a second block that can move on three different axes and be easily adjusted so that the optical coupling can be optimized. The last block holds the connecting optical fiber that can move in two different directions, also for a proper alignment. This fiber allows an analysis of the waveguide performance thanks to its connection with an optical spectrum analyser (OSA).

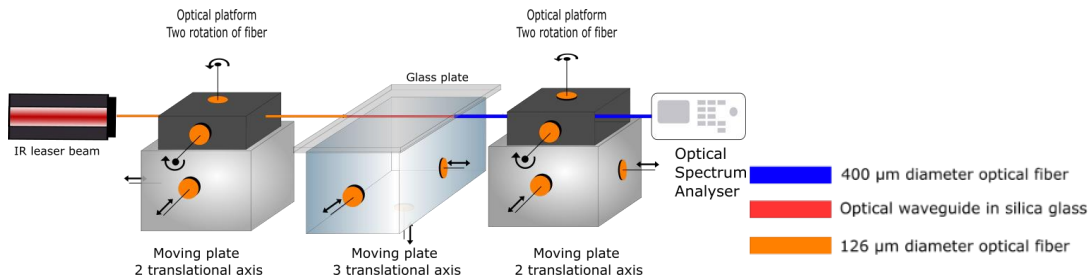


Figure 2. Experimental set-up for the determination of the transmission signal.

## Experimental results

In this section, we present our experimental results. Figure 3 shows a microscope image of a waveguide written in bulk silica glass. To create this structure, the parameters of the Femtoprint were optimized following a trial and error approach. It turns out that appropriate parameters are a pulse energy of 130 nJ, a repetition rate of 1 MHz, a speed of inscription of 20 mm/min with planar movements of the tightly-focused laser beam and a space between the different laser paths of 0.5  $\mu\text{m}$ .

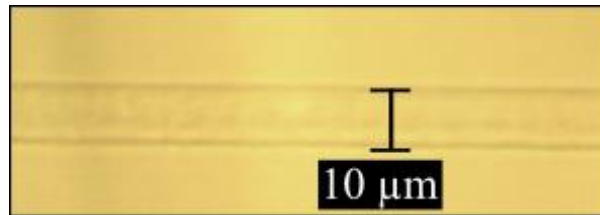


Figure 3. Microscope picture of a waveguide (refractive index densification) created by tightly-focused femtosecond pulses laser in a planar silica substrate.

To properly connect this femtosecond laser-induced waveguide with external characterization equipment and thereby analyse its performance, a mechanical holder was designed and manufactured at one edge of the planar substrate to host the connecting optical fiber. Figure 4a shows the conceptual design that is a succession of 3 cavities of 1 mm side with a small tunnel (0.5 mm in length and 126  $\mu\text{m}$  of diameter) in between to allow the easy insertion of a telecommunication-grade single-mode optical fiber. This mechanical structure was obtained with pulses of 230 nJ, a repetition rate of 1 MHz and a speed of inscription of 950 mm/min. After the laser process, a KOH (0.1 M) etching was performed for 6 hours at 85  $^{\circ}\text{C}$ . Figure 4b depicts the obtained mechanical holder.

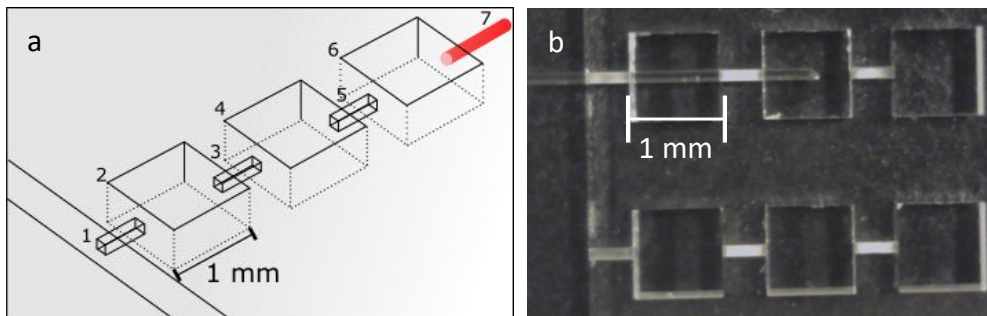


Figure 4. Scheme representing the design of the optical fiber holder at one edge of the glass plate (1,3 and 5 represent the cavity for the optical fibre whereas 2, 4 and 6 are the cavities allowing the KOH to spread more quickly) (a), Picture of the actual implementation (b).

Now that the waveguide and the optical fiber connector are produced in line within the glass substrate, they can be optically characterized. The goal of the measurements is primarily to observe the efficiency of the waveguide in terms of transmission. To do so, Bragg gratings inscribed in the connecting optical fiber are used. They are first measured directly with the fiber connected to the OSA. These measurements correspond to the blue bars displayed in Fig. 5 for 3 different gratings. The connecting fibers are then aligned with the optical waveguide made in the glass substrate and a similar characterization is

performed. This yields the green bars of Fig. 5. Comparing blue and green bars reveals that the optical loss is less than 1 dB, which is very satisfactory for us as we intend to use the waveguides for sensing purposes.

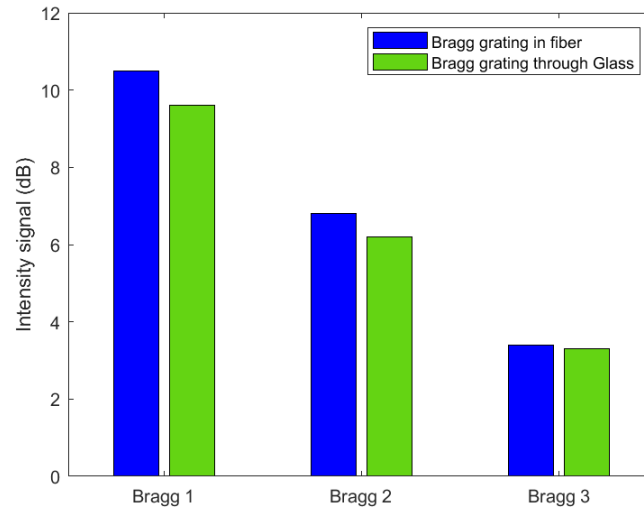


Figure 5. Optical characterization of the waveguide performance in bulk silica thanks to the use of fiber Bragg gratings written in the connecting optical fiber.

## Conclusion

In conclusion, we have created an optical waveguide that is fully working and can transmit at least 90 % of the signal. The created mechanical structure allows us to properly align the waveguide and the coupling optical fiber. The next step of our experimental work is now the inscription of a Bragg grating into the core of an optical waveguide. The targeted application is mostly focused on physical sensing (temperature and strain) based on the in-built Bragg grating.

Authors acknowledge the financial support of the F.R.S.-FNRS.

## References

- [1] Akhmanov, Sergei Aleksandrovich, et al. Optics of femtosecond laser pulses. New York: American Institute of Physics, 1992.
- [2] Sheeba Rajesh and Yves Bellouard. "Towards fast femtosecond laser micromachining of fused silica: The effect of deposited energy" *Optics Express*, 18(20):21490–21497, 2010.
- [3] DM Krol, "Femtosecond laser modification of glass" *Journal of Non-Crystalline Solids*, 354(2-9):416–424, 2008.
- [4] Lawrence Shah, Alan Y Arai, Shane M Eaton, and Peter R Herman, "Waveguide writing infused silica with a femtosecond fibre laser at 522 nm and 1 MHz repetition rate", *Optics express*, 13(6):1999–2006, 2005.
- [5] Vibhav Bharadwaj, Ottavia Jedrkiewicz, JP Hadden, Belén Sotillo, María Ramos Vázquez, Paola Dentella, Toney T Fernandez, Andrea Chiappini, Argyro N Giakoumaki, Thien Le Phu, et al. "Femtosecond laser written photonic and microfluidic circuits in diamond" *Journal of Physics: Photonics*, 1(2):022001, 2019.
- [6] Y Bellouard, A Champion, B Lenssen, M Matteucci, Allison Schaap, M Beresna, C Corbari, M Gecevičius, P Kazansky, O Chappuis, et al. The femtoprint project. *Journal of Laser Micro/Nanoengineering*, 7(1):1–10, 2012.

# Insulin detection with plasmonic optical fiber sensor

H. Fasseaux,<sup>1</sup> M. Loyez,<sup>1,2</sup> and C. Caucheteur<sup>1</sup>

<sup>1</sup> University of Mons, Department of Electromagnetism and Telecommunication, 31 Bd Dolez, 7000 Mons, Belgium

<sup>2</sup> University of Mons, Department of Proteomics and Microbiology, 6 Av. Du Champs de Mars, 7000 Mons, Belgium

*Gold-coated tilted fiber Bragg gratings (Au-TFBGs) can detect surrounding refractive index (SRI) changes by surface plasmon resonance (SPR) shift following a similar principle found in commercial devices, based on the Kretschmann prism. While the Au-TFBG is functionalized with appropriate bioreceptors, it can detect molecular events and act as a biosensor. In this paper, we show that the use of the Jones formalism combined with fictive polarizer emulation can improve the detection process. We experiment our method for the detection of insulin at a concentration ranging from 0.1 to 100 ng/mL.*

## Introduction

Insulin is an anabolic hormone playing an essential role in the regulation of glycemia. Abnormal levels of insulin in the body can lead to serious health problems such as diabetes, obesity or cancers [1]. Its normal concentration in blood for a fasting person lies between 0.3-0.4 ng/mL. A lower concentration suggests type I diabetes while patients with type II diabetes (T2D) present a higher insulin concentration. The T2D accounts for 90 % of people suffering from diabetes. In the early stages of this disease, the insulin concentration increases to compensate for the increase in glucose levels. However, the T2D diagnosis is primarily based on fasting blood glucose concentration measurements. Nevertheless, measurement of insulin concentration would allow early diagnosis of this type of disease but the actual techniques usually require expensive equipment and trained people. Standard telecommunication-grade fiber with tilted Bragg grating inside its core act as sensitive refractometer [2] which can be used for biosensing. The sensitivity is further enhanced if the surface of the fiber is coated with a noble metal to take advantage of surface plasmon resonance (SPR). Indeed, gold-coated tilted fiber Bragg gratings (Au-TFBGs) functionalized with specific receptors are platforms that have already shown promising results in the detection of analytes at low concentration. This is especially true using a spectral demodulation based on the phase difference between two orthogonal polarization states [3]. In this work, we show that by functionalizing the fiber with a matrix of anti-human insulin antibodies, we can achieve insulin detection at concentrations down to 0.1 ng/mL.

## Theoretical Concepts

The insertion loss spectra of Au-TFBGs display characteristic attenuation area while the direction of a linear polarization state matches the tilted angle of the grating inside the core of the optical fiber (see Fig. 1a). Thus, the usual read-out set-up contains a linear polarizer. However, to extract the phase difference spectra, the polarizer should be removed from the set-up and spectral features are retrieved thanks to the Jones formalism. Indeed, for a given wavelength, the Jones formalism can be used to model a totally coherent field that propagates through an optical system. Let us consider the input Jones

vector  $|\alpha\rangle \in \mathbb{C}^{2 \times 1}$  (written using the Dirac representation). Thus, the output one  $|\beta\rangle \in \mathbb{C}^{2 \times 1}$  satisfies

$$|\beta\rangle = \mathbb{J} |\alpha\rangle, \quad (1)$$

where  $\mathbb{J} \in \mathbb{C}^{2 \times 2}$  is the Jones matrix. This matrix represents the modification on the input polarized state due to the whole system under test. In the case of Au-TFBGs, the corresponding Jones matrices are obtained from an optical vector analyzer (OVA, OVA CTE from Luna Technologies Inc.) while the fiber is connected in transmission without any additional device. To extract the p-polarized state, we numerically add a linear polarizer  $\mathbb{P}(\theta)$  that makes an angle  $\theta$  with respect to the x-axis of the Cartesian coordinate where the Jones elements are given. Thus, the new Jones matrix  $\mathbb{J}_p$  becomes

$$\mathbb{J}_p = \mathbb{J} \mathbb{P}, \quad (2)$$

with

$$\mathbb{P} = \begin{pmatrix} \cos^2 \theta & \cos \theta \sin \theta \\ \sin \theta \cos \theta & \sin^2 \theta \end{pmatrix}. \quad (3)$$

The transmitted intensity  $I(\lambda, \theta)$  is finally computed via the following Rayleigh quotient

$$I(\lambda, \theta) = \frac{\langle \alpha | \mathbb{J}_p^\dagger \mathbb{J}_p | \alpha \rangle}{\langle \alpha | \alpha \rangle}. \quad (4)$$

Usually, the insertion loss spectrum is monitored, and it can be extracted using the following relationship [4]:

$$IL(\lambda) = 10 \log \left( \frac{\rho_1(\lambda) + \rho_2(\lambda)}{2} \right), \quad (5)$$

where  $\rho_1(\lambda), \rho_2(\lambda)$  are the eigenvalues of the Hermitian matrix  $\mathbb{J}_p^\dagger \mathbb{J}_p$ . By varying the angle  $\theta$  and looking at the insertion loss spectrum, one can determine the Jones vectors  $|\alpha_p\rangle = (\cos \theta_p \quad \sin \theta_p)^T$  corresponding to the p-polarized state as well as  $|\alpha_s\rangle = (\cos \theta_s \quad \sin \theta_s)^T$  where  $\theta_s = \theta_p \pm \frac{\pi}{2}$  for the s-one. Since the phase analysis is known to be more sensitive than the intensity-based demodulation, we take advantage of the known Jones vectors to compute the phase difference between the two orthogonal states using the Pancharatnam connection [5]

$$\delta\varphi(\lambda) = \arg(\langle \alpha_p | \mathbb{J} | \alpha_p \rangle) - \arg(\langle \alpha_s | \mathbb{J} | \alpha_s \rangle) \quad (6)$$

The phase difference spectrum shown in Fig. 1b displays multiple peaks with amplitude dependency to the SRI. The demodulation of that spectrum consists in following the amplitude between two neighboring peaks (i.e.  $\Delta\varphi = \delta\varphi(\lambda_2) - \delta\varphi(\lambda_1)$  highlighted in red in the Fig. 1b). This method has shown an enhancement of the real-time detection precision and sensitivity of more than 45000 degrees/RIU [3].

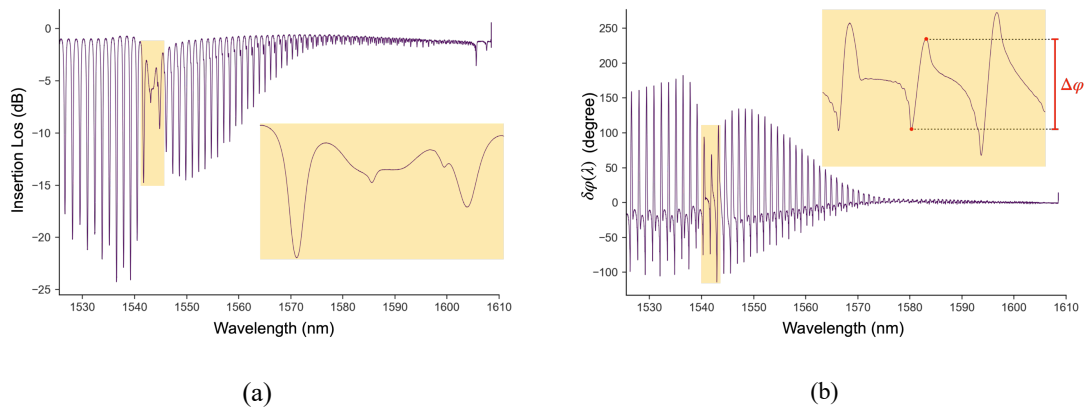


Figure 1. Au-TFBG spectra. (a) Insertion loss spectrum of the p-polarized state showing the characteristic attenuation highlighted in the inset. (b) Phase difference between the p and the s-polarization state. The inset displays a focus on the highest sensitive area and the amplitude  $\Delta\varphi$  with is followed during the detection.

## Materials and Methods

The physical platform is made of telecommunication-grade silica optical fiber (Corning SMF-28) including an  $8^\circ$  tilted Bragg grating with a period of 555.41 nm inside the core to have comb-shaped insertion loss spectrum in short-wave infrared (SWIR) region. The inscription process consists in using the phase mask technique with a 193 nm excimer laser (Noria from Northlab Photonics) after having hydrogen loaded the fiber at 200 bar and  $60^\circ\text{C}$  for 30h to enhance the fiber photosensitivity. Then, hydrogen excess has been removed by a heating process at  $100^\circ\text{C}$  for 24h. A  $\sim 50$  nm gold layer has been deposited using a sputter-coater Spuco with 2'' magnetron modules with 250 W RF power supply and an inbuilt quartz microbalance with resolution of 0.1 nm (Tetra gmbh, Germany). A matrix of 11-mercaptoundecanoic acid (Sigma-Aldrich) is bonded to the gold surface by immersion for 16 h in pure ethanol. The matrix is then activated to give a reactive succinimide esters by immersion in a mixture of 1-ethyl-3 (3-dimethylaminopropyl) carbodiimide (EDC, Sigma-Aldrich) and N-hydroxysuccinimide (NHS, Sigma-Aldrich) for 10 min. Mouse anti-human insulin antibodies (Apollo Scientific) are then passed over the surface and are covalently linked to the matrix by spontaneous reaction with the esters. Remaining active esters are finally deactivated using ethanolamine-HCl (Sigma-Aldrich). Between each solution, a rinsing with buffer (mix of HPES, NaCl, EDTA and surfactant) has been performed. The resulting biosensor has been placed into a  $120 \mu\text{L}$  microfluidic chamber (microfluidic ChipShop) where the detection has been performed.

## Results and Discussion

During the first 10 min, the sensor is immersed in a continuous flow of  $30 \mu\text{L}/\text{min}$  of buffer to ensure stability. Then, insulin at a concentration of  $0.1 \text{ ng}/\text{mL}$  gradually replaces the buffer for 20 min before the sensor is immersed again in the physiological solution. As shown in Fig. 2a, after the rinsing process,  $\Delta\varphi$  does not retrieve its original level. The difference ( $\sim 1.865^\circ$ ) is attributed to remaining analyte-receptors bonds. By repeating this sequence (buffer - analytes - buffer) for increasing concentrations up to  $100 \text{ ng}/\text{ml}$ , the difference in level decreases. Although the difference between the initial buffer level (before immersion in a solution at a concentration of  $0.1 \text{ ng}/\text{ml}$ ) and the buffer level after immersion in each concentration increases until saturation is reached. This is due to the

number of free receptors decreases, and saturation is reached when almost all of them have been bound to an analyte. Figure 2b shows this result in a semi-logarithmic scale.

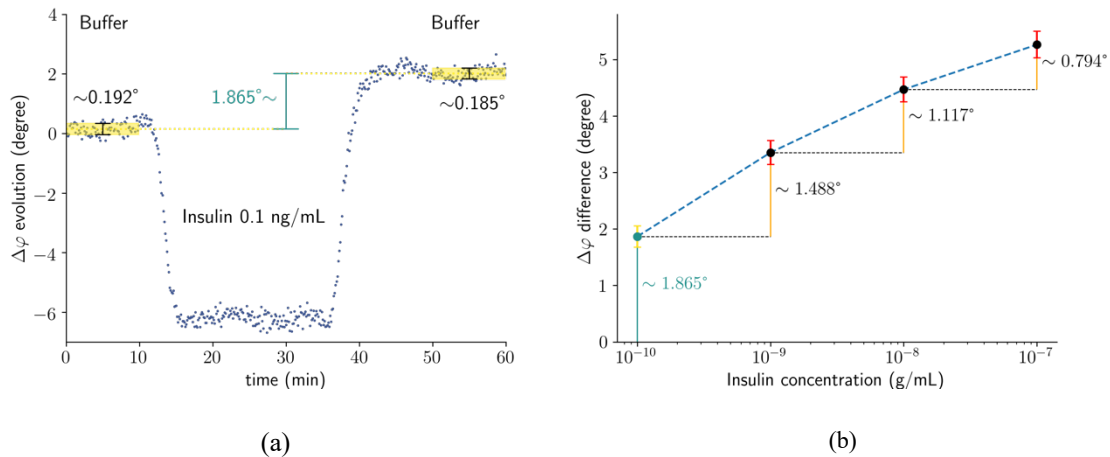


Figure 2. Insulin detection. (a) sensorgram obtained using the phase difference analysis. (b) Evolution of the shift between the initial level (while the sensor is immersed for the first time in the buffer) and after each immersion into analyte solutions with different concentrations. The green point corresponds to the shift of 1.865° displayed in (a).

## Conclusion

Using the phase difference spectra between two polarization states of a functionalized Au-TFBG, we have shown that it is possible to detect insulin at concentrations down to 0.1 ng/mL. Those spectra are extracted using an OVA and the Jones formalism coupled with polarizer emulation. The functionalization using matrix of 11-mercaptoundecanoic acid bound with anti-insulin receptors limit the transient nature of insulin and showing a shift due to bindings between analyte and receptor that saturate at concentration slightly higher than 100 ng/mL.

## Acknowledgments and fundings

This work was financially supported by the Fonds de la Recherche Scientifique - F.R.S.-FNRS under Senior Research Associate Grant of Christophe Caucheteur and the postdoctoral research grant of M d ric Loyez (C.R.), and the PDR Mosaic and EOS n O001518F (EOS-convention 30467715).

## References

- [1] K. Lian, H. Feng, S. Liu, K. Wang, Q. Liu, L. Deng, G. Wang, Y. Ghen, G. Liu, "Insulin quantification towards early diagnosis of prediabetes/diabetes," *Biosens. Bioelectron.*, vol. 203, no. January, p. 114029, 2022, doi: 10.1016/j.bios.2022.114029.
- [2] C. Caucheteur, J. Villatoro, F. Liu, M. Loyez, T. Guo, and J. Albert, "Mode-division and spatial-division optical fiber sensors," *Adv. Opt. Photonics*, vol. 14, no. 1, p. 1, Mar. 2022, doi: 10.1364/AOP.444261.
- [3] H. Fasseaux, M. Loyez, K. Chah, and C. Caucheteur, "Phase interrogation of plasmonic tilted fiber Bragg grating biosensors through the Jones formalism," *Opt. Express*, vol. 30, no. 19, p. 34287, 2022, doi: 10.1364/oe.463140.
- [4] A. Bialiyayeu, A. Ianoul, and J. Albert, "Polarization-resolved sensing with tilted fiber Bragg gratings: Theory and limits of detection," *J. Opt. (United Kingdom)*, vol. 17, no. 8, Aug. 2015, doi: 10.1088/2040-8978/17/8/085601.
- [5] J. C. Guti rrez-Vega, "Optical phase of inhomogeneous Jones matrices: retardance and ortho-transmission states," *Opt. Lett.*, vol. 45, no. 7, p. 1639, 2020, doi: 10.1364/ol.387644.

# Parameter Analysis in Continuous-Variable Quantum Key Distribution with Arbitrary Modulation

João dos Reis Frazão<sup>1</sup>, Aaron Albores-Mejia<sup>1</sup>, Boris Škorić<sup>1</sup>, and Chigo Okonkwo<sup>1</sup>

<sup>1</sup> Eindhoven Hendrik Casimir Institute, Eindhoven University of Technology, the Netherlands

*Continuous-variable quantum key distribution (CV-QKD) represents a solution to distribute quantum-secure secret random keys, where weak coherent states can be encoded with Gaussian or discrete modulation. Using readily available and mature commercial off-the-shelf components, it is possible to achieve high secret key rates for practical short-reach optical communications. From the security proof perspective, it is possible to analyse the Gaussian modulation performance considering finite size effects. More recently, a security proof for arbitrary discrete modulation was proposed, but only in the asymptotic regime. In this work, finite size effects and confidence intervals are included in the models in order to get realistic bounds for relevant hardware implementation parameters for CV-QKD with arbitrary modulation. Furthermore, the optimum secret key rates were studied according to different Alice/Bob implementation parameters such as receiver clearance, channel loss, system excess noise, signal/LO lasers phase noise, signal modulation variance and quantum/calibration data lengths, with the Gaussian linear channel assumption.*

## Introduction

The first CV-QKD protocol to make use of coherent states with Gaussian modulation [1] was introduced in 2002, with security against individual attacks. The security proof was further extended and improved to that of composable security against collective and coherent attacks in [2]. In order to lower the complexity of CV-QKD, discrete modulation formats like BPSK and QPSK have been proposed in [3] considering security against collective attacks. However, their performance is reduced when compared to Gaussian modulation, due to the lower cardinality of BPSK and QPSK. To close the gap between Gaussian and discrete modulations, an analytical bound for the asymptotic secret key ratio (SKR) of protocols with arbitrary modulation has been proposed [4]. In this work, we analyse such analytical bounds under a realistic scenario with trusted noise and finite-size effects.

## Protocol & optimisation

In CV-QKD, Alice starts the protocol by randomly encoding a finite number of weak coherent states, according to the modulation format and optimised modulation variance ( $V_A$ ). She transmits the data to Bob via the quantum channel, that has a length/loss according to each use case. To measure the quantum states, Bob uses double homodyne detection with maximised quantum efficiency and optimised clearance, the ratio between receiver shot and electronic noise. Excess noise due to Alice's equipment or Eve's attack cannot be distinguished or calibrated. For the post-processing steps, Alice and Bob use an authenticated classical channel to publicly share information for parameter estimation, error correction (EC) and privacy amplification (PA). In parameter estimation, Alice and Bob estimate the secret key ratio by publicly revealing 50% of the data. Here, the quantum block length needs to be optimised according to the impact of finite-size effects and limitations of the system. Lastly, Alice and Bob perform error correction and privacy amplification to make sure they have the same key and to minimize Eve's potential knowledge. In error correction and privacy amplification, the algorithms need to be as

efficient as possible to prevent further degradation of the protocol's performance. The key management service (KMS) should be implemented with minimized key consumption processes. A summary of the parameter requirements is presented in Table 1, where the  $\uparrow$  and  $\downarrow$  mean maximize and minimize, while  $*$  means the parameter requires optimisation according to theoretical model or use case.

Transmitter (Alice)	Quantum channel	Receiver (Bob)	Post-Processing
Modulation Format $\uparrow$	Distance $\uparrow$	Clearance $*$	Block length $*$
Modulation Variance $*$	Fiber type	Quantum Efficiency $\uparrow$	EC/PA efficiency $\uparrow$
Symbolrate $*$	Channel Loss $\downarrow$	Total Excess Noise $\downarrow$	KMS consumption $\downarrow$

**Tab. 1:** CV-QKD requirements for transmitter, quantum channel, receiver and post-processing.

## Gaussian channel & Finite-size effects

This paper uses the assumption that Alice's ( $x$ ) and Bob's ( $y$ ) data follow the normal linear model:  $y = tx + z$  with  $t = \sqrt{\eta T/2}$  and Gaussian noise  $z$ , with variance  $\sigma_z^2 = \frac{\eta T}{2} \xi_A + N_0 + v_{el}$ . Where  $T$  corresponds to the transmittance of the channel,  $N_0 + v_{el}$  the receiver trusted noise and  $\xi_A$  the excess noise at Alice's output, where the optimal attack by Eve is performed. Finite-size effects are considered according to [5]. A lower bound on the secret key ratio is obtained assuming the worst-case estimators with confidence intervals for excess noise, transmittance and trusted noise. The following expression is used to evaluate the secret key ratio assuming reverse reconciliation and collective attacks with  $\epsilon$  security:  $K_{finite} = \frac{n}{N} [\beta I_{BA} - \chi_{EB} - \Delta]$ . The fraction  $\frac{n}{N}$  is the amount of data after parameter estimation,  $\beta$  the reconciliation efficiency,  $I_{BA}$  the mutual information between Alice and Bob,  $\chi_{EB}$  the Holevo bound and  $\Delta$  a parameter related to the security of privacy amplification. The analytical bound for a discrete modulation format is given in [4].

## Receiver Trusted Noise

In a realistic CV-QKD scenario, one can assume that the receiver side is safe from an attacker (Eve)[3]. This means Bob operates under the trusted noise assumption and calibrates his detectors regularly by disconnecting the quantum channel and measuring his total and electronic receiver noise with the LO on and off, respectively [6]. Bob can further analyse the shot noise and clearance levels of the receiver to calibrate his data accordingly. From the perspective of a theoretical model, the trusted quantities are perceived as quantum efficiency  $\eta$ , shot noise  $N_0$  and electronic noise  $v_{el}$ . These parameters are used to obtain the final excess noise expression:  $\xi_A = \frac{2}{\eta T} (\sigma_z^2 - N_0 - v_{el})$ .

## Modulation Format

At the transmitter, Alice needs to either implement a Gaussian or discrete modulation format. In Gaussian modulation, the coherent state is an arbitrary complex number chosen according to a Gaussian probability distribution. One discrete example is quadrature amplitude modulation (QAM), where the constellation consists of  $M$  points distributed over a square grid. It is important that each coordinate of the coherent state is chosen independently according to a discrete Gaussian distribution (Probabilistic Constellation Shaping). The coherent states are centered at  $M$  possible equidistant points of the form  $\alpha = x + ip$  with probability:  $p_{x,p} \approx \exp(-\nu(x^2 + p^2))$ . By fixing the overall variance per coordinate to  $\frac{V_a}{4}$ , the probability distribution depends only on the free parameter  $\nu$ , which is numerically optimised according to Fig. 1a. An analysis of the impact of the worst-case assumption and clearance levels is given in Fig. 2, with enhanced  $\nu$  for 64/256 QAM.

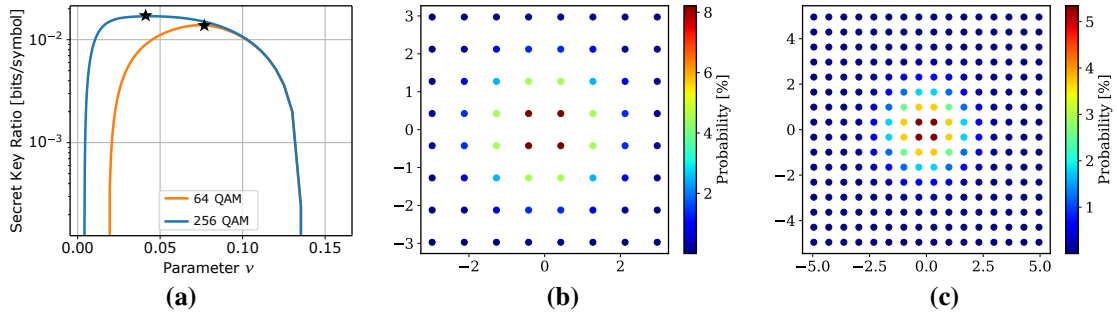


**Fig. 1:** (a) Optimisation of  $\nu$  for maximum secret key ratios. Fixed parameters: distance = 30 km,  $\alpha = 0.2$  dB/km,  $V_A = 4.6$  SNU,  $\xi_B = 0.01$  SNU,  $v_{el} = 0.05$  SNU,  $N = 2 \times 10^7$ ,  $N_{cal} = 10^6$ ,  $\eta = 60\%$ ,  $\beta = 95\%$ ,  $\epsilon = 10^{-10}$ . (b) Probabilistic constellation shaping 64 QAM with  $\nu = 0.0747$ . (c) Probabilistic constellation shaping 256 QAM with  $\nu = 0.046$ .

## Residual Phase noise

Initial CV-QKD implementations multiplexed the quantum signal with strong transmitter-side LO (TLO). This, enables a shot-noise calibration attack on the distributed LO, compromising the security [7]. To circumvent this problem, Bob uses an independent laser to provide the LO (LLO). With pilot-tone-aided techniques, Bob can recover the relative phase between both lasers. Even so, excess phase noise exists which cannot be compensated [8] given by:  $\xi_{phase} = 2V_A(1 - e^{-V_{est}/2})$  where,  $V_{est}$  is the variance of the residual phase noise after phase estimation/correction. For a sequential-LLO scheme,  $V_{est}$  depends on, the symbol rate, the amplitude of reference signal (or pilot) and the sum of the linewidths of the two free-running lasers. In order to minimize the impact of  $\xi_{phase}$  on the secret key ratio, these parameters need to be optimised as shown in Fig. 3.

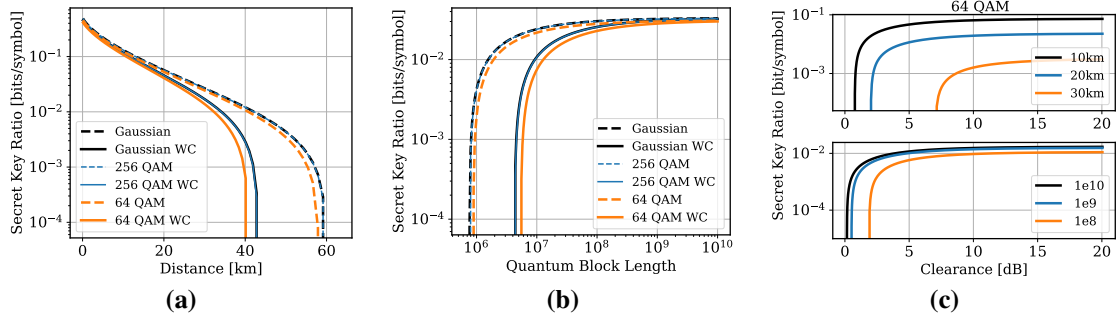


**Fig. 2:** (a) Impact of worst-case (WC) scenario on SKR vs Distance. (b) Worst-case analysis of SKR vs Quantum block length. (c) SKR for 64 QAM Modulation versus Clearance for different transmission distances and block lengths. Same fixed parameters as Fig. 1.

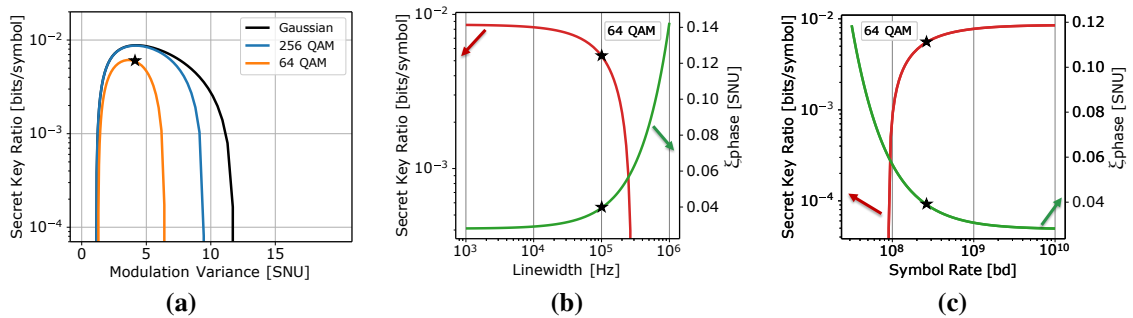


**Fig. 3:** (a) Comparison of SKR vs  $V_A$  for different modulation formats. (b) SKR (left) and  $\xi_{phase}$  (right) variation with LO linewidth. (c) SKR (left) and  $\xi_{phase}$  (right) for different symbol rates. Same fixed parameters as Fig. 1 with 250 Mbaud and 50 kHz linewidth for both lasers.

## Results

The star symbol in each plot represents the input value in the theoretical model. For the optimisation of the modulation format, in Fig. 1a,  $\nu$  is chosen according to the maximum secret key ratio, given the fixed parameters. For 64/256 QAM  $\nu$  is equal to 0.0747 and 0.046, respectively.

In Fig. 2 we can see the impact of the worst-case estimators on the secret key ratio, with transmission distance in Fig. 2a and quantum block length in Fig. 2b. The larger the block size ( $> 10^8$ ), the less the finite size effects will deteriorate the performance of CV-QKD. However, if the block size is increased, eventually hardware memory and processing speeds will not be sufficient for a realistic implementation. Also, the higher the modulation format the closer performance is to Gaussian, as expected from [4]. The clearance analysis is given in Fig. 2c, where we note that for large distances ( $> 30$  km) and reasonable block sizes ( $2 \times 10^7$ ) high-end low noise receivers will be required. Additionally, if the receiver clearance is low, trade-offs are required by increasing block lengths.

On the transmitter side, Alice optimises the modulation variance according to the security proof and excess phase noise Fig. 3a. For this plot, the increasing excess noise is considered as we increase the modulation variance, and the used optimum value is 4.6 SNU for 30 km and  $N = 2 \times 10^7$ . Further optimisation to minimize the excess phase noise can be achieved by reducing the linewidth  $< 10$  kHz and increasing symbol rates  $> 10^8$ , as seen in Fig. 3b and Fig. 3c.

## Conclusion

In this paper, an in-depth multidimensional optimisation analysis is presented for a practical CV-QKD implementation focusing on modulation format, clearance, block length, symbol rate, linewidth and modulation variance. We showcase significant gains for the secret key ratio extraction in realistic cost-effective CV-QKD. To our knowledge, this is the first time that such optimisation analysis has been realized for these discrete modulation formats considering receiver trusted noise and finite-size effects.

*This work was supported by the Dutch Ministry of Economic Affairs and Climate Policy (EZK), as part of the Quantum Delta NL programme.*

## References

- [1] F. Grosshans and P. Grangier, “Continuous Variable Quantum Cryptography Using Coherent States”, vol. 88, no. 5, 057902, p. 057 902, 2002. DOI: 10.1103/PhysRevLett.88.057902.
- [2] N. Jain, H.-M. Chin, H. Mani, *et al.*, “Practical continuous-variable quantum key distribution with composable security”, *Nature Communications*, vol. 13, Aug. 2022. DOI: 10.1038/s41467-022-32161-y.
- [3] A. Leverrier, “Theoretical study of continuous-variable quantum key distribution”, Theses, Télécom ParisTech, 2009. [Online]. Available: <https://pastel.archives-ouvertes.fr/tel-00451021>.
- [4] A. Denys, P. Brown, and A. Leverrier, “Explicit asymptotic secret key rate of continuous-variable quantum key distribution with an arbitrary modulation”, *Quantum*, vol. 5, p. 540, 2021, ISSN: 2521-327X. DOI: 10.22331/q-2021-09-13-540.
- [5] P. Jouguet, S. Kunz-Jacques, E. Diamanti, and A. Leverrier, “Analysis of imperfections in practical continuous-variable quantum key distribution”, *Phys. Rev. A*, vol. 86, p. 032 309, 3 2012.
- [6] M. Rueckmann and C. G. Schaeffer, “Calibration of receiver noise in cv-qkd systems”, in *Photonic Networks; 21th ITG-Symposium*, 2020, pp. 1–4.
- [7] P. Jouguet, S. Kunz-Jacques, and E. Diamanti, “Preventing calibration attacks on the local oscillator in continuous-variable quantum key distribution”, *Phys. Rev. A*, vol. 87, p. 062 313, 6 2013. DOI: 10.1103/PhysRevA.87.062313.
- [8] A. Marie and R. Alléaume, “Self-coherent phase reference sharing for continuous-variable quantum key distribution”, *Phys. Rev. A*, vol. 95, p. 012 316, 1 2017. DOI: 10.1103/PhysRevA.95.012316.

# Event-based vision for improved classification accuracy in label-free flow cytometry

Muhammed Gouda,<sup>1</sup> Alessio Lugnan,<sup>1</sup> Joni Dambre,<sup>2</sup> Gerd Van den Branden,<sup>3</sup> Christoph Posch<sup>3</sup> and Peter Bienstman<sup>1</sup>

<sup>1</sup> Ghent University-imec, Photonics Research Group, Ghent, Belgium

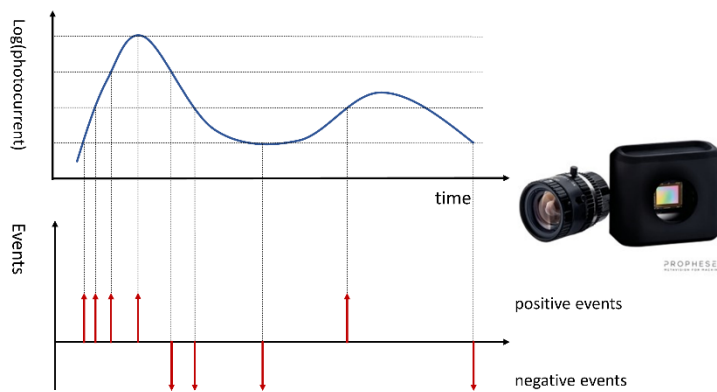
<sup>2</sup> Ghent University, IDLab, Ghent, Belgium

<sup>3</sup> PROPHESEE, Paris, France

## Abstract

Event-based cameras are cutting-edge, bio-inspired vision sensors that differ from conventional frame-based cameras in their operating principles. In the field of machine learning, the switch from CMOS cameras to event-based cameras has improved accuracy in settings with critical illumination and rapid dynamics. In this work, we examine the combination of event cameras with extreme learning machines in the context of imaging flow cytometry. The experimental setup, with the exception of the image sensor, is similar to a set-up we utilized in a previous work in which we demonstrated that a simple linear classifier can achieve an error rate of about 10% on background-subtracted cell frames. Here, we demonstrate that by utilizing an event camera's capabilities, the error rate of this basic imaging flow cytometer could be reduced to the order of  $10^{-3}$ . Additionally, advantages like increased sensitivity and effective memory utilization are obtained. Finally, we make further suggestions for potential upgrades to the experimental setup that records events from moving microparticles which will enable more precise and reliable cell sorting.

## Introduction



The biomedical sector employs a tool called flow cytometry to analyze a large number of cells or particles [1]. The technique has been used in a variety of applications, including the progression of cancer therapy and cancer detection, as well as the categorization of microparticles and microalgae [2,3].

In this work, we use PROPHESEE's event-based camera (also called a dynamic vision sensors DVS) in imaging flow cytometry to overcome two main drawbacks faced by systems which rely on traditional CMOS (or frame-based) sensors. The two drawbacks of continuously capturing consecutive frames are memory usage and the difficulty of filtering the background noise. Since the machine learning training can be very sensitive to noise, not filtering noise properly could result in lower achievable classification accuracies. Since event-based cameras only capture the changes in the scene (Figure 1),

the background noise is automatically removed and the memory usage is much more efficient.

## Methods

A laser source generating light with a 632.8 nm wavelength makes up the configuration created for this work as seen in figure 2. The light is directed onto a PMMA microfluidic channel after passing via a lens and a 25  $\mu\text{m}$  pinhole. A manual syringe pump attached to the top port of the channel is used to pump flowing microparticles. One syringe was used for particle A, another for particle B, and a third one was used to wash out the system with water. The movement of the particles changes the diffraction pattern which is captured by a Prophesee event camera. We used two different classes of spherical microparticles (class A of diameter 16  $\mu\text{m}$  and class B with a diameter of 20  $\mu\text{m}$ ).

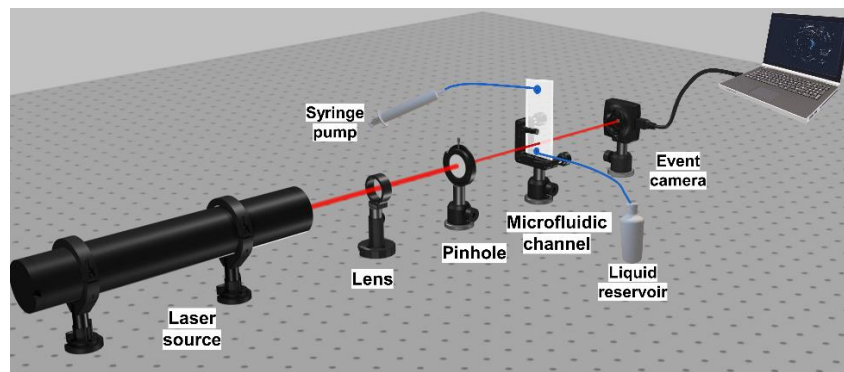


Fig. 2: The experimental setup built to generate the training and test datasets. Light coming from a 1550 nm He-Ne laser passes through a lens then a 25  $\mu\text{m}$  pinhole. Behind the pinhole is a vertically-mounted PMMA microfluidic channel inside which microparticles are flowing downwards. The diffraction pattern caused by a flowing particle is captured by the event-based camera which is connected to a laptop with a dedicated software for recording the events fired at different pixels.

## Results

The events fired by the camera upon the passage of different particles inside the microfluidic channel were recorded by a laptop. We then build a machine learning pipeline which starts by first framing all the different events belonging to a certain sample as shown in figure 3. We compared such samples with a simulation model that was done in ASAP<sup>1</sup> using gaussian beam propagation method. The generated frames then went through different preprocessing steps (downsampling, flattening, standardization, feature

---

<sup>1</sup> ASAP is an optical simulation software for predicting real-world performance

selection), then a simple regularized logistic regression (a classification algorithm) was applied on the resulted feature matrix.

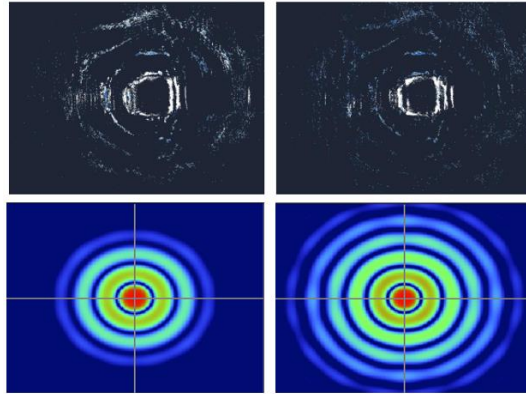


Fig. 3: Experimental (top) and simulated (down) data of the diffraction pattern caused by the flowing microparticles. Particles with two different diameters were used,  $16\ \mu\text{m}$  (left) and  $20\ \mu\text{m}$  (right). The model was simulated using ASAP's waveoptics simulator. Notice the first disc of the airy pattern appears in the simulation model but not in the experimental frames. This is because the events in the center are not fired due to the fixed illumination.

In machine learning, it is crucial to split the data into three different categories for training, validating and testing our model. At first, we had only one single measurement session from which we collected those three types of samples. However, we found that models trained and validated this way give misleading high accuracy when tested on the same measurement session's data. However, when we test such models on data from new experiments, we found that the accuracy drops significantly. Therefore, we decided to train our classifier in an intertwined way making it see data from different experiments while testing was done on data from unseen experiments during training. Figure 4 shows the error rates achieved by our trained classifier.

Finally, we compared the error rates of the current system with the one we had previously in [3] which used a CMOS camera. We found that we could decrease error rate by 2 orders of magnitude.

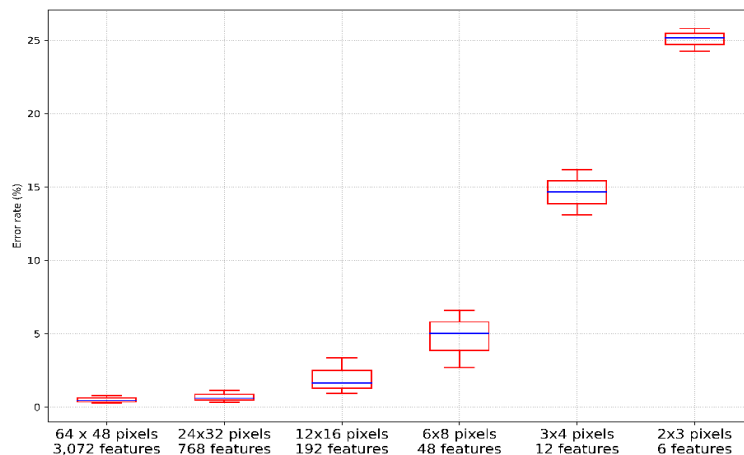


Fig. 4: Test error rates for different classifier models trained using samples from different measurement sessions. The trained models were tested on unseen data from different sessions than those in either training or validation. On the x-axis are the resolutions of the frames sent to the linear classifier.

## **Conclusion**

In this work we have demonstrated experimentally the different benefits novel event-based sensors bring to the field of flow cytometry. These included higher accuracy, lower background noise and more efficient memory utilization. We compared the new results with the results from previous work which used a frame-based camera. Future work encompass classifying biological cells and training spiking neural networks on the signal from the DVS sensor.

## **ACKNOWLEDGMENTS**

This work was performed in the context of the European H2020 Neoteric project (grant agreement 871330).

## **References**

- 1 M. Doan, I. Vorobjev, P. Rees, A. Filby, O. Wolkenhauer, A. E. Goldfeld, J. Lieberman, N. Barteneva, A. E. Carpenter, and H. Hennig, “Diagnostic potential of imaging flow cytometry,” *Trends in Biotechnology*, vol. 36, no. 7, pp. 649–652, 2018.
- 2 Y. Han, Y. Gu, A. C. Zhang, and Y.-H. Lo, “Imaging technologies for flow cytometry,” *Lab on a Chip*, vol. 16, no. 24, pp. 4639–4647, 2016.
- 3 A. Lugnan, E. Gooskens, J. Vatin, J. Dambre, and P. Bienstman, “Machine learning issues and opportunities in ultrafast particle classification for label-free microflow cytometry,” *Scientific Reports*, vol. 10, no. 1, pp. 1–13, 2020.

# Towards a Fourier-Domain mode-locked laser system with an integrated Mach-Zehnder interferometer as frequency filter

J.Hazan,<sup>1</sup> A. Nassar<sup>1</sup>, K.A.Williams<sup>1</sup> and E. A. J. M. Bente<sup>1</sup>

<sup>1</sup> Eindhoven University of Technology, Dept. of Electrical Engineering, De Rondom, 5630 MB Eindhoven, The Netherlands

*The use of an InP based integrated asymmetric Mach-Zehnder interferometer (AMZI) in a Fourier Domain Mode-Locked fiber-based laser for optical coherence tomography (OCT) application is discussed and characterization results are shown. The need for high-speed scanning source is crucial for OCT images, since it helps to avoid blurriness and artifacts due to the motion of biological tissue during in-vivo measurements. In this work, we observed that replacing the commonly used piezo-driven Fabry-Perot filters (FFP) with monolithically integrated ones, enables a laser system with higher tuning speed and consequentially reduced cavity length. The laser consists of a fiber ring cavity containing a semiconductor optical amplifier and the integrated AMZI. The laser wavelength is tuned at the cavity roundtrip frequency by applying reverse bias voltage on an electro refractive modulator present in one of the arms of the integrated AMZI. A preliminary characterization reveals a 3 nm comb width around 1530 nm, together with 83.3 ns output pulses for a 16 m fiber-based laser with a 12 MHz repetition rate.*

**Keywords:** InP, Semiconductor Lasers, Fourier-Domain Mode-Locked laser

## Introduction

Fourier domain mode-locked (FDML) lasers are among the fastest wavelength-swept light sources. They are used in many applications, like optical coherence tomography (OCT) [1] and Raman or two photon microscopy [2]. FDML lasers consist of long ring fiber cavities with tunable Fabry-Perot bandpass filters (FFPs). The transmission wavelength of the mechanically tunable FFPs is modulated sinusoidally with a repetition period equal to the fundamental cavity round trip time. In this way, these lasers overcome the limitation of the buildup time of the laser signals from spontaneous emissions, allowing for fast sweeps up to 290 kHz [3]. The slow scans of FFPs are currently limiting the tuning speed and the dimensions of the laser cavities. New approaches introduced lithium-niobate Mach-Zehnder interferometers [4] as wavelength-tunable comb filters in such FDML fiber ring lasers. In this work we show preliminary data on an integrated AMZI bandpass tunable filter with reversely bias driven InP based phase modulators in a fiber based FDML laser. The phase modulators allow for faster scanning of the AMZI as well as using other time dependencies of the maximum transmission wavelength as a function of time than sinusoidal. The AMZI characteristics and the laser schematics are reported. Optical and electrical spectra, and output pulse duration obtained from the FDML. These results can be considered as a milestone for the monolithic integration of FDML laser on InP, to achieve GHz scan speeds, as theoretically modeled [5], [6]. Moreover, the use of an InP based integrated AMZI, increases the possibility of using different driving voltage waveforms, which leads to different power distributions over the modes of the generated frequency combs.

## Laser Design and DC operation

The fiber-based laser design, with schematics in Fig. 1 (a), consists of ring cavity with the AMZI as a tunable bandpass filter. The gain medium is a discrete component semiconductor optical amplifier (SOA), where its substrate temperature is stabilized to 20° trough Peltier and water cooling. Two optical isolators are included inside the ring cavity to ensure only counterclockwise (CCW) propagation of the light. The output of the AMZI is connected to 2x2 output coupler where 90% of the optical power is fed back to the laser cavity and 10% is extracted as the output signal. A Single Mode fiber (SMF) delay line leads to a total cavity length of 16.071 m which corresponds to a cavity FSR of around 12.038 MHz calculated as:

$$FSR_{cavity} = \frac{c}{n_{g1}L_{AMZI} + n_{g2}(L_{total} - L_{AMZI})} \quad (1)$$

Where  $n_{g1}=3.66$  is the group index of InP waveguides at 1550 nm,  $n_{g2}=1.55$  is the group index of SMF and  $L_{AMZI} = 4.6 \text{ mm}$  is the optical path length on the InP chip. The free spectral range (FSR) of 6 nm of the AMZI is determined by the geometrical length mismatch  $\Delta L$  (97  $\mu\text{m}$ ) between the two arms. The wavelength tuning of the laser is done by applying a reverse bias voltage to one of the phase modulators of the AMZI, with a linear phase change of 15°/V.mm [7]. It is important to mention that to achieve FD-MLL operation in the proposed design, it is essential that the modulation is applied only on one arm of the AMZI to exploit both the effects of wavelength filtering and phase modulation. In this way it is possible to obtain a fixed phase relation between adjacent modes.

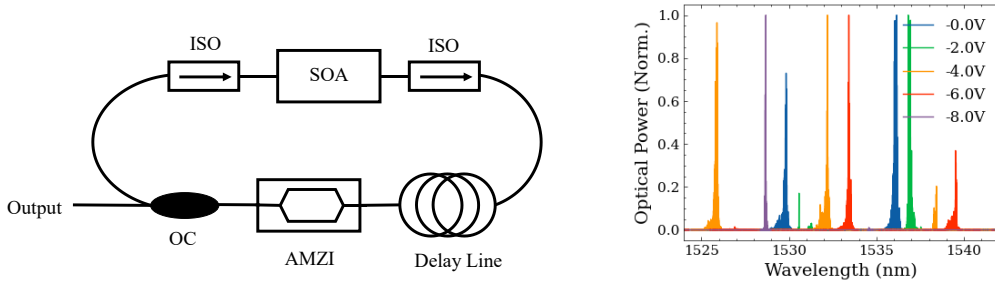


Fig.1 (a) Schematics of the fiber-based Fourier Domain Mode-locked laser investigated in this work. (b) Laser spectra for different DC bias conditions applied to the AMZI.

The laser threshold current is 200 mA, and the optical power measured on the photodetector is 110  $\mu\text{W}$  at 320 mA. The optical power is mainly hampered by the coupling loss between InP chip and the fiber, and it has been measured at the output of the AMZI where the highest cavity loss occurs. The laser tuning is investigated applying reverse bias voltage to the filter between 0 V and -7 V with 1 V step. In Fig. 1 (b) is possible to observe different spectra as function of the reverse bias voltage measured with a resolution of 20 MHz (APEX 2641-B). From the plots, we can observe three spectral mode groups with 6 nm spacing corresponding to different AMZI transmission periods. From the wavelength tuning we observe that lasing modes are hopping between the different filter maxima. This is since the lasing wavelength occurs where the minimum loss is present and small variations in loss for the different maxima occur during tuning. This behavior is a limitation to the FDML operation, since the laser hopping between different wavelengths will occur then as well.

## Fourier Domain Mode-Locking Operation

The mode-locking operation of the laser is investigated tuning the AMZI filter with a sinusoidal drive signal with the same frequency as the FSR of the ring laser cavity. Electrical spectra from a 12.5 GHz photodetector, monitoring the laser output are

recorded to investigate the mode-locking operation with respect to the modulation frequency of the AMZI tunable filter. The optimal frequency was found to be 11.975 MHz, for an SOA current of 318 mA. The blue curve in Fig 2 (a) shows the electrical spectrum when the modulation of 11.975 MHz is applied to the AMZI. RF power at the cavity repetition rate is measured to be -15.7 dBm, which is 85 dB higher than the noise floor (-100 dB). This is used as a clear indication of mode-locking operation of the laser. As we detune the modulation frequency by 10% we observe (red curve in Fig 2 (b)) the presence of beating frequencies between the laser fundamental frequency and the modulation frequency. A high-resolution scan of the modulation frequency is made to observe the effect of smaller detuning on the RF power. We see that a detune of 5 KHz, 15 KHz and 60 KHz results in 1 dB, 3 dB and 5 dB of RF power drop respectively. In the same way, a detuning of  $\pm 5$  KHz results in a 3-4 dB drop of the optical spectral power. Fig. 2 (b), shows the optical spectrum of this FDML laser measured at 20 MHz resolution for different AMZI modulation depths ( $V_{pp}$ ). It is clear how the optical power is concentrated at the edges of the frequency comb generated by the filter sweep. This is a characteristic result for a sinusoidal drive signal applied to the AMZI filter as we predicted from optical simulations [6]. The asymmetric shape of the comb with respect to the center can be explained with the residual absorption of phase modulators as function of the reverse bias voltage [8]. The effect of the modulation depth is observed by the increase in the comb width and a simultaneous decrease in the average power. This happens since the larger the modulation depth, the shorter the fraction of time the laser is operating at one of the cavity modes, as theoretically explained in [6].

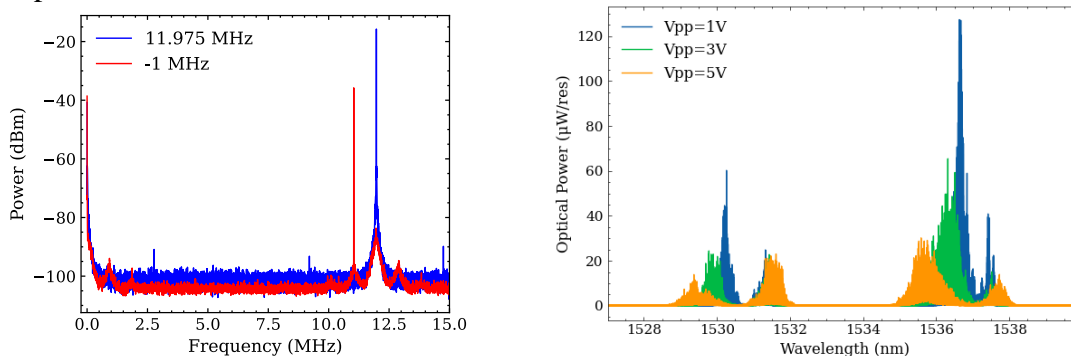


Fig. 2 (a) Electrical spectrum for FD-ML operation at the fundamental frequency ( $F_{Mod}=11.975$  MHz) and for 1 MHz detuning. b) Optical spectra for different  $V_{PP}$  applied to the AMZI

The output pulses, after passing through an Erbium doped fiber amplifier (EDFA) are recorded with a 12.5 GHz bandwidth photodiode and studied to identify the FDML operation. The RF signal applied to the AMZI filter is used to trigger the oscilloscope acquisition and the time traces were averaged over 600 sweeps. The obtained output pulses, shown in Fig. 3 (a) reveal how the output power is distributed over the whole pulse period of 83.3 ns (11.975 MHz repetition rate). This can be interpreted as a second indication for FDML operation. The presence of drops in output power occurring at the maximum drive voltage of -5V may be due to the fact that the laser is operating outside of the gain window of the EDFA. This happens due to mode-hopping between different maxima of the periodic filter function as shown for DC laser operation in Fig. 1 (b). To evaluate the phase relation between different spectral modes in the obtained combs, the output comb is spectrally filtered over different modes to determine the relative time delay of different spectral components. During the wavelength sweep of

FD-MLL, we expect the existence of two pulses at a specific filtered wavelength within the sweep range of the laser. The time delay between the two pulses  $\delta t$  can be linked to the filtered wavelength  $\lambda_{filter}$  by:  $\delta t = \frac{\lambda_0 - \lambda_{filter}}{\lambda_1 - \lambda_0} \cdot T_{period}$  where  $\lambda_0 = 1528.3 \text{ nm}$  and  $\lambda_1 = 1531.40 \text{ nm}$  corresponds to the wavelengths at the edge of the sweep range of the obtained frequency and  $T_{period}$  is the round trip time. Fig. 3 (b) shows 500 ns output time trace corresponding to filtered output spectrum at 1530.40 nm. We observe the existence of two pulses in the round-trip time of 83.3 ns and the time delay between them is found to be 56 ns which is the delay between the two pulses at 1531.40 nm.

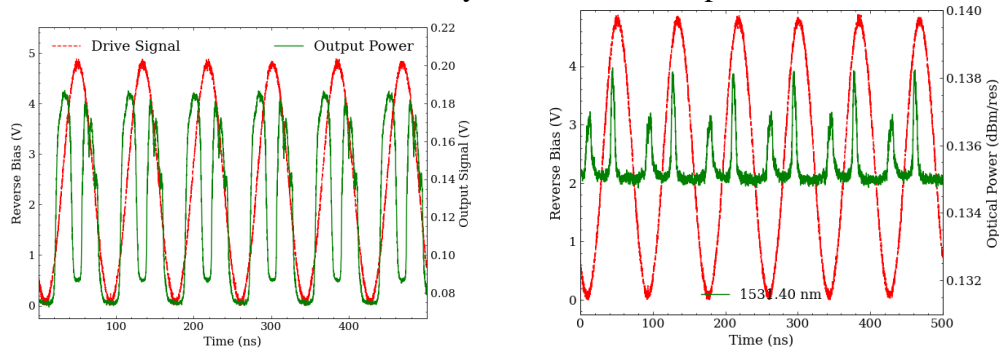


Fig.3 (a) 500 ns recorded signal time traces (green) overlapped with the drive signal applied to the AMZI.(red) (b) 500 ns recored signal time traces for sinusoidal same driving and a filtered spectrum at 1530.4 nm (ISOA=318 mA,  $F_{Modulation}=11.975 \text{ MHz}$ ,  $V_{PP}=5$ ,  $V_{Offset}=-2.5 \text{ V}$ ,  $G_{EDFA}=11 \text{ dB}$ )

## Conclusions

This first results on the use of an integrated AMZI as a fast tunable filter in FDML laser are here presented. A 3 nm frequency comb together with 83 ns long pulses have been experimentally observed. This work is intended to be a first step into the realization of a fully integrated FDML laser with GHz scan rates to be used as a source for OCT endoscopy and imaging.

## Acknowledgments

This work is part of the research program 'An integrated Optical Coherence Tomography system for medical imaging at 1300nm' with project number 16251, which is (partly) financed by the Dutch Research Council (NWO).

## References

- [1] R. Huber, "Fourier domain mode locking (FDML): A new laser operating regime and applications for biomedical imaging, profilometry, ranging and sensing," *Opt. InfoBase Conf. Pap.*, vol. 14, no. 8, pp. 1981–1983, 2009, doi: 10.1364/assp.2009.ma1.
- [2] S. Karpf, M. Eibl, W. Wieser, T. Klein, and R. Huber, "A Time-Encoded Technique for fibre-based hyperspectral broadband stimulated Raman microscopy," *Nat. Commun.*, pp. 6–11, 2015, doi: 10.1038/ncomms7784.
- [3] D. Huang, Y. Shi, F. Li, and P. K. A. Wai, "Fourier Domain Mode Locked Laser and Its Applications," *Sensors*, vol. 22, no. 9, p. 3145, 2022, doi: 10.3390/s22093145.
- [4] J. Dong, K. S. Chiang, and K. Chen, "Wavelength-tunable multi-wavelength fiber laser with an electro-optic lithium-niobate waveguide comb filter," *Asia Commun. Photonics Conf. ACPC 2015*, pp. 5–7, 2015, doi: 10.1364/acpc.2015.asu2a.51.
- [5] M. J. R. Heck and J. E. Bowers, "Integrated fourier-domain mode-locked lasers: Analysis of a novel coherent comb laser," *IEEE J. Sel. Top. Quantum Electron.*, vol. 18, no. 1, pp. 201–209, 2012, doi: 10.1109/JSTQE.2011.2113371.
- [6] J. Hazan, A. Nassar, K. Williams, and E. Bente, "Monolithically integrated InP 2 . 5 GHz Fourier Domain Mode-Locked Laser at 1530nm," no. c, pp. 2–3, doi: 10.1117/12.2610120.R.
- [7] S. Latkowski *et al.*, "Novel Widely Tunable Monolithically Integrated Laser Source," *IEEE Photonics J.*, vol. 7, no. 6, 2015, doi: 10.1109/JPHOT.2015.2493722.
- [8] S. Andreou, K. A. Williams, and E. A. J. M. Bente, "Steady-state analysis of the effects of residual amplitude modulation of InP-based integrated phase modulators in pound-drever-hall frequency stabilization," *IEEE Photonics J.*, vol. 11, no. 3, pp. 1–14, 2019, doi: 10.1109/JPHOT.2019.2915163.
- [9] Y. Barbarin *et al.*, "Realization and modeling of a 27-GHz integrated passively mode-locked ring laser," *IEEE Photonics Technol. Lett.*, vol. 17, no. 11, pp. 2277–2279, 2005, doi: 10.1109/LPT.2005.857228.

# Low-loss photonic integrated circuits for UV applications

W.A.P.M. Hendriks, M. Dijkstra, S. Mardani, I. Hegeman, Sonia M. Garcia-Blanco

Integrated Optical Systems Group, MESA+ Institute, University of Twente, P.O. Box 217, 7550 AE, Enschede, The Netherlands

*We present a low propagation loss aluminium oxide integrated photonics platform enabling applications with operation down to the UV wavelength range (i.e.,  $>250$  nm). Single mode fully etched waveguides were fabricated with losses down to 2 dB/cm at 405 nm. The influence of waveguide dimensions on the propagation losses are presented, indicating that losses are sidewall roughness limited. Lower losses can be achieved by further optimization of the cross-section of the waveguides. In this paper, the aluminium oxide platform is introduced together with the characterization of the waveguides at near-UV wavelengths.*

## Introduction

Silicon photonics has led to the development of devices in a range of fields including signal processing [1], nonlinear optics [2] and quantum information processing [3]. Amongst the different silicon photonic platforms, devices based on silicon nitride are quite mature, particularly for visible and near infrared (NIR) wavelengths [4], [5]. However, the high material absorption in the blue and UV have prevented their utilization at near-UV wavelengths. A need for low loss photonic integrated circuits (PICs) in the UV exists with applications such as quantum ion traps [6], atomic clocks [7] and spectroscopy. Aluminium oxide ( $\text{Al}_2\text{O}_3$ ) exhibits a bandgap between 5.1 and 7.6 eV ( $\lambda \sim 163 - 243$  nm) depending on the layer morphology [8], facilitating devices down to 250 nm. In addition, an moderate refractive index contrast with silicon dioxide ( $\text{SiO}_2$ ) facilitates reduced scattering losses from roughness while the minimum device features are still reasonable as it scales with the wavelength. Using atomic layer deposition (ALD) deposited  $\text{Al}_2\text{O}_3$  with  $\text{SiO}_2$  cladding, losses down to 1.8 dB/cm at 405 nm have been demonstrated [9]. With air cladding, losses as low as 3 dB/cm have been reached at 370 nm [10]. These losses demonstrate the feasibility for  $\text{Al}_2\text{O}_3$  PICs in the UV. ALD is however an slow [11] and relatively expensive process. Here we present a low-loss reactive sputtered  $\text{Al}_2\text{O}_3$  UV PIC platform. First, the waveguide design is discussed ensuring single mode operation. Next, slab losses in the UV of the deposited layers is discussed. Finally, channel propagation losses measured at 405 nm using a cutback method are presented.

## Design

Single transverse mode operation is a requirement for most PIC components. We have therefore chosen the investigated waveguide dimensions to support single mode operation. We choose to fix the layer thickness at 70 nm as this is the minimum thickness that still supports mode propagation at 377 nm, thereby allowing for quality control of the layer after deposition. For quality control, the layer propagation losses are measured using a Metricon M2010 prism coupling setup. For the results presented here the losses after deposition were found to be 0.7 dB/cm at 377 nm. To determine suitable waveguide widths for 405 nm light, finite difference eigenmode simulations are

performed to determine the refractive index as a function of waveguide width. The results shown in *Figure 1* indicate that a higher order mode starts at a width of 670 nm. For this reason we choose a maximum waveguide width of 700 nm as the higher order TE mode is not supported when even a slight bend is applied. The minimum waveguide width is chosen at 400 nm as this still exhibits negligible bend losses at a bend radius of 500  $\mu\text{m}$ .

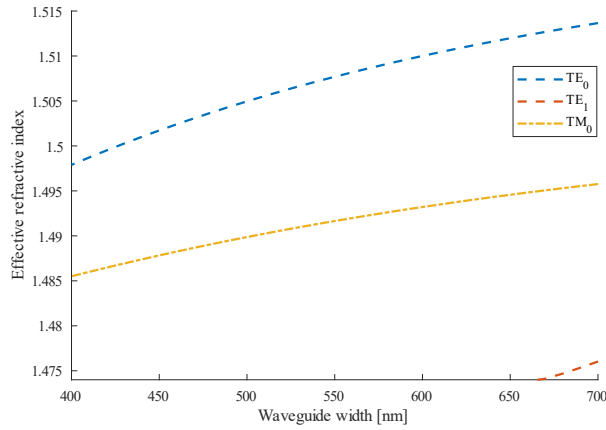


Figure 1 Effective index of an 70 nm high  $\text{Al}_2\text{O}_3$  waveguide as a function of its width for light at 405 nm.

## Results

We will demonstrate the performance of the  $\text{Al}_2\text{O}_3$  waveguides for UV applications by UV-Vis transmission measurements as well as waveguide loss measurements using a cutback method at 405 nm. The UV-Vis transmission measurement is performed on an quartz substrate coated with an  $\sim 850$  nm  $\text{Al}_2\text{O}_3$  layer and an quartz reference. The resulting transmission loss as presented in *Figure 2* shows that the absorption of the  $\text{Al}_2\text{O}_3$  layer starts to markedly increase from  $\sim 250$  nm demonstrating the feasibility for waveguide operation below 250 nm.

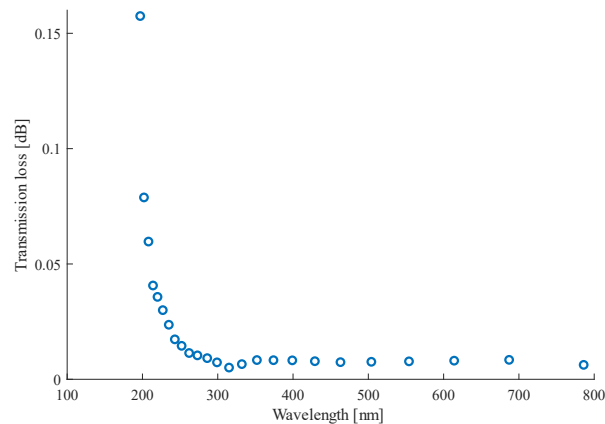
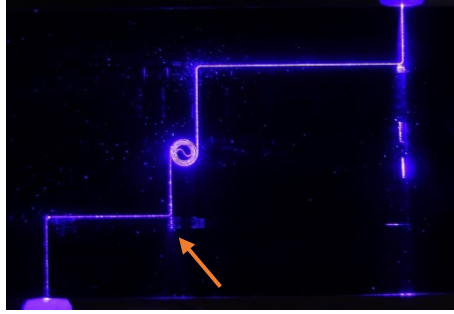


Figure 2 Transmission loss spectrum of sputter coated  $\text{Al}_2\text{O}_3$ . The observed dip at 310 nm is caused by the switching between the halogen and deuterium lamp.

The PICs for the waveguide loss measurements are fabricated by electron beam lithography. They consist of a circuit with spirals of varying propagation length from 3.3 to 14 cm. After development, the waveguides pattern is transferred into the  $\text{Al}_2\text{O}_3$  using reactive ion etching. Next, a  $\text{SiO}_2$  cladding is deposited and the circuits are diced. For the

cutback measurements light from a polarization maintaining (PM) fiber-coupled 405 nm laser source is butt-coupled to the chip using pm-s350-hp fibers. Although taper couplers are implemented in the circuits, high coupling losses in excess of 30 dB per facet are observed. We expect the facet roughness to be a major contributor to these losses as the end facets are not polished. In addition, bend losses can be observed in the camera image taken from the propagation through the waveguide in *Figure 3*.



*Figure 3* Top view of 405 nm light coupled into an  $\text{Al}_2\text{O}_3$  PIC. The arrow indicates light lost at the bend scattering from waveguides that are routed perpendicular.

To determine the propagation losses, the power transmitted (in dB) as a function of channel length is plotted and a linear fit is used to determine the propagation losses. The results for the given waveguide widths for both TE and TM polarization are shown in *Figure 4*. We observe a clear loss reduction when the waveguide width is increased from 400 to 500 nm, indicating an significant sidewall roughness contribution to the losses. Observed losses for the consecutive widths have clearly overlapping confidence intervals making any further conclusion precarious.

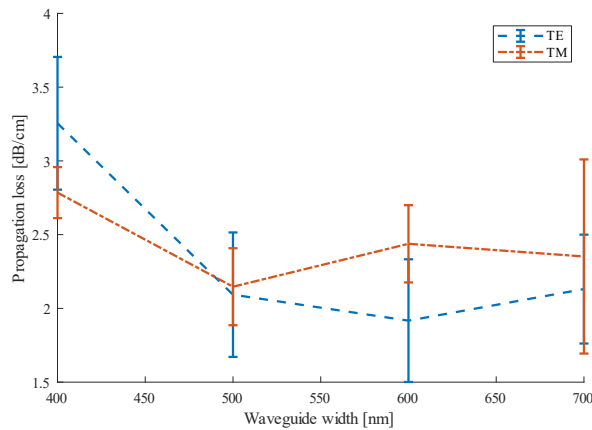


*Figure 4* Propagation loss as a function of waveguide width for launched light of 405 nm. Error bars are the 95% confidence interval of the linear least squares fit.

## Conclusion

We have demonstrated low loss sputter coated  $\text{Al}_2\text{O}_3$  waveguides with  $\text{SiO}_2$  cladding, with losses down to  $2 \pm 0.5$  dB/cm, comparable to the best results obtained with ALD deposited  $\text{Al}_2\text{O}_3$ . In addition the transmission bandgap down to 250 nm is verified showing the possibility for PICs in the UV.

## Funding

The research was funded under the ERC Asindo Proof of Concept program. ID:964006

## References

- [1] W. Bogaerts *et al.*, “Programmable photonic circuits,” *Nature*, vol. 586, no. 7828, pp. 207–216, Oct. 2020, doi: 10.1038/S41586-020-2764-0.
- [2] H. Zia, N. M. Lüpken, T. Hellwig, C. Fallnich, and K. J. Boller, “Supercontinuum Generation in Media with Sign-Alternated Dispersion,” *Laser Photonics Rev.*, vol. 14, no. 7, p. 2000031, Jul. 2020, doi: 10.1002/LPOR.202000031.
- [3] C. Taballione *et al.*, “20-Mode Universal Quantum Photonic Processor,” Mar. 2022, doi: 10.48550/arxiv.2203.01801.
- [4] A. Leinse *et al.*, “TriPlex photonic platform technology: Low-loss waveguide platform for applications from UV to IR,” *16th Eur. Conf. Integr. Opt.*, vol. 4, pp. 6–7, 2012.
- [5] M. J. R. Heck *et al.*, “Ultra-low-loss high-aspect-ratio Si<sub>3</sub>N<sub>4</sub> waveguides,” *Opt. Express Vol 19 Issue 4 Pp 3163-3174*, vol. 19, no. 4, pp. 3163–3174, Feb. 2011, doi: 10.1364/OE.19.003163.
- [6] K. R. Brown, J. Chiaverini, J. M. Sage, and H. Häffner, “Materials challenges for trapped-ion quantum computers”, doi: 10.1038/s41578-021-00292-1.
- [7] N. Hinkley *et al.*, “An Atomic Clock with 10–18 Instability,” *Science*, vol. 341, no. 6151, pp. 1215–1218, Sep. 2013, doi: 10.1126/science.1240420.
- [8] E. O. Filatova and A. S. Konashuk, “Interpretation of the Changing the Band Gap of Al<sub>2</sub>O<sub>3</sub> Depending on Its Crystalline Form: Connection with Different Local Symmetries,” *J. Phys. Chem. C*, vol. 119, no. 35, pp. 20755–20761, Aug. 2015, doi: 10.1021/acs.jpcc.5b06843.
- [9] G. N. West *et al.*, “Low-loss integrated photonics for the blue and ultraviolet regime,” *APL Photonics*, vol. 4, no. 2, p. 026101, Feb. 2019, doi: 10.1063/1.5052502.
- [10] C. Lin *et al.*, “UV photonic integrated circuits for far-field structured illumination autofluorescence microscopy,” *Nat. Commun. 2022 131*, vol. 13, no. 1, pp. 1–9, Jul. 2022, doi: 10.1038/s41467-022-31989-8.
- [11] M. M. Aslan *et al.*, “Low-loss optical waveguides for the near ultra-violet and visible spectral regions with Al<sub>2</sub>O<sub>3</sub> thin films from atomic layer deposition,” *Thin Solid Films*, vol. 518, no. 17, pp. 4935–4940, Jun. 2010, doi: 10.1016/j.tsf.2010.03.011.

# Towards integration of a Pound Drever Hall frequency stabilized laser system on the InP platform

R. Jones,<sup>1</sup> E. Bente,<sup>1</sup> and K. Williams<sup>1</sup>,

<sup>1</sup> Eindhoven University of Technology, Dept. of Electrical Engineering, Photonic Integration Group, Groene Loper 19, 5612 AP Eindhoven, the Netherlands

Laser frequency stabilization schemes are opto-electronic control systems which enable the reduction of frequency noise and typically provide the long term ( $> \mu\text{s}$ ) frequency stability of the laser output. Such systems consist of several optical components, yet only the semiconductor laser has thus far been successfully integrated. In this paper we present our work towards the further integration of other optical components, namely the electrical optical phase modulator (EOPM) of the Pound Drever Hall (PDH) frequency stabilization scheme onto a single monolithically fabricated PIC on the Smart Photonics InP platform. Previous attempts have been unsuccessful due to the electrical cross talk between the EOPM and the semiconductor laser. In this paper, we investigate whether fabrication on a semi-insulating InP substrate integration platform and the use of adjacent short circuited EOPMs sufficiently reduce the cross talk for frequency locking to be achieved.

## Introduction

Optical sources with good frequency stability (linewidth  $< 100\text{kHz}$ ), over short ( $< 10\mu\text{s}$ ) and long ( $> 10\mu\text{s}$ ) timescales are vital for sensing and metrology. Although free running lasers with intrinsic linewidths at  $10\text{kHz}$  have been monolithically integrated [1], their stability will significantly deteriorate over time due to environment disturbances and electrical noise. To enable stable sources over longer timescales, it is necessarily to employ a frequency stabilizing feedback system such as the Pound Drever Hall (PDH) system [2].

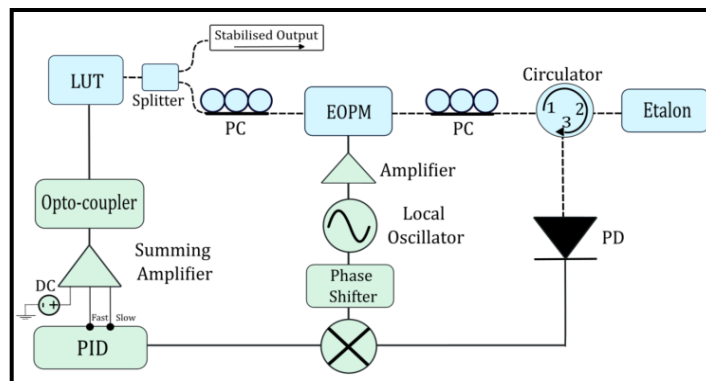


Figure 1: Schematic of the PDH locking scheme. The blue and green boxes indicate the optical and electrical components respectively.

Figure 1 is a basic schematic of the PDH system. Composed of large and expensive components, it is often advantageous to miniaturize the footprint of the circuit in terms of

cost, size and power consumption. Whilst the integration of the electronic circuitry on a single CMOS IC has been demonstrated [3], with regards to the optical circuit, thus far, only the light source has been successfully integrated on a PIC [4]. Integration has been limited by electrical cross talk between the stabilized laser and other actives. In this work, we aim to investigate whether the EOPM, in addition to the laser, can be integrated on chip.

## Circuit Design

Previous work on the n doped platform identified two explanations for the occurrence of electrical cross talk [4]. Firstly, under reverse bias voltage, the resistance of the EOPM ( $50M\Omega$ ) far outweighs the resistance of the isolation sections (few  $M\Omega$ ). This allowed current to leak through the connecting waveguide leading to the laser cavity, effectively making the waveguide a weak EOPM. This changed the length of the lasing cavity causing the frequency mode to be modulated. To prevent the flow of leakage current, we have included adjacent EOPMs, of length  $50\mu\text{m}$ , either side of the external EOPM, which are shorted on chip [5]. We will refer to these as shorted blocks.

The second issue relates to the common ground shared between all active components. An EOPM is a PIN diode, which has an associated capacitance. In addition to this capacitance, a finite resistance exists between the diode and the common ground. When current flows from the n doped InP layer to the ground it causes an elevation of the common ground and subsequent tuning of all actives. To establish greater isolation of the grounds, we have fabricated on a semi-insulating platform. On this platform the n doped layer is on top of a semi-insulating substrate. Active components are grounded by etching to the n doped layer close ( $\approx 10\mu\text{m}$ ) to the P contact, allowing for a low resistance contact. So, although the common ground remains, the current should flow through a loop close to the device.

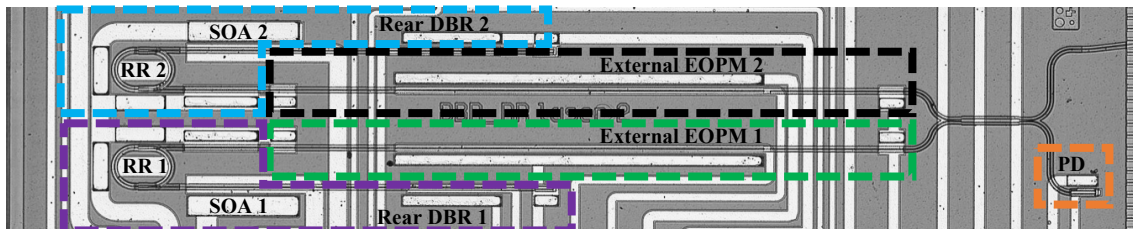


Figure 2: Microscopic image of InP PIC. The purple box and green boxes indicate the laser 1 and external EOPM 1 respectively. The blue and black boxes show the laser 2 and external EOPM 2 respectively. The orange box indicates a PD, used for monitoring purposes. Metallization is made from the topside.

Figure 2 shows a microscopic image of the integrated optical circuit. The green box encircles the EOPM structure (comprising the external EOPM 1 and the two adjacent shorted blocks) and the purple box encircles the narrow intrinsic linewidth semiconductor laser which we wish to frequency lock. EOPM 1 has a length of  $1.5\text{mm}$  and a measured efficiency of  $13.3\text{ }^\circ/\text{mm}\cdot\text{V}$ . As was shown in figure 1, there are two electrical inputs to the circuit. A reverse bias control signal from the PID controller is applied through an opto-coupler to one of the tuning elements (ring resonator or rear DBR) to correct for any frequency deviations, and a sinusoidal signal is applied to the external EOPM to modulate the carrier. To successfully integrate both the laser and the external EOPM onto the same PIC we must limit the electrical cross talk between the EOPM and the fine-tuning elements.

## Measurement

To establish the presence of electrical cross talk in our circuit, we first examined the optical spectrum. The PIC in figure (2) was mounted on an aluminum sub-mount and wire bonded to a PCB to allow for electrical inputs. A lensed fibre was coupled to the angled facet to collect the optical signal. Figure 3 shows the spectrum from laser 2 (encircled by the blue box in figure 2) when EOPM 1, of circuit 1, was modulated with a 30MHz sinusoidal signal with an offset of -5V and an amplitude of 2V. Two effects are seen. Firstly, sidebands are induced on the carrier wave showing that EOPM 2 was being unintentionally frequency modulated and secondly the lasing mode is shifted 260 MHz. The DC and AC modulation respectively suggest that we have both resistive and capacitive coupling of electrical signals.

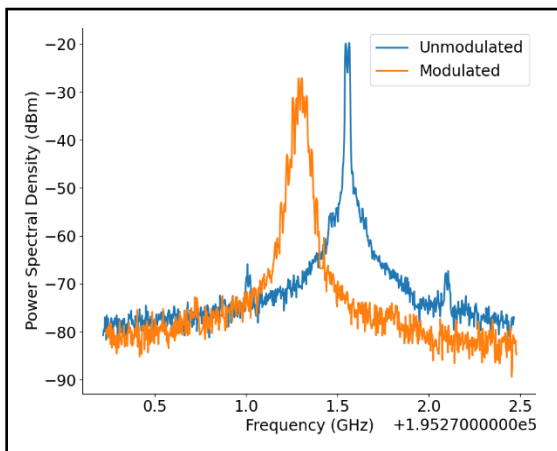


Figure 3: Spectrum of the laser 2 when the EOPM 1 is unmodulated (blue) and modulated (orange).

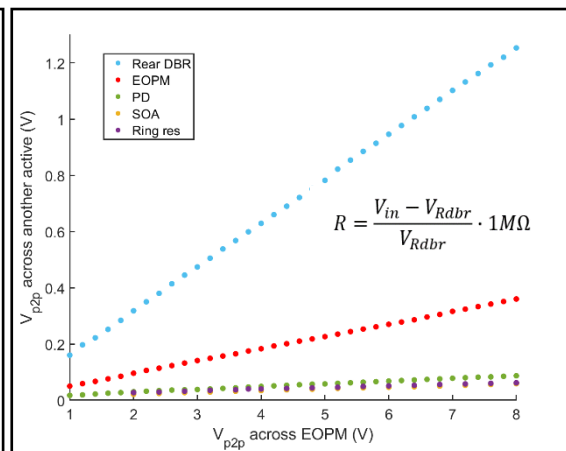


Figure 4:  $V_{p2p}$  across other active components (rear DBR, EOPM 2, Photodiode, SOA and RR) as a function of  $V_{p2p}$  across EOPM 1.

To measure the resistance between the EOPM 1 and the active components in laser 1, a slow sinusoidal modulation of 100kHz (detectable using our equipment) was applied to the external EOPM. The voltage across one of the active components in the circuit 1, either the SOA 1, ring resonator 1, rear DBR 1 or PD was measured, whilst the other actives were grounded, including the shorted blocks, to the ground of the signal generator. We additionally measured the voltage across the EOPM 2 in circuit 2 which is connected via a waveguide that combines the output of the two laser systems. Figure 4 shows the peak-to-peak voltage ( $V_{p2p}$ ) across the active component, connected via a waveguide to the EOPM 1, plotted against the  $V_{p2p}$  applied to EOPM 1. It can be seen that the rear DBR is most strongly affected. A 1V  $V_{p2p}$  to the EOPM results in 0.160mV  $V_{p2p}$  across the rear DBR. Using this data, we can estimate the resistance between the EOPM and the measured active. For the rear DBR this was found to be a resistance of 5.25M $\Omega$ . As a diode under reverse bias typically has a resistance of 10 times this value, it suggests there is a short circuit between the EOPM 1 and the rear DBR.

The final measurement taken was to determine the capacitance of the circuit. We placed a 1k $\Omega$  resistor on the output of the signal generator and measured the voltage across it, allowing for the calculation of the current (I) through the EOPM (see figure 5). On an

oscilloscope we recorded the  $V(t)$  across the EOPM and took the time derivative to determine the capacitance. Figure 6 shows a plot of the current across the EOPM, as a function of the time derivative of the voltage across it, the gradient of which is equal to the capacitance of the EOPM 1. This was calculated to be  $190\text{pF}$ .

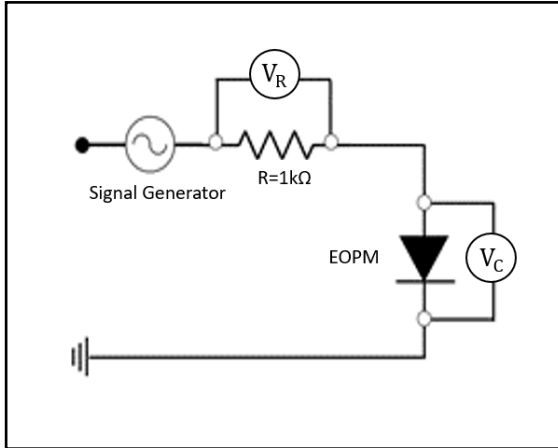


Figure 5: Circuit diagram of the measurement setup. Voltages across the  $1\text{k}\Omega$  resistor and the EOPM are measured as a function of time using a real time oscilloscope.

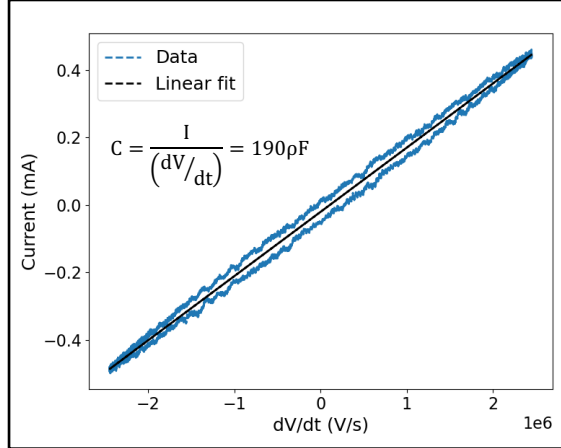


Figure 6: Plot of the current through the external EOPM vs time derivative of the voltage across it using an output impedance from the signal generator of  $1\text{k}\Omega$ .

## Conclusion

Our results show that there is still significant electrical cross talk present on the semi-insulating platform and in the configuration presented here it does not allow for the integration of the EOPM and semi-conductor laser on a single monolithic PIC. In this work we have started to measure and identify the mechanisms in which electrical signals from one device are transmitted to others on the PIC. In future work, we will investigate how the use of an etch through the n doped layer, and a greater decoupling between the grounds, impacts the measured electrical cross talk.

## References

- [1] R. Kumar et al., "A 10-kHz intrinsic linewidth coupled extended-cavity DBR laser monolithically integrated on an InP platform," *Optics Letters*, vol. 47, no. 9, p. 3, 2022.
- [2] C. L. R.W.Fox, "Stabilising Diode lasers to High Finesse Cavities," in *Experimental Methods in the Physical Sciences: Cavity-Enhanced Spectroscopies*, Elsevier Science, 2003.
- [3] F. M.H.Idjadi et al., "Integrated Pound–Drever–Hall laser stabilization system in silicon," *Nature Communications*, no. 8, 2017.
- [4] S. Andreou, K. Williams and E. Bente, "Frequency stabilization of an InP-based integrated diode laser deploying electro-optic tuning," *IEEE Photonics Technology Letters*, vol. 31, no. 24, pp. 1983-1986, 2019.
- [5] R.Pajkovic, S. E.Bente and T.Van.Schaijk, "Improved building block for electro-optical integrated indium-phosphide based phase modulator". Patent W0 2020/162754 A1, 13 August 2020.

# Facet-coupled heterogeneous integration of GaAs SOAs on silicon nitride through micro-transfer printing for near-visible applications

M. Kiewiet,<sup>1,2</sup> S. Cuyvers,<sup>1,2</sup> G. Roelkens,<sup>1,2</sup> K. van Gasse,<sup>1,2,3</sup> and B. Kuyken<sup>1,2</sup>

<sup>1</sup>Photonics Research Group, INTEC Department, Ghent University - imec, 9052 Ghent, Belgium

<sup>2</sup>Center for Nano- and Biophotonics, Ghent University, Belgium

<sup>3</sup>E. L. Ginzton Laboratory, Stanford University, Stanford, CA, USA

*Integrated Silicon Nitride (SiN) photonic circuits offer high flexibility, low losses, and a wider wavelength operating range compared to silicon-based waveguides. The possibility to use wavelengths down to less than 800 nm can enable applications such as Optical Coherence Tomography and fully integrated optical Rubidium clocks. Central to this promise is the integration of (low-linewidth) laser sources operating in these shorter wavelength ranges. By integrating Gallium-Arsenide (GaAs) semiconductor optical amplifiers (SOAs) on the low-loss platform SiN, ultra-narrow linewidth extended-cavity lasers can be created on a fully integrated platform. However, the integration of GaAs with SiN has shown to be challenging due to the high refractive index mismatch between the two materials, making evanescent coupling practically impossible. This work proposes a novel facet-coupling based approach to integrating GaAs SOAs operating at 780 nm on a SiN platform using micro-transfer printing into an etched recess. By optimizing the spatial overlap of the SOA mode with the SiN mode, direct non-adiabatic broad-band facet coupling can be achieved with simulated theoretical coupling between III-V and SiN of up to 72%. This work shows the integration method, as well as the simulations of the coupling between the SOA and the waveguide platform.*

## Introduction

In the past years, a great push has been made to extend integrated photonics to the shorter wavelength spectrum. While silicon-based infrared and mid-infrared photonics have offered many technical solutions, most notably in telecom/datacom fields, many fully integrated sensing applications requiring visible wavelengths have been firmly out of reach due to the relatively narrow bandgap of silicon. At a wavelength of 800 nm, optical coherence tomography and fully integrated optical Rubidium clocks are two of the main envisioned applications for photonics. To accommodate such wavelengths, Silicon Nitride (SiN) based waveguides are used, offering transparency well through the visible spectrum. Central to these sensing solutions is the integration of a narrow-linewidth laser on the silicon nitride platform. Since silicon nitride is a passive dielectric, gain at these wavelengths must come from the heterogeneous integration of III-V materials, most notably Gallium Arsenide (GaAs) semiconductor optical amplifiers (SOAs) at 800 nm.

Unfortunately, the integration of GaAs on SiN is difficult, mostly due to the mismatch in refractive index, making direct evanescent coupling impossible. Most commonly, III-V materials are integrated on top of patterned SiN wafers through (die-to-)wafer bonding or micro-transfer printing and coupled using evanescent fields [1, 2]. To couple from the high-index III-V materials to the low-index SiN, an intermediate layer with a taper is generally used. For mid-IR, coupling between Indium Phosphide integrated on SiN using micro-transfer printing has been frequently demonstrated using an amorphous silicon

intermediate layer. However, selection of such layers for sub-micron wavelengths is much more difficult. In other recent work, integration of bonded GaAs on SiN was shown using an intermediate dielectric coupling structure that is butt-coupled to the GaAs SOA and evanescently coupled to the SiN [3].

This work proposes instead to forgo the coupling structure and directly butt-couple the SOA to the SiN waveguide. This is made possible by using the flexible micro-transfer printing approach, which can print a small fully pre-fabricated structure into a recess, allowing for vertical alignment of the SOA and waveguide modes. In this paper, the fabrication approach for butt-coupling through micro-transfer printing is laid out and verified through simulations, showing more than 70% maximum coupling efficiency. Furthermore, it shows that, within reasonable alignment tolerances, more than 50% theoretical coupling efficiency is possible.

### Device integration procedure

The GaAs SOAs are designed as edge-coupled devices. To this end, both ends of the SOA are dry-etched to form facets. On the back-side of the SOA, the facet is straight and coated with a layer of gold to form a broad-band mirror. The front-side facet is used to couple to the SiN waveguide and is etched at an angle to prevent reflections into guided modes. The SOAs are designed to be heterogeneously integrated on a SiN-on-oxide feedback chip to form low-noise extended-cavity lasers, as shown in Figure 1(a). Here, an example design is pictured of a Fabry-Perot-type extended-cavity laser using the SOA, a taper for matching the mode shapes of the SOA and SiN modes for butt-coupling, a SiN waveguide spiral, and a narrow-band Bragg reflector.

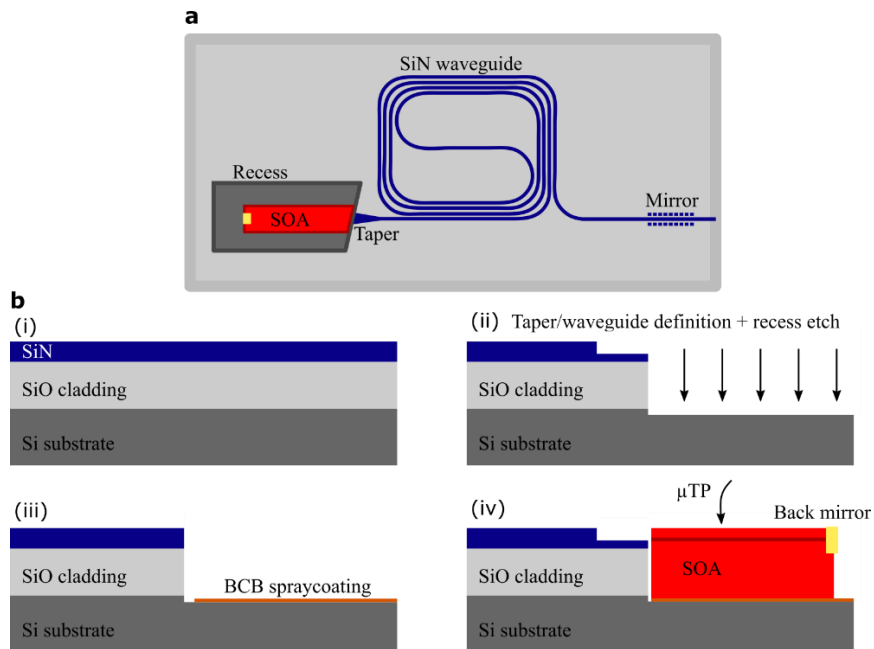


Figure 1: a) example of an heterogeneously integrated extended-cavity laser with a micro-transfer printed SOA in a recess, a SiN waveguide spiral, and a narrow-band Bragg grating. b) fabrication steps for SOA integration showing (i) unprocessed target wafer, (ii) taper/waveguide definition and recess etching, (iii) BCB bonding layer spray-coating and patterning, and (iv) micro-transfer printing of SOA into the recess using a polymer stamp.

The SOAs are coupled to the SiN feedback chip by micro-transfer printing them. Here, fully-processed SOA's are transferred into an etched recess, thereby aligning the SOA

mode with the SiN both horizontally and vertically. This shows the relative flexibility of the micro-transfer printing approach. The complete process flow for integration is shown in Figure 1(b). First, the waveguides are etched in the SiN, as well as the taper. To align the SOA mode with the SiN waveguide mode vertically, a recess is etched in the target chip. Since the (usually positive) slope of the sidewall of this recess will determine the minimum distance between the SOA facet and the SiN facet, the sidewall should be as straight as possible. Subsequently, a polymer bonding layer of benzocyclobutene (BCB) is spray-coated and patterned so it only covers the recess floor. This patterning can also allow to remove any sloping of the BCB up to the recess sidewall, which would complicate the transfer-printing alignment. Next, the pre-fabricated SOA is printed in the recess. Lastly, the whole chip can be cladded in oxide or BCB to further reduce reflections and the chip is metallized to form electrical contacts for the SOA.

The horizontal alignment is done using the transfer printer. Since the height of the quantum wells and thus the optical mode in the SOA is known very precisely, the depth of the recess can be made to match this to vertically align the SOA. Since the SOA is placed in a recess, it can be directly placed on the silicon (Si) substrate. In other methods, the SOA is always placed above the SiN and SiO layers, the latter insulates heat very well. This means this method provides much better heat sinking of the SOA to the Si substrate. Since heat generation is usually the main factor limiting with how much current a heterogeneously integrated laser can be pumped, this will allow for higher pump currents and thus laser output power.

### **Alignment simulations**

The most important consideration for the direct butt-coupling approach is the alignment tolerance. To verify the potential of this approach, therefore, finite-difference time domain (FDTD) simulations were performed using Lumerical's software suite. From optical mode simulations, the ideal cross-section for the SiN taper end was found to be 3000 nm by 80 nm, resulting in a mode overlap of 95% with the SOA mode, which is shown in Figure 2(a). This geometry was then used in an FDTD simulation to find the coupling efficiency between the two geometries for different misalignments. The optical propagation from the SOA to the SiN is plotted in Figure 2(b). To reduce reflections within the laser cavity, the GaAs waveguide is angled by 7 degrees and the SiN by the corresponding optimal angle following from Snell's law. Furthermore, a layer of SiN is present on the GaAs facet. This layer is an inherent product of the fabrication method of the SOA and can be tuned to form a simple anti-reflective (AR) coating.

The ideal case, where the SOA is printed directly against the recess edge, is plotted in Figure 2(c). However, in practice, this is very hard to realize. In work by Juvert et al. [4], coupons were shown to be printed within 1  $\mu\text{m}$  of the recess edge and mostly within a 1  $\mu\text{m}$  spread in lateral misalignment. In Figure 2(d), the coupling values for a facet distance of 1  $\mu\text{m}$  are therefore plotted. Clearly, within these misalignment values, theoretical coupling values in excess of 50% can be expected, showing the feasibility of this integration method.

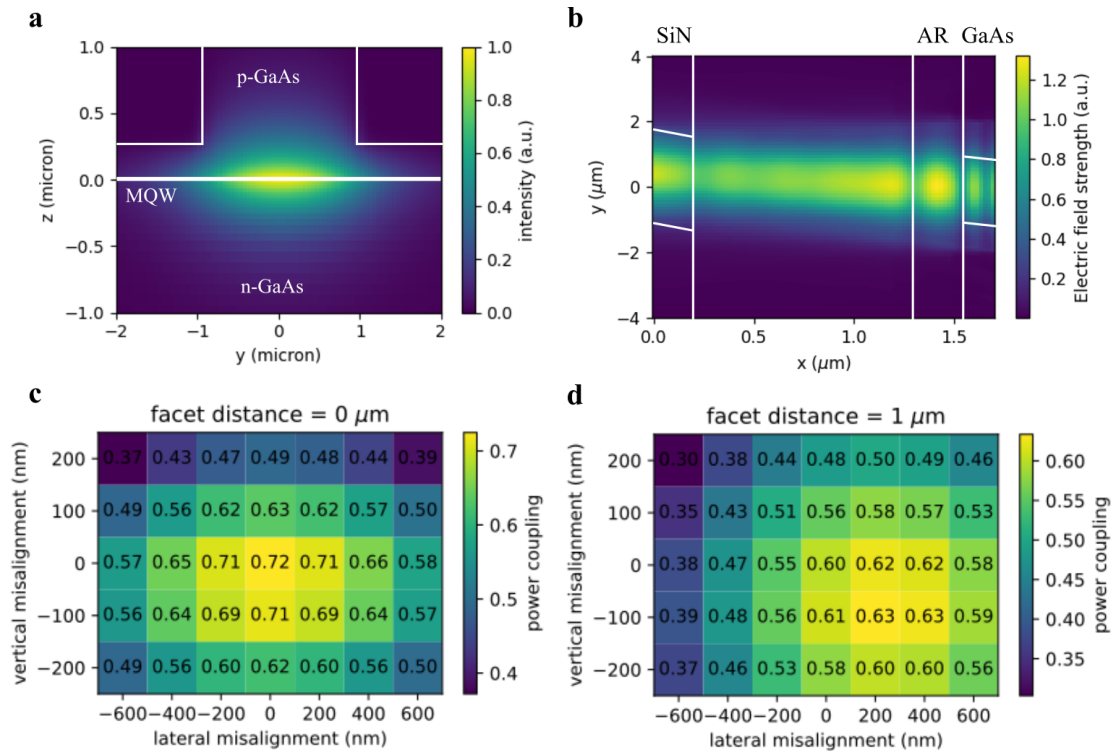


Figure 2: a) Optical mode of the GaAs SOA with outlines for the multiple quantum wells (MQW) and the ridge waveguide. b) Top-down view of the optical propagation from the GaAs to the SiN with outlines for the SiN waveguide and GaAs ridge, as well as the SiN AR coating. c) Power coupling heat map for a facet distance of  $0 \mu\text{m}$  (ideal case) for different alignments. d) Power coupling values for a facet distance of  $1 \mu\text{m}$  (realistic case).

## Conclusions

In conclusion, we demonstrate a novel coupling method for GaAs on SiN heterogeneously integrated lasers, using direct facet-coupling of GaAs SOAs micro-transfer printed in a recess. Here, we outline the integration method and show FDTD coupling simulations for misalignment in three dimensions, showing larger than 50% coupling efficiencies for realistic misalignment values. This method may allow for easier integration of GaAs on the SiN platform, allowing for applications such as OCT and Rubidium optical clocks.

## References

- [1] Xiang, Chao, Joel Guo, Warren Jin, Lue Wu, Jonathan Peters, Weiqiang Xie, Lin Chang et al. "High-performance lasers for fully integrated silicon nitride photonics." *Nature communications* 12, no. 1 (2021): 1-8.
- [2] de Beeck, Camiel Op, Bahawal Haq, Lukas Elsinger, Agnieszka Gocalinska, Emanuele Pelucchi, Brian Corbett, Günther Roelkens, and Bart Kuyken. "Heterogeneous III-V on silicon nitride amplifiers and lasers via microtransfer printing." *Optica* 7, no. 5 (2020): 386-393.
- [3] Tran, M.A., Zhang, C., Morin, T.J. et al. Extending the spectrum of fully integrated photonics to submicrometre wavelengths. *Nature* 610, 54–60 (2022).
- [4] Joan Juvert, Tommaso Cassese, Sarah Uvin, Andreas de Groote, Brad Snyder, Lieve Bogaerts, Geraldine Jamieson, Joris Van Campenhout, Günther Roelkens, and Dries Van Thourhout, "Integration of etched facet, electrically pumped, C-band Fabry-Pérot lasers on a silicon photonic integrated circuit by transfer printing," *Opt. Express* 26, 21443-21454 (2018)

# Design and optimization of an Er-doped Al<sub>2</sub>O<sub>3</sub> adiabatic waveguide taper for double layer integration with Si<sub>3</sub>N<sub>4</sub> platform

C. E. Osornio-Martínez, D. B. Bonneville, and S. M. García-Blanco

Integrated Optical Systems, MESA+ Institute for Nanotechnology, University of Twente, 7500 AE Enschede, The Netherlands.

*The integration of active-passive material platforms is needed to increase the number of optical components on-chip, i.e. achieve more functionalities on PICs. Adiabatic waveguide tapers are of great interest for applications that require short and low-loss transitions between different material platforms. In this work, an Er-doped Al<sub>2</sub>O<sub>3</sub> adiabatic waveguide taper is designed for the integration with the standard asymmetric double stripe (ADS) Si<sub>3</sub>N<sub>4</sub> TriPleX technology. The tolerance of the taper design to fabrication variations is studied in the wavelength range of 980 nm – 1630 nm. The simulated total loss of the final taper design is  $\leq 0.1$  dB per coupler.*

## Introduction

The integration of active-passive material platforms allows for more functionalities on Photonic Integrated Circuits (PICs). There are two main schemes for material integration, namely hybrid and monolithic integration. The monolithic integration scheme allows the incorporation of all the optoelectronic components on a single chip which results in compact devices and cost reductions [1]. For commercial applications, the transitions between the different material platforms should be compact and with low optical losses. One of the common techniques to achieve high-performance coupling between two waveguides is using adiabatic transitions [2]. In an adiabatic transition, the change from one waveguide to another should be smooth and gradual, e.g. by using a tapered section. With the slow variation of the geometry, the mode from the first waveguide evolves adiabatically (i.e. with negligible power losses) to the mode of the second waveguide.

## Device design

A 3D schematic of the double-layer integration of Er<sup>3+</sup>:Al<sub>2</sub>O<sub>3</sub> and Si<sub>3</sub>N<sub>4</sub> is shown in Fig. 1(a). The Er<sup>3+</sup>:Al<sub>2</sub>O<sub>3</sub> channel waveguides are separated by a thin SiO<sub>2</sub> layer from standard asymmetric double stripe (ADS) Si<sub>3</sub>N<sub>4</sub> TriPleX waveguides [3]. The thickness of the SiO<sub>2</sub> spacer is controlled by a chemical-mechanical polishing (CMP) step that is used to achieve a good surface uniformity. Typical thickness values are in the range of 200-300 nm. However, the spacer thickness can be further reduced down to 100 nm by locally etching in buffered HF.

Fig. 1(b-c) shows the cross-section (CS) schematic of the structure with the corresponding electric field intensity distribution of the fundamental TE mode at four distinct positions along the adiabatic coupler. The cross-sections are shown at the ADS Si<sub>3</sub>N<sub>4</sub> waveguide core [CS (i)], the ADS Si<sub>3</sub>N<sub>4</sub> waveguide core and tip of the Er<sup>3+</sup>:Al<sub>2</sub>O<sub>3</sub> lateral taper [CS (ii)], the tip of the ADS Si<sub>3</sub>N<sub>4</sub> lateral taper and the Er<sup>3+</sup>:Al<sub>2</sub>O<sub>3</sub> waveguide core [CS (iii)], and the Er<sup>3+</sup>:Al<sub>2</sub>O<sub>3</sub> waveguide core [CS (iv)]. The fundamental TE mode at the beginning/end of the coupler, i.e. CS (ii) or CS (iii), has a slightly different effective refractive index from the mode at the Si<sub>3</sub>N<sub>4</sub> waveguide [CS (i)] or Er<sup>3+</sup>:Al<sub>2</sub>O<sub>3</sub> waveguide [CS (iv)]. The change in effective refractive index produces a mode mismatch loss, visible in their electric field intensity distribution. Then, the mode continues propagating in the tapered region, where the power of the mode is transferred adiabatically from one

waveguide to the other. Therefore, the total loss of the coupler is the sum of the mode mismatch losses and the losses occurring in the tapered region.

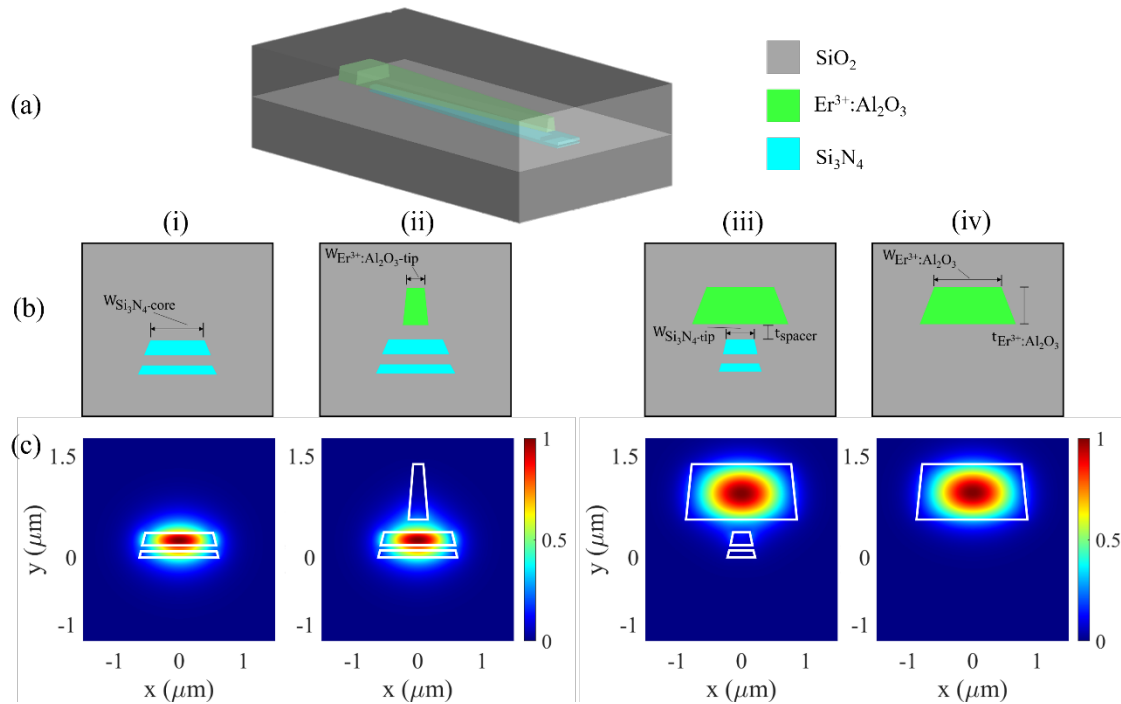


Fig 1. (a) 3D schematic of the coupling region for the double-layer integration of Si<sub>3</sub>N<sub>4</sub> and Er<sup>3+</sup>:Al<sub>2</sub>O<sub>3</sub>. (b) Schematic cross-sections at (i) the Si<sub>3</sub>N<sub>4</sub> core, (ii) the Si<sub>3</sub>N<sub>4</sub> core and tip of the Er<sup>3+</sup>:Al<sub>2</sub>O<sub>3</sub> taper, (iii) the tip of the Si<sub>3</sub>N<sub>4</sub> taper and the Er<sup>3+</sup>:Al<sub>2</sub>O<sub>3</sub> core, (iv) the Er<sup>3+</sup>:Al<sub>2</sub>O<sub>3</sub> core. (c) E-field intensity of the fundamental TE mode at the respective cross-sections.

## Simulation results

Simulations using Lumerical Mode Solutions software were performed to study the performance of the optical couplers considering fabrication tolerances. The methodology combines the Finite Difference Eigenmode (FDE) solver, for the mode field calculations and extracting the mode mismatch losses, and the EigenMode Expansion (EME) solver to calculate the losses in the tapered region.

For the design, the standard width of 1.1 μm was used for the Si<sub>3</sub>N<sub>4</sub> waveguide core. The Si<sub>3</sub>N<sub>4</sub> width is tapered laterally down to 300 nm with a taper angle of ~0.039° (i.e. taper length of 800 μm) based on previous work [4]. The minimum Si<sub>3</sub>N<sub>4</sub> width is limited by the resolution of the stepper lithography process. For the Er<sup>3+</sup>:Al<sub>2</sub>O<sub>3</sub> channel waveguide, a thickness of 800 nm was chosen for its application in waveguide amplifiers since it will allow for a high overlap (~80%) between the fundamental TE mode of the signal wavelength and gain material resulting in higher gain. The Er<sup>3+</sup>:Al<sub>2</sub>O<sub>3</sub> core width of 1.6 μm is tapered laterally down to 150 nm, with the same taper length as Si<sub>3</sub>N<sub>4</sub>, resulting in a taper angle of ~0.057°. The taper width was chosen based on the current achievable dimensions using Electron Beam Lithography (EBL, Raith EBP5150).

Five wavelengths are considered in the simulations: 980 nm and 1480 nm (i.e., pumping wavelengths for Er<sup>3+</sup>); 1532 nm, 1550 nm and 1630 nm (i.e., Er<sup>3+</sup> emission band). The refractive indices for the materials are extracted from experimental measurements (Woollam M-2000UI ellipsometer) and are summarized in Table 1. The simulation analysis focuses on the influence of the EBL process in lateral misalignment ( $\Delta x$ ) between

$\text{Si}_3\text{N}_4$  and  $\text{Er}^{3+}:\text{Al}_2\text{O}_3$ , the taper width variation of the  $\text{Er}^{3+}:\text{Al}_2\text{O}_3$  waveguide, and the thickness variation in the  $\text{SiO}_2$  spacer dependent on the CMP process.

Table 1. List of refractive indices used in the simulations.

Material	$\lambda = 980 \text{ nm}$	$\lambda = 1480 \text{ nm} - 1630 \text{ nm}$
$\text{Er}^{3+}:\text{Al}_2\text{O}_3$	1.726	$1.720 \pm 0.001$
$\text{Si}_3\text{N}_4$	1.993	$1.983 \pm 0.001$
$\text{SiO}_2$	1.455	$1.452 \pm 0.001$

In Fig. 2a the mode mismatch loss as a function of misalignment and  $\text{SiO}_2$  spacer thickness of the fundamental TE mode for case 1, i.e. comparison between [CS (i)] and [CS (ii)], and case 2, i.e. comparison between [CS (iii)] and [CS (iv)]. It is observed that the loss is below 0.06 dB for all the simulated wavelengths, misalignments and  $\text{SiO}_2$  spacer thicknesses. For case 1, the fundamental TE mode at 980 nm is highly confined to the  $\text{Si}_3\text{N}_4$  core and therefore the mode mismatch is lower compared to the longer wavelengths. It is observed that when the misalignment increases, the mode mismatch losses decrease. This is because the  $\text{Er}^{3+}:\text{Al}_2\text{O}_3$  taper tip has less influence in the effective refractive index change. A similar trend is observed for case 2, although with a 100 nm  $\text{SiO}_2$  spacer the mode mismatch at 980 nm wavelength and shorter misalignments is higher compared to the longer wavelengths. In this case, the  $\text{Si}_3\text{N}_4$  tip is closer to the  $\text{Er}^{3+}:\text{Al}_2\text{O}_3$  and it induces a relatively bigger change in the effective refractive index compared to the longer wavelengths. In Fig. 2b the mode mismatch loss, for case 1, as a function of misalignment and  $\text{Er}^{3+}:\text{Al}_2\text{O}_3$  taper tip width variation is shown. For these simulations, a  $\text{SiO}_2$  spacer of 200 nm was considered. A similar trend as described above is observed. As expected, for wider  $\text{Er}^{3+}:\text{Al}_2\text{O}_3$  taper tip widths, the change in effective refractive index is higher and therefore the mode mismatch loss is also higher. However, for all the taper tip width variations, the mode mismatch loss was below 0.1 dB.

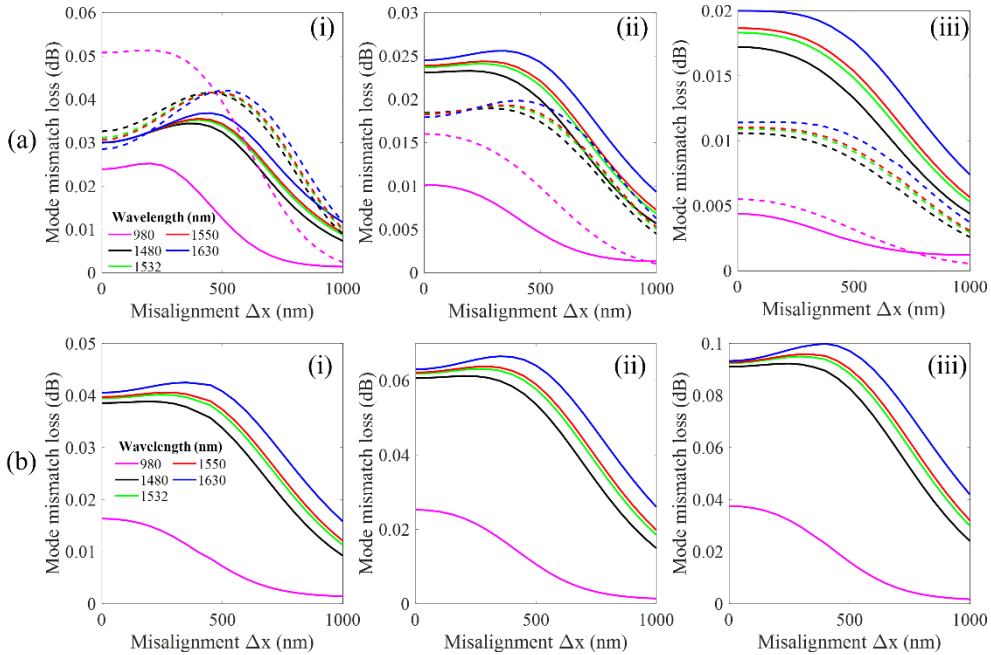


Fig 2. Mode mismatch losses for (a) A 150 nm wide  $\text{Er}^{3+}:\text{Al}_2\text{O}_3$  tip with  $\text{SiO}_2$  spacer thickness of (i) 100 nm, (ii) 200 nm, and (iii) 300 nm. Solid lines are for case 1 and dashed lines for case 2. (b) A 200 nm thick  $\text{SiO}_2$  spacer and  $\text{Er}^{3+}:\text{Al}_2\text{O}_3$  tip width of (i) 200 nm, (ii) 250 nm, and (iii) 300 nm.

The loss in the tapered region as a function of misalignment is presented in Fig. 3a. It is observed that for both considered  $\text{Er}^{3+}:\text{Al}_2\text{O}_3$  taper tip widths (150 nm and 300 nm) the loss is below 0.03 dB for the wavelength range of 1480 nm – 1630 nm. For 980 nm wavelength, the loss increases up to 1.8 dB for misalignment  $> 800$  nm. The total coupler loss, i.e. mode mismatch loss and the loss in the tapered region, is displayed in Fig. 3b. For the considered misalignments and taper widths, the total coupler loss is  $\leq 0.1$  dB for the wavelength range of 980 nm -1630 nm.

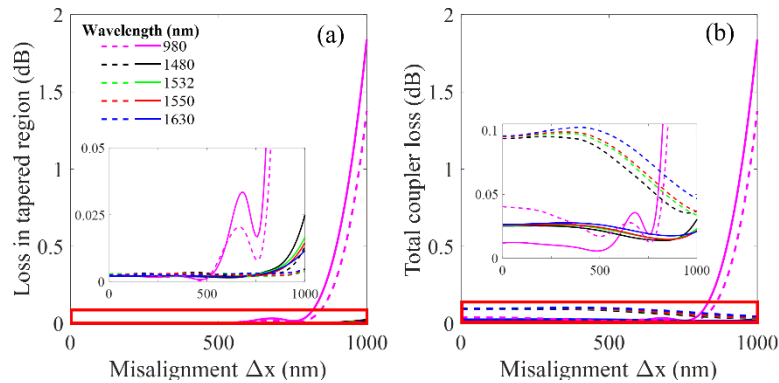


Fig 3. (a) Loss in 800  $\mu\text{m}$  long tapered region and (b) Total coupler losses for an  $\text{Er}^{3+}:\text{Al}_2\text{O}_3$  tip width of 150 nm (solid lines) and 300 nm (dashed lines). A  $\text{SiO}_2$  spacer thickness 200 nm was considered. Inset correspond to the section of the red boxes.

## Conclusion

In conclusion, an adiabatic optical coupler design for the integration of  $\text{Er}^{3+}:\text{Al}_2\text{O}_3$  in the commercial  $\text{Si}_3\text{N}_4$  TriPleX platform has been presented. The simulations show a low-loss ( $\leq 0.1$  dB) over a broad wavelength range (980 nm – 1630 nm) for an 800  $\mu\text{m}$  long taper section. The design high fabrication tolerances such as misalignment during the EBL process,  $\text{Er}^{3+}:\text{Al}_2\text{O}_3$  taper tip width variations, and thickness variations in the  $\text{SiO}_2$  spacer. The taper length could be further reduced by using different taper shapes by applying numerical methods as shown in [5].

## Funding

This project has received funding from the European Union’s Horizon 2020 research and innovation programme under grant agreement No 101017136. This result reflects only the author's view and the European Commission is not responsible for any use that may be made of the information it contains.

## References

- [1] N. Bamiedakis, K. A. Williams, R. V. Pentyl, and I. H. White, *Integrated and Hybrid Photonics for High-Performance Interconnects*, Sixth Edit., vol. 5A. Elsevier Inc., 2013.
- [2] X. Sun, H. Liu, and A. Yariv, “Mode Transformer in a Coupled-Waveguide System,” *Opt. Lett.*, vol. 34, no. 3, pp. 280–282, 2009.
- [3] C. G. H. Roeloffzen *et al.*, “Low-Loss  $\text{Si}_3\text{N}_4$  TriPleX Optical Waveguides: Technology and Applications Overview,” *IEEE J. Sel. Top. Quantum Electron.*, vol. 24, no. 4, pp. 1–21, 2018.
- [4] J. Mu, M. Dijkstra, J. Korterik, H. Offerhaus, and S. M. García-Blanco, “High-gain waveguide amplifiers in  $\text{Si}_3\text{N}_4$  technology via double-layer monolithic integration,” *Photonics Res.*, vol. 8, no. 10, p. 1634, 2020.
- [5] T. L. Liang *et al.*, “A fully numerical method for designing efficient adiabatic mode evolution structures (Adiabatic Taper, Coupler, Splitter, Mode Converter) applicable to complex geometries,” *J. Light. Technol.*, vol. 39, no. 17, pp. 5531–5547, 2021.

# Noise-induced pulse-timing statistics in an integrated two-section semiconductor laser with saturable absorber

L. Puts<sup>1</sup>, D. Lenstra<sup>1</sup>, W. Yao<sup>1</sup>

<sup>1</sup> Photonic Integration Group, department of Electrical Engineering, Eindhoven University of Technology, P.O. Box 513, Eindhoven 5600 MB, The Netherlands

Corresponding author: [l.puts@tue.nl](mailto:l.puts@tue.nl)

*We have analyzed and explained the generation of irregularly timed, spontaneous-emission triggered optical pulses from a two-section semiconductor laser with saturable absorber, operating near threshold in a regime of excitability. Here we focus on the statistics of the spontaneously emitted pulses. The numerical simulations and analytical theory are based on the Yamada model. The observed irregular pulse train intervals exhibit an initial refractory time, followed by a time interval until the next emitted pulse. The latter is analyzed in terms of a first-passage-time distribution for the intensity to diffuse from its equilibrium value to hit a larger threshold intensity for the first time. Analytic asymptotic short-time and long-time approximations have been derived.*

## Introduction

For decades, the human brain has been an inspiration to develop artificial neural networks, which consist of a highly interconnected network of neurons arranged in layers. After training the network with a specific dataset, a neural network is used to perform classification of input data. At the heart of such a network is the neuron itself, which effectively performs a non-linear operation. It was previously shown that from a dynamical perspective, a two-section semiconductor laser shows similar dynamics and spiking capabilities as biological neurons when operated close to its threshold [1]–[3]. Consequently, an integrated semiconductor laser may be a suitable candidate for a spiking neural network (SNN).

The dynamics are the result of the intracavity loss element next the gain element in an optical resonator, of which the recovery rate is different compared to the gain section recovery rate. When the laser is operated close to its threshold, it may be triggered by an external optical trigger, which means the laser is excitable. At this operation point, spontaneous emission is relatively high, and thus optical noise is present. The effect of optical noise on the spiking behavior of an excitable two-section laser was studied before in terms of jitter and amplitude deviations [4]. Recently, analytical expressions to describe the time distributions were derived based on the initial relative refractory period and a first passage time (FPT) principle [5]. In this paper, we present simulation results when the level of absorption in an excitable two-section laser is changed using a modified and normalized Yamada model, which includes a term for optical noise injection. We also present how the timing distributions change due to different absorption values and fit the asymptotic approximations based on previously developed theory [5].

## Normalized Yamada Rate Equations with Noise Injection

The structure under investigation is a two-section laser, consisting of a gain and saturable absorber section in an optical cavity, as shown schematically in Figure 1.



Figure 1: Schematic overview of the two section laser structure model. The optical cavity is formed by the two mirrors R, a loss section Q, and gain section G. The optical output is marked with I.

Under the assumption the optical intensity is uniform along the longitudinal axis, the loss and gain dynamics as well as the optical intensity can be modeled using the normalized Yamada model, which comprises a set of coupled differential equations for the gain  $G$ , loss  $Q$  and intensity  $I$  [3]:

$$\dot{G} = \gamma_G [A - G(t) - G(t)I(t)] \quad (1)$$

$$\dot{Q} = \gamma_Q [B - Q(t) - aQ(t)I(t)] \quad (2)$$

$$\dot{I} = \gamma_I [G(t) - Q(t) - 1]I(t) + \epsilon f(G) + \theta(t) + F_I(t) \quad (3)$$

with gain  $A$ , absorption  $B$ , recovery rates  $\gamma_G$ ,  $\gamma_Q$ , and  $\gamma_I$  for the gain, loss and intensity equations respectively, differential absorption relative to the differential gain  $a$ , spontaneous emission  $\epsilon f(G)$ , and optical injection  $\theta(t)$ . The influence of noise on the excitable responses is modeled using the white-noise fluctuating delta-correlated Langevin noise term  $F_I(t)$ . This term satisfies the following conditions for the first and second moments [6]:

$$\langle F_I(t) \rangle = 0 \quad (4)$$

$$\langle F_I(t)F_I(u) \rangle = 2D_{II}\delta(t - u) \quad (5)$$

with  $D_{II}$  the intensity diffusion coefficient. To find the numerical solution to the set of rate equations, on every integration step a random number is drawn from a Gaussian distribution with  $\mu = 0$  and  $\sigma^2 = 2R_S I \Delta t$ . Here,  $R_S$  is the average spontaneous emission rate, and  $\Delta t$  the fixed numerical integration timestep.

In Figure 2 and Figure 3, two simulated timetraces in units of photon lifetimes  $\tau_p$  for different values of  $B$  are shown. Depending on the absorption, the density of intensity pulses changes. From visual inspection it is clear that the time between consecutive pulses (indicated by the inset in Figure 3) seems more consistent at a low level of absorption.

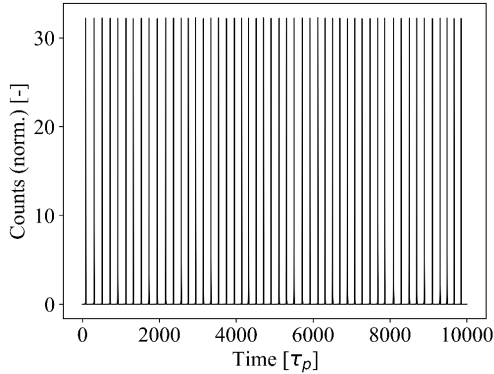


Figure 2: Simulated timetrace using  $B=3.6540$ ,  $A=4.5$ ,  $\gamma_G=0.05$ ,  $\gamma_Q=0.1$ ,  $\gamma_I=1$ ,  $a=5$ .

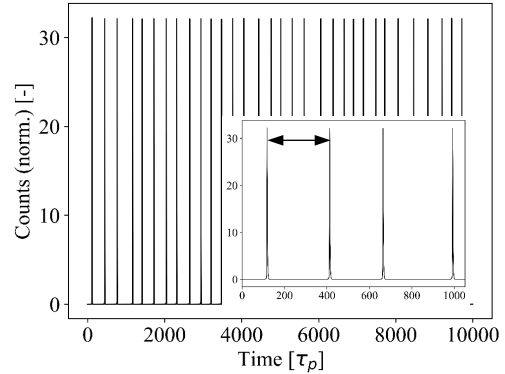


Figure 3: Simulated timetrace using  $B=3.6740$ ,  $A=4.5$ ,  $\gamma_G=0.05$ ,  $\gamma_Q=0.1$ ,  $\gamma_I=1$ ,  $a=5$ .

Inset: zoomed in timetrace indicating the time between consecutive pulses.

## Timing Statistics

Next, the timing statistics are further investigated. Figure 4 shows the time distributions for eight different levels of absorption, ranging from  $B=3.6500$  (low) to  $B=3.6780$  (high). The distributions are obtained by simulating 170 timetraces while registering the time between consecutive pulses. In all cases, the distributions are asymmetric and positively skewed, which means the distributions are characterized by a sharp onset followed by a long tail. For low absorption (in blue) the distribution is relatively narrow, whereas for high absorption (in yellow) the distribution is spread out in time. The dead-time before the sharp onset occurs is related to the relative refractory period, which is the time needed for the gain and absorption to recover to a steady state, and the first passage time, which is a stochastic quantity. The latter follows a first-passage-time-distribution (FPTD) [5] and from Figure 4 it follows that this quantity is shortest when the absorption is low.

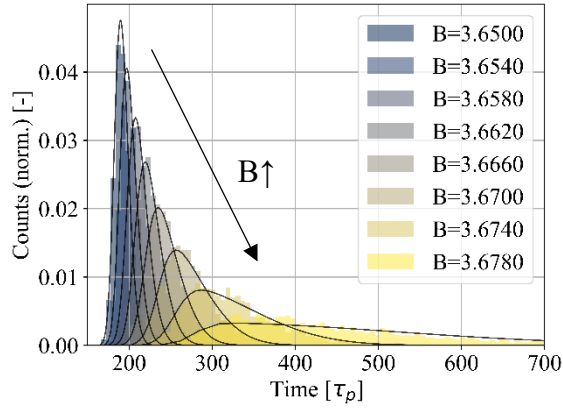


Figure 4: Simulated histograms for 8 values of  $B$ ,  $A=4.5$ ,  $\gamma_G=0.05$ ,  $\gamma_Q=0.1$ ,  $\gamma_I=1$ ,  $a=5$ , and corresponding fits. The number of samples for every histogram is 8699, 8336, 7869, 7383, 6799, 6056, 5051, and 3497, respectively.

The sharp onset and long tail of the simulated histograms in Figure 4 can be expressed by two analytical approximations, which are the short-time Eq. (6) and large-time approximation Eq. (7), and are given by [5]:

$$P_{first}(T; I_i, I_C) = \frac{(I_C - I_i)}{\sqrt{4\pi\mathcal{D}T^3}} e^{-\frac{(I_C - I_i)^2}{4\mathcal{D}T}} \quad (6)$$

$$P_{first}(T; I_0, I_C) = e^{-\left(1 + \frac{T}{T_{I_0, I_C}}\right)} \frac{I_{Bessel,1} \left( 2 \sqrt{\frac{T}{T_{I_0, I_C}}} \right)}{\sqrt{T_{I_0, I_C} T}} \quad (7)$$

with excitability threshold value  $I_C$ , initial intensity  $I_i$ , diffusion coefficient  $\mathcal{D} = 2R_s I_0$ , time  $T$ , the characteristic time related to the first passage from  $I_0$  to  $I_C$ ,  $T_{I_0, I_C}$ , and the modified Bessel function of the first kind  $I_{Bessel,1}$ .

For two of the cases shown in Figure 4 the short-time and large-time approximations are fitted to the simulated histograms, which are shown in Figure 5 and Figure 6 using the dashed and dash-dotted lines, respectively. The simulation parameters are the same as mentioned before.

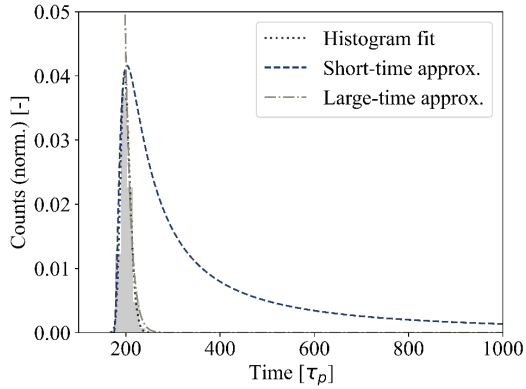


Figure 5: Simulated histogram using  $B=3.6540$  and fitting parameters  $I_C=13.0$ ,  $I_0=1.8$ ,  $R_s=0.18$ , and  $T_{10,IC}=8.0$ .

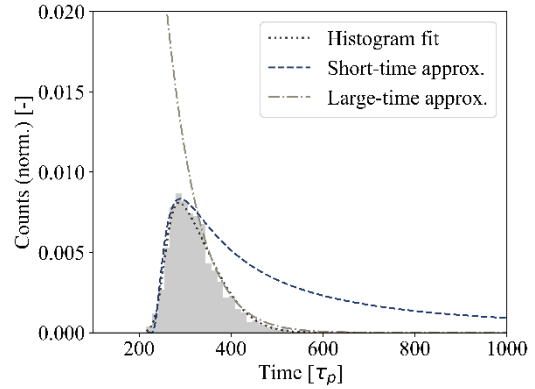


Figure 6: Simulated histogram using  $B=3.6740$  and fitting parameters  $I_C=18.6$ ,  $I_0=1.8$ ,  $R_s=0.18$ , and  $T_{10,IC}=41.0$ .

In both cases, the short-time and large-time approximations fit the simulated histogram accurately, indicating the asymptotic models accurately describe the noised induced spiking distributions.

## Conclusion

A two-section laser, or integrated optical neuron operated in the excitable regime, close to its lasing threshold, can be triggered by noise to generate an optical pulse. We have shown using the normalized Yamada model with an optical noise term that the pulse density and timing statistics are a function of the level of absorption. Asymptotic analytical models, based on the initial relative refractory period and a first passage time (FPT) principle, accurately describe the short-time and large-time behavior of the simulated timing histograms.

## References

- [1] L. Puts, D. Lenstra, and W. Yao, "Measurements and modeling of a monolithically integrated self-spiking two-section laser in InP," *IEEE Journal of Quantum Electronics*, Accepted.
- [2] L. Puts, W. Yao, and D. Lenstra, "Modeling a Spiking Optical Neuron using Normalized Yamada Rate Equations," in *25th Annual Symposium of the IEEE Photonics Benelux*, Mons, Belgium, Nov. 2021, p. 4.
- [3] M. A. Nahmias, B. J. Shastri, A. N. Tait, and P. R. Prucnal, "A Leaky Integrate-and-Fire Laser Neuron for Ultrafast Cognitive Computing," *IEEE J. Sel. Top. Quantum Electron.*, vol. 19, no. 5, pp. 1–12, Sep. 2013, doi: 10.1109/JSTQE.2013.2257700.
- [4] J. L. A. Dubbeldam, B. Krauskopf, and D. Lenstra, "Excitability and coherence resonance in lasers with saturable absorber," *Phys. Rev. E*, vol. 60, no. 6, pp. 6580–6588, Dec. 1999, doi: 10.1103/PhysRevE.60.6580.
- [5] D. Lenstra, L. Puts, and W. Yao, "First-passage-time analysis of the pulse-timing statistics in a two-section semiconductor laser under excitable and noisy conditions," *Photonics*, Accepted.
- [6] G. H. M. van Tartwijk and D. Lenstra, "Semiconductor lasers with optical injection and feedback," 1995. *Quantum Semiclassical Opt. J. Eur. Opt. Soc. Part B*, 7 87-143. <https://iopscience.iop.org/article/10.1088/1355-5111/7/2/003>

# Design and analysis of high-density SOA arrays on indium phosphide

S.F.G. Reniers,<sup>1</sup> W.P. Voorthuijzen,<sup>1,2</sup> M.J.R. Heck<sup>1</sup> and Y. Jiao<sup>1</sup>

<sup>1</sup> Eindhoven University of Technology, De Groene Loper 19, 5612 AP Eindhoven, The Netherlands

<sup>2</sup> SMART Photonics, HTC 29, 5656 AE Eindhoven, The Netherlands

*Applications such as optical switch matrices and optical phased arrays require many integrated components, e.g. semiconductor optical amplifiers (SOAs). We present a novel solution for increasing the density of SOAs using the open-mask regrowth technique which can eliminate the loading effect and growth rate enhancement which are typically seen for large-area or high-density active blocks. We designed SOA arrays using the proposed technique on a generic indium phosphide platform. In parallel, a systematic approach towards enabling transfer printing of SOA arrays on a single coupon is introduced. Thermal simulations of SOA arrays on a substrate and coupon show that arrays with several SOAs on a single coupon are possible with minor thermal penalty. Finally, the experimental plan on a generic indium phosphide platform is presented.*

## Introduction

A monolithically integrated light amplification component is a key advantage of indium phosphide (InP) based photonic integration platforms. With the rapid developments of LiDAR and the ever-increasing bandwidth requirements for various applications, e.g. for optical switch matrices [1], neural networks [2] and programmable photonic circuits [3], the density on our optical chips is being pushed continuously. On integrated photonic platforms, the placement of highly dense SOA arrays can be challenging for several reasons, which can be categorized as optical, thermal, electrical and fabrication [4] limitations. For the scope of this paper, we will focus on the thermal and fabrication limitations of high-density arrays.

Micro-transfer-printing enables the integration of III-V coupons on silicon-based platforms [5], which combines the active components on the coupon with the low-loss silicon platform. In this paper, SOA arrays on InP substrates and InP coupons will be compared.

## Fabrication challenges and solutions

On a typical InP integration platform, a regrowth step is carried out to define where the active and passive components are placed in the circuit. When placing SOA building blocks in dense arrays, one runs into issues with the regrowth of the passive layers, due to an effect called growth rate enhancement (GRE). This GRE appears when SOA arrays are densely spaced, which is named the loading effect, or when the active area that is covered during the regrowth process is too large [6]. These effects can cause issues in the butt-joint connection between the SOAs and passive waveguides, which can lead to high coupling losses and reflections.

To avoid the GRE effect, an improvement to the regrowth process is proposed. This method is introduced for the first time in [4], and utilizes a hollow-mask approach to prevent GRE around close to the active islands. As a result, the GRE is not impacted by

the size of the active islands. To illustrate this solution, a schematic step-by-step view of this solution is shown in Fig. 1.

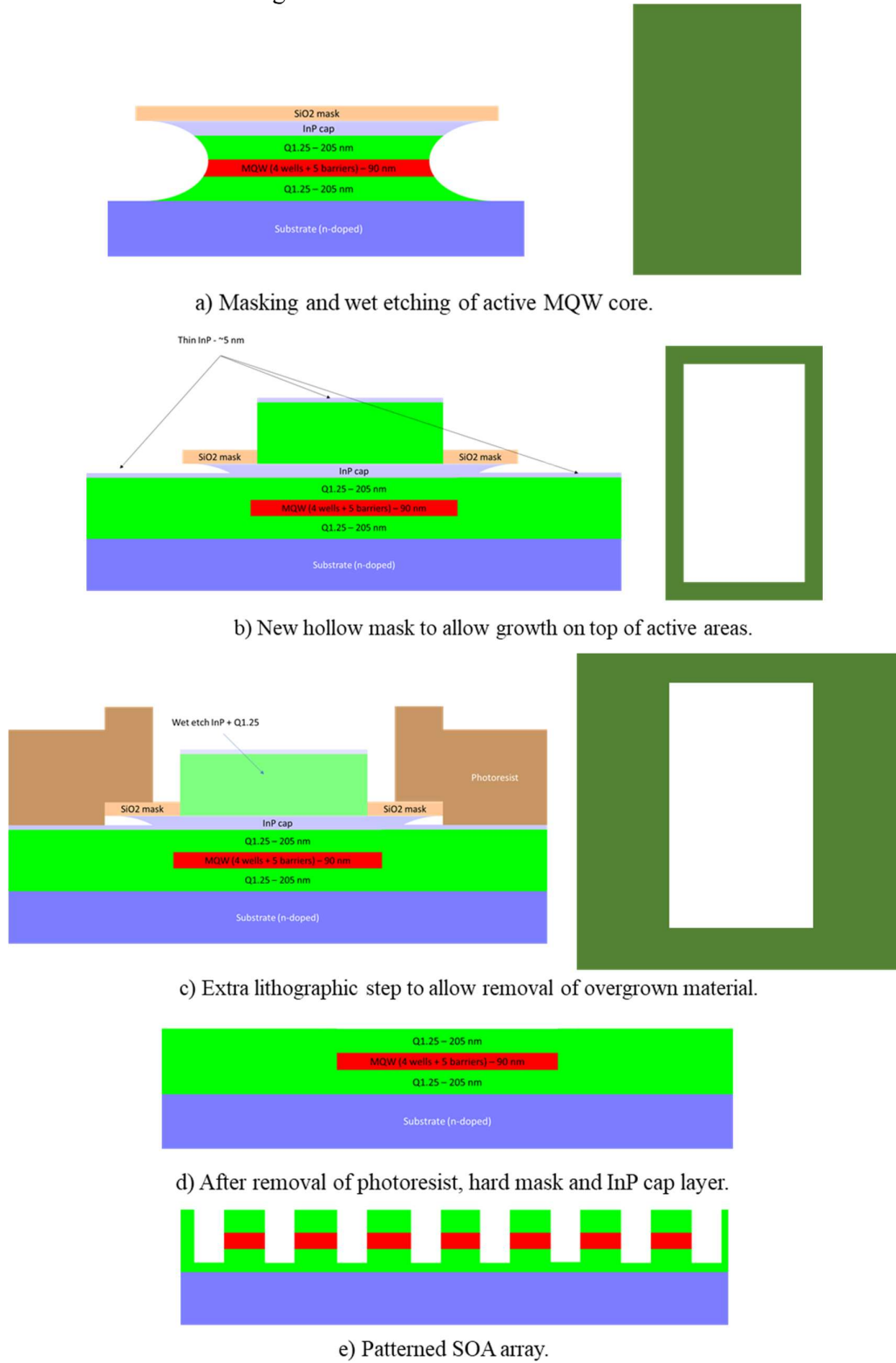


Figure 1 – Key steps of the hollow-mask regrowth scheme (not drawn to scale).

## Thermal challenges and solutions

Placing multiple SOAs in a dense array, results in higher thermal crosstalk and a more challenging thermal management. We investigated the thermal performance of SOA arrays on InP substrates and transfer-printed coupons using commercial simulation software.

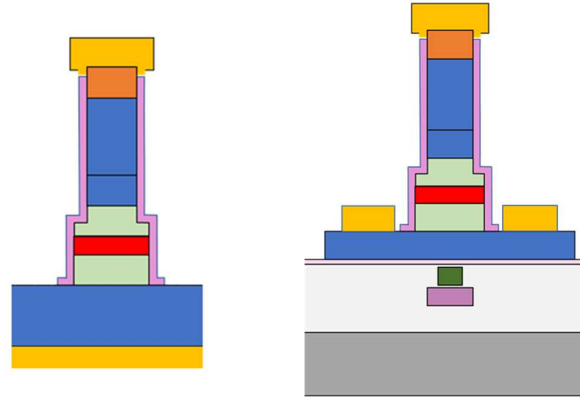


Figure 2 – Cross section of a monolithically integrated SOA (left) and micro-transfer-printed SOA (right).

For substrate based arrays and coupons, the cross section is shown in Fig. 2. Since the typical upper limit of a coupon width for micro-transfer-printing is around  $100\ \mu\text{m}$ , the pitch of the SOAs in the array has to be chosen carefully. The thermal input power for each SOA is chosen to be  $100\ \text{mW}$  for an SOA length of  $500\ \mu\text{m}$ , which is around the typical operating point. The output of the simulation provides the temperature increase in the SOA core, for each SOA in the array. We are showing the highest temperature reached in the array, typically of the center SOA. The temperature increase of substrate-based and transfer-printed SOAs is shown in Fig. 3.

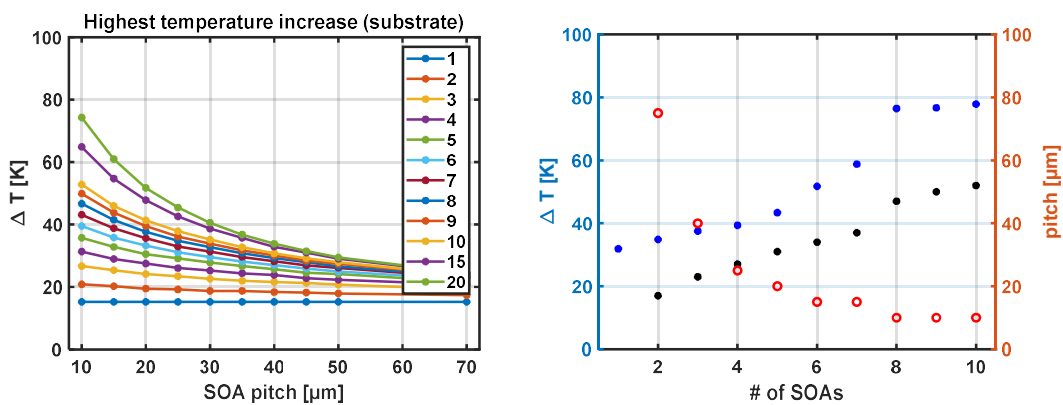


Figure 3 – The temperature increase in the center SOA of an array on substrate (left) and on a transfer-printed coupon (right). On the left  $\Delta T$  is shown for various SOA pitches (x-axis) and number of SOAs in array (legend). On the right  $\Delta T$  is shown for a  $100\ \mu\text{m}$  wide coupon with one to ten SOAs (x-axis) with optimized pitch. In black, the equivalent is shown for substrate-based arrays.

From the substrate-based figure, we can conclude that with a 70  $\mu\text{m}$  pitch the thermal penalty is as low as 10°C up to arrays with 20 SOAs. When decreasing the pitch, the thermal penalty is increases as expected. The impact on the SOA performance is still to be experimentally investigated for transfer-printed SOAs.

The coupon-based arrays demonstrate a more dramatic impact. For example, if placing 10 SOAs with 10  $\mu\text{m}$  pitch on a coupon, the thermal penalty is almost 80°C, where on a substrate this only gives a slightly over 50°C increase in temperature. In Fig. 3 (right) the increased thermal penalty of the coupon-based arrays with respect to the substrate-based ones can be observed. In this case, the pitch on the substrate is chosen equal to the pitch on the coupon. The increase in thermal penalty is between 12 and 32 degrees, depending on the number of SOAs in the array. The increase in thermal penalty from one to five SOAs on a single coupon is only slightly above 10°C, which indicates that up to this array size, the thermal penalty is expected to give acceptable SOA performance. An experimental plan to verify these simulations has been designed on both a monolithic InP and coupon-based platform.

## Conclusion

In this paper, we present the main thermal challenges and fabrication challenges for making dense SOA arrays on InP substrates and transfer-printed coupons. Solutions to overcome these challenges have been presented, and supporting simulations are carried out to identify the possibilities on both platforms. An experimental plan is crafted to verify the novel regrowth strategy to enable dense SOA arrays on active-passive indium phosphide platforms, and to verify the simulated thermal behavior of dense arrays.

## Acknowledgements

The authors acknowledge the Horizon 2020 INSPIRE project.

## References

- [1] R. Stabile, A. Rohit, and K. A. Williams, "Dynamic multi-path WDM routing in a monolithically integrated  $8 \times 8$  cross-connect," *Opt. Express*, vol. 22, no. 1, p. 435, Jan. 2014, doi: 10.1364/OE.22.000435.
- [2] B. Shi, N. Calabretta, and R. Stabile, "Deep Neural Network Through an InP SOA-Based Photonic Integrated Cross-Connect," *IEEE J. Sel. Top. Quantum Electron.*, vol. 26, no. 1, pp. 1–11, Jan. 2020, doi: 10.1109/JSTQE.2019.2945548.
- [3] W. Bogaerts *et al.*, "Programmable photonic circuits," *Nature*, vol. 586, no. 7828, pp. 207–216, Oct. 2020, doi: 10.1038/s41586-020-2764-0.
- [4] F. Lemaitre, S. Kleijn, A. J. Millan-Mejia, K. Williams, and V. Dolores-Calzadilla, "High Density Integration of Semiconductor Optical Amplifiers in InP Generic Photonic Integration Technology," *IEEE J. Sel. Top. Quantum Electron.*, pp. 1–6, 2022, doi: 10.1109/JSTQE.2022.3210663.
- [5] C. A. Bower, M. Meitl, and D. Kneeburg, "Micro-Transfer-Printing: Heterogeneous integration of microscale semiconductor devices using elastomer stamps," in *IEEE SENSORS 2014 Proceedings*, Valencia, Spain, Nov. 2014, pp. 2111–2113. doi: 10.1109/ICSENS.2014.6985454.
- [6] Y. Wang *et al.*, "Versatile butt-joint regrowth for dense photonic integration," *Opt. Mater. Express*, vol. 11, no. 8, p. 2478, Aug. 2021, doi: 10.1364/OME.431963.

# Monolithically Integrated Temperature Sensor in an InP-based Generic Integration Technology

W. Tian,<sup>1\*</sup> B. J. A. Bas,<sup>1</sup> D. A. Harmsen,<sup>1</sup> P. van den Berg,<sup>1</sup> R. de Meulder,<sup>1</sup>  
D. Pustakhod,<sup>2</sup> K. A. Williams,<sup>1</sup> and X. J. M. Leijts<sup>1</sup>

<sup>1</sup> Eindhoven Hendrik Casimir Institute, Eindhoven University of Technology,  
5600 MB Eindhoven, The Netherlands

<sup>2</sup> Photonic Integration Technology Center (PITC), 5600 MB Eindhoven, The Netherlands

*We have developed various monolithically integrated temperature sensors to locally measure the temperature of InP-based photonic integrated circuits. These sensors are based on InP diodes with either an active multi-quantum well structure or a passive bulk quaternary structure. They have been fabricated in the generic integration process of SMART Photonics. We theoretically and experimentally explored the temperature dependence in the diode characteristics. Our results show that the devices are suitable for on-chip monitoring of the operating temperature of photonic integrated circuits. Integrating a temperature sensor on-chip enables a more local temperature measurement compared to using an external temperature sensor. This should be advantageous for temperature control of photonic integrated circuits.*

## Introduction

Photonic integrated circuits (PICs) have received considerable interest and are finding their way into many applications, such as optical communications, LIDAR, and quantum information processing [1-3]. PICs, with a broad range of functionalities, can be created using generic integration technology. Based on indium phosphide (InP), this technology is an integration process with basic building blocks, such as semiconductor optical amplifiers (SOAs), phase modulators (PMs), and photodetectors. The generic integration technology helps reduce the prototyping costs and throughput time of PICs by using highly standardized processes [1].

High-performance and multi-functional PICs are sensitive to temperature changes, such as SOAs, micro-ring resonators, and lasers [4]. Accurate thermal measurement and temperature control of PICs are important for many applications. Conventionally, discrete temperature sensors, such as thermistors, thermocouples, and resistive temperature detectors, have been used [5, 6]. However, they are bulky and add to the complexity of a system. In addition, these bulk sensors are placed separately in photonic modules and are at some distance from the PICs, which increases the overall module size and measures the temperature at a different location.

Integrated temperature sensors are favorable because of their compact size and local thermal measurement, which therefore provides more precise temperature control of the PICs. A diode temperature sensor is a basic and accurate integrated temperature sensor. The diode sensor is a commonly used integrated temperature sensor in CMOS technology [6]. However, such a diode structure is not being used for temperature sensing and monitoring purposes for InP-based PICs.

In this work, we designed various monolithically integrated temperature sensors based on InP pin diodes. We exploited the temperature dependence of the diode current-voltage (I-V) characteristics. Experimental results confirm that this can be used for local thermal measurement and temperature control of InP-based PICs.

## Concept

The forward voltage of a diode has a linear dependency on temperature when the diode is driven by a constant current [5, 6]. Two types of integrated temperature sensors are proposed which stem from two diode basic building blocks in the InP-based generic integration technology: an SOA with an active multi-quantum well (MQW) structure, and a PM with a passive bulk quaternary structure (Q1.25). Figure 1 shows a simplified schematic of the two different layer structures. Both building blocks are pin diodes and can be used for temperature sensing.

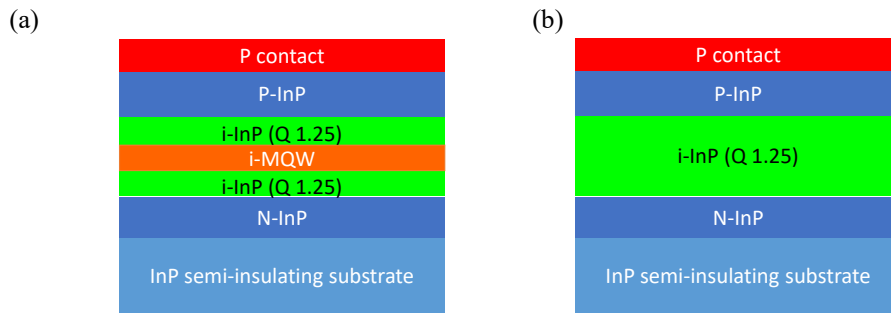


Figure 1. Simplified schematic of the layer stacks of the integrated temperature sensors stemming from two basic building blocks in the InP-based generic integration technology: (a) The SOA-type: layer stack of the active multi-quantum well structure; (b) The PM-type: layer stack of the passive bulk quaternary structure.

The integrated temperature sensor is schematically depicted in Figure 2. It is composed of either an SOA or PM building block and an etched trench around it. The trench is designed to prevent leaking currents and scattering light from surrounding devices. Note that the PM-type sensor is less affected by light on the chip. The sensors were fabricated by SMART Photonics which offers InP-based generic integration technology.

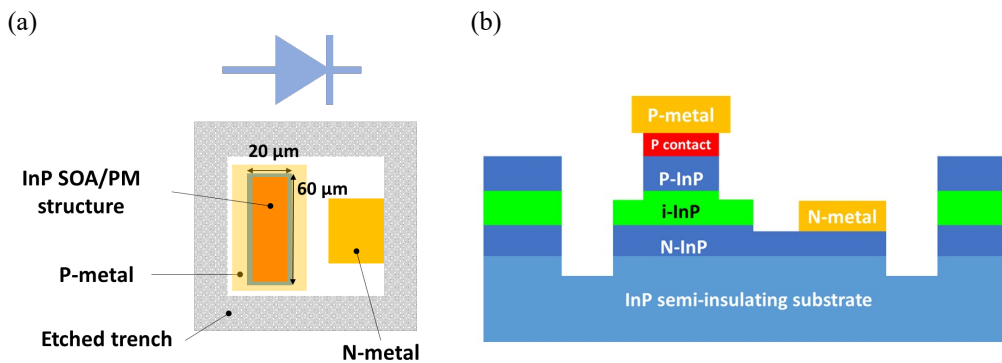


Figure 2. Schematic of an integrated temperature sensor: (a) Simplified top-view layout of an integrated temperature sensor of width = 20 μm and length = 60 μm.; (b) Simplified cross-section view of an integrated temperature sensor with the PM-type passive layer stack.

## Simulation

We simulated both types of diodes in Harold software from Photon Design which is an advanced hetero-structure simulator. In the simulation, we constructed the layer stacks of both diodes shown in Figure 1. Low current densities were used ranging from  $1 \times 10^{-4}$  A/cm<sup>2</sup> to 50 A/cm<sup>2</sup>, which corresponds to currents of  $1 \times 10^{-9}$  A to  $5 \times 10^{-4}$  A in a diode that measures 10 μm x 100 μm. Using low currents can minimise self-heating in the diodes. Then, the forward voltages of the diodes were simulated at temperatures ranging from 0 - 300 °C. The simulation results are shown in Figure 3.

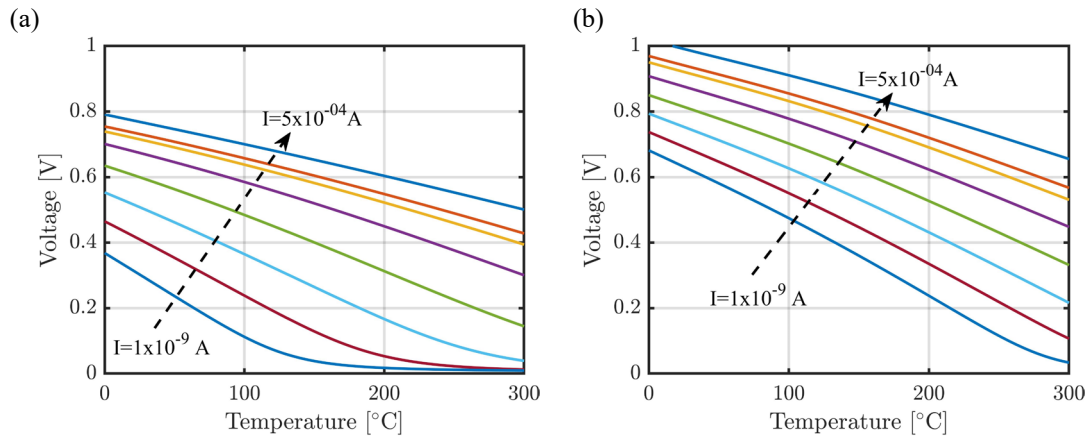


Figure 3. Simulated forward voltage-temperature (V-T) relation of two types of integrated temperature sensors ( $10 \mu\text{m} \times 100 \mu\text{m}$ ) operated in forward current mode over temperature range of 0 - 300 °C: (a) The SOA-type sensor with an active multi-quantum well structure; (b) The PM-type sensor with a passive bulk quaternary structure. In both plots: 8 curves, from bottom left to top right, represent currents of  $1 \times 10^{-9}$ ,  $1 \times 10^{-8}$ ,  $1 \times 10^{-7}$ ,  $1 \times 10^{-6}$ ,  $1 \times 10^{-5}$ ,  $5 \times 10^{-5}$ ,  $1 \times 10^{-4}$ ,  $5 \times 10^{-4}$  A.

For both types of integrated temperature sensors, a linear dependency between forward voltage and temperature was observed. Besides that, using a higher forward-bias current leads to a wider linear range. However, there is a trade-off between the linear range and the sensitivity depending on the forward-bias currents. The sensitivity of a diode temperature sensor is given by the slope of the voltage-temperature (V-T) curve in the linear dependency range. For both types of sensors, using a lower forward-bias current leads to a steeper slope, which represents a higher sensitivity. In detail, the sensitivity of the SOA-type sensor varies from  $-0.9$  to  $-2.6 \text{ mV}/^\circ\text{C}$  in correlation with the variation in current from  $5 \times 10^{-4}$  to  $1 \times 10^{-9}$  A. For the PM-type sensor driven by the same current range, its sensitivity varies from  $-1.1$  to  $-2.1 \text{ mV}/^\circ\text{C}$ . Overall, the sensitivity of both types of InP-based integrated temperature sensors is in the same range as CMOS sensors, which is  $-1.2$  to  $-2.2 \text{ mV}/^\circ\text{C}$  [6].

## Experimental Results

A chip with several integrated temperature sensors was mounted on a copper block, of which the temperature is controlled by a thermoelectric cooler (TEC) and monitored by a reference thermistor. The electrical signals to the diode were set and measured by Keithley 2402B source meter. At first, we measured the I-V characteristics of both types of sensors with the same dimension at temperatures of 20, 40, and 60 °C. Results are shown in Figure 4(a) and (b): in both types of sensors, the forward voltage decreases with increasing temperature at the same current levels, for example, at 100  $\mu\text{A}$ .

Then, we measured the V-T relation of both types of integrated temperature sensors in a wider temperature range of 18 to 60 °C, using four constant driving currents of 10, 50, 100, and 500  $\mu\text{A}$ , as shown in Figure 4(c) and (d). The voltage was measured during temperature rising (18 to 60 °C) and temperature falling (60 to 18 °C), which is a typical operating temperature range of PICs. Both types of sensors show linear dependency between forward voltage and temperature. Besides, the slopes of V-T curves in Figure 4(d) are steeper than the slopes in Figure 4(c). It means that the sensitivity of the PM-type sensor,  $-1.7$  to  $-2.2 \text{ mV}/^\circ\text{C}$ , is higher than the sensitivity of SOA-type,  $-1.0$  to  $-1.4 \text{ mV}/^\circ\text{C}$ , at currents of 10, 50, 100, and 500  $\mu\text{A}$ .

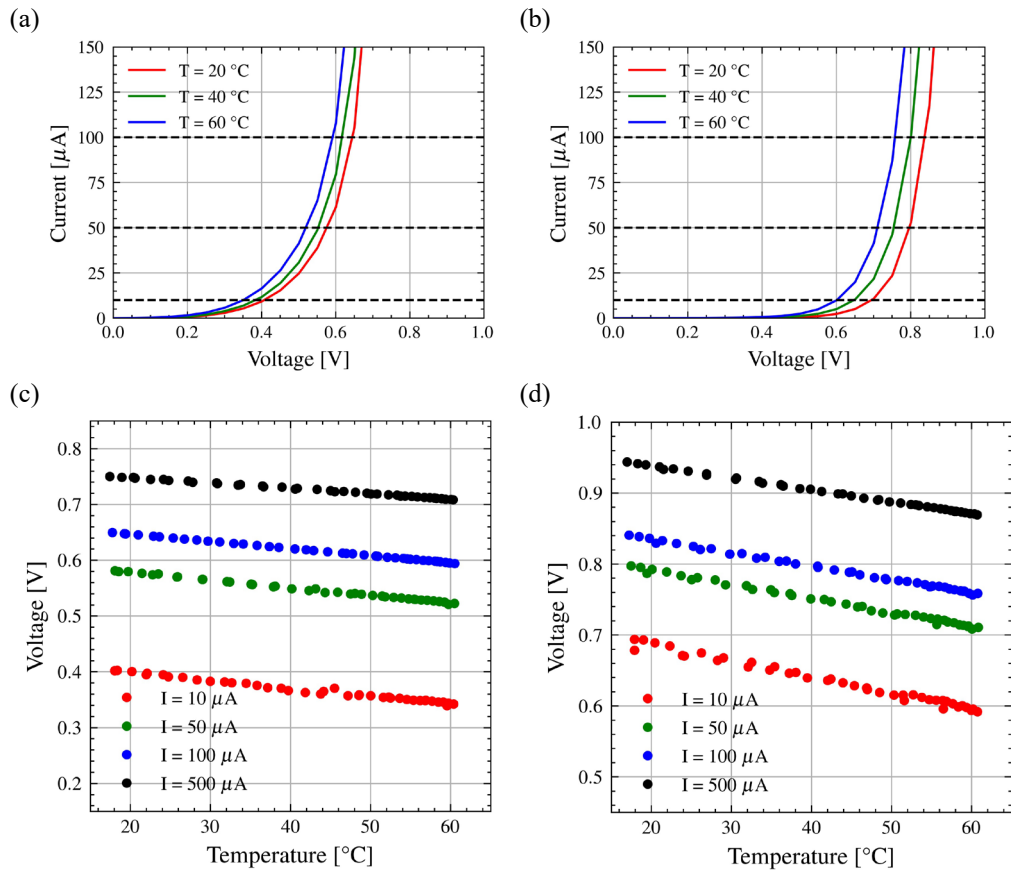


Figure 4. Experimental results. (a) and (b): Comparison of I-V characteristics of (a) the SOA-type and (b) the PM-type of integrated temperature sensors at temperatures of 20, 40, and 60 °C. (c) and (d): Comparison of V-T relation of (c) the SOA-type and (d) the PM-type of integrated temperature sensors at temperature ranging from 18 to 60 °C. Both diodes have the same dimension of 20 x 60  $\mu\text{m}$ .

## Conclusion

In this paper, we proposed integrated temperature sensors based on pin diodes stemming from two basic building blocks, SOA and PM, in the InP-based generic integration technology. Both types of sensors show linear dependency between forward voltage and temperature at the current injection mode. Their sensitivity is comparable to CMOS sensors [6]. Especially, the PM-type sensor shows higher sensitivity and is less affected by light on the chip which is more favorable than the SOA-type sensor. The results are promising for on-chip thermal management and temperature control of PICs.

## References

- [1] M. Smit, X. Leijtens, et. al., "An introduction to InP-based generic integration technology," *Semiconductor Science and Technology*, vol. 29, no. 8, 2014.
- [2] T. Baba, et. al., "Silicon Photonics FMCW LiDAR Chip with a Slow-Light Grating Beam Scanner," *IEEE Journal of Selected Topics in Quantum Electronics*, vol. 28, no. 5, pp. 1-8, 2022.
- [3] A. Elshaari, et. al., "Hybrid integrated quantum photonic circuits," *Nat Photonics*, vol. 14, no. 5, 2020.
- [4] L. Carroll, J.-S. Lee, et. al., "Photonic Packaging: Transforming Silicon Photonic Integrated Circuits into Photonic Devices," *Applied Sciences*, vol. 6, no. 12, 2016.
- [5] G. C. M. Meijer, "Thermal sensors based on transistors," *Sensors and Actuators*, vol. 10, no. 1, pp. 103-125, 1986/09/10/, 1986.
- [6] F. Udrea, S. Santra, and J. W. Gardner, "CMOS temperature sensors - concepts, state-of-the-art and prospects." in 2008 International Semiconductor Conference, vol. 1, 2008, pp. 31-40.

# Improving Alignment of Free-Space Coupling of Multi-Mode Fibres using Off-Axis Digital Holography

Menno van den Hout<sup>(1,\*),</sup> Sjoerd van der Heide<sup>(1),</sup> Thomas Bradley<sup>(1),</sup>  
Amado M. Velazquez-Benitez<sup>(1),(2),</sup> Ali Mefleh<sup>(3),</sup> and Chigo Okonkwo<sup>(1)</sup>

<sup>(1)</sup> High Capacity Optical Transmission Laboratory, Electro-Optical Communications Group,  
Eindhoven University of Technology, the Netherlands <sup>(\*)</sup> [m.v.d.hout@tue.nl](mailto:m.v.d.hout@tue.nl)

<sup>(2)</sup> Instituto de Ciencias Aplicadas y Tecnología, Universidad Nacional Autónoma de México, Mexico

<sup>(3)</sup> KPN, Technology, Innovation, Roadmap & Architecture, The Hague, the Netherlands

*Off-axis digital holography is employed to align multi-mode fibers in a free-space optical setup that can be used for space-division multiplexing (SDM) transmission. We show that alignment based on power coupling measurements alone does not guarantee a low mode-dependent loss, limiting the system capacity. The alignment method we proposed previously enables reliable fiber coupling with low mode-dependent loss and cross-talk for few-mode to multimode fiber alignment, by using digital holography to capture the full complex optical field at the output of the fiber of interest. After capturing the full complex field, by means of digital demultiplexing, we can calculate relevant parameters such as mode-dependent loss and cross-talk. Here we extend these results with few-mode to few-mode fiber alignment measurements and look at alternative optimization metrics such as the cross-talk between the mode groups of interest and all guided modes. The proposed method allows for precise (automated) alignment of space-division multiplexing components, devices and subsystems.*

## Introduction

It has been demonstrated that space-division multiplexing (SDM) can largely increase the capacity of optical fiber communication<sup>[1]</sup>. For mode-division multiplexing (MDM), a subset of SDM, different modes in few-mode fibers (FMFs) and multi-mode fibers (MMFs) are used as independent spatial paths to increase the throughput with respect to single-mode fibers. However, as these modes have a complex spatial distribution, this has to be taken into account when coupling between SDM components. Using total coupled power as an optimization metric might disproportionately impact certain modes, resulting in increased impairments such as mode-dependent loss (MDL) and cross-talk (XT).

A complete description of the spatial distribution of light can be retrieved using digital holographic measurements. Off-axis digital holography (DH) measures the amplitude and phase for both polarizations of a free-space signal by recording the interference between the signal field and a flat-phase reference<sup>[2]-[4]</sup>. Analysis of the measured interference subsequently reveals important metrics for SDM systems such as MDL and XT.

Previously<sup>[5]</sup>, we demonstrated the use of off-axis DH for the alignment of free-space coupling between a FMF and a MMF. Coupling was evaluated at various fiber positions. At each position, the total coupled power was measured and DH was used to calculate MDL and XT. In this work, we extend these results with additional measurements on FMF to FMF coupling and look at an additional optimization metric. It is shown that maximizing the total coupled optical power does not provide adequate coupling and MDL penalties of up to 20 dB are observed. Therefore, to ensure reliable coupling, the spatial distribution of the light must be taken into account when the coupling is optimized in SDM systems. Off-axis DH is demonstrated to provide the necessary measurements for reliable automated alignment of SDM devices and subsystems.

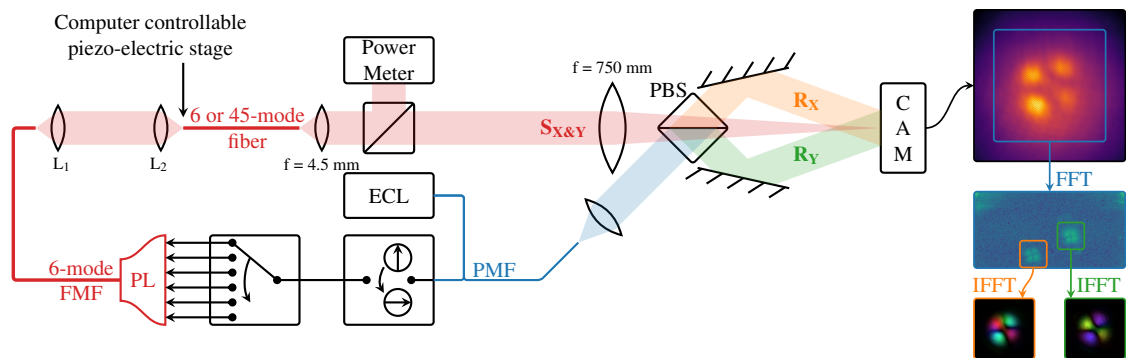


**Fig. 1:** Experimental setup.  $S_{X\&Y}$  denotes the dual-polarization signal to be characterized,  $R_X$  and  $R_Y$  are the reference beam for x- and y-polarization, respectively. Note that the signal  $S_{X\&Y}$  passes over the PBS.

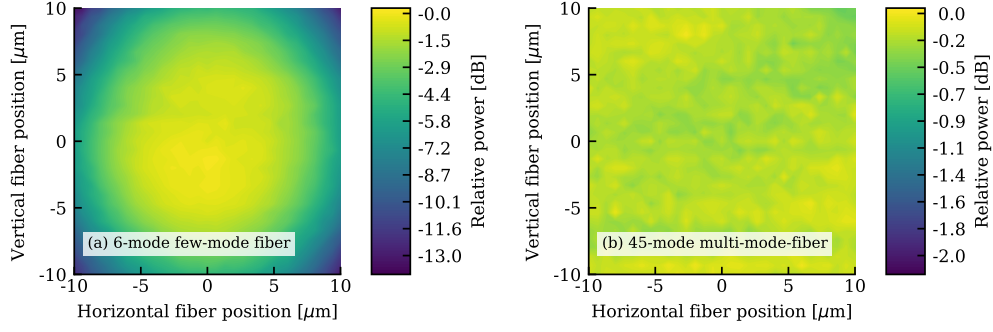
## Experimental setup

Fig. 1 shows the experimental free-space optical setup. A photonic lantern (PL)<sup>[6]</sup> multiplexes light from six single-mode fibers to a 6-mode FMF<sup>[7]</sup>. The light exiting the 6-mode FMF is coupled into a short piece of either 6-mode FMF or 45-mode MMF<sup>[8]</sup> in free space using collimator lenses mounted on computer-controllable piezo-electric 3-axis stages. The light exiting this fiber is collimated, split, and measured using a free-space power meter and off-axis DH. The DH setup is comprised of a lens for the signal beam  $S_{X\&Y}$ , a large collimator for the reference beams  $R$ , a polarization beam splitter (PBS), mirrors, and a camera. By interfering with the signal field with two off-axis flat-phase reference beams, this setup is capable of measuring the signal field in both amplitude and phase for both polarizations. The digital field extraction process is visually explained in Fig. 1. More details on the measurement technique can be found in<sup>[2],[3]</sup>.

To optimize coupling, the x- and y-position of the 3-axis stage are swept. Coupling efficiency is measured using two methods. Firstly, light is inserted into one of the inputs of the PL and the total coupled optical power exiting the fiber is measured using the free-space power meter. Secondly, the light exiting the fiber is measured using off-axis DH, providing a full description of the signal light which is used for subsequent modal analysis. The modal decomposition of the signal light is obtained through *digital demultiplexing* into target mode fields, obtained for the employed FMF and MMF using a scalar numerical mode solver. This process is repeated for each input port and polarization of the PL to construct a complex-valued dual-polarization transfer matrix from PL input port to output mode. Analysis of this transfer matrix can be used to assess the quality of the transmission channel and free-space coupling therein.

## Results

Fig. 2 shows the total coupled optical power measured using the free-space optical power meter when only the linearly polarized (LP)  $LP_{01}$  port of the PL is excited for both coupling to the FMF and MMF fiber. From Fig. 2a, for coupling to the FMF, it can be seen that there is a relatively broad optimum coupling position where the measured power stays constant. However, for coupling to the MMF, in Fig. 2b, there is no distinct optimum position visible for the measured range of  $-10 \mu\text{m}$  to  $10 \mu\text{m}$  in both the horizontal and vertical direction. This can be explained by the fact that the  $LP_{01}$  mode will couple into the higher-order modes of the MMF, however, this results in severe MDL penalties not seen from these power measurements. As in both coupling scenarios, there is no significant variation of the metric over the variation of the fiber, it is not suitable for accurate alignment.



**Fig. 2:** Relative powers measured at the output of the two different fiber types when launching the  $LP_{01}$  mode. Powers are normalized to the maximum measured powers.

In Fig. 3 alignment metrics obtained using the DH setup are shown. Here MDL is calculated through singular value decomposition (SVD) of the complex-valued dual-polarization transfer matrix  $T$  from PL input port to MMF output mode:

$$\text{MDL [dB]} = 10 \cdot \log_{10} \left( \frac{\lambda_0}{\lambda_{2N_k-1}} \right)^2 \quad (1)$$

with  $\lambda_0$  and  $\lambda_{2N_k-1}$  the largest and smallest singular value, respectively. The full transfer matrix  $T$  can be converted into a mode-group intensity transfer matrix  $\hat{T}$ , from which XT can be calculated using:

$$\text{XT [dB]} = 10 \cdot \log_{10} \left( \frac{\text{tr}(\hat{T})}{\Sigma \hat{T} - \text{tr}(\hat{T})} \right) \quad (2)$$

with  $\text{tr}$  the trace operator. This definition of XT describes the ratio between of power coupled to the intended mode-group and the other mode-groups. When coupling a FMF to a MMF, it is possible that modes will be coupled to higher order modes supported by the MMF, and therefore increasing MDL. Therefore, we also introduce the higher-order modes (HOM) XT, defined as the ratio between the power in the transmitted modes of the output fiber and the power in the other supported modes of the fiber-coupled into as

$$\text{XT HOM [dB]} = 10 \cdot \log_{10} \left( \frac{\sum_{i=0, j=0}^n \hat{t}_{i,j}}{\Sigma \hat{T} - \sum_{i=0, j=0}^n \hat{t}_{i,j}} \right). \quad (3)$$

Here,  $n$  is the number of transmitted modes. As for coupling to the FMF, the number of modes supported equals  $n$ , this metric is only evaluated for coupling into the MMF.

A clear optimum fiber position is observed for all metrics in Fig. 3 near zero offsets in both horizontal and vertical directions. For fiber position offsets within the large optimum power areas of Figs. 2a and 2b, Figs. 2b and 3b show an MDL penalty of up to 20 dB, demonstrating that power measurements only do not guarantee adequate coupling. Furthermore, Figs. 3a and 3d show the measured XT and a distinct optimal location for the fiber position is observed, which coincides with the optimum position obtained based on MDL for the FMF scenario, however for the MMF scenario, the optimum in Fig. 3c is slightly shifted with respect to Fig. 3e. However, for the HOM XT in Fig. 3d the optimum coincides with the one from Fig. 3e. Thus, both MDL and XT can be used as optimization metrics for alignment since they both directly measure the quality of coupling, however, when the supported modes in the fiber-coupled into is larger than the number of transmitted modes, the HOM XT is the more relevant metric.

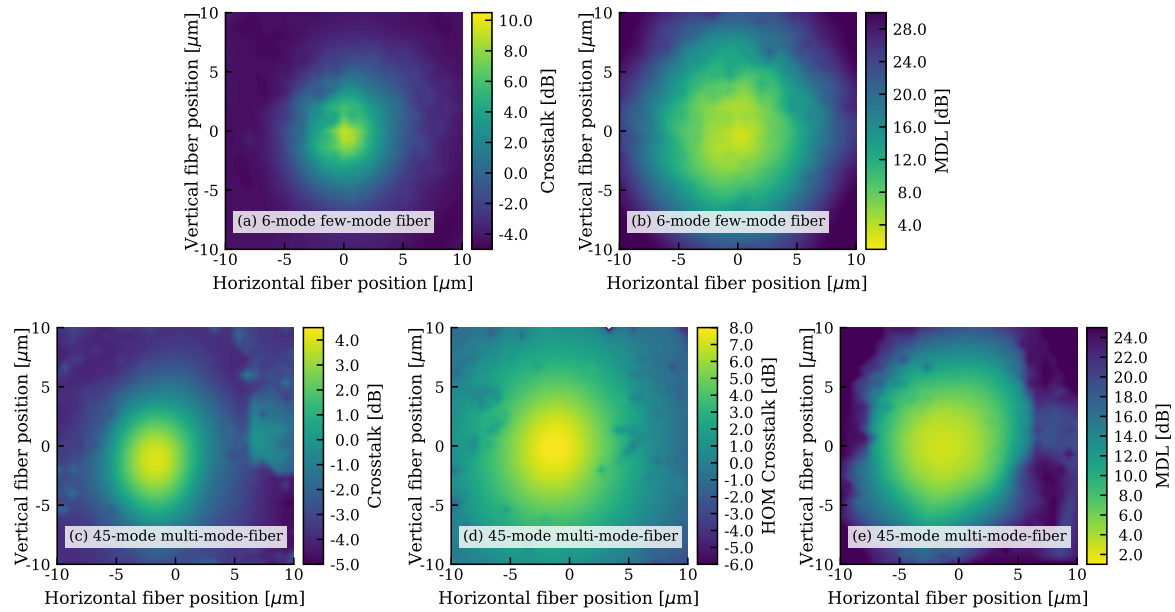


**Fig. 3:** Measured XT and MDL when coupling from FMF to FMF or MMF.

## Conclusions

The optimization of free-space coupling between mode-division multiplexing fibers is investigated. When only the total coupled optical power is maximized, the spatial distribution of the light is not taken into account and adequate coupling with low mode-dependent loss and cross-talk cannot be guaranteed. Off-axis digital holography provides a full description of optical fields and is demonstrated to provide relevant metrics for the investigated coupling scenario. The proposed method can be used for reliable automated alignment of SDM components, devices, and subsystems enabling the effective coupling of amplifiers and multiplexers into transmission fibers.

Partial funding is from the Dutch NWO Gravitation Program on Research Center for Integrated Nanophotonics (Grant Number 024.002.033), from the KPN-TU/e Smart Two program and from the Dutch NWO Visitor's program (Grant number 040.11.743).

## References

- [1] B. J. Puttnam *et al.*, "Space-division multiplexing for optical fiber communications", *Optica*, vol. 8, no. 9, 2021. doi: 10.1364/OPTICA.427631.
- [2] S. van der Heide, "Space-division multiplexed optical transmission enabled by advanced digital signal processing", Ph.D. dissertation, Electrical Engineering, Apr. 2022, ch. 3, ISBN: 978-90-386-5491-1. doi: 10.6100/2d04a1e9-15e1-40fb-8e6d-7b22444397bc.
- [3] S. van der Heide, B. van Esch, M. van den Hout, *et al.*, "Optical field characterization using off-axis digital holography", in *Optical Fiber Communication Conference (OFC) 2022*, Optica Publishing Group, 2022, M3Z.6. doi: 10.1364/OFC.2022.M3Z.6.
- [4] N. K. Fontaine *et al.*, "Laguerre-Gaussian mode sorter", *Nature Communications*, vol. 10, no. 1, 2019, ISSN: 2041-1723. doi: 10.1038/s41467-019-09840-4.
- [5] M. van den Hout, S. van der Heide, *et al.*, "Alignment of free-space coupling of few-mode fibre to multi-mode fibre using digital holography", in *ECOC*, 2022. doi: 10.48550/ARXIV.2208.02904.
- [6] A. M. Velázquez-Benítez *et al.*, "Scaling photonic lanterns for space-division multiplexing", *Scientific Reports*, vol. 8, no. 1, 2018, ISSN: 2045-2322. doi: 10.1038/s41598-018-27072-2.
- [7] P. Sillard, D. Molin, M. Bigot-Astruc, H. Maerten, D. Van Ras, and F. Achten, "Low-DMGD 6-LP-mode fiber", in *OFC 2014*, IEEE, 2014, pp. 1–3. doi: 10.1364/OFC.2014.M3F.2.
- [8] P. Sillard, D. Molin, M. Bigot-Astruc, A. Amezcua-Correa, K. de Jongh, and F. Achten, "50  $\mu\text{m}$  Multimode Fibers for Mode Division Multiplexing", *J. Lightwave Technol.*, vol. 34, no. 8, pp. 1672–1677, Mar. 2016. doi: 10.1109/JLT.2015.2507442.

# Receiver Calibration and Quantum Random Number Generation for Continuous-variable Quantum Key Distribution

Sjoerd van der Heide<sup>(1,\*),</sup> Aaron Albores-Mejía<sup>(1),</sup> João Frazão<sup>(1),</sup> and Chigo Okonkwo<sup>(1)</sup>

<sup>(1)</sup> High Capacity Optical Transmission Laboratory, Electro-Optical Communications Group, Eindhoven University of Technology, the Netherlands <sup>(\*)</sup> [s.p.v.d.heide@tue.nl](mailto:s.p.v.d.heide@tue.nl)

*The desire for secure communications and the advent of quantum computing has spurred innovation into key-distribution technologies that are secure against future quantum computers. Computationally secure solutions based on post-quantum algorithms and physically-secure solutions using either discrete-variable or continuous-variable quantum key distribution (CV-QKD) have been proposed. The attraction with CV-QKD systems in particular is the potential to leverage the vast knowledge base and access scaling benefits of photonic integration for conventional coherent optical communication for key distribution. CV-QKD requires detailed characterization of coherent receiver hardware, specifically noise generated by electronics and shot noise caused by the local oscillator (LO) laser. This work investigates the temporal stability of the receiver noise power which defines the amount of trusted noise in the quantum link used to compute the secret key rate (SKR). Depending on the noise power's stability, this characterization must be repeated often, typically in the order of seconds. Therefore, this work explores the possibility of using the shot noise measurement as a source of quantum random numbers, which is required by a CV-QKD transceiver. This work enables further integration of the CV-QKD hardware, removing the need for a separate quantum random number generator (QRNG).*

## Introduction

Current key-exchange mechanisms employed are based on public key cryptography and could be potentially compromised by future quantum computers. A proposed alternative secure method is QKD. In particular, CV-QKD is of interest because it utilizes hardware and digital signal processing (DSP) similar to conventional coherent optical communications. By leveraging knowledge and components from current classical fiber-optical communication systems, future CV-QKD systems may become highly-integrated and low-cost.

To ensure security, CV-QKD receivers require thorough characterization. Under the trusted noise assumption, they must be calibrated frequently<sup>[1]</sup>, typically in the order of

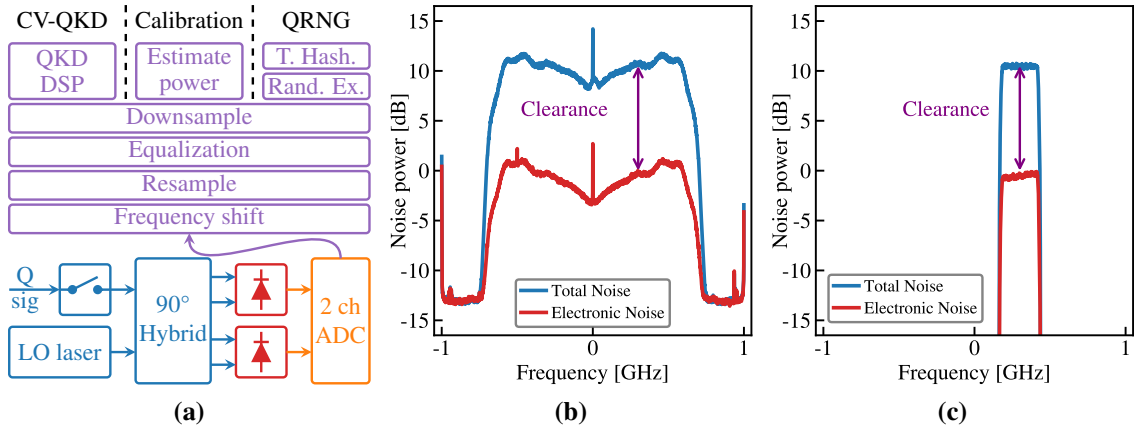


**Fig. 1:** Experimental CV-QKD receiver (a) with measured spectra before (b) and after (c) DSP.

seconds, but this can be traded off against raw SKR. It also depends on the temporal stability of receiver noise. Furthermore, a CV-QKD receiver requires secure random numbers, usually provided by a separate QRNG. Many QRNGs use vacuum-state fluctuations as a source of randomness by measuring shot noise using a balanced photo-diode (BPD)<sup>[2]-[4]</sup>.

In this paper, a detailed characterization of CV-QKD receiver hardware is presented, including its noise spectrum and clearance. Furthermore, the temporal stability of noise sources is investigated, indicating that calibration needs to be performed every couple of seconds. A method is then introduced to generate quantum random numbers during the calibration procedure. Finally, the randomness of the QRNG is verified.

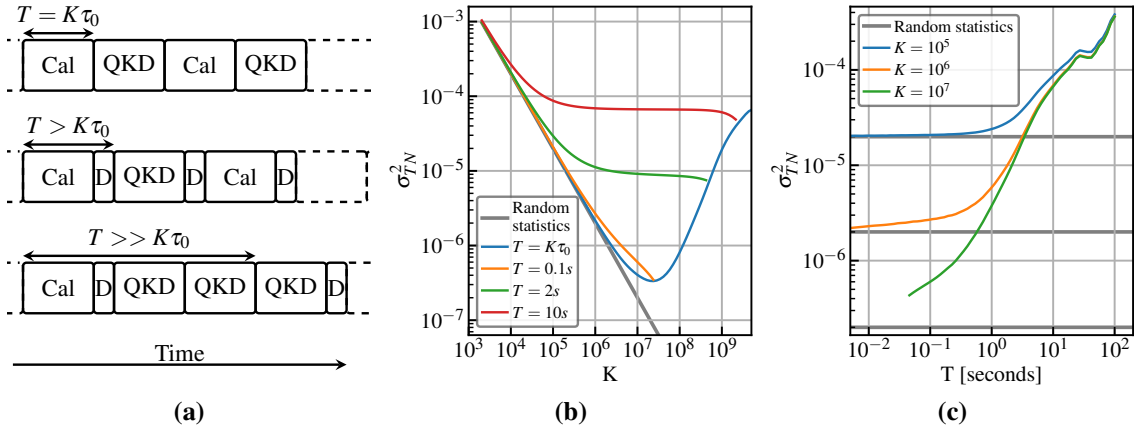
## Experimental setup

Fig. 1a shows the experimental CV-QKD setup with a conventional single-polarization coherent receiver. A  $<100$  kHz external cavity laser (ECL) is used as LO. During calibration, the quantum signal into the 90-degree hybrid is blocked by an optical switch. Two BPDs detect the optical signals, whose electrical signals are then digitized using a 2-channel 2 GS/s analog-to-digital converter (ADC). Note that the experimental setup can be easily extended to be polarization-diverse, but we did not have the extra ADC channels to do so. Furthermore, the employed 90-degree hybrid is a dual-polarization model, thus, half of the optical power is directed towards unused ports.

Fig. 1a also shows most signal processing steps are common for CV-QKD transmission, calibration, and QRNG. DSP starts by frequency shifting the digitized signal by 300 MHz. Then, the signal is resampled to 2 samples per symbol (SPS), filtered by a static equalizer to a 250 MBaud 10% rolloff root-raised-cosine (RRC) pulse shape, and downsampled to 1 SPS. Fig. 1b and Fig. 1c show the spectra of electronic noise and total noise, i.e. shot noise plus electronic noise, before and after DSP, respectively. Note that the spectrum of Fig. 1c is upshifted for illustrative purposes to show the assumed quantum signal is modulated on a digital subcarrier to avoid disturbances around direct current (DC), similar to<sup>[5]</sup>.

## Calibration

Fig. 2a outlines three scenarios for CV-QKD calibration with varying time delay  $T$ . The required temporal stability is at least equal to the QKD block length  $K$  multiplied by the symbol time  $\tau_0$ , but may be longer if switching delay causes dead time  $D$  between



**Fig. 2:** (a) Three scenarios with varying required calibration time delays  $T$ , depending on the calibration (Cal), quantum key distribution (QKD), and switching delay (D). Allan variance of total noise ( $\sigma_{TN}^2$ ) as a function of block size  $K$  (b) and as a function of time delay  $T$  (c).

KKD and calibration. Finally, a much greater temporal stability enables multiple QKD transmission blocks for each calibration block, greatly decreasing calibration overhead.

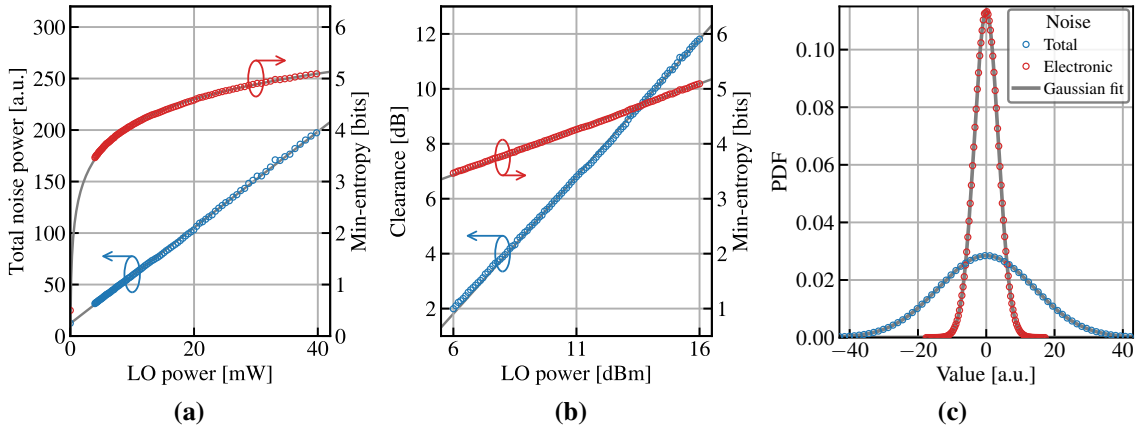
Temporal receiver stability  $T$  is investigated using the overlapped Allan variance method<sup>[6]</sup>. After DSP as explained in the previous section, the power of the extracted noise symbols is calculated ( $y_n$ ) and the cumulative sum is taken using  $x_n = \sum_{i=0}^n y_i$ . Then, the Allan variance is given by  $\sigma_{TN}^2 = \frac{1}{(N-K-L)K^2} \sum_{n=0}^{N-K-L-1} (x_{n+K+L} - x_{n+L} - x_{n+K} + x_n)^2$  with  $L = \frac{T}{\tau_0}$ . Fig. 2b and Fig. 2c show the Allan variance of the total noise versus QKD block length  $K$  and time delay  $T$ , indicating that for the tested hardware, calibration needs to be performed at least every 2 seconds if  $K = 10^7$  and  $\sigma_{TN} = 10^{-5}$  are assumed. Note that underestimating the Allan variance  $\sigma_{TN}^2$  is a security concern and overestimation lowers SKRs. Therefore, SKR and time between calibrations can be traded off.

Fig. 3a demonstrates a linear relation between LO power and observed total noise power after DSP. This one-time characterization is required to ensure the BPDs are adequately balanced. Unbalanced operation is a security concern and would violate this linearity. Fig. 3b shows the clearance, the ratio between shot and electronic noise, achieving 12 dB clearance at 16 dBm LO power into the 90-degree hybrid.

## Quantum random number generation

A QRNG based on vacuum-state fluctuations is implemented using the same noise symbols as used for calibration. The min-entropy per symbol can be calculated using  $H_{min} = \text{erf}\left(\frac{\delta}{2\sqrt{2}\sigma_q}\right)$ , with  $\sigma_q$  the standard deviation of the shot noise and  $\delta$  the sampling resolution<sup>[4]</sup>. Figs. 3a and 3b show that more than 5 random bits can be extracted per 1D-symbol at highest LO power. Extraction requires re-binning with identical sampling resolution as initially used by the ADC, here performed using 8 bits. Note that this equation for min-entropy only holds if the noisy symbols are Gaussian distributed and the sampling range is sufficiently large to capture the tails. Fig. 3c shows excellent agreement between a Gaussian fit and the observed probabilities and Gaussianity is further confirmed by the quantile-quantile plot of Fig. 4a.

After re-binning, Toeplitz hashing with  $2^{19}$  input bits and  $2^{18}$  output is performed to remove any correlations left after equalization or introduced by binning. This reduces the number of extracted bits from 8 to 4 per 1D-symbol, leaving a large safety margin to the



**Fig. 3:** (a) Total noise power and min-entropy versus LO power. (b) Clearance and min-entropy versus LO power. (c) Empirical and fitted probability density function (PDF) for the total and electronic noise.

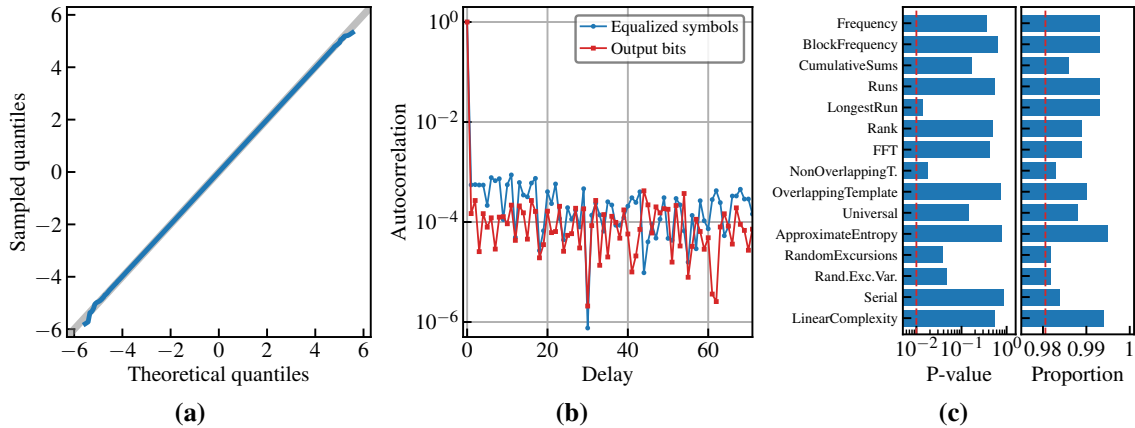


**Fig. 4:** (a) Quantile-quantile plot showing Gaussianity of normalized equalized symbols. (b) Autocorrelation of equalized symbols and QRNG output bits. (c) NIST-STS randomness test results.

min-entropy. Fig. 4b confirms that correlations are removed by the equalizer and Toeplitz hashing. To reduce computational complexity, Toeplitz hashing is performed using fast Fourier transforms (FFTs) instead of matrix multiplications<sup>[7]</sup>.

Finally, Fig. 4c shows the result of the National Institute of Standards and Technology: Statistical Test Suite (NIST-STS) randomness test<sup>[8]–[10]</sup> for 1000 sequences of 1 Mbit, indicating the generated bits are statistically random. Note that some sub-tests occasionally fail, as is to be expected, even for truly random numbers<sup>[11]</sup>.

## Conclusion

A CV-QKD receiver capable of performing calibration and quantum random number generation simultaneously is presented. Furthermore, a detailed analysis into its noise characteristics and the temporal stability thereof is given, indicating calibration needs to be performed every couple of seconds. Finally, the QRNG implementation is described and its successful operation is verified.

This work was supported by the Dutch Ministry of Economic Affairs and Climate Policy as part of the Quantum Delta NL programme.

## References

- [1] A. Leverrier, “Theoretical study of continuous-variable quantum key distribution”, Theses, Télécom ParisTech, Nov. 2009.
- [2] T. Gehring *et al.*, “Homodyne-based quantum random number generator at 2.9 Gbps secure against quantum side-information”, *Nature Communications*, 2021. DOI: 10.1038/s41467-020-20813-w.
- [3] A. Kordts *et al.*, “Security verification for vacuum fluctuation based quantum random number generator”, *CLEO*, 2018. DOI: 10.1364/CLEO\_AT.2018.JTh2A.10.
- [4] J. Y. Haw *et al.*, “Maximization of Extractable Randomness in a Quantum Random-Number Generator”, *Phys. Rev. Applied*, 2015. DOI: 10.1103/PhysRevApplied.3.054004.
- [5] F. Roumestan *et al.*, “Demonstration of Probabilistic Constellation Shaping for Continuous Variable Quantum Key Distribution”, *OFC*, 2021. DOI: 10.1364/OFC.2021.F4E.1.
- [6] W. J. Riley, “NIST Special Publication 1065”, *Handbook of frequency stability analysis*, 2008.
- [7] M. Hayashi *et al.*, “More Efficient Privacy Amplification With Less Random Seeds via Dual Universal Hash Function”, *IEEE Trans. Inf. Theory*, 2016. DOI: 10.1109/TIT.2016.2526018.
- [8] L. Bassham *et al.*, *A Statistical Test Suite for Random and Pseudorandom Number Generators for Cryptographic Applications*, 2010.
- [9] M. Sýs *et al.*, *Faster randomness testing*, <https://randomness-tests.fi.muni.cz/>.
- [10] M. Sýs *et al.*, “Algorithm 970: Optimizing the NIST Statistical Test Suite and the Berlekamp-Massey Algorithm”, *ACM Trans. Math. Softw.*, vol. 43, 2016. DOI: 10.1145/2988228.
- [11] K. Marton *et al.*, “On the interpretation of results from the NIST statistical test suite”, *Science and Technology*, vol. 18, no. 1, pp. 18–32, 2015.

# Design, Characterisation, and Demonstration of a Hot-Air-Based Optical Turbulence Generator

V. van Vliet, M. van den Hout, S.P. van der Heide, and C.M. Okonkwo

High-Capacity Optical Transmission Laboratory, Electro-Optical Communications Group,  
Eindhoven Hendrik Casimir Institute, Eindhoven University of Technology, the Netherlands

*The performance of free-space optical communication links is impaired by atmospheric effects such as optical turbulence. Several techniques are being investigated for emulating the effects of turbulence in the laboratory. Here we explore the use of an optical turbulence generator, facilitating the investigation of turbulent effects and the development and evaluation of mitigation strategies. In this work, the design of a hot-air-based optical turbulence generator is discussed. The characterisation is performed using an off-axis digital holography measurement setup, allowing measurements of the perturbed complex optical field. The measured data can be further analysed in the digital domain. The results of an experimental investigation of mode diversity reception, a technique to improve free-space-to-fibre coupling, are presented.*

## Introduction

Free-space optical (FSO) communication is regarded as a promising solution for the limitations faced by radio frequency (RF)- and fibre-optic-based communication systems<sup>[1]</sup>. Benefitting from large bandwidth, high data rate, license-free spectrum, inherent security against eavesdropping, quick deployability, and low equipment size, weight, and power consumption, FSO communication is appealing for applications such as space communications, backhaul for cellular networks, quantum key distribution, disaster recovery, and last mile access<sup>[2]</sup>. However, the performance of FSO communication links is impaired by atmospheric effects such as optical turbulence. Consequently, the development of impairment mitigation techniques to improve link availability and reliability is essential. To facilitate the investigation of turbulent effects and enable efficient development and evaluation of these techniques, in-laboratory emulation of turbulent atmospheric channels is desired. A turbulent-fluid-based optical turbulence generator (OTG) is a device in which real, physical, naturally evolving turbulence is created in a confined space<sup>[3]</sup>. In this work, we describe the design, characterisation, and demonstration of an OTG based on hot air.

## Design

In a hot-air-based OTG, turbulence is produced through the forced mixing of two laminar air flows, with temperature difference  $\Delta T$ , in a compact chamber<sup>[4],[5]</sup>. The strength of the produced turbulence is, at equal and constant air volumes, a function of and controlled

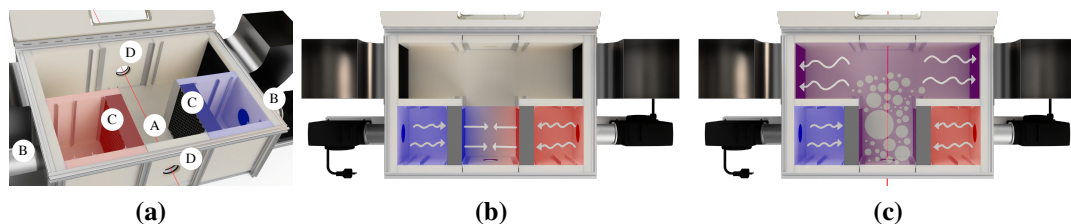


**Fig. 1:** (a) Design of the OTG (opened). (A): mixing chamber, (B): (hot-)air blowers, (C): metal mesh to laminarise flow, (D): laser window panels. (b) Top view illustrating the two air flows upon collision in the mixing chamber and (c) illustrating the produced turbulence (purple and grey) and signal path (red line).

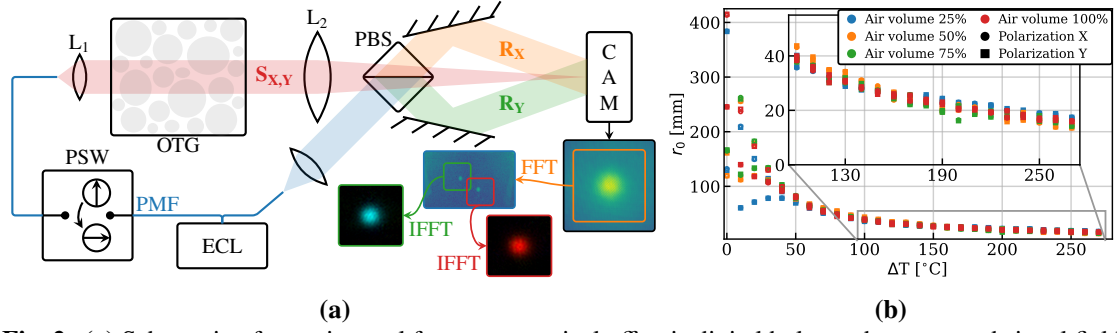


**Fig. 2:** (a) Schematic of experimental free-space optical off-axis digital holography setup and signal field extraction digital signal processing.  $L_1$  and  $L_2$ : lenses with focal distances  $f_1 = 4.51$  mm and  $f_2 = 750$  mm,  $S_{X,Y}$ : signal to be characterised,  $R_X$  and  $R_Y$ : reference beams, ECL: external cavity laser, PMF: polarisation-maintaining fibre, PBS: polarisation beam splitter. Note that  $S_{X,Y}$  passes over the PBS. (b) Characterisation results of  $r_0$  over a temperature difference range from 0 to 270 °C. Results are shown for different air volumes and polarisations.

with  $\Delta T$ . Fig. 1a shows the design of the OTG discussed in this work<sup>[6]</sup>. It is a rectangular box with two air inflow channels, a mixing chamber (A) and two air outflow channels. The air flows are produced by industrial hot-air blowers (Leister Hotwind System), denoted (B), and laminarised by stainless steel honeycomb structures (C). Fig. 1b illustrates the two air flows upon collision in the mixing chamber. Due to the temperature difference between the flows, turbulence is produced (depicted in Fig. 1c). A PID control loop ensures that  $\Delta T$ , which can range from 0 to 275 °C, remains constant at a set value. Anti-reflection coated windows, denoted (D) in Fig. 1a, allow light to be propagated through the produced turbulence, emulating a turbulent FSO channel. The clear aperture of the windows is 45.72 mm, defining the upper limit for beam diameter  $D$ . Aluminium deflectors guide the outflowing air away from the setup to avoid parasitic turbulence.

Essential to the emulation of a FSO turbulent channel is the preservation of characteristic ratios, most prominently the ratio of the beam diameter,  $D$ , and the turbulence coherence length,  $r_0$ , which is an indicator of the turbulence strength<sup>[5]</sup>. To achieve optimal emulation, the ratio achieved in the OTG laboratory setup is equal to the ratio expected or measured in a deployed FSO link.

The turbulence produced in the OTG represents a single layer with uniform turbulence strength. To emulate more consecutive layers with a single OTG, each having a different turbulence strength, it is necessary to design a multi-pass approach where  $D$  is changed for each pass.

For a more detailed description of the design of the OTG, the reader is referred to<sup>[6]</sup>.

## Characterisation

The strength of the turbulence produced in the OTG is characterised using the beam wander variance characterisation technique<sup>[7],[8]</sup>. Here, the corresponding turbulence strength in a satellite uplink (ground-to-satellite) channel is determined based on the variance of the displacement of the beam's centroid after propagation through the turbulent channel, as<sup>[9]</sup>

$$r_0 = D \left( \frac{0.54 L^2 \lambda^2}{D^2 \langle r_c^2 \rangle} \right)^{3/5} \quad (1)$$

where  $L$  is the length of the turbulent channel,  $\lambda$  the wavelength, and  $\langle r_c^2 \rangle$  the beam wander displacement variance.

The experimental setup used for the characterisation of the OTG is shown in Fig. 2a. By employing off-axis digital holography (DH)<sup>[10]</sup>, this setup allows the measurement of the complete optical field for both polarisations of signal field  $S$ . For this,  $S$  is interfered with flat-phase orthogonally-polarised reference beams  $R_X$  and  $R_Y$ . Subsequent digital signal processing (DSP) allows the extraction of amplitude and phase information of the orthogonally-polarised parts of  $S$ . A polarization switch (PSW) alternates between  $x$ - and  $y$ -polarised signals for each subsequent frame, which are recorded at 333 fps. To determine the beam centroid in the spatial (position on camera) and angular domain (angle of incidence), the power of the overlap integral between a digitally-generated TEM<sub>00</sub> field and the extracted  $S_{X,Y}$  field is maximised. Through back-propagation the beam centroid position in the plane of lens  $L_2$  is determined, enabling the application of the beam wander variance characterisation technique.

During an automated measurement, captures consisting of 10 000 frames are recorded for a range of OTG settings ( $\Delta T$ , air volume). Applying the described characterisation method with  $L = 430$  mm,  $\lambda = 1550$  nm, and  $D = 0.88$  mm results in the characterisation curve shown in Fig. 2b. It was found that for  $\Delta T \leq 50$  °C the outputs of the digital-to-analog converters (DACs) providing the control signal to the hot-air blowers to maintain  $\Delta T$  at a set value are unstable. Although a temperature offset was applied to the cold-air side to circumvent this issue, further investigation must be performed to determine if the data in that  $\Delta T$  range is accurate. Apart from that, stronger turbulence is produced for larger  $\Delta T$ , as expected.

Assuming  $D = 0.1$  m to 0.6 m and  $r_0 = 0.05$  m to 0.2 m ( $\lambda = 1550$  nm) as realistic values for a FSO satellite uplink, we can conclude that with the current setup it is not possible to achieve  $D/r_0$  ratios corresponding to the strongest turbulent conditions. However, the lower range of  $D/r_0$ , corresponding to weaker turbulence, can be emulated successfully with this setup.

The characterisation procedure and results are described in more detail in<sup>[6],[8]</sup>.

## Mode diversity reception

Although the usage of commercial, typically single-mode fiber (SMF)-based, fibre-optic components can catalyse the development of FSO communication systems, the free-space-to-SMF coupling is severely impaired by turbulent effects<sup>[11]</sup>, resulting in signal fading. It has been demonstrated that receiving additional spatial modes, using a multi-mode fiber (MMF), has the potential to improve the fibre coupling efficiency and thus improve the link performance<sup>[12]-[14]</sup>. A de-multiplexer and coherent recombination provide compatibility with SMF-based components. This technique, known as mode diversity reception, is especially promising for satellite-to-ground and ground-to-ground FSO links, where the received optical field can exhibit higher-order aberrations.

Here, an experimental investigation<sup>[15]</sup> of mode diversity reception is performed using the perturbed optical fields  $S_{X,Y}$  measured during the characterisation procedure. Fibre coupling is performed digitally by demultiplexing  $S_{X,Y}$  into the propagating modes of a 50  $\mu$ m core diameter graded-index (GI) MMF<sup>[16]</sup>, generated using a numerical scalar linearly polarized (LP) mode solver.  $S_{X,Y}$  are scaled for optimal coupling to the LP<sub>01</sub> fibre mode, mimicking an ideal optical beam expander maximising the coupling efficiency between the fundamental modes of the transmitting SMF and receiving MMF.

The resulting coupling losses for the weakest and strongest turbulent conditions we

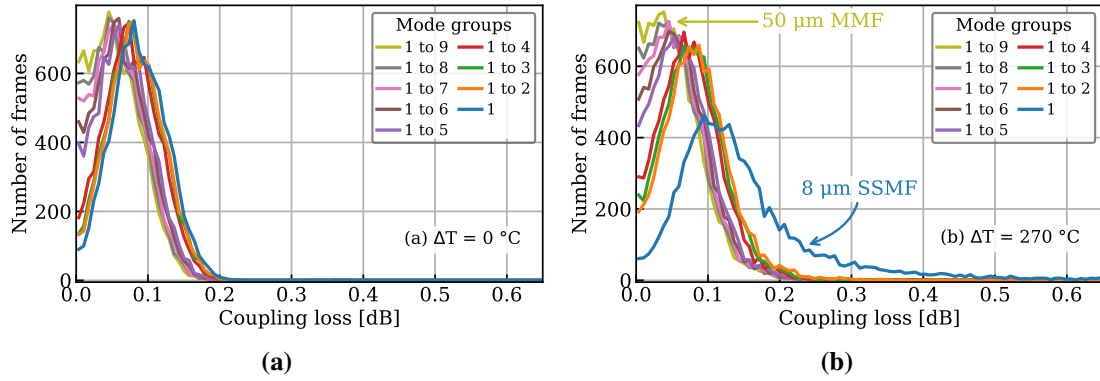


**Fig. 3:** Histograms of coupling loss over 10 000 frames for  $\Delta T = 0^\circ\text{C}$  and  $270^\circ\text{C}$  (air volume 50 %).

can produce in the OTG are displayed in Figs. 3a and 3b, respectively. It is clear that while coupling to a SMF and MMF show similar performance in weak turbulent conditions, receiving higher order modes results in improved free-space-to-fibre coupling efficiency when stronger turbulence is present in the channel. For the related outage probabilities, please refer to<sup>[15]</sup>.

It must be noted that the beam diameter used during characterisation is small compared to the turbulence coherence length. Consequently, the main induced effect is beam wander. Because of this, the incorporation of mode groups beyond the second does not yield significant improvement. It is expected that such an improvement will be observed when higher-order aberrations are present in the received optical fields. For this, one can for example use an increased beam diameter.

## Conclusions

In this work, we discussed the design of a hot-air-based OTG. Furthermore, a characterisation method allowing the simultaneous measurement of the complete perturbed optical field using off-axis DH was presented, along with the characterisation results for a satellite uplink. Lastly, the results of an experimental investigation of mode diversity reception confirm that the reception of higher-order spatial modes can improve the free-space-to-fibre coupling efficiency under turbulent conditions.

Funding received from NWO Perspectief project Optical Wireless Superhighways: Free photons, the KPN-TU/e Smart Two Program and the Dutch NWO Gravitation Program (Grant Number 024.002.033).

## References

- [1] H. Kaushal *et al.*, 2017. DOI: 10.1109/COMST.2016.2603518.
- [2] M. A. Khalighi *et al.*, 2014. DOI: 10.1109/COMST.2014.2329501.
- [3] L. Jolissaint, 2006. DOI: 10.1086/507849.
- [4] E. Masciadri *et al.*, 1997. DOI: 10.1364/AO.36.001320.
- [5] O. Keskin *et al.*, 2003. DOI: 10.1117/12.506430.
- [6] V. van Vliet, 2022. DOI: 10.6100/10631f35-e821-4ab5-9033-2c6947dc35ba.
- [7] H. Kaushal *et al.*, 2011. DOI: 10.1109/LPT.2011.2166113.
- [8] V. van Vliet *et al.*, 2022. DOI: 10.1364/SPPCOM.2022.SpTu3G.1.
- [9] L. C. Andrews *et al.*, 2006. DOI: 10.1117/1.2219470.
- [10] S. van der Heide, 2022. DOI: 10.6100/2d04a1e9-15e1-40fb-8e6d-7b22444397bc.
- [11] Y. Dikmelik *et al.*, 2005. DOI: 10.1364/AO.44.004946.
- [12] D. Zheng *et al.*, 2016. DOI: 10.1364/OE.24.018739.
- [13] N. K. Fontaine *et al.*, 2019. DOI: 10.1049/cp.2019.1015.
- [14] D. J. Geisler *et al.*, 2018. DOI: 10.1117/12.2294039.
- [15] V. van Vliet *et al.*, 2022. DOI: 10.48550/arXiv.2209.06821.
- [16] P. Sillard *et al.*, 2016. DOI: 10.1109/JLT.2015.2507442.

# Quad photodiode array for optical wireless communication

M. Wolny<sup>1</sup>, S. Henader,<sup>2</sup> J. Mink<sup>2</sup>, T. Koonen<sup>1</sup>, E. Tangdiongga<sup>1</sup>

<sup>1</sup> Eindhoven University of Technology, De Groene Loper 19, 5612 AP Eindhoven

<sup>2</sup> VTEC Lasers & Sensors, Kastanjelaan 400, 5616 LZ Eindhoven, The Netherlands

## Abstract

*Optical spectrum offers bandwidths far beyond the radio-frequency (RF) technologies. Optical Wireless Communication (OWC) is meant to serve many users in small areas with high-capacity connection. Due to its ultrahigh capacity, OWC can help unload the traffic from the RF channels so that the RF spectrum can be freed for other services. Receivers used in indoor OWC scenario must have a wide field-of-view (FoV) and high sensitivity to be able to capture light from different directions at eye safety levels. VTEC Lasers & Sensors B.V. developed a quad photodiode array with 100  $\mu\text{m}$  diameter. Each photodiode has a shape of 90° sector of a circle and has a separate Trans-Impedance Amplifier (TIA). Such choice allows the system to retain the bandwidth of a single photodiode while increasing the aperture. At -8 dBm incident power, where TIA saturates, the device achieved an error free ( $\text{BER} < 10^{-9}$ ) transmission at 16 Gbps, and 20 Gbps below the error-free FEC floor ( $\text{BER} < 10^{-3}$ ). Incidence angle of the beam was varied between 0° and 16° and no penalty was observed in this range. Hence it can be concluded that the device has a full angle FoV greater than 32°. The results prove that the presented quad photodiode can be used in the indoor OWC communication scenario.*

## Introduction

The demand for wireless communication has been growing for the past decades. There are more and more devices connected to the wireless networks. Most of the traffic is generated indoors. OWC is a promising solution for high-density high-throughput user scenarios and it can also be used to unload the traffic from existing radio frequency technologies [1]. Optical spectrum is unlicensed, so it is free to use with the only limitation being eye safety limits. There is huge amount of bandwidth available and by keeping whole communication system in the optical domain the latency of the communication link can be decreased. In an optical beam steered system proposed by Koonen et al [2] the light beam is only directed where and when needed thus conserving the energy. Optical beam steering also makes wireless communication secure and private, due to the fact that light does not propagate through walls and that information is only transmitted on the line of sight so eavesdropping is extremely difficult.

In the indoor optical communication system the light is transmitted at wide range of angles and at eye-safe power levels. For that reason the optical receiver in such system must accept beam incoming from wide FoV and must have a high sensitivity due the eye-safe power transmission and high coupling loss to a receiver.

VTEC Lasers & Sensors has developed a quad photodiode array with 100  $\mu\text{m}$  diameter. Each of the four PDs has a separate TIA. The benefit of separate TIAs is the possibility to measure the direction of the incident light beam. Such PD array could be used simultaneously for data transfer and localization.

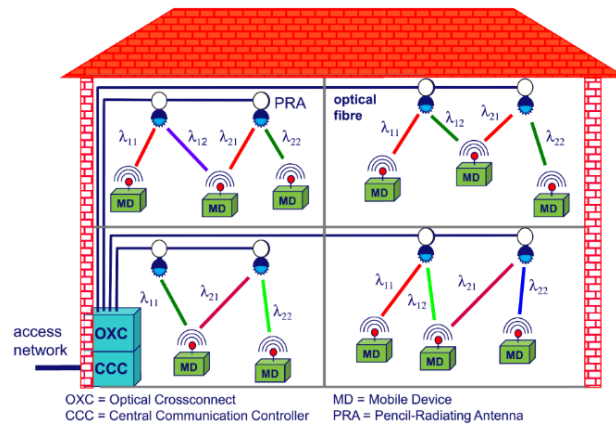


Figure 1 Indoor optical wireless beam steered communication scenario.

## Experimental setup

The quad photodiode array was characterized by injecting light from a fibre mounted on a platform with 6 degrees of freedom, so that the angle and position of the fibre could be controlled. The diagram of the experimental setup is shown in Figure 2. Tunable laser source which emitted light at 1530 nm with 12 dBm output power was connected to a Polarization Controller to optimize the transmission power for the modulator inside Bit Error Rate Tester (BERT). Modulated light from the BERT was then amplified with Erbium Doped Fibre Amplifier (EDFA) to compensate for the losses of the components in the link. Then Variable Optical Attenuator (VOA) was placed to control the incident power level on the photodiode array. Fibre was then aligned to the photodiode with a mount with which the position and the angle of the fibre could be precisely controlled as shown in the Figure 3. The RF output of the photodiode array was then connected back to the BERT through a DC block to keep threshold voltage around 0 V.

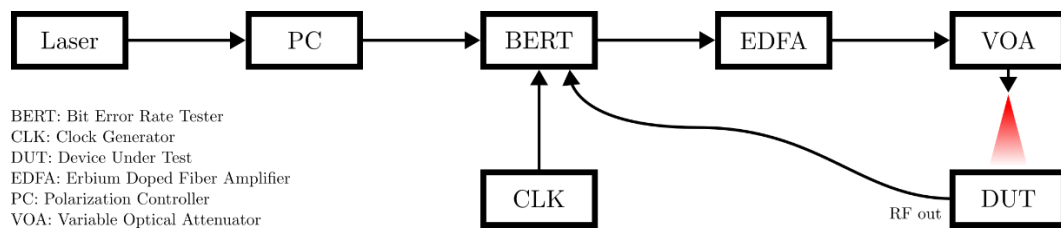


Figure 2 Diagram of the experimental setup used to characterize the photodiode.

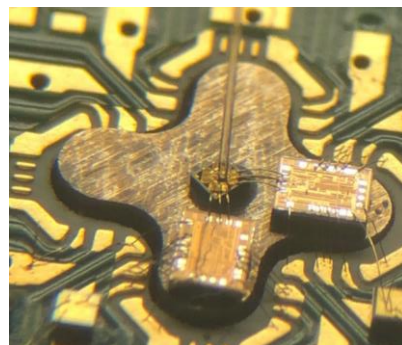


Figure 3 Picture of the fibre aligned to the photodiode array.

The first objective of the experiment was to verify the FoV of the device. FoV was verified by changing the angle of the fibre on the mount with respect to the photodiode. The maximum angle which is supported by the mounting is 16 degrees relative to the normal incidence (half angle). Figure 3 shows the fibre aligned to the photodiode at 0 degrees incidence angle. The data rate in the FoV measurement was 1 Gbps. The only modulation format which was considered is OOK NRZ.

The second objective was to verify the bit error rate dependency on the incident light power for various bit rates. The light power output by the BERT was swept by the VOA, and the bit rate was controlled by the BERT. The signal was transmitted in OOK NRZ format. In this measurement the photodiode array was illuminated at normal incidence angle.

## Results

Setup described in the previous section was used to measure the FoV of the Quad Photodiode and the BER relation with the incident power level. In the Figure 4 BER curves vs received power are shown. At 1 Gbps the BER curves for incidence angles of 0 degrees and 16 degrees overlap. Hence, in this range of angles there is no penalty for receiving signal in the range of angles which are supported by the fibre mount. Figure 5 shows eye diagrams for selected bit rates of the RF output of the photodiode array. The input light power in all the cases is -8 dBm, at this power the TIA reached saturation. Hence, increasing the power would not increase the eye opening. At 10 Gbps and 16 Gbps eye opening is sufficient to achieve error free data transmission. Data rates of 20 Gbps and 23 Gbps are further beyond the bandwidth of the photodiode so the eye opening is smaller and error-free data transmission was not achieved.

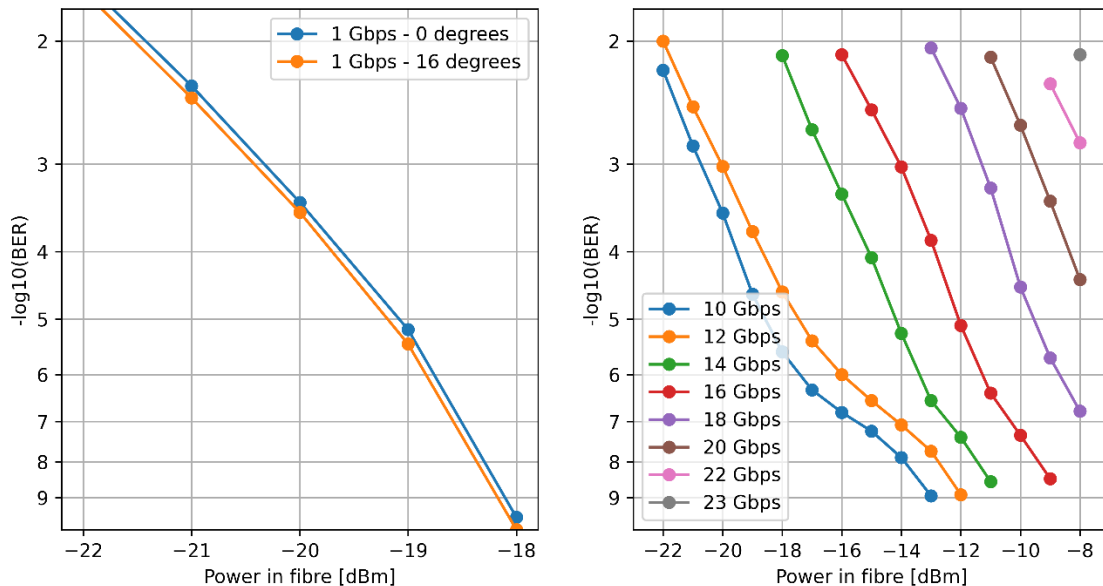


Figure 4 Left: BER vs received power measurement at 1 Gbps at normal incidence and angled at 16 degrees. Right: BER vs received power measurement for bit rates ranging from 10 Gbps to 23 Gbps. 'Power in fibre' is measured after the BERT.

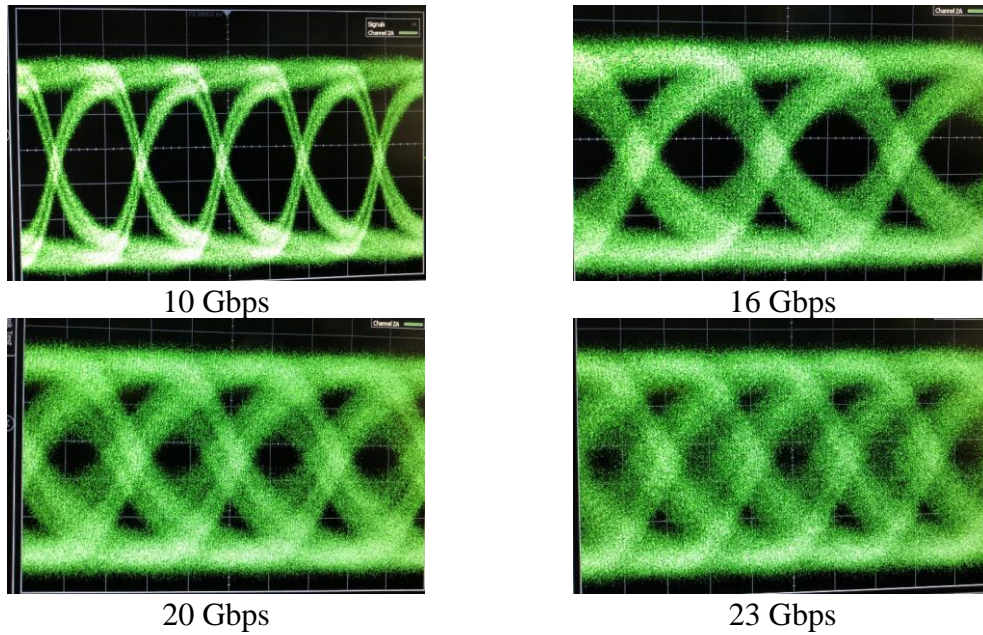


Figure 5 Eye diagrams for selected bit rates measured on the RF output of the photodiode at 0 deg launching.

## Discussion and Conclusions

The results obtained in this experiment show an improvement compared to the previous experiments done in the indoor optical wireless communication scenario. The previous experiment of Koonen et al. [2] achieved a maximum bit rate of 1.25 Gbps (Gigabit Ethernet speed) with error free data transmission. The Quad Photodiode array used in this work allowed to receive the data rates up to 16 Gbps with error free transmission. By using hard decision Forward Error Correction (FEC) data rates could be increased up to 20 Gbps, and by using soft decision FEC up to 23 Gbps. All the data transmission was performed at eye safe power levels. Also, the FoV of the DUT is wider than of the photodiode array presented in [2]. Therefore, the Quad photodiode array shown in this paper can potentially replace it as a receiver in an indoor OWC system.

In the future work, higher order modulation formats will be used to increase the spectral efficiency and to increase the bit rates. It is possible to receive coherent symbols with direct detection by using Kramers-Kronig relations [3]. Hence, it will be possible to use the Quad Photodiode, which used in this work, in a coherent data transmission system for indoor OWC.

## References

- [1] T. Koonen, "Indoor Optical Wireless Systems: Technology, Trends, and Applications," in *Journal of Lightwave Technology*, vol. 36, no. 8, pp. 1459-1467, 15 April 2018
- [2] T. Koonen, K. A. Mekonnen, Z. Cao, F. Huijskens, N. Q. Pham and E. Tangdiongga, "Beam-Steered Optical Wireless Communication for Industry 4.0," in *IEEE Journal of Selected Topics in Quantum Electronics*, vol. 27, no. 6, pp. 1-10, Nov.-Dec. 2021
- [3] Antonio Mecozzi, Cristian Antonelli, and Mark Shtaif, "Kramers–Kronig coherent receiver," *Optica* 3, 1220-1227 (2016)

*This work is supported in part by the Netherlands Organization for Scientific Research (NWO) under grant 12128 Optical Wireless Superhighways: Free Photons.*

# Comparison between Laser Doppler and Sagnac-based vibrometers from the view of velocity noise density

Zhizhi Yang,<sup>1,2</sup> Emiel Dieussaert,<sup>1,2</sup> Roel Baets,<sup>1,2</sup> and Yanlu Li<sup>1,2</sup>

<sup>1</sup> Photonics Research Group, Ghent University-Imec, Technologiepark-Zwijnaarde 126, 9052 Ghent, Belgium

<sup>2</sup> Center for Nano- and Biophotonics (NB-Photonics), Ghent University, 9052 Ghent, Belgium

*Non-destructive testing is a group of analytic techniques widely used to evaluate and characterize the properties of a material, structure, or system. Conventional non-destructive testing often uses an ultrasound transducer in contact with the target, which is unsuitable for many applications. The non-contact testing methods, however, can provide more flexibility since they evaluate targets distantly. Laser Doppler vibrometry (LDV) and Sagnac-based vibrometry are two common non-contact testing methods utilizing the interferometer structure. In this paper, we compare the velocity noise density of the LDV and the Sagnac-based vibrometry, considering the shot noise limitation in simulation. We also review the advantages and disadvantages of both methods.*

## Introduction

Non-destructive testing (NDT) is a group of testing methods used in many realms, including material engineering, pipe and tube inspection, and defects characterization. Laser Doppler vibrometry (LDV) [1] is a well-recognized NDT technique widely used for defect characterization in evaluating composite materials. Sagnac-based vibrometry, which is widely used has been reported to show an outstanding performance in [2]. As shown in Fig. 1 (a) and (b), both Sagnac-based vibrometry and LDV are based on the principle of interference, which gives them great sensitivity and enables them to measure sub-nanometer or sub-picometer displacement in vibration.

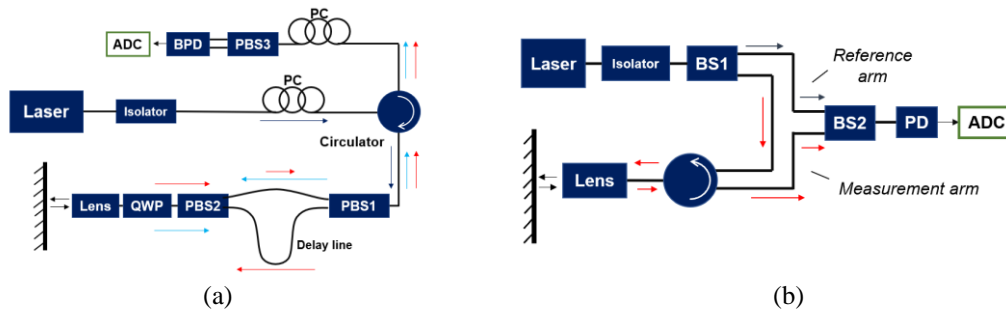


Figure 1: (a) The schematics of Sagnac-based vibrometer; (b) the schematics of laser Doppler vibrometer, QWP: quarter wave plate, PBS: polarization beam splitter, BPD: balanced photodiode, BS: beam splitter, PD: photodiode, ADC: analog-to-digital converter.

The LDV was first used to study fluid dynamics to measure the flow speed in high resolution without disturbing the liquid [3]. The light scattered by the particles in a flowing liquid undergoes the process of the Doppler effect. A laser beam is focused on a target to measure the vibration of a solid surface. By collecting the reflected or scattered light and mixing it with reference light, the frequency shift brought by the vibration of the target can be obtained after a demodulation process [4]. The Sagnac interferometer, first demonstrated for its potential in fiber-based gyroscopic sensing, is now utilized in

vibration sensing, hydrophone, and many other domains [5]. The sameness of the clockwise and counterclockwise loop directions of Sagnac-based vibrometry makes it capable of operating using a low coherent light source [2, 5], which is not applicable for laser Doppler interferometer since its measurement beam needs a mutually coherent reference to beat with. In 2014, I. Pelivanov reported a balanced fiber-optic Sagnac interferometer to inspect the laser ultrasonic on a composite material with an excellent noise equivalent pressure of 400 Pa over 1 MHz to 10 MHz [2], which has attracted much attention from the NDT world. To further investigate the potential of Sagnac-based vibrometry, we model Sagnac-based vibrometry and LDV and compare them from the perspective of shot noise limit.

## Velocity noise analysis of Sagnac-based vibrometry and LDV

As shown in Fig. 1 (b), the Sagnac-based vibrometry structure consists of a light source that can be coherent or incoherent, three polarization beam splitters, a circulator, and a balanced PD (BPD) using balanced detection. The light source is a CW laser with the power of  $P_0$ . The splitting ratios of  $PBS1$  and  $PBS2$  are set as 50:50 to ensure the system's optimal performance. Then we can obtain the signal at the BPD as

$$I(t) = 2\mu\sqrt{P_c \cdot P_{cc}} \cdot \cos(\theta(t - \Delta T) - \theta(t))$$

where  $P_c$  and  $P_{cc}$  are the clockwise and the counterclockwise light power in Sagnac.  $\Delta T$  is the time delay brought by the fiber delay line of Sagnac structure and  $\mu$  is the responsivity of BPD. The time delay can be derived as  $\Delta T = \frac{l \cdot n}{c}$ , where  $l$  is the length difference of the two fibers,  $c$  is the speed of light, and  $n$  is the effective refractive index of fiber. Since the lights of both the clockwise and counterclockwise directions travel through the same devices, their power  $P_c$  and  $P_{cc}$  can be obtained as  $P_c = P_{cc} = \frac{1}{2}P_0L$ , where  $L$  is the percentage of optical power transmitted via the optical link of the clockwise and counter-clockwise paths. The  $\theta(t)$  and  $\theta(t - \Delta T)$  are the phase shifts brought by the vibration of measured target in the directions of clockwise and counterclockwise, respectively. The DC component of each PD can be derived as

$$I_{DC} = \mu \frac{P_0L}{2}$$

And amplitude density of the total shot noise of the BPD can be expressed as

$$I_{shot\ noise}(\omega) = \sqrt{2q\mu P_0L}$$

We assume that the interferometer is working at the most sensitive point of  $\theta(t - \Delta T) - \theta(t) = \frac{\pi}{2}$ . Since the phase change brought by the shot noise is sufficiently small, we can approximate the phase change equals to the current of shot noise divided by  $2\mu\sqrt{P_c \cdot P_{cc}}$ . Therefore, the amplitude density of the noise in the demodulated displacement  $\rho_{Dnoise}(\omega)$  can be obtained as is

$$\rho_{Dnoise}(\omega) = \frac{\lambda}{4\pi} \cdot \sqrt{\frac{2q}{\mu P_0L}} \cdot \frac{1}{(e^{j\omega\Delta T} - 1)}$$

where  $\lambda$  is the wavelength of the light source. The nonlinear factor  $\frac{1}{(e^{j\omega\Delta T} - 1)}$  at the right side of the equation originates from the time delay between the clockwise and counterclockwise signals. Moreover, the amplitude noise in the velocity signal is

$$\rho_{v_{noise}}(\omega) = \frac{\lambda}{4\pi} \cdot \sqrt{\frac{2q}{\mu P_0 L}} \cdot \frac{1}{(e^{j\omega\Delta T} - 1)} \cdot \omega$$

The same analysis can be applied to LDV. Since the two arms of LDV have very different optical losses, the best splitting ratio  $S$  is not 50:50 in practice. The noise amplitude of the velocity output of an LDV is

$$\rho_{v'_{noise}}(\omega) = \frac{\lambda}{4\pi} \sqrt{\frac{q\mu(P_{ref} + P_{mea})}{P_{ref} \cdot P_{mea}}} \cdot \omega$$

where the  $P_{ref} = P_0 \cdot S$  is the optical power on the reference arm, and the  $P_{mea} = P_0 \cdot (1 - S)L$  is the light power on the measurement arm before the beam splitter 2 (BS2), as shown in Fig. 1(b). Based on the analysis above, we are able to derive the velocity noise density of both techniques, and make a side-by-side comparison of them.

### Comparison between the Sagnac-based vibrometry and LDV

According to the analysis above, we calculate the theoretical velocity noise density of the Sagnac-based vibrometer and LDV. The light source of LDV and Sagnac is operating on 1550 nm and the optical powers coupled into both the systems are set to be 1 mW, and the responsivity  $\mu$  of PD is 1 A/W. The length difference between the two fibers of the Sagnac-based vibrometer is 10 m long with the effective refractive index of 1.5. We consider the frequency range of the detected vibration is from 0.1 MHz to 100 MHz, which can cover a wide frequency range, including the measurement range in [2]. Firstly, we consider the ideal situation: that is, the optical link of both the Sagnac-based vibrometer and LDV are lossless, and the splitting ratio  $S$  of LDV is set 50:50 to match the lossless condition.

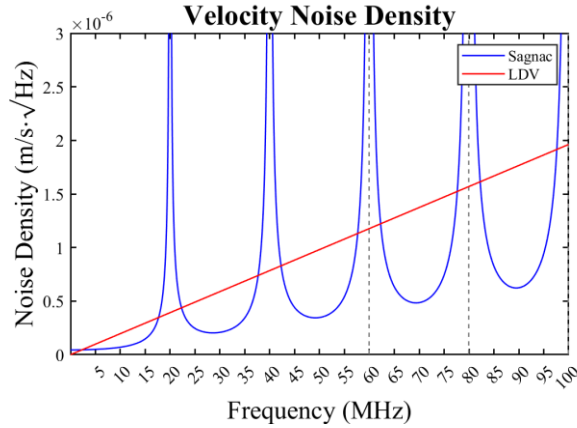


Figure 2: Comparison of the velocity noise density of Sagnac-based vibrometer and LDV in an ideal setup: the light source is operating on 1550 nm with the power of 1 mW, the optical path is lossless, the splitting ratio  $S$  of LDV is 50:50, and the fiber delay line in Sagnac is 10 m with the effective refractive index of 1.5.

From the result in Fig. 2, we can observe that with the ideal setup of light source and loss from measurement, the Sagnac-based vibrometry shows better performance for most of the frequency points with the lower noise level, since the velocity noise density of Sagnac-based vibrometry is nonlinear to the frequency. Because of the periodic property of the velocity noise density of Sagnac-based vibrometry, the noise level deteriorates around the frequency of 20 MHz, 40 MHz, 60 MHz, and 80 MHz. Then, we consider a more practical

setup in that the loss brought by the measurement is 20 dB. Meanwhile, the splitting ratio  $S$  of LDV is set to be 10:90, which is the optimal splitting ratio cooperating with the loss.

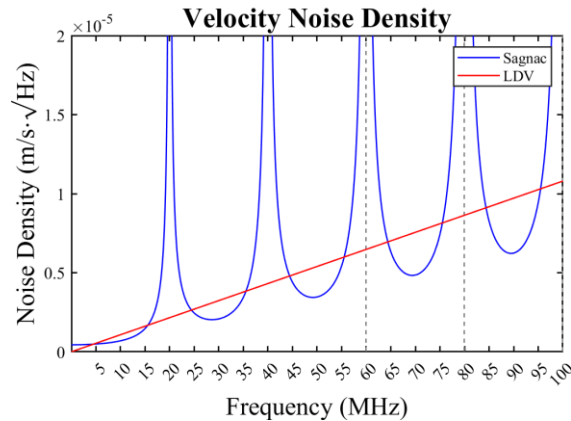


Figure 3: Comparison of velocity noise density of the Sagnac-based vibrometer and LDV in a pragmatic setup: the light source is operating on 1550 nm with the power of 1 mW, the loss brought by the measurement is 20 dB, the splitting ratio  $S$  is 10:90, and the fiber delay line in Sagnac is 10 m with the effective refractive index of 1.5.

As shown in Fig. 3, the performance of both Sagnac-based vibrometry and LDV deteriorated with the higher noise level. However, even with a certain loss, the velocity noise of the Sagnac-based vibrometer and LDV remain roughly the same, which convinces the potential of the Sagnac-based vibrometry.

## Conclusion

In this paper, we model, calculate and compare the velocity noise density of Sagnac-based vibrometry and LDV. We observed that with the same amount of optical power, the noise floor of shot-noise-limited Sagnac-based vibrometry and LDV is at roughly the same level over the frequency range from 0.1 MHz to 100MHz. However, at some frequency points, the Sagnac-based vibrometry provides a slightly lower noise level due to its periodic property in velocity noise density. Moreover, a setup with lower loss also helps in improving the performance of the system. Considering the implementation of the system, Sagnac has the advantage of using a broadband light source because the clockwise and the counterclockwise light undergo the same path. Although a broadband light source can also be applied for an interferometer like the LDV, it cannot be named an LDV as its optical source is no longer a laser source.

## References

- [1] M. Johansmann, G. Siegmund, and M. Pineda, "Targeting the limits of laser Doppler vibrometry," Proc. IDEMA, 1-12, 2005.
- [2] I. Pelivanov, T. Buma, J. Xia, C.W. Wei, and M. O'Donnell, "A new fiber-optic non-contact compact laser-ultrasound scanner for fast non-destructive testing and evaluation of aircraft composites," Journal of Applied Physics, 115(11), 113105, 2014.
- [3] L.E. Drain, "Introduction," in The Laser Doppler Technique, Chichester, pp. 1-4, 1980.
- [4] L. Yanlu, E. Dieussaert, and R. Baets, "Miniaturization of Laser Doppler Vibrometers—A Review," Sensors 22, no. 13: 4735, 2022.
- [5] B. Culshaw "The optical fibre Sagnac interferometer: an overview of its principles and applications," Measurement Science and Technology, 17 R1, 2006.

# Towards wafer-scale integration of InP membrane photonics on InP substrates for high-speed datacenter applications

S. Abdi<sup>1</sup>, V. Nodjiadjim<sup>2</sup>, R. Hersent<sup>2</sup>, M. Riet<sup>2</sup>, C. Mismar<sup>2</sup>, T. de Vries<sup>1</sup>, K.A. Williams<sup>1</sup>, and Y. Jiao<sup>1</sup>

<sup>1</sup> Eindhoven University of Technology, De Rondon 70, 5612 AP Eindhoven, The Netherlands

<sup>2</sup> III-V Lab, joint lab of Nokia Bell Labs, Thales R. and T. and CEA Leti, Palaiseau, France

*In this paper, we discuss challenges faced towards wafer-scale co-integration of InP membrane photonics with InP electronics. We start by addressing thin film coatings for protecting the InP electronics wafer during wet etching removal of InP photonics wafer. We then investigate the evolution of BCB residual stress for different BCB thicknesses and treatment times. Finally, we assess the effect of residual stress of BCB and SiO<sub>2</sub> on the performance of HBT devices to validate the co-integration plan.*

## Introduction

Vertical co-integration of InP-based membrane photonics with InP-based electronics paves the way towards scalable compact high-speed devices. This technique relies on wafer-scale adhesive bonding and <20 μm long through-polymer vias gold interconnects to create a 3D monolithic circuit. Here, the sandwiched polymer ensures high thermal and electrical insulation while the gold interconnections drive the RF signal and acts as heat sink for photonics. This reduces the parasitic effects with increased device and interconnect integration density [1]

There are several challenges related to this integration scheme. First, we rely on wet etching and etch-stop layer to reach precise membrane thickness after bonding. For InP membranes on Silicon (InP), the chemical selectivity is high. Here, the InP electronics wafer itself is the carrier, thus high-quality hermetic protective coatings are needed to ensure the wafer is not damaged during the wet-etch of the InP photonics side. Secondly, BCB is cured during bonding at temperatures above 240°C. The resulting residual stress build-up need to be studied for different bonding conditions to ensure that the fabrication and performance of bonded devices on both sides are not affected.

In this paper, we discuss our investigation of these challenges starting by protective coatings for selective wet etching. We then discuss the residual stress of BCB vs BCB thickness and treatment time. Finally, we test the DC and RF performance of electronics undergoing this stress to validate the feasibility of this co-integration scheme.

## Thin film protective coatings for InP wafer wet-etching

Wafer removal by wet etching is a key process to reach a InP membrane-thick layer for photonics with precise thickness. Etching is done using concentrated HCl at an extended time. For InP-InP bonded wafers, this requires backside protection to block the solution from damaging one of the substrates, e.g., the electronics wafer. The chemical reaction leads to forming concentrated PH<sub>3</sub> gas that can create or aggravate weak spots in the protective coating, which in-turn can complicate further processing. Thus, low-stress hermetic coatings are needed. Having these considerations in mind, we systematically investigated different combinations of protective layers. A schematic illustration of the tested coatings is shown in Fig.1. The pre-bond SiO<sub>2</sub> and ALD coatings are intended to

reach conformal coverage of the wafers sidewalls and increase hermicity, other coatings are used to strengthen the protection.

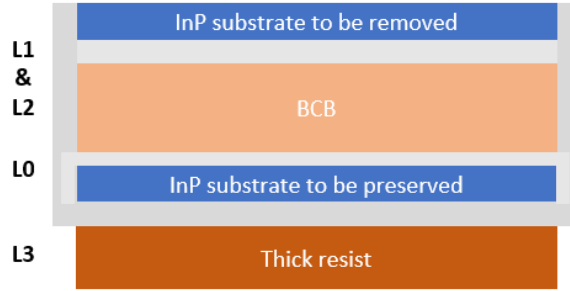


Figure 1: Schematic illustration of the layer stack. L:0-3 indicates the deposition order of these layers. We first investigated the required SiO<sub>2</sub> thickness for BCB adhesion before bonding (L0), the tested thicknesses are 50 and 500nm. Results show that 50nm thickness leads to BCB lift-off and higher damage to the InP wafer underneath. Therefore, 500nm thickness of the SiO<sub>2</sub> is required to fully encapsulate the InP wafer. Next, we investigated (<100Mpa) stress SiO<sub>2</sub> coatings on the backside (L1, L2). L1 is a thin 30 nm ALD-deposited layer that conformally covers the entire backside and wafer edges, while L2 is >1μm-thick SiO<sub>2</sub> to preserve the ALD-deposited SiO<sub>2</sub>. Results show that both of these layers are required to fully preserve the wafer edges, while L2 is more flexible in terms of thickness. However, given that the wafers are extensively processed up to the point of bonding, SiO<sub>2</sub> protective coating were not sufficient to fully cover the backside due to the presence of particles. Therefore, an extra resist layer is needed to cover the surface.

## Evaluation of residual stress in adhesive bonding

In this section, we assess the residual stress of BCB for unbonded wafers and relate it the post-bonding case. In adhesive bonding with soft-baked BCB, the BCB reaches a low viscous state and reflows before full curing. This reflow is ideal for planarizing structured interfaces. However, it also well accommodates for non-uniformities in the compression forces applied during bonding, which translates into large thickness non-uniformities [2]. For unbonded stacks, the BCB thickness non-uniformity after full cure is below 5%. Moreover, any mismatch in CTEs (coefficient of thermal expansions) between the two bonded wafers can contribute to this residual stress. Thus, we focused on the comprehensive study of residual stress of unbonded stacks to decouple these effects.

The evolution of BCB stress vs baking temperatures was previously studied [3]. However, the relationships between BCB stress and its thickness, and BCB stress and its treatment time have not been investigated. Hence, we fixed our treatment temperature at 280 °C and studied these relationships to have a full view on bonding-induced residual stresses. The investigated thickness range is 1-16 μm, whereas the treatment time range corresponds to 95% crosslinking to well beyond full crosslinking. We also used Si and InP carriers for higher accuracy. The stress is assessed by measuring the variation in wafer bow. We used Stoney's formula to extract the stress values given by [4]:

$$\sigma = \frac{E_s}{6(1 - \nu_s)} \frac{h_s^2}{h_f^2} \left( \frac{1}{R} - \frac{1}{R_s} \right)$$

Here,  $E_s$  and  $\nu_s$  are the Young modulus and Poisson ratio of the substrate,  $h_s$  and  $h_f$  are the thicknesses of the substrate and deposited thin film, and  $R_s$  and  $R$  are the substrate curvature radius before and after deposition (or thermal treatment in some cases of this study). The bow profiles are measured using profilometry and automatically fitted to

extract accurate bow values. The process flow consists of cleaning the wafers and depositing and outgassing 50 nm SiO<sub>2</sub>. BCB is then deposited and cured for different periods. The bows are tracked between each deposition or curing step. The BCB thickness is tracked with reflectometry. We measured bows in both directions perpendicular and parallel to the wafer major flat to increase the accuracy. The average bow of the two directions are plotted for each thickness and curing time for Si and InP carriers in Fig.2.a) and Fig.2.b), respectively. We identify each wafer by its BCB thickness after the full cure. The dashed line represents the stress expected from CTE mismatch between BCB and the carrier wafer given by:

$$\sigma = \left( \frac{E_{BCB}}{1 - \nu_{BCB}} \right) (\alpha_{BCB} - \alpha_{carrier}) \Delta T$$

Where  $E_{BCB}$  and  $\nu_{BCB}$  are the Young's modulus and Poisson ratio of BCB,  $\alpha_{BCB}$  and  $\alpha_{carrier}$  are the coefficients of thermal expansion of BCB and the carrier wafer, and  $\Delta T$  is the temperature window.

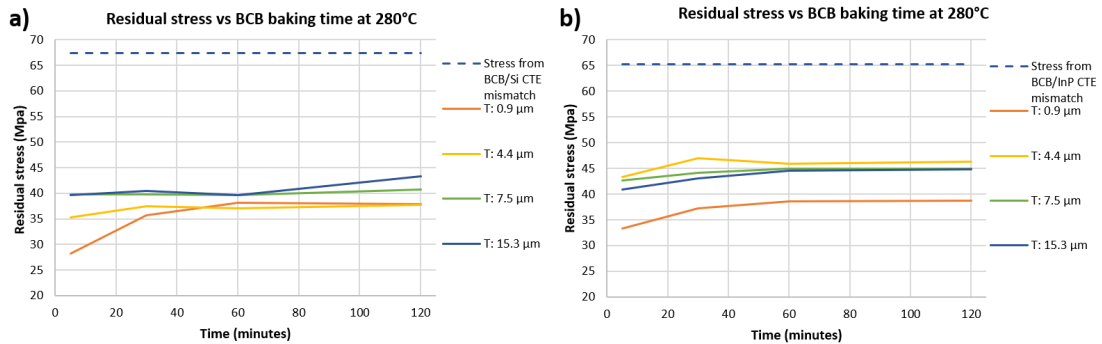


Figure 2: Residual stress vs baking time for different BCB thicknesses for: a) Si carrier, b) InP carriers. Results show the residual stress is tensile-strained, because of the higher stretching and contracting of BCB. From Fig.2, it can be seen that the residual stress values are similar for various BCB thicknesses. All of these values are below the stress expected from CTE mismatch between BCB and the carrier wafer, signifying a partial stress relaxation given the mobility of polymer chains at this temperature, which is also in agreement with results from [3]. The stress increases with increasing treatment time in the range of 5 to 30 minutes and then stabilizes, signifying that the polymer chains are no longer mobile and the full cure is achieved between 5 and 30 minutes when BCB is treated at 280°C. These findings also suggest that the residual stress is mainly dominated by the CTE mismatch between BCB and the carrier wafer, which is in-turn is dominated by the large thermal expansion of BCB compared to any other solid-state substrates. Here, the difference in obtained stress values for Si and InP carriers is below 10 MPa. Therefore, in the case of InP-Si or InP-InP bonding, we expect the stress values to be similar to or lower than these values regardless of the high BCB non-uniformities after bonding.

### Effect of SiO<sub>2</sub> and BCB residual stress on InP electronics performance

To validate the possibility of this co-integration scheme, we tested the performance of HBTs under this residual stress. For this, we received two InP HBT samples from III-V Lab. We tested the stress of 500 nm SiO<sub>2</sub> as reference (required as protective coating), and compared it to adding 12μm BCB after full cure (required for planarization). We used the same flow as discussed before and photolithography to open only the pad areas as shown in Fig.3. Devices are then characterized for their DC and RF performance.

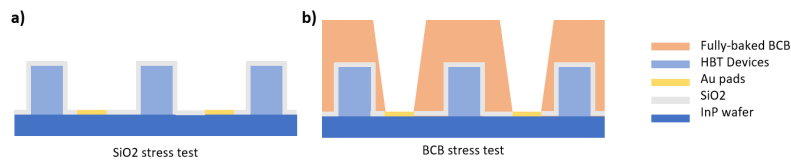


Figure 3: Schematic representation of the stacks dedicated for testing the stress of: a) SiO<sub>2</sub>, b) BCB

Based on our previous investigations, temperatures for thermal treatments on HBTs need to be lower than 250°C to avoid significant performance degradations. Therefore SiO<sub>2</sub> outgassing and BCB full-cure both required baking at 240°C for 10h.

DC and RF characteristics of several tested HBTs are shown in Fig.4.

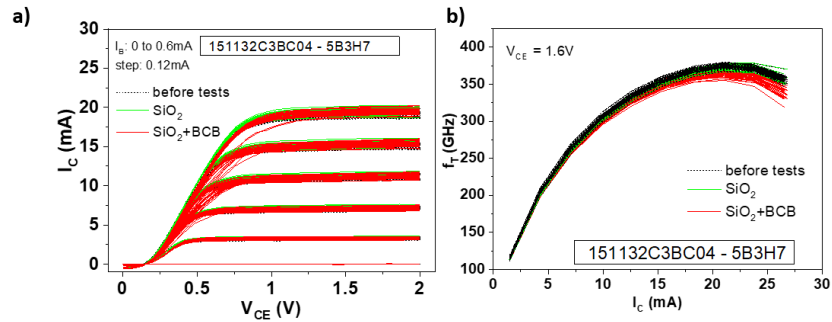


Figure 4: a) DC and b) RF characteristics of HBTs before and after adding SiO<sub>2</sub> and SiO<sub>2</sub> +BCB. Number of characterized transistors: 80 before tests, 26 after SiO<sub>2</sub>, 36 after SiO<sub>2</sub> +BCB

Measurements on the SiO<sub>2</sub> sample showed that the transistors were not affected by the deposition while ones performed on SiO<sub>2</sub>+BCB showed a slight degradation of the transistor emitter resistance, and thus  $f_T$ . This degradation is linked to the hard baking conditions used for BCB with double the thermal budget delivered to the first sample.

## Conclusions

To conclude, we investigated processing steps for co-integration of InP electronics and photonics. Using 500nm SiO<sub>2</sub> before bonding and multi-coatings on the backside is optimal as protective coating. The residual stress of BCB is mainly dominated by BCB/substrate mismatch, regardless of the treatment time and BCB thickness. BCB partial stress relaxation yields values below 50 MPa. This stress had no effect on the performance of HBTs, thereby further validating our co-integration plan.

## Acknowledgements

This work was supported by the H2020 ICT TWILIGHT Project (contract No. 781471) under the Photonics PPP.

## References

- [1] M. Smit, K. Williams, and J. van der Tol, "Past, present, and future of InP-based photonic integration," *APL Photonics*, vol. 4, no. 5, p. 050901, May 2019, doi: 10.1063/1.5087862.
- [2] F. Niklaus *et al.*, "Adhesive Wafer Bonding Using Partially Cured Benzocyclobutene for Three-Dimensional Integration," *J. Electrochem. Soc.*, vol. 153, no. 4, p. G291, Feb. 2006, doi: 10.1149/1.2168409.
- [3] I. Yadav, S. Dutta, A. Katiyar, M. Singh, R. Sharma, and K. K. Jain, "Evolution of residual stress in benzocyclobutene films with temperature," *Mater. Lett.*, vol. 158, pp. 343–346, Nov. 2015, doi: 10.1016/j.matlet.2015.06.032.
- [4] D. Quirion, M. Manna, S. Hidalgo, and G. Pellegrini, "Manufacturability and Stress Issues in 3D Silicon Detector Technology at IMB-CNM," *Micromachines*, vol. 11, no. 12, Art. no. 12, Dec. 2020, doi: 10.3390/mi1121126.

# Optically Programmable Microring Resonator Filter

A. Bahari<sup>1</sup>, M. Spiegelberg<sup>1</sup>, D.R.D. Van Luijk<sup>2</sup>, R.P. Sijbesma<sup>2</sup>, O. Raz<sup>1</sup>

<sup>1</sup>Eindhoven University of Technology, Dept. of Electrical Engineering, Groene Loper 19, 5612 AP Eindhoven, The Netherlands

<sup>2</sup>Eindhoven University of Technology, Dept. of Chemical Engineering and Chemistry, Het Kranenveld 14, 5612 AZ Eindhoven, The Netherlands

*This paper demonstrates a method to program photonic integrated circuits (PICs) by using a tunable cladding. It is based on using photoswitchable molecules called diarylethenes (DAE), which induce a photoisomerization. The use of DAEs is promising as the optical properties change after light stimulation is applied. Optical tuning can be easily realized with light sources in the visible and long ultra-violet (UV-a) range. Rapid programming times and a reversible group index change of approximately  $\Delta n_g \approx 0.04$  have been achieved between the two states of the DAE cladding which has been applied to a microring resonator (MRR).*

## Introduction

**P**HOTONIC integrated circuits are used in key applications such as data communication, biomedical, metrology[1], [2], and show great promise in the fast-growing fields of neural networks and quantum information processing[3], [4]. PICs have been bespoke devices and only in recent years the growing maturity of the technology has introduced the idea of *programmable* photonic integrated circuits[4]. Programming can be achieved through numerous mechanisms such as electrical or thermal tuning as well as using more complex means like MEMS technology[5]. Unfortunately, all these solutions can only maintain their state while constant power is applied to the system. Thus, a need has been created for a programming mechanism that is sustainable as well as reversible. This introduces the idea of using a programmable layer to rectify or optimize the output characteristics of a photonic device. These layers change their optical characteristics through physical stimulation. This enables the possibility to compensate for process tolerances. The method in this paper focuses on photoswitchable compounds, in particular diarylethenes (DAEs). The DAE molecules undergo photoisomerization when they are irradiated with light of a certain wavelength. This results in a refractive index change of the DAE molecule and

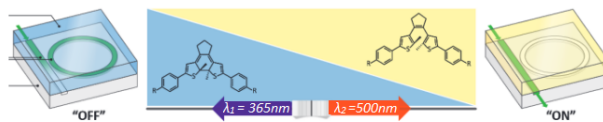


Figure 1. Example of switching due to light stimulation of the optical sensitive cladding

therefore of the cladding. The light-induced isomerizations also exhibit different absorption spectra. When combining this chemical compound with an integrated photonic component, such as a waveguide, the refractive index change of the cladding will influence the optical properties of the component. The strength of the effect depends on the sensitivity of the PIC's surface.

In this paper it is shown that the use of programmable waveguide cladding is promising. Physical and optical properties change when light stimulation is applied.

### Optical tunable compound

The compounds that have been investigated belong to the group of diarylethenes (DAEs). DAEs are optically sensitive. Two different isomer configurations of the DAEs can be seen in Figure 2. This paper tests these DAE variations called DAE 1 and DAE 2. The first one is based on a perfluorocyclopentene derivative. The second one is structurally similar but without fluorine atoms.

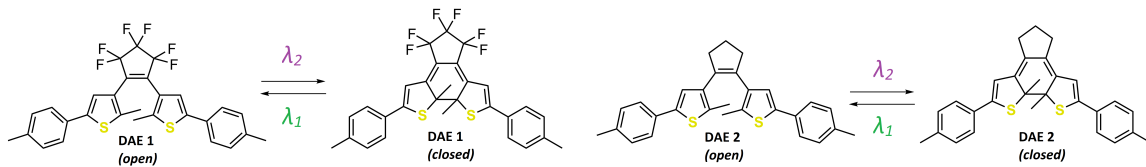


Figure 2. Structural formulas of DAE 1 and DAE in the open and closed forms

The quantum yield is a parameter specifically used in photochemical reactions and is defined as the ratio between the number of molecules undergoing a transition from state A to state B, and the number of photons that are absorbed for this reaction. This applies to a molecule undergoing a photoisomerization from an isomer A to isomer B. The DAEs in this paper have two isomer configurations, a closed-ring and an open-ring form. The molecule will switch to its closed-ring form when illuminated with UV-light, or to its open-ring form using light in the visible spectrum.

### Method and Results

The DAEs have been analyzed by spinning them as a cladding layer on a PIC. This device is based on a silicon on insulator (SOI) platform enabling high interaction of the guided waveguide mode with the surface. The PIC that has been used for testing is an MRR which operates as a wavelength filter. By changing the state of the DAE the refractive index of the cladding changes and therefore a shift of the filtered wavelength can be measured. To characterize the MRR a transmission measurement is performed. Therefore light is coupled in and out of the PIC via single mode fibers using TE optimized grating couplers. As light source, a tunable laser is used and the transmitted signal is measured with an optical power meter. As a reference, a fiber Bragg grating (FBG) is used for any wavelength discrepancies. This FBG filters at a wavelength of 1547.75nm. The wavelength range has been chosen to be 1540 to 1550 nm. The input power is fixed for all wavelengths at 5 dBm. A polarization controller is used to tune the polarization state.

The PIC contains a 24  $\mu\text{m}$  MRR with a 55 nm separation gap between the ring and the

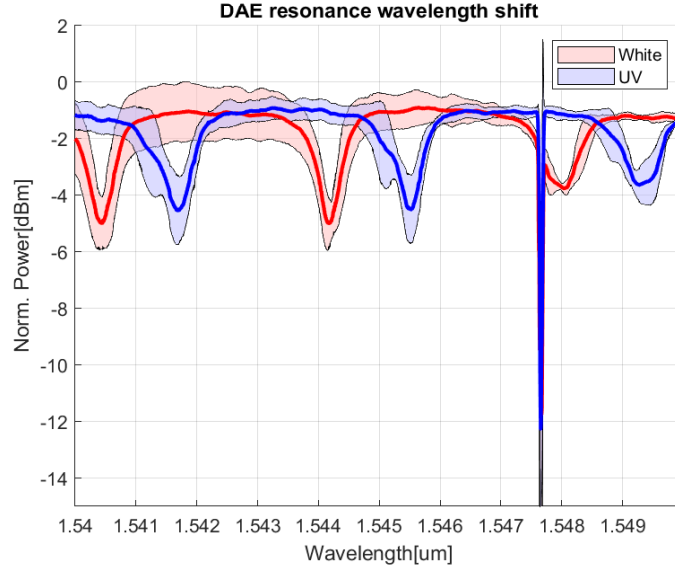


Figure 3. Mean and standard deviation of congregate data

buswaveguide. The photoswitching has been achieved by a common small desk-lamp (2700 K, 220 lumen) as the white light source, and a 390 nm UV lamp with a radiant flux of 6 W. The DAE sample has been measured through multiple cycles. Each cycle the MRR has been measured between and after each exposure of white light for 5 minutes, and UV for 1 minute. This data has been normalized against the wavelength dependent propagation loss. Some discrepancies still exist between cycles due to external factors such as ambient light and too long/short exposure times. The DAE is highly sensitive, measuring for longer/short timeframes will give different results. In Figure 3 the mean and standard deviation of the transmission measurement are shown. The two colors (red and blue) represent the two programming states. A wavelength shift in a MRR will scale linearly with the refractive index. The refractive index change can be approximated by analyzing the group index:

$$n_g = \frac{\lambda^2}{FSR \cdot L} \quad (1)$$

$FSR$  is the free spectral range,  $L$  is the optical path length of the MRR. This results in an  $\Delta n_g$  of approximately 0.04. The Q-factor of the ring is  $Q \approx 4500$ .

To evaluate the usability of the DAE an estimation can be made regarding the quantum yield and maximum programming time. The quantum yields for the two DAEs are calculated using an estimation of the photon flux determined by the LED driver current and quantum efficiency of the laser setup. It can be estimated roughly with the following equation:

$$photon\ flux = \frac{I_{driver} \cdot QE}{q_e \cdot area} \quad (2)$$

where  $I_{driver}$  is the LED driver current,  $q_e$  is the elementary charge in Coulombs, and QE is the quantum efficiency. The quantum yield of the solid films of DAE 1 is approximately 50% and for DAE 2 30%.

The maximum programming time rounds to 60 minutes for both DAEs for visible light. The programming time using the UV source is a factor 10 smaller at 5 minutes. However, the largest measured refractive index change occurs within 10 minutes for visible light and within 1 minute for UV light.

## Discussion

To enable better modeling of the system consisting of the PIC and the DAE cladding layer it is important to know the effective refractive index change instead of the group index change. It has estimated to be  $\Delta n_{eff} \approx 0.03$  at 1550 nm. This is slightly lower than the measured refractive group index of 0.04. This is because the group index is expected to be higher for Si[6], and also due to approximation errors of the fitting software. With regards to the sustainability of the DAE layers, it needs to be considered that while its optical behaviour seems ideal for photonic programming, it is limited in the amount of cycles it can switch states. Another limitation of the system is the fact that the DAE is easily affected by ambient light, reducing the remaining cycle life of the molecules even further. It is therefore vital that the DAE films are not exposed to external light sources for experimental as well as potential industrial applications.

## Conclusion

The DAE shows great potential for photonic programming. For the used PIC a group index change of  $\Delta n_g \approx 0.04$  has been measured. The resonance wavelength shift of the tested MRR was controllable, reversible, and maintains its state if not exposed to light sources.

## Acknowledgment

The authors of this paper would like to thank Prof. Stefan Hecht and Bart Saes, who provided the material used for this research.

## References

- [1] M. A. Mohammed, C. C. Sproncken, B. Gumí-Audenis, E. Lazdanaitė, R. Stabile, I. K. Voets, and O. Raz, "Reversibly Programmable Photonics via Responsive Polyelectrolyte Multilayer Cladding," *Advanced Optical Materials*, vol. 8, no. 16, 2020. [Online]. Available: <https://doi.org/10.1002/adom.202000325>.
- [2] "Birth of the programmable optical chip," p. 1, dec 2016. [Online]. Available: <https://www.nature.com/articles/nphoton.2015.265>
- [3] S. Xu and J. Wang, "Performance evaluation of an integrated photonic convolutional neural network based on delay buffering and wavelength division multiplexing."
- [4] J. Capmany, I. Gasulla, and D. Pérez, "Microwave photonics: The programmable processor," pp. 6–8, dec 2016. [Online]. Available: <https://www.nature.com/articles/nphoton.2015.254>
- [5] W. Bogaerts, H. Sattari, P. Edinger, A. Y. Takabayashi, I. Zand, X. Wang, A. Ribeiro, M. A. Jezzini de Anda, C. Errando-Herranz, G. Talli, K. Saurav, M. A. Garcia Porcel, P. Verheyen, B. Abasahl, F. Niklaus, N. Quack, K. B. Gylfason, P. O'Brien, and M. U. Khan, "MORPHIC: Programmable photonic circuits enabled by silicon photonic MEMS." *SPIE-Intl Soc Optical Eng*, feb 2020, p. 1.
- [6] E. Dulkeith, F. Xia, L. Schares, W. M. J. Green, and Y. A. Vlasov, "Group index and group velocity dispersion in silicon-on-insulator photonic wires," *Optics Express*, vol. 14, no. 9, p. 3853, may 2006. [Online]. Available: <https://opg.optica.org/viewmedia.cfm?uri=oe-14-9-3853&seq=0&html=true> <https://opg.optica.org/abstract.cfm?uri=oe-14-9-3853> <https://opg.optica.org/oe/abstract.cfm?uri=oe-14-9-3853>

# Phase modulation improves performance of delay-based reservoir computing with semiconductor lasers

I. Bauwens,<sup>1</sup> K. Harkhoe,<sup>1</sup> P. Bienstman,<sup>2</sup> G. Verschaffelt,<sup>1</sup> and G. Van der Sande<sup>1</sup>

<sup>1</sup> Vrije Universiteit Brussel, Applied Physics Research Group, Pleinlaan 2, 1050 Brussels, Belgium

<sup>2</sup> Ghent University-IMEC, Photonics Research Group, Department of Information Technology, Technologiepark Zwijnaarde 126, 9052 Ghent, Belgium

*In photonic reservoir computing, semiconductor lasers with delayed feedback can be used to efficiently solve difficult and time-consuming problems. We show numerically that the performance depends heavily on how the data is modulated on the optical input signal [1]. We compare different input configurations for injecting the input signal into the reservoir and evaluate their performance on the one-step ahead Santa Fe prediction task. Based on simulations, we show that better performance can be achieved by using an unbalanced Mach-Zehnder modulator, which modulates both intensity and phase, as compared to a balanced Mach-Zehnder modulator, which only modulates the intensity. This implies that modulating the phase of the injected field is essential to get good computational performance in this type of reservoir computers. We also observe a further improvement in performance when using a phase modulator alone. We can thus conclude that using only a phase modulator as input configuration, with well-chosen modulation amplitude, is ideal for solving tasks using semiconductor lasers with delay, both performance-wise as well as in simplicity of implementation.*

## Introduction

In our current technological society, we are becoming increasingly able to process and analyze information using machine learning. The concept of reservoir computing (RC) within this machine learning field offers a simple, yet powerful technique to use recurrent networks for computing. RC systems have shown good performance in various benchmark tasks. An RC system consists of a large recurrent neural network with fixed interconnections. Its topology can be described in three separate components: an input layer, the reservoir, and an output layer. In the input layer, the data is injected into the system and is sent to the reservoir, which consists of a recurrently connected network of non-linear nodes. The processed information is then sent to the output layer, where the output weights are optimized to match the output with a corresponding target output. The optimization of weights, and thus the training phase, occurs only in the output layer, whereas the internal weights of the reservoir itself are not altered. This makes training much more straightforward compared to other artificial neural networks and simplifies RC in its implementation. Using photonics for implementing RC offers several advantages, ranging from a low-energy consumption, high-speed performance and the possibility of high inherent parallelism [2,3]. The injection of input data into this reservoir can be performed via several methods. The input data can e.g. be injected electronically. In this work, however, we will focus on optically injected data, which has the advantage of allowing higher data injection rates. This latter method can be performed by modulating the phase of the injected electric field by using a phase modulator or by modulating the amplitude of the electric field. In this work, we numerically investigate

the effect of the optical data injection configurations on the performance of delay-based reservoir computing system [1].

## Numerical implementation of delay-based reservoir computing

RC using semiconductor lasers with delayed feedback relies on a time-multiplexing approach to implement the reservoir. This delay-based technique has been implemented in several types of electronic or photonic reservoirs. Fig. 1 shows the topology of a photonic delay-based RC using a single mode semiconductor laser as non-linear node, which will be studied in this paper, and consists of an input layer, reservoir and output layer.

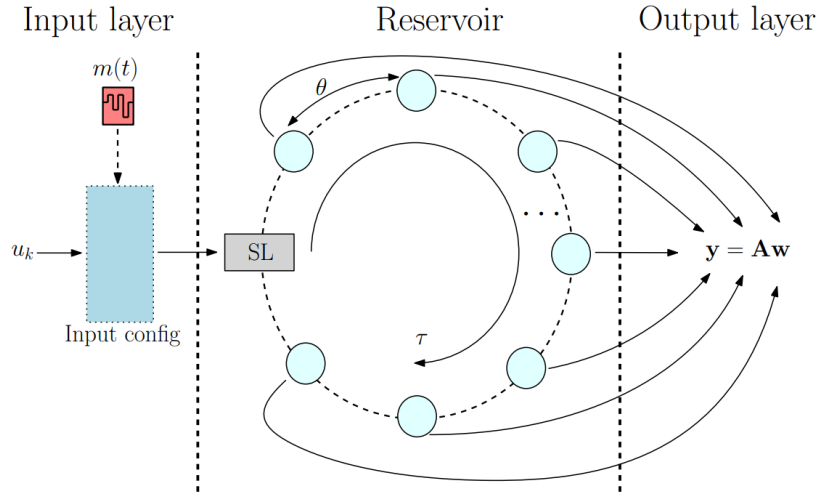


Figure 1. Illustration of a delay-based RC system using a semiconductor laser (SL), with input data  $u_k$ , preprocessing mask  $m(t)$ , node separation  $\theta$  and delay time  $\tau$ . The light blue circles represent the virtual nodes and the output layer is defined by the reservoir output  $A$  and output weights  $w$ .

We use the intensity of the nodes, which are measured by sampling the output of the reservoir with a time separation  $\theta$ . We can find the output weights  $w$  corresponding to the  $N$  nodes of the reservoir in the training phase. In order to achieve this, we use the output of the RC system  $A$ , which represents the node responses to the training input data, and the expected target data  $y^{\text{train}}$ . In practice, the weights  $w$  can be retrieved by calculating  $w = A^\dagger y^{\text{train}}$ , where  $^\dagger$  denotes the pseudo-inverse. In the input layer, we optically inject the discrete input data  $u_k$ , with  $k$  the index of the data sample, via an input configuration which we will vary in this work. Due to the time-multiplexing, we need to make use of a preprocessing mask  $m(t)$  before injecting the input data into the reservoir. The delay-based RC system with a single-mode semiconductor laser as non-linear node, can be accurately modeled using rate-equations [4]

$$\begin{aligned} \frac{dE(t)}{dt} &= \frac{1}{2} (1 + i\alpha) \xi n(t) E(t) + \eta E(t - \tau) e^{-i\Omega_0 \tau} + \tilde{F}_\beta + \mu E_{in j}(t) \\ \frac{dn(t)}{dt} &= \Delta J - \frac{n(t)}{\tau_c} - [g + \xi n(t)] |E(t)|^2, \end{aligned}$$

where  $E(t)$  and  $n(t)$  are the complex valued electric field of the laser and the excess amount of available carriers (both dimensionless).  $\alpha$  represents the linewidth enhancement factor, and  $\xi$  and  $g$  the differential gain and threshold gain. Parameters  $\eta$  and  $\mu$  are the feedback

rate and the injection rate.  $\Delta J$  represents the excess pump current rate, and is defined as  $\Delta J = I_{\text{thr}}\Delta I/e$ , where  $I_{\text{thr}}$  is the threshold pump current,  $e$  the elementary charge and  $\Delta I$  the dimensionless pump current excess,  $\Delta I = (I - I_{\text{thr}})/I_{\text{thr}}$ . We use a single feedback phase, which is not varied in our work,  $\Omega_0 \tau = 0$ .  $F_{\beta}$  represents complex Gaussian white noise to simulate the spontaneous emission noise strength.  $F_{\beta}$  has a zero mean and autocorrelation equal to  $\langle F_{\beta}(t)F_{\beta}^*(t') \rangle = \beta/\tau_c \delta(t - t')$ , where  $\beta$  controls the spontaneous emission noise and where  $\tau_c$  is the carrier lifetime. Furthermore, the input data is injected through an optical input signal  $E_{\text{inj}}(t)$  with the same wavelength as the free running laser, i.e. the injection frequency detuning is therefore equal to zero and not varied in this work. Following previous work in Ref. [5] we have chosen a value of 20 ps as the standard value for the node separation. In order to simulate the injection of data in the rate-equations, we specify the term  $E_{\text{inj}}(t)$ . For the unbalanced MZM  $E_{\text{inj}}(t) \propto (1 + e^{iB_{\text{MZM}}(t)})$ , for the balanced MZM  $E_{\text{inj}}(t) \propto (e^{iB_{\text{MZM}}(t)/2} + e^{-iB_{\text{MZM}}(t)/2})$ , for the balanced MZM combined with PM  $E_{\text{inj}}(t) \propto (e^{iB_{\text{MZM}}(t)/2} + e^{-iB_{\text{MZM}}(t)/2})e^{iB_{\text{PM}}(t)}$  and for the PM  $E_{\text{inj}}(t) \propto e^{iB_{\text{PM}}(t)}$ . The terms  $B_j(t)$  ( $j \in \{\text{MZM}, \text{PM}\}$ ) represent the masked time-dependent modulator signal which is used as input for the different input configurations of the RC system. We define the modulator signal  $B_j(t)$ , corresponding to input configuration  $j$ , from the masked data signal  $S_j(t)$  using an amplitude  $A_j$  and bias  $\Phi_j$ ,  $B_j(t) = A_j S_j(t) + \Phi_j$ . In order to compare our results for tasks which have different ranges for their input data, we will introduce in our discussions the range of  $B_j$ , marked by  $\Delta B_j$ . For the simulations of our delay-based RC system we numerically integrate the rate-equations [1].

## Numerical results: Santa Fe time-series prediction task

In order to compare the performance of the different input configurations, we use a one-step ahead time-series prediction task. The input dataset used for this task is the Santa Fe dataset, which consists of data points sampled from a far-IR laser in a chaotic regime. The goal is to find the input configuration which results in the lowest error, and thus the best performance for this particular task. The performance is quantified by the NMSE (normalized mean square error), where typical values for the NMSE for the Santa Fe one-step ahead predictions via simulations of RC systems are around 0.01. We have taken 3000 data samples from the discrete Santa Fe dataset,  $u_k^{\text{train}}$ , where  $k \in \{1, \dots, 3000\}$ , as the training set in the RC system. As test set  $u_k^{\text{test}}$ , we have taken 1000 different data samples. We have repeated each numerical experiment 10 times, from which we calculate the average NMSE and its standard deviation (shown as error bars). If we consider a balanced MZM as input configuration, we find an  $\text{NMSE} = 0.134 \pm 0.044$ , and if we use an unbalanced MZM,  $\text{NMSE} = 0.019 \pm 0.0047$ . This result is in agreement with typical NMSE values found in literature. This is shown in Fig. 2, where we show the NMSE versus the total range of the phase modulator signal  $\Delta B_{\text{PM}}$  for different input configurations. In this figure, we have indicated the performance of the (un)balanced MZM as a horizontal line. We also observe in this figure that, for the input configuration consisting of a PM and a balanced MZM, the NMSE initially decreases when increasing  $\Delta B_{\text{PM}}$ , reaches an optimal point (with lowest NMSE) and again increases for larger  $\Delta B_{\text{PM}}$ .

As we achieve a large improvement by adding a phase modulator, the question can be raised whether an MZM is required at all to obtain good RC performance. Ultimately, this allows for a simpler input configuration that only uses a phase modulator. We observe in Fig. 2 that the input configuration where only a PM is used results in the best mean

NMSE. This shows that replacing the MZM with a PM for the input configuration, and thus reducing the complexity of the input system, an improved performance can be achieved. We observe that the lowest NMSE values occur for input configurations with PMs around the broad range of  $\Delta B_{PM} = \pi/2$  to  $\pi$ . Therefore, we achieve an improvement within this large  $\Delta B_{PM}$  range. This optimal NMSE can be explained by two factors. For small  $\Delta B_{PM}$  (around  $\pi/4$ ), the system is limited by noise, so that it becomes difficult for the system to distinguish noise from different sublevel mask values. For large  $\Delta B_{PM}$ , the phase modulated signal will stand to wrap on itself. Both of these phenomena will have a negative effect on the achieved performance and explain the existence of the optimal range in the modulator signal range  $\Delta B_{PM}$ .

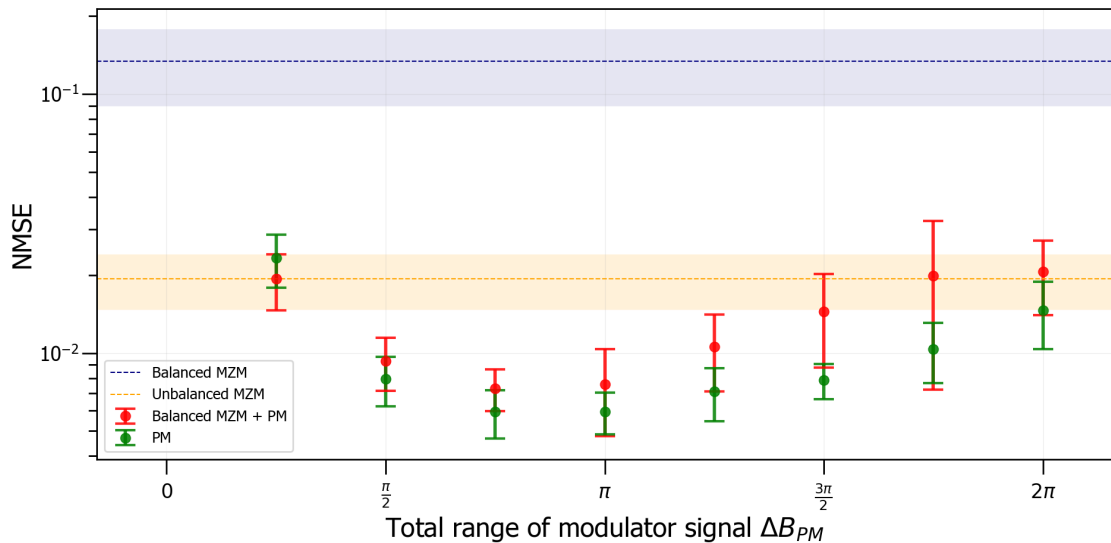


Figure 2. NMSE in function of the total range  $\Delta B_{PM}$  of the phase modulator (PM) signal for one-step ahead prediction of Santa Fe data for different input configurations, showing improved performance when a PM is used.

## Conclusion

We have numerically investigated the effect of modulating the phase when optically injecting data, with the goal of improving delay-based reservoir computing with semiconductor lasers. Using a phase modulator to inject the signal into the reservoir, resulted in an improved performance compared to literature. We therefore conclude that modulating the injected signal's phase increases the performance of optical RC for the one-step ahead prediction Santa Fe task.

## References

- [1] Ian Bauwens, Krishan Harkhoe, Peter Bienstman, Guy Verschaffelt, and Guy Van der Sande, "Influence of the input signal's phase modulation on the performance of optical delay-based reservoir computing using semiconductor lasers", *Opt. Express* 30, 13434 (2022)
- [2] Van der Sande, G., Brunner, D., and Soriano, M. C., "Advances in photonic reservoir computing," *Nanophotonics* 6(3), 561–576 (2017).
- [3] De Lima, T. F., Shastri, B. J., Tait, A. N., Nahmias, M. A., and Prucnal, P. R., "Progress in neuromorphic photonics," *Nanophotonics* 6(3), 577–599 (2017).
- [4] Lenstra, D. and Yousefi, M., "Rate-equation model for multi-mode semiconductor lasers with spatial hole burning," *Optics express* 22(7), 8143–8149 (2014).
- [5] Harkhoe, K. and Van der Sande, G., "Delay-based reservoir computing using multimode semiconductor lasers: Exploiting the rich carrier dynamics," *IEEE Journal of Selected Topics in Quantum Electronics* 25(6), 1–9 (2019).

# Silicon nitride based guided-acoustic stimulated Brillouin scattering for microwave photonic signal processing

R.A. Botter, K. Ye, Y. Klaver, O.F.P. Daulay, P.J.M. van der Slot and D. Marpaung  
University of Twente, Nonlinear Nanophotonics, PO Box 217, 7500 AE, Enschede, the Netherlands.

*In this work we present a microwave photonic notch filter created with our on-chip SBS gain. By combining the gain with a microring resonator in the same platform, we create a notch filter with a rejection of more than 60 dB. The filter can be tuned by tuning the ring resonator and pump laser. The filter has a link gain of -10 dB, an SFDR of 100.5 dB/Hz<sup>2/3</sup>, and a noise figure of 43.7 dB.*

## Stimulated Brillouin scattering in silicon nitride waveguides

Stimulated Brillouin scattering (SBS) is a third order nonlinear optical process, based on interacting acoustic and optical waves [1]. The interest in SBS induced in integrated photonic circuits has been grown in the past few years, as it has shown promising uses in signal processing [2], high-precision sensors [3], non-reciprocal control of light propagation [4], and ultra-narrow linewidth laser sources [5]

Silicon nitride has emerged as a leading platform for microwave photonic signal processing [6]. Adding SBS to the existing toolbox in this platform would open up new ways of improving the performance of the processing, and open up new possibilities. SBS in silicon nitride waveguides is weak however, because acoustic waves are not guided in a silicon oxide cladded silicon nitride waveguide [7].

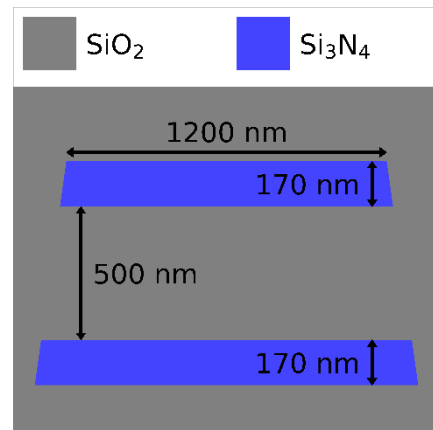


Figure 1: The geometry of our symmetric double-stripe waveguide.

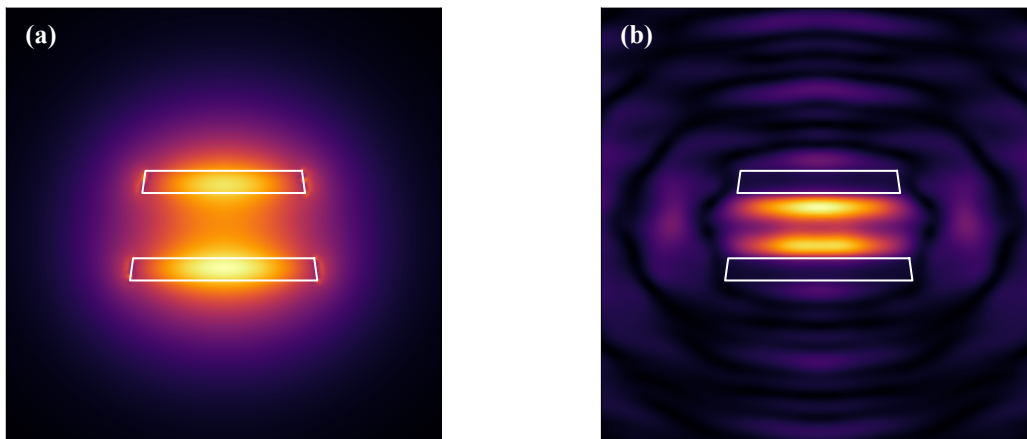


Figure 2: (a) the optical mode of our waveguide. (b) the acoustic response of the waveguide.

We have recently shown the first example of guided-acoustic SBS in silicon nitride waveguides [8]. The geometry of our waveguide, the symmetric double stripe (SDS) can be seen in Figure 1. By using two layers of silicon nitride, we are able to prevent the acoustic wave from leaking, creating acoustic guidance. Figure 2 (a) shows the optical mode of (SDS) waveguide. The corresponding acoustic response is depicted in Figure 2 (a). Note how the acoustic wave is trapped in between the two silicon nitride layers.

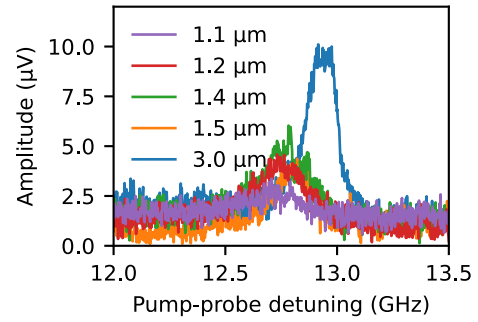


Figure 3: The measured SBS response of waveguides with different widths.

Using this geometry, we are able to achieve a Brillouin gain coefficient of  $0.24 \text{ m}^{-1}\text{W}^{-1}$ . Further enhancement of the acoustic guiding, and therefore of the Brillouin gain can be achieved by making the waveguide wider than the  $1.2 \text{ }\mu\text{m}$  depicted in Figure 1. Increasing the width to  $3.0 \text{ }\mu\text{m}$  leads to the highest measured Brillouin gain, as depicted in Figure 3. The Brillouin gain coefficient of this waveguide is  $0.40 \text{ m}^{-1}\text{W}^{-1}$ , which is a record for silicon nitride based waveguides, and 4 times higher than previous results [7].

## Microwave photonic notch filter with SBS

The linewidth of the Brillouin response in our waveguide is 130 MHz, making it very promising for signal processing. To demonstrate the potential of our waveguides we combined it with a ring resonator in the same platform to create a microwave photonic notch filter [9]. Figure 4 shows the working principle of the filter. The ring resonator is used to impart a  $\pi$  phase shift into one of the sidebands. The SBS process, with its narrow linewidth, is uniquely able to counteract the ring losses. This leads to destructive interference at the desired frequency.

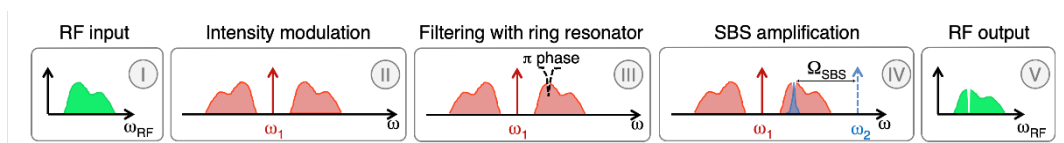


Figure 4: Working principle of the filter. The RF signal (I) is modulated using intensity modulation (II). Then, an over-coupled ring resonator processes the upper sideband, creating a notch with  $\pi$  phase shift (III). The SBS amplification is then used to compensate for the ring losses (IV). When the signal beats at the photodiode, the  $\pi$  phase shift results in a notch in the RF spectrum (V)

Figure 5 shows the setup we used to implement the filter. The ring resonator is made from the same SDS waveguide geometry, showing that these elements can readily be integrated.

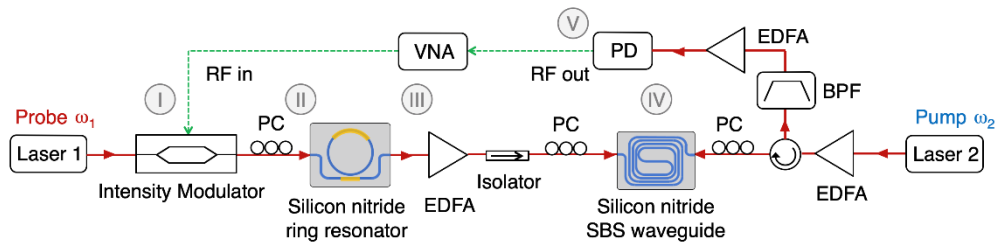


Figure 5: Schematic overview of our setup. BPF: band-pass filter, EDFA: erbium doped fiber amplifier, PC: polarization controller, PD: photodiode, VNA: vector network analyzer.

Figure 6 shows the resulting notch filter. The rejection is more than 60 dB. Tuning of the center wavelength of the filter can be achieved by simultaneously tuning the ring resonator and the pump laser. The filter has a 3 dB-bandwidth of 2.4 GHz, a link gain of -10 dB, an SFDR of  $100.5 \text{ dB/Hz}^{2/3}$ , and a noise figure of 43.7 dB. These numbers are comparable to previously reported numbers of similar SBS notch filters in suspended silicon waveguides [10].

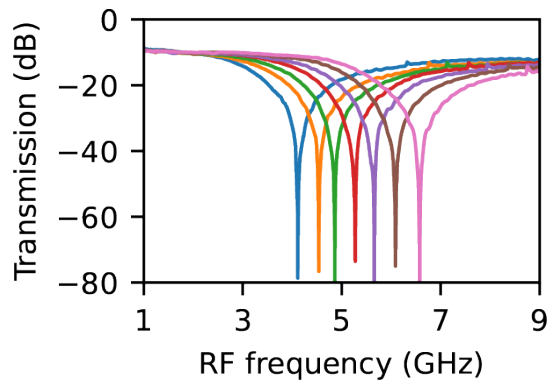


Figure 6: The notch filter created with our SBS setup. The center wavelength is tunable.

## Conclusion and outlook

We have shown the first guided-acoustic stimulated Brillouin scattering in silicon nitride waveguides, which we further enhanced by increasing the waveguide width. Using this Brillouin gain, we were able to demonstrate the first microwave photonic notch filter using SBS in the platform. This filter is on par with similar filters in other platforms.

From here we will work on further enhancing the Brillouin gain. An increased gain will lead to more use cases, such as for high precision sensing, and narrow linewidth lasers.

## Acknowledgements

This work was funded by the Nederlandse Organisatie voor Wetenschappelijk Onderzoek (NWO), project numbers 1570 and 740.018.021

## References

- [1] B. J. Eggleton, C. G. Poulton, P. T. Rakich, M. J. Steel, and G. Bahl, “Brillouin integrated photonics,” *Nat. Photonics*, vol. 13, pp. 664–677, 2019.
- [2] D. Marpaung, J. Yao, and J. Capmany, “Integrated microwave photonics,” *Nat. Photonics*, vol. 13, no. 2, pp. 80–90, 2019.
- [3] Y. H. Lai *et al.*, “Earth rotation measured by a chip-scale ring laser gyroscope,” *Nat. Photonics*, 2020.
- [4] E. A. Kittlaus, N. T. Otterstrom, P. Kharel, S. Gertler, and P. T. Rakich, “Non-reciprocal interband Brillouin modulation,” *Nat. Photonics*, vol. 12, no. 10, pp. 613–619, 2018.
- [5] S. Gundavarapu *et al.*, “Sub-hertz fundamental linewidth photonic integrated Brillouin laser,” *Nat. Photonics*, vol. 13, no. January, 2019.
- [6] C. G. H. Roeloffzen *et al.*, “Low-Loss Si<sub>3</sub>N<sub>4</sub> TriPleX Optical Waveguides: Technology and Applications Overview,” *IEEE J. Sel. Top. Quantum Electron.*, vol. 24, no. 4, pp. 1–21, 2018.
- [7] F. Gyger *et al.*, “Observation of Stimulated Brillouin Scattering in Silicon Nitride Integrated Waveguides,” *Phys. Rev. Lett.*, vol. 124, no. 1, 2020.
- [8] R. Botter *et al.*, “Guided-acoustic stimulated Brillouin scattering in silicon nitride photonic circuits,” *Sci. Adv.*, vol. 8, no. 40, p. eabq2196, 2022.
- [9] Y. Liu, A. Choudhary, D. Marpaung, and B. J. Eggleton, “Integrated microwave photonic filters,” *Adv. Opt. Photonics*, vol. 12, pp. 485–555, 2020.
- [10] S. Gertler *et al.*, “Narrowband microwave-photonic notch filters using Brillouin-based signal transduction in silicon,” *Nat. Commun.*, vol. 13, no. 1, p. 1947, 2022.

# Towards broadband optical wafer-level testing system with on-chip micro-parabolic mirror

Y. Kong<sup>1</sup>, H.L. Offerhaus<sup>2</sup>, M. Dijkstra<sup>1</sup>, S.M. García Blanco<sup>1</sup>, L. Chang<sup>1</sup>

<sup>1</sup> Integrated Optical Systems Group, MESA+ Institute for Nanotechnology, University of Twente, 7500 AE Enschede, The Netherlands

<sup>2</sup> Optical Sciences Group, MESA+ Institute for Nanotechnology, University of Twente, 7500 AE Enschede, The Netherlands

*Reflection of light by a 3D-printed parabolic mirror overcomes the in-plane limitation of end-facet coupling between two photonic devices (such as on-chip waveguides, and optical fibers). In this study, a parabolic mirror base is 3D printed using a 3D-Nanoscribe two-photon polymerization printer. The reflection layer is formed by an aluminum coating. Studies on printed mirror shape and aluminum coating roughness will be presented.*

## 1. Introduction

Wafer-level testing of optical waveguide devices is an important enabling technology to reduce testing time compare with die-level testing. This leads to a cheaper and faster development cycle. It also benefits the production process, where we can identify problematic devices easily, minimizing waste during subsequent assembly steps. In the Si waveguide platform, grating couplers have been used to couple the light out of the wafer plane for wafer-level testing [1]. However, grating couplers are based on an interference effect that is highly wavelength dependent, thus, limiting the bandwidth, especially in a relatively low-contrast waveguide material platform. Several studies have shown 3D printed solutions to redirect and collimate broadband light from a waveguide based on total internal reflection and/or refraction effect [2-4]. However, they cannot be used in the UV region, since light needs to pass through the 3D-printed polymer, which absorbs the UV light. In our design, an aluminum coating is used as the reflection layer, and the light does not pass through the polymer, thus, in principle, our design is capable from UV to infrared.

Our previous work [5] is summarized in Fig. 1, where preliminary design, fabrication, and optical characterization are shown. As shown in Fig. 1 (a), light can leave the wafer plane vertically. This enables wafer-level optical testing. Furthermore, with the proper curvature design, the mirrors generate a bigger beam waist than the mode sizes at the waveguide end-facet, which reduces the requirements for alignment accuracy. This also enables the optical coupling to another photonic chip, which is flip-chip bonded on top. In order to achieve the desired optical beam parameters it is import to investigate the printed mirror shape and the reflection coating properties. Our investigation results are discussed in this work and indicate future study direction.

## 2. Mirror shape measurement

It is important to know if the fabricated curved mirror surface has the same shape as designed. Stand-alone mirror is printed on a flat Si chip (without Al coting) for this study, as shown in Fig. 2 (a). White light interferometry (Bruker WLI Contour GT-I) is used to measure the mirror surface. However, as shown in Fig. 2 (b), no data is obtained on the curved surface (the white region in the surface plot) since the incoming light from the

white light interferometer is not reflected or scattered back to the instrument. Therefore, this technique cannot be used to measure this kind of structure.

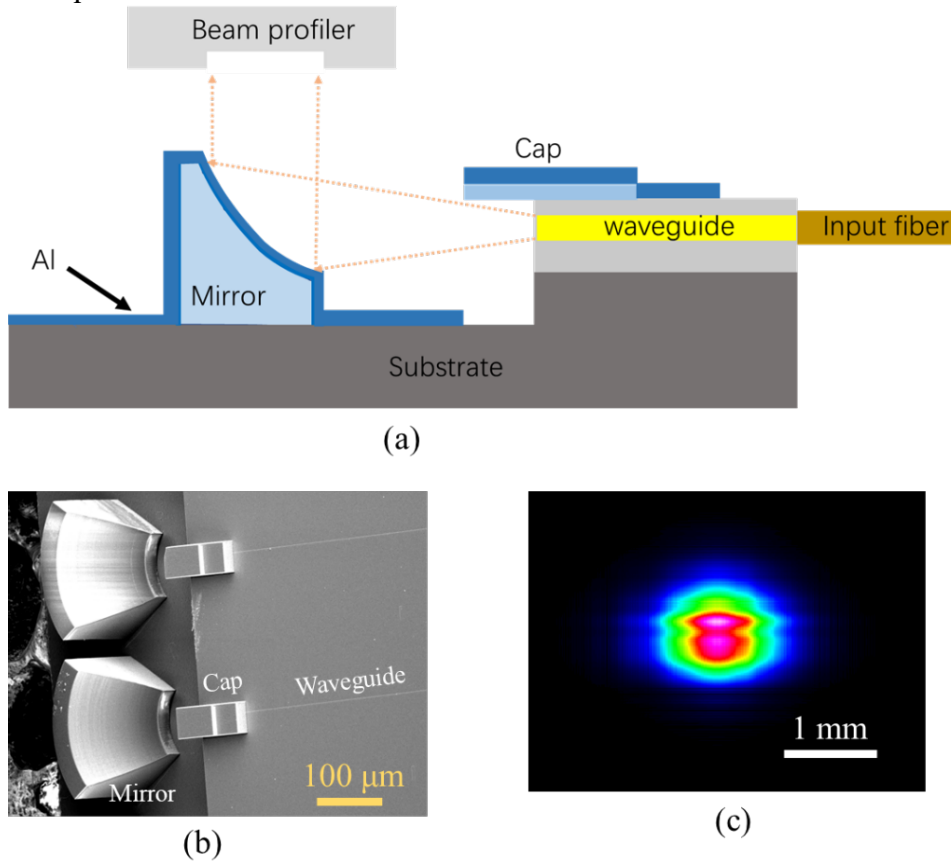


Fig. 1. (a) The cross-section view of the waveguide and the parabolic mirror. The aluminum deposition is a directional process, thus, a 3D-printed cap is positioned on top of the waveguide facet to prevent aluminum (Al) from covering the end facet. (b) SEM image of the fabricated mirrors on a waveguide chip. (c) A beam profile measured with a Thorlabs beam profiler BP209IR1(/M) at the location shown in (a) with a few centimeters distance on top of the chip.

A Dektak 8, surface profiler, is used to scan across the structure as shown in Fig. 2 (c). In order to measure the parabolic shape of the mirror surface, the scanning tip should pass through the rotation axis of the structure. Therefore, a 15  $\mu\text{m}$  high dot is printed at the rotation center as a reference point for the Dektak scan measurement. Based on the result shown in Fig. 2 (c), two conclusions can be made. First, the printed polymer has a small amount of shrink since the measured height of 138  $\mu\text{m}$  is slightly shorter than the designed value of 140  $\mu\text{m}$ . Second, the measured mirror side wall does not have 90-degree respect to the wafer surface due to the finite tip size. This means we cannot use the scanned data directly to model the true mirror surface. The scanned data is a combination of the mirror surface shape with the tip shape and the contact angle at the corresponding point. In order to obtain the true reflecting surface shape, detailed modeling is needed for future development.

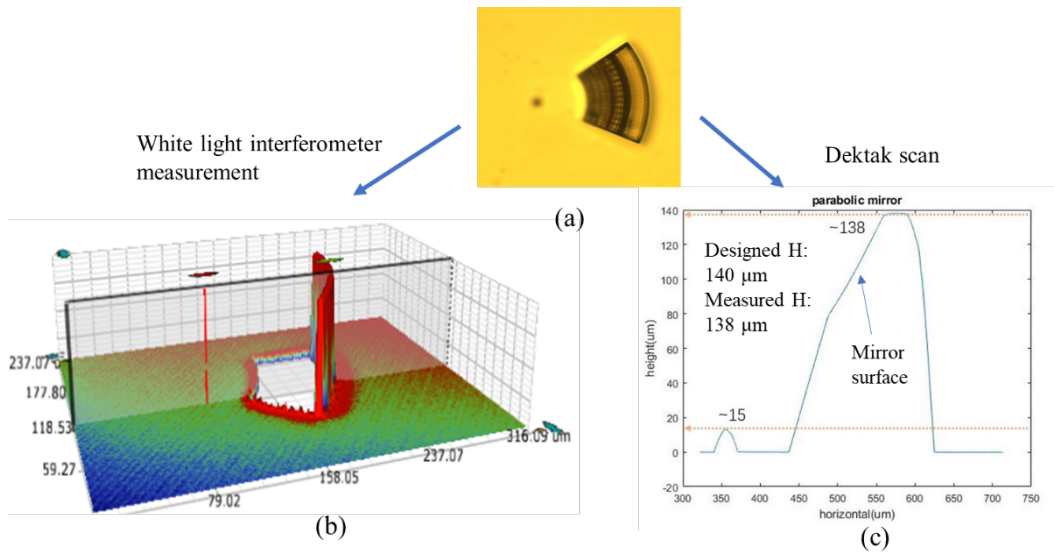


Fig. 2. (a) Optical microscope top view image of a printed mirror base without the aluminum coating. (b) White light interferometry measurement on a mirror base. (c) Dektak scan data of a mirror base.

### 3. Aluminum coating roughness

The surface roughness of the aluminum layer is an important parameter for reflectivity. During our study, we notice the Al layer becomes milky as the layer thickness increases as shown in Fig. 3. Aluminum surface SEM images of different layer thicknesses have been shown in Fig. 4. Sputtering and evaporation deposition are compared at every layer thickness as shown in Fig. 4. Based on these SEM images, it is clear that the grain size, thus, surface roughness increases as the layer thickness increases. This explains why the thicker aluminum layer looks milkier and less reflecting. This comparison also indicates that the evaporation deposition resulting a smoother aluminum layer than sputtering deposition at the same layer thickness.

These results conclude that evaporation deposition is preferred over sputtering deposition and the layer thickness should be kept as thin as possible in order to obtain the most smooth layer.

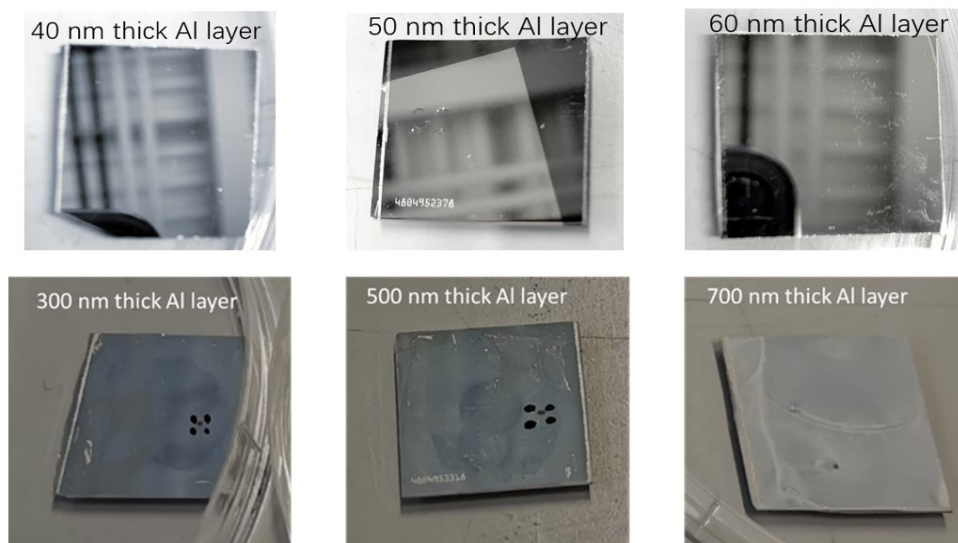


Fig. 3. Appearance comparison of sputtering deposited aluminum layers with different thicknesses on Si chips.

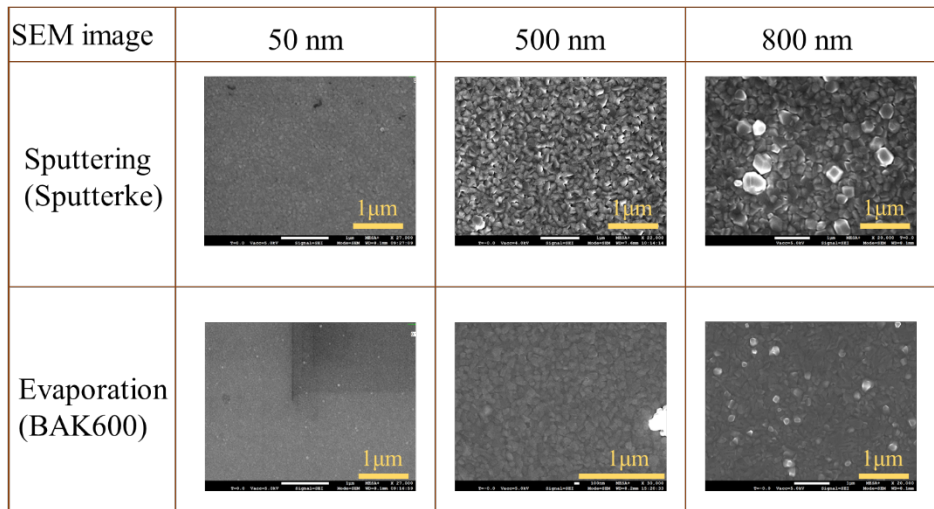


Fig. 4 Aluminum layer surface roughness comparison between different deposition methods and layer thickness.

#### 4. Conclusion and Outlook

In this research, we demonstrate 3D-printed parabolic mirrors on a waveguide chip for out-of-plane light coupling. Measurement of the exact reflecting surface shape remains a challenge. White light interferometry has been proven not a suitable method for this kind of structure. The physical tip scanning method needs further research in order to obtain the real shape of the surface. The aluminum deposition method and layer thickness have a significant influence on its surface roughness, thus, reflectivity. This will be increasingly important in shorter wavelength applications.

#### References:

- [1] A. Mekis *et al.*, "A Grating-Coupler-Enabled CMOS Photonics Platform," *IEEE Journal of Selected Topics in Quantum Electronics*, vol. 17, no. 3, pp. 597-608, 2011.
- [2] M. Blaicher *et al.*, "3D-printed ultra-broadband highly efficient out-of-plane coupler for photonic integrated circuits," in *CLEO: Science and Innovations*, 2018: Optical Society of America, p. STh1A. 1.
- [3] H. Gehring *et al.*, "Low-loss fiber-to-chip couplers with ultrawide optical bandwidth," *APL Photonics*, vol. 4, no. 1, p. 010801, 2019.
- [4] H. Gehring, A. Eich, C. Schuck, and W. H. Pernice, "Broadband out-of-plane coupling at visible wavelengths," *Opt. Lett.*, vol. 44, no. 20, pp. 5089-5092, 2019.
- [5] Y. Kong, H. L. Offerhaus, M. Dijkstra, S. M. G. Blanco, and L. Chang, "3D printed on-chip parabolic mirror for chip-to-fiber and chip-to-chip coupling," presented at the European Conference on Integrated Optics, Milano, Italy, 4 - 6 May 2022, 2022.

# Design optimization and fabrication tolerance analysis of a polarization insensitive spot-size converter for InP-membrane-on-silicon platform

Z. Chen, D.W. Feyisa, S. Abdi, P. Stabile and Y. Jiao

Eindhoven Hendrik Casimir Institute, Eindhoven University of Technology, PO Box 513, 5600MB, Eindhoven, The Netherlands

## Abstract

*We report on the design optimization and fabrication tolerance analysis of a broadband, low-loss and polarization insensitive integrated fiber-to-chip coupling spot-size converter(SSC) on InP-membrane-on-silicon (IMOS) platform. The proposed SSC consists of a laterally tapered InP waveguide and a SiN secondary waveguide. The fundamental TE-polarized and TM-polarized mode is efficiently converted from the high-confinement single-mode InP waveguide with the cross-section of  $0.4 \mu\text{m} \times 0.3 \mu\text{m}$  to the low-confinement SiN waveguide with a cross-section of  $4 \mu\text{m} \times 3 \mu\text{m}$  via a lateral InP taper. The calculated transmittance for TE-fundamental mode is up to 97.2% and 84.5% for TM-fundamental mode (from InP to SiN). The influence of the fabrication error, e.g., the critical dimension deviation of the InP taper, the spatial misalignment of the SiN secondary waveguide with respect to the InP taper, and the verticality of SiN waveguide side-wall, has been numerically analyzed via eigenmode expansion (EME) method.*

## Introduction

Polarization insensitive, broadband, efficient chip-to-fiber coupling remains to be challenging to integrated photonics. Silicon photonics offers low-loss, compact edge couplers[1-3] but lacks high-performance, native amplifiers and modulators, which hinders the integrity of the photonic integrated circuit (PIC). The conventional III-V technologies can provide monolithic integrated photonic system but lacks broadband, polarization independent chip-to-fiber couplers, which however is important in modern high speed telecom industry. A novel InP membrane platform, on which the light can be confined into the compact waveguide, can offer monolithic integration solution with its native active photonic components[4-5].

In this work, we report on the design optimization and fabrication tolerance analysis of an integrated index-matching SSC on InP-membrane-on-silicon (IMOS).

## Design Optimization

The proposed SSC consists of an adiabatic inverse InP taper as the core, and a bulk SiN secondary waveguide as the low-index cladding waveguide, as shown in Figure 1(a-b). The wider side of the inverse InP taper connects to the IMOS waveguide, while the narrower side (tip) points towards the chip facet. A SiN bulk waveguide covers the InP taper and ends at the chip facet. As shown in Figure 1(c), the mode propagates from IMOS waveguide will be compressed when the light is going through the inverse InP taper, as the taper cross-section is gradually shrinking. When the InP taper becomes too small to sustain the mode, the mode will partially distribute in the outer region of the InP taper and confined in the SiN waveguide, which has a larger cross-section but smaller index contrast to the surrounding (usually air or polymer). Till then, the modal size conversion from a high-confinement nano-waveguide ( $0.4 \times 0.3 \mu\text{m}^2$ ) to a low-confinement bulk waveguide ( $4 \times 3 \mu\text{m}^2$ ) is completed.

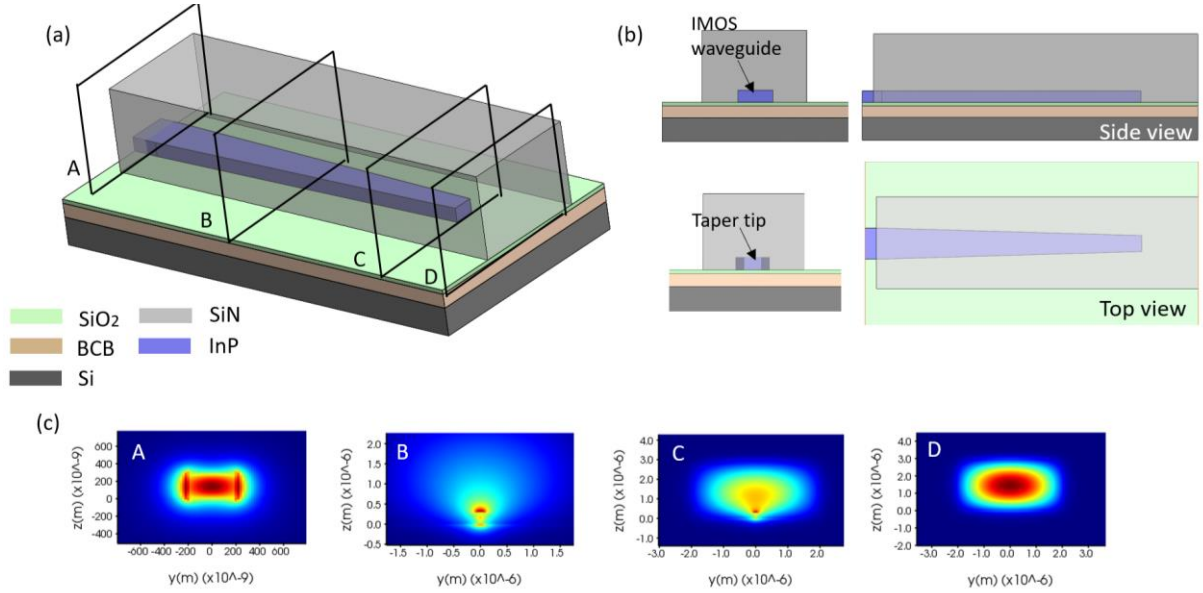


Figure 1: (a) the 3D demonstration (not-to- scale), (b) the orthographic projection (not-to-scale) and (c) the mode slices of the proposed SSC (note that scales are different in the four slices)

There are several design parameters which can essentially influence the mode conversion efficiency of an SSC from design aspect, namely the width of the taper tip, the lateral slope of the taper and the dimension of the SiN waveguide cross-section. Each of these parameters has been systematically studied for fundamental TE and TM mode via eigenmode expansion (EME) method and will be introduced in the following. To define the terminology, the conversion efficiency in this paper refers to the transmittance when the InP waveguide mode adiabatically converts to the SiN waveguide mode. Polarization conversion will not be discussed if not specified.

A joint study on the tip width and the taper length has been performed in this work, the tip width varies from 200 nm to 50 nm with a step-size of 50 nm, and the length of the taper is swept from 1  $\mu\text{m}$  to 401  $\mu\text{m}$  with a step-size of 10  $\mu\text{m}$ . Figure 2 reveals the tip width dependency and the lateral slope dependency of the conversion efficiency for both fundamental TE and TM mode. Both plots clearly prove that longer taper is preferable in a SSC because of lower optical loss in propagation. For fundamental TE mode, the maximum conversion efficiency is only 40% when the tip is 200 nm wide, but it can be significantly improved to 97% by narrowing the tip down to 150 nm. For TM fundamental mode, the conversion efficiency reaches 85% when the tip width is below 100 nm. In order to achieve balanced efficiency for both fundamental TE and TM mode, and also to take the fabrication feasibility into consideration, the optimal tip width is set to be 100 nm in this design.

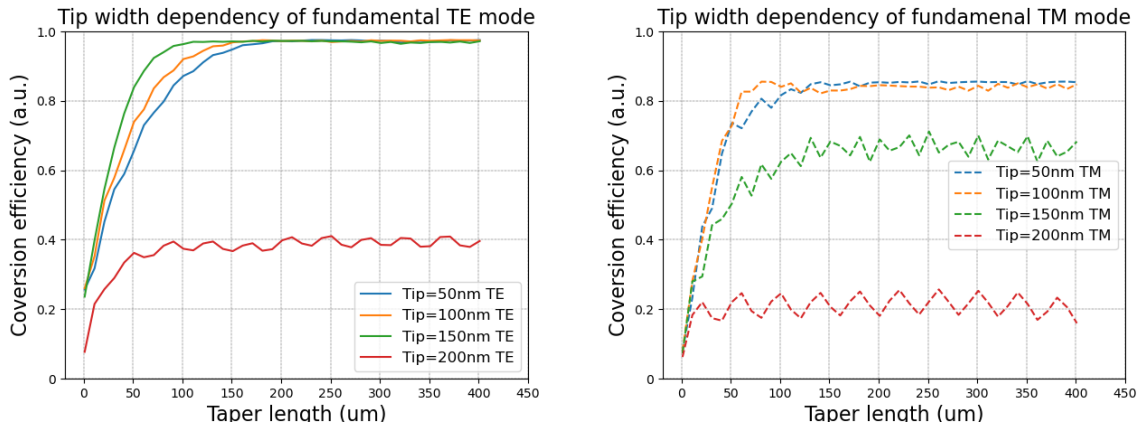


Figure 2: the tip width dependency of the conversion efficiency of the fundamental TE mode (left) and of the fundamental TM mode (right)

The dimension of the SiN waveguide determines the mode distribution inside the SiN waveguide. Considering the modal size in the off-chip coupling devices (fibers, couplers, etc.) is usually larger than  $3\ \mu\text{m}$ , and the output facet of SSC should match to the off-chip couplers. Hence, designs with varying cross-section with minimal dimension of  $3\ \mu\text{m}$  have been verified in EME simulation. The design of InP taper has been fixed as  $100\ \text{nm}$  according to the results introduced above. The InP taper length is set to be  $200\ \mu\text{m}$ , to compromise the foot print of SSC and its conversion efficiency. The simulation results plotted in Figure 3 reveal that  $4\ \mu\text{m} \times 3\ \mu\text{m}$  (*width*  $\times$  *thickness*) is an optimal design choice which balances the conversion efficiency of the fundamental TE and TM mode. The wavelength dependence is plotted in Figure 3, bottom, showing a broadband up to  $300\ \text{nm}$ .

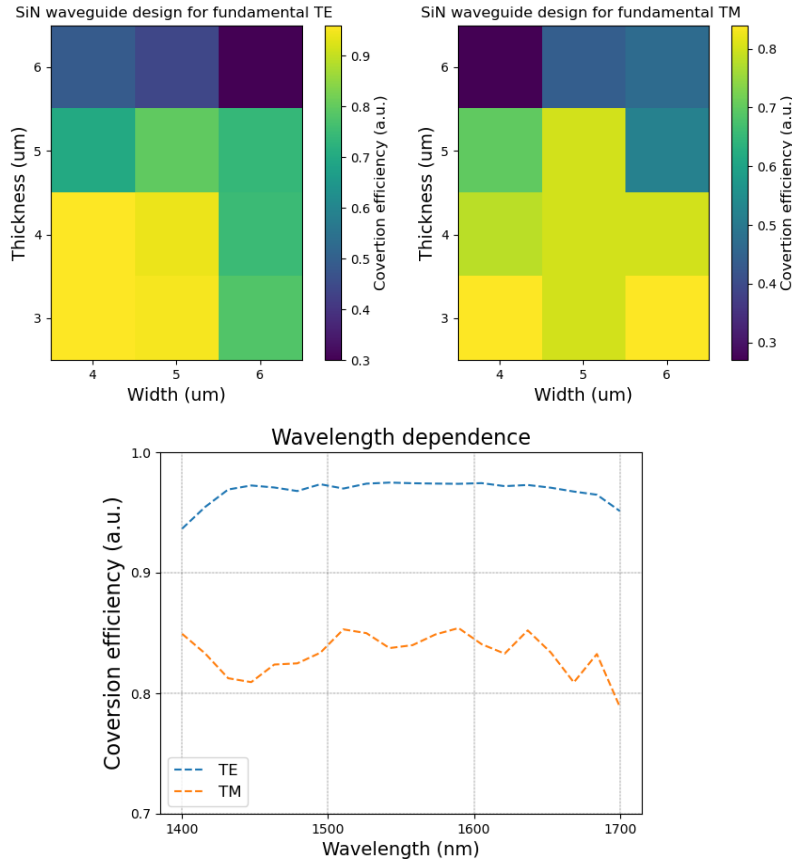


Figure 3: SiN waveguide cross-section dimension analysis for fundamental TE (top left) mode and fundamental TM mode (top right) and the wavelength dependence of the optimum design (bottom)

## Fabrication tolerance analysis

The fabrication tolerance analysis in this work is mainly focused on three aspects: the critical dimension (CD) tolerance of the InP taper tip width, the sidewall verticality of the SiN waveguide, and the spatial misalignment between the InP taper and the SiN waveguide.

The deviation in CD is inevitable during fabrication, as the fabricated structure can suffer from CD loss in any uncalibrated process step. And the CD loss is usually in the order of a few nanometers. Therefore, we set up a small range modification ( $\pm 5\ \text{nm}$  and  $\pm 10\ \text{nm}$ ) around the optimum design width ( $100\ \text{nm}$  in this work), to emulate the CD loss during fabrication.

As shown in Figure 4, the change of the conversion efficiency, which comes from tip width small variation, is ignorable for both fundamental TE and TM modes.

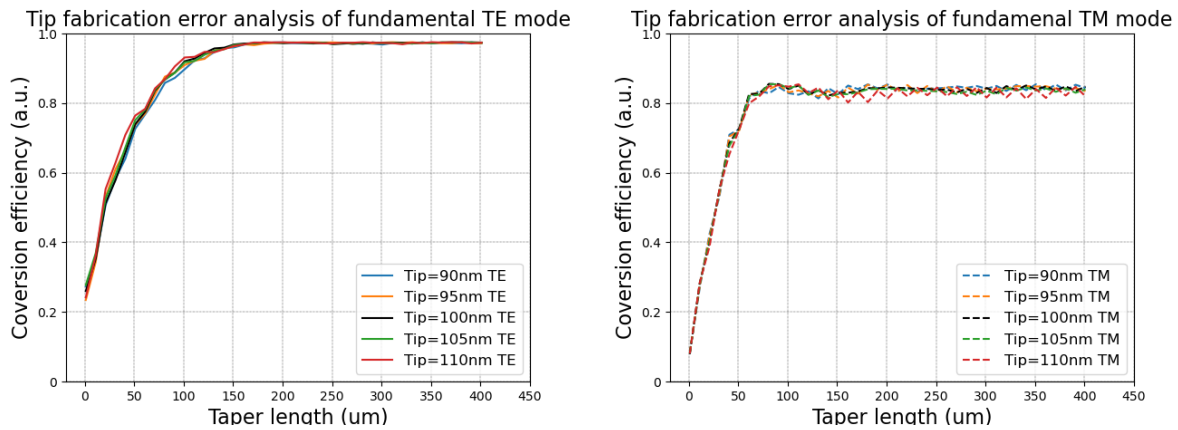


Figure 4: tip width CD tolerance analysis for fundamental TE (left) and TM (right) mode

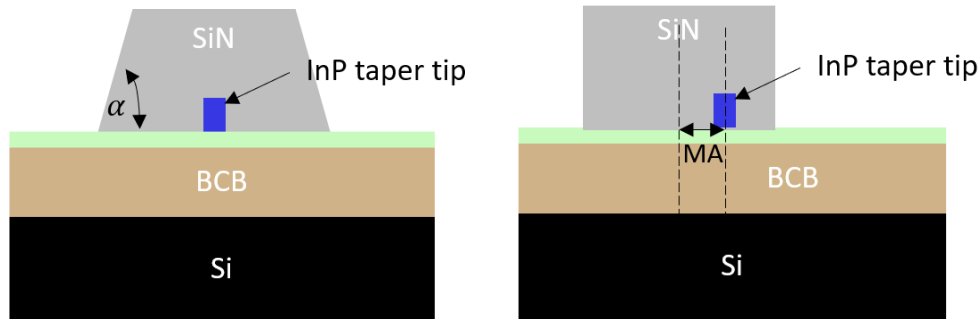


Figure 5: the schematic demonstration of the sidewall non-verticality (left) and the spatial misalignment of the SiN waveguide with respect to the InP taper

The influence of a sloped SiN sidewall has been investigated by varying the geometric model of the SSC in EME simulation. The sidewall angle  $\alpha$  varies from  $45^\circ$  to  $90^\circ$  (vertical) with a step-size of  $15^\circ$ , as shown in Figure 5, left. The width of the taper tip is fixed as  $100\text{ nm}$ . The results are plotted in Figure 6. As we can see in the left plot in Figure 6, the conversion efficiency of the fundamental TE mode fluctuates a lot when the sidewall angle is  $45^\circ$ , which is an extreme case for an unsatisfied sidewall verticality. When the sidewall angle is beyond  $60^\circ$ , the TE mod conversion becomes stable. Compare with the best-case scenario, i.e., the waveguide with perfectly vertical sidewall ( $\alpha = 90^\circ$ ), a  $15^\circ$  deviation on sidewall is tolerable for the fundamental TE mode, as its conversion efficiency doesn't differ much. For the fundamental TM mode, the proposed SSC can tolerate even more verticality deviation, as the electric field of a TM mode oscillates vertically in the waveguide, thus a TM mode is less sensitive to the lateral sidewall. As shown in the right plot in Figure 6, the modal conversion efficiency of SSCs with different sidewall angle shows very high consistency when the taper length is above  $150\ \mu\text{m}$  and no evident efficiency degradation is observed.

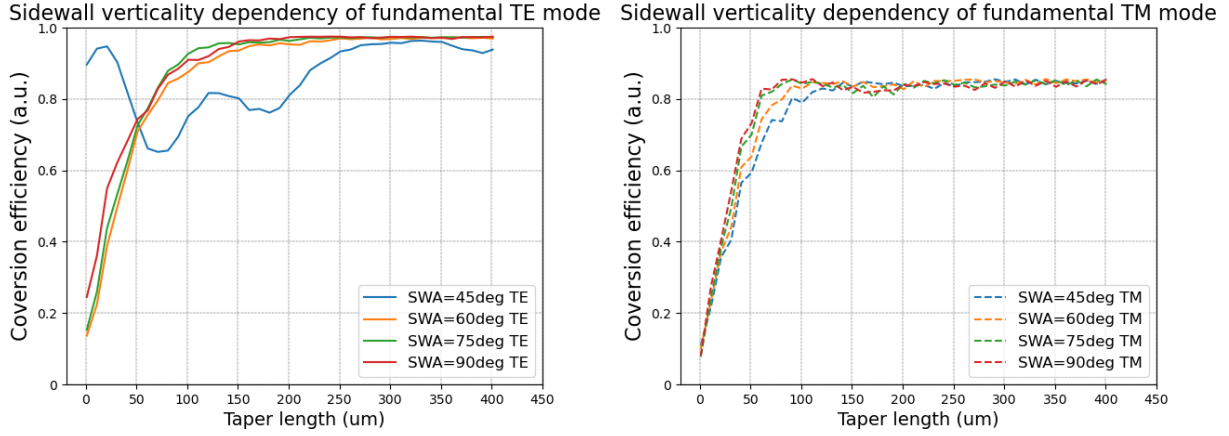


Figure 6: the sidewall verticality dependency of the conversion efficiency of the fundamental TE mode (left) and of the fundamental TM mode (right)

To investigate the spatial misalignment tolerance of the proposed SSC, an offset between the SiN waveguide and the InP taper is introduced, as shown in Figure 5, right. The offset varies from 0 to  $1.8 \mu\text{m}$  with a step-size of  $0.45 \mu\text{m}$ . The width of the taper tip is fixed as  $100 \text{ nm}$ . As indicated in both plots in Figure 7, the conversion efficiency for both fundamental modes degrades enormously when the SiN waveguide is  $1.8 \mu\text{m}$  off from the InP taper, in which case the InP taper locates at the edge of the SiN waveguide. Despite this extreme case, the proposed SSC shows acceptable spatial misalignment tolerance, namely  $0.45 \mu\text{m}$  for fundamental TE mode and  $0.9 \mu\text{m}$  for TM mode.

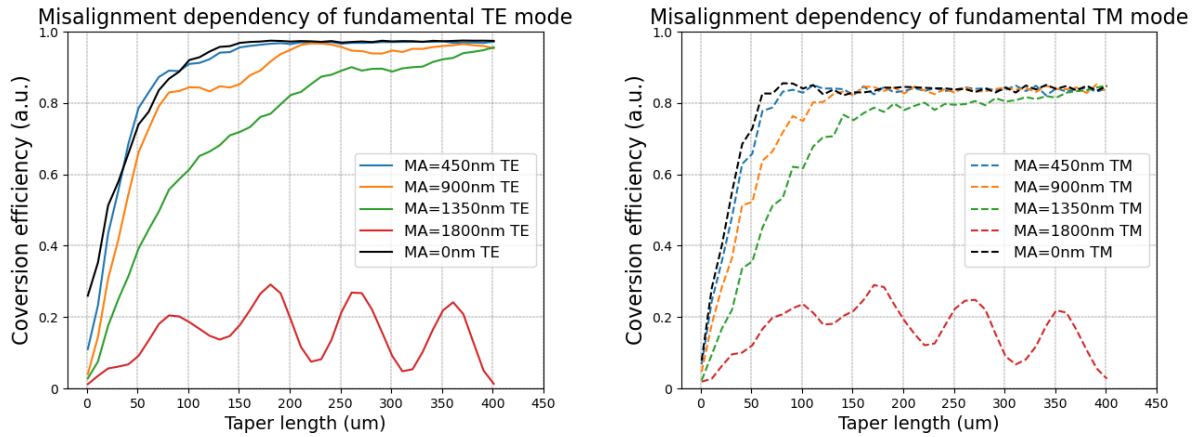


Figure 7: the spatial misalignment tolerance of the SSC in the case of fundamental TE mode (left) and of the fundamental TM mode (right)

## Conclusion and outlook

In this work, we designed and optimized a polarization insensitive broadband SSC for IMOS platform. The fabrication tolerance analysis proved its feasibility. This design will be further verified in an on-going IMOS MPW fabrication run. In the future, further study will be performed to increase the conversion efficiency of the fundamental TM mode.

## Acknowledgement

This work was supported by the H2020 ICT TWILIGHT Project (contract No. 781471) under the Photonics PPP [6].

## Reference:

- [1] G. Ren et al, "Study on inverse taper based mode transformer for low loss coupling between silicon wire waveguide and lensed fiber," *Optics Communications*, Vol 284, Issue 19, (2011)
- [2] M. Papes et al, "Fiber-chip edge coupler with large mode size for silicon photonic wire waveguides," *Opt. Express* 24, 5026-5038 (2016)
- [3] J. Wang et al, "Low-loss and misalignment-tolerant fiber-to-chip edge coupler based on double-tip inverse tapers," in *Optical Fiber Communication Conference, OSA Technical Digest (online)* (Optica Publishing Group, 2016), paper M2I.6.
- [4] Y. Jiao et al., "Indium phosphide membrane nanophotonic integrated circuits on silicon," *physica status solidi (a)* 217.3 (2020): 1900606.
- [5] J. J. G. M. van der Tol et al., "Indium Phosphide Integrated Photonics in Membranes," in *IEEE Journal of Selected Topics in Quantum Electronics*, vol. 24, no. 1, pp. 1-9, Jan.-Feb. 2018, Art no. 6100809, doi: 10.1109/JSTQE.2017.2772786.
- [6] Spyropoulou, Maria, et al. "Towards 1.6 T datacentre interconnect technologies: the TWILIGHT perspective." *Journal of Physics: Photonics* 2.4 (2020): 041002

# Polarization-sensitive reflectometer for distributed magnetic field measurement in tokamaks: impact of reflectometer's dynamic range

P. Dandu,<sup>1</sup> A. Gusarov,<sup>2</sup> S. Kim,<sup>1</sup> and M. Wuilpart<sup>1</sup>

<sup>1</sup> University of Mons, Dept. of Electromagnetism & Telecommunications, Blvd. Dolez 31, 7000 Mons, Belgium

<sup>2</sup> Belgian Nuclear Research Center SCK-CEN, Boeretang 200, B-2400 Mol, Belgium

*In this paper, we investigate a fully passive polarization-sensitive reflectometry-based optical fibre sensor for measuring the spatial distribution of magnetic field in tokamaks. The measurement principle exploits the Faraday magneto-optic effect occurring in the optical fibres in the presence of magnetic field. Experimental data from the Tore Supra (now WEST) reactor is presented. Based on the analysed experimental data, a discussion on the impact of the reflectometer's dynamic range on the magnetic field measurement accuracy is presented.*

Magnetic diagnostics play an indispensable role in the safe operation of tokamak-based thermonuclear reactors like ITER [1]. Nonetheless, in the future tokamaks like ITER and DEMO, the measurement accuracy of the conventional electromagnetic sensors may be compromised due to the combined effect of quasi steady-state operation and nuclear radiation. Optical fibres, thanks to their advantages over conventional methods like relative immunity to temperature and radiation effects, are a potential solution for measuring the magnetic field in the future burning plasma installations. This paper discusses a method for measuring the spatial distribution of magnetic field in tokamaks using the state of polarization (SOP) evolution of the Rayleigh backscattered light in the sensing optical fibre installed around a section of the tokamak's Vacuum Vessel (VV).

It is well known that a Polarization-Sensitive Reflectometer (PSR) can provide information about the spatial distribution of a measurand which can change the SOP of the light propagating in an optical fibre. In the presence of the magnetic field, the SOP of a linearly polarized light is rotated proportional to the axial magnetic field strength, thanks to the *Faraday effect*. The principle of the PSR consists in converting the Rayleigh backscattered SOP evolution into the light power fluctuations, thanks to the polarizer. When the influence of the perturbing effects is insignificant compared to the Faraday magneto-optic effect, the normalized backscattered power recorded at the PSR such as POTDR (Polarization Optical Time-domain reflectometer) or POFDR (Polarization Optical Frequency-domain reflectometer) is given by:

$$P_B(z) = \left( \cos \left( 2 \int_0^z \rho(l) dl \right) \right)^2 \quad (1)$$

where  $z$  is the distance along the fibre and  $\rho(l) = VH(l) \cos(\theta(l))$  is the local Faraday rotation per unit length.  $V$  is the Verdet constant ( $\sim 6.8 \times 10^{-7}$  rad/A in silica fibres operating at 1550 nm [2]),  $H(l)$  is the local magnetic field strength and  $\theta(l)$  is the angle between the magnetic field and the fibre axis. The above equation can be exploited to measure the plasma current in a tokamak even in the presence of perturbing effects [3]. However, by slightly modifying the equation it can also be used for distributed magnetic field measurement:

$$P_B(z) = (\cos(2 \rho(z) dz + \varphi(z)))^2 \quad (2)$$

where  $\varphi(z) = 2 \int_0^{z+dz} \rho(l) dl$  and  $dz$  is the length of the local section of the fibre along which the magnetic field can be considered constant. By locally fitting the normalized measured trace,

of length  $dz$ , with the analytical equation, i.e. Eq. (2), one can measure the local  $\rho(z)$  which indeed gives the local axial magnetic field strength along the fibre axis,  $H(z) \cos(\theta(z))$ . The best local fit is decided based on the Least Mean Square Error, by sweeping  $\rho$  and  $\varphi$  over the chosen range. It is worth stressing here that as the analytical equation, i.e. Eq. (2), is a cosine function and therefore insensitive to the sign of  $\rho$ , which changes according to the direction of magnetic field w.r.t the fibre axis, consequently, the technique is insensitive to the direction of the magnetic field. Note that in general  $\varphi$  is swept over 0 to  $2\pi$  and the sweep step  $\Delta\varphi$  should be chosen small enough such that the required magnetic field accuracy is achieved. The results reported in this paper are based on  $\Delta\varphi = 0.001$  rad. The range of  $\rho$  should be higher than the  $\rho$  corresponding to the highest magnetic field to be measured. The sweep step used in this paper is  $\Delta\rho = 0.001$  rad, which translates to  $\Delta H \approx 1.5$  kA/m ( $\Delta B \sim 1.9$  mT).

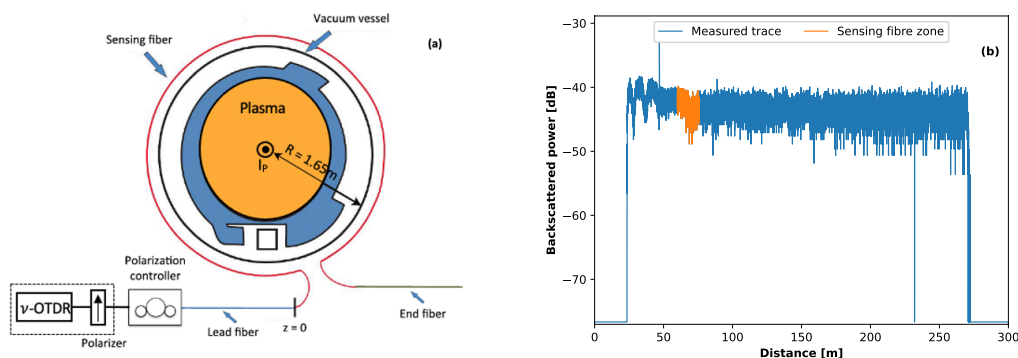


Fig.1 (a) Schematic of the experimental arrangement of the  $\nu$ -POTDR setup at Tore Supra tokamak; (b) Measured  $\nu$ -POTDR trace for a 1.5 MA plasma current.

Fig. 1(a) depicts a graphic representation of the experimental arrangement of the photon counting POTDR ( $\nu$ -POTDR) based setup for the magnetic field measurement at the Tore Supra tokamak. A lo-bi sensing fibre, with a beat length of 420m, is installed on the VV thermal shield with a radius  $R \approx 1.65$  m. More details on the experiment can be found in [4, 5]. Fig. 1(b) shows the measured  $\nu$ -POTDR trace for a 1.5 MA plasma current circulating in the Tore Supra tokamak. Note that the bending induced linear birefringence, for a bending radius of 1.65 m is too small compared to the intrinsic birefringence of the lo-bi fibre, which is itself more than 5 times smaller than the non-reciprocal circular birefringence resulting from the magnetic field generated by the 1.5 MA plasma current. The  $\nu$ -POTDR used for the experiment has a 4 dB dynamic range (DR) and the measured data has a spatial resolution of  $\sim 1.3$  cm. Nevertheless, Savitzky-Golay (SG) filtering is used to improve the SNR of the experimental data. The results presented in this paper are based on an SG filter of order 2 with a filtering window of  $\sim 9$  cm. In the rest of the paper, SG filter implies an SG filter with the aforementioned parameters.

Fig. 2(a) shows the impact of repeatedly filtering the sensing fibre zone of the measured trace with the SG filter. Repeated filtering is done in the following way: each filtered signal is input to the next filtering iteration until the end, except in the beginning where the noisy measured signal is the input to the filter. It can be noticed that the higher the number of times SG filtering is repeated the smoother is the trace. For repeatedly filtering 15 million times, SNR of the signal in the sensing fibre zone has a significant improvement. Note that by further increasing the number of times filtering is performed, beyond 15 million times, there is no significant improvement in the SNR on one hand but on the other hand this over filtering will affect the local frequency of the trace which in turn affects the magnetic field measurement accuracy.

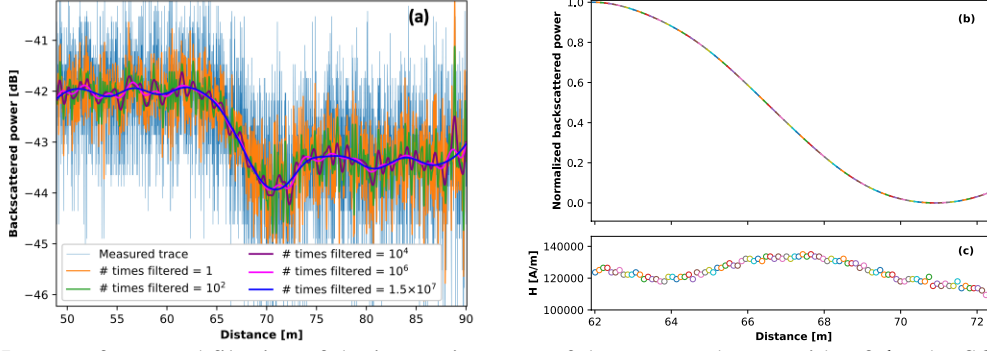


Fig. 2(a) Impact of repeated filtering of the interesting zone of the measured trace with a 2<sup>nd</sup> order SG filter of 9 cm filtering window; (b) Fitting of the normalized backscattered trace of the measurement from the sensing fibre after applying SG filtering (of order 2 and 9 cm filtering window) for  $1.5 \times 10^7$  times; (c) Distributed magnetic field measurement

Fig. 2(b) shows the result of fitting (using Eq. (2)) the normalized trace of the fibre in the sensing region, after filtering 15 million times. Note that the fitting is performed over 9 cm (which corresponds to the SG filtering window length) and the best fitting curve of each of the 9 cm section of the trace is plotted in a different colour than its neighbouring section to facilitate identification of successive sections. Fig. 2 (c) shows the magnetic field measured (with 9 cm spatial resolution) from the (local) frequency  $\rho(z)$  of the local best fittings shown in Fig. 2(b). Recall that the (local) frequency  $\rho(z)$  of the local best fitting is obtained by sweeping  $\rho(z)$  in Eq. (2) over the chosen range. In this case the range is (0, 0.16) where the maximum value of  $\rho$ , i.e. 0.16 rad, corresponds to twice the magnetic field calculated ( $H_E$ ) considering the plasma current (1.5 MA) as a point source located in the centre of the VV. Thus, according to Amperes law, the magnetic field can be estimated as  $H_E = \frac{I_P}{2\pi R}$ , where  $I_P$  is the plasma current, and  $R$  is the radius of the VV thermal shield over which the sensing fibre is installed. Let us note that in practice, the actual magnetic field is not just induced by the plasma current but also by the eddy currents circulating in the VV shell and the currents circulated in various coils installed in the tokamak. The accuracy of the measured magnetic distribution profile cannot be reported yet due to the lack of a reference measurement. It is a perspective of this work to compare the obtained measurement data with that of the conventional magnetic field sensors installed on the tokamak. Nevertheless, the preliminary analysis of the experimental data from the Tore Supra tokamak indicates a potential solution for the distributed magnetic field measurement.

To understand the influence of the PSR's DR on the magnetic field measurement accuracy, simulation approach is considered. The details of the approach are as following: a simulation model for PSR, based on the Jones formalism, is developed considering the intrinsic and bending induced birefringence of the fibre besides the Faraday magneto-optic effect resulting from the 1.5 MA plasma current. Note that the magnetic field used in the simulations is obtained by considering plasma current as a point current source in the centre of the 1.65 m circular VV section. A detailed discussion on the development of the PSR simulation model can be found elsewhere [3,4]. Assuming the noise of the PSR has a gaussian distribution, the

DR of the device can be used to get the standard deviation of the random noise  $\sigma = \left( \frac{DR}{P_{Max}} \right)^{-1}$ ,

where  $P_{Max}$  is the maximum power in the linear scale, which for a normalized trace is 1. Thus, the effect of the DR on the normalized trace is included by adding gaussian noise with zero mean and the standard deviation  $\sigma$ . Also, note that the spatial resolution of the simulation data matches the  $\nu$ -OTDR used in the experiment.

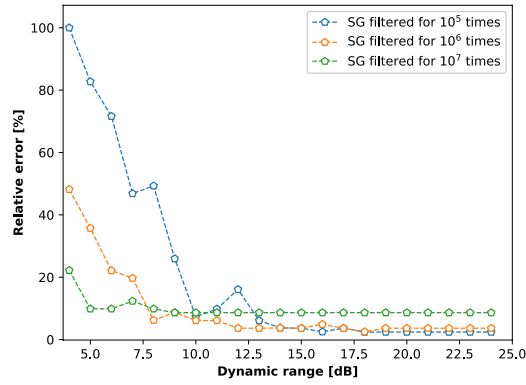


Fig. 3 Impact of dynamic range on the relative error in magnetic field measurement; SG: Savitzky-Golay.

Fig. 3 shows the maximum relative error ( $\varepsilon_r = \frac{|H_M - H_E|}{H_E} \times 100$ ) made in the magnetic field measurement ( $H_M$ ) from the simulated traces at different dynamic ranges (while all the other simulation parameters are constant), for SG filtering repeated at 3 different number of times. Note that the SG filter used in the simulations is same as the one used for the experimental data. The figure clearly depicts that the relative error in magnetic field measurement decreases as the dynamic range increase. For example, in the case of filtering  $10^5$  times at 4 dB DR we make 100% error, but with a DR of 10 dB the error drops to less than 10% which is a significant improvement. At 15 dB the  $\varepsilon_r$  drops to less than 5% and after that there is no significant improvement seen in the relative error. Besides, the results also indicate that over filtering will compromise the accuracy of the measurement in the high DR range, while this is also true for low DR range, but the effect is not relatively as pronounced as it is in the high DR range. In practice, it is quite common to have 10-15 dB DR PSR devices over a distance range of 200 m, which is normally sufficient for the magnetic field measurement in tokamaks. In addition to this, most of the PSR with DR in this range has better spatial resolution which eventually leads to an improved spatial resolution in the measurement. In particular, the low spatial resolution will be of great help in tokamaks where the magnetic field shows strong local variations. Thus, the simulation results infer that a high DR, i.e. 10-15 dB, PSR is desirable for the magnetic field measurement in tokamaks.

In conclusion, a fully passive distributed magnetic field sensor in the form of a PSR-based optical fibre sensor is investigated. Preliminary results of the measurement from the Tore Supra tokamak taken with a 4 dB dynamic range  $\vartheta$ -POTDR has provided magnetic field measurement with a 9 cm spatial resolution, thus, showing the feasibility of the approach. The simulation results demonstrate that the measurement technique can provide magnetic field measurement with good accuracy when using commercially available PSR's with DR around 10-15 dB.

*This work was supported by Fonds de la Recherche Scientifique – FNRS under the convention PDR T.0252.19. A. Gusarov received financial support under the grant from the Federal Public Service of Economy of the Belgian Federal Government.*

[1] Moreau, Ph, et al. "Development of a magnetic diagnostic suitable for the ITER radiation environment." *Ist Inter. Conf. on Advancements in Nuclear Instrumentation, Measurement Methods and their App.* IEEE, 2009.  
[2] Cruz, J. L., M. V. Andres, and M. A. Hernandez. "Faraday effect in standard optical fibers: dispersion of the effective Verdet constant." *Applied optics* 35.6 (1996): 922-927.  
[3] Dandu, Prasad, et al. "Plasma current measurement in ITER with a polarization-OTDR: impact of fiber bending and twisting on the measurement accuracy." *Applied Optics* 61.9 (2022): 2406-2416.  
[4] Wuilpart, Marc, et al. "Plasma current measurement in thermonuclear fusion reactors using a photon-counting POTDR." *IEEE Photonics Technology Letters* 29.6 (2017): 547-550.  
[5] Moreau, Ph, et al. "Test of fiber optic based current sensors on the Tore Supra tokamak." *Fusion engineering and design* 86.6-8 (2011): 1222-1226.

# Bragg gratings for phase-mismatch compensation in phase-sensitive Four-Wave Mixing

T. David,<sup>1</sup> P. Kockaert,<sup>2</sup> and S. Clemmen<sup>1,2,3</sup>

<sup>1</sup> Laboratoire d'information quantique, Université libre de Bruxelles, 50 Av. F. D. Roosevelt CP 224, 1050 Brussels, Belgium.

<sup>2</sup> OPERA-Photonique, Université libre de Bruxelles, 50 Av. Franklin D. Roosevelt, CP 194/5, 1050 Brussels, Belgium.

<sup>3</sup> Photonics Research Group, Department of Information Technology, Ghent University-imec, Technologiepark-Zwijnaarde 126, 9052 Ghent, Belgium

*Abstract: Bragg gratings (BG) are resonant structures that exhibit a strong dispersion close to their transmission stopband, enabling wave-vector modifications. Integrated BG can be made by coupling evanescently from a straight waveguide to an auxiliary periodic structure. This can be exploited either to enable phase-mismatch compensation in an OPA [1], or quasi-phase matching in hybrid waveguides [2]. Here, we develop a method to design a grating that allows phase-mismatch compensation for a Bragg-Scattering Four-Wave-Mixing process (BS-4WM). As a result, we can predict by means of numerical simulations that this grating-assisted phase-matching allows unprecedented conversion bandwidth. We also design structures allowing an experimental demonstration with existing technologies.*

Four-Wave Mixing (4WM) finds applications in frequency conversion [3] or quantum entanglement [4] and Bragg-Scattering Four-Wave Mixing (BS-4WM) is a specific 4WM process that is phase-sensitive. BS-4WM is therefore theoretically noise free as it transfers directly energy from signal to idler waves as depicted in figure 1. It can preserve quantum states during the conversion [5] and has been used for optical switches [6]. BS-4WM has already been demonstrated in highly nonlinear fibers [7] and SiN waveguides [8]. Fibers exhibit a low nonlinear coefficient  $\gamma$ , so that meters of fiber are typically needed to observe an efficient conversion. Meanwhile, waveguides have a higher  $\gamma$  and typically sub-meter interaction lengths, hence lower accumulated dispersion. In both cases, efficient conversion requires to satisfy the phase-matching condition:  $\Delta\beta L < 2\pi$ . This condition is expressed as a function of the wave vectors (momenta)  $\beta_k = n(\omega_k) \frac{\omega_k}{c}$ ,

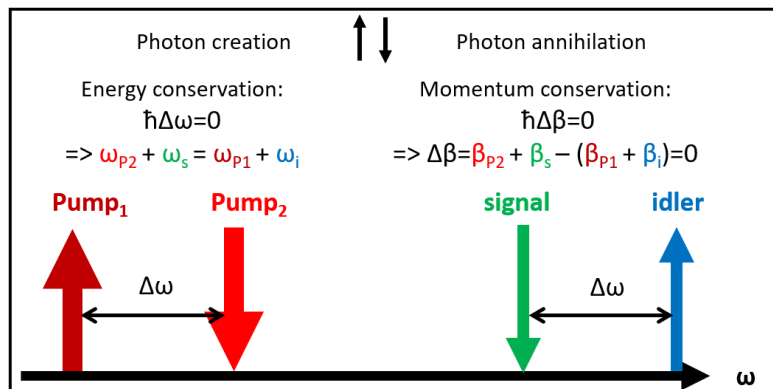


Figure 1. Bragg scattering Four Wave Mixing. Two intense light fields (“pump” fields, at  $\omega_{P1}$ ,  $\omega_{P2}$ ) and a weaker one (at  $\omega_s$ ) propagate inside the material. Two photons (at  $\omega_{P2}$ ,  $\omega_s$ ) are annihilated and two photons

are generated (at  $\omega_{P1}, \omega_i$ ) while satisfying energy and momentum conservation laws:  $\hbar\Delta\omega = 0$  and  $\hbar\Delta\beta=0$  with  $\Delta\omega = (\omega_{P1} + \omega_i) - (\omega_{P2} + \omega_s)$  and the phase mismatch  $\Delta\beta = (\beta_{P1} + \beta_i) - (\beta_{P2} + \beta_s)$ .

with  $n$  the refractive index associated to each wave frequency  $\omega_{P1}, \omega_{P2}, \omega_s, \omega_i$ , and is expressed as  $\Delta\beta = (\beta_{P1} + \beta_i) - (\beta_{P2} + \beta_s)$  in the configuration depicted in figure 1. In that typical configuration, the pump wavelengths and the single photon wavelengths have to be on opposite sides of the 0-group velocity dispersion (0-GVD) wavelength. That condition can be challenging or even impossible for some set of wavelengths due to the limited control on the 0-GVD by dispersion engineering. Indeed, if phase engineering has been extensively applied for optimization of 4WM in SiN and Si waveguides, it typically requires affecting both the width and the thickness of the core materials. This is not always possible because of fabrication constraints, or bare availability of the process for multi projects wafer run (MPW) services. The influence of a Bragg Grating on the generation of solitons has been studied more than two decades ago [9], while its positive effects on OPA operation was reported more recently [1]. Non-resonant gratings have also been exploited, including in four wave mixing demonstrations [2]. Similarly to dispersion engineering used for 4WM [10,11], we engineer a grating to allow phase matching of a given BS-4WM process.

The wavelength conversion efficiency  $\eta$  via BS-FWM can be simply expressed as [5]

$$\eta = |2\gamma PL|^2 \text{sinc}^2(\sqrt{(2\gamma P)^2 + \Delta\beta^2} L) \quad (\text{eq. 1})$$

when pump powers  $P$  are equal [12],  $\gamma$  is the non-linear coefficient,  $L$  the interaction length and  $\Delta\beta$  the phase-mismatch. The conversion is unity when  $\gamma PL = \frac{\pi}{4}$  and  $\Delta\beta = 0$ . This maximum conversion can be hard to reach. Indeed, choosing the frequencies of photons that interact will constrain the phase-mismatch  $\Delta\beta$ , as the wave vectors are function of the frequency:  $\beta = n(\omega) \frac{\omega}{c}$ , with  $n$  the optical index. A Bragg grating exhibits a spectral domain (bandgap) where transmission is forbidden around a resonance frequency  $\omega_{res} = \frac{\pi c}{n_{mean}\Lambda}$  with the grating period  $\Lambda$  and the mean index  $n_{mean}$ [13].

Outside of this bandgap, the grating has a strong influence  $q(\omega)$  on the wave vector  $\beta$  of the propagating fields. It is defined in a linear regime by:

$$q^2(\omega) = \delta^2 - \kappa^2 \quad (\text{eq. 2})$$

With  $\delta = \beta(\omega) - \frac{\pi}{\Lambda}$  and the strength of the grating  $\kappa \approx \frac{2\pi}{\lambda} dn$ , dependent of the index modulation amplitude  $dn$ . In practice,  $q(\omega)$  is calculated using a Taylor expansion around the resonance frequency  $\omega_{res}$  [13]. These analytical formulas can be included in the expression of effective wave vectors

$$\beta_{eff} = \beta + q(\omega) \quad (\text{eq. 3})$$

as long as the nonlinear interaction is weak enough. Indeed,  $q$  should be corrected for the Kerr-induced nonlinear phase:  $q = -\frac{\kappa(1-f^2)}{2f} - \frac{\gamma P(1-f^2)}{2(1+f^2)}$  and  $\delta = -\kappa \frac{(1+f^2)}{2f} - \frac{3\gamma P}{2}$ , with  $f$  a real parameter that quantifies the energy distribution between transmitted and reflected fields. We have  $|q_{non\ linear} - q_{linear}| = \frac{\gamma P}{2} \left| \frac{1-f^2}{1+f^2} \right|$ . Because  $h(x) = \left| \frac{1-x^2}{1+x^2} \right|$  maps the real numbers onto  $[0;1]$ ,  $h(x) \leq 1$  so we deduce that  $|q_{non\ linear} - q_{linear}| \leq \frac{\gamma P}{2}$  irrespective of the details of the grating or the wavelength detuning between the field and the grating resonance. As  $P = \frac{\pi}{4\gamma L}$  for unity efficient BS-4WM, we have that  $\Delta q = |q_{non\ linear} - q_{linear}| \leq \frac{\pi}{8L}$ . That nonlinear correction is significantly smaller than the phase mismatch that we can accept:  $\Delta q \ll 2\pi/L$ . Thus, the linear expression for the

grating-induced dispersion is a good approximation in our case. Therefore, equations (2) and (3) can be combined to seek the proper phase matching  $\Delta\beta < 2\pi/L$  demanded

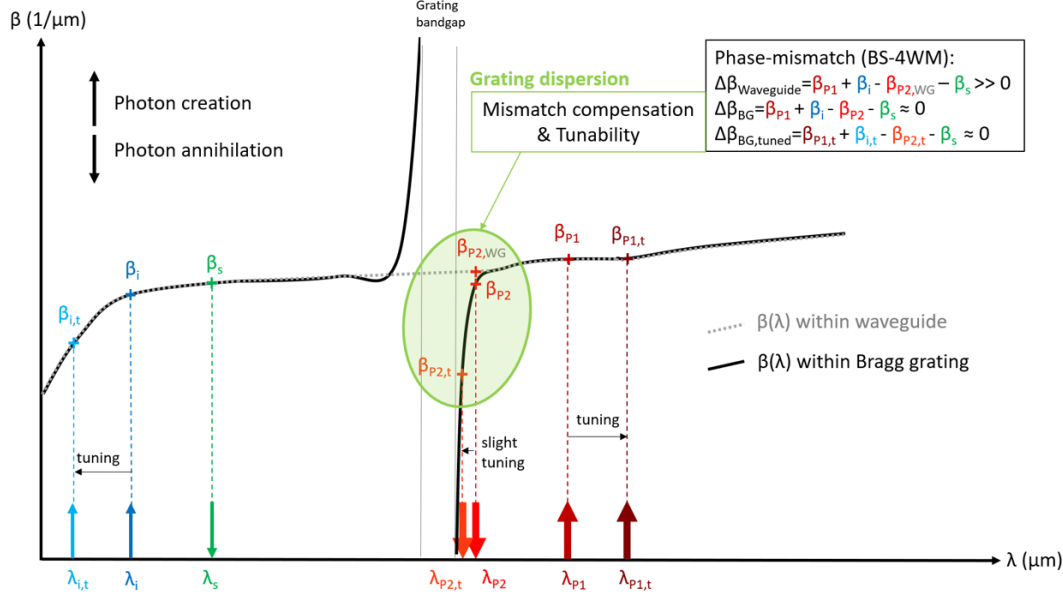


Figure 2. Schematic example of BS-4WM in presence of a grating. The light grey dotted line represents the waveguide dispersion  $\beta(\lambda)$  without any grating, while the continuous black curve represents the dispersion in the presence of the grating. Close to the bandgap (vertical thin gray lines) the grating resonance change  $\beta(\lambda_{P2})$  and allows phase-matching. If we want to tune some wavelengths of the system (ex.  $\lambda_i$  &  $\lambda_{P1}$ ), the newly induced mismatch can be compensated by slightly tuning  $\lambda_{P2}$  resulting in a high tunability of the system.

by eq 1. Hence, for a typical 1cm-long grating, and  $\gamma PL = \frac{\pi}{4}$ , the linear formula of  $\beta_{eff}$  gives an error of  $0.4 \text{ cm}^{-1}$  much smaller than the phase mismatch bound of  $6.28 \text{ cm}^{-1}$ .

We now can examine a practical situation for which the grating resonance is close to the pump field at  $\omega_{P1}$ . In that scenario,  $\beta_{P1}$  undergoes the grating influence so that  $\beta_{P1,eff} = \beta_{P1} + q(\omega)$  while other waves remain unaffected by the presence of the grating (principle illustrated in figure 2). One can then express the modified phase mismatch as  $\Delta\beta_{BG} = (\beta_{P1,eff} + \beta_i) - (\beta_{P2} + \beta_s) = \Delta\beta + q(\omega)$  implying that the influence of the grating  $q(\omega)$  directly comes in the phase mismatch.

To illustrate the benefit of this design, we focus on a particular configuration involving pump fields at  $\lambda_{P1}=2090 \text{ nm}$  and  $\lambda_{P2}=1750 \text{ nm}$  with an initial signal photon at  $\lambda_s=1550 \text{ nm}$  and a final idler wavelength  $\lambda_i=1350 \text{ nm}$ . If we allow unrestricted dispersion engineering via the width and thickness of the waveguide, the phase mismatch for that process is minimized for a cross section of  $1.25\mu\text{m} \times 0.9\mu\text{m}$  (width x height) which correspond to a phase mismatch of  $\Delta\beta=0.15 \text{ cm}^{-1} < 2\pi/L=6.28 \text{ cm}^{-1}$  for a 1cm-long interaction. However, the tunability of the process is low: a change of  $\omega_s$  requires a similarly large change of  $\omega_{P1}$ . As an example, if we allow tuning of the pump over  $\pm 0.5 \text{ nm}$  (something typical from a semiconductor laser diode), the signal can be tuned by  $1.2 \text{ nm}$ .

For a grating assisted waveguide, we are starting from a standard monomode waveguide cross section (as available via common MPW services) of  $1\mu\text{m} \times 0.8 \mu\text{m}$ . Without accounting for the grating, the phase mismatch would be  $90 \text{ cm}^{-1}$ . This can be brought down to  $0.26 \text{ cm}^{-1}$  thanks to a grating with an index modulation  $dn = 2,4 \cdot 10^{-3}$  and a resonant wavelength  $\lambda_{res} = 2091.296 \text{ nm}$ . Not only this offers more fabrication freedom but also improves the tunability. Because  $\beta_{P1,eff}$  exhibits a resonant behavior, a slight

tuning of  $\lambda_1$  will indeed results in a larger impact on phase-mismatch than in the previous case (similarly to figure 2). More specifically, a tuning of the pump wavelength by 0.1 nm provides signal tunability over 30 nm.

Without the presence of the grating, such a tuning would require the pump to be modified by a similar amount thus requiring a change of technology for the laser (external cavity laser or OPO). A demonstration is under investigation using a Bragg grating made from equally spaced pillars evanescently coupled to a straight SiN waveguide ( $1\mu\text{m} \times 0.8\mu\text{m}$ ). We then expect  $\Delta\beta \leq 0.60 \text{ cm}^{-1}$  for wavelengths  $\lambda_s \in [1530, 1560] \text{ nm}$ ,  $\lambda_i \in [1340; 1360] \text{ nm}$ ,  $\lambda_{p1} \in [2090.01; 2089.99] \text{ nm}$  and  $\lambda_{p2} = 1750 \text{ nm}$ .

To conclude, we demonstrate that the linear formula of Bragg gratings can be used in the nonlinear regime required for efficient conversion via BS-4WM. This allows easy predictions and designs of gratings dedicated to correct a given phase-mismatch for a given BS-4WM configuration. We simulated such a grating and observed in these simulations the correction of the phase-mismatch as well as a high tunability potential.

In the future, the improvement of the acceptance bandwidth is another parameter to be maximized. The simultaneous use of several grating periods (a.k.a aperiodic gratings) might also bring additional tunability and possible other benefits. Moreover, we foresee that Bragg gratings can be exploited to forcefully mismatch spurious processes such as parametric fluorescence.

### Acknowledgements

Stéphane Clemmen is a research associate of the Fonds De La Recherche Scientifique - FNRS. This work was supported by the Fonds de la Recherche Scientifique – FNRS under Grant MIS F.4506.20

### References

- [1] Choi, J. W., Sohn, B. U., Sahin, E., Chen, G. F., Xing, P., Ng, D. K., ... & Tan, D. T. An optical parametric Bragg amplifier on a CMOS chip. *Nanophotonics*, 10(13), 3507-3518, 2021.
- [2] Kwon, M. S. Quasi-Phase-Matched Four-Wave Mixing Enabled by Grating-Assisted Coupling in a Hybrid Silicon Waveguide. *IEEE Access*, 10, 83440-83451, 2022.
- [3] Boyd, R. W. *Nonlinear optics*. Academic press, 2020.
- [4] Sharping, J. E., Fiorentino, M., Coker, A., Kumar, P., & Windeler, R. S. Four-wave mixing in microstructure fiber. *Optics letters*, 26(14), 1048-1050, 2001.
- [5] McKinstrie, C. J., Harvey, J. D., Radic, S., & Raymer, M. G. Translation of quantum states by four-wave mixing in fibers. *Optics express*, 13(22), 9131-9142, 2005.
- [6] Zhao, Y., Lombardo, D., Mathews, J., & Agha, I. All-optical switching via four-wave mixing Bragg scattering in a silicon platform. *Appl Photonics*, 2(2), 026102, 2017.
- [7] McGuinness, H. J., Raymer, M. G., McKinstrie, C. J., & Radic, S. Quantum frequency translation of single-photon states in a photonic crystal fiber. *Physical review letters*, 105(9), 093604, 2010.
- [8] Agha, I., Davanço, M., Thurston, B., & Srinivasan, K. Low-noise chip-based frequency conversion by four-wave-mixing Bragg scattering in SiN x waveguides. *Optics letters*, 37(14), 2997-2999, 2012.
- [9] Eggleton, B. J., De Sterke, C. M., & Slusher, R. E. Bragg solitons in the nonlinear Schrödinger limit: experiment and theory. *JOSA B*, 16(4), 587-599, 1999.
- [10] Foster, M. A., Moll, K. D., & Gaeta, A. L. (2004). Optimal waveguide dimensions for nonlinear interactions. *Optics Express*, 12(13), 2880-2887.
- [11] Foster, M. A., Turner, A. C., Salem, R., Lipson, M., & Gaeta, A. L. Broad-band continuous-wave parametric wavelength conversion in silicon nanowaveguides. *Optics Express*, 15(20), 12949-12958, 2007.
- [12] Clemmen, S. Coherent frequency conversion for quantum information processing. In *Real-time Measurements, Rogue Phenomena, and Single-Shot Applications V* (Vol. 11265, pp. 17-23). SPIE, 2020.
- [13] Agrawal, G. P. *Applications of nonlinear fiber optics*, ch1, p 11-21, Elsevier, 2001.

# Design of a Focusing Multi-Wavelength Grating Coupler on a SiN Photonic Integrated Circuit

D. De Vocht, Y. Jiao, and E.A.M. Bente

Photonic Integration Group, Department of Electrical Engineering, Eindhoven University of Technology,  
PO Box 513, 5600 MB Eindhoven, The Netherlands.

[d.j.y.d.vocht@tue.nl](mailto:d.j.y.d.vocht@tue.nl)

## Abstract

*We describe a design approach for multi-wavelength grating couplers that emit a near-Gaussian beam that is focused at several millimeters above the chip. To obtain this intensity profile at multiple wavelengths, we optimize the filling factors over the grating, which is based on optimized single-wavelength grating couplers. We design such a grating coupler on a SiN technology platform which can operate at wavelengths of 635 nm, 780 nm and 850 nm. The beams are emitted in the same direction and focus to a near-Gaussian distribution with a diameter of 27.6  $\mu\text{m}$ , 30.0  $\mu\text{m}$  and 32.4  $\mu\text{m}$ , respectively.*

Monolithically integrating a coupler on a photonic integrated circuit that can emit or receive free-space beams focussed at a long working distance, enables further miniaturization of optical devices by reducing the need for external optics such as lenses or gratings. Integrated grating couplers are widely used to couple light out of a chip into e.g an optical fiber. However, their emittance angle is highly wavelength sensitive [1] and the output beam is highly divergent due to their small size. This limits focusing beams to the same target far away from a chip at multiple wavelengths from the same grating. This is relevant for e.g. a number of optical sensing and free-space communication applications.

Previously, we published an algorithm to design a Computer-Generated Waveguide Holograms (CGWH) – a “pixelized” grating coupler - that can focus light from an on-chip waveguide to a distance of 10 mm above the chip at a wavelength of 1300, 1450 and 1600 nm [2]. Near-vertical focusing for single- [3] and multi-wavelength CGWH was demonstrated. However a large part of the light passed the holograms without being transmitted due to a low scattering strength used. Using a low strength the waveguide grating emits its light fairly uniformly. In this paper, we describe how to use the concepts of optimizing the local scattering strength in single-wavelength grating couplers to obtain the emission of a near-Gaussian intensity profile for a multi-wavelength coupler. We have designed grating couplers in the SiN platform as shown in Figure 1 using a double strip waveguide. By using the SiN photonic integration platform, we enable the advancement of many optical sensing applications in the visible regime.

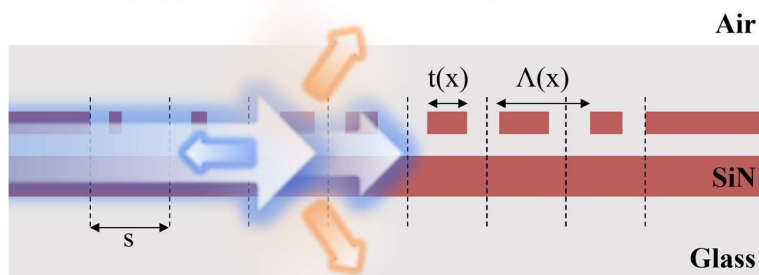


**Figure 1 Schematic of our grating coupler.** Each cell (dashed lines) contains one and exceptionally two grating lines, the sum of their widths is  $t(x)$  and the period with their neighbour is  $\Lambda$ . The arrows show how a grating line scatters some light of the guided mode back-, up- or downward.

## Analytical Model of Grating Couplers

When a guided mode in a grating coupler passes a scatterer, a part of its light will be reflected in the waveguide or emitted up- or downward (Figure 1). We can represent the strength of these events by the coupling strengths  $\alpha_{refl}$ ,  $\alpha_{up}$  and  $\alpha_{down}$ , respectively. They depend on many factors of the grating coupler: the period  $\Lambda$ , the filling factor  $ff$  (equal to  $t/s$  in Fig. 1), the layer properties and the etch depth.

The effect of the coupling strengths on the power of the guided mode  $A(x)$  over the propagation length  $x$  can be mathematically expressed as

$$\frac{dA(x)}{dz} = -2\alpha(x)A(x) \quad (1)$$

where  $\alpha = \sum \alpha_{refl} + \alpha_{up} + \alpha_{down}$  and the factor 2 is conventionally added. So, the guided power in a grating coupler exponentially decays from  $A_0$  at its starting point  $x_0$

$$A(x) = A_0 \exp\left(-2 \int_{x_0}^x \alpha(x) dx\right) \quad (2)$$

Since the radiated power  $B(x)$  represents the leaked guided light, it is given by

$$B(x) = -\frac{dA(x)}{dx} = 2\alpha(x)A_0 \exp\left(-2 \int_{x_0}^x \alpha(x) dx\right) \quad (3)$$

However, this  $B(x)$  represents the local scattering of light. The total reflection/emission is only strong if the contributions of all the scatterers constructively interfere with each other. For a grating with period  $\Lambda$ , the light constructively interferes if

$$k_{out,x} \Lambda = k_{guided,x} \Lambda + 2\pi m \quad (4)$$

with  $k_{ou,x}$  and  $k_{out,x}$  the wave vector contributions in the  $x$  direction of the guided and output mode and  $m$  is the diffraction order. We can rewrite Eq. (4) to determine the period  $\Lambda$  needed to emit a beam upward above the chip (in the air) with an angle  $\theta$

$$\Lambda = \frac{m\lambda_0}{n_{eff} - \sin \theta} \quad (5)$$

where  $\lambda$  is the wavelength in vacuum and  $n_{eff}$  the effective refractive index of the waveguide.

To obtain a Gaussian emission profile, we can derive from Eq. (1) and (3) how the profile of the required coupling strength should look like [4]

$$\alpha_{required}(x) = \frac{B(x)}{2 \left[ A_0 - \int_{x_0}^x B(t) dt \right]} \quad (6)$$

## Designing multi-wavelength grating couplers

As our target, we want our coupler to emit a Gaussian beam with a spot size of 164, 200 and 218  $\mu\text{m}$  at the wavelengths of 635, 780 and 850 nm, respectively, and focus it to a 30  $\mu\text{m}$ -narrow Gaussian beam 5 mm above the chip. Figure 2b shows the required coupling strengths  $\alpha_{required}$ . To determine how  $\alpha$  depends on the filling factor  $ff$  and the period  $\Lambda$ , we simulate utilizing Lumerical's Finite-Difference Time-Domain (FDTD) method a series of 100  $\mu\text{m}$ -long grating couplers. We determine  $\alpha$  by fitting the exponential decay of the guided mode's power (Eq. (2)). We then optimized the layer thicknesses of the grating coupler (Fig. 1) such that  $\alpha(ff, \Lambda)$  can sufficiently reach  $\alpha_{required}$ .

Figure 2(a) shows the resulting profile  $\alpha(ff, \Lambda)$ . For most periods,  $\alpha$  changes slowly with  $\Lambda$ . But around  $\Lambda = 390 \text{ nm}$ , suddenly a second maximum occurs with  $\alpha$  reaching a very low value. This line closely matches the analytically expected condition

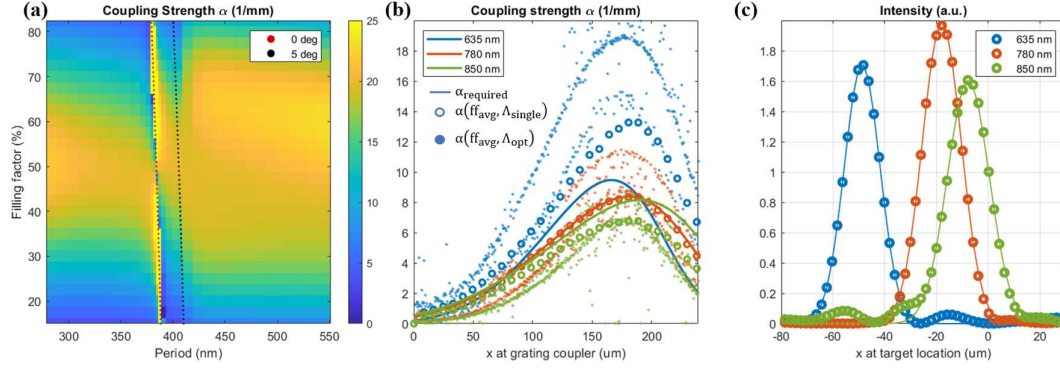


**Figure 2 Optimization of the multi-wavelength coupler.** (a) Influence of the filling factor and period on the coupling strength at 635 nm. The dots indicate the grating parameters required to emit a beam with an angle of 0 or 5°. Note the colour scale is saturated. The coupling strength can be as high as 83 1/mm around the 0° line. (b) Required coupling strength (lines) vs after taking the average of  $ff_{single}$  whilst assuming  $\Lambda_{single}$  (circles) and after also optimizing the period  $\Lambda$  (dots) to focus the light at multiple wavelengths. (c) Intensity profile of the focused beams at target location with Gaussian fit (lines).

for vertical emission and backward reflection. To avoid such strong reflections, we design our coupler to emit a beam at a slight angle of 5° (Fig. 2(a)). So, for each location  $x$  on the grating coupler, we want to focus the light to a narrow spot 5 mm above the chip shifted 592  $\mu\text{m}$  of the coupler's centre. Thus, at each  $x$  we need a different  $\theta$ . Since  $n_{eff}$  varies with  $ff$ , a range of  $(ff, \Lambda)$  points will give desired  $\theta$  (Eq. (5)). We then select the optimal  $(ff_{single}, \Lambda_{single})$  for which the  $\alpha$  matches the closest to  $\alpha_{desired}$  (Eq. (6)).

To design the multiwavelength coupler, we take for each  $x$  the average of  $ff_{single}$  over the different wavelengths. When we heuristically consider  $\Lambda_{single}$  at each  $\lambda$ , we notice already that  $\alpha(635 \text{ nm})$  increases,  $\alpha(850 \text{ nm})$  decreases whilst  $\alpha(780 \text{ nm})$  remains constant (Fig. 2(b)). Next, we optimize the local grating period  $\Lambda(x)$  using a semi-analytical algorithm as described in [2], [5]. This algorithm optimizes  $\Lambda(x)$  to focus the light at the three wavelengths all to the same target. As a result, the optimized  $\Lambda$  strongly fluctuates. Because  $\alpha$  depends on  $\Lambda$ , it moves further away from  $\alpha_{required}$  and also fluctuates (Fig. 2(b)). Figure 2(c) show the intensity profile at the target location. They are near-Gaussian with beam diameters 8% within the design target of 30  $\mu\text{m}$  (Table 1).

Figure 3 compares the targeted  $B(x)$  with our calculated (Eq. (3)) and simulated result of our optimized multiwavelength grating coupler. As expected, the data points in our result largely fluctuate, but we do still observe a Gaussian distribution. First, we see that the peak of the semi-analytically and FDTD Gaussian distribution is within 24  $\mu\text{m}$  and 41  $\mu\text{m}$  of the target location, respectively. The deviations between the peaks of the FDTD results are up to 4  $\mu\text{m}$  identical to those of the profiles at the target location (Fig. 2(c)). Thus, the coupler emits the beams in the same direction. Secondly, we observe that the beam diameter  $w$  of the beam emitted by our model is up to 1.8x lower than our target value. This indicates how largely  $\alpha$  deteriorates after independently optimizing  $\Lambda$ . However, we notice that our model underestimates the emission of the scatterers in the first 70  $\mu\text{m}$  as compared to rigorous FDTD simulations. One reason is that our model assumes a uniform array of scatterers vs a strong fluctuating  $\Lambda$ . As a result,  $w$  of the simulated intensity profile is 1.2-1.8x wider than our model predicts (Table 1). Only  $w$  at  $\lambda = 850 \text{ nm}$  is below the target with 12% compared to 56% as our model predicted.

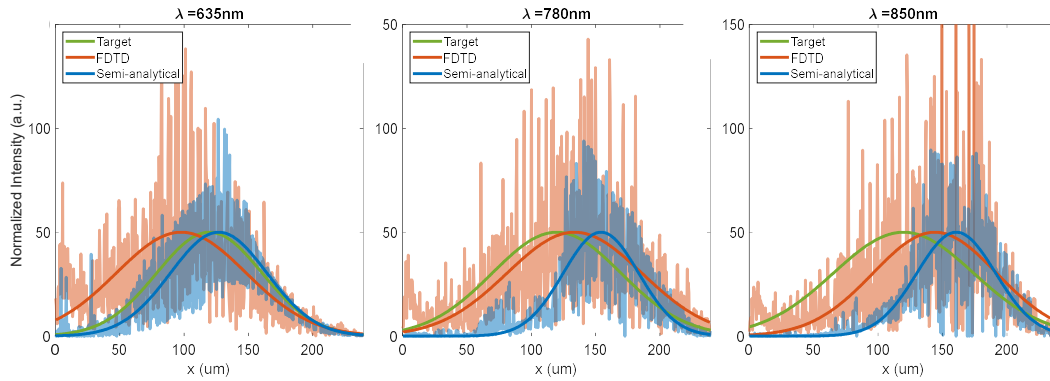


**Figure 3 Validating our semi-analytical model.** Comparing upward emitted intensity profile at wavelengths of (a) 635, (b) 780 and (c) 850 nm as targeted (green) and calculated by FDTD (red) or our semi-analytical model (blue). The solid lines represent Gaussian fits through the data points.

**Table 1** Comparison of the beam diameters of the intensity profile at the near-field and focus location.

Location	Method	635 nm	780 nm	850 nm
Near-chip plane	Design target	164 $\mu\text{m}$	200 $\mu\text{m}$	218 $\mu\text{m}$
	FDTD Simulation	202 $\mu\text{m}$	210 $\mu\text{m}$	192 $\mu\text{m}$
	Semi-analytical Calculation	150 $\mu\text{m}$	117 $\mu\text{m}$	122 $\mu\text{m}$
At focus location	FDTD Simulation	27.6 $\mu\text{m}$	30.0 $\mu\text{m}$	32.4 $\mu\text{m}$

## Conclusion

We designed a grating coupler that emit a near-Gaussian beam that is focused 5 mm above the chip at a wavelength of 635 nm, 780 nm and 850 nm. The beams are emitted in the same direction with an angle of  $5^\circ$  to avoid strong Bragg reflections. They have a diameter of 28-33  $\mu\text{m}$ , within 8% of the design target. At the start of the grating coupler, our semi-analytical model underestimates the strength of the scatterers. We think this is caused because our model assumes a uniform grating profile. In the future, we will investigate how sensitive our model is to variations in the grating period.

## Acknowledgements

This publication is part of the project FreeSense with project number 17971 of the research program HTSM which is financed by the Dutch Research Council (NWO). We thank professor Irwan Setija for the insightful discussions.

## References

- [1] L. Cheng, S. Mao, Z. Li, Y. Han, and H. Y. Fu, "Grating Couplers on Silicon Photonics: Design Principles, Emerging Trends and Practical Issues," *Micromachines* 2020, Vol. 11, Page 666, vol. 11, no. 7, p. 666, Jul. 2020.
- [2] T. Liu, Y. Jiao, and E. Bente, "Design of a computer-generated waveguide hologram for integrated free space sensing," *Proceedings of the International Conference on Numerical Simulation of Optoelectronic Devices, NUSOD*, vol. 2021-September, pp. 95–96, Sep. 2021.
- [3] D. De Vocht, T. Liu, Y. Jiao, and E. A. M. Bente, "Integrated Computer Generated Waveguide Hologram for Versatile Free-Space Beam Projection," in *European Conference on Integrated Optics*, 2022, pp. 134–137.
- [4] R. Waldhä, B. Schnabel, P. Dannberg, E.-B. Kley, A. Brä, and W. Karthe, "Efficient coupling into polymer waveguides by gratings," 1997.
- [5] J. Backlund, J. Bengtsson, C.-F. Carlström, and A. Larsson, "Incoupling waveguide holograms for simultaneous focusing into multiple arbitrary positions," *Applied Optics*, Vol. 38, Issue 27, pp. 5738–5746, vol. 38, no. 27, pp. 5738–5746, Sep. 1999.

# Proposal for non-contact photoacoustics using silicon photonics-based Laser Doppler Vibrometers

Emiel Dieussaert,<sup>1,2</sup> Roel Baets,<sup>1,2</sup> and Yanlu Li<sup>1,2</sup>

<sup>1</sup> Photonics Research Group, Ghent University-IMEC, Belgium

<sup>2</sup> Center for Nano- and Biophotonics, Ghent University, Belgium

*Photoacoustics has proven to be an important technique for realizing new sensing and imaging solutions. Conventional methods rely on an ultrasound detector in contact with the sample. Contact-based methods increase however the risk of contamination or reaction with the sample. This is a major drawback for many applications, especially in the biomedical field. Interferometric techniques have proven to enable non-contact photoacoustics, but these free-space or fiber-based systems are usually too bulky. In this paper, we present silicon photonics-enabled on-chip Laser Doppler Vibrometers (LDV) as a compact and non-contact solution for photoacoustic sensing or imaging. A design of silicon photonics-based LDVs is proposed and its performance is analyzed and compared to other ultrasound detector solutions for non-contact photoacoustics. From these performance metrics, we discuss the benefits and limitations of LDVs for the detection of photoacoustic signals and propose how an on-chip LDV array can provide compact and non-contact photoacoustic imaging.*

## Introduction

In the last decade, it has been demonstrated that photoacoustic techniques can enable new biomedical sensing and diagnostic tools to go beyond conventional techniques [1]. In photoacoustics, a modulated or pulsed laser excitation source illuminates a sample that may contain a part that can strongly absorb the excitation light. Because of the photo-thermal effect, local heating occurs where the light is absorbed. This local heating induces a sudden local stress which will be propagated to the surface of the sample as an acoustic wave. The acoustic waves can be detected and processed to retrieve the absorption profile of the excitation source [2]. This combination of optical excitation and acoustical detection allows for retrieving the absorption information far beyond the ballistic regime, which is usually the limit in conventional optical imaging systems relying on optical reflection (e.g. optical coherence tomography, optical imaging,...). Using multiple different excitation wavelengths, spectroscopic information can be retrieved from the absorption profile at different wavelengths.

A photoacoustic system for biomedical applications requires sensitive and compact ultrasound detectors. Due to a large impedance mismatch between air and sample, and very poor ultrasound transmission in air, conventional ultrasound detectors require to be in contact with the sample and often, a contact gel is used to improve ultrasound transmission from sample to detector [3]. In biomedical applications, contact with any sample creates a risk of infection and contamination [4]. In recent years, laser doppler vibrometers (LDV) have been used to demonstrate non-contact photoacoustics [5]. In this interferometric technique, a beam of light probes the movement of a remote target. These optical systems consist of several optical elements such as splitters/combiners, optical hybrids, photodetectors... Usually, these systems are made using free space optics or fiber-based components. However, increasing the number of probe beams drastically increases the number of optical elements and fibers and increases complexity, cost, and

size. In this paper, we propose silicon photonics-based LDVs as a non-contact and compact solution for photoacoustic applications, even with multiple probe beams. Silicon photonics uses CMOS-like techniques to create optical components and waveguides on a small silicon chip [6]. For medium to large-volume production, the cost of a chip can be relatively low. It also allows the creation of on-chip LDVs with multiple probe beams on a chip smaller than  $1 \text{ mm}^2$  [7]. In the next part, we introduce the on-chip LDV working principle and calculate the theoretical limits of on-chip LDVs. Thereafter, we discuss the benefits and drawbacks of using on-chip LDVs for photoacoustic biomedical applications.

## Silicon photonics-based LDVs

The general layout of an on-chip homodyne LDV is depicted in figure 1a. An external laser couples light into the chip using a grating or edge coupler. The coherent light is split into a reference beam measurement beam. The measurement light goes to a transmitting antenna to direct light toward a target. After reflection from the target, the collected light is combined with the reference light into a  $90^\circ$  optical hybrid. On-chip photodetectors connected to each port of the hybrid convert the intensity into currents. From these photocurrents, one can retrieve a pair of signals with a quadrature phase relation (i.e. I and Q signals). After a demodulation procedure, the phase difference between the reference and measurement beams can be obtained. A change in the phase difference denotes a change in the path length and the displacement can be retrieved. When the chip remains static, we can thus remotely record the movement of the target. As seen in figure 1b, recent demonstrations include a six-beam silicon photonic-based LDV system and indicates the potential for on-chip silicon photonics LDV with multiple beams [8].

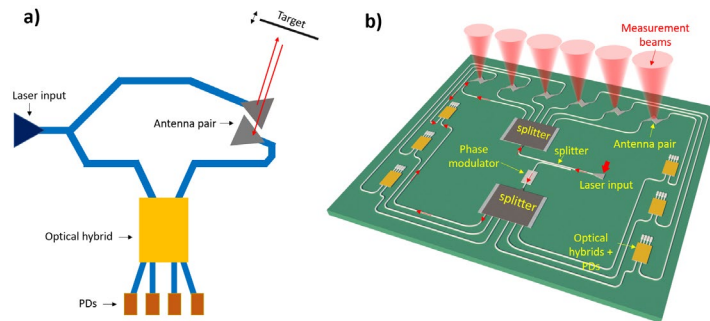


Figure 1 a) Schematic of an on-chip LDV layout b) Reproduced from [8], layout of a six beam on-chip LDV

Assuming a homodyne LDV limited by the shot noise in the photodetector, one can estimate the noise limit of an LDV, as can be seen in Figure 2. Considering a white noise spectrum of the shot noise, this results in a flat phase- and flat displacement noise spectrum. The flat displacement noise spectrum can be translated into a linearly increasing velocity noise spectrum, and using a specific acoustic impedance this can be converted into a pressure noise spectrum. The following equation describes the relation between the sample-air boundary velocity ( $u$ ) and the pressure amplitude of an incident acoustic plane wave ( $p$ ), through the specific acoustic impedance of the sample ( $Z_{sample}$ ), assuming  $Z_{sample} \gg Z_{air}$ .

$$p = \frac{Z_{sample}}{2} \cdot u$$

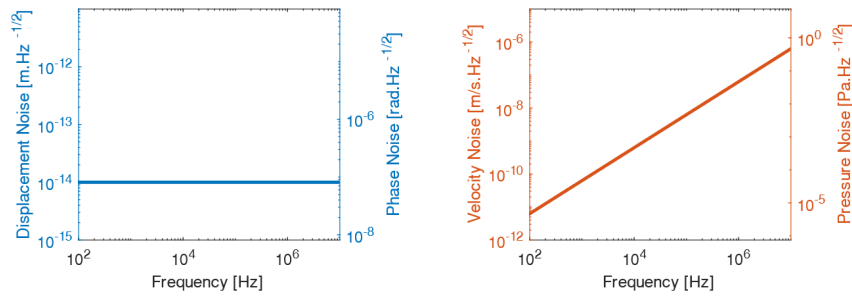


Figure 2 a) Flat displacement and phase noise spectrum for LDV due to shot noise, assuming a 10 mW probing beam and 1% collection efficiency. b) The subsequent pressure noise can be calculated by multiplying the velocity noise by the specific acoustic impedance (1.5 MRayl for tissue)

## Silicon photonics-based LDVs for non-contact Photoacoustics

In figure 3, we propose a compact non-contact photoacoustic system for imaging vascularization, using the silicon photonics-based LDV technology described in the previous section.

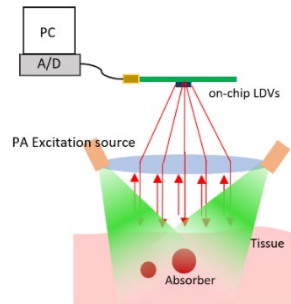


Figure 3 A schematic demonstrating a compact and non-contact biomedical photoacoustic imaging system using silicon photonics based LDVs connected to a digitizer (A/D) and signals are saved and processed into a PC.

The benefits of a system using on-chip LDVs can be clear. First of all, the non-contact nature is desirable in many biomedical applications to mitigate any risks or discomforts from contact methods [4]. Secondly, the on-chip implementation of this system allows for a compact detector system, even for multi-point vibrometers. Combining this with a compact excitation source allows for a completely non-contact compact photoacoustic system [9]. On the other hand, the contactless approach mitigates any interference between the detector to the ultrasound waves and allows for delivering the excitation light directly underneath the probe beams.

The conventional detectors (piezoelectric transducers,..) in contact generally have a better noise floor compared to LDV, but are not suitable for remote detection due to the 1000-fold reduction of the signal pressure due to the impedance mismatch between air and tissue [3] and the very poor transmission of ultrasound frequencies (>MHz) in the air [10]. Optical detection techniques seem more promising for remote detection. However, wideband detection with laser doppler vibrometers results in poor SNR due to the increasing pressure noise floor with the frequency. It is therefore important to consider the application requirements of the detector bandwidth and look at the expected signal strength. Considering a  $0.01 \frac{pm}{\sqrt{Hz}}$  noise limit LDV, a system with a bandwidth from 0 to 2 MHz results in a total noise of around 150 Pa of noise equivalent pressure (assuming  $Z=1.5$  MRayl). Consider an application for imaging vascularization under the skin, the initial pressure due to a photoacoustic excitation can be estimated. For short laser

excitations (<10 ns for tissue), one can assume we are in the stress and thermal confinement region. Now, initial pressures can be estimated by multiplying the Grüneisen parameter and the pulse energy [2]. For  $10 \frac{mJ}{cm^2}$  pulses (below the safety limit for NIR light), and considering all light perpendicularly incident on the skin, the initial pressures are in Pa to kPa range for 0 to 5 mm depths. Comparing this to the noise equivalent pressure (NEP) of the LDV, it can be seen that often averaging will be necessary to detect blood vessels at larger depths. Decreasing the LDV bandwidth decreases the noise, but the bandwidth determines the fundamental resolution limit for acoustic resolution photoacoustic microscopy (AR-PAM). A 0 to 2 MHz acoustic detector results in a resolution of around 0.6 mm [1]. Based on these results, it can be seen that LDV can be a suitable detector solution for limited resolution AR-PAM.

## Conclusion

Silicon photonics-based LDVs have been proposed as a non-contact detector solution for photoacoustic imaging and sensing. Theoretical limits of LDV noise were calculated and translated into a pressure noise spectrum. The noise of an LDV system with 2 MHz bandwidth was compared with typical photoacoustic-induced pressures and the benefits and drawbacks of on-chip LDV as a detector solution were discussed. From the calculations, it is clear that LDV is a potential detector solution for building contactless and compact photoacoustic sensing or imaging system within the constraints of limiting system bandwidth to limit LDV noise.

## References

- [1] M. Xu and L. V. Wang, "Photoacoustic imaging in biomedicine," *Review of Scientific Instruments*, vol. 77, no. 4, p. 041101, 2006.
- [2] L. V. Wang, *Photoacoustic Imaging and Spectroscopy*, CRC Press, 2009.
- [3] M. Rayann, L. Saint-Martin and K. Avanaki, "Couplants in Acoustic Biosensing Systems," *Chemosensors*, vol. 10, no. 5, pp. 2227-9040, 2022.
- [4] T. Sartoretti, E. Sartoretti, C. Bucher, A. Doert, C. Binkert, K. Hergan, M. Meissnitzer, J. Froehlich, O. Kolokythas, S. Matoori, C. Orasch, S. Kos, S. Sartoretti-Schefer and A. Gutzeit, "Bacterial contamination of ultrasound probes in different radiological institutions before and after specific hygiene training: do we have a general hygienical problem?," *Eur Radiol.*, vol. 27, no. 10, pp. 4181-4187, 2017.
- [5] J. Eom, S. J. Park and B. H. Lee, "Noncontact photoacoustic tomography of in vivo chicken chorioallantoic membrane based on all-fiber heterodyne interferometry," *J. Biomed. Opt.*, vol. 20, no. 10, p. 106007, 2015.
- [6] S. Y. Siew, B. Li, F. Gao, Y. H. Zheng, W. Zhang, P. Guo, S. W. Xie, A. Song, B. Dong, L. W. Luo, C. Li, X. Luo and G.-Q. Lo, "Review of Silicon Photonics Technology and Platform Development," *J. Lightwave Technol.*, vol. 39, no. 13, pp. 4374-4389, 2021.
- [7] Y. Li and R. Baets, "Homodyne laser Doppler vibrometer on silicon-on-insulator with integrated 90 degree optical hybrids," *Optics Express*, vol. 21, no. 11, pp. 13342-13350, 2013.
- [8] Y. Li, J. Zhu, M. Duperron, P. O'Brien, R. Schüler, S. Aasmul, d. M. Mirko, K. Mathias and R. Baets, "Six-beam homodyne laser Doppler vibrometry based on silicon photonics technology," *Optics Express*, vol. 26, no. 3, pp. 3638-3645, 2018.
- [9] M. K. A. Singh and W. Xia, "Portable and Affordable Light Source-Based Photoacoustic Tomography," *Sensors*, vol. 20, no. 21, p. 6173, 2020.
- [10] H. E. Bass, L. C. Sutherland, A. J. Zuckerwar, D. T. Blackstock and D. M. Hester, "Atmospheric absorption of sound: Further developments," *The Journal of the Acoustical Society of America*, vol. 97, no. 1, pp. 680-683, 1995.

# Monolithic 16 GHz DBR mode-locked laser in an InP generic foundry platform: simulation and experiment

Jiaxing Dong,<sup>1,2</sup> Y Durvasa Gupta,<sup>3</sup> Braulio Gomez Saavedra,<sup>1</sup> Francisco M. Soares,<sup>4</sup> André Richter,<sup>1</sup> and Francisco J. Diaz-Otero<sup>2</sup>

<sup>1</sup> VPIphotonics GmbH, Carnotstr. 6, Berlin, Germany

<sup>2</sup> University of Vigo,atlanTTic Research Center, EI Telecommunication, 36310 Vigo, Spain

<sup>3</sup>Fraunhofer Heinrich Hertz Institute, Einsteinufer 37, 10587 Berlin, Germany

<sup>4</sup> Soares Photonics, Lisbon, Portugal

## Abstract

*This paper presents a 16 GHz passive quantum well-based passive mode-locked laser (MLL) with an extended cavity, and Distributed Bragg reflectors (DBR) fabricated in the generic integration platform from Fraunhofer HHI. The performance of different operation regimes (Q-switching, mode-locking, and harmonic mode-locking) and pulse shape was studied for multiple lengths of the saturable absorber (SA). Characteristics for the gain and absorption spectra of the gain region and SA under various bias conditions were obtained from measurements of stand-alone devices and used to fit the analytical models applied in the simulations of the devices. The outcomes of these simulations of the MLL based on the Traveling Wave Equation and Transmission Line model are in good agreement with the measurements for the repetition rate and the behavior of different operation regimes.*

## Introduction

Semiconductor mode-locked lasers (MLLs) can produce a pulse at radio frequency (RF). They are used, for instance, in medical cutting, data communications, lidar, and metrology. Passive MLLs can be realized using linear or ring geometries [1]. They modulate the losses of the whole cavity by using a saturable absorber (SA) to synchronize the phase of the lasing modes. Inside the SA, the counterpropagating interaction of the light will cause a higher saturation by utilizing the colliding pulse mode-locking (CPM) configuration. Adding a passive component to a two-section linear MLL with cleaved facets acting as mirrors can improve its performance. First, it allows flexibility in selecting the total length of the cavity which defines the repetition rate. Second, it reduces self-phase modulation (SPM). Further improvements can be achieved by using the Multimode Interference Reflector (MIR) as a broadband reflector or the distributed Bragg reflector (DBR) as a narrow-band but wavelength-tunable reflector. Third, extending the cavity with an optical filter gives additional bandwidth control and can result in harmonic MLL operation. Finally, using other passive components enables the effective implementation of programmable photonics circuits [2].

In this paper, we theoretically and experimentally investigate the performance of operation regimes of a 16 GHz passive DBR mode-locked laser fabricated in the multi-project wafer (MPW) platform at Fraunhofer HHI. We further present optimization results of the SA length.

## MLL operation regimes

The monolithic 16 GHz DBR mode-locked laser simulations have been performed using VPIcomponentMaker Photonics Circuits. We used the photonics transmission-line model (TLM) to simulate the behavior in the multi-quantum well (MQW) active region. The

Traveling-wave equations (TWE) were solved to obtain the electric field inside the active region.

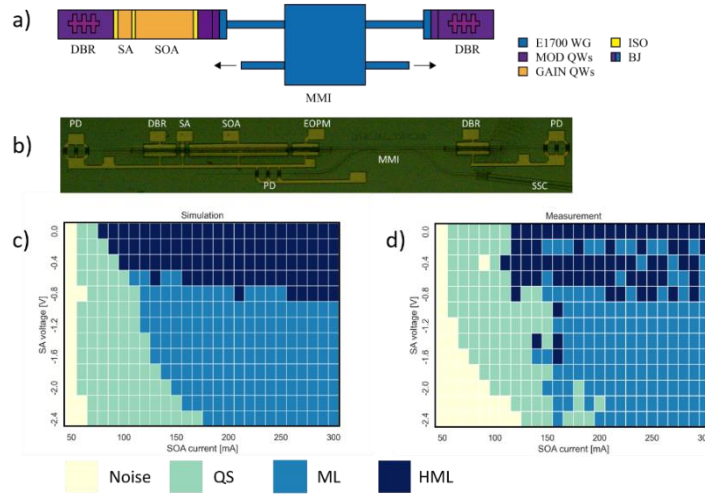


Fig. 1. (a) Schematic diagram of the DBR mode-locked laser with an extended cavity: semiconductor optical amplifier (SOA); saturable absorber (SA); electrical isolation (ISO); Multi-mode interference coupler (MMI); distributed Bragg grating reflector (DBR); (b) Microscope image of the fabricated device; (c) Simulation results of different operation regimes: Q-switching (QS), mode-locking (ML), and harmonic mode-locking (HML); (d) measurement of different operation regimes.

Fig. 1(a) shows the schematic diagram of the fabricated 16 GHz DBR mode-locked laser. Fig. 1(b) shows the microscope image of the device under test (DUT). The MLL consists of a 900  $\mu\text{m}$  SOA and a 50  $\mu\text{m}$  reversely biased SA section separated by a 30  $\mu\text{m}$  electrical isolation section (ISO). Two identical 300  $\mu\text{m}$  distributed Bragg grating reflectors with 1550 nm center wavelength are used as mirrors. A 2x2 Multimode Interference coupler is used to transport the light out of the device. Deeply etched passive waveguides were included to extend the cavity. We investigated the mode-locking operation regimes by varying separately from each other the SOA current (50 mA to 300 mA) and the SA voltage (0 V to -2.6 V).

The carrier lifetime of the SA is dominated by the sweep-out time ( $\tau$ ) and is assumed to

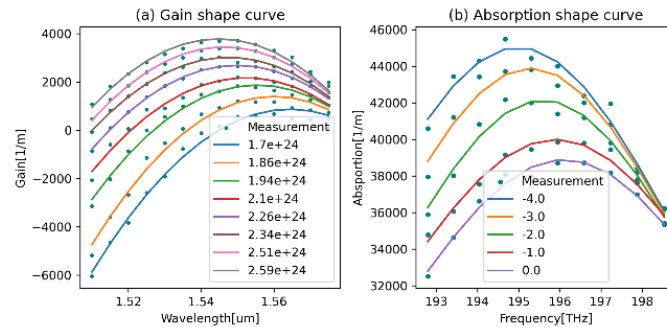


Fig. 2. (a) Measurement and fitting curves of the SOA gain spectrum with carrier density from 1.7E24 to 2.59E24  $1/m^3$ . (b) Measurement and fitting curve of the SA absorption spectrum under -4 V to 0 V.

follow a linear relationship with voltage in the logarithmic scale [3]. Fig. 2 shows the measured gain and absorption spectra of InGaAsP/InP SOAs with eight quantum wells for a range of injection currents and reverse biased voltage, as indicated above.

In the simulations, the following parabolic analytical model was used to fit the measured gain spectra:

$$g(f, N) = g_{peak}(N) \cdot \left\{ 1 - \left[ \frac{f - f_{peak}(N)}{\Delta f(N)/2} \right]^2 \right\}$$

where  $g_{peak}$  is the gain peak of the spectra,  $N$  is the carrier density inside the TLM sections,  $f_{peak}$  is the gain peak frequency, and  $\Delta f$  is the gain bandwidth.

A Lorentzian analytical model was used to fit the absorption spectra of the SA:

$$\alpha_e(f, V_k) = \alpha_p(V_k) \cdot \frac{(\Delta f(V_k)/2)^2}{(f - f_p(V_k))^2 + (\Delta f(V_k)/2)^2}$$

where  $\alpha$  is the absorption coefficient,  $f_p$  is the voltage-dependent absorption peak frequency, and  $\Delta f$  is the absorption bandwidth.

We determine the operation classification of the MLL based on the simulated pulse shape and measured electrical spectrum [4,5]. Fig. 1(c) shows simulation results of the different operation regimes of the MLL. At low  $V_{sa}$  ( $< 0.4$  V), the MLL worked in QS mode when the current was above the threshold and began lasing in the HML mode with the current increasing. As  $V_{sa}$  varies from 0.6 V to 0.8 V, which corresponds to  $\tau$  varying from 25.11 ps to 15.84 ps, the carrier density of the SA cannot be reduced to zero in the ML mode, which means that the absorption ability of the SA is partially recovered within one round-trip time within the laser cavity. Consequently, this leads to a chirped pulse with a duration comparable to the round-trip time. In the HML mode, the net amplification is strong enough to support two pulses inside the cavity simultaneously. Because of the pulse duration time, the adjacent two pulses will overlap partially. When  $0.8$  V  $< V_{sa}$   $< 2.4$  V,  $\tau$  ranges from 15.84 ps to 0.39 ps, and a wide and stable ML operation region was observed. When  $\tau < 6.30$  ps, which corresponds to  $V_{sa} < 1.2$  V, the carrier density inside the SA decreases to zero before the next pulse front enters the SA. With the increase of  $V_{sa}$ , the 3 dB bandwidth of the optical spectrum increases and results in narrower pulse generation.

The DUT was mounted on a temperature-controlled copper chuck and measured at 20 °C. A spot size converter (SSC) facilitated the coupling of the device to an optical fiber and reduced the coupling loss. We placed the SSC on the chip with a 7° tilt related to the chip edge to minimize the impact of back reflections from the interface to the laser cavity. The optical signal was detected using a THORLABS RXM40AF photoreceiver with 40 GHz bandwidth. The RF signal generated was recorded by a 50 GHz bandwidth electrical spectrum analyzer (ESA) Agilent 8565EC. Fig. 1(d) shows the different operation regimes derived from the experimental characterization of the MLL which are in good agreement with the simulations.

The MLL becomes unstable and operates between the ML and HML regimes for  $V_{sa} < 0.8$  V. The highest fundamental RF peak of -10.66 dBm/res was found at  $I_{soa} = 185$  mA and  $V_{sa} = 1.4$  V. When  $V_{sa} > 1.6$  V, the high starting lasing  $I_{soa}$  can be explained by the unexpected high loss inside the cavity.

## Influence of SA length

We also studied the influence of the SA length  $L_{SA}$  on the operation regimes and pulse quality. Fig. 3(a, b, c) presents a simulation pulse train for various  $L_{SA}$  from 19  $\mu$ m to 90  $\mu$ m. All other parameters were kept the same as described in the previous section. A stable ML can be obtained for  $L_{SA}$  from 20  $\mu$ m to 80  $\mu$ m. When  $L_{SA} < 20$   $\mu$ m, a stable HML can

be observed. The peak power has a positive correlation and the pulse duration time has a negative correlation with  $L_{SA}$ . The highest peak power (106.51 mW) and the sharpest full width at half maximum (FWHM) pulse duration (6.66 ps) can be observed at 19  $\mu\text{m}$ .

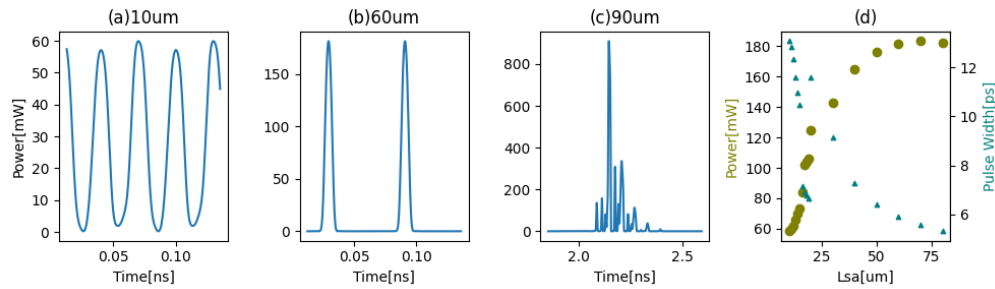


Fig 3. (a, b, c) Simulated pulse train of SA length from 10  $\mu\text{m}$  to 90  $\mu\text{m}$ . (d) detected simulation peak power and FWHM of the pulse with different SA lengths. (all plots for  $I_{\text{soa}} = 220 \text{ mA}$  and  $V_{\text{sa}} = 2.0 \text{ V}$ )

When  $L_{SA} > 20 \mu\text{m}$ , a stable ML pulse train can be observed. A jump in pulse width can be observed at the threshold of ML. After the threshold length, the highest peak power (183.40 mW) was obtained by 70  $\mu\text{m}$ , and the sharpest FWHM (5.30 ps) can be observed at 80  $\mu\text{m}$ . When  $L_{SA} > 90 \mu\text{m}$ , QS is observed, and the peak power significantly increases to 0.91 W. The average output peak power and FWHM as a function of  $L_{SA}$  are shown in Fig. 3(d).

## Conclusion

We realized a 16 GHz MLL with a DBR reflector as an InP photonic integrated circuit. The operation condition at the passive mode-locking regime was theoretically and experimentally studied. Our simulations can qualitatively predict the different operation regimes of the MLL. For the ML region, we found the highest peak power of 183.4 mW at  $L_{SA} = 70 \mu\text{m}$ , and the sharpest pulse with FWHM = 5.3 ps at  $L_{SA} = 80 \mu\text{m}$  by varying the length of the SA section.

## Acknowledgments

This work has been funded by the H2020-MSCA-ITN-2019 program of the European Union under the Grant Agreement N860763 (Drive-In). The authors express their gratitude to Fraunhofer Heinrich Hertz Institute for fabricating the devices analyzed in this paper.

## References

- [1] K. Van Gasse *et al.*, "Recent Advances in the Photonic Integration of Mode-Locked Laser Diodes," *IEEE Photonics Technol. Lett.*, vol. 31, no. 23, pp. 1870–1873, Dec. 2019.
- [2] W. Bogaerts *et al.*, "Programmable photonic circuits," *Nature*, vol. 586, no. 7828, pp. 207–216, Oct. 2020.
- [3] K. R. Lefebvre and A. F. M. Anwar, "Electron and hole escape times in single quantum wells," *J. Appl. Phys.*, vol. 80, no. 6, pp. 3595–3597, Sep. 1996.
- [4] U. Bandelow, M. Radziunas, A. Vladimirov, B. Hüttel, and R. Kaiser, "40 GHz Mode-Locked Semiconductor Lasers: Theory, Simulations and Experiment," *Opt. Quantum Electron.*, vol. 38, no. 4–6, pp. 495–512, Mar. 2006.
- [5] V. Moskalenko, S. Latkowski, S. Tahvili, T. de Vries, M. Smit, and E. Bente, "Record bandwidth and sub-picosecond pulses from a monolithically integrated mode-locked quantum well ring laser," *Opt. Express*, vol. 22, no. 23, pp. 28865–28874, Nov. 2014.

# Narrow-band electroluminescence of resonant-cavity avalanche-mode silicon LEDs

S. Dutta,<sup>1</sup> R.J.E. Hueting,<sup>2</sup> and G.J. Verbiest<sup>1</sup>

<sup>1</sup> Delft University of Technology, Dept. of Precision and Microsystems Engineering, Mekelweg 2, 2628 CD Delft, The Netherlands.

<sup>2</sup> University of Twente, Faculty of EEMCS, 7522 NB Enschede, The Netherlands

*Monolithic integration of light-emitting diodes (LEDs) in silicon (Si) is gaining attention in various on-chip optoelectronic applications e.g. optical links, micro-displays, and chemical sensing. Operating Si LEDs in avalanche mode leads to electroluminescence (EL) with photon energies exceeding the indirect bandgap of Si, although at low efficiencies. The optical wavelength ( $\lambda$ ) of these photons span a wide range of 450 nm - 950 nm, well-matched to the responsivity of Si photodiodes in CMOS technology. A knowledge gap exists on how to enhance the EL intensity within a desired narrow  $\lambda$ -band. Here, we show our recent study on the effect of optical cavity resonances on the phonon-assisted hot-carrier EL in Si LEDs. By employing Fabry-Pérot (FP) resonances in micro-ring diodes in a silicon-on-insulator (iSiPP50G) technology, we show (at room temperature) : (i) the EL peak  $\lambda$  can be tuned across a 100 nm range, (ii) the FWHM of the peak  $\lambda$  can be as low as 50 nm, and (iii) a 1-order-of-magnitude increase in optical power efficiency is achieved. Further, by combining FP resonance with carrier injection in a light-emitting transistor, we report on quasi-monochromatic light-emission near  $\lambda \approx 760$  nm with a record low FWHM of 38 nm.*

## Introduction

Efficient light-generation in standard silicon (Si) has been a key challenge for monolithic integration of photonic systems in CMOS technology. Despite its low optical power efficiency ( $\eta \sim 10^{-6}$ ), electroluminescence (EL) from Si p-n junctions, in particular during avalanche-mode (AM) operation, has gained attention in recent years due to its broad-spectrum ( $400 < \lambda < 900$  nm). This spectrum has a significant overlap with the responsivity of Si photodetectors (PDs), which has made the Si AM light-emitting diode (LED) a viable non-coherent light-source in monolithically integrated systems, e.g., optical interconnects, micro-displays and pigment sensors. Nonetheless, it is highly desirable to increase  $\eta$  within a desired (narrow) range of  $\Delta\lambda$  for such AMLEDs to boost the performance metrics of the aforesaid systems. In this paper we present our recent findings [1],[2] on  $\eta$ -enhancement and  $\lambda$ -tuneability in AMLEDs and AM light-emitting transistor (LET). Specifically, we show the effect of optical cavity resonances on the phonon-assisted hot carrier EL spectra, that occur during avalanche breakdown of Si p-n junctions.

## Experimental devices in iSiPP50G Si photonics technology

*Micro-ring LEDs:* Each Si micro-ring unit of radius  $R$  and width  $w$  consists of symmetrically doped half-rings, forming p-n junctions at two opposite ends (Fig. 1a). Highly doped p+ and n+ implants offer ohmic contacts to metal layers routed to bond pads for biasing. For each LED, eleven such ring units are connected in parallel to increase the total device area, and thus light-output. The vertical SOI layer thickness post-fabrication is 0.21  $\mu\text{m}$ . Design variations were included in  $R$  (0.6 – 2.0  $\mu\text{m}$ ),  $w$  (0.16 –

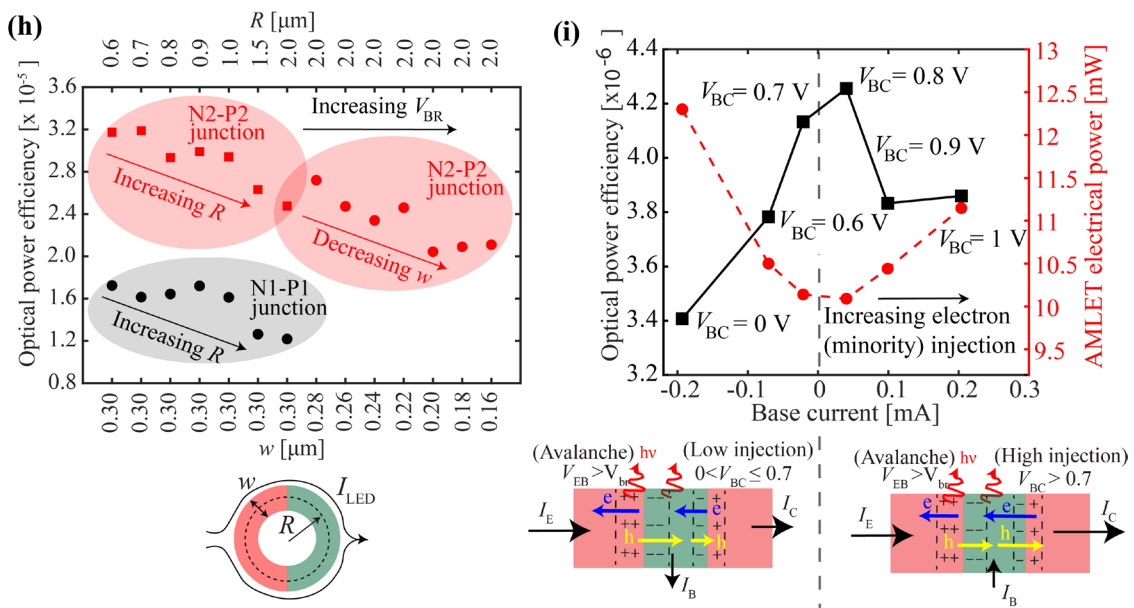
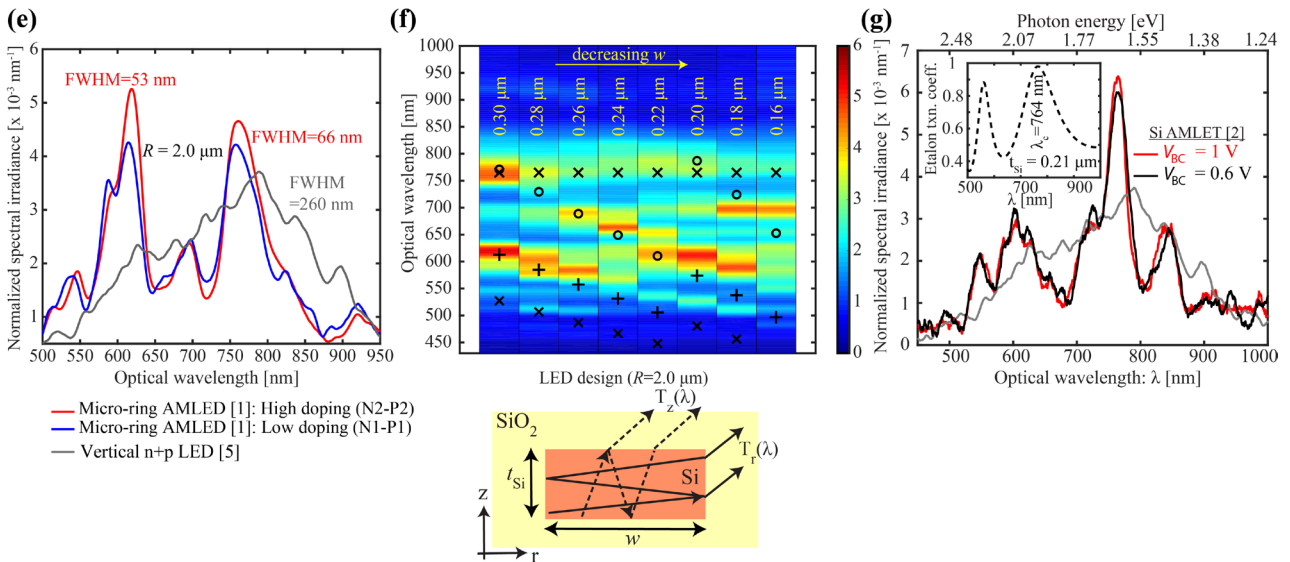
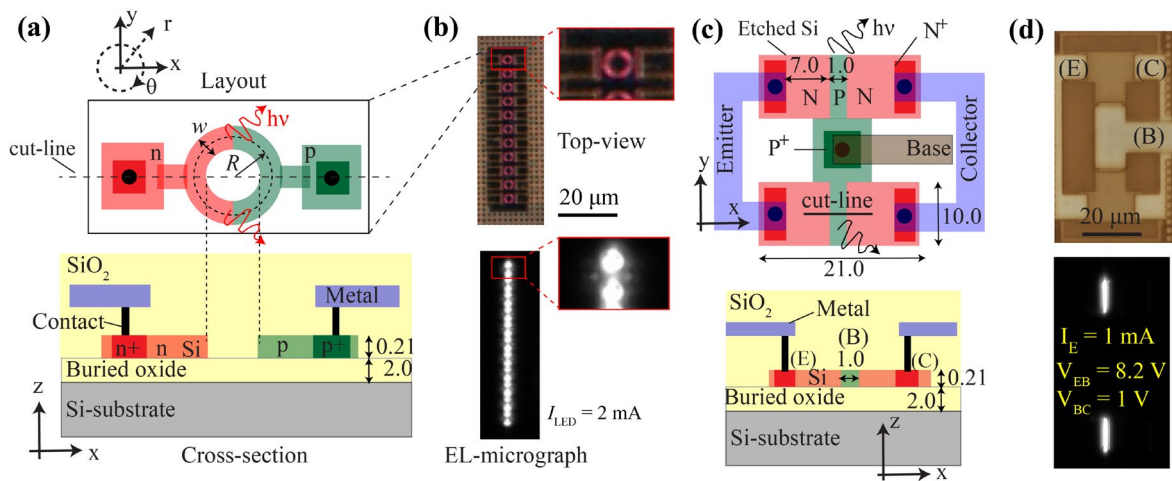
0.30  $\mu\text{m}$ ) and doping levels (lightly doped N1/P1 and highly doped N2/P2). The N1/P1 (N2/P2) LEDs show avalanche breakdown voltages ( $V_{\text{BR}}$ ) near  $\sim 7$  V ( $\sim 14$  V). The micro-rings emit light in AM operation (Fig. 1b).

Avalanche-mode light-emitting transistor (AMLET): The AMLET consists of lateral n-p-n bipolar junctions with symmetrically doped emitter (E), base (B), and collector (C) regions (Fig. 1c,d). The base length is 1.0  $\mu\text{m}$ . The device is placed in a 21  $\mu\text{m}$  x 10  $\mu\text{m}$  Si island surrounded by  $\text{SiO}_2$  on all faces.

## Key results

Micro-ring LEDs: AM-EL from each micro-ring LED was observed as localized bright twin spots from the p-n junctions (Fig. 1b). The EL mechanism is phonon-assisted recombination of hot carriers generated by the electric field at the junction [3],[4]. The intensity of the spots attenuates sharply along the  $\theta$ -axis of the ring due to the short attenuation length (1-10  $\mu\text{m}$ ) of light at short  $\lambda$  in Si, which is close to the round-trip length of the rings. Fig. 1e shows the normalized spectral irradiance  $\varepsilon(\lambda)$  of the ring LEDs with  $R=2.0$   $\mu\text{m}$  and  $w=0.3$   $\mu\text{m}$ . Irrespective of the doping level, two dominant narrow spectral bands were observed:  $\lambda_{\text{VIS}} \approx 620$  nm with FWHM of 53 nm, and  $\lambda_{\text{NIR}} \approx 764$  nm with FWHM of 66 nm. The relative intensities of these bands are 2-3 times higher than in prior reported Si AMLEDs [5]. Two minor bands near 550 nm and 700 nm were additionally observed. Further, the peak EL wavelengths  $\lambda_{\text{m}}$  of the ring LEDs in the 500 – 700 nm spectral range showed a consistent blue-shift with decreasing  $w$ . These results can be explained by FP resonances along the r-axis and z-axis of the Si cavity (Fig. 1f), where the Si-SiO<sub>2</sub> interfaces act as reflective boundaries. The calculated  $\lambda_{\text{m}}$  corresponding to integral resonance modes are in good agreement with the experiment. For a fixed ring geometry, the optical power efficiency ( $\eta_{\text{opt}} = P_{\text{opt}}/P_{\text{LED}}$ ) was higher for the higher (N2/P2) doping level, due to the lower  $V_{\text{BR}}$  (and so, lower  $P_{\text{LED}}$ ). Further,  $\eta_{\text{opt}}$  increased with decreasing  $R/w$  ratio (Fig. 1h), which is attributed to a decrease in  $V_{\text{BR}}$  as the series resistance ( $\propto R/w$ ) is lowered. A maximum  $\eta_{\text{opt}}$  of  $3.2 \times 10^{-5}$  at  $P_{\text{LED}} = 360$   $\mu\text{W}$  per p-n junction, was obtained for  $R=0.6$   $\mu\text{m}$  and  $w=0.3$   $\mu\text{m}$ , a 1-order-of-magnitude improvement compared to that of state-of-the-art Si AMLEDs (Fig. 1j) in various CMOS technologies.

AM light-emitting transistor (AMLET): The AMLET was measured in dc-operation at 298 K in common-base configuration. The E-B junction was set in AM ( $V_{\text{EB}} > V_{\text{BR}}$ ,  $I_{\text{E}} = 1$  mA) to emit light (Fig. 1d), whereas the B-C junction was forward biased in steps from 0 to 1 V, to inject minority carriers into the base. The AMLET EL spectrum showed three bands (Fig. 1g): Y-band ( $\lambda \approx 600$  nm), R-band ( $\lambda \approx 764$  nm), and NIR band ( $\lambda \approx 850$  nm). The R-band is significantly (2 times) brighter than the other bands. Further, the FWHM of the R-band is only 38 nm, with EL suppression in 650 – 700 nm  $\lambda$ -range, due to FP-resonance in the 0.21  $\mu\text{m}$  thick SOI layer. As  $V_{\text{BC}}$  increased from 0 to 0.8 V,  $\eta_{\text{opt}}$  increased (Fig. 1i) and reached a maximum at  $V_{\text{BC}}=0.8$  V, coinciding with a minimum in  $P_{\text{LED}}=I_{\text{C(E)}}V_{\text{EC}}$ , and a reversal in the direction of  $I_{\text{B}}$ . For  $V_{\text{BC}} > 0.8$  V,  $\eta_{\text{opt}}$  decreased due to a subsequent increase in  $P_{\text{LED}}$ . These are explained as follows. For  $V_{\text{BC}} < 0.8$  V, hot electrons (holes) generated in the E-B junction are swept to the E(B) region by the electric field. Only a small fraction of holes are injected into the collector ( $I_{\text{B}} < 0$ ). For  $V_{\text{BC}} > 0.8$  V, more holes can transit through the narrow base into the collector, thus  $I_{\text{B}} > 0$ . The injected cool electrons from the collector diffuse through the base and initiate avalanche at lower  $V_{\text{EB}}$ , thereby reducing  $P_{\text{LED}}$  by transistor action. Recombination of either hot (or cool) electrons with cool (or hot) holes are, thus, the dominant EL-mechanism (favoring the R-band).



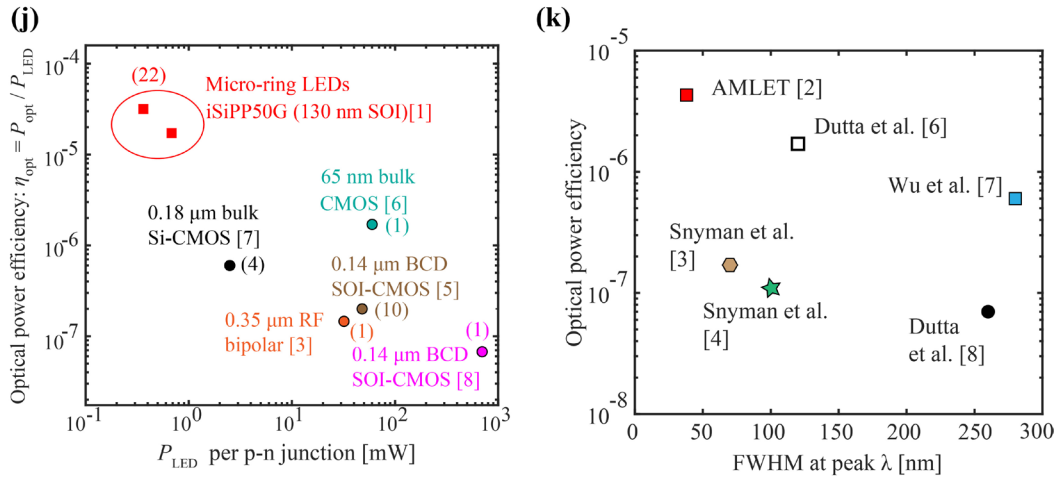


**Figure 1:** (a) Schematic layout along with the device cross-section of a micro-ring LED unit [1]. Indicated dimensions are in  $\mu$ m. Doping levels n/p, ring width  $w$  and radius  $R$  were varied in the LED designs. (b) Top-view of a micro-ring LED and its AM-EL micrograph captured at the indicated electrical bias. (c) Schematic layout and device cross-section of the AMLET [2] realized with a n-p-n bipolar junction. (d) AMLET top-view and its AM-EL micrograph at the indicated electrical bias. All devices were fabricated in the iSiPP50G Si photonics technology. The EL micrographs were captured with a 20 s integration time. (e) Normalized  $\varepsilon(\lambda)$  of ring LEDs with identical geometry ( $R=2 \mu$ m,  $w=0.3 \mu$ m), but with different doping levels. The  $\varepsilon(\lambda)$  of a prior-reported n<sup>+</sup>p AMLED [5] is shown in grey for comparison. (f)  $\varepsilon(\lambda)$  versus  $w$  for N2/P2 doped ring LEDs. The symbols o,+,x denote the calculated Fabry-Pérot (FP) resonance peak wavelengths corresponding to each  $w$  and to the 0.21  $\mu$ m thickness of Si layer. (g) Normalized  $\varepsilon(\lambda)$  of the AMLET at the indicated biasing, showing peak emission at 764 nm. (h)  $\eta_{opt}$  versus  $R$  and  $w$  for the micro-ring LEDs. (i) AMLET  $\eta_{opt}$  (black) and  $P_{LED}$  (red) at  $I_E=1$  mA and varying  $I_B$ . The schematic at the bottom shows the AMLET operation under low and high injection. (j) Benchmark of  $\eta_{opt}$  versus  $P_{LED}$  per p-n junction against prior art for Si AMLEDs [3],[5]-[8]. (k) Benchmark for  $\eta_{opt}$  versus FWHM at peak emission  $\lambda$  of the AMLET against those for prior art Si AM LED(T)s [3],[4],[6]-[8].

## Conclusion

We reported on narrow band electroluminescence (EL) of avalanche-mode (AM) silicon (Si) p-n junction devices, by employing Fabry-Pérot (FP) resonances and carrier injection. Micro-ring cavity LEDs were studied to optically confine the light along two dimensions, leading to narrow-band EL peaks within the visible (500-700 nm) and near-infrared spectra (750-800 nm), with a 2-3 fold higher intensity and a 10-fold higher optical power efficiency compared to state-of-the-art AM Si LEDs. The peak EL-wavelengths depend on the ring width, as predicted by a FP resonator model. Further, we realized an AM Si light-emitting transistor. A high injection current density through a narrow base region combined with FP resonance in the optically thin SOI layer, resulting in near quasi-monochromatic light-emission centered at 764 nm with a record low bandwidth of 38 nm.

## References

- [1] S. Dutta and G.J. Verbiest, *Optics Express*, vol. 30, no. 23 (in press), 2022.
- [2] S. Dutta, R.J.E. Hueting, and G.J. Verbiest, *IEEE Electron Device Lett.*, vol. 43, no. 10, pp. 1701-1704, 2022.
- [3] L.W. Snyman et al., *IEEE J. Quantum Electron.*, vol. 53, no. 5, p. 7100209, 2017.
- [4] L.W. Snyman, K. Xu, and J.-L. Polleux, *IEEE J. Quantum Electron.*, vol. 56, no. 4, p. 3200210, 2020.
- [5] S. Dutta et al., *IEEE Trans. Electron Devices*, vol. 64, no. 4, pp. 1612-1618, 2017.
- [6] S. Dutta et al., *IEEE Electron Device Lett.*, vol. 38, no. 7, pp. 898-901, 2017.
- [7] K. Wu et al., *IEEE Electron Device Lett.*, vol. 42, no. 4, pp. 541-544, 2021.
- [8] S. Dutta et al., *Optics Express*, vol. 25, no. 5, pp. 5440-5456, 2017.

# Amorphous Si Side-wall Grating DFB InGaAs/GaAs Nano-ridge Laser Epitaxially Grown on a Si Wafer

E. M. B. Fahmy<sup>1</sup>, Z. Ouyang<sup>1</sup>, and D. Van Thourhout<sup>1</sup>

<sup>1</sup> Photonics Research Group, Department of information technology (INTEC), Ghent University - IMEC, Belgium

*Epitaxial growth of InGaAs/GaAs nano-ridges allows monolithic integration of laser sources on silicon wafers [1]. This opens up the possibility for integrated silicon photonics applications on a single chip. In this paper, we study the possibility of improving the design of DFB nano-ridge lasers, by adding a silicon grating on the side walls of the nano-ridge structure. The fundamental TE mode of the nano-ridge extends to the side walls of the structure, resulting in a stronger interaction with a side wall grating, compared to the top grating used in previous work [1]. The mode simulations show a bigger overlap of the electric field with the side-wall grating resulting in an increased mode effective index and hence, higher reflectivity from the grating, allowing for a smaller device.*

## Introduction

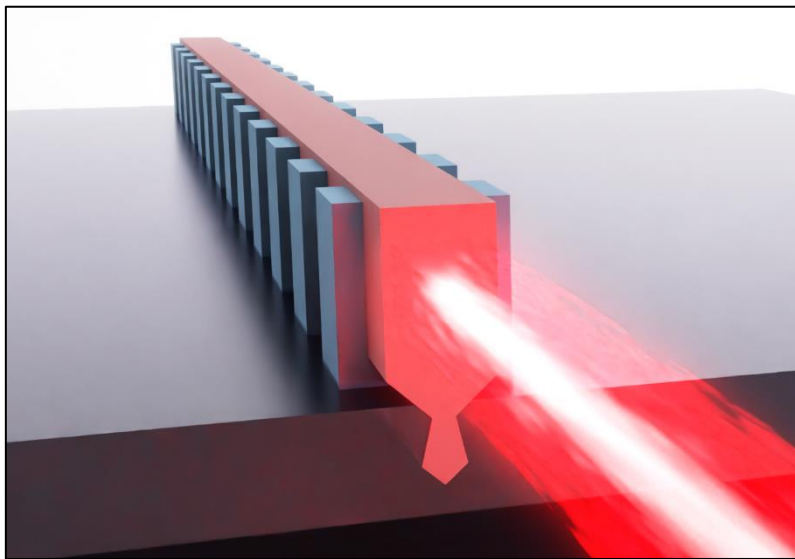


Figure 1: An illustration of the proposed nano-ridge laser with side-wall gratings.

To make full use of the potential offered by silicon photonic ICs, we need a method to integrate lasers on the same silicon platform. This can be achieved through heterogenous integration. An example is transfer printing [2], where the active material is fabricated on a different wafer in the form of coupons, that are then transferred and bonded on a silicon chip.

Monolithic integration on the other hand offers an advantage as the active material is directly grown on the Si wafer. But comes with a challenge, the lattice mismatch between the active material and silicon causes crystal dislocations and defects, resulting in non-radiative recombination. One way to solve this issue is by using aspect ratio trapping (ART) and nano-ridge engineering (NRE). In this approach, the dislocations are trapped

in narrow trenches, allowing the growth of defect-free active material in the form of nano-ridges [1].

Here, we introduce an improvement on the design of the nano-ridge DFB lasers reported earlier [3]. We show that introducing an amorphous Si side-wall grating to the nano-ridge structure, instead of the previously used top grating, allows for higher interaction of the DFB grating with the fundamental TE mode of the device. A single nano-ridge device (figure 1) comprises a GaAs waveguide with InGaAs quantum wells embedded in the

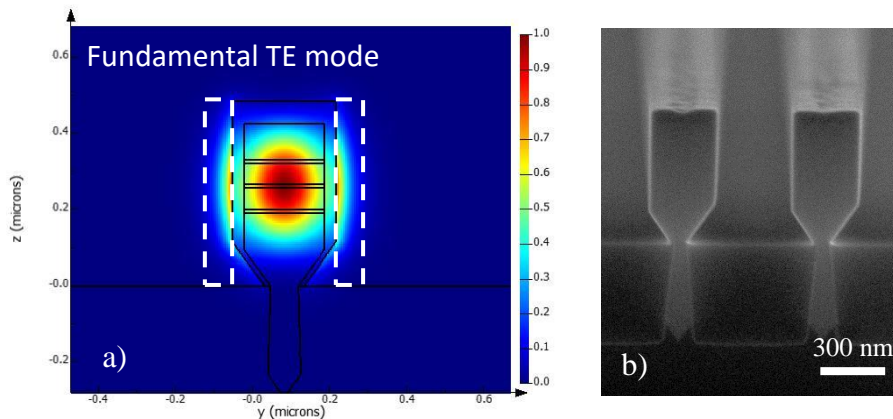


Figure 2: a) The fundamental TE mode is extending outside the sides of the structure. b) SEM image of Nano-ridge structure.

middle of the device, providing the gain medium needed for lasing (figure 2b). The waveguide can support multiple modes with different mode profiles. The fundamental TE mode has a higher overlap with the quantum wells and lower losses [3]. Additionally, the electric field is parallel to the quantum wells plane, making it the dominant lasing mode (figure 2a). To achieve lasing, a form of resonator structure is needed. In a Fabry-Perot laser, the resonator is formed using two mirrors at both ends of the gain medium to provide the feedback, in this case, reflection between the two mirrors [4]. Another way to achieve the necessary feedback is by using a periodic structure along the length of the device. The modulation of the mode effective index due to the grating causes Bragg scattering at the designed wavelength [4].

## Designing a smaller device

Making a smaller device required two modifications. First, the grating was added on the two sides of the nano-ridge, allowing for higher interaction with the TE mode. For a nano-ridge of 220 nm width, 70 nm trench width, and 485 nm height, a side grating of 50 nm width results in a mode power overlap of 7.035% per side (~14% total). This can be compared to a top grating of 50 nm, for which the overlap is only 1.8%. Increasing the top grating thickness to 100 nm, improved the overlap to 6.1%, but it is still less than half of that found for the side grating.

Secondly, the nano-ridge width needed to be reduced to increase the index contrast of the grating even more. An FDTD simulation for different nano-ridge widths shows the change in the frequency of the fundamental TE mode (Figure 3). The simulations show that at smaller nano-ridge widths (<300 nm) the change in the resonance frequency is

higher and the bandgap strongly increases. Using this information we can choose a width, which is still possible to fabricate, and maximizes the difference between the mode supported in the

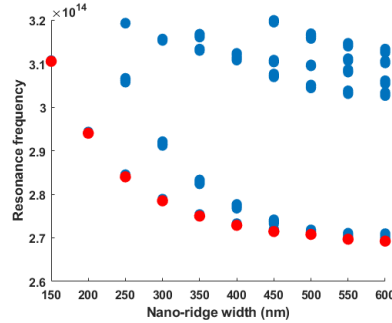


Figure 3: A band-edge (vertical slice of the bandstructure) simulation sweep showing the fundamental TE mode (red) frequency changing rapidly at smaller nano-ridge width and the increasing bandgap.

grating region and the mode in the waveguide region (figure 4 a, b). The grating period ( $\Lambda$ ) is then calculated according to the Bragg formula,  $\Lambda = \lambda_0 / 2n_{avg}$ . A  $\lambda/4$  phase shift section is used to force single longitudinal mode operation.

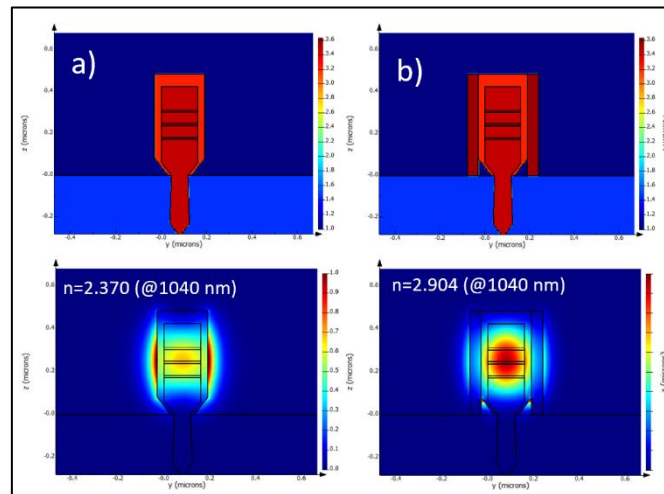


Figure 4: Mode profiles in the region without a) and with b) a-Si sidewall.

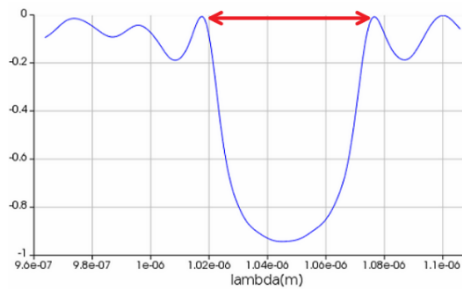


Figure 5: Reflection spectrum for 25 grating periods (one side of the device).

These modifications result in high reflectivity of 94% (figure 5) over a bandwidth of 59 nm for a side-grating of 25 periods ( $\Lambda=200$  nm). In previous work [4], a reflectivity of 90% was achieved for a top grating with 300 periods. This is a one order of magnitude reduction in the device length.

The reflectivity isn't the only factor that will dictate the device length, but also the material gain volume. The reduction of the nano-ridge width reduces the amount of gain material (quantum wells) available, which adds a limit on the minimum device length. Further investigation is needed in that regard.

The quality factor of the proposed device was also calculated. The Q-factor shows a significant improvement for a smaller number of grating periods (figure 6) compared to the top grating.

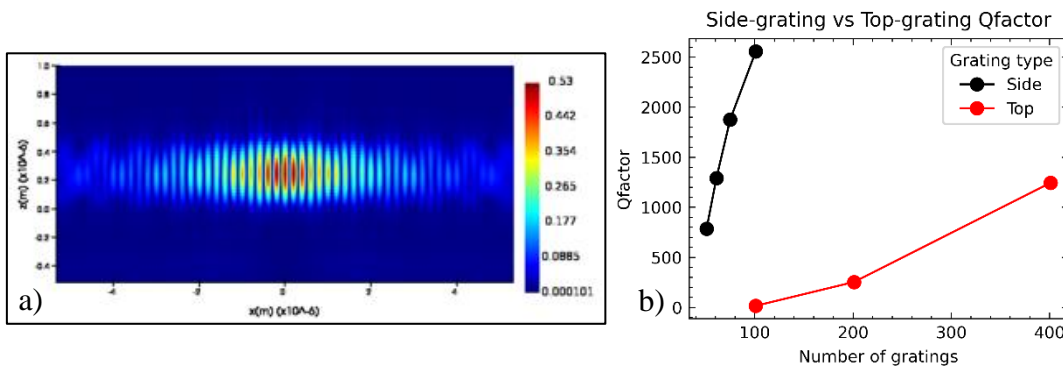


Figure 6: a) Calculated mode profile along the device at 1044 nm, showing the electric field localized at the  $\lambda/4$  phase shift section in the center of the device (25 grating periods at both sides). b) Q-factor calculations show a significant improvement for a side-grating ( $\Lambda=200$  nm, nano-ridge width of 220 nm, 485 nm height and a grating thickness of 50 nm) vs. a top grating ( $\Lambda=164$  nm, nano-ridge width of 410 nm, 485 nm height and a grating thickness of 100 nm).

## Conclusion

We demonstrated a significant improvement in the device miniaturization by using a higher index contrast side gratings on both sides of the nano-ridge structure.

## Acknowledgement

This project has received funding from the European Union's Horizon 2020 research and innovation program under grant agreement No. 884963 (ERC AdG NARIOS)

## References

- [1] D. Van Thourhout, Y. Shi, M. Baryshnikova, Y. Mols, N. Kuznetsova, Y. De Koninck, M. Pantouvaki, J. Van Campenhout, R. Langer, and B. Kunert, "Nano-ridge laser monolithically grown on (001) si," *Future Directions in Silicon Photonics*, pp. 283–304, 2019.
- [2] B. Corbett, R. Loi, J. O'Callaghan, and G. Roelkens, "Transfer printing for Silicon Photonics," *Semiconductors and Semimetals*, pp. 43–70, 2018.
- [3] Y. Shi, Z. Wang, J. Van Campenhout, M. Pantouvaki, W. Guo, B. Kunert, and D. Van Thourhout, "Optical pumped InGaAs/GaAs Nano-ridge Laser epitaxially grown on a standard 300-mm Si Wafer," *Optica*, vol. 4, no. 12, p. 1468, 2017.
- [4] H. Kogelnik and C. V. Shank, "Stimulated emission in a periodic structure," *Applied Physics Letters*, vol. 18, no. 4, pp. 152–154, 1971.

# InP-based optical phased array with on-chip amplification

M. Gagino,<sup>1</sup> A. Millan-Mejia,<sup>2</sup> L. Augustin,<sup>2</sup> K. Williams,<sup>1</sup> E. Bente,<sup>1</sup> V. Dolores-Calzadilla<sup>1,3</sup>

<sup>1</sup> Technical University Eindhoven, Dept. of Electrical Engineering, Groene Loper 19, 5612 AP Eindhoven, The Netherlands

<sup>2</sup> SMART Photonics, High Tech Campus 29, AE Eindhoven, The Netherlands

<sup>3</sup> Photonic Integration Technology Center, Groene Loper 19, 5612 AP Eindhoven, The Netherlands

*We present an optical phased array (OPA) photonic integrated circuit based on an InP generic platform with on-chip amplification. To the best of our knowledge, it is the OPA with the highest on-chip optical gain reported in literature. The proof-of-principle OPA chip has 8 channels and includes a booster semiconductor optical amplifier (SOA), and in-line SOAs for amplification in all arms. We investigated the optical amplification performance at different current injection levels in an 80nm wavelength range. We measured a maximum on-chip optical gain of 8.6dB at 1530nm for an on-chip input laser power of 5dBm, delivering a total output power of 23mW. The results are promising for OPA-based LiDAR systems where output power is critical to increase the sensing range.*

## Introduction

Optical phased arrays (OPA) have gained popularity for their potential use in LiDAR sensing [1,2]. Photonic integrated circuit (PIC) OPAs offer a solid-state and non-mechanical solution for optical beam steering which, compared to existing and available solutions in the market, is potentially advantageous in reducing reliability issues linked to mechanical vibrations.

Several requirements must be met to produce a LiDAR sensor with the range and angular resolution necessary for autonomous driving applications [3]. The optical output power requirement is often limiting the sensing range of PIC-based OPA technologies, due to non-negligible optical losses in currently available PIC platforms [4]. Moreover, a wide operational spectral range is desirable to achieve beam steering in two dimensions via dispersive gratings [5].

We propose an OPA photonic integrated circuit with on-chip amplification through semiconductor optical amplifiers (SOAs), which was developed on a generic InP photonic platform [6]. Although similar design concepts were explored in previous publications [5,7,8], in this work we present a characterization of the on-chip amplification performances in the 1490-1570nm range, and we show a broadband operation of the active OPA through calibration and beam steering.

## PIC design and measurement setup

We designed the proof-of-principle OPA shown in Figure 1a, which was fabricated on a generic InP photonic platform by SMART Photonics. The chip consists of an edge-coupled input waveguide, a star coupler, 8 arms with amplitude and phase control, and an output edge emitter. The input laser signal, and the light guided in each OPA arm, are amplified by 500 $\mu$ m long SOAs. The phase in the OPA arms is controlled by 2.2mm long electro-optical phase modulators (EOPMs).

The OPA emitter is an array of  $1.2\mu\text{m}$  wide waveguides which are equally distanced at a pitch of  $2.2\mu\text{m}$ , giving a simulated (*Lumerical MODE/FDTD*) field of view of  $\pm 20^\circ$  before the main lobe and the first order grating lobe are of equal intensity (i.e., aliasing condition).

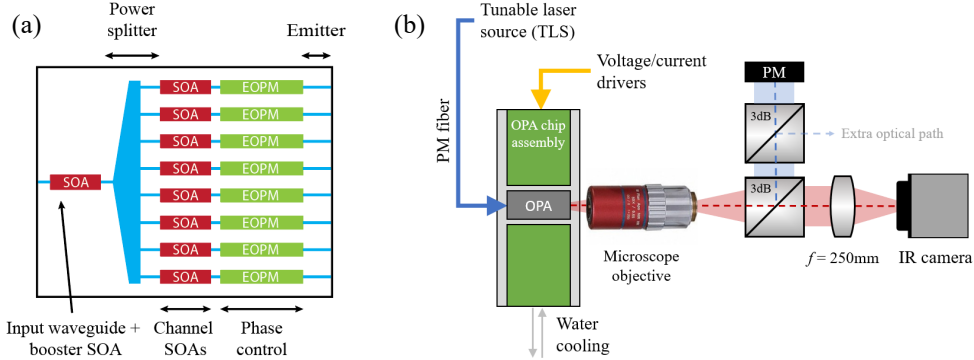


Figure 1: (a) Schematic diagram of the OPA under test. (b) Schematic diagram of the free-space measurement setup.

We assembled the PIC onto a water-cooled Aluminium-Copper mount with conductive epoxy, and we wire-bonded the PICs electrical pads to two PCBs which routed the driving signals to the electrical instrumentation (*Nicslab XDAC-120MUB*, and *NI PXIe-4145*). We optically characterized the OPA's far-field by means of the setup shown in Figure 1b. The setup consists in a 0.7 NA microscope objective ( $f = 2\text{mm}$ ) and a 250mm focal length plano-convex lens which form a  $4f$  optical system that focus light on an IR camera. A series of two 50:50 free-space splitters bring collimated light to a free-space powermeter (*Thorlabs S122C*); we used the same powermeter to calibrate the loss of our free space optics. Light from a tunable laser source is input through a lensed polarization maintaining fiber.

## Characterization of OPA amplification

We investigated the OPA on-chip amplification level in the 1490-1570nm range, and at SOAs current injection levels in the  $3 - 10\text{kA}/\text{cm}^2$  range. The 8 channel SOAs were operated under the same bias condition, while the input booster SOA's current density was fixed to  $10\text{kA}/\text{cm}^2$  to maximize the output power level. We set the temperature of the water-cooler to  $10^\circ\text{C}$  with a thermal stability of  $0.1^\circ$ , and the on-chip input power to  $5\text{dBm}$  (Figure 2a).

We measured the highest on-chip gain level of 8.6dB by operating the channel SOAs at a  $7.1\text{kA}/\text{cm}^2$  current density, and at 1530nm wavelength; the total output power under these conditions is 13.6dBm. To the best of our knowledge, it is the highest on-chip gain recorded in a solid-state optical phased array. Moreover, for channel SOAs current densities in the  $6.2 - 9\text{kA}/\text{cm}^2$  range, the on-chip gain is greater than 4.5dB at all wavelengths in the 80nm range, delivering an output power higher than 9.5dBm.

From *Lumerical MODE/FDTD* simulation results, we calculated the losses due to the presence of diffraction orders and grating sidelobes, which are between 3.2dB and 1.9dB in the steering range.

Furthermore, we observe a decrease in the output power and on-chip gain at currents in the  $6 - 10\text{kA}/\text{cm}^2$  range for all wavelengths, and we attribute it to thermal roll-over associated to the number of SOAs operating simultaneously and their proximity ( $160\mu\text{m}$  pitch). To estimate the decrease in amplification, we measured the total OPA output

power by operating the channel SOAs one by one, while the remaining 7 SOAs were shorted and absorbing light in the active medium. The process was repeated for all arms. By summing the output power contributions of all channels, we calculated an on-chip gain of  $10.5\text{dB}$ , under the same driving conditions mentioned before (i.e.,  $7.1\text{kA}/\text{cm}^2$  current density in the channel SOAs, and  $1530\text{nm}$  wavelength), and a maximum on-chip gain of  $11.5\text{dB}$  with channel SOAs driven at  $10\text{kA}/\text{cm}^2$ . As Figure 2b shows, thermal roll-over induces a decrease in amplification between  $1\text{dB}$  and  $3.4\text{dB}$ , whereas at a higher substrate temperature of  $18^\circ\text{C}$ , the effects of thermal roll-over are more pronounced, reducing the gain by up to  $4.5\text{dB}$ .

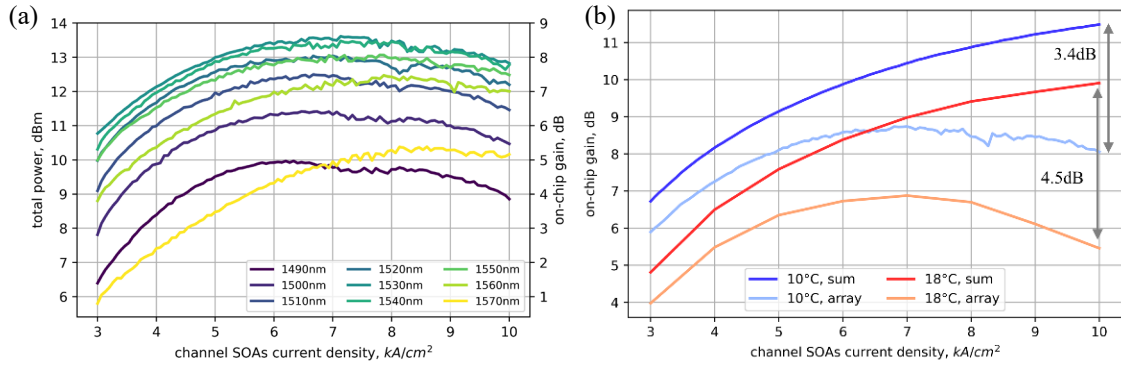


Figure 2: (a) Measured output power and gain of the OPA. Channel SOAs are driven at the same current density. (b) On-chip gain measured with all arms in forward bias (array), and by summing the contribution of single arms (sum).

## Calibration and beam steering

We demonstrated the beam calibration and beam steering in the  $80\text{nm}$  wavelength range. To do so, we operated the optical phased array at a substrate temperature of  $18^\circ\text{C}$ , we set the on-chip input power at  $5\text{dBm}$ , and we biased the booster SOA and channel SOAs with  $10\text{kA}/\text{cm}^2$  and  $6\text{kA}/\text{cm}^2$  respectively.

We employed the modified Rotating Element Electric Field Vector (*mREV*) method to calibrate the OPA at  $0^\circ$  steering, and to extract the EOPMs phase information to steer at any angle in the field of view [9]. We calibrated the beam at 20 wavelengths in the  $80\text{nm}$  range, and we steered the beam at 20 angles in the  $\pm 20^\circ$  field of view. Figure 3 shows beam steering at 7 angles and at three wavelengths.

From the far-field images we collected through the setup shown in Figure 1, we extracted the beam properties at all wavelengths and steering angles. The angular resolution, which is measured at the full-width at half-maximum (FWHM), fluctuates in the  $4.63^\circ - 4.97^\circ$  range, giving a pixel resolution of 7 points. The FWHM variations are within the  $\pm 0.2^\circ/\text{pixel}$  resolution of the free-space optical system and are attributed to the vibrations induced by the water-cooler system, and the calibration accuracy. The OPA beam's diffraction sidelobe suppression ratio (SSR) is below  $-10.7\text{dB}$  for all wavelengths and steering angles. We recorded the lowest SSR of  $-14.9\text{dB}$  at  $1526\text{nm}$ .

We compared the measurements to the optical simulation results of the OPA emitter obtained through *Lumerical MODE/FDTD*. We estimated a far-field beam with a FWHM of  $4.8^\circ$ , and an SSR better than  $-14.5\text{dB}$  for all steering angles in the field of view. The

measurements and simulation results are in agreement, and the SSR discrepancy is accredited to the limited calibration accuracy.

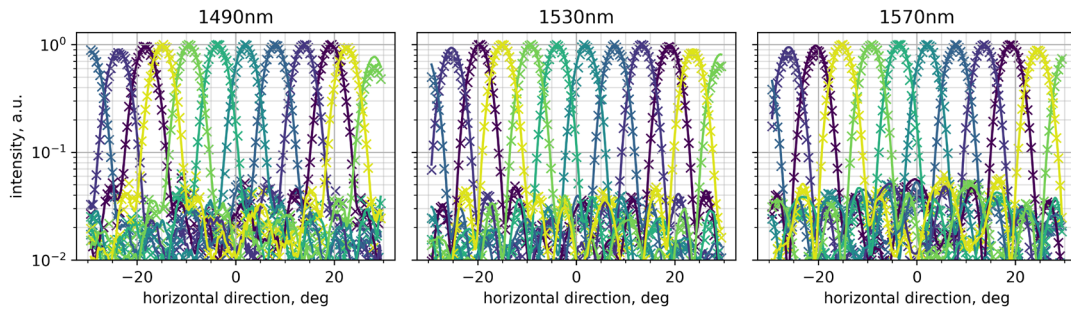


Figure 3: 1D cross section of measured far-field beam at 7 steering angles (color of the plots) in the OPA's field-of-view, at three wavelengths in the tuning range.

## Conclusions

We designed an optical phased array with on-chip amplifiers, and we demonstrated its beam steering operation in an 80nm wavelength range with a maximum measured SSR of -14.9dB. We measured, to the best of our knowledge, the highest power recorded at the output of an OPA (13.6dBm), and the highest on-chip gain (8.6dB).

The results are promising for LiDAR sensing applications that require high optical power for reaching long range, and to allow 2D beam scanning through dispersive gratings. Moreover, the design is scalable, and a higher number of OPA arms, as well as the use of a longer booster SOA, can significantly increase the output power level.

Thermal roll-over in the OPA was observed, therefore future improvements may include the design of more efficient SOA devices. Packaging and an ad-hoc cooling system will also be beneficial for the thermal stability of high-power OPAs.

## Acknowledgments

This work has received funding support from the European Union's Horizon 2020 program through the NewControl project under grant no. 826653.

## References

- [1] Y. Guo, et al., "Integrated Optical phased arrays for beam forming and steering," *Applied Sciences*, vol. 11, no. 9, p. 4017, 2021.
- [2] M. J. R. Heck, "Highly integrated optical phased arrays: Photonic integrated circuits for optical beam shaping and beam steering," *Nanophotonics*, vol. 6, no. 1, pp. 93–107, 2017.
- [3] Z. Dai, et al., "Requirements for automotive lidar systems," *Sensors*, vol. 22, no. 19, p. 7532, 2022.
- [4] C. V. Poulton, et al., "Large-scale silicon nitride nanophotonic phased arrays at infrared and visible wavelengths," *Optics Letters*, vol. 42, no. 1, p. 21, 2016.
- [5] J. C. Hulme, et al., "Fully integrated hybrid silicon two-dimensional beam scanner," *Optics Express*, vol. 23, no. 5, p. 5861, 2015.
- [6] L. M. Augustin, et al., "InP-based generic foundry platform for photonic integrated circuits," *IEEE J. Sel. Topics Quantum Electron.*, vol. 24, no. 1, pp. 1–10, Jan. 2018.
- [7] C.-W. Chow, et al., "Actively controllable beam steering optical wireless communication (OWC) using Integrated Optical Phased Array (OPA)," *Journal of Lightwave Technology*, pp. 1–7, 2022.
- [8] K. A. McKinzie, et al., "INP high power monolithically integrated widely tunable laser and SOA array for hybrid integration," *Optics Express*, vol. 29, no. 3, p. 3490, 2021.
- [9] M. Gagino, et al., "Broadband operation of an INP optical phased array," *IEEE Photonics Technology Letters*, vol. 34, no. 10, pp. 541–544, 2022.

# Quantum Secured Control Plane Communications

Carlos Rubio García<sup>1</sup>, Idelfonso Tafur Monroy<sup>1</sup>, J.J. Vegas Olmos<sup>2</sup>, Simon Rommel<sup>1</sup>

<sup>1</sup> Department of Electrical Engineering, Eindhoven University of Technology, Eindhoven, The Netherlands

<sup>2</sup> Software Architecture, NVIDIA Corporation, Yokneam, Israel

*In current networks, the security of critical information depends primarily on a mix of conventional public key encryption (PKE) whose security is based on very complex mathematical models. Nonetheless, as proven by Shor's algorithm, the rapid development of quantum computers is seriously threatening PKE schemes. This is something that exposes new security issues on Software Defined Networks (SDN), where the control plane is separated from the data plane. Since the behavior of the network is based on the information collected and transmitted by the control plane, it is of high importance that these communications remain secure against any attacker. This paper explains the problem that SDN networks are facing in the advent of quantum computers and the reason why quantum key distribution (QKD) and post-quantum cryptography (PQC) need to be combined for enabling quantum secured control plane communications. Finally, we describe a user scenario in which a strategy is proposed for integrating QKD and PQC into the control plane.*

## Introduction

Over the last few years, there has been an unexpected growth in quantum technologies. The need for more powerful machines in some areas of research is leading the industry to strongly push for the development of quantum computers [1]. In such a case, current cryptography algorithms will no longer be secure. The development of Shor's polynomial-time algorithms for prime factorization and discrete logarithms transform problems that were thought to be hard for classical computers, into something doable with a mature-enough quantum computer [2]. The National Institute of Standard and Technology (NIST) predicts that by 2030, a quantum computer built with a budget of around 1 billion dollars will be able to break 2000-bit Rivest-Shamir-Adleman (RSA) cryptography. Moreover, this report also predicts that by 2036, sufficiently large quantum computers will be able to break all public key schemes that are currently in use within communication systems [3], [4]. The reason to address this now is commonly known as the "harvest now, decrypt later" problem, in which a quantum-mature adversary can collect encrypted versions of long-lived private information to decrypt it later in the future. This implies a critical need for implementing quantum-safe communications [4].

## Software Defined Networks

Increasingly demanding cloud services, network virtualization and Internet of Things (IoT) applications demand service providers to develop new services that can keep up with high quality of service (QoS) requirements [5]. While this is rather difficult to do in conventional network architectures [6], Software Defined Networking (SDN) has emerged as the network paradigm that provides the programmability and flexibility long needed. As depicted in Fig. 1, since the behavior of the network is logically centralized in an entity called SDN controller, service providers can easily manage, configure and

optimize network resources with dynamic, automated and open-source programs [5]. SDN is enabled by four key features [6]:

- Separation of control plane from the data plane
- Centralized controller that has a global view of the network
- Open interfaces between the control plane (controller) and the data plane (network devices)
- Programmability of the network by external applications

Although SDN allows more simple, flexible and dynamic network deployments, there are also several challenges that need to be addressed, such as performance, scalability, security and interoperability. While all of them are of capital importance, this paper focuses on the security vulnerabilities of SDN. We propose a strategy on how to augment the security of the SDN control plane communications by means of QKD, and thus, explain how SDN can remain secure in the advent of quantum computing.

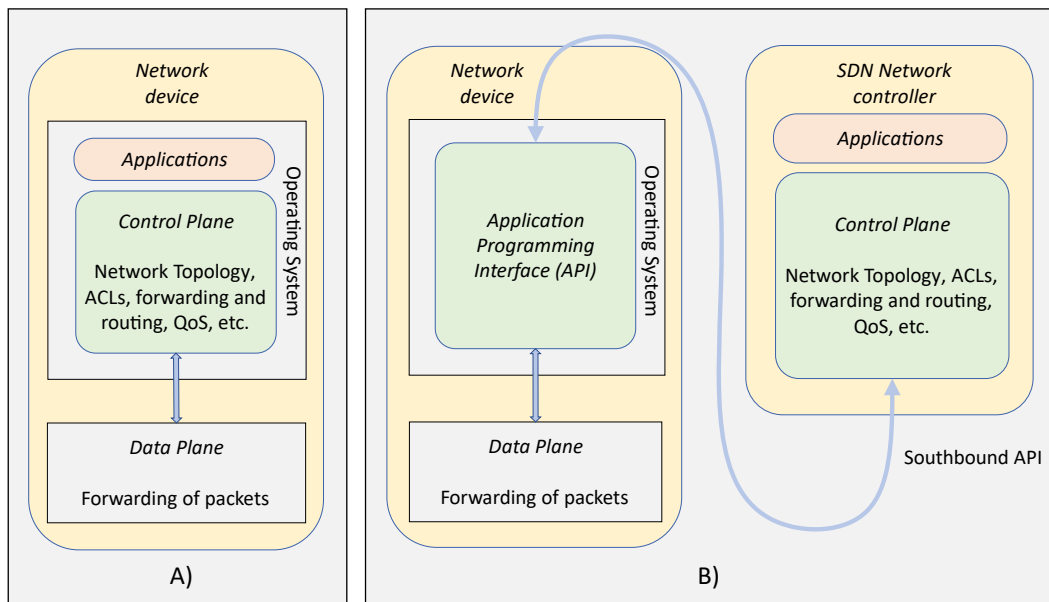


Figure 1. A) Traditional control approach; B) SDN control approach [6].

## Quantum Key Distribution

A solution to overcome this challenge is by employing Quantum Key Distribution (QKD). This technology allows establishing a secure communication channel whose security is guaranteed by the laws of quantum physics, instead of a challenge on how to solve a complex mathematical problem. Due to the uncertainty principle and the no-cloning theorem, the observation of a quantum signal causes a perturbation in its state. That means, if a third party (Eve) wants to obtain any information about the message exchanged in the quantum channel, it causes a perturbation to the sequence of qubits, which changes its final state. After the transmission of the encoded message, both transmitter and receiver can estimate how much of the message has been leaked. If the difference between the first and final state of the qubits surpasses a certain threshold, the secret quantum key cannot be distilled. The fact that the integrity of the messages can be guaranteed following quantum physics suggests the unconditional security of the messages, independently of Eve's computational resources [7].

## Architecture of quantum secured networks

It is vital that the introduction of quantum technologies in the data plane can coexist with current optical infrastructure. As it happens with traditional equipment, QKD networks need an effective management and control plane that can coordinate the QKD resources, support the dynamic allocation of quantum links among nodes, and orchestrate the integration with already existing telecommunications infrastructure. The data plane must ensure the correct forwarding of the quantum keys. On the other hand, QKD can be implemented to secure control plane communications against quantum-mature attackers. Therefore, SDN-QKD is considered a mutually beneficial relationship. In order to enable the integration of QKD within SDN control plane, we propose the architecture shown in fig. 2:

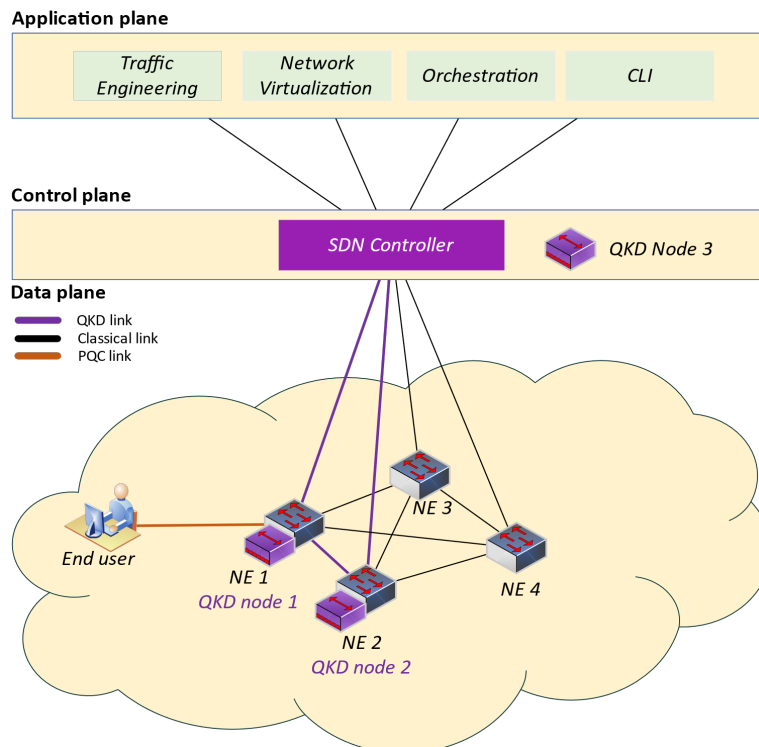


Figure 2. SDN-QKD-PQC architecture

- For implementing fully secure QKD-based communications, there needs to be an authentication phase in which both applications using QKD keys can use PKE (certificates) to identify themselves as the rightful endpoints of the communication. Authentication is a task that QKD cannot address, and thus, another quantum safe alternative needs to be used. We propose the use of post-quantum cryptography (PQC) for the authentication of multiple parties. While there are many different post-quantum algorithms that can handle authentication, the use of Crystals-Dilithium [8] algorithm is recommended by NIST [9].
- While QKD has established itself as the most secure option for key distribution, it is a relatively “new” technology that also brings constraints to the networks (limited distance, expensive equipment, complex integration with traditional infrastructure, etc.). It is recommended that QKD should be combined with other cryptographic algorithms for augmented security. Here, we propose that network security protocols such as Transport Layer Security (TLS) could be modified, so that they combine classical cryptography (Elliptic Curve Diffie-Hellman) with QKD. On top of that,

since there are also PQC alternatives for the key exchange such as Crystals-Kyber [10], PQC can also be integrated into authenticated key exchange (AKE) mechanisms. We propose the implementation of a quantum-safe TLS, which combines classical cryptography, PQC and QKD. Hence, achieving a level of security backed up by three different cryptographic assumptions.

- Although free space QKD is also an alternative for implementing QKD in wireless scenarios, it is still a challenging subject. In implementations where end-to-end quantum security must be achieved, we propose to implement PQC (i.e. Crystals-Kyber) as the AKE mechanism in those areas of the networks where optical fiber links are not available.

## Conclusions

Since SDN allows more flexible, programmable and dynamic networks, it remains the technology of choice while introducing QKD for securing communications. This adds requirements on the QKD equipment, which needs: (i) be equipped with interfaces that can interpret and respond to the network controller commands, and (ii) be able to react accordingly to these commands. At the same time, QKD is one of the best options to secure control plane communication. Its integration/combination with classical cryptography, as well as PQC, will give SDN networks the security needed to guarantee and provide ultra-safe communications in the 6G and beyond era, where quantum computers will already be a mature technology.

## Acknowledgements

This work was supported by the EC H2020 MSCA ITN-ETN IoTalentum (grant no. 953442) and Dutch Ministry of Economic Affairs and Climate Policy (EZK), as part of the Quantum Delta NL programme.

## References

- [1] J. Preskill, “Quantum Computing in the NISQ era and beyond,” *Quantum*, vol. 2, p. 79, Aug. 2018, doi: 10.22331/q-2018-08-06-79.
- [2] P. W. Shor, “Polynomial-Time Algorithms for Prime Factorization and Discrete Logarithms on a Quantum Computer,” *SIAM J. Comput.*, vol. 26, no. 5, pp. 1484–1509, Oct. 1997, doi: 10.1137/S0097539795293172.
- [3] L. Chen *et al.*, “Report on Post-Quantum Cryptography,” National Institute of Standards and Technology, NIST IR 8105, Apr. 2016. doi: 10.6028/NIST.IR.8105.
- [4] D. Ott, C. Peikert, and other workshop participants, “Identifying Research Challenges in Post Quantum Cryptography Migration and Cryptographic Agility.” arXiv, Sep. 16, 2019. doi: 10.48550/arXiv.1909.07353.
- [5] M. Karakus and A. Durresi, “A survey: Control plane scalability issues and approaches in Software-Defined Networking (SDN),” *Comput. Netw.*, vol. 112, pp. 279–293, Jan. 2017, doi: 10.1016/j.comnet.2016.11.017.
- [6] S. Sezer *et al.*, “Are we ready for SDN? Implementation challenges for software-defined networks,” *IEEE Commun. Mag.*, vol. 51, no. 7, pp. 36–43, Jul. 2013, doi: 10.1109/MCOM.2013.6553676.
- [7] V. Scarani, H. Bechmann-Pasquinucci, N. J. Cerf, M. Dusek, N. Lutkenhaus, and M. Peev, “The Security of Practical Quantum Key Distribution,” *Rev. Mod. Phys.*, vol. 81, no. 3, pp. 1301–1350, Sep. 2009, doi: 10.1103/RevModPhys.81.1301.
- [8] P. Schwabe, “Dilithium.” <https://pq-crystals.org/dilithium/> (accessed Nov. 09, 2022).
- [9] “NIST Announces First Four Quantum-Resistant Cryptographic Algorithms,” *NIST*, Jul. 2022, Accessed: Nov. 09, 2022. [Online]. Available: <https://www.nist.gov/news-events/news/2022/07/nist-announces-first-four-quantum-resistant-cryptographic-algorithms>
- [10] P. Schwabe, “Kyber.” <https://pq-crystals.org/kyber/> (accessed Nov. 09, 2022).

# SWIR GaSb Photodiode integration on Si Photonics through Micro-Transfer-Printing

X. Guo<sup>1,2</sup>, A. De Groote<sup>3</sup> and G. Roelkens<sup>1,2</sup>

<sup>1</sup>Photonics Research Group, INTEC, Ghent University - IMEC, 9052 Ghent, Belgium

<sup>2</sup>Center for Nano- and Biophotonics, Ghent University - IMEC, 9052 Ghent, Belgium

<sup>3</sup>Brolis Sensor Technology, Bollebergen 2B/Box 11, 9052 Ghent, Belgium

*We investigate the possibility to integrate GaSb photodiodes on a Ge-SOI platform via micro-transfer printing. The germanium layer is used as an intermediate waveguide/taper to couple light from the underlying silicon waveguide to the III-V active region. We have successfully transfer-printed GaSb photodiode coupons and electrical measurements are performed.*

## Introduction

The short-wave infrared (SWIR) wavelength range and especially the 2-2.5  $\mu\text{m}$  range is of particular interest for spectroscopic sensing applications [1]. Various molecules including glucose, lactate, urea and ethanol have absorption peaks in this spectral region. Therefore SWIR lasers and photodiodes are of great interest.

In recent years, GaSb, as the 4<sup>th</sup> generation of the III-V material, has proven its excellent electrical and optical properties in the SWIR range [2-4]. GaSb and its related alloys are able to efficiently cover a spectral range from 1.7 to 3  $\mu\text{m}$ , which is in line with the absorption bands of multiple molecules. Compared to the InP system, the current most mature choice in the near-infrared, GaSb can probe further into the SWIR and has better performance diode lasers in the 2-2.5  $\mu\text{m}$  range [5].

Here, we present a GaSb based p-i-n photodiode that fits the target spectral range (2 to 2.5  $\mu\text{m}$ ). We integrate the GaSb photodiode on a Ge-SOI platform via micro-transfer printing technology [6, 7]. This technology allows for the efficient use of III-V materials and enables pre-testing of the devices on the source wafers and the integration of a wide range of materials/devices on wafer scale in a massively parallel way.

## Design & Fabrication

The GaSb p-i-n photodiodes are integrated on a Ge-SOI platform, where 500 nm germanium is grown on top of standard 220 nm SOI wafers. The schematic of the device is depicted in Fig. 1. The germanium and silicon waveguides are patterned by Electron-beam lithography (EBL). After EBL patterning the germanium and silicon layer are etched by Reactive-ion etching (RIE).

The GaSb epitaxial layer is supplied by Brolis Sensor Technology. The GaSb photodiode structure consists of a 200 nm thick highly-doped GaSb p-contact layer and cladding, a pair of AlGaAsSb SCH layers, an active region with quantum wells separated by AlGaAsSb barriers and a 275 nm n-GaSb contact layer. A 1.5  $\mu\text{m}$  thick intrinsic InAsSb layer is used as the release layer for the transfer printing. The overall thickness of the III-V layer stack that is printed onto the target photonic circuit is around 4  $\mu\text{m}$ .

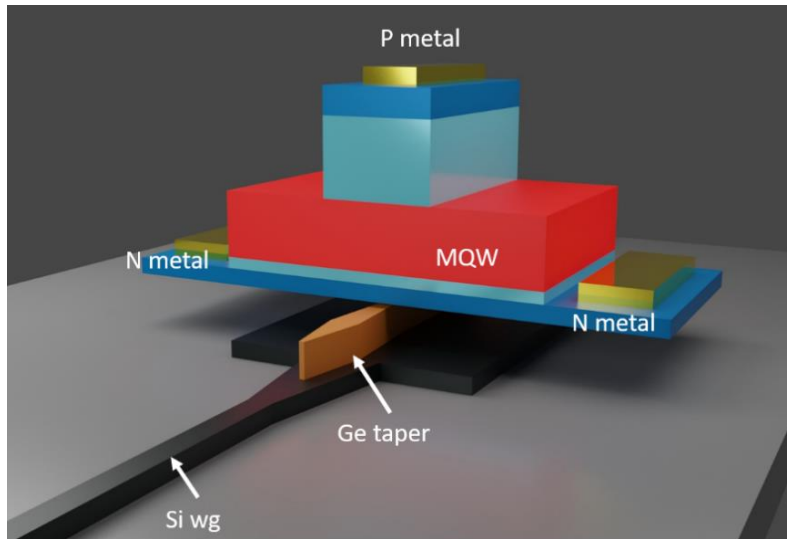


Figure 1: Rendering of the layout of the GaSb on Ge-SOI Photodiode.

The III-V process flow is described in Fig. 2. It starts by depositing a SiN hard mask. The hard mask is then patterned using optical lithography to define the mesa of the photodiode. The III-V is then etched through Inductively Coupled Plasma (ICP) etching (Fig 2(a)). This mesa etch defines the III-V waveguide and it is stopped before the quantum wells are reached. After this, a second mesa is defined to pattern the quantum well region (Fig. 2(b)). The dry etch process stops when the n-GaSb contact layer is exposed. Subsequently, a layer of 400 nm SiN is deposited to protect the side walls of the mesa. This protective layer is then patterned by optical lithography, followed by ICP etching to make the vias for metallization. Ti/Pt/Au contacts are formed on p-GaSb and n-GaSb contact layers simultaneously through a lift-off process (Fig. 2(c)). At this stage the GaSb photodiode is formed on the native source sample and will be followed by steps to make it transfer-printable. A SiN layer is again deposited as the hard mask to define the boundaries of the transfer-printable coupon (Fig 2(d)). The etching stops at the release layer. Afterwards, the release layer is etched through the same method: mask deposition, optical lithography and dry etching (Fig. 2(e)). After over-etching 200 to 300 nm into the GaSb substrate, a 650 nm SiN layer is deposited and patterned to form tethers that will hold the device after the under-etching of the release layer (Fig. 2(f)). In order to form a flat-top surface for the transfer-printing step, a thick photoresist of 4.2  $\mu\text{m}$  is spin-coated on the sample and patterned to encapsulate the device. To mitigate the attack from the etchants during the under-etching, the photoresist also requires a hard bake at 150° for 5 minutes to get better chemical stability. Afterwards, a citric acid solution is used to under-etch the InAsSb release layer. This wet-etching process is performed at 60° C which gives an etching rate of 25  $\mu\text{m}$  per hour. The coupons at this point stand on the SiN tethers as the anchors.

These coupons are fabricated in a dense array with a vertical pitch of 110  $\mu\text{m}$  and the length of the coupon varies from 200 to 400  $\mu\text{m}$  with a step of 100  $\mu\text{m}$ , where the lengths of the III-V waveguide are 120  $\mu\text{m}$ , 220  $\mu\text{m}$  and 320  $\mu\text{m}$  respectively.

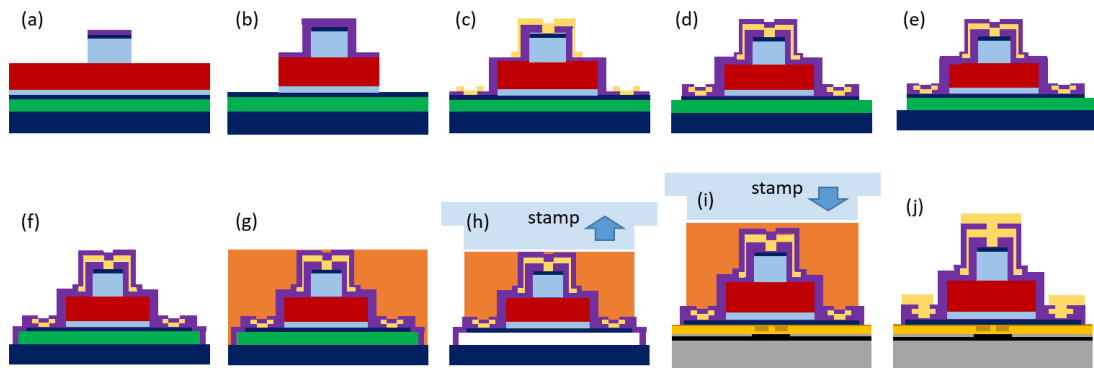


Figure 2: Process flow of the integration of GaSb photodiode coupons via micro-transfer printing.

Fig. 3(a) shows the top view of patterned and released coupons on the GaSb source sample, where the coupons have a width of  $45\ \mu\text{m}$ . In the current design there are two variants of our coupons: one with two n-contacts on both sides and the other with only one n-contact at the side. To transfer-print these coupons, PDMS stamps with a post of  $200, 300$  and  $400 \times 50\ \mu\text{m}^2$  in size are used for the corresponding size of coupons, using an X-Celeprint  $\mu\text{TP-100}$  tool. The photodiode coupons are printed on a Ge-on-SOI photonic waveguide circuit. The Germanium layer is  $500\ \text{nm}$  thick and the waveguides are etched  $300\ \text{nm}$  deep.

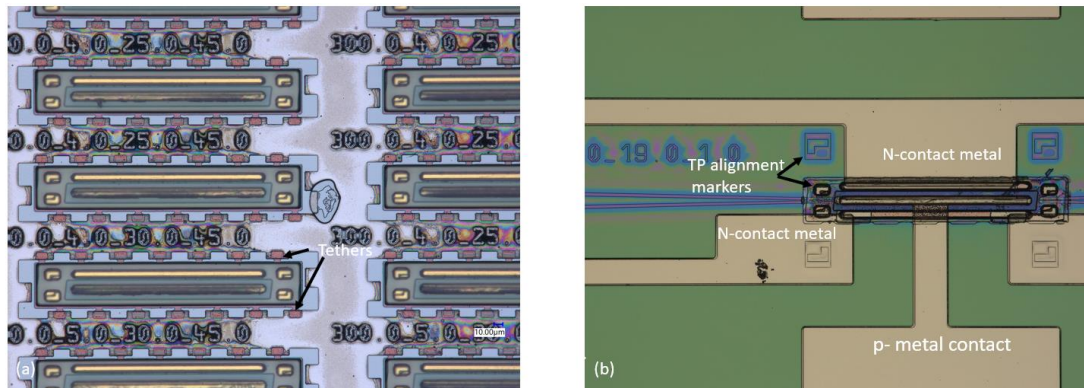


Figure 3: Microscope top images of GaSb coupons (a) before transfer-printing; (b) after transfer-printing and post-process.

To ensure a high printing yield, the target sample is spin-coated with a DVS-BCB: mesitylene 1:4 solution at  $3000\ \text{rpm}$ , followed by a soft bake at  $150^\circ\text{C}$  and cooling down to room temperature. Both the GaSb source sample and the Ge-on-SOI target sample are loaded into the micro-transfer-print tool after preparation. The source and the target samples need to be aligned before the actual transfer-printing. Once they are aligned and all the parameters are set properly, the stamp can pick up the coupons from the source sample and print them on the target sample (Fig. 2(h) and 2(i)).

One of the advantages of micro-transfer-printing is that all III-V processes are carried out on the native sample, which simplifies the process and allows us to know the quality of the III-V devices before transfer-printing by putting testing structures on the source sample (for example TLM structures). The first step of post-processing is removing the

encapsulated photoresist using an oxygen plasma RIE. After that, the DVS-BCB bonding layer is fully-cured at 210° C for 9 hours. Then, metal vias is made by etching the SiN layer to expose the p-contact metal and n-contact metal. As the last step of the whole process, a final lift-of process is executed to form a Ti/Au metal stack as the electrical contacts for probing, as shown in Fig. 3(b).

## Device characterization

So far we characterized the test structures on the source sample and performed *I-V* measurements. The testing structures were characterized at room temperature using electrical contact probes and a Keithley 2400A voltage-current source. As shown in Fig. 4, a dark current below 1  $\mu\text{A}$  was measured at a reverse bias voltage of 2 V for all 3 test photodiodes with a maximum length of 320  $\mu\text{m}$ . The next step is to measure the real transfer-printed photodiode.

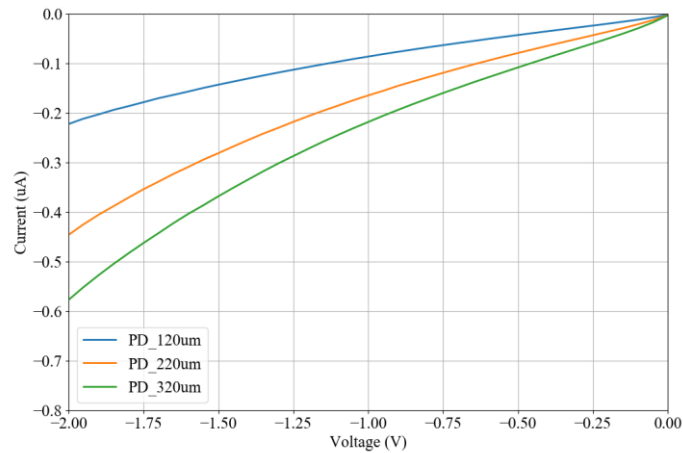


Figure 4: Measured dark currents of testing PD devices

## References

- [1] L.S. Rothman, et al. "The HITRAN2012 molecular spectroscopic database," *Journal of Quantitative Spectroscopy and Radiative Transfer*, vol. 130, 4-50, 2013.
- [2] A. Vizbaras, "Infrared laser spectroscopy at your fingertips," *Compound Semiconductor Magazine*, vol. 28, 18-26, 2022.
- [3] R. Wang, et al. "Compact GaSb/silicon-on-insulator 2.0x  $\mu\text{m}$  widely tunable external cavity lasers," *Optics express*, vol. 24, 28977-28986, 2016.
- [4] N. Hattasan, et al. "GaSb-based integrated lasers and photodetectors on a Silicon-On-Insulator waveguide circuit for sensing applications in the shortwave infrared," in *Proceedings of Photonics Global Conference (PGC)*. IEEE, 1-4, 2012.
- [5] A. Vizbaras, "GaSb-based chips promise a sensing revolution," *Compound Semiconductor Magazine*, vol. 27, 16-22, 2021.
- [6] B. Haq, et al. "Micro-transfer-printed III-V-on-silicon C-band semiconductor optical amplifiers," *Laser & Photonics Reviews*, vol 14, 1900364, 2020.
- [7] J. Zhang, et al. "Transfer-printing-based integration of a III-V-on-silicon distributed feedback laser," *Optics express* vol. 26, 8821-8830, 2018.

# Grating engineering for self-referenced Al<sub>2</sub>O<sub>3</sub> microring resonator sensors

B. Jongebloed, W.A.P.M. Hendriks, M. Dijkstra, S.M. García-Blanco

Integrated Optical Systems Group, MESA+ Institute for Nanotechnology,  
University of Twente, 7500 AE Enschede, The Netherlands.

*Microring resonators can be used in biosensing applications. Including a Bragg grating in the resonator results in frequency splitting of the resonances, creating a self-referenced sensor. The grating has to be designed such that the reflectivity is uniform. In that case, changes in the frequency splitting can be ascribed solely to the presence of biomarkers. To achieve this behaviour, the grating design is optimized by chirping and apodization. The resulting resonance splitting is constant over a bandwidth of 5 nm. The RIU sensitivity of this sensor is 209.22 pm/RIU, with a limit of detection of  $\sim 7 \cdot 10^{-6}$  RIU.*

## Introduction

Microring resonator sensors are a promising candidate for biosensing applications [1]. A microring resonator (MRR) sensor is a device that can sense changes in the environment of the device by measuring shifts in the resonance spectrum. The resonances shift when the optical path length of the MRR changes, which happens as a result of external perturbations to the system. In the case of a biosensor, the MRR is typically covered with acceptor molecules, that selectively bind to a particular biomarker [1]. The biomarker is a molecule found in bodily fluids, blood or tissue that is a sign for a specific disease. The optical path length of the MRR changes as biomarker molecules attach to acceptor molecules. As a result of the changed optical path length, the resonances shift.

In biosensing applications, one would often try to show the presence of a specific biomarker molecule. It would seem straightforward to do so by recording shifts of the resonances. However, more parameters influence the effective refractive index of the waveguides, for instance, temperature fluctuations and bulk refractive index changes. To ascribe changes in the resonance spectrum to the presence of biomarker molecules, referencing can be used to distinguish between different signal sources. Typically two transducers are used, of which one is sensitive to the biomarker and one is not. This however leaves uncorrelated noise contributions. To compensate for the uncorrelated noise contributions, a self-referenced MRR can be designed.

The self-referenced MRR consists of a Bragg grating inside the path of the MRR. The resonances of the MRR with Bragg grating now occur as resonance doublets. The frequency splitting, the frequency separation between the two resonances in the doublet, is directly related to the grating reflectivity [2]. Therefore, by recording the amount of frequency splitting, any signal that causes a change in the grating reflectivity can be measured. When the periodicity of the Bragg grating is filled with (or alternatively formed by) acceptor molecules, the reflectivity of the Bragg grating changes upon adhesion of biomarker molecules. Furthermore, since the splitting is much less sensitive to temperature and bulk refractive index variations than the MRR resonances, the MRR with Bragg grating exhibits self-referencing behavior. Figure 1 (b) depicts the splitting of the resonances in resonance doublets.

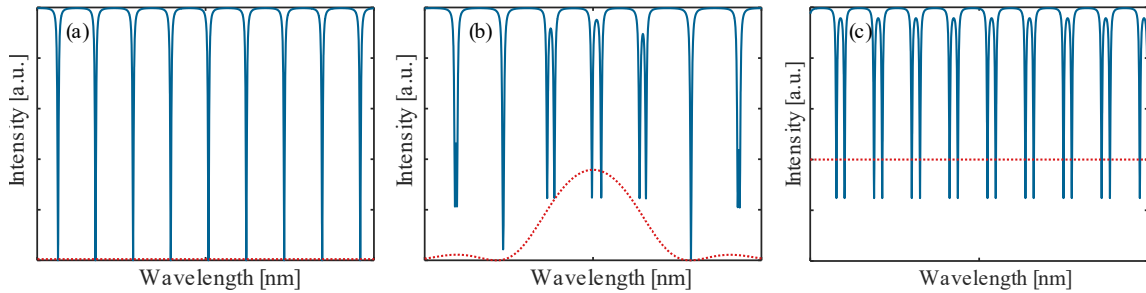


Figure 1 Transmission spectrum of (a) a MRR without a grating, (b) a self-referenced MRR, (c) self-referenced MRR with idealized grating. In all cases, the blue line represents the transmitted power and the red line represents the reflectivity of the Bragg grating

## Grating Engineering

The working principle of the Bragg grating can be understood as follows. The Bragg grating lifts the degeneracy between the clockwise and counterclockwise propagating modes in the MRR. A standard single periodicity and fill factor Bragg grating will have a frequency response as indicated by the red line in figure 1 (b). A flat response is required, shown in figure 1 (c), to ascribe changes in the frequency splitting to the presence of biomarker molecules. If the grating response is not flat, any shift of the MRR resonance will change the encountered grating reflectivity as shown in figure 1 (b). The amount of frequency splitting in this case remains sensitive to temperature and bulk refractive index changes.

A flat grating response, as shown in figure 1 (c), can be achieved by engineering the Bragg grating response. Two ways of manipulating the spectral response of a Bragg grating are chirping and apodization [3, 4, 5]. By chirping, the grating period of the Bragg grating increases along the grating length indicated in figure 2 (a). As a result, the bandwidth of the reflection increases. Apodizing the grating changes the duty cycle of a grating period along the length of the grating, as indicated in figure 2 (b). By changing the duty cycle, the grating strength is varied along the length of the grating. Apodization causes the reflectivity to flatten over the bandwidth.

The gratings are placed on top of a MRR that has a circumference of  $3384 \mu\text{m}$ . The  $\text{Al}_2\text{O}_3$  waveguides have a height of  $0.4 \mu\text{m}$  and a width of  $1.6 \mu\text{m}$ . In total, the length of the PMMA grating is  $200 \mu\text{m}$ , while the thickness of the PMMA layer is  $250 \text{nm}$ . For this thickness, the overlap of the fundamental TE mode with the PMMA grating is  $22.86\%$ . The chirp parameter is set to  $600 \mu\text{m}/\text{m}$  and the grating is apodized with a hyperbolic tangent duty cycle apodization profile [4] with parameters  $D_a = 1.8$  and  $D_b = 2.9$ . Using the grating parameters, the self-referenced MRR sensor is fabricated.

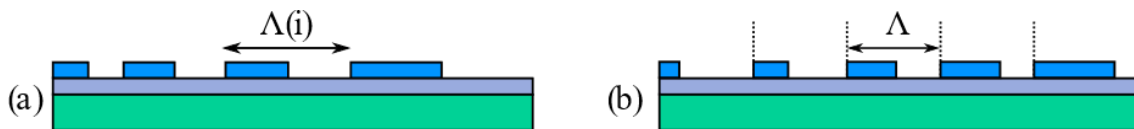


Figure 2 Schematic depiction of (a) chirped PMMA grating, and (b) apodized PMMA grating.

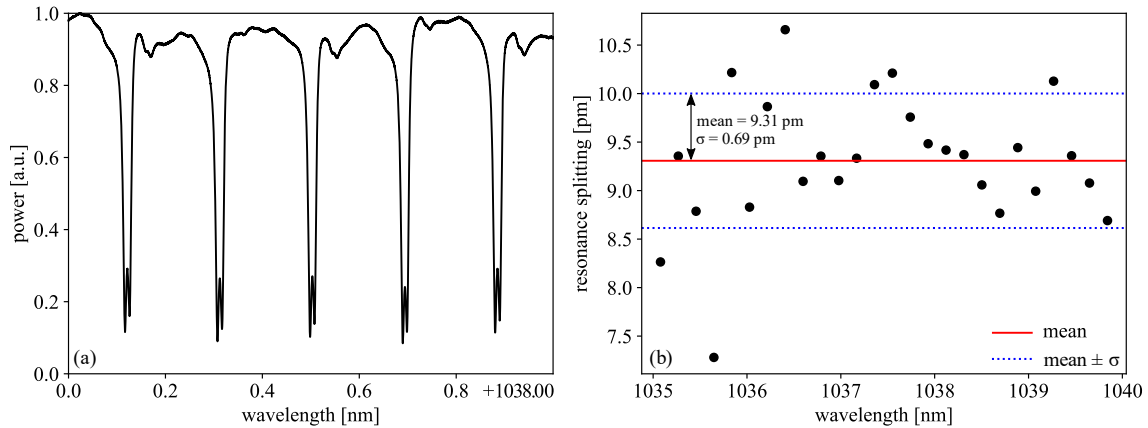


Figure 3 Transmission spectrum of (a) a self-referenced MRR with a DI water cladding, and (b) the resonance splitting of each resonance doublet in the wavelength range 1035 – 1040 nm.

## Characterization device

In order to characterize the self-referenced MRR, the transmission spectrum is studied. The transmission of light of different wavelengths is measured with a photodetector. A TOPTICA CTL 1050 source allows scanning over a wavelength range of 1020 to 1070 nm. The light is guided through single-mode polarization-maintaining (PM) fibers. These fibers are butt-coupled to the end facets of the chip using index matching fluid.

In order to introduce aqueous samples, the device is equipped with a PDMS pool. The PDMS pool allows for the introduction of different fluids, to have a controlled bulk refractive index. Furthermore, the device is placed on top of a heater, that is controlled with a PID controller, to keep the temperature of the sensor as constant as possible. The resonance spectrum is measured with a DI water cladding at a temperature of 22 °C. A small section of the transmission spectrum is shown in figure 3 (a). This figure shows that the resonances are split into resonance doublets.

In figure 3 (b), the resonance splitting is shown for each of the resonance doublets in the wavelength range of 1035 to 1040 nm. The resonance splitting is determined by finding the minima of the measured power. Since the wavelength resolution of the transmission spectrum is limited, the resonance splitting can only be determined with limited accuracy in this method. The mean resonance splitting is found to be 9.31 pm, with a standard deviation of 0.69 pm. The standard deviation is identical to the wavelength resolution of the transmission spectrum. In other words, within the detection limits, the resonance splitting is constant over a 5 nm bandwidth.

## Sensitivity analysis

The performance of the sensor is quantified by determining its sensitivity and the limit of the detection (LOD). The sensitivity of the resonance splitting to temperature variations and bulk refractive index changes is measured. Since the sensor is not yet functionalized, the grating trenches will also be filled with the different fluids that are flushed through the PDMS pool. As a result, during the sensitivity measurement, not only the bulk RIU is changed, but the refractive index contrast in the grating changes as well. The change in index contrast results in a change in reflectivity, resulting in a change in resonance splitting.

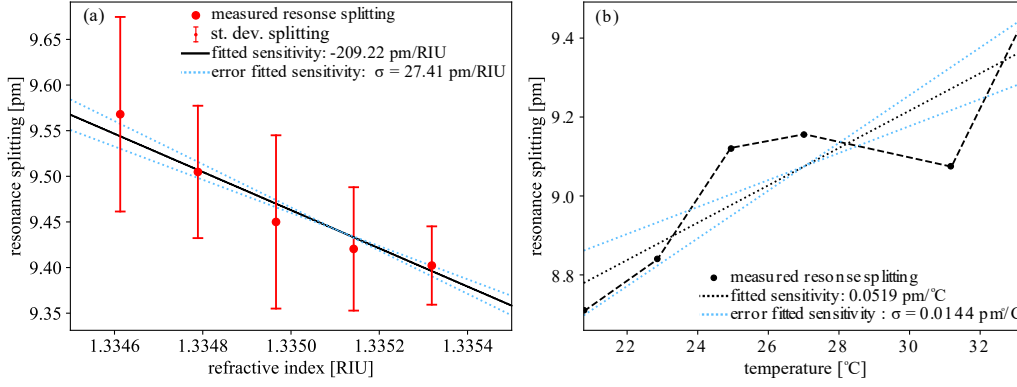


Figure 4 Resonance splitting as a function of (a) bulk refractive index and (b) temperature.

In figure 4, the measured resonance splitting as a function of the refractive index of the cladding solution and as a function of temperature are plotted. From these plots, both the bulk refractive index sensitivity and temperature sensitivity can be obtained as the slope of the linear fit. A bulk refractive index sensitivity of  $209.22 \pm 27.41$  pm/RIU and a temperature sensitivity of  $0.0519 \pm 0.0144$  pm/°C were measured. From these two values, the LOD can be calculated.

The LOD depends on the noise floor of the measurements. Due to the self-referencing, the noise floor is expected to reduce significantly. Assuming that only the temperature noise contribution is to be considered for an estimation of an expected limit of detection, the LOD is given by

$$LOD = \frac{3\sigma}{S_{bulk\ RIU}} = \frac{3 \cdot S_{temperature} \cdot \Delta T}{S_{bulk\ RIU}}. \quad (1)$$

In equation (1), the parameter  $\Delta T$  represents the practically achievable temperature stability, set to 10 mK. Calculating the LOD results in a value of  $\sim 7 \cdot 10^{-6}$  RIU.

## Conclusion

The self-referenced MRR of this work consists of a Bragg grating that is optimized to have a flat frequency response. The constant frequency response is obtained by chirping and apodizing the grating. The characterisation of the sensor shows that the resonance splitting is constant over a bandwidth of 5 nm. Additionally, a RIU sensitivity of  $209.22 \pm 27.41$  pm/RIU, with a temperature sensitivity of  $0.0519 \pm 0.0144$  pm/°C were experimentally demonstrated. Combining these two sensitivities results in a limit of detection of  $\sim 7 \cdot 10^{-6}$  RIU.

## References

- [1] M. de Goede et al., "Al<sub>2</sub>O<sub>3</sub> microring resonators for the detection of a cancer biomarker in undiluted urine," *Opt. Express*, vol. 27, no. 13, p. 18508, Jun. 2019.
- [2] De Goede, M. et al. Mode-splitting in a microring resonator for self-referenced biosensing. *Opt. Express*, vol 29, (2021).
- [3] A. Tehranchi et al., "Engineered gratings for flat broadening of second-harmonic phase-matching bandwidth in mgo-doped lithium niobate waveguides" *Opt. Express*, vol 16, Nov. 2008.
- [4] I. Navruz and A. Altuncu, *New trends in computer networks*, Imperial College Press, ch 12, pp. 114 - 123, 2005.
- [5] S. S. A. Khan and M. S. Islam, "Determination of the Best Apodization Function and Grating Length of Linearly Chirped Fiber Bragg Grating for Dispersion Compensation," *Journal of Communications*, vol. 7, pp. 840–846, Nov. 2012.

# Evaluation of Attenuation Methods for an Integrated, Weak Coherent Source for Quantum Key Distribution

J. König, H. O. Çirkinoglu, E. A. J. M. Bente, K. A. Williams, and X. J. M. Leijtens

Eindhoven University of Technology, Eindhoven Hendrik Casimir Institute, 5612 AZ, Eindhoven, The Netherlands

*Quantum key distribution (QKD) systems that use weak coherent states often rely on attenuated lasers to generate signals with an average of less than one photon per pulse. Two ways of attenuating laser light in a weak, coherent, integrated QKD transmitter chip are compared in terms of noise, namely attenuation with Mach-Zehnder (MZ) interferometers and attenuation with semiconductor optical amplifiers (SOAs) biased as attenuators. Results from simulations and experiments on the optical spectrum of the output of the transmitter chip show that under reverse bias conditions the SOAs result in similar noise levels as the MZs. The footprint of the SOAs on the chip, however, is more than 50 times smaller than that of the MZs. This makes them the better candidate for the integrated, weak coherent QKD source.*

## Introduction

Quantum Key Distribution (QKD) allows the exchange of inherently secret cryptographic keys. Using quantum particles to exchange these keys, QKD schemes can guarantee key secrecy through the detectability of eavesdroppers, instead of assumptions on the computational power available to a potential, undetected eavesdropper [1], [2]. Most current QKD implementations rely on attenuated lasers to generate weak coherent states with an average of less than one photon per pulse [1]. QKD systems using different attenuation methods to achieve this have been demonstrated. To the authors' best knowledge, however, the influence of the different attenuation methods on the signal quality has not yet been investigated. This work aims to investigate the influence of two different on-chip attenuation methods on the noise in the signal of an integrated QKD transmitter chip [3], [4]. The two attenuation methods investigated are semiconductor optical amplifiers (SOAs) biased as absorbers and destructive interference after phase modulation in the arms of a Mach-Zehnder (MZ) interferometer. The goal is to compare the two methods for QKD in terms of noise.

The influence of the attenuation methods on the signal noise is investigated through the optical spectrum of the output of the QKD chip. The power at the signal wavelength and the level of the noise floor of the optical spectrum for different attenuation levels are compared for the different attenuation methods. The attenuation methods are first compared in simulations and then in measurements.

## Simulations

Simulations are carried out in the time domain traveling wave (TDTW) simulation software PICWave from Photon Design [5] (version 6.1), using the SMART Photonics gen 2 process design kit (PDK) [6] (version 1.0). Light from an ideal, narrow linewidth laser at a wavelength of 1550 nm and a power of 0 dBm with no noise, is joined with the output of a SMART SOA, biased at 10 mA, to generate laser light with a spontaneous emission noise floor. This light is split and guided through a SMART SOA of 100  $\mu\text{m}$ , a

SMART saturable absorber (SA) of 100  $\mu\text{m}$  (necessary to simulate a reverse-biased SOA), and an MZ interferometer. The MZ interferometer is constructed using two lossless equal splitting ratio Y-junctions and SMART electro-optic phase modulators (EOPM) of 3040  $\mu\text{m}$  in both arms.

The simulations run for different bias currents on the SOA, different bias voltages on the SA, and different bias voltages on one arm of the MZ interferometer while keeping the other arm biased at 0 V. The bias current on the SOA is swept from 15 mA to 0 mA. The voltage on the SA is swept from -0.1 V to -3 V. The voltage on the MZ arm is swept from -0.1 V to -3.5 V. The spectrum is obtained at each step. From these results, the peak and floor levels are obtained for comparison of the attenuation methods.

## Simulation Results

The obtained spectra for MZ attenuation and SOA attenuation are shown in Fig. 1a. The simulated spectra show wavelength and bias-dependent noise figures as characterized in [6]. From these spectra, the peak and floor levels are determined. Peak levels for different bias levels are taken from the spectrum at 1550 nm. Floor levels for different attenuation bias levels are determined by averaging over the values of the spectrum between 1549 nm and 1549.5 nm and between 1550.5 nm and 1551 nm. The floor levels as a function of the signal levels for the two attenuation methods are shown in Fig. 1b. The MZ interferometer shows a linear relation between the floor and peak levels. The SOA, when positively biased, shows floor levels that are approximately 3 dB higher than for the MZ interferometer, indicating worse performance in terms of noise. When reverse-biased, the floor levels change to similar levels as for the MZ interferometer, indicating equal performance. For QKD transmission, attenuation in the order of -60 dB is necessary [3], warranting reverse bias on the SOA and therefore rendering the performance of the SOA equal to the MZ in terms of noise measured in this experiment.

## Measurements

Measurements on the optical spectrum of the QKD transmitter chip are carried out using an optical setup with a bare chip. The chip used for measurements is produced by SMART

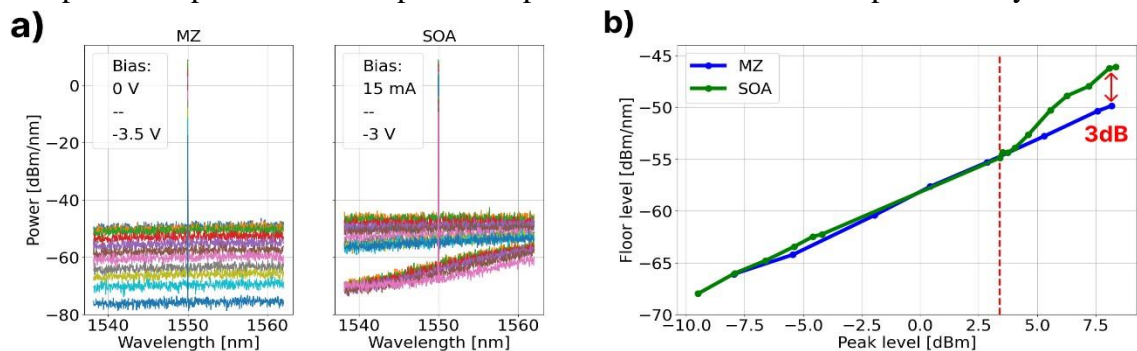


Figure 1. a) Simulated spectra for different attenuation methods. MZ (left), SOA (right). b) Simulated optical spectrum noise floor power as a function of the power at the signal wavelength for SOA and MZ attenuators. The signal powers are taken at 1550 nm, the noise floor powers are averaged values from between 1549 nm and 1549.5 nm and between 1550.5 nm and 1551 nm. The transition from positive bias to reverse bias for the SOAs is indicated in red.



Figure 2. Simplified overview of the chip used for measurements. Light from a DBR laser is guided towards an MZ modulator that can guide the light either towards Port 1 or towards an SOA section containing three SOAs. From the SOAs the light is guided towards Port 2.

Photonics on a multi-project wafer run (SP27). An overview of the chip is shown in Fig. 2 and the chip is described in more detail in [3]. Light from a distributed Bragg reflector (DBR) laser with a gain section of 500  $\mu\text{m}$  is guided through a waveguide to an MZ interferometer

containing EOPMs of 3040  $\mu\text{m}$  long. At the output of the MZ, light is guided either towards an output at the facet of the chip (Port 1) or towards a waveguide containing three 100- $\mu\text{m}$ -long SOAs. After the three SOAs, the light is guided toward the second output of the chip (Port 2). The elements on the chip are contacted using probe needles on gold pads. The voltage and current supplies used are Keithley Model 2400 source meters and a Thorlabs Pro8000 Current module LDC80xx. The output light is coupled to a lensed single-mode fiber placed on a Thorlabs BPC203 piezo-controlled fiber stage.

To measure the spectra for different attenuations with the MZ as an attenuator, Port 1 is connected to an OSA (Yokogawa AQ6375). The laser bias is kept constant at 95 mA and the bias voltage on one arm of the MZ is swept from maximum output (-3.7 V) to minimum output (-6.7 V). At every step of the sweep, the optical spectrum is acquired. To measure the spectra for different attenuations using the SOAs, the output from Port 2 is connected to the OSA. The MZ is biased at a constant bias value for maximum input into the SOAs (-6.7 V). The SOA bias is swept from the transparency current (set to equal the maximum output at Port 1, measured at 29.4 mA) to 0 mA and from -0.1 V to -8.5 V. At each step of the sweep, the optical spectrum is acquired. The spectrum is measured on a range of 20 nm around a center wavelength of 1550 nm, taking 1001 points with a resolution of 2 nm. The relatively wide resolution is necessary to reach the sensitivity needed to measure noise down to levels in the order of -80 dBm/nm.

As an additional attenuation method, the coupling efficiency between the chip facet and the lensed fiber is reduced to attenuate the light coupled into the single-mode fiber. The laser is biased at a constant current of 95 mA and the MZ is biased for maximum output power at Port 1 (-3.7 V). The lensed fiber is slowly retracted to decrease the coupling efficiency, in steps of 1  $\mu\text{m}$ , for a total of 40  $\mu\text{m}$ . After each retraction, the optical spectrum is acquired.

## Measurement Results

The measured spectra for MZ attenuation, attenuation with SOAs, and attenuation by retracting the lensed fiber are shown in Fig. 2a from left to right respectively. The peak levels are determined from these optical spectra by taking the value measured at 1550 nm. The noise floor levels are determined from the optical spectra by taking the value measured at 1544 nm. The noise floor levels as a function of the peak levels for the three attenuation methods are shown in Fig. 2b. The measurement results of the MZ interferometer as attenuator and the attenuation by retraction of the lensed fiber are very similar. The peak level and the noise floor level show a linear relation. The attenuation with SOAs shows

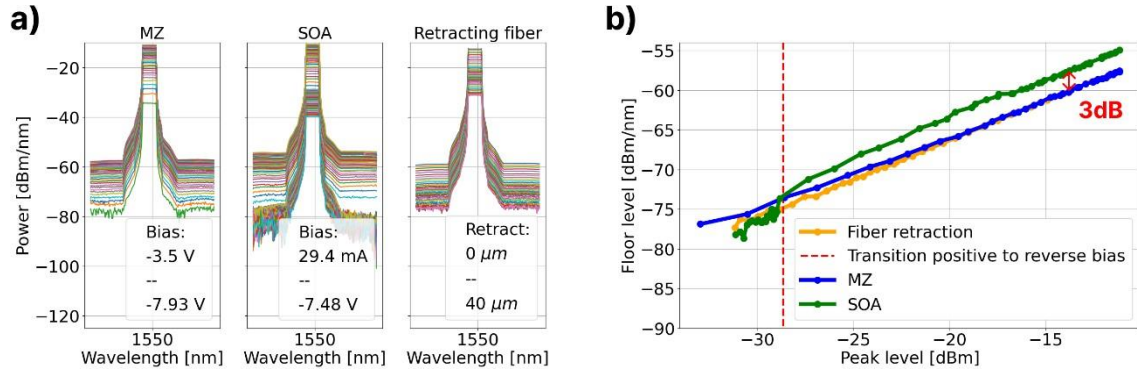


Figure 3. a) Measured optical spectra for different attenuation levels with different attenuation methods. The spectra are obtained on a range of 20 nm around a center wavelength of 1550 nm, taking 1001 points with a resolution of 2 nm. From left to right: SOAs, MZ, fiber retraction. b) Measured optical spectrum noise floor levels as a function of the levels at signal wavelength for SOAs, MZ, and fiber retraction. The signal powers are measured at 1550 nm and the noise floor values are measured at 1544 nm. The transition from positive bias to reverse bias for the SOAs is indicated in red.

similar behavior as found in the simulations. For positively biased SOAs, the noise floor levels are approximately 3 dB higher than for the other two attenuation methods. When reverse-biased, the noise floor levels drop to similar levels as for the other two attenuation methods. This confirms the finding from the simulations that for reverse bias, the SOAs show similar performance to the MZ attenuators. A possible explanation for the higher noise of the SOAs as attenuators at positive bias is that additional spontaneous emission is caused by the excess carriers in the SOAs as a result of the forward bias.

## Conclusion

By comparing the power at signal wavelength to the power level of the noise floor of the optical spectrum, two different on-chip attenuation methods for an integrated weak coherent QKD transmitter are compared. Simulations and measurements show that for reverse bias, SOA attenuators show similar performance as MZ attenuators. To reach attenuation levels needed for QKD, the SOA attenuators will be reverse-biased. This is encouraging for the use of SOAs as attenuators in the QKD chip, since the footprint of the SOA attenuators is more than 50 times smaller than that of the MZ interferometers, making them the better candidate.

## References

- [1] H. Lo, M. Curty, and K. Tamaki, "Secure Quantum Key distribution," *Nature Photonics*, vol. 8, 595604, 2014.
- [2] S. Pirandola, et al., "Advances in quantum cryptography," *Adv. Opt. Photon.*, vol. 12, 1012-1236, 2020.
- [3] H.O. Çirkinoglu, R. Santos, K. Williams and X. Leijtens "Monolithically integrated differential phase shift transmitter for quantum key distribution," in *Proceedings of the 22nd European Conference on Integrated Optics*, 2020.
- [4] M. Smit, et al., "An introduction to InP-based generic integration technology," *Semiconductor Science and Technology*, vol. 29, 083001, 2014.
- [5] Photon Design, PICWave, [Online]. Available: <https://www.photond.com/products/picwave.htm>
- [6] PICWave SMART Photonics Gen2 PDK [Online]. Available: [https://www.photond.com/products/picwave/picwave\\_features\\_09\\_3.htm](https://www.photond.com/products/picwave/picwave_features_09_3.htm)

# Design and modeling of a fabrication tolerant and broadband directional coupler

Yichen Liu,<sup>1,2</sup> Umar Khan,<sup>1,2</sup> and Wim Bogaerts<sup>1,2</sup>

<sup>1</sup>Photonics Research Group, Ghent University-IMEC, Ghent, Belgium

<sup>2</sup>Center of Nano and Biophotonics, Ghent, Belgium

\*Yichen.liu@ugent.be

*We present a design for a fabrication tolerant and broadband directional coupler in photonic integrated circuits based on IMEC's iSiPP50G silicon photonics platform. We demonstrate that such a design can be tolerant to fabrication errors on waveguide width and at the same time has a uniform coupling ratio around the operating wavelength of 1550 nm. Based on the finite difference eigenmode and finite-difference time-domain simulation results, we analyze the effects of fabrication errors on the coupling of these directional couplers.*

## 1 Introduction

Photonic Integrated Circuits (PIC) route light between different optical functions on a chip, and these circuits are becoming increasingly complex with the growing maturity of the fabrication technology and the design/simulation platforms. The high refractive index contrast between the waveguide core and the cladding on the one hand facilitates the high integration of chip fabrication, but on the other hand, makes the transmission characteristics of the on-chip optical components more sensitive to fabrication errors<sup>[1]</sup>. For example, fabrication errors in waveguide width of a directional coupler (DC), one of the most fundamental components on a chip, can lead to very large errors in the power coupling. Therefore, designing and manufacturing on-chip components that are insensitive to manufacturing errors is of great significance for improving product yield and reducing manufacturing costs.

## 2 Structure model of the directional coupler

A DC consists of two waveguides that are brought in close proximity, so the evanescent fields can couple the light from one waveguide to the other. The model [2] that describes the cross-transmission characteristics of the coupler:

$$P = \sin^2(\kappa' L + \kappa_0) \quad (1)$$

Where  $P$  is the overall power coupling,  $\kappa'$  is the coupling per unit length of the straight coupler section,  $L$  is the length of the straight section of the DC, and  $\kappa_0$  is the coupling from the curved section.

The corresponding schematic diagram is as figure 1(a)

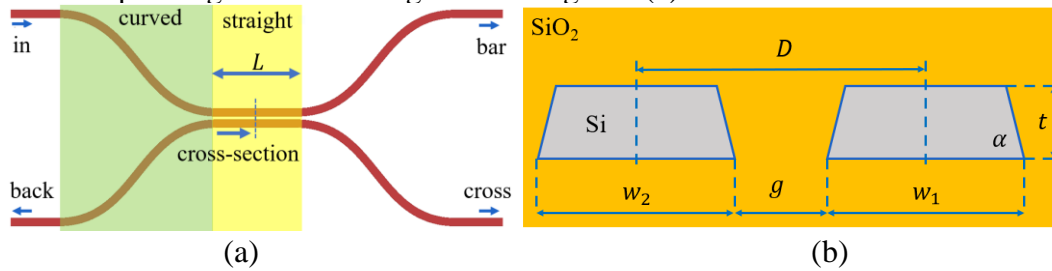


Figure 1: (a) Schematic diagram of a directional coupler showing the straight and the curved sections.  
(b) Diagram showing the cross-section through the straight section of the directional coupler.

## 3 Waveguide width fabrication errors

Figure 1(b) shows the cross-section through the straight section of a directional coupler with silicon waveguides and silica cladding all around.  $D$  is the distance between the center lines of the two waveguides;  $w_1, w_2$  are the widths of two waveguides;  $t$  is waveguides thickness;  $g$  demonstrates the base gap of the waveguides; the sidewall angle  $\alpha$  is  $85^\circ$ .

Based on IMEC's silicon photonics platform iSiPP50G, we use some approximations here: both waveguides are symmetrical trapezoids (side angle ( $\alpha$ ) is same on the outside

and in the gap), and we assume that when the width changes due to a fabrication variation, the change is the same (in absolute numbers) for both waveguides and it occurs symmetrically on the left and right sides of the waveguide. That means that we assume that  $D$  is invariant under fabrication variations.

When the waveguides become wider, the mode confinement in the waveguide becomes stronger, which will lead to lower coupling strength. But on the other hand, widening the waveguides will make the gap between the two waveguides smaller (for constant  $D$ ), which will lead to a larger coupling strength. Therefore, if these two factors that affect the coupling can achieve balance in the range of waveguide widths that we can fabricate, then we can achieve an equilibrium region where the coupling strength is not sensitive to a change in the waveguide width.

## 4 Tolerant coupler

We performed a set of simulations to validate the idea of this tolerant design, and to identify the tolerant design space. For a given  $D$  of a symmetric directional coupler, we scanned the width of the waveguides and observed how the transmission changed with the width of the waveguides.

### 4.1 Finite difference eigenmode simulations

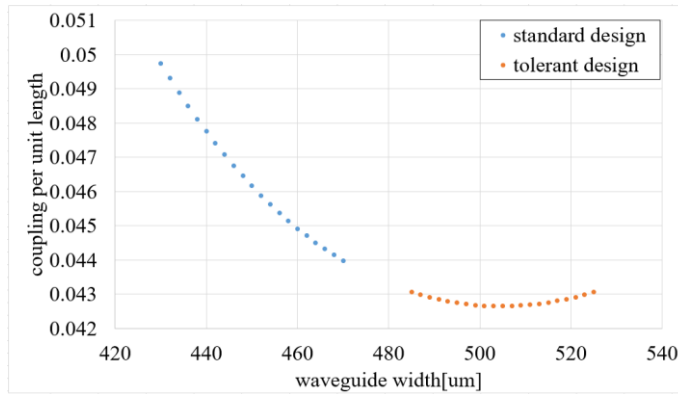


Figure 2 Calculated coupling per unit length ( $\kappa'$ ) using finite difference eigenmode (FDE) solver for different waveguide widths of both the standard and the tolerant designs.

We first present a fast and accurate simulation result using the finite difference eigenmode (FDE) solver from Ansys Lumerical Mode. It is worth noting that the simulation result only represents the coupling strength per unit length ( $\kappa'$ ) from the straight coupler section, not the total power coupling after a given length.

Figure 2 shows the simulation results calculated by the FDE solver. The standard design we used is  $D = 700\text{nm}$ ,  $w_1 = w_2 = 450\text{nm}$ , and  $t = 214\text{nm}$ .

We can see that within a width variation of  $\pm 20\text{nm}$  around  $450\text{nm}$ , the standard design leads to a 6% relative difference  $\left(\frac{\max-\min}{\max+\min}\right)$ , while we observe a tolerant region around  $505\text{nm}$  which only has a 0.5% relative difference. After a quick simulation with the FDE solver, we were able to ascertain that this tolerant design is feasible. The next step is to simulate the complete coupler with the curved sections. We do not expect the results to be quite different from the straight waveguide section, since the coupling strength is dominated by the straight waveguide section, except when the coupler is very short.

### 4.2 Finite-difference time-domain simulations

We used Ansys Lumerical finite-difference time-domain (FDTD) to simulate the complete coupler with the bend sections shown in Figure 1(a). We have simulated different lengths of the DC to find out the influence of the curved section on the tolerant region.

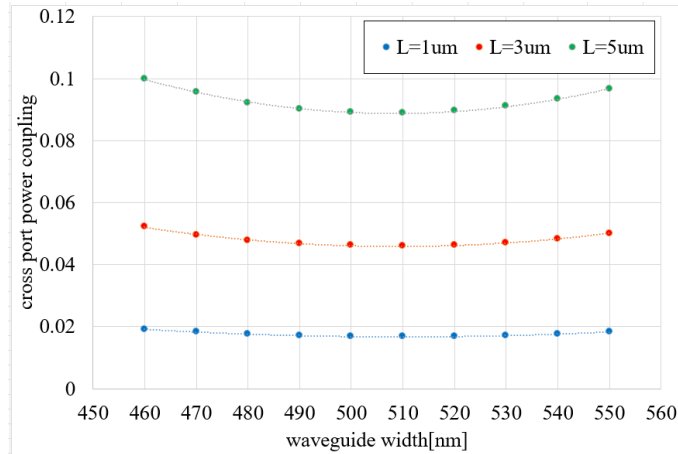


Figure 3 Calculated cross port power coupling using finite difference time domain (FDTD) solver for different waveguide widths and lengths of the tolerant design.

From the simulations, we can see that the tolerant region of the complete coupler has several nano-shifts compared with that of the straight section. The relative differences for a width variation of  $\pm 45\text{nm}$  are 9.9%, 6.5%, and 6.4% for  $L = 1, 3,$  and  $5\mu\text{m}$  respectively. The relative differences decrease with increasing coupler lengths. We think the reason might be that the curved section of coupler is more sensitive to the width variations.

## 5 Broadband-tolerant coupler

We want our directional coupler to be both fabrication tolerant, and broadband, i.e., it has a constant coupling strength over a wide wavelength range. For that, we make the directional coupler asymmetric:  $w_1 \neq w_2$  [3]. We use the simplest and most easily fabricated asymmetric coupler as the basis for our design of the broadband-tolerant coupler. The asymmetry will lead to a maximum power cross-coupling of less than 1. We can use the asymmetry to get the desired maximum cross coupling for the center wavelength; as the power coupling follows a sinusoidal response as function of length, the top of this sine curve (at max cross coupling) is also quite tolerant to wavelength variations. It is worth noting that for these simulations, we use a rectangular waveguide, so the sidewall angle  $\alpha$  is  $90^\circ$ .

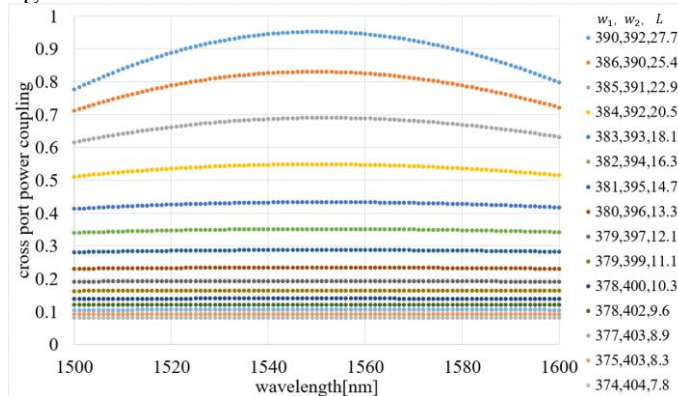


Figure 4 Calculated cross port power coupling for the designed tolerant-broadband coupler.

We show one group of tolerant-broadband design parameters for different desired power coupling in figure 4. The center line distance ( $D$ ) between two waveguides is fixed at  $700\text{nm}$ . The legend shows the used design parameters, the first two numbers are the widths [nm] of the waveguides ( $w_1, w_2$ ) and the third number is the length[um] of the straight section waveguides ( $L$ ).

From figure 4, we can see that the larger the mismatch between the waveguide widths is, the lower is the maximum power coupling, but broader is the bandwidth. The relative difference within the  $\pm 50\text{nm}$  wavelength band around  $1550\text{nm}$  changes from 10% to 0.2% when the maximum coupling efficiency changes from 95% to 8%.

Figure 5 shows the relationship between desired maximum cross power coupling, width difference between two waveguides and the coupler length. We can see that, for a particular desired coupling, we need the specific width difference and coupler length.

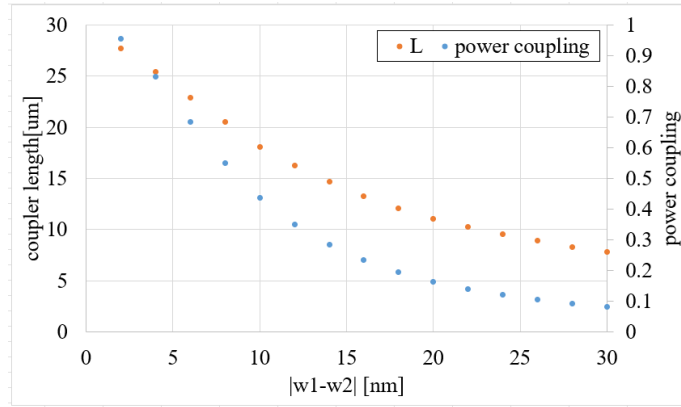


Figure 5 Relationship between desired maximum coupling, width difference and the coupler length. We select one of the designs in this group and scan the waveguide widths to test the fabrication tolerance. During the sweep, the mismatch between the two waveguides is fixed at 10nm. The horizontal axis below shows the shifts between averaged waveguide width and 388nm.

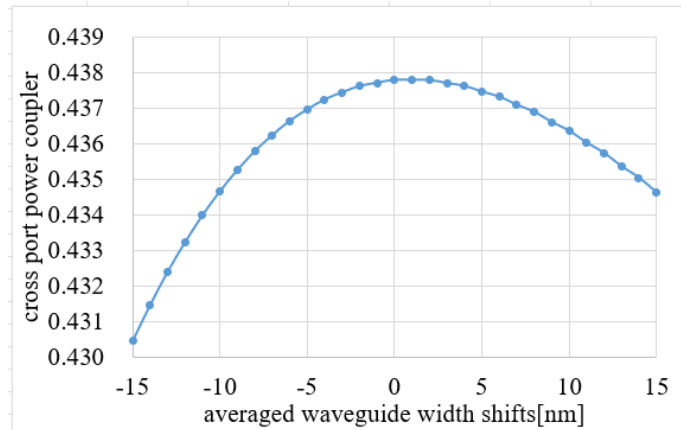


Figure 8 Waveguide width sweep for the tolerant-broadband coupler.

We can see that the relative difference within  $\pm 15$ nm width variation around the tolerant region ( $w_1 = 383$ nm,  $w_2 = 393$ nm) is 0.84%. Unlike the symmetrical coupler (non-broadband coupler simulation results shown in Figure 2), the tolerant region of the non-broadband coupler shows a minimal value while the tolerant region of the broadband coupler shows a maximal value.

The reason is that the tolerance of the non-broadband coupler is the optical confinement of the waveguide and the effect of the waveguide gap that cancel each other. We should consider that a broadband coupler requires a particular coupler length and waveguide width to get maximal coupling efficiency. The change in width will reduce the coupling efficiency.

## 6 Conclusions

To conclude, the design of the tolerant-broadband directional coupler is presented and validated using FDE and FDTD simulations. We validated the design space and identified regions of broadband and tolerant operation. We currently do not have an experimental verification, but this is planned for the near future. If the measurement results support the simulation results, the presented design parameters can be used in our future manufacturing platform.

## References

- [1] Programmable photonic circuits. *Nature* 586, 207–216 (2020). <https://doi.org/10.1038/s41586-020-2764-0>
- [2] Y. Xing, U. Khan, A. Riberio and W. Bogaerts, "Behavior model for directional coupler", *Proc. Symp. IEEE Photon. Soc. Benelux*, pp. 128-131, 2017.
- [3] A. Takagi, K. Jinguji, and M. Kawachi, "Broadband silica based optical waveguide coupler with asymmetric structure," *Electron. Lett.*, vol. 26, p. 132, 1990.

# Optical Receiver Front-end Design Choices to Enhance Throughput of LiFi

X. Liu<sup>1</sup>, L. Azarkh<sup>1</sup>, J. P. M. G. Linnartz<sup>1,2</sup>

<sup>1</sup>Electrical Engineering, Eindhoven University of Technology, 5600 MB Eindhoven, The Netherlands

<sup>2</sup>Signify (Philips Lighting) Research, 5656 AE Eindhoven, The Netherlands

## Abstract

The optical front end (OFE) is a critical part in most Optical Wireless Communication (OWC) systems. It captures the incoming light flux, converts it and amplifies it into an electrical signal. Its photodiode (PD) and transimpedance amplifier (TIA) can limit the throughput, determined by the noise levels and the (gain-) bandwidth. This paper starts with a refined model of the PD and the TIA, in order to analyze in detail the strength and frequency characteristics of the relevant noise sources. At high frequencies signal-to-noise ratio (SNR) degrades due to the capacitance of the PD. This limits the useful modulation bandwidth, though equalization and frequency-dependent power and bit loading can mitigate this. To some extent, SNR can be traded for bandwidth by choosing an appropriate PD size. We investigate different optical receiver design strategies, where single PD is segmented into pieces, and connected to one or more TIAs. Numerical analysis on channel quality is carried out to compare between various design strategies.

## I. INTRODUCTION

The increasing demand for wireless data in mobile and Internet-of-Things services puts pressure on the Radio Frequency (RF) spectrum. Optical Wireless Communication (OWC), is drawing great research attention as an alternative to RF in tackling the spectrum congestion challenge. In earlier work we studied limitations caused by the LED [1], where its low-pass frequency characteristics restricts the bandwidth. If increasingly lasers are used, the optical receiver may start to limit performance. In the OFE, which usually consists of a PD and TIA, several noise sources exist. The spectral power density of these noise sources differ [2]. Moreover, these noise contributions are amplified and filtered by the TIA, which changes the output noise spectral power density. Also, the capacitance of the PD significantly influences the signals and noise, particularly at high frequencies [3].

We study various noise sources at the OFE, especially their spectral characteristics and amplification effect of TIA, referenced to the noise input. Together with all the noise sources, an equivalent input noise model with both current and voltage noise sources is built that helps to compute the total output noise power spectral density. Next, we investigate the trade-off of PD capacitance by PD segmentation, in the means of dividing one PD into  $N$  pieces, thus decrease the capacitance of each PD. In this case, total output noise spectral density that is amplified by TIA and capacitance of PD is compared between the segmented and non-segmented scenarios. The paper ends with a brief discussion on throughput optimization by means of different modulation strategies based on the channel spectral information, which we will elaborate later. While previous papers describe the impact of the PD area on signal bandwidth, we focus on the impact on the noise.

## II. SYSTEM DESCRIPTION

An OFE with PD and TIA is illustrated in Fig. 1. Photons that arrive at the PD are converted into a current, which is fed into the TIA, which converts it into a voltage

output.  $R_S$ ,  $C_S$  are the parasitic source resistance and capacitance of the PD, which in parallel are responsible for the source impedance  $Z_s = R_s || 1/j\omega C_S$ . The resistor  $R_F$  and capacitor  $C_F$  of the TIA create the feedback impedance  $Z_F = R_F || 1/j\omega C_F$ .

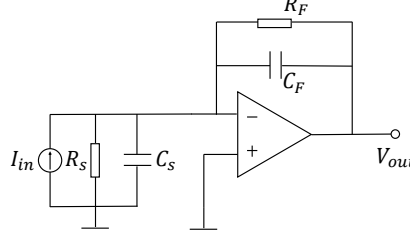


Fig. 1. Optical Receiver Front End

Noise is generated by different sources within the optical receiver front end, from the PD, from the amplifier and from the discrete character of photons. Specifically, five types of input noise sources are identified:

- 1) Shot noise originates from the statistical nature of light as a statistical arrival of photons. The generated current will also fluctuate with time. It is mostly considered as white noise over the relevant modulation spectrum. However, it is not additive but signal dependent. Its power spectral density is expressed as ( $q$  is the electron charge) [4]:  $S_{sh}(f) = 2qi_{in}(t)$ , where  $i_{in}$  denotes the incoming current in time-domain.
- 2) Dark current noise, which is a relatively small current  $I_d$  exists when even no photon is detected by the PD. It is also treated as white and its power spectral density is calculated by [4].
- 3) Thermal noise for resistors  $R_F$ ,  $R_S$ , generally treated as white noise with power spectral density:  $S_{th}(f) = 4kT/R$  where  $T$  is the absolute temperature, and  $k$  is the Boltzmann's constant.
- 4) Input current noise of the amplifier. There are number of noise sources in the amplifier. These noise are modelled as an input current and voltage (see below) externally to a noise-free amplifier. The frequency spectrum of the input current noise is colored, where at low frequency it is  $1/f$  noise and white noise at high frequency [5].
- 5) Input voltage noise of the amplifier. The spectrum is similar to input current noise. The noise power spectral density of the input current and voltage noise is denoted as [5]:  $S_{e_{in}, i_{in}}(f) = kf_c/f$  where  $k$  is the rms input noise power at high frequency,  $f_c$  is the corner frequency of the  $1/f$  noise.

The above noise sources are illustrated in Fig. 2. Summing up the input noise, Fig. 3 shows the noise analysis model for the optical receiver front end.  $i_n$  includes shot noise, dark current noise, thermal noise, and input current noise of the amplifier.  $e_n$  denotes the input voltage noise. The total output noise can be derived via

$$V_{Nout}(f) = G_e(f)e_n(f) + G_i(f)i_n(f) \quad (1)$$

where the amplification of current and voltage noise are

$$G_i(f) = \frac{A(f)Z_F(f)}{1 + A(f)}, G_e(f) = \frac{A(f)}{1 + A(f)\beta(f)} = \frac{A(f)(Z_s + Z_F)}{(Z_s + Z_F) + A(f)Z_s}. \quad (2)$$

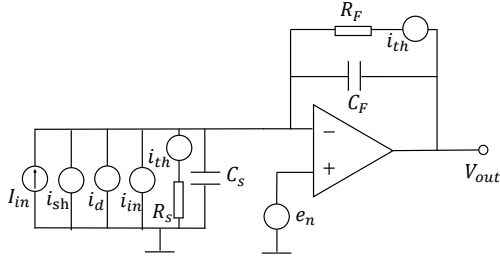


Fig. 2. Noise Sources in OFE

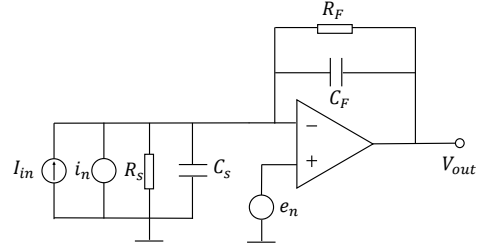


Fig. 3. Noise Model for OFE

where  $A(f) = \frac{A_{amp}}{1+f/f_{amp}}$  is the open loop gain for the op-amp, and  $\beta = \frac{Z_S}{Z_F+Z_S}$  is the feedback factor of the TIA.

### III. PD SEGMENTATION

High capacitance of the PD increases the voltage noise at high frequency because with higher  $C_S$ , the voltage noise  $e_n$  will be amplified more. As  $Z_F$  is fixed, we can expect a degradation of SNR at high frequency. Since the capacitance of PD is in good approximation proportional to the PD area, an effective approach to reduce the noise at high frequency will be to decrease the size of the PD. However, a smaller PD also has a decreased detection area. To maintain a large total detection area while mitigating high frequency noise, one possible solution is to divide the PD into several segments, to connect each segment to its own dedicated TIA, while all the outputs of all amplifiers are summed together.

This section quantifies this effect. One motivation for such study is that as the number of amplifiers increases, more noise contributions will be added. Even if the noise at high frequency is less amplified, the total noise may still be higher than the case without segmentation. In order to address this problem, we consider to use a lens to focus the light on one or several of the PDs, and turn off the receivers with no signal received. Multiple segments are nonetheless needed if the angle of arrival is unknown during design. We consider a number of scenarios for different PD designs:

- 1) *Single PD* Only one large PD is used, connected with one TIA;
- 2) *Segmented, non-imaging* The PD is divided into  $N$  pieces, each connected to one TIA; All segments receive light, in an equal amount as scenario *Single PD*;
- 3) *Segmented, imaging*: The PD is segmented similar to scenario 2), but a lens is deployed to focus optical signal to one of the PD segments. PDs and their connected TIAs that do not receive optical power are switched off;

### IV. CALCULATION & DISCUSSION

To quantify the noise levels, we model the op-amp AD8099 with a gain bandwidth = 3.8GHz ( $A_{amp} = 85\text{dB}$ ,  $f_{amp} = 0.2\text{MHz}$ ), and PD s-5980-10 with source capacitance  $C_S = 40/N$  pF and source resistance  $R_S = 5M\Omega$ . The feedback circuit for TIA is set as  $R_F = 1k\Omega$ . Fig. 4 shows the noise power spectral density from different noise sources in scenario *Single PD*. Op-amp noise dominates over PD and thermal noise due to the significant amplification of  $e_n$  at high frequencies. With the finite gain-bandwidth of op-amp, beyond a certain frequency  $f = |Z_S A_{amp} - 1| f_{amp}$  the noise level decreases. Fig. 5 shows the total output noise power spectral density for three PD segmentation

configurations, with segmentation factor  $N = 1, 4, 9, 16$ . Although *Segmented, non-imaging* shows the highest noise level over the spectrum due to the application of several TIAs, the total noise is less amplified at high frequency compared to *Single PD* since  $C_S$  decreases. *Segmented, imaging* has the lowest noise level, since redundant TIAs are switched off as well as the decreased PD capacitance.

In this paper, we did not describe the frequency dependant signal gains, which we include in future work to derive gain-noise ratios and throughput. The frequency characteristics of noise versus size of PD, as addressed here, in combination with signal amplification models give insight in how to design an OFE for best link quality. This allows an optimization of the throughput, for example optimization of OFE design topologies [6], [7], in combination with the modulation scheme including adaptive bandwidths and adaptive bit loading [8]–[10].

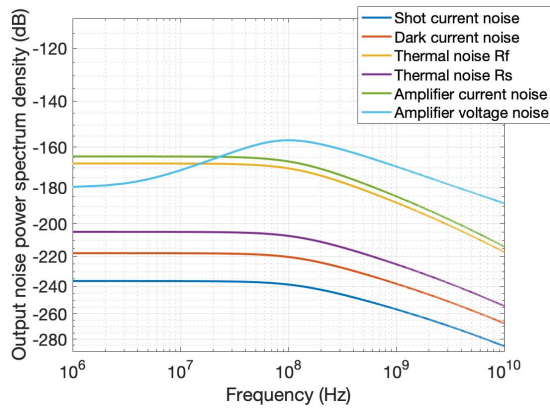


Fig. 4. Output Noise from Different Noise Sources

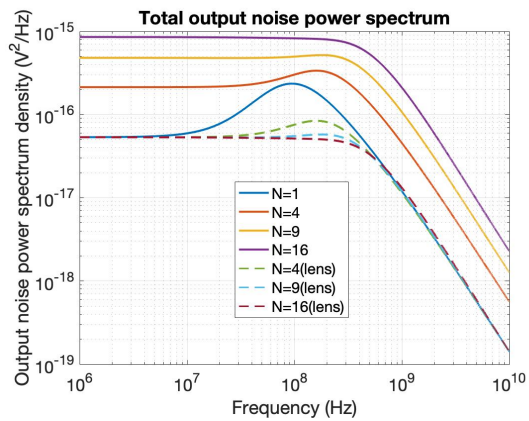


Fig. 5. Total Output Noise Under Different PD Segmentation Scenario

## REFERENCES

- [1] J.-P. M. G. Linnartz, X. Deng, A. Alexeev, and S. Mardanikorani, "Wireless communication over an led channel," *IEEE Communications Magazine*, vol. 58, no. 12, pp. 77–82, 2020.
- [2] *Transimpedance Amplifier Noise Considerations*, Analog Devices, 2002.
- [3] G. Royo, A. Martínez-Pérez, C. Sánchez-Azqueta, C. Aldea, and S. Celma, "Noise reduction technique using multiple photodiodes in optical receivers for pof communications," in *2021 IEEE 12th Latin America Symposium on Circuits and System (LASCAS)*, 2021, pp. 1–4.
- [4] R. Hui, *Introduction to fiber-optic communications*. Academic Press, 2019.
- [5] B. Carter, "Op amp noise theory and applications," in *Op amps for everyone*. Elsevier, 2009, pp. 163–188.
- [6] T. Koonen, K. Mekonnen, F. Huijskens, Z. Cao, and E. Tangdiongga, "Novel broadband owc receiver with large aperture and wide field-of-view," in *2020 European Conference on Optical Communications (ECOC)*, 2020, pp. 1–4.
- [7] M. D. Soltani, H. Kazemi, E. Sarbazi, H. Haas, and M. Safari, "Optimal imaging receiver design for high-speed mobile optical wireless communications," in *2022 IEEE International Conference on Communications Workshops (ICC Workshops)*, 2022, pp. 01–06.
- [8] T. E. B. Cunha, J.-P. M. G. Linnartz, and X. Deng, "Achievable rate of led-based distributed mimo owc systems under a per-led power constraint," in *2021 17th International Symposium on Wireless Communication Systems (ISWCS)*, 2021, pp. 1–6.
- [9] S. Mardanikorani, X. Deng, and J.-P. M. G. Linnartz, "Optimization and comparison of m-pam and optical ofdm modulation for optical wireless communication," *IEEE Open Journal of the Communications Society*, vol. 1, pp. 1721–1737, 2020.
- [10] —, "Sub-carrier loading strategies for dco-ofdm led communication," *IEEE Transactions on Communications*, vol. 68, no. 2, pp. 1101–1117, 2020.

# Extreme Learning Machines based on Optical Frequency Combs

A. Lupo,<sup>1</sup> M. Zajnulina,<sup>1</sup> and S. Massar<sup>1</sup>

<sup>1</sup> Laboratoire d'Information Quantique, CP 224, Université libre de Bruxelles, Av. Roosevelt 50, 1050, Bruxelles, Belgium

*Artificial Neural Networks (ANN) are powerful neuromorphic, i.e. brain-inspired, algorithms already successfully deployed in a plethora of fields including computer vision and natural language processing. Extreme Learning Machines (ELM) are a type of ANNs suitable for classification tasks. Contrary to traditional ANNs, ELMs have mostly fixed, untrained, connections: only the output weights are trained, making the network easier to implement on non-electronic substrates. We developed two schemes for photonic ELMs based on frequency combs, where neurons are encoded in complex amplitudes of comb lines. A Programmable Spectral Filter (PSF) encodes input information by setting the initial line amplitudes and/or phases. The subsequent mixing of encoded information occurs via interference between comb lines, which can be achieved either by applying a phase modulation or by propagating the comb through a nonlinear Kerr medium such as optical fiber. The output weights are applied by a second PSF, attenuating each comb line proportionally to the required weight. The weighted comb is then measured by a photodiode, introducing a quadratic nonlinearity. A preliminary comparison of the two different schemes of information mixing shows the superiority of the Kerr-medium approach.*

## Introduction

Human activities generate an increasing demand for computational power that cannot be satisfied by traditional digital computers anymore. Electronic chip miniaturization, following the Moore law, will eventually stagnate, mainly due to quantum and thermal limits [1]. Also, traditional digital computing architectures, despite being relatively easy to deploy, constitute a bottleneck in terms of energy and computational time consumption when it comes to the processing of big amounts of data.

The human brain is known to outperform traditional computers on tasks such as speech or visual data recognition. This suggests that for certain problems, brain-inspired algorithms and/or architectures can be advantageously used for data processing. In fact, non-digital brain-inspired algorithms, in particular Artificial Neural Networks (ANNs), have been already successfully deployed in the above-mentioned tasks, and more [2]. ANNs process information and approximate the desired output by transforming the input data as it propagates in a network composed of trainable weighted connections and nonlinear activations.

Extreme Learning Machines (ELMs, Fig. 1a) are a subclass of feedforward ANN algorithms in which most of the connections remain untrained [3]. Only output connections are trained to approximate the desired behavior. This approach has two main advantages. First, it simplifies and speeds up the training procedure (which often reduces to a linear regression problem). Second, it allows for the network to be easily implemented in unconventional computational substrates. ELM networks are organized into three layers: the input, hidden, and output layer.

Many physical systems that exhibit nonlinear behavior can be exploited as ELM (Fig. 1b). To this end, initial information is injected into the system via the input layer using a

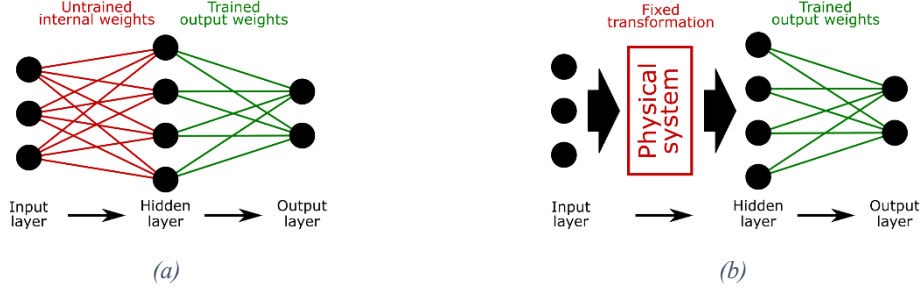


Figure 1. (a) The scheme of an Extreme Learning Machine. The number of neurons per layer is arbitrary. Connections between input and hidden layers (red) are fixed, while the connections between hidden and output layers (green) are trained. (b) The scheme of an Extreme Learning Machine implemented through an arbitrary physical system. The input layer is injected in the system and gets transformed in a fixed way (red), according to its internal rules. The state assumed by the system in response to the input is considered to represent the hidden layer. Multiplication by trained output weights (green) is performed in the readout layer.

suitable perturbation mechanism. The response to the perturbation is considered to be the hidden layer. The way in which perturbations are applied and the way in which responses are measured depend on the parameters of the system. In photonic systems, the perturbation could be a modulation of light, while the response could be given by a measurement of amplitudes or intensities. Hence, the physical system performs the transformation from input layer to hidden layer. A properly designed readout mechanism can measure the system response (hidden layer) and perform multiplication by trained output weights, thus generating the output layer of the ELM. Multiple photonics-based implementations of ELMs have been reported, which exploit propagation of light in free space [4], in multimode fibers [5], in time multiplexing systems [6], and more.

We presented a scheme of a photonic ELM based on wavelength multiplexing. In this scheme, each neuron is encoded in the amplitude of a line of an Optical Frequency Comb (OFC). The input layer is generated by properly shaping the OFC through a spectral filter, and the (untrained) information mixing occurs via OFC line interference stimulated by periodic phase modulation [7]. In the present work, we introduce a novel mixing method that exploits the Kerr nonlinearity of a standard telecom fiber. In the next section, we describe the experimental setup and the experimental procedure; then, we present and discuss the results; finally, we summarize our work in the conclusion.

## Methods

The experimental setup is represented in Fig. 2. An OFC is generated by periodically phase modulating a monochromatic CW laser radiation. The laser wavelength, that determines the center of the OFC, is  $\lambda_0 = 1554.6nm$ . The periodic phase modulation is generated by a  $LiNbO_3$  Phase Modulator (PM1) driven by a RF signal (power  $P_1 = 32.7dBm$  and frequency  $\Omega/2\pi = 16.969GHz$ ). The span of the OFC depends on the RF signal intensity  $P_1$ . We chose  $P_1$  to generate 31 usable comb lines with spectral spacing of  $\Omega$ . Input information is encoded in the central lines of the OFC by a Programmable Spectral Filter (PSF1, II-VI WaveShaper). The inputs for each neuron are always normalized in the range of values  $[0,1]$ , then linearly remapped in the range of attenuations  $[-30dB, 0dB]$ . The modulated OFC constitutes the input layer of our ELM. Our system is designed to test three different schemes for information mixing: phase modulation, Kerr nonlinearity in fiber, and both. The mixing based on phase modulation

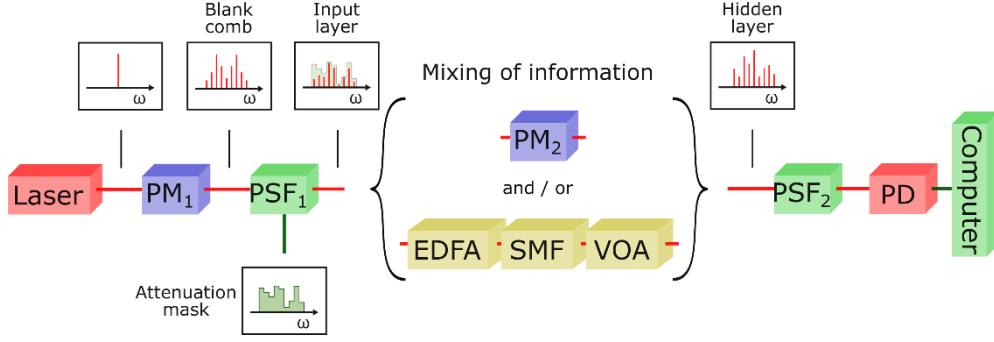


Figure 2: Experimental realization of a photonic Extreme Learning Machine. PM: Phase Modulator, PSF: Programmable Spectral Filter; SMF: Single Mode Fiber spool; VOA: Variable Optical Attenuator; PD: Photodiode

is obtained by propagating the OFC through another  $LiNbO_3$  Phase Modulator (PM2) that is driven at the frequency  $\Omega$  and RF power  $P_2 = 21.4dBm$ . The phase modulation generates interference between comb lines, and, thus, provides the required mixing of information [7]. The mixing based on the Kerr effect is obtained by amplifying the signal up to  $27dBm$  through an Erbium-Doped Fiber Amplifier (EDFA) and then propagating it along a standard telecom Single Mode Fiber (SMF) with a length of  $540m$ . In the fiber, the information is mixed due to the Kerr-effect-based self- and cross-phase modulation. A Variable Optical Attenuator (VOA), placed immediately after SMF, reduces the intensity to a power level safe for the rest of the system. When both mixing methods are tested at the same time, the phase modulation is applied after the propagation in fiber. The OFC obtained after information mixing encodes the hidden layer of the ELM. The last part of the optical circuit is the readout layer implemented via a second Programmable Spectral Filter (PSF2, II-VI WaveShaper) and a Photodiode (PD). PSF2 is employed as a programmable bandpass filter. The OFC lines are measured individually, and their intensities are recorded on a computer by tuning the filter. The set of OFC line intensities constitutes the hidden layer. Multiplication by optimal output weights is performed on the computer. The multiplication by output weights can also be done all-optically as described in [7].

The proposed system is tested using three benchmark classification tasks (Iris classification [8], Wine classification [9], and Heart disease classification [10]). Their performances are evaluated in terms of accuracy, i.e. percentage of correct classifications. For each task, we split the set of available samples, using 70% of the samples to train the output weights and the remaining 30% to evaluate the accuracy. The output weights are trained using a ridge regression model (cf. [7]).

## Results and discussion

We compare three different mixing schemes (phase modulation, Kerr nonlinearity, and both) using three different classification tasks (Wine, Iris and Heart disease classifications). Also, we compare our experimental results with the performance obtained by a software ELM having a similar topology (25 hidden neurons, quadratic nonlinearity). To acquire better statistics, the accuracy values are measured as the average score calculated over  $10^3$  random repartitions of the samples into training and testing sets. Results are reported in Table 1.

The presence of Kerr nonlinearity clearly boosts the performance with respect to the presence of only phase modulation. The presence of both mixing schemes does not always

Classification task	Experimental Photonic ELM Mixing method			Software ELM
	PM [7]	K	K + PM	
Wine	97.5 %	99.3 %	98.9 %	96.1 %
Iris	93.9 %	98.3 %	99.6 %	96.0 %
Heart Disease	Not measured	83.2 %	79.1 %	81.0 %

Table 1: Accuracy measured on the benchmark tasks for the different configurations. PM: Phase Modulation; K: Kerr nonlinearity. The results described in column PM have been obtained in our previous experiment [7]. Experimental performances are compared with the performances measured on a similar software ELM (25 hidden neurons and quadratic nonlinearity).

produce an improvement in the results. This could be due to the nature of the tasks and to the decrease of the signal-to-noise ratio caused by the second phase modulator. The Kerr-based photonic ELM outperforms the software ELM: we believe that this is because the nonlinear mixing introduced by Kerr nonlinearity is more complex, and thus more effective, than the one provided by our simple software ELM.

## Conclusion

We introduced and tested a novel scheme for a fiber-based Extreme Learning Machine (ELM). Information is encoded in the intensities of frequency comb lines and mixed by Kerr nonlinear effects arising from the propagation in a standard telecom single-mode fiber. This new scheme outperforms the previously proposed one [7], as well as a software ELM with a similar dimension but a quadratic nonlinearity. The advantage of this all-optical scheme (compared to the optoelectronic one based on phase modulation) will be further studied and explored in future work.

## Acknowledgment

The authors acknowledge financial support from the European Commission grant 860360-POSTDIGITAL.

## References

- [1] M. M. Waldrop, "More than Moore," *Nature*, vol. 530, issue 7589, pp. 144-148, 2016.
- [2] Y. LeCun, Y. Bengio, and G. Hinton, "Deep learning," *Nature* vol. 521, pp. 436-444, 2015.
- [3] G.-B. Huang, Q.-Y. Zhu, and C.-K. Siew, "Extreme learning machine: theory and applications," *Neurocomputing*, vol. 70, issues 1-3, pp. 489-501, 2006.
- [4] D. Pierangeli, G. Marcucci, and C. Conti, "Photonic extreme learning machine by free-space optical propagation," *Photonics Res.*, vol. 9, issue 8, pp. 1446-1454, 2021.
- [5] U. Teĝin, M. Yıldırım, İ. Oĝuz, et al., "Scalable optical learning operator," *Nat. Comput. Sci.*, vol. 1, pp. 542-549, 2021.
- [6] S. Ortín, M. Soriano, L. Pesquera, et al., "A Unified Framework for Reservoir Computing and Extreme Learning Machines based on a Single Time-delayed Neuron," *Sci Rep*, vol. 5, no. 14945, 2015.
- [7] A. Lupo, L. Butschek, and S. Massar, "Photonic extreme learning machine based on frequency multiplexing," *Opt. Express*, vol. 29, pp. 28257-28276, 2021.
- [8] R. A. Fisher., "Iris Data Set," UCI Machine Learning Repository [Online], 1988. Available: <https://archive.ics.uci.edu/ml/datasets/iris>
- [9] M. Forina et al., "Wine Data Set," UCI Machine Learning Repository [Online], 1991. Available: <https://archive.ics.uci.edu/ml/datasets/wine>
- [10] R. Detrano et al., "Heart Disease Data Set," UCI Machine Learning Repository [Online], 1988. Available: <https://archive.ics.uci.edu/ml/datasets/heart+disease>

# Time and frequency multiplexed implementation of a deep Reservoir Computer

E. Picco,<sup>1</sup> A. Lupo,<sup>1</sup> M. Zajnulina,<sup>1</sup> and S. Massar<sup>1</sup>

<sup>1</sup> Laboratoire d'Information Quantique, CP 224, Université libre de Bruxelles, Av. Roosevelt 50, 1050, Bruxelles, Belgium

*Reservoir Computing (RC) is a popular class of recurrent neural networks characterized by having most of the connections untuned and only output weights trained. RCs drew attention because of their advantageous training costs and for being easily implementable in unconventional substrates, constituting a possible work-around for the limits of electronics. We demonstrated two schemes for photonic RC, differentiated by the way in which neurons are encoded and connected. Both have been tested on tasks such as chaotic time-series predictions or nonlinear distortion-compensation. The first scheme is based on frequency multiplexing: neurons are encoded in lines of a frequency comb and are mixed by making lines interfere via phase modulation. The second scheme is based on time multiplexing: neurons are encoded in different timeslot of a signal propagating in a fiber spool and the mixing is achieved by making timeslots overlap during propagation. Organizing RCs in "deep" architectures, i.e.: in series, has the effect of increasing the complexity of their dynamics, thus enhancing their effectiveness. We propose a deep-RC architecture based on the concatenation of our two different RC schemes. Preliminary results show a significative performance improvement on benchmark tasks, showing that the deep architecture benefit from being composed of two RCs with different dynamics.*

## Introduction

Artificial Neural Networks (ANN) are a powerful brain-inspired computational tool setting the benchmark in multiple challenging tasks. Huge ANNs, composed of thousands of neurons, deliver high performances but require power and time expensive tunings [1]. Randomized Neural Networks (RNN) are ANNs partially consisting of fixed and untrained connections. The RNNs approach has two advantages. First, the training procedure is cheaper. Second, as the internal connections are not required to vary, RNNs can be implemented on various physical substrates, beyond digital electronic platforms. Reservoir Computing (RC) is a recurrent RNN algorithm implemented in various non-conventional substrates [2]. The untrained recurrent network is called "reservoir" and constitutes a dynamical system exhibiting memory about past inputs. The output of the network is a linear combination of the states of the reservoir neurons, in some cases passed through a nonlinear output function.

Among many possible hardware platforms, photonics is highly suitable for the implementation of reservoir computers, allowing to perform high-bandwidth tasks with reduced energy consumption using commercial-grade devices for light manipulation.

We elaborated two schemes for fiber-optics-based photonic RC. The schemes differ by the way in which neurons are encoded in the light. The first system uses Frequency-Multiplexing (FM-RC) to encode neurons in different wavelengths [3]. The second system deploys Time-Multiplexing (TM-RC) to encode the neurons in different timeslots of a light signal propagating through a fiber loop [4].

Empirical analysis reported in literature [5] show that a "deep" RC, a concatenated network consisting of several RCs, may provide advantages not achievable by a simple

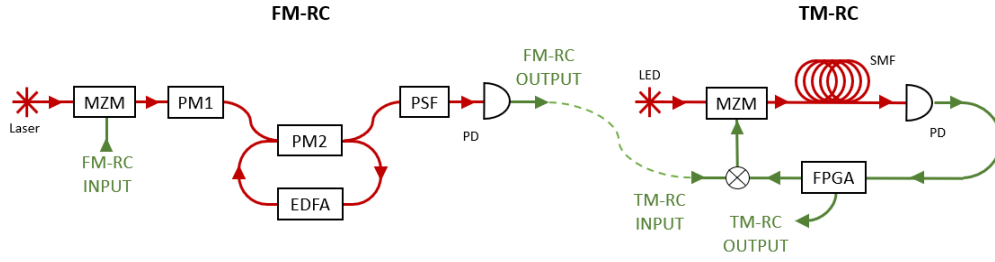


Figure 1. FM-RC: Frequency-Multiplexing Reservoir Computer; TM-RC: Time-Multiplexing Reservoir Computer. MZM: Mach Zehnder Modulator, PM: Phase Modulator; EDFA: Erbium-Doped Fiber Amplifier; PSF: Programmable Spectral Filter; PD: Photodiode; FPGA: Field-Programmable Gate Array. The connections in red are optical, the connections in green are electrical. The FM-RC output drives the TM-RC.

increase of the dimension of one single RC network. Here, we report our first results on a photonic deep-RC obtained by stacking together two physical RC. These preliminary results are a hybrid between experiment and simulation. In particular, the processing through the FM-RC is performed experimentally while the processing through the TM-RC is performed through a realistic simulation. The physical connection between the two RC experiments is feasible and will be the next step of this work.

In the next section, we describe our experimental setups and show how the connection between the two physical RCs is obtained; then we present and discuss our results; finally, in the conclusion, we summarize our findings and perspectives.

## Methods

The aim of this work is to explore the concept of concatenating two different photonic RCs to constitute a dual-layer deep-RC. To do so, we employed two experimental systems already presented in the past: a Frequency-Multiplexing RC (FM-RC) [3] and a Time-Multiplexing RC (TM-RC) [4].

In the FM-RC, neurons are encoded in the complex lines of a frequency comb. A monochromatic C-band CW radiation is intensity-modulated according to the input signal by a Mach-Zehnder Modulator (MZM). Afterwards, the radiation is periodically phase-modulated at frequency of  $\Omega/2\pi \approx 17\text{GHz}$  using a Phase Modulator (PM1). This radio-frequency phase-modulation expands our originally monochromatic radiation into a frequency comb with spectral line separation of  $\Omega$  and a range that depends on the phase-modulation intensity (we have approximately 25 usable lines). The frequency comb, encoding the input signal, is injected into a fiber loop (polarization maintaining fiber, 15 m long). The loop contains a second Phase Modulator (PM2) and an Erbium-Doped Fiber Amplifier (EDFA). PM2 operates at the same frequency as PM1, generating interference between the lines of the frequency comb which mixes the encoded information. The EDFA partially compensates the losses in the loop, its gain is optimized to obtain the best possible performance. The comb circulating in the fiber loop represents a reservoir state with neurons being encoded in the complex amplitude of the comb lines. The input rate is adjusted to the cavity roundtrip time such that a timestep in the input timeseries fills the cavity. For each roundtrip, the new comb shape (i.e.: the new reservoir state) is determined by the previous state (modified by the passage through PM2) and by the new input. 10% of the radiation is extracted from the loop and directed to a readout circuit composed of a Programmable Spectral Filter (PSF) and a Photodiode (PD). The PSF acts as a tunable band-pass filter allowing to measure independently each comb line to

reconstruct the full evolution of the reservoir. The collected data are later used to train the output weights and produce the overall output of the RC.

In the TM-RC, the neurons are time-multiplexed in the intensity of light traveling through a fiber spool. The reservoir has a ring topology with next-nearest-neighbor coupling. The information flows into an optoelectronic loop composed of the fiber spool and electronic hardware (a Field-Programmable Gate Arrays board, FPGA). The radiation from a Light Emitting Diode (LED) is intensity-modulated via a MZM and injected into a 1.7 km long spool of a Single-Mode Fiber (SMF), connected, on the other end, to a photodiode (PD). The length of the fiber allows for 50 time-multiplexed neurons. The FPGA reads out the neurons at the PD, mixes them with new inputs, and drives consequently the MZM, which introduces a sine nonlinearity. Also, the FPGA records the full reservoir evolution that is subsequently used to train the output weights and produce the overall output of the RC. As mentioned, the data processing in the FM-RC was obtained experimentally, while the data processing through the TM-RC was performed in simulation. We use an accurate TM-RC simulation that contains a realistic model for the MZM, PD, and possible desynchronization in the fiber propagation.

The deep-RC scheme that we tested is depicted in Fig. 1. The input signal is supplied to the first reservoir (FM-RC). The FM-RC states,  $\mathbf{X}_{FM}(t)$ , are multiplied by a set of weights  $\mathbf{W}_{int}$  to obtain a single-dimensional timeseries:  $u_{int}(t) = \mathbf{W}_{int} \cdot \mathbf{X}_{FM}(t)$ . The timeseries  $u_{int}(t)$  is then injected as an input in the second reservoir (TM-RC). The states of the first RC layer,  $\mathbf{X}_{FM}(t)$ , and the states of the second RC layer,  $\mathbf{X}_{TM}(t)$ , are then concatenated,  $\mathbf{X}(t) = [\mathbf{X}_{FM}(t), \mathbf{X}_{TM}(t)]$ , such that the vector  $\mathbf{X}(t)$  contains the value of the neurons of both reservoirs at the timestep  $t$ . We use these “total reservoir” states to train the set of output weights  $\mathbf{W}_{out}$  by means of a ridge regression model.

The choice of  $\mathbf{W}_{int}$  that represent the connection between the reservoirs is crucial. We tested three possible choices: a random set of weights, a set of weights such that the first layer output already approximates the target, and a set of weights learned via a genetic optimization algorithm (CMA-ES).

The performance of the system is evaluated on a benchmark task consisting in compensating the distortion induced by a nonlinear noisy channel in a simulated communication system (cf. [3]). The Signal-to-Noise Ratio (SNR) can be tuned, thus varying the difficulty of the task.

For each run, 45000 distorted symbols are injected in the deep-RC. The first 1000 outputs are discarded, to avoid evaluating the system during the warm-up transient state. Then, 12000 symbols are employed for training  $\mathbf{W}_{out}$ , while the remaining 32000 are used for testing. The score is provided in terms of the Symbol-Error Rate (SER) that denotes the rate of incorrect symbols received. To improve the statistics, the performance values are evaluated as an average over 1000 random repartitions in training and testing set.

## Results and discussion

We analyzed the performance of a dual-layer deep-RC using the nonlinear channel equalization as a task. In particular, we tested three different ways of choosing a suitable set of weights  $\mathbf{W}_{int}$  that connect the first reservoir network layer with the second one. For each technique, we measured the Symbol-Error Rate for different values of the Signal-to-Noise Ratio (SNR) in the simulated channel. The results are shown in Fig. 3.

We first note that the noise in the channel is, in general, detrimental. Hence, for low SNR values the performances are tendentially worse (high SER). For low SNR, the system performance tends to saturate at a minimum SER value. This is because the results depend

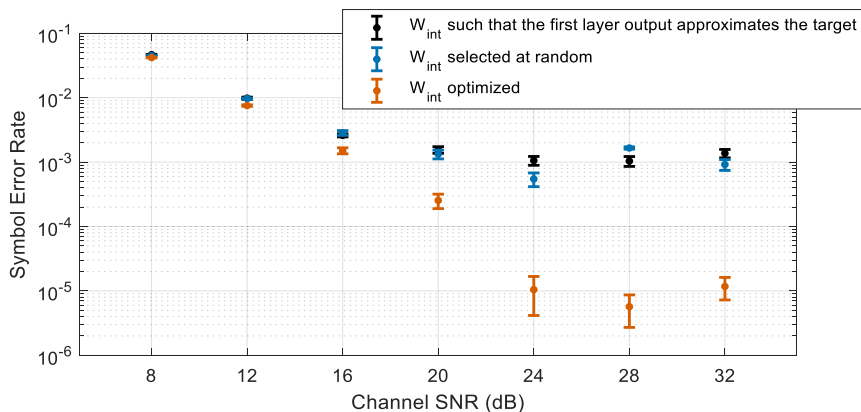


Figure 2. Symbol Error Rate (SER) measured varying the amount of noise in the channel, for three different choices of  $W_{int}$ .

uniquely on the capability of the system to correct for nonlinear distortions once the noise becomes negligible. The biggest difference between the three ways of choosing  $W_{int}$  can be observed in the low-noise regime.

Training  $W_{int}$  in such a way that the first layer output approximates the target gives approximately the same result of a random choice for  $W_{int}$ . Instead, when  $W_{int}$  is properly optimized through the CMA-ES algorithm, improvements of up to two orders of magnitude in SER can be observed.

## Conclusion

We presented a preliminary study for a scheme of a photonic deep-RC. We showed that stacking two different RCs generates an increase in the overall performance on an idealized channel equalization task. We experimented with different ways of connecting both RC layers observing that a black-box optimization algorithm (in our case, CMA-ES) is necessary to exploit the full power of the deep-RC.

At present, the first layer of the deep-RC is executed in a physical experiment, while the second layer is executed in a realistic simulation.

The positive results obtained in the present work motivate us to pursue in future work a fully experimental implementation of the scheme. Future work will also investigate other architectures, such as stacking two or more layers of the same kind of reservoirs, instead of using heterogeneous ones as in the present work.

## Acknowledgement

The authors acknowledge financial support from the European Commission grant 860360-POSTDIGITAL.

## References

- [1] Y. LeCun, Y. Bengio, and G. Hinton, “Deep learning,” *Nature* vol. 521, p. 436, 2015.
- [2] K. Nakajima, “Physical reservoir computing—an introductory perspective,” *Jpn J Appl Phys*, vol. 59, issue 6, p. 60501, 2020.
- [3] L. Butschek, A. Akrouf, E. Dimitriadou, A. Lupo, M. Haelterman, and S. Massar, “Photonic reservoir computer based on frequency multiplexing,” *Opt. Lett.*, vol. 47, issue 4, p. 782, 2022.
- [4] P. Antonik, M. Haelterman, and S. Massar, “Brain-Inspired Photonic Signal Processor for Generating Periodic Patterns and Emulating Chaotic Systems,” *Phys. Rev. Appl.*, vol. 7, issue 5, 2017.
- [5] M. Freiberger, P. Bienstman, and J. Dambre, “Towards Deep Physical Reservoir Computing Through Automatic Task Decomposition And Mapping,” arXiv:1910.13332, 2019.

# Micro-Transfer-Printed Photodiodes on Silicon Nitride for High-Speed Communications

D. Maes,<sup>1,2,3</sup> G. Roelkens,<sup>1</sup> S. Lemey,<sup>2</sup> E. Peytavit,<sup>3</sup> B. Kuyken<sup>1</sup>

<sup>1</sup> Photonics Research Group, Department of Information Technology (INTEC), Ghent University — imec, Technologiepark-Zwijnaarde 126, 9052 Ghent, Belgium

<sup>2</sup> Internet Technology and Data Science Lab (IDLab), INTEC, Ghent University — imec, Technologiepark-Zwijnaarde 126, 9052 Ghent, Belgium

<sup>3</sup> Institute of Electronics, Microelectronics and Nanotechnology (IEMN), Université de Lille, 59652 Villeneuve d'Ascq, France

*Silicon photonics is a key technology for high-speed interconnects. Its small footprint, integrated nature, and CMOS-compatible manufacturing make it a technological platform that is rapidly being embraced by industry. Silicon Nitride (SiN) flavored platforms have some extra benefits, including low-loss waveguides, allowing high-Q filters, and no two-photon absorption (TPA), greatly improving its power handling. However, the functionality of this passive platform needs to be extended to feature active components, and as such relies on heterogenous integration techniques for detectors and light sources.*

*To this end, we have transfer-printed uni-travelling-carrier photodiodes (UTC PDs) on a SiN photonic integrated circuit (PIC). These evanescently coupled photodiodes have a waveguide-referenced responsivity of 0.3 A/W, a dark current of 10 nA at -1 V bias and a 3-dB bandwidth of 155 GHz and 135 GHz at -1 V and zero bias, respectively.*

*In this paper, we show that such a high-bandwidth heterogeneously integrated photodetector can be used for direct photomixing at sub-mmWave (sub-THz) frequencies, enabling data rates beyond 100 Gbit/s.*

## 1. Introduction

Optical technologies have since long been important in communication systems. The internet is unimaginable without high-speed fiber interconnects. However, the optical subsystem in these interconnects has only in recent years been growing beyond the optical fiber and necessary peripheral components. Silicon Photonics (SiPh) accelerates this change: complex and cost-effective photonic circuits are possible thanks to the CMOS-compatible manufacturing and the small footprint of these chips.

Silicon-Photonic technologies not only enable more sophisticated, more efficient, and faster transceivers for fixed datacom and telecom. It also finds its way to wireless communication systems, e.g. next-generation wireless networks (6G). The field of microwave photonics leverages the fact that high-bandwidth radio signals are relatively narrowband in the optical domain. Compared to their electronic counterparts, this allows for easy filtering and manipulation of millimeter wave (mmWave) signals and even terahertz (THz) signals.

Silicon Nitride (SiN) is one particular flavor of Silicon Photonics that is increasingly gaining popularity thanks to its noticeable benefits. SiN waveguides are very low loss, allowing high-Q filters, and the absence of two-photon absorption (TPA) greatly improves the linearity at high optical powers. On the other hand, many SiN platforms

only excel for their passive components (waveguides, filters...) and require hybrid or heterogeneous integration of active components (lasers, modulators, photodetectors...).

In this paper, we show that a low-loss passive SiN platform can be extended with very high-bandwidth photodetectors using the micro-transfer-printing technology. We further demonstrate that this device can be used in future THz systems by setting up a link at 300 GHz with a bit rate beyond 100 Gbit/s. The remainder of this paper is divided in two sections: Section 2 describes the integration of the high-bandwidth photodetectors on SiN, and in Section 3 we demonstrate a THz data link leveraging this device.

## 2. High-bandwidth photodetectors on SiN

Multiple technologies have been developed to bring high-speed detectors to SiN platforms. Oftentimes these approaches start from a high-speed photodetector developed on a III-V platform, e.g. based on InP and InGaAs. One particular type of photodetector, the uni-travelling-carrier photodiode (UTC PD), is a great choice for high-speed high-power applications. By limiting the carrier transport to high-mobility electrons, the transit-time-limited bandwidth is greatly increased, making the RC-time limit dominant. Furthermore, the UTC PD only shows carrier-screening effects at much higher powers – compared to traditional PIN photodiodes – making it a perfect suitor for a SiN platform.

Yu et al. [1] have shown that waveguide-coupled UTC PDs can be integrated on a SiN platform by means of wafer-bonding. Their approach yielded a high responsivity of 0.8 A/W and a respectable 3-dB opto-electric bandwidth of 20 GHz.

In our work, we use micro transfer-printing ( $\mu$ TP) as heterogenous integration technology. In this technology, first a fully operational photodiode is created on the III-V wafer (the *source* wafer). Next, the photodiode is encapsulated in a passivation layer and under-etched to create a suspended chiplet, i.e. a *coupon*. This coupon can then be picked up using a polymer stamp and is printed on top of the desired photonic structure. In our design it is printed on top of a SiN waveguide on the SiPh wafer (the *target* wafer). Compared to wafer bonding this offers some additional benefits: the chiplet can be fully made on the source wafer without alteration of the original process flow, multiple chiplets of different source wafers can be printed close to each other on the target wafer allowing for multi-material integration, and this process is more efficient by requiring less source wafer material [2].

In our previous work [3] we reported a UTC PD on SiN with a 3-dB bandwidth beyond 100 GHz, a responsivity of 0.45 A/W at 1550 nm and a dark current of 10 nA. The smooth roll-off at high frequencies makes this device a great component for sub-mmWave (sub-THz) signal generation.

## 3. On-chip photomixing for THz generation

Generating continuous-wave radiation at frequencies beyond 100 GHz is not easy for electronic ICs, especially in CMOS. Monolithic microwave integrated circuits (MMICs) are fabricated in advanced technological nodes and mostly rely on high-electron-mobility transistors (HEMTs) made using GaAs and AlGaAs. In microwave photonics, an alternative approach called photomixing is used to generate high-frequency microwave signals. By beating two optical tones on a photomixer, i.e. a photodetector with a high

electrical bandwidth, an electrical signal at the beat note of the two optical frequencies is generated. As such, if two tunable lasers are used, the only limit on the maximum frequency that can be generated is the efficiency of the photomixer at this frequency.

This approach is not limited to continuous wave (CW) signals, but also data can easily be upconverted to (sub-)THz frequencies this way. One of the two optical lines is modulated and the resulting data signal is then heterodyne-mixed to the desired THz carrier by choosing the appropriate wavelength for the second laser. We demonstrated that this approach for high data-rate THz communication is possible with a SiN photonic integrated circuit (PIC) featuring our high-speed UTC PD (Fig. 1).

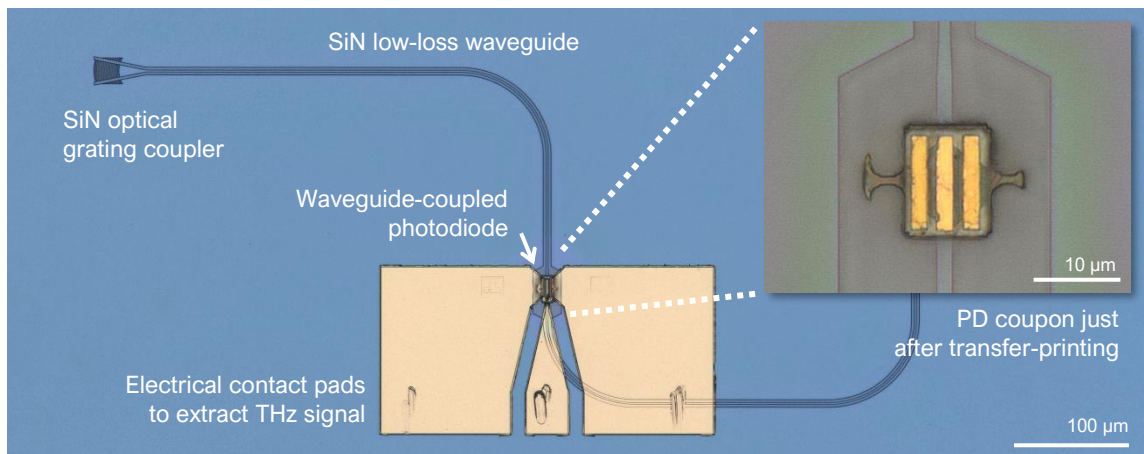


**Figure 1. The SiN PIC consists of an optical grating coupler, SiN waveguide and electrical contact pads to probe the waveguide-coupled UTC PD.**

Fig 2. shows the setup we used for this photomixing experiment. Two optical lines are generated using tunable C-band lasers at a wavelength of 1547.9 nm and 1550.1 nm (193.68 THz and 193.40 THz respectively). A Mach-Zehnder Modulator (MZM) is used to modulate the data generated by the Arbitrary Waveform Generator (AWG) on the optical carrier. To overcome the optical losses of coupling into the PIC using a grating coupler, an optical Erbium-Doped Fiber Amplifier (EDFA) was used to increase the power. After photomixing, the sub-THz (sub-mmWave) signal with a center frequency of 280 GHz is fed over a waveguide channel (WR3) before being mixed down at the receiver side. The signal is mixed down again to an intermediate frequency (IF) that is within the bandwidth of the real-time oscilloscope.

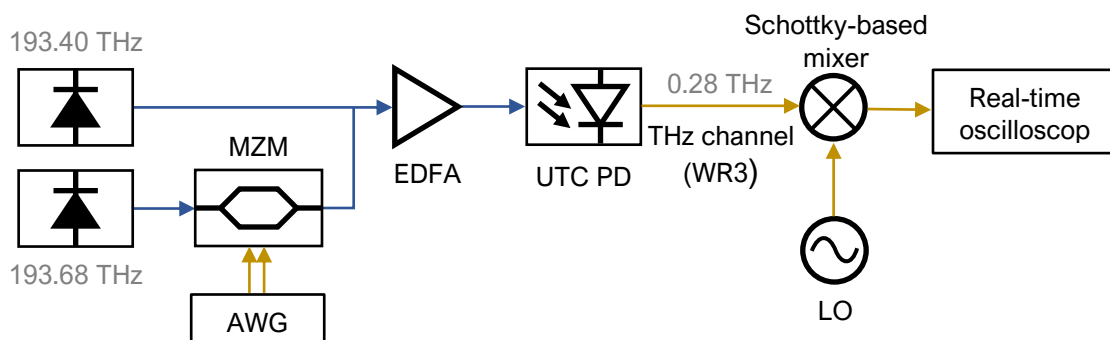


**Figure 2. The photomixing experiment consists centrally of the optically and electrically probed PIC containing the UTC PD.**

With this setup, we were able to transmit data back-to-back at a rate up to 140 Gbit/s. A 16-point quadrature amplitude modulation (16-QAM) scheme was deployed at symbol rate of 35 GBaud. This resulted in a low error vector magnitude (EVM) of 11%, below the 12.5% EVM forward-error-correction (FEC) limit. Also higher order modulation (32-QAM) yielded high bit rate transmission (125 Gbit/s at 25 GBaud) with low EVM (7%). Fig. 3 shows the constellation diagrams.

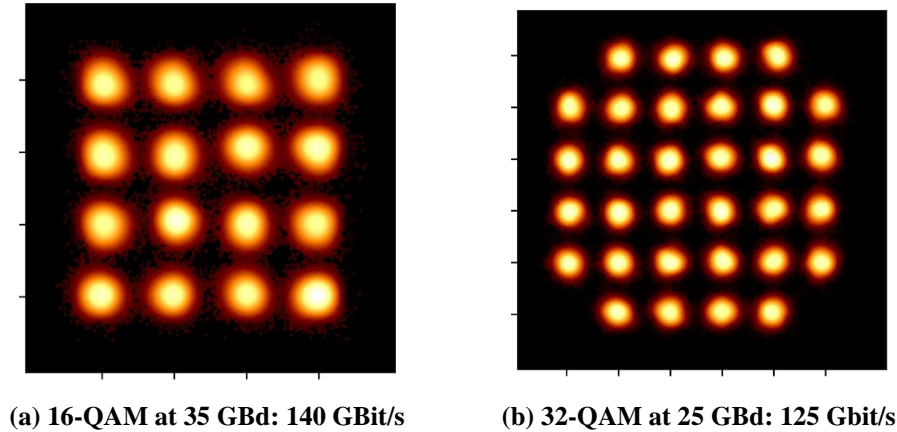


Figure 3. Constellation diagrams for both configurations show a low EVM.

#### 4. Conclusion

Silicon photonics offers many technological benefits for future fixed and wireless networks. We have demonstrated that low-loss passive SiN platforms can be extended with state-of-the-art photodetectors by heterogeneous integration of a UTC PD using the micro-transfer-printing technology. We further demonstrate that these devices on a SiN PIC are ready to be used in a sub-THz communication link at 280 GHz. For this a back-to-back link with a data rate up to 140 Gbit/s was set up.

#### References

- [1] Q. Yu et al., "Heterogeneous Photodiodes on Silicon Nitride Waveguides with 20 GHz Bandwidth," 2020 Optical Fiber Communications Conference and Exhibition (OFC), 2020.
- [2] G. Roelkens et al., "Micro-Transfer Printing for Heterogeneous Si Photonic Integrated Circuits," Journal of Selected Topics in Quantum Electronics, 2022.
- [3] D. Maes et al. "High-Speed Photodiodes on Silicon Nitride with a Bandwidth beyond 100 GHz," 2022 Conference on Lasers and Electro-Optics (CLEO), 2022.

# Semi-nonlinear waveguides for three waves mixing

Romain Morleghem<sup>1</sup>, Simone Napolitano<sup>4</sup> and Stéphane Clemmen<sup>1,2,3</sup>

<sup>1</sup>Laboratoire d'Information Quantique, CP 225, Université libre de Bruxelles (U.L.B.), Belgium

<sup>2</sup>OPERA-Photonique, CP 194/5, Université libre de Bruxelles (U.L.B.), Brussels, Belgium

<sup>3</sup>Photonics Research Group, Department of Information Technology, Ghent University-imec, Belgium

<sup>4</sup>Experimental Soft Matter and Thermal Physics (EST), Université libre de Bruxelles, Brussels, Belgium

## Abstract

*Silicon nitride (SiN) has emerged as a mature photonics platform due to its very low losses and large transparency but lacks a significant  $\chi^{(2)}$  nonlinearity [1]. Hence, the integration of ultra-high  $\chi^{(2)}$  thin films on SiN waveguides, resulting in so-called semi-nonlinear waveguides, would open the way for many functionalities such as second harmonic (SH) generation and single photons frequency conversion [2]. We design semi-nonlinear waveguides that achieve modal phase matching between a spatially fundamental mode ( $TE_{00}$ ) at an initial frequency and a spatially 2 lobe-mode ( $TE_{01}$ ) at the SH [3]. We thoroughly compare the predicted SH conversion efficiency in that situation to usual situation of a fully nonlinear waveguide requiring phase matching between the same  $TE_{00}$  mode and the  $TE_{20}$  mode at the SH (the lowest possible order of non-vanishing modal phase matching). Our simulations show that semi-nonlinear waveguides result in a higher SH conversion efficiency than fully nonlinear waveguides.*

## Silicon nitride platform and hybrid integration with $\chi^{(2)}$ materials

Silicon nitride (SiN) is a mature and versatile platform, exhibiting a lot of attractive features for integrated nonlinear and quantum photonics: a high bandgap (transparent down to 400 nm), very low losses ( $\sim 0.1$  dB/cm) and state-of-the-art  $\chi^{(3)}$  platform [4]. Still, SiN lacks a  $\chi^{(2)}$  nonlinearity due to its centrosymmetric structure, preventing the SiN platform from key  $\chi^{(2)}$  applications like high-speed electro-optic modulation and frequency conversion (sum/difference frequency generation).

Although it is possible to induce an effective  $\chi^{(2)}_{\text{eff}}$  in SiN by several methods (strain, electric field, all-optical poling [5], ...), the resulted  $\chi^{(2)}_{\text{eff}}$  and on-chip SH conversion efficiency are several orders of magnitude lower than material platforms possessing an intrinsic  $\chi^{(2)}$  coefficient [5].

Another strategy consists in the integration of a high  $\chi^{(2)}$  material on existing SiN waveguides, resulting in a semi-nonlinear structure as depicted in figure 1. Several materials already used to fabricate nanophotonics circuits like  $\text{LiNbO}_3$ , AlN, SiC, GaP, InGaP [6] are potential candidates for this hybrid integration with SiN. However, the aforementioned  $\chi^{(2)}$  materials are not ideal for different reasons: AlN and SiC have a relatively low  $\chi^{(2)}$  coefficient (not exceeding 20 pm/V). The very high tensorial component  $\chi^{(2)}_{\text{xyz}}$  of GaP and InGaP ( $\sim 200$  pm/V) is difficult to exploit effectively. The ferroelectric  $\text{LiNbO}_3$  constitute arguably the state-of-the-art because its etching has reached a certain maturity resulting in very low loss waveguides and it also offers possibilities of phase matching via periodic poling. Yet,  $\text{LiNbO}_3$  is far from being perfect for processes such as sum frequency generation because of the limitations associated to a photorefractive effect and a moderate  $\chi^{(2)}$  (55 pm/V). Besides those  $\chi^{(2)}$  semiconductor materials, organic materials like OH1(2-(3-(4-hydroxystyryl)-5,5-dimethylcyclohex-2-

enylidene)malononitrile) and BNA (N-benzyl-2-methyl-4-nitroaniline) fulfill the required features for the hybrid integration with SiN waveguides : a transparency range extending in the visible and near infrared, a bandgap high enough to avoid linear and two photons absorption at telecom wavelength, a  $\chi^{(2)}$  coefficient significantly higher than that of LiNbO<sub>3</sub> (bulk  $\chi^{(2)} \sim 150\text{-}250$  pm/V), a refractive index closed to the one of SiN ( $\sim 2$ ) and finally, a convenient processability and good thermal stability. BNA thin films exhibiting a  $\chi^{(2)}$  of the order of 150 pm/V at 1550 nm have already been demonstrated [7] but the control of their processing conditions and their interfacing to existing SiN integrated circuits is currently lacking. Thus, the integration of a ultra-high organic  $\chi^{(2)}$  thin film (BNA or OH1) on top of SiN waveguides would undoubtedly transform the SiN platform into an all-nonlinear photonics champion.

## Second harmonic generation via modal phase matching

The  $\chi^{(2)}$  response is usually assessed using second harmonic generation (SHG), where an input fundamental wave at  $\omega$  (1550 nm) is upconverted to a second harmonic wave at  $2\omega$  (775 nm). Moreover, to have an efficient SH conversion, the fundamental and second harmonic need to be phase matched, i.e., travel at the same phase velocity. This phase matching condition is fulfilled when the effective refractive index of the fundamental and the SH mode equal each other —  $n(\omega) = n(2\omega)$ . Yet, due to dispersion, the effective refractive index increases with frequency for a given spatial mode of the waveguide. The modal phase matching strategy is based on having the SH wave in a higher order spatial mode, allowing to have  $n(\omega) = n(2\omega)$ . In practice, modal phase matching is achieved by carefully engineering the geometric dimensions of the waveguide, which add up to 3 parameters in our case: the SiN core width and thickness as well as the  $\chi^{(2)}$  overlay thickness. For this  $\chi^{(2)}$  overlay, we investigate first the organic BNA whose highest tensorial component is the  $\chi^{(2)}_{xxx}$  as depicted on figure 1, which means that the spatial modes involved are (quasi) TE modes. A key advantage of the semi-nonlinear structure is the use of the first higher order TE<sub>01</sub> mode for the SH wave (assuming a fundamental TE<sub>00</sub> mode). The TE<sub>01</sub> mode can easily be excited using on-chip mode converters [8]. As depicted in the top left inset of figure 3, the SH TE<sub>01</sub> mode consists of 2 vertically stacked lobes: a negative-valued lobe lying in the SiN core and a positive-valued lobe lying in the BNA overlay. Having only one lobe in the  $\chi^{(2)}$  overlay allows to reach significant nonlinear modal overlap integral, and consequently high SH conversion efficiency as it has already been experimentally demonstrated using semi-nonlinear TiO<sub>2</sub>/LiNbO<sub>3</sub> waveguides [3].

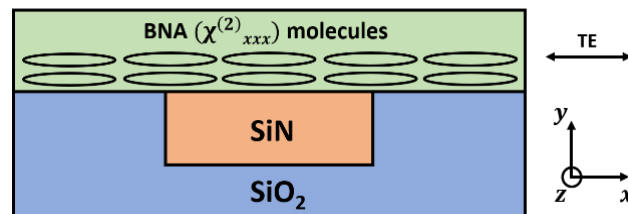


Figure 1: Semi-nonlinear waveguide made of a SiN core and a high  $\chi^{(2)}$  overlay. The  $\chi^{(2)}$  thin film is based on a crystalline arrangement of organic BNA molecules oriented along the x direction. Therefore, this high  $\chi^{(2)}_{xxx}$  component can be exploited by using TE modes for the fundamental and second harmonic waves.

## Second harmonic conversion efficiency in semi-nonlinear waveguides

As evidence of the suitability of those new semi-nonlinear waveguides in nonlinear photonics, we theoretically compare (assuming modal phase matching) the SH

conversion efficiency between semi-nonlinear SiN/BNA waveguides (SH in TE<sub>01</sub>) to the simpler situation of a hypothetical monolithic BNA waveguide requiring phase matching in the TE<sub>20</sub> (or TE<sub>02</sub>) SH mode in order to have a non-vanishing overlap with the fundamental TE<sub>00</sub> mode. This SH conversion efficiency map is depicted in figure 2 and further explained in the caption. This map shows that, within a certain range of geometric dimensions, the best waveguides are the semi-nonlinear ones, which is mostly due to a higher confinement of the two phase matched waves.

In figure 3, we plot the theoretical SH conversion efficiency as a function of the  $\chi^{(2)}$  nonlinearity of the BNA thin films. The bulk  $\chi^{(2)}$  of BNA has been reported to 160 pm/V at a fundamental wavelength of 1550 nm [9], shown by a vertical dotted line on figure 3. On the same figure, we also add the theoretical SH conversion efficiency of state-of-the-art LiNbO<sub>3</sub> waveguides (PPLN [10,11] and dual layer thin film LiNbO<sub>3</sub> [12]). Thanks to the very high nonlinearity of BNA (almost 3 times the one of LiNbO<sub>3</sub>), it is predicted that these semi-nonlinear SiN/BNA waveguides lead to SH conversion efficiency much higher than the ones of current PPLN waveguides.

In conclusion, we have theoretically demonstrated that ultra-high  $\chi^{(2)}$  semi-nonlinear SiN/BNA waveguides lead to much higher SH conversion efficiency compared to their fully nonlinear counterparts and current PPLN waveguides. The next step in our analysis is to consider tolerances to fabrication (variation of waveguide dimensions), in order to estimate the phase matching bandwidth of the SHG process.

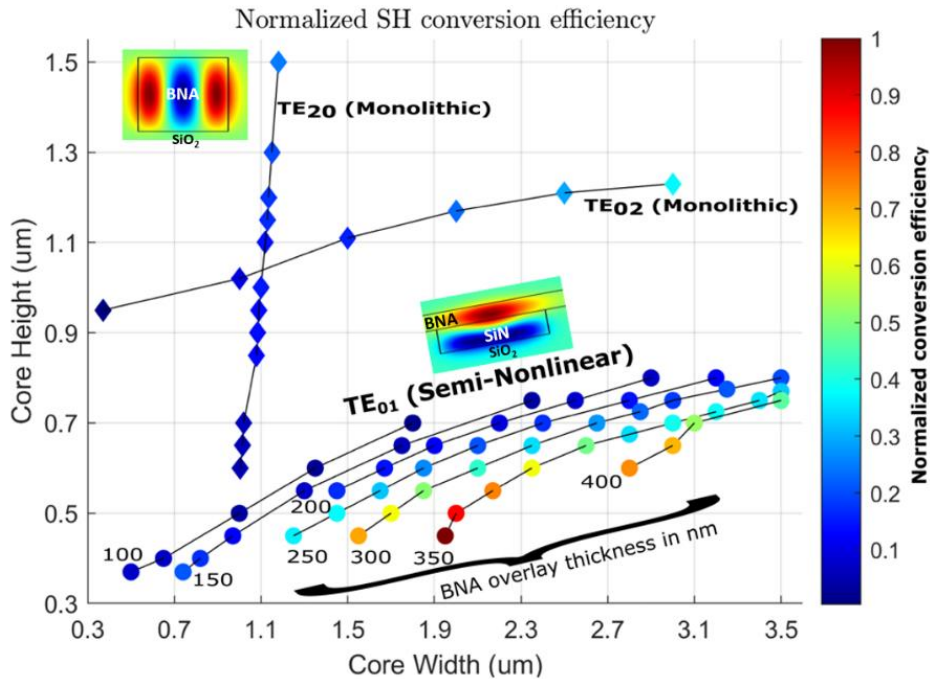


Figure 2: Second harmonic conversion efficiency map (1550 nm  $\rightarrow$  775 nm) for monolithic (diamond) and semi-nonlinear modal phase matched waveguides (circle). The core dimensions correspond to the  $\chi^{(2)}$  core (BNA) for the monolithic case and to the SiN core for the semi-nonlinear case. The values near the TE<sub>01</sub>(semi-nonlinear) curves correspond to the BNA overlay thickness (in nm) for the semi-nonlinear case. The conversion efficiency is normalized by the highest value found in the simulation (29000 % W<sup>-1</sup>cm<sup>-2</sup> for the waveguide with SiN width = 1.95  $\mu$ m / SiN height = 450 nm / BNA height = 350 nm). In the SH mode profiles (TE<sub>20</sub> mode for monolithic and TE<sub>01</sub> mode for semi-nonlinear), red (blue) lobes correspond to a positive (negative) field value.

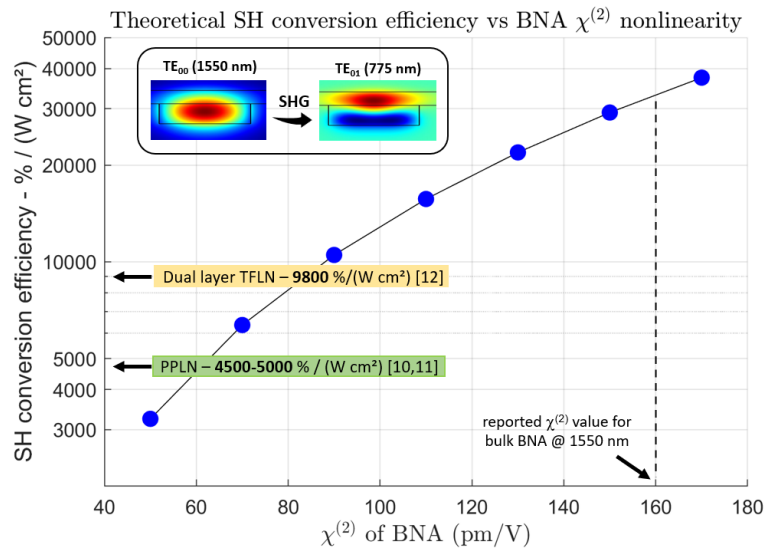


Figure 3: Theoretical second harmonic (SH) conversion efficiency (in %  $W^{-1}cm^{-2}$ ) plotted as a function of the  $\chi^{(2)}$  nonlinearity of the BNA overlay (circles). The semi-nonlinear waveguide (SiN core with BNA overlay) with the mode profiles are depicted in the top left inset of the figure. We also report on the graph the bulk  $\chi^{(2)}$  of BNA ( $\sim 160$  pm/V at 1550 nm) on the horizontal axis as well as state-of-the-art theoretical SH conversion efficiency with LiNbO<sub>3</sub> ( $\chi^{(2)} \sim 55$  pm/V) waveguides on the vertical axis. Thanks to the very high nonlinearity of BNA (almost 3 times the one of LiNbO<sub>3</sub>), these semi-nonlinear SiN/BNA waveguides outperform nanophotonic LiNbO<sub>3</sub> waveguides with respect to the theoretical SH conversion efficiency.

**Acknowledgement** Stéphane Clemmen is a research associate of the Fonds De La Recherche Scientifique — FNRS. This work was supported by the Fonds de la Recherche Scientifique – FNRS under Grant MIS F.4506.20.

## References

- [1] Abdul Rahim et al. “Expanding the silicon photonics portfolio with silicon nitride photonic integrated circuits”. In: *Journal of lightwave technology* 35.4 (2017), pp. 639–649.
- [2] Anaïs Dréau et al. “Quantum frequency conversion of single photons from a nitrogen-vacancy center in diamond to telecommunication wavelengths”. In: *Physical review applied* 9.6 (2018), p. 064031.
- [3] Rui Luo et al. “Semi-nonlinear nanophotonic waveguides for highly efficient second-harmonic generation”. In: *Laser & Photonics Reviews* 13.3 (2019), p. 1800288.
- [4] Xingchen Ji et al. “Exploiting ultralow loss multimode waveguides for broadband frequency combs”. In: *Laser & Photonics Reviews* 15.1 (2021), p. 2000353.
- [5] Edgars Nitiss et al. “Optically reconfigurable quasi-phase-matching in silicon nitride microresonators”. In: *Nature Photonics* 16.2 (2022), pp. 134–141.
- [6] Galan Moody et al. “2022 Roadmap on integrated quantum photonics”. In: *Journal of Physics: Photonics* 4.1 (2022), p. 012501.
- [7] Artur Hermans et al. “Growth of organic crystalline thin films with strong second-order nonlinearity for integrated optics”. In: *21st European Conference on Integrated Optics (ECIO 2019)*.
- [8] Aseema Mohanty et al. “Quantum interference between transverse spatial waveguide modes”. In: *Nature communications* 8.1 (2017), pp. 1–7.
- [9] Takashi Notakel et al. “Ultra-precise processing and Maker fringe measurements of organic N-Benzyl-2-Methyl-4-Nitroaniline crystal”. In: *2018 43rd International Conference on Infrared, Millimeter, and Terahertz Waves (IRMMW-THz)*. IEEE, 2018, pp. 1–2.
- [10] Cheng Wang et al. “Ultrahigh-efficiency wavelength conversion in nanophotonic periodically poled lithium niobate waveguides”. In: *Optica* 5.11 (2018), pp. 1438–1441.
- [11] Ashutosh Rao et al. “Actively-monitored periodic-poling in thin-film lithium niobate photonic waveguides with ultrahigh nonlinear conversion efficiency of 4600%  $W^{-1}cm^{-2}$ ”. In: *Optics express* 27.18(2019), pp. 25920–25930.
- [12] Lei Wang, Xiuquan Zhang, and Feng Chen. “Efficient Second Harmonic Generation in a Reverse Polarization Dual-Layer Crystalline Thin Film Nanophotonic Waveguide”. In: *Laser & Photonics Reviews* 15.12 (2021), p. 2100409.

# Performance Evaluation of Beam Steering using Piezoelectric Actuators.

E. Muller<sup>1</sup>, Y. Song<sup>1</sup>, T. Koonen<sup>1</sup>, E. Tangdiongga<sup>1</sup>

<sup>1</sup> Eindhoven University of Technology, Dept. of Electrical Engineering, De Groene Loper 19, 5612 AP, Eindhoven, Netherlands

## Abstract

*Optical wireless communication (OWC) has been considered the technology of choice to realize ultra-high bitrates and low latency for wireless communication. Therefore, we have the objective to develop an optical transmitter capable of serving an indoor area, meaning that it must track and connect to multiple nomadic users. A narrow light beam delivers the best power to the receiver, but because of its size, it must be steered to the receiver aperture. We are part of the NWO optical superhighways project, under grant 12128 Optical Wireless Superhighways: Free Photons.*

*One of the proposed solutions is the use of a pair of piezoelectric actuators coupled with an optical fiber. By controlling each actuator, we can achieve two-dimensional freedoms of movement. Steering the beam with this method is done by decentralizing the fiber from the center of the magnifying lens. This is challenging, due to the limited movement of the actuator, consequently, the lenses must be in the micrometer dimension. This system has been simulated with results of a steering beam angle of around 10 degrees. Furthermore, the lenses are being designed and will be produced for a practical experiment.*

## Introduction

Current data consumption grows at an exponential rate, and so overloads the wireless network infrastructure. These networks are limited due to the legally defined frequencies and the overcrowding of them by the huge number of users, this is also a consequence of the expansion of the internet-of-things (IoT) [1]. As a possible solution for the end-user congestion, we propose the use of OWC technology, which will offload the RF frequencies [2]. Optical communication also has the advantages of having huge bandwidths, low latency, high privacy, and low interference from neighboring networks.

To develop this novel indoor network, we are proposing a transmitter that must track and connect to multiple users. The data throughput is defined by the laser bandwidth and the power delivered to the receiver, therefore, to have the best data throughput it is necessary to deliver the maximum power to it. But, due to eye safety concerns [3], the beam power must be maintained below a certain threshold. Therefore, it is not possible to illuminate the whole room and get the desired signal to the receiver. Then a narrow light beam is a solution that delivers high levels of power to the receiver while maintaining the power in a safe zone [4]. But, because of its size, the beam must be steered to the receiver aperture.

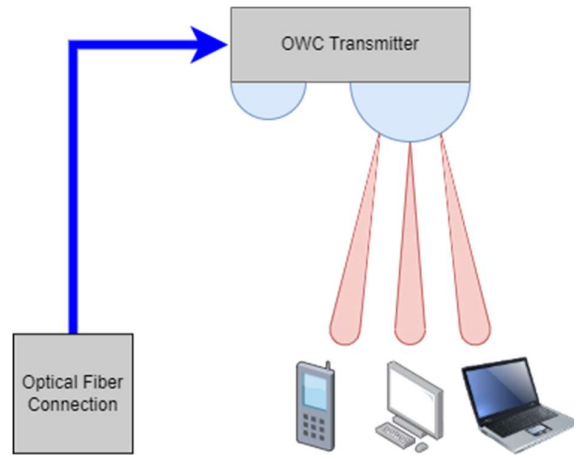


Figure 1 OWC Indoor concept

For the construction of a feasible OWC network, the transmitter must fulfill many requirements such as multi-beam capability, 2D steering, a wide field of view, and large throughput. For these requirements, many viable solutions can be found for beam steering, such as Array Waveguide Gratings [5], Micro Electrical-Mechanical systems [6], Meta-Surfaces [7], Optical Phased Arrays [8], Polarization Gratings [4], Spatial Light Modulators [9].

This paper intends to give an overview of technologies used in a beam steered OWC transmitter. This is an extensive field, as previously commented, with several workable solutions. All the technologies can, in some form, fulfill the requirements for the OWC, and the most advanced now is the use of a pair of piezoelectric actuators to steer the beam. After discussing the concept of the beam steering transmitter concept, I will demonstrate a simulation and show the design of a future experiment. This work is supported in part by the Netherlands Organization for Scientific Research (NWO) under grant 12128 Optical Wireless Superhighways: Free Photons.

## System Concept

To keep the costs and time-to-market down, we will utilize the most from the standard fiber communications and adapt it to an indoor OWC system. And because of its wide implementation, we will be using the 1550nm C-band communication equipment as the base for this project. The basic concept is that we need to serve an optical signal, with enough quality to keep the data throughput, to individual users. At the same time tracking its movements and updating the localization to the steering control.

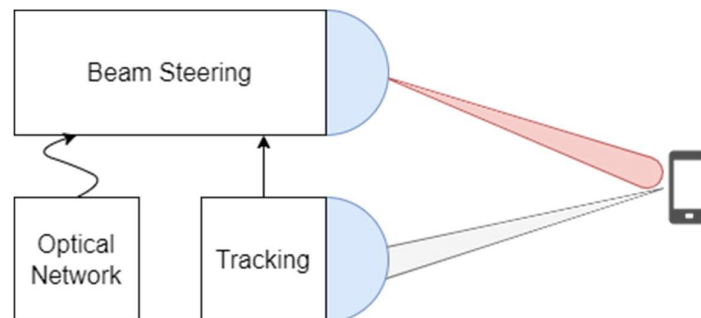


Figure 2 Beam-steering system diagram

Figure 2 is the basic scheme of our transmitter. The tracking module has the responsibility to track and separate each user and update this data to the beam steering control unit. Then, with the localization information each beam is moved to the receiver aperture of a user. Following the system requisites, the steering unit must steer multiple beams or be small enough where many units can work in parallel in a single transmitter. Also, there are several ways of sending signal to the transmitter, such as, multiple optical cables, multicore fibers, or a multiplex signal split with an AWGr, separating the wavelengths for different the users.

A pair of piezoelectric actuators, each controlling one axis of movement, is a solution to the steering problem. Because they fit the prerequisites, while being small enough to be implemented in parallel, and having a good steering angle in 2D. The actuators steer a beam by moving the source of the light, here being an optical fiber. But, to have several parallel elements in the same transmitter, with each responsible for one user, the actuators are small. And because of their size, the actuators have a limited range of movement, in the micron range. Therefore, there is the need to amplify this tiny move to a usable larger area of service. We can achieve this magnification by using a lens in the same size range as the movement, this means that we also need a lens in the  $\mu\text{m}$  range.

## Simulation

The simulation was designed to demonstrate beam steering using actuators. This is done by moving the output of a standard optical fiber from the center of a fixed lens [10]. In this manner the lens acts as an angle magnifier, amplifying the tiny movement from the actuators into a more useful angle. The microlenses and their modeling were investigated and manufactured in [11]. The system was simulated in Optical Studio 16, using a model of a polymer microlenses on a silicon substrate, the lens has a radius of fifty  $\mu\text{m}$  and a focal length of 111  $\mu\text{m}$ . After the initial setup, the fiber output was moved to its maximum extension of twenty  $\mu\text{m}$ , in steps of 2.5  $\mu\text{m}$ .

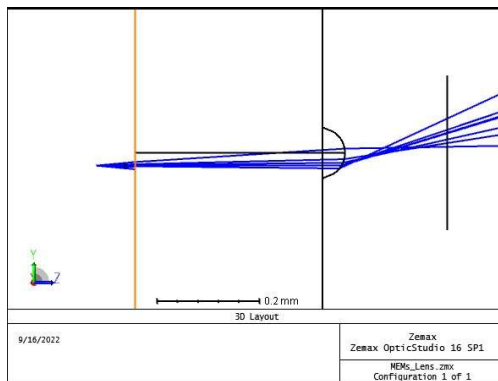


Figure 3 Lens setup

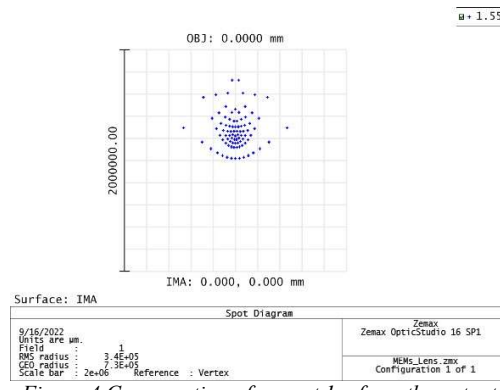


Figure 4 Cross section of rays at 1m from the output

Figure 3 shows the elements being simulated using raytracing, the first element is the output of an optical fiber, which is simulated as a Gaussian beam. This beam then goes through the silicon substrate that has a thickness of 410 $\mu\text{m}$ , then, hits the microlenses with a determined offset of 20  $\mu\text{m}$  in the figure. This offset, in conjunction with the lens focal length, will determine the total deflection angle of the optical beam. Figure 4 is the cross-section of the ray-traced beams

at a target at 1m from the lens, this is useful to calculate the beam angle of deflection and angle of dispersion.

As expected by moving the fiber from the center of the lens the output beam is steered. At the end of propagation, we achieved a deflection angle of 12 degrees and an angular dispersion of 36 degrees. This simulation also showed that the system is limited not only by the movement of the actuators but also by the size of the lens. A smaller lens has a smaller focal lens, therefore increasing the deflection angle. But at the same time the closer the beam gets to the edge of the lens; the greater distortion will happen at the target.

With the simulation results in hand, we will continue to a proof-of-concept experiment using the same setup simulated. Using a pair of voltage-controlled actuators to move the fiber against a grid of lenses with several varied sizes, thus giving the ability to evaluate multiple focal lengths in the same setup. And using an IR camera as the target to measure the resulting steering.

## Conclusion

In the development of an OWC indoor network, it was concluded that there is a need for a form of beam steering to deliver the best signal to the receiver. As part of the research, several active forms of beam steering were observed to be capable of meeting most of the requirements set for the system. The most advanced system at hand was the one that steered the beam with the use of a pair of actuators. As a primary evaluation, a simulation in Optical Studio was made, with results in the expected range of angle magnification, therefore justifying the advancement of this method to a real experiment.

## References

- [1] "Radio Regulations - Articles - Edition of 2020," p. 442.
- [2] T. Koonen, "Indoor Optical Wireless Systems: Technology, Trends, and Applications," *J. Light. Technol.*, vol. 36, no. 8, pp. 1459–1467, Apr. 2018, doi: 10.1109/JLT.2017.2787614.
- [3] "Laser safety," *Wikipedia*. Aug. 08, 2022. Accessed: Nov. 03, 2022. [Online]. Available: [https://en.wikipedia.org/w/index.php?title=Laser\\_safety&oldid=1103030189](https://en.wikipedia.org/w/index.php?title=Laser_safety&oldid=1103030189)
- [4] C. Hoy, J. Stockley, J. Shane, K. Kluttz, D. McKnight, and S. Serati, "Non-Mechanical Beam Steering with Polarization Gratings: A Review," *Crystals*, vol. 11, no. 4, p. 361, Mar. 2021, doi: 10.3390/cryst11040361.
- [5] T. Koonen, F. Gomez-Agis, Z. Cao, K. Mekonnen, F. Huijskens, and E. Tangdiongga, "Indoor ultra-high capacity optical wireless communication using steerable infrared beams," in *2017 International Topical Meeting on Microwave Photonics (MWP)*, Beijing, Oct. 2017, pp. 1–4. doi: 10.1109/MWP.2017.8168719.
- [6] S. Cardarelli, N. Calabretta, R. Stabile, K. Williams, X. Luo, and J. Mink, "Wide-Range 2D InP Chip-to-Fiber Alignment Through Bimorph Piezoelectric Actuators," in *2018 IEEE 68th Electronic Components and Technology Conference (ECTC)*, San Diego, CA, USA, May 2018, pp. 1124–1129. doi: 10.1109/ECTC.2018.00172.
- [7] J. R. Sanford and J. D. Evans, "Two-Dimensional Scanning Liquid Crystal Infrared Reflect Array," in *2022 IEEE International Symposium on Antennas and Propagation and USNC-URSI Radio Science Meeting (AP-S/URSI)*, Denver, CO, USA, Jul. 2022, pp. 359–360. doi: 10.1109/AP-S/USNC-URSI47032.2022.9886992.
- [8] R. Fatemi, A. Khachaturian, and A. Hajimiri, "A Nonuniform Sparse 2-D Large-FOV Optical Phased Array With a Low-Power PWM Drive," *IEEE J. Solid-State Circuits*, vol. 54, no. 5, pp. 1200–1215, May 2019, doi: 10.1109/JSSC.2019.2896767.
- [9] M. J. Escuti and W. M. Jones, "A polarization-independent liquid crystal spatial light modulator," presented at the SPIE Optics + Photonics, San Diego, California, USA, Aug. 2006, p. 63320M. doi: 10.1117/12.681213.
- [10] X. Cao, G. Qiu, K. Wu, M. Cai, C. Li, and J. Chen, "A Lidar System Based on Integrated Lens Assisted Twodimensional Beam Steering," in *Conference on Lasers and Electro-Optics*, Washington, DC, 2020, p. SM1O.2. doi: 10.1364/CLEO\_SI.2020.SM1O.2.
- [11] J. M. Pavia, M. Wolf, and E. Charbon, "Measurement and modeling of microlenses fabricated on single-photon avalanche diode arrays for fill factor recovery," *Opt. Express*, vol. 22, no. 4, p. 4202, Feb. 2014, doi: 10.1364/OE.22.004202.

# Low-optical-pumping-threshold InGaAs/GaAs nano-ridge laser monolithically grown on 300 mm silicon substrate

Z. Ouyang,<sup>1</sup> E. M. B. Fahmy,<sup>1</sup> D. Colucci,<sup>1,2</sup> A. A. Yimam,<sup>1</sup> B. Kunert<sup>2</sup> and D. Van Thourhout<sup>1</sup>

<sup>1</sup> Gent University-imec, Photonics Research Group, INTEC department, iGent, Technologiepark-Zwijnaarde 126, 9052 Ghent, Belgium

<sup>2</sup> IMEC, Kapeldreef 75, 3001 Heverlee, Belgium

## Abstract

*The monolithic growth of III-V materials directly on a Si substrate is a promising approach for realizing complex silicon photonic integrated circuits (PICs) including sources and amplifiers. It remains challenging to realize practical, reliable and efficient light emitters however, due to defect formation during the epitaxial process. Exploiting the aspect ratio defect trapping (ART) technique and nano-ridge engineering (NRE), nano-ridges with high crystal quality were achieved. In earlier work we used etched gratings to create distributed feedback (DFB) lasers from these nano-ridges<sup>[1]</sup>. Here we deposited an amorphous silicon (a-Si) grating on the top of nano-ridge. Under pulsed optical pumping,  $\sim 2.8 \text{ kW/cm}^2$  lasing turn-on threshold was observed, more than 10 times smaller compared to etched grating devices. This low-optical-pumping-threshold again demonstrates the high quality of the epitaxial material and provides an alternative route towards realizing electrically-driven devices.*

## Introduction

Leveraging well-developed processes from the complementary metal-oxide semiconductors (CMOSs) industry, silicon photonics circuits incorporating various optical components, including high-efficiency grating couplers, high-response-speed photodetectors and excellent modulators<sup>[2-4]</sup> are now widely studied. However, the lack of a high-performance laser is a main bottleneck for further development of the silicon photonic platform. Direct-bandgap III-V semiconductors are the promising candidate for realizing a practical and compact light source but not easy to integrated on silicon. Several methods, including flip-chip, bonding, transfer printing and direct epitaxy of III-V materials utilizing a buffer layer<sup>[5-8]</sup>, were explored to achieve this but all have their limitations. The novel nano-ridge engineering (NRE) technique<sup>[9-10]</sup> has been shown to enable the growth of high-quality III-V material directly on Si substrates without any buffer layer, and compared to other methods shows advantages in terms of device scalability, integration density and cost.

In our previous work, although the nano-ridge cavity with etching grating had been realized, the threshold of these devices were still high<sup>[1]</sup>. One of the reasons is that the etched structure caused the damage to InGaP passivation layer, which introduced more surface recombination centers. It is necessary to understand the non-radiative surface recombination mechanism and reduce the damage to passivation for improving laser performance further. Therefore, in this work, high-refractive-index, but ‘weak’ and small a-Si grating were deposited on the top of nano-ridge rather than etched grating inside nano-ridge. The design of a-Si grating considered the light interaction with grating and

more mode overlap with quantum wells into account, which contributed to form nano-ridge cavity with behaving low lasing turn-on.

## Experiment

### 1. GaAs nano-ridge epitaxial growth

The box-shaped nano-ridges with high crystal quality and large III/V material volume were grown by metal organic vapor phase epitaxy (MOVPE) on a silicon substrate containing narrow trenches patterned in a SiO<sub>2</sub> layer. The details of the epitaxy process can be found in previous reports<sup>[1,9-10]</sup>. Figure 1(a)-(b) give the image of the overall structure, the InGaAs quantum wells inside nano-ridge and the trench part of the nano-ridge<sup>[1]</sup>. Figure 1(c) shows that the oxide sidewall effectively blocks threading dislocations, avoiding extension of these defects into the large III/V material volume above the trench, as shown in Figure 1(b). Figure 1(d) and (e) show a top-view of nano-ridges with different sizes and a cross-section view of a nano-ridge with 60 nm trench size (485 nm-high and 411 nm-width nano-ridge). All of the nano-ridges in these two figures were used to design nano-ridge lasers with a top a-Si grating. The basic transverse electric (TE)-like mode in a 485 nm-high nano-ridge without and with a-Si grating on the top are given in figure 1(f) and (g). Both TE modes exhibit high confinement and negligible substrate leakage loss, 0.46 dB/cm and 0.21 dB/cm, respectively. This low substrate leakage loss contributes to a low-optical-pumping-threshold.

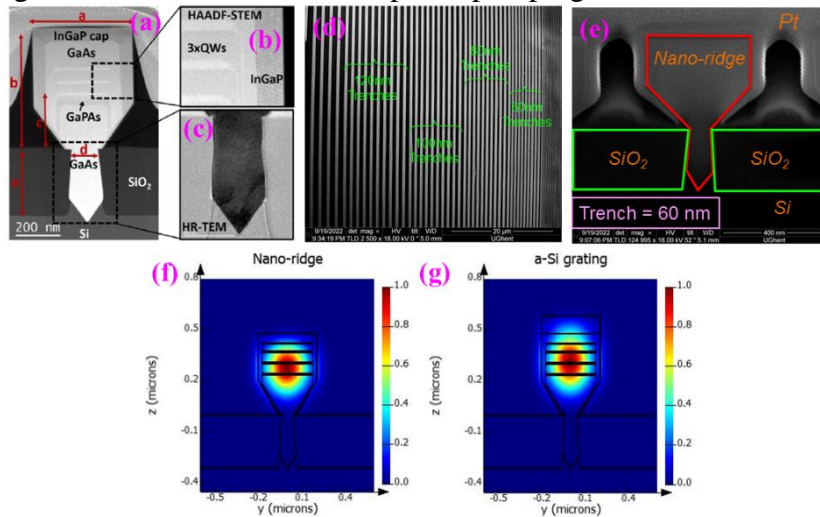


Figure 1(a) The HAADF-STEM image of nano-ridge structure from reference [1]. (b) Zoomed-in HAADF-STEM image of the quantum wells part in (a). (c) The HR-TEM image of the trench region from reference [1]. (d) Top view SEM image of nano-ridge array with trench width from 60 nm to 120 nm. (e) Cross-section SEM image of 485 nm-high nano-ridge (with 60 nm trench width). The basic transverse electric (TE)-like mode in a 485 nm-high nano-ridge without (f) and with (g) a-Si grating on the top.

### 2. Photoluminescence and fabrication process

The material quality of the nano-ridge was characterized by photoluminescence measurements at the room temperature. The nano-ridges were excited by a 532 nm continuous-wave (CW) solid state diode laser (MGL-FN-532-1.5W model, Changchun New Industries Optoelectronics Technology Co., Ltd). The emission from the nano-ridges was collected and detected with a monochromator (Oriel MS257 1/4m, Newport) and a thermo-electric-cooled InGaAs detector (Oriel, 70328NS model, Newport). Figure 2(a) presents the normalized photoluminescence spectrum from nano-ridges with

different trench sizes under  $4.20 \text{ W/cm}^2$  pumping power density. The photoluminescence spectrum contains a broad peak extending from 1000 nm to 1060 nm.

After optimizing the trade-off between light interaction with the a-Si grating on the top of nano-ridge and mode confinement in quantum wells with a 3D-finite difference time domain (3D-FDTD) solver, the 100 nm a-Si thin film was deposited on nano-ridge chips by plasma-enhanced chemical vapor deposition (Advanced Vacuum Vision 310 PECVD, Plasma-Therm) after acetone, isopropyl alcohol (IPA) and DI water cleaning. Due to the reaction between the a-Si layer and the developer (AZ400K:DI water = 1:3) of hydrogen silsesquioxane resist (HSQ, Dow Corning),  $\sim 50 \text{ nm}$  cured benzocyclobutene (BCB) was added as protection layer before  $\sim 150 \text{ nm}$  HSQ resist spin coating and the electron beam lithography (EBL, Voyager, Raith). Then, 800 grating periods in total were patterned into HSQ resist after EBL and the development. The patterned structures were transferred from HSQ resist to the a-Si layer by reactive-ion etching of the BCB layer and the a-Si layer with  $\text{SF}_6/\text{O}_2$  and  $\text{CF}_4/\text{H}_2/\text{SF}_6$ , respectively. The successfully fabricated devices, including a 200-period second-order grating added at one side to couple light out, are shown in Figure 2(b). Figure 2(c) present zoomed-in tilted scanning electron microscope (SEM) images. Figure 2(d) shows the vertical sidewall and smooth surface of the a-Si grating, which benefits the low-optical-pumping-threshold.

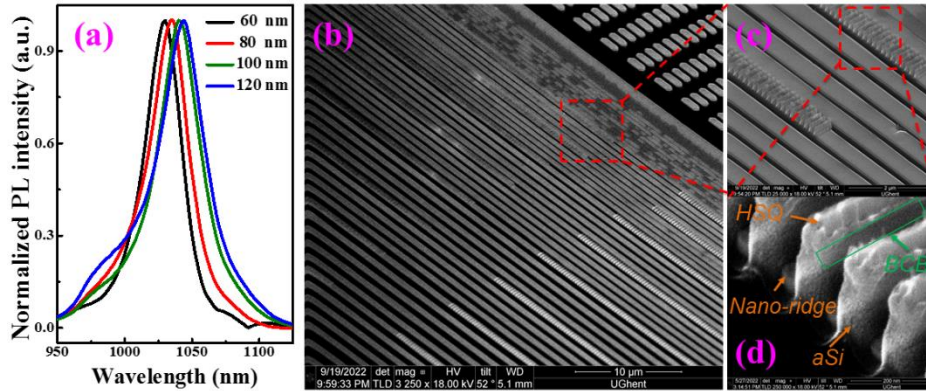


Figure 2(a) Normalized room-temperature photoluminescence spectra of nano-ridges with different trench widths. (b) Tilted SEM image of all DFB lasers with different trench sizes. (c) Zoomed-in tilted SEM image of DFB laser with 60 nm trench size. (d) Zoomed-in tilted SEM image of a-Si grating on the top of 485 nm-high nano-ridge (with 60 nm trench size).

## Results and discussion

The devices were excited by a Nd:YAG 532-nm nanosecond pulsed laser (7 ns pulse width, 938 HZ repetition rate, NL200 series laser, EKSPLA, Lithuania) at room temperature. The emission from the devices was collected and detected with the same monochromator and InGaAs detector, as mentioned before. Figure 3(a) shows a microscope picture of a full array of devices excited simultaneously by a  $200 \mu\text{m}$ -radius pump spot. For single device characterization, a rectangle slit was utilized to control the pump spot size, as presented in Figure 3(b). Figure 3(c) shows the photoluminescence spectrum of the DFB laser based on 485 nm-high nano-ridges, 100 nm-high a-Si grating and 165 nm a-Si grating period under different 532nm pulsed pumping power densities. The 1028 nm lasing peak becomes apparent when the pumping density reaches  $11 \text{ kW/cm}^2$  and the peak intensity increases strongly with the further increase of the pumping density. At the pumping power density of  $61 \text{ kW/cm}^2$ , the lasing peak reaches more than 22 dB side-mode suppression ratio, demonstrating excellent laser performance. The line width of the laser is 4.5 nm, limited by the input slit width setting. A clear change of slope

in the light in (pumping power density) - light out (integrated photoluminescence intensity) curve on linear and logarithmic (inset) scale from the same DFB laser illustrates lasing turn-on behavior, as shown in Figure 3(d). Figure 3(e) shows the photoluminescence spectrum of the DFB laser based on nano-ridges with 120 nm trench size (539 nm-high and 582 nm-width nano-ridge), 100 nm-high a-Si grating and 161 nm a-Si grating period under 2.8 kW/cm<sup>2</sup> pulsed pumping power density and the 1044 nm lasing peak appears. This threshold value is more than 10 times smaller than that reported earlier<sup>[1]</sup>. This is because the a-Si grating deposited on the top of nano-ridge avoids any damage to the InGaP surface passivation layer and does not induce surface recombination centers during the etching process.

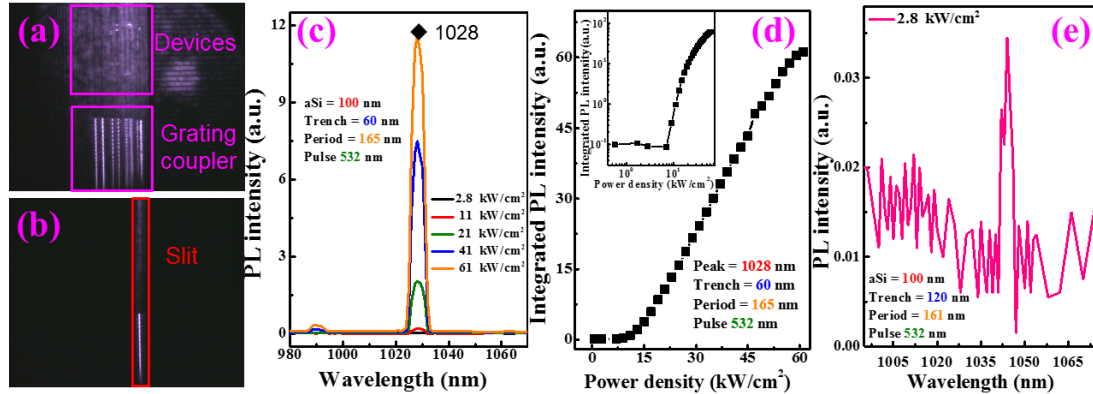


Figure 3(a) The image of all excited DFB laser with different trench sizes under 532 nm pulsed pumping. (b) The image of one excited DFB laser with slit under 532 nm pulsed pumping. (c) Photoluminescence spectrum from the DFB laser with 60 nm trench size under different 532 nm pulsed pumping densities. (d) Light in -Light out curve on linear and logarithmic (inset) scale of the DFB laser with 60 nm trench size. (e) Photoluminescence spectrum from the DFB laser with 120 nm trench size under 2.8 kW/cm<sup>2</sup> pulsed pumping density.

## Conclusion

In conclusion, in order to achieve low-optical-pumping-threshold nano-ridge laser monolithically grown on a standard 300-mm Si wafer, 100nm-high a-Si grating was deposited on the top of nano-ridge. Room temperature measurement shows clear laser operation with a side-mode-suppression ratio better than 22 dB side-mode suppression ratio and 2.8 kW/cm<sup>2</sup> lasing threshold. This lasing threshold is more than 10 times smaller than DFB laser with etched grating, which is ascribed to a-Si grating deposition on the top avoiding damaging InGaP passivation cladding and introducing more surface recombination paths. This low-optical-pumping-threshold nano-ridge laser demonstration proves high quality of the III-V-on-silicon epitaxial material again and open up the road towards achieving high-performance electrically-driven devices.

## Acknowledgment

This project has received funding from the European Union's Horizon 2020 research and innovation programme under grant agreement No. 884963 (ERC AdG NARIOS) and China Scholarship Council.

## References

- [1] Y. Shi, Z. Wang, J.V. Campenhout, et al, "Optical pumped InGaAs/GaAs nano-ridge laser epitaxially grown on a standard 300-mm Si wafer", *Optica*, vol. 4, 1468-1473, 2017.

- [2] R. Marchetti, C. Lacava, A. Khokhar, et al, "High-efficiency grating-couplers: demonstration of a new design strategy", *Scientific Report*, vol. 7, 16670:1-8, 2017.
- [3] N. Youngblood, C. Chen, S. J. Koester and M. Li, "Waveguide-integrated black phosphorus photodetector with high responsivity and low dark current", *Nature Photonics*, vol. 9, 247-252, 2015.
- [4] Y. Terada, K. Kondo, R. Abe and T. Baba, "Full C-band Si photonic crystal waveguide modulator", *Optics Letter*, vol. 42, 5110-5112, 2017.
- [5] H. Lu, J. Lee, Y. Zhao et al, "Flip-chip integration of tilted VCSELs onto a silicon photonic integrated circuit", *Optics Express*, vol. 42, 5110-5112, 2017.
- [6] M. R. Billah, M. Blaicher, T. Hoose, et al, "Hybrid integration of silicon photonics circuits and InP lasers by photonic wire bonding", *Optica*, vol. 5, 876-883, 2018.
- [7] J. Zhang, G. Muliuk, J. Juvert, et al, "III-V-on-Si photonic integrated circuits realized using micro-transfer-printing", *APL Photonics*, vol. 4, 11803:1-10, 2019.
- [8] J. Yang, P. Jurczak, F. Cui, et al, "Thin Ge buffer layer on silicon for integration of III-V on silicon", *Journal of crystal growth*, vol. 514, 109-113, 2019.
- [9] B. Kunert, W. Guo, Y. Mols, et al, "Integration of III/V Hetero-Structures by Selective Area Growth on Si for Nano- and Optoelectronics", *ECS Transactions*, vol. 35, 679-681, 2010.
- [10] B. Kunert, R. Alcotte, Y. Mols, et al, "Application of an Sb Surfactant in InGaAs Nano-ridge Engineering on 300 mm Silicon Substrates", *Crystal Growth and Design*, vol. 21, 1657-1665, 2021.
- [11] D. Colucci, M. Barysgbujiva, Y. Shi, et al, "Unique design approach to realize an O-band laser monolithically integrated on 300mm Si substrate by nano-ridge engineering", *Optics Express*, vol. 30, 13510-13521, 2021.

# Fiber-tip electric field sensors based on semiconductor photonic crystals

L.Picelli,<sup>1</sup> P.J. van Veldhoven,<sup>1</sup> E. Verhagen<sup>1,2</sup> and A.Fiore<sup>1</sup>

<sup>1</sup> Department of Applied Physics and Eindhoven Hendrik Casimir Institute, Eindhoven University of Technology, PO Box 513, 5600 MB, Eindhoven, The Netherlands

<sup>2</sup> Center for Nanophotonics, AMOLF, Science Park 104, 1098 XG Amsterdam, The Netherlands

*Sensors based on the measurement of electric field or voltage are commonly used in a wide variety of applications. Use of these devices in harsh environments and remote locations is limited by the need for electrical cables. In this work we show the possibility of transducing electric field to an optical signal in a fiber with a semiconductor-based fiber-tip device. A thin InP membrane is embedded with a photonic crystal, with resonance wavelength in the near-infrared, and transferred to the cleaved facet of an optical fiber. The fiber-tip device is immersed in a frequency-modulated electric field. Through the Pockels effect, this leads to a change in the resonant wavelength, which can be sensed via the fiber using a probe laser tuned at the side of the resonance. We describe the theoretical modeling of the electro-optic effect in a photonic crystal. We validate the model by comparison of finite-element simulations with experiments. We suggest the application of the electric field sensor to the optical interrogation of electrical circuits.*

## Introduction

The importance of sensors in modern technology has rapidly increased over the course of the last decades. They are used in a large variety of devices and applications [1]. Most of the developed sensors are based on electrical circuits. Their metallic contacts and the electrical wiring, required to read them out, leads to signal loss over long distances and to electromagnetic interference and makes them incompatible with high temperatures and extreme environments. Optical fiber sensors (e.g. fiber Bragg gratings, FBGs) do not suffer from these drawbacks and are applied in different fields[2]. Fiber-tip sensors have also been widely explored as they have the additional advantage of very small footprint, direct contact with the surrounding medium, and large freedom in sensor design [3,4]. We have previously demonstrated the possibility of fabricating the sensing element with a wafer-scale semiconductor process and then easily transfer it to the optical fiber facet [5]. These fiber sensors are limited by the relatively small response (wavelength shift) to external stimuli and high cost of the interrogation system needed to measure it. Electrical sensors, instead, typically display a large relative change of an electrical parameter (e.g. resistance) to an external stimulus. It would thus be convenient to develop a platform which combines electrical sensing and optical read-out via a fiber. This can be done with a fiber-tip structure which transduces voltage to a change in the reflectance, easily detectable with a fixed-wavelength interrogation set-up. This could be achieved by exploiting the electro-optic effect, already used to realize fiber-tip electric field sensors with a LiNbO<sub>3</sub> photonic crystal slab [6]. In this work we focus on determining the electric field response of a fiber-tip device based on an InP photonic crystal slab using the electro-optic effect. This is a first step towards the development of the proposed platform. In fact, this semiconductor (differently from LiNbO<sub>3</sub>) can be easily doped to realize p-n and p-i-n junctions, which can act as current sources upon illumination with visible light. The

combination of current generation and voltage read-out could be used as a basis for an optically-interrogated fiber-tip electrical sensor.

### Electro-optic effect in a photonic crystal

The proposed sensor is based on the Pockels effect, a nonlinear (second-order) optical phenomenon in which a static, or low-frequency, electric field ( $E$ ) causes the change of the refractive index ( $n$ ) of the material [7]. The effect is determined by the linear electro-optic tensor of the material  $r_{hk}$  where  $k$  indicates the direction of the field (1, 2, 3 or  $X$ ,  $Y$ ,  $Z$ ) and  $h$  indicates the directions in which the refractive index is modified (1-6, where 4, 5, 6 represent  $XY$ ,  $XZ$  and  $YZ$  directions). The crystalline structure of the material strongly influences which elements of the tensor are non-null. Only non-centrosymmetric materials such as  $\text{LiNbO}_3$  and  $\text{InP}$  exhibit the effect. For  $\text{InP}$  only terms  $r_{41} = r_{52} = r_{63}$  are non-null. The application of a field along one of the main crystal axis (e.g.  $Z$ ) causes a rotation of the two perpendicular optical axes by  $45^\circ$  with respect to the crystallographic axes, and the change of refractive index along these new directions ( $x$  and  $y$ ) according to  $n_{x,y} = n_0 \pm \frac{1}{2} n_0^3 r_{41} E_Z$ . To study the interaction of the electro-optic effect with the photonic crystal (PhC) we adopt a perturbative approach [8] to determine the change in resonance wavelength caused by the field. In the rotated reference frame ( $x, y, Z$ ) the permittivity tensor of the material is diagonal, and  $\epsilon_{x,y} = n_{x,y}^2$  (where  $\epsilon_{x,y}, n_{x,y}$  are real since in the wavelength region of our interest the material can be considered non-absorptive). We write the wavelength perturbation as

$$\delta\lambda = -\frac{\lambda_0 \int \left( |\mathcal{E}_x(\mathbf{r})|^2 - |\mathcal{E}_y(\mathbf{r})|^2 \right) n_0^4 r_{41} E_Z(\mathbf{r}) d\mathbf{r}}{2 \int \epsilon(\mathbf{r}) |\mathcal{E}(\mathbf{r})|^2 d\mathbf{r}}, \quad (1)$$

where  $\lambda_0$  is the unperturbed wavelength,  $\mathcal{E}_{x,y}$  are the in-plane components of the electric field of the PhC mode in the rotated reference frame and we neglected a small second-order term. From Eq.1 it is evident that the perturbation depends on the difference between the magnitudes of the mode electric field components in the rotated frame. To efficiently exploit the electro-optic effect in a photonic crystal sensor, it is necessary to define a mode with a strong polarisation asymmetry. For this reason, we used a photonic crystal slab (thickness of 250 nm) characterized by a rectangular unit cell. This geometry presents a mode which is strongly polarized (Fig. 1a), making it sensitive to the applied field. In addition, the mode is isolated from other spectral features and can effectively couple to the optical fiber [5]. The rectangular unit cell is obtained by shifting every other hole of a square lattice (lattice constant  $a=350$  nm, hole radius  $r=126$  nm) by a small quantity ( $s=17.5$  nm) in each row. To determine the electro-optic response of the proposed device, a photonic crystal with the described design was fabricated on a  $\text{InP}$  membrane and transferred to the tip of an optical fiber tip (Fig 1b,c), using the method described in Ref. 5. Light from a tunable infrared (IR) laser is directed to the device through a circulator and a polarization controller. The circulator directs the reflected light to an  $\text{InGaAs}$  amplified detector. The voltage output of the detector is measured with a digital multimeter and an electrical spectrum analyzer (ESA). To apply the electric field, the fiber-tip device is positioned halfway the 5 mm air gap ( $\Delta z$ ) between two metal plates (lateral dimensions 10 cm x 10 cm), perpendicularly to them. A sinusoidal AC voltage is applied to the plates using a resonant high-voltage source which can apply  $\sim 230 V_{p-p}$  at a frequency  $\sim 53$ -55 kHz. The applied external field is calculated as  $E = V_{p-p}/\Delta z \approx 46$  kV/m. The measurement principle is represented in Figure 2a.

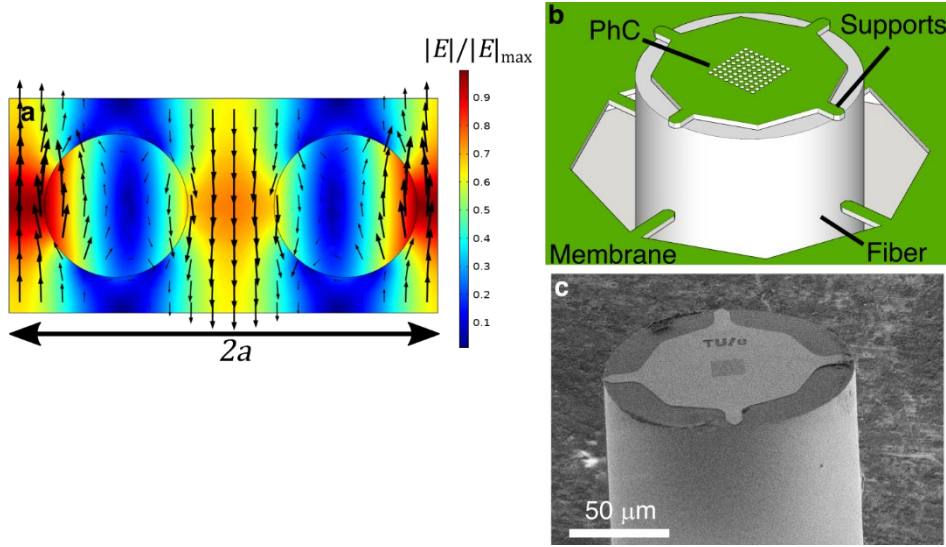


Figure 1: (a) Mode field profile for the studied rectangular cell photonic crystal. Arrows indicate field lines, color scale indicates normalized amplitude. (b) Sketch illustrating the transfer process and sensor geometry. (c) SEM image of the assembled fiber-tip sensor.

The oscillating field shifts the resonance wavelength by  $\Delta\lambda$  causing a change in the reflected power (change in the detector output voltage  $\Delta V$ ) at the fixed probe laser wavelength  $\lambda_L$  ( $\sim 1.54 \mu\text{m}$ ). The modulated signal can be detected and resolved with the ESA and converted into the wavelength shift spectral density ( $S_{\lambda\lambda}$ ) knowing the slope of the resonance ( $110 \pm 7 \text{ mV/nm}$  for  $0.45 \text{ mW}$  of incident optical power). Figure 2b shows the response of a fiber-tip device with the photonic crystal designed to maximize the electro-optic response (black solid line) and one with the crystal rotated by  $45^\circ$  respect to the optical axis (red dashed line). The correctly oriented crystal shows a strong response to the applied electric field. From the integration of the peak in the ESA spectrum we calculate the peak-peak wavelength perturbation to be  $\delta\lambda_{exp} = (3.8 \pm 0.4) \cdot 10^{-5} \text{ nm}$ , corresponding to an electric field sensitivity of  $(8.3 \pm 0.9) \cdot 10^{-10} \text{ nm/(V/m)}$  (referred to the field in air between the electrodes). The  $45^\circ$  rotated crystal still shows small response, which we attribute to the imprecision in the orientation of the crystal during the fabrication process. Due to the presence of the PhC,  $E_z$  in Eq. 1 is not uniform in the slab and the theoretical value of the wavelength shift must be calculated using finite elements method simulations. This is done by including the effect of the field in an eigenfrequency simulation of an infinite PhC to determine the perturbed mode wavelength. The effect of the fiber in the spatial distribution of the electric field within the plates is taken into account in the estimation of the static electric field in the PhC membrane. We determine a wavelength change of  $\delta\lambda_{sim} = 9.7 \cdot 10^{-5} \text{ nm}$ , which is in the same range, but a factor 2.5 higher than the experimental value. We attribute the discrepancy to the uncertainty in the estimation of electric field at the fiber position, sub-optimal orientation of the crystal and imprecise knowledge of the material refractive index. From the noise observed in Fig.2b ( $\sqrt{S_{\lambda\lambda}^N} \sim 8 \cdot 10^{-7} \text{ nm}/\sqrt{\text{Hz}}$ ) and the sensitivity, we estimate the external electric field measurement imprecision to be  $\sim 1 \text{ kV}/(\text{m}\sqrt{\text{Hz}})$ . This value is higher than the sensor reported in Ref.6 due to the 30 times smaller electro-optic coefficient of InP ( $r_{41} = -1.63 \text{ pm/V}$  [9]). Despite this drawback, the fact that p-i-n junctions are easily realized in InP, and the relatively large internal fields are generated by small voltages in the junction, makes this interrogation scheme viable for the measurement of voltages across a fiber-tip electrical device.

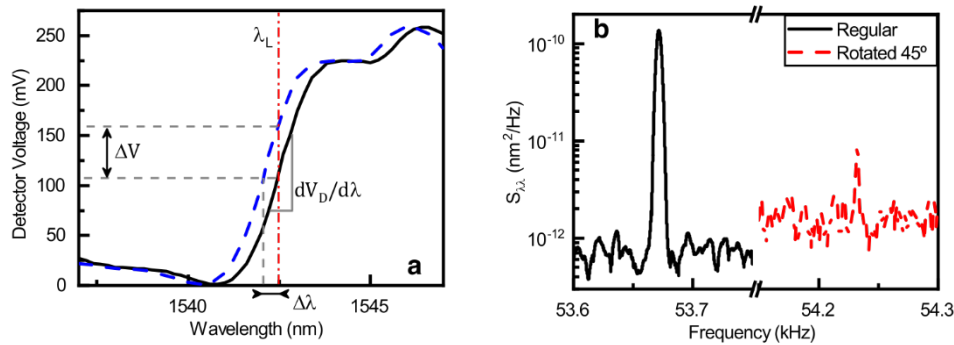


Figure 2 : (a) Optical spectrum of the photonic crystal (black curve). The blue dashed curve is artificially shifted to illustrate the fixed wavelength detection scheme. The interrogation laser is set at wavelength  $\lambda_L$  (red dot-dashed line). The incident optical power is 0.45 mW. (b) Frequency response of fiber-tip devices immersed in the AC electric field. The crystal aligned to the rotated optical axes (black solid line) is compared to a crystal rotated 45° around its center (red dashed line). The incident optical power on the device is 0.45 mW for both devices, the measurement bandwidth is 5 Hz (regular) and 3 Hz (rotated).

## Conclusions

We showed the possibility to optically sense an electric field with a semiconductor InP photonic crystal membrane using a fixed-wavelength optical interrogation system. We obtain field imprecision of  $1 \text{ kV}/(\text{m}\sqrt{\text{Hz}})$ . We propose the combination of this detection scheme, based on the Pockels effect, with a p-i-n junction embedded on a membrane of the same thickness where small voltages in mV range produce internal fields in the order of 10 kV/m. This approach would therefore allow the optical detection of the photovoltage generated across the junction by absorption of visible light. When combined with resistors or other electrical components integrated on the fiber tip, it opens the way to the optical read-out of electrical sensors.

## Acknowledgements

We thank T.Huiskamp and R.Serra (TU/e) for the help in the realization of the electric field measurement set-up. This work was funded by the NWO Zwaartekracht Research Center for Integrated Nanophotonics.

## References

- [1] M. Alam, M. M. Tehranipoor, and U. Guin, "TSensors Vision, Infrastructure and Security Challenges in Trillion Sensor Era," *J. Hardw. Syst. Secur.*, vol. 1, no. 4, pp. 311–327, Dec. 2017.
- [2] M. A. Riza, Y. I. Go, S. W. Harun, and R. R. J. Maier, "FBG Sensors for Environmental and Biochemical Applications - A Review," *IEEE Sens. J.*, vol. 20, no. 14, pp. 7614–7627, 2020.
- [3] G. Kostovski, P. R. Stoddart, and A. Mitchell, "The optical fiber tip: An inherently light-coupled microscopic platform for micro- and nanotechnologies," *Adv. Mater.*, vol. 26, no. 23, pp. 3798–3820, 2014.
- [4] P. Vaiano *et al.*, "Lab on Fiber Technology for biological sensing applications," *Laser Photonics Rev.*, vol. 10, no. 6, pp. 922–961, 2016.
- [5] L. Picelli *et al.*, "Scalable wafer-to-fiber transfer method for lab-on-fiber sensing," *Appl. Phys. Lett.*, vol. 117, no. 15, 2020.
- [6] V. Calero *et al.*, "An ultra wideband-high spatial resolution-compact electric field sensor based on Lab-on-Fiber technology," *Sci. Rep.*, vol. 9, no. 1, p. 8058, 2019.
- [7] J. Coutaz and L. Duvillaret, "Electro-optic sensors for electric field measurements. II. Choice of the crystals and complete optimization of their orientation'," vol. 19, no. 11, pp. 2704–2715, 2002.
- [8] J. Bravo-Abad, S. Fan, S. G. Johnson, J. D. Joannopoulos, and M. Soljačić, "Modeling nonlinear optical phenomena in nanophotonics," *J. Light. Technol.*, vol. 25, no. 9, pp. 2539–2546, 2007.
- [9] N. Suzuki and K. Tada, "Electrooptic Properties and Raman Scattering in InP," *Jpn. J. Appl. Phys.*, vol. 23, no. 3, pp. 291–295, 1984.

# Design of a 32Gbit/s O-band high sensitivity receiver

Senbiao Qin,<sup>1,2</sup> Laurens Bogaert,<sup>1,2</sup> and Gunther Roelkens<sup>1,2</sup>

<sup>1</sup> Photonics Research Group, INTEC, Ghent University - imec, Ghent, Belgium

<sup>2</sup> Center for Nano- and Biophotonics, Ghent University - imec, Ghent, Belgium

*We propose a receiver design to achieve high sensitivity by minimizing the capacitance and improving the responsivity. Through micro-transfer printing, the trans-impedance amplifier can be compactly integrated side by side with the photodiode, which can significantly reduce the capacitance of the connection between the two. The interconnect capacitance can be as low as 9.6 fF with a connection length of 150  $\mu\text{m}$  taken into consideration. A short grating coupler with a length of 5  $\mu\text{m}$  and an efficiency of 80% is also designed on the imec SiN platform to support a small surface illuminated photodiode with an area of 30  $\mu\text{m}^2$  and junction capacitance of 4.5 fF. Aiming at 32 Gbit/s non-return-to-zero On-Off keying in the O-band, the InGaAs absorption layer thickness is optimized to be 0.85  $\mu\text{m}$ , corresponding to a responsivity of 0.69 A/W. Implementation of a partially doped absorption layer can further enhance the photodiode for higher responsivity.*

## Introduction

From long-haul fiber links to on-chip photonics interconnection, optical systems are calling for a highly power-efficient solution. The SiN PIC platform is known for its low-loss waveguides, broad transparency window and absence of two-photon absorption in the telecom wavelength range, attracting lots of attention in the fields of optical interconnect, sensing, non-linear optics, etc. To realize fully integrated circuits on this platform, active components should be integrated onto it. Micro transfer printing is an emerging solution, by which a series of laser [1] and photodetector [2] integration on Si or SiN platforms have been demonstrated.

Optical receiver noise typically comes from the feedback resistor and feedback amplifier of the TIA front-end. The receiver sensitivity can be considerably improved by reducing the input capacitance for a low TIA input referred noise. In this paper, we present a high-sensitivity receiver design, including an InGaAs photodiode coupon and a SiGe BiCMOS trans-impedance amplifier coupon. The micro transfer printing of the SiGe BiCMOS electronic integrated circuits has recently been developed by X-Celeprint [3], which provides an excellent opportunity to bring the TIA chiplet close to the PD coupon, leading to an ultra-low interconnect capacitance and high sensitivity. A short grating coupler is also implemented to minimize the photodiode dimension to reduce the junction capacitance. In addition, the responsivity improvement of implementing a partially doped InGaAs absorption layer is also evaluated.

## Receiver design

Figure 1a shows the schematic of the high-sensitivity receiver. Both the InGaAs photodiode coupon and the SiGe BiCMOS trans-impedance amplifier coupon can be integrated on the imec SiN photonics platform by micro-transfer printing. Thus, a compact layout is realized to minimize the capacitance from the metal leads. Spray-coated DVS-BCB helps to planarize the  $\sim 15$   $\mu\text{m}$  height difference between the TIA coupon and the PD coupon for the metal connection. Figure 1b is a detailed schematic of the surface-illuminated photodiode. The optical power is coupled from the SiN waveguide to the PD

coupon by a grating coupler. The dimensions of the PD coupon and the grating coupler are limited to reduce the junction capacitance of the photodiode. An additional aSi layer is implemented to increase the grating coupler strength to achieve a short coupling length with a decent coupling efficiency. The absorption InGaAs layer is partially doped, containing an intrinsic layer and another p-doped layer, which can boost the photodiode to a higher responsivity under a certain bandwidth requirement. When the p-doped InGaAs absorption layer thickness is set to zero, the layer stack returns to a normal p-i-n case.

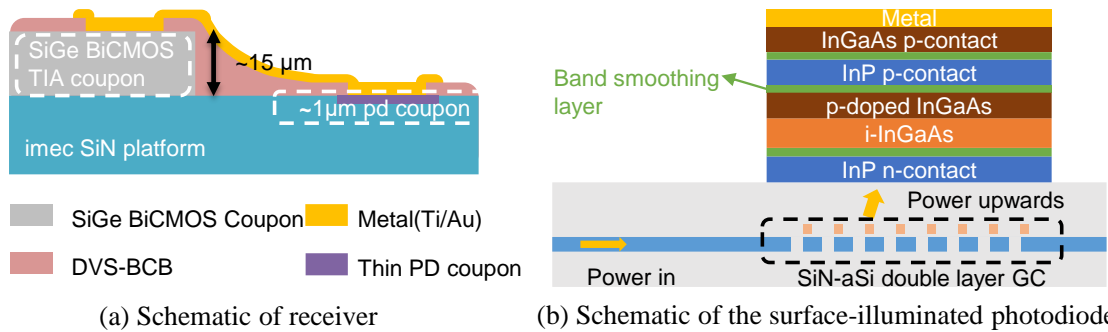


Figure 1: Plots of a) schematic of the high sensitivity receiver with SiGe BiCMOS trans-impedance amplifier coupon and InGaAs photodiode coupon transfer printed on imec SiN platform and b) schematic of the surface-illuminated photodiode containing 5 μm length SiN-aSi double layer grating coupler and a partially doped InGaAs absorption layer

## Capacitance and responsivity optimization

The capacitance introduced by the taper metal connection between the PD and TIA pads is studied as shown in figure 2a and 2b. In figure 2a, the dimension of the PD side GSG pads is 5 μm × 6 μm with 1 μm gap, while for the TIA side it is 10 μm × 10 μm with 10 μm gap. The metal connection is a taper structure, whose length varies from 5 μm to 150 μm. Figure 2b gives the simulated taper capacitance as a function of the taper length. Considering a taper length of 150 μm, which should be a relatively relaxed condition for processing, the taper capacitance is still only 9.6 fF.

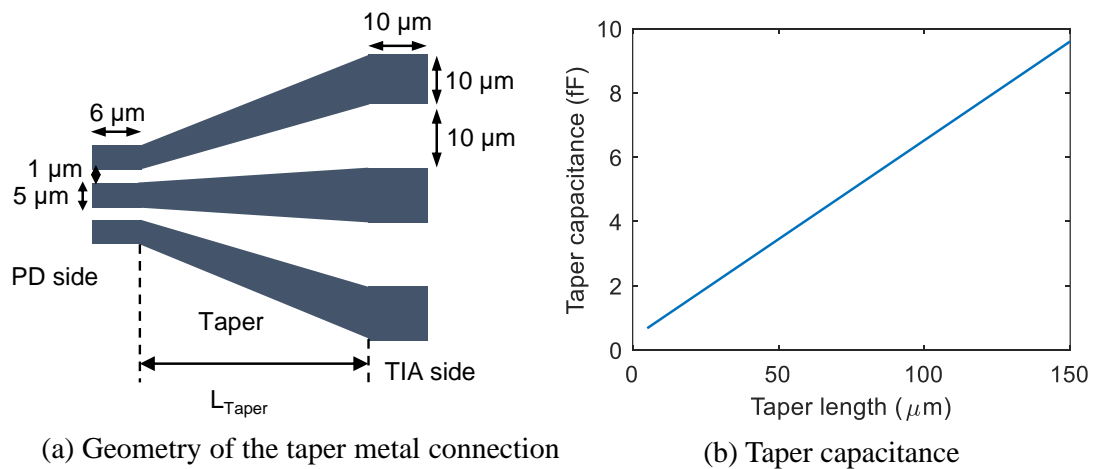


Figure 2: Plots of a) schematic of PD and TIA sides GSG pads and the taper metal connection and b) taper capacitance when the taper length is changed from 5 - 150 μm

Junction capacitance, mainly determined by the geometric dimensions of the photodiode, also contributes to the total capacitance of the receiver. With the implementation of a short grating coupler, the PD length can be considerably limited, as well as the junction capacitance. As shown in figure 3a, the grating coupler is designed based on the imec 400 nm SiN photonics platform, which includes another 330 nm aSi layer. The grating pitch is 617 nm, with a SiN tooth width of 430 nm and an aSi tooth width of 147 nm. The coupling efficiency of this grating coupler is presented in figure 2b. A 5- $\mu\text{m}$  grating coupler with 8 periods can provide a coupling efficiency of 80% at a wavelength of 1.3  $\mu\text{m}$ . Using a thick InGaAs absorption layer can also reduce the junction capacitance. Figure 3c shows the bandwidth for different p-i-n type mesa sizes, compared with the transit-limited bandwidth. When the InGaAs layer is thicker than 0.6  $\mu\text{m}$ , the carrier transit time becomes the dominant factor. For this p-i-n photodiode, the maximum thickness of the InGaAs layer is 0.85  $\mu\text{m}$  due to the bandwidth requirement of 25 GHz for 32 Gbit/s. The simulation result of the junction capacitance as a function of InGaAs layer thickness is in figure 3d. Considering a small photodiode with an area of 30  $\mu\text{m}^2$ , the minimum junction capacitance is 4.5 fF.

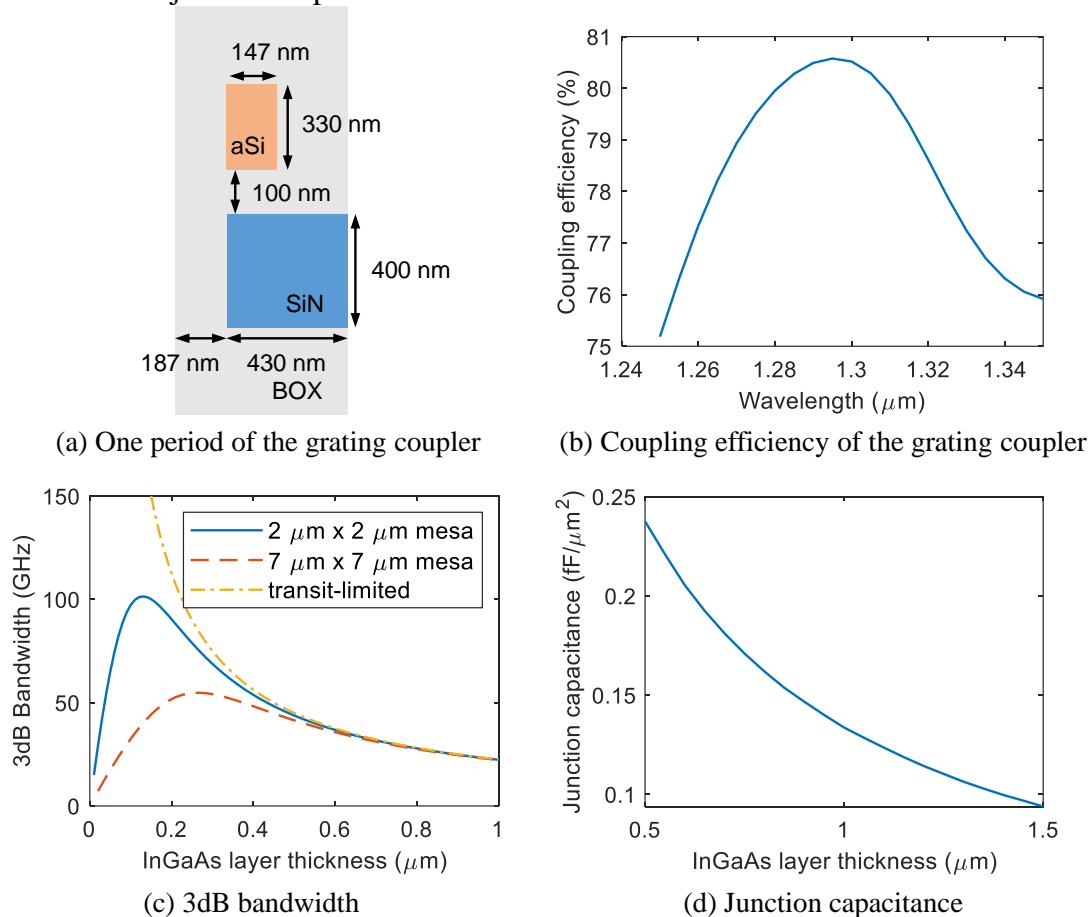


Figure 3: Plots of a) structural dimension of one period of the grating coupler, b) coupling efficiency as a function of wavelength, c) 3 dB bandwidth (assuming a 50 Ohm load) for 2  $\mu\text{m} \times 2 \mu\text{m}$  and 7  $\mu\text{m} \times 7 \mu\text{m}$  p-i-n type mesas when InGaAs layer thickness is changed and d) dependency of the InGaAs p-i-n photodiode junction capacitance on the InGaAs layer thickness

For the normal p-i-n photodiode with an InGaAs layer thickness of 0.85  $\mu\text{m}$ , the responsivity is 0.69 A/W. By implementing a partially p-doped InGaAs absorption layer, a 25 GHz bandwidth can be achieved with a thicker absorption layer thickness because neutral and depleted layers have different carrier transport mechanisms [4], which can further improve the photodiode to higher responsivity. As illustrated in figure 4a, the 1.90  $\mu\text{m}$  partially doped InGaAs absorption layer at the ratio of 0.47 has the same bandwidth as the 0.85  $\mu\text{m}$  intrinsic InGaAs absorption layer. In this case, according to the simulation results in figure 4b, the responsivity is enhanced to 0.78 A/W.

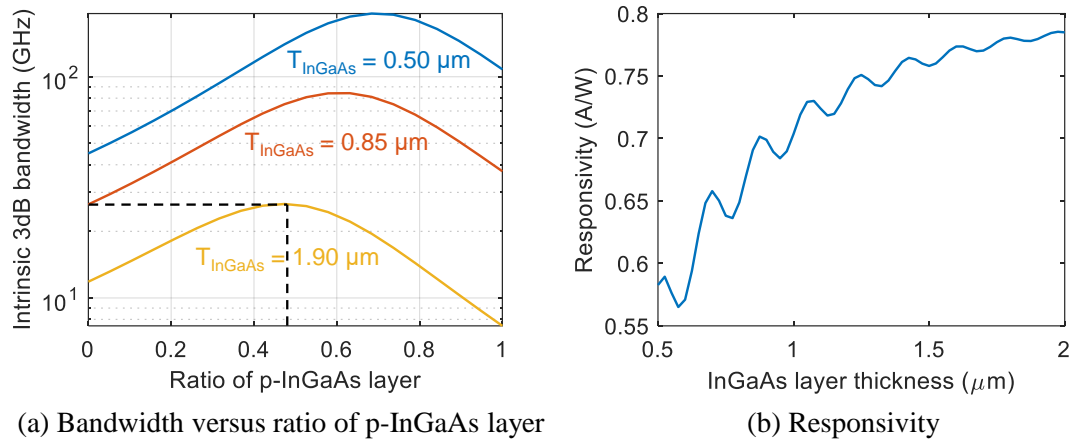


Figure 4: Plots of a) ratio of p-InGaAs layer dependence of bandwidth for different total InGaAs layer thicknesses and b) responsivity as a function of total InGaAs layer thickness

## Conclusions

We put forward a high-sensitivity receiver design. The trans-impedance amplifier and photodiode can be compactly integrated on imec SiN platform to realize a metal lead capacitance of 9.6 fF for the connection length of 150  $\mu\text{m}$ . The SiN-aSi double-layer grating coupler can provide a decent coupling efficiency of 80% within a length of 5  $\mu\text{m}$ , which can support a small surface-illuminated photodiode with an area of 30  $\mu\text{m}^2$  and junction capacitance of 4.5 fF. The adoption of a partially doped InGaAs layer helps increase the total absorption layer thickness from 0.85  $\mu\text{m}$  to 1.90  $\mu\text{m}$  while still meeting the 25 GHz bandwidth requirement. The corresponding responsivity is improved from 0.69 A/W to 0.78 A/W.

## References

- [1] E. Soltanian, G. Muliuk, S. Uvin, D. Wang, G. Lepage, P. Verheyen, J. Van Campenhout, S. Ertl, J. Rimbock, N. Vaissiere, D. Neel, J. Ramirez, J. Decobert, B. Kuyken, J. Zhang, and G. Roelkens, "Micro-Transfer-Printed Narrow-Linewidth III-V-on-Si Double Laser Structure with Combined 110 nm Tuning Range," *Optics Express*, vol. 30, 39329-39339, 2022.
- [2] S. Cuyvers, A. Hermans, M. Kiewiet, J. Goyvaerts, G. Roelkens, K. Van Gasse, D. Van Thourhout, and B. Kuyken, "Heterogeneous integration of Si photodiodes on silicon nitride for near-visible light detection," *Optics Letters*, vol. 47, 937-940, 2022.
- [3] R. Loi, P. Ramaswamy, A. Farrell, A. Jose Trindade, A. Fecioru, J. Rimböck, S. Ertl, M. Pantouvaki, G. Lepage, J. Van Campenhout, T. Pannier, Y. Gu, D. Gomez, P. Steglich and P. Ossieur, "Micro transfer printing of electronic integrated circuits on Silicon photonics substrates," in *Proceedings of the European Conference on Integrated Optics*, 2022.
- [4] M. Nada, H. Yokoyama, Y. Muramoto, T. Ishibashi, and H. Matsuzaki, "50-Gbit/s vertical illumination avalanche photodiode for 400-Gbit/s Ethernet systems," *Optics Express*, vol. 22, 14681-14687, 2014.

# An experimental demonstration of a passively mode-locked laser using an integrated graphene saturable absorber.

**T. Reep<sup>1,2,3</sup>, C. Wu<sup>1,2,3</sup>, E. Vissers<sup>1,2,3</sup>, S. Brems<sup>3</sup>, D. Yulistira<sup>3</sup>,  
J. Van Campenhout<sup>3</sup>, M. Pantouvaki<sup>3</sup>, D. Van Thourhout<sup>1,2,3</sup>, and B. Kuyken<sup>1,2,3</sup>**

<sup>1</sup>*Photonics Research Group, Department of Information Technology, Ghent University-IMEC, Gent B-9000, Belgium*

<sup>2</sup>*Center for Nano- and Biophotonics (NB-Photonics), Ghent University, Ghent, Belgium*

<sup>3</sup>*IMEC, Kapeldreef 75, 3001 Leuven, Belgium*

*Tom.Reep@UGent.be*

## Abstract

Graphene has many promising properties for use as a saturable absorber in mode-locked lasers, such as a low saturation power, a broad optical bandwidth and a fast carrier recombination time. Passively mode-locked lasers using graphene saturable absorbers have been demonstrated, but the graphene integration methods used require complex manufacturing steps and do not support mass-production of these devices. In this paper we demonstrate experimentally that an integrated graphene saturable absorber on a silicon waveguide can passively mode-lock a hybrid laser. This integrated graphene saturable absorber was manufactured on wafer-scale, demonstrating that this graphene integration approach is a reliable and scalable method for manufacturing graphene saturable absorber assemblies for both integrated and fibre based passively mode-locked lasers.

## I. INTRODUCTION

Mode-locked lasers generate optical pulse-trains which produce a large number of equally spaced laser lines locked together in phase and frequency. This type of laser is beneficial for many applications such as for telecom systems, gas spectroscopy and biomedical applications [1]–[3]. Optical pulses inside the cavity are formed through loss and/or gain modulation inside a laser cavity at an integer multiple of the roundtrip time [4]. This can be achieved either through active mode-locking, in which the loss or gain is electrically modulated resulting in pulses forming inside the cavity, or by using a passive mode-locking regime in which a saturable absorber (SA) modulates the loss inside the cavity.

Saturable absorption is a nonlinear effect where the optical transmission of a SA increases with an increase in optical power. A pulse passing through a SA saturates its absorption resulting in a short window where the loss inside the cavity is reduced, which in turn favours the pulse's propagation. There are various approaches to making saturable absorbers. The most common SA assemblies used in passively mode-locked lasers at the time of writing are based on semiconductor devices, with free-space, fibre and VCSEL mode-locked lasers often using semiconductor saturable absorber mirror assemblies (SESAM) [5] and integrated photonic circuits often using a reverse biased electrically isolated section of a III/V semiconductor amplifier [6]–[8]. These semiconductor based saturable absorbers have a limited optical operating bandwidth however, and reverse biased amplifiers have been reported having recovery times exceeding 2.5 ps which has been theorised to limit the achievable pulsewidth of mode-locked lasers [8][9]. This has motivated research to find new saturable absorber materials, one of which is graphene.

Since the exfoliation of graphene in 2004 [10], it was found that graphene has many promising properties for use as a saturable absorber, such as a broadband operating region (covering full IR and NIR bands), low saturation intensity, fast recovery times (around 200 fs) and a tunable modulation depth [11][12]. Initial experimental demonstrations of passively mode-locked lasers using graphene-based saturable absorbers used chemical vapour deposition (CVD) grown single- and few-layer graphene flakes on a fibre ferrule [11], and later single- and few-layer graphene-oxide flake composites [13]. A downside of these graphene integration methods is that light interacts with the graphene at a normal incidence, which due to the atomic thickness of graphene (0.7 nm) significantly limits the saturable modulation depth due to the short optical interaction length. This modulation depth can be increased by placing the graphene sheet in the evanescent tail and along the propagation direction of a propagating mode. This has been demonstrated through D-shaped and micro-fibres [14]–[16].

Graphene integrated on semiconductor waveguides works through the same principle, which is that a graphene sheet placed on top of an integrated waveguide interacts with the evanescent tail of the propagating mode. Using this approach integrated electro-absorption modulators (EAM) and photo-detectors have been demonstrated [17][18]. Advantages of the integration of graphene onto semiconductor waveguides are the scalability and manufacturing reproducibility as was demonstrated in the 300 mm fab at imec [19].

Graphene integrated on semiconductor waveguides has been experimentally demonstrated to have saturable absorption effects in both TE, TM and slot waveguides [20]–[23]. By adding a gate the chemical potential of graphene can be controlled resulting

in control over the insertion loss and saturable absorption depth [24][25]. However, to our knowledge, actual demonstrations of active or passive mode-locking using an integrated graphene saturable absorber have not yet been reported.

In this report, we experimentally demonstrate that an integrated single-layer graphene modulator can be used to passively mode-lock a hybrid laser. This graphene SA integration approach shows potential for reliable production of the SA devices on a wafer scale and the compatibility for use in fully integrated mode-locked lasers.

## II. GRAPHENE ASSEMBLY AND EXPERIMENTAL SETUP

The saturable absorber assembly used in our experiment was manufactured using imec's 220 nm thick silicon on 2  $\mu\text{m}$  BOX silicon photonics platform and the graphene integration was performed in a 300 mm fab using standard CMOS production tools. A schematic cross-section of the single-layer graphene saturable-absorber is shown in Figure 1a. The optical mode is confined in a planarised 500 nm wide socket waveguide and this silicon waveguide is used as a gate to electrically control the chemical potential of graphene. Three separate ion doping implantation steps were used to reduce the electrical resistance of this gate while keeping optical losses to a minimum. The graphene was electrically isolated from the gate by a 5nm thick SiOx layer. Graphene was CVD grown on a 6 inch wafer and transferred onto the patterned 300 mm silicon wafer by Graphenea, after which the graphene was encapsulated with a 30 nm thick ALD-AIOx layer. This graphene and AIOx stack was patterned by dry-etching using a SiOx hardmask. In order to contact the doped silicon and graphene, a 600 nm thick pre-metal dielectric was deposited in which via's were etched. A Ti/TiN/W stack was deposited followed by a Tungsten chemical mechanical polishing step. Finally the final metal layer was deposited through a Cu-oxidation step. A microscope photo showing the top of the silicon device is shown in Figure 1b. Coupling to and from a 50  $\mu\text{m}$  long SLG device is achieved through TE-optimised grating couplers, which are connected to the device through a total of 800  $\mu\text{m}$  long 450 nm wide silicon strip waveguides. More information on the manufacturing steps, EAM performance and wafer reliability can be found in ref. [19].

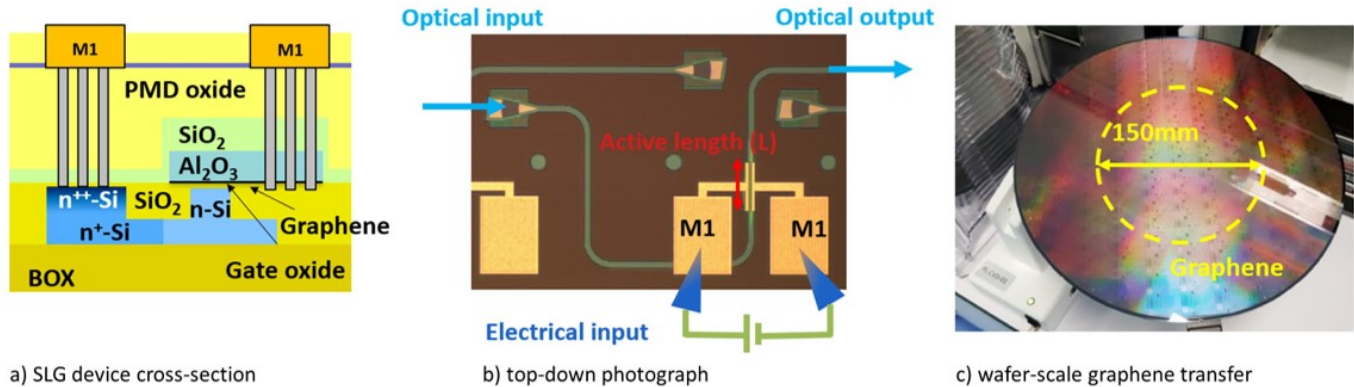


Fig. 1: The graphene saturable absorber assembly used for passive mode-locking [19]. Figure a) shows the schematic cross-section of the graphene modulator, Figure b) shows a top-down photograph of the device used as a saturable absorber. And Figure c) shows the 300mm patterned silicon wafer on which a 6 inch graphene sheet is placed.

A schematic setup of the mode-locked laser cavity used is shown in Figure 2. The cavity consists of an Opto-Link C-band EDFA having approximately 28 m of internal fibre with 27 dB of small-signal gain and an integrated internal isolator. After the EDFA an optical splitter is used to couple 10% of the light out of the cavity after which 90% is passed to a polarisation controller to couple light to the integrated silicon waveguides through a grating coupler having a 45 nm 3 dB bandwidth centered at 1560 nm. The graphene modulator is biased using a Keithley source measurement unit. The output of the integrated graphene modulator is passed back to the input of the EDFA completing the laser cavity. The output optical signal is measured on an Alphasas 25 GHz photodetector of which the electrical signal is split using a 3 dB splitter to simultaneously measure the electrical spectrum on an R&S electrical spectrum analyser (ESA) and the temporal response on a Keysight oscilloscope. The optical spectrum is measured with a Yokogawa AQ6310 optical spectrum analyser. In order to measure the optical pulsewidth the output from the laser is amplified by a second Opto-link CW-EDFA, after which the optical signal is measured using an APE autocorrelator.

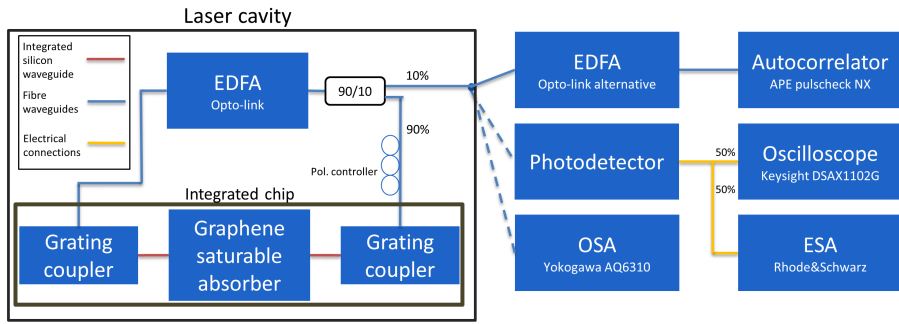
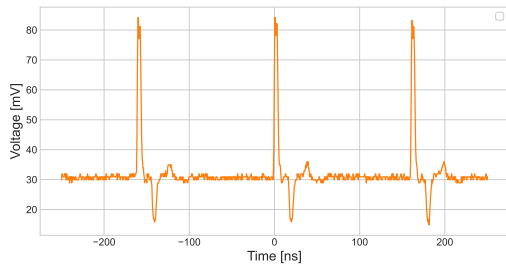
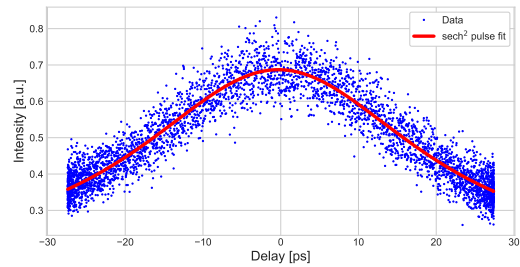


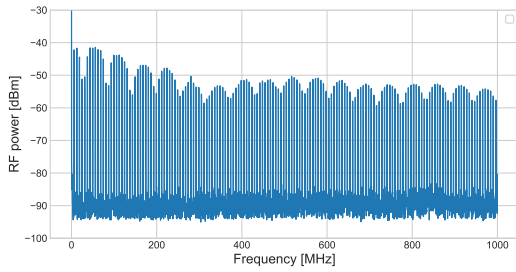
Fig. 2: Schematic of the experimental setup. The section in the black box indicates the laser cavity, and the section on the right the measurement equipment used



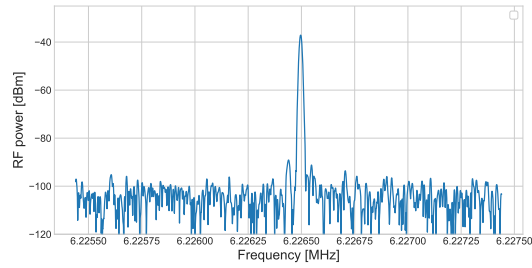
(a) Temporal pulsetrain measured using an oscilloscope



(b) Autocorrelation trace of the optical pulse after passing through an EDFA. The  $\text{sech}^2$  fit gives a FWHM pulsewidth of 26ps.



(c) RF spectrum of the ESA at a 10kHz BW.



(d) RF spectrum of the first harmonic, measured with a 10Hz bandwidth. The image shows a side-mode suppression ratio of 52dB.



(e) Optical spectrum of the mode-locked laser.

Fig. 3: Measurement results of the passive mode-locked laser result.

### III. RESULTS

The mode-locked laser described in section II passively mode-locks with a repetition rate of 6.23 MHz, which is consistent with the cavity length dominated by 28 m of fibre inside the EDFA. The temporal signal coming from the photo-detector

measured using an oscilloscope is shown in Figure 3a, which shows a stable pulse-train. The electrical spectrum measured using the ESA is shown in Figure 3c, which shows RF comb lines spaced by 6.23 MHz combined with an approximate 100 MHz intensity modulation. The fundamental RF peak is shown in Figure 3d and has >50 dB signal-to-noise ratio indicating stable mode-locking. The optical pulse-width measured using the auto-correlator was fitted with a  $\text{sech}^2$  pulse, which is shown in Figure 3b showing a 26 ps wide optical pulse, where it should be noted that this pulse is broadened due to the amplification of a second CW-type EDFA at the output. The optical spectrum of the output signal is shown in Figure 3e, which shows a 6 nm wide optical bandwidth centered at 1554 nm, which is expected to be limited by the bandwidth of the grating-couplers.

#### IV. CONCLUSION

Passive spontaneous mode-locking was demonstrated in a hybrid laser cavity using an integrated graphene electro-absorption modulator manufactured using standard CMOS tools. These results demonstrate that integrated graphene modulators can be used as a saturable absorber in fibre lasers. Furthermore by further integrating an amplifier and a passive extended cavity onto a semiconductor platform a fully integrated actively and passively mode-locked laser using graphene saturable absorbers should be able to be realised.

#### REFERENCES

- [1] N. Picqué and T. W. Hänsch, *Frequency comb spectroscopy*, Mar. 2019.
- [2] M. A. Abbas, Q. Pan, J. Mandon, *et al.*, “Time-resolved mid-infrared dual-comb spectroscopy,” *Scientific Reports*, vol. 9, no. 1, Dec. 2019.
- [3] T. Bajraszewski, M. Wojtkowski, M. Szkulmowski, *et al.*, “In vivo corneal high-speed, ultra high-resolution optical coherence tomography,” *Tech. Rep.* 120, 2007, pp. 889–894.
- [4] H. A. Haus, “Mode-locking of lasers,” *IEEE Journal on Selected Topics in Quantum Electronics*, vol. 6, no. 6, pp. 1173–1185, Nov. 2000.
- [5] U. Keller, K. J. Weingarten, F. X. Kärtner, *et al.*, “Semiconductor saturable absorber mirrors (SESAM’s) for femtosecond to nanosecond pulse generation in solid-state lasers,” *IEEE Journal on Selected Topics in Quantum Electronics*, vol. 2, no. 3, pp. 435–451, Sep. 1996.
- [6] K. Van Gasse, S. Uvin, V. Moskalenko, *et al.*, “Recent Advances in the Photonic Integration of Mode-Locked Laser Diodes,” *IEEE Photonics Technology Letters*, vol. 31, no. 23, pp. 1870–1873, Dec. 2019.
- [7] S. Cuyvers, B. Haq, C. Op de Beeck, *et al.*, “Low Noise Heterogeneous III-V-on-Silicon-Nitride Mode-Locked Comb Laser,” *Laser and Photonics Reviews*, vol. 15, no. 8, Aug. 2021.
- [8] M. L. Davenport, S. Liu, and J. E. Bowers, “Integrated heterogeneous silicon/III–V mode-locked lasers,” *Photonics Research*, vol. 6, no. 5, p. 468, May 2018.
- [9] R. P. Green, M. Haji, L. Hou, *et al.*, “All-optical wavelength conversion by electroabsorption modulator,” *IEEE J. Sel. Top. Quantum Electron.*, vol. 6, pp. 278–284, 2004.
- [10] K. S. Novoselov, A. K. Geim, S. V. Morozov, *et al.*, “Electric Field Effect in Atomically Thin Carbon Films,” *Phys. Rev. Lett.*, vol. 306, no. 5696, pp. 666–669, 2004. [Online]. Available: <http://science.sciencemag.org/>.
- [11] Q. Bao, H. Zhang, Y. Wang, *et al.*, “Atomic-layer graphene as a saturable absorber for ultrafast pulsed lasers,” *Advanced Functional Materials*, vol. 19, no. 19, pp. 3077–3083, Oct. 2009.
- [12] F. Bonaccorso, Z. Sun, T. Hasan, *et al.*, “Graphene photonics and optoelectronics,” *Nature Photonics*, vol. 4, no. 9, pp. 611–622, Sep. 2010.
- [13] Z. Sun, T. Hasan, F. Torrisi, *et al.*, “Graphene mode-locked ultrafast laser,” in *ACS Nano*, vol. 4, Feb. 2010, pp. 803–810.
- [14] Y. W. Song, S. Y. Jang, W. S. Han, *et al.*, “Graphene mode-lockers for fiber lasers functioned with evanescent field interaction,” *Applied Physics Letters*, vol. 96, no. 5, 2010.
- [15] J. D. Zapata, D. Steinberg, L. A. Saito, *et al.*, “Efficient graphene saturable absorbers on D-shaped optical fiber for ultrashort pulse generation,” *Scientific Reports*, vol. 6, Feb. 2016.
- [16] X. M. Liu, H. R. Yang, Y. D. Cui, *et al.*, “Graphene-clad microfiber saturable absorber for ultrafast fibre lasers,” *Scientific Reports*, vol. 6, May 2016.
- [17] M. A. Giambra, V. Soriano, V. Misiak, *et al.*, “High-speed double layer graphene electro-absorption modulator on SOI waveguide,” *Optics Express*, vol. 27, no. 15, p. 20 145, Jul. 2019.
- [18] I. Goykhman, U. Sassi, B. Desiatov, *et al.*, “On-Chip Integrated, Silicon-Graphene Plasmonic Schottky Photodetector with High Responsivity and Avalanche Photogain,” *Nano Letters*, vol. 16, no. 5, pp. 3005–3013, May 2016.
- [19] C. Wu, S. Brems, D. Yudistira, *et al.*, “Graphene electro-absorption modulators integrated at wafer-scale in a CMOS fab,” in *Symposia on VLSI Technology and Circuits*, vol. 59, 2020, pp. 94–100.
- [20] Z. Shi, C. Y. Wong, Z. Cheng, *et al.*, “In-plane saturable absorption of graphene on silicon waveguides,” in *Pacific Rim Conference on Lasers and Electro-Optics, CLEO - Technical Digest*, 2013.
- [21] Z. Cheng, H. K. Tsang, X. Wang, *et al.*, “In-plane optical absorption and free carrier absorption in graphene-on-silicon waveguides,” *IEEE Journal on Selected Topics in Quantum Electronics*, vol. 20, no. 1, 2014.
- [22] J. Wang, Z. Cheng, H. K. Tsang, *et al.*, “In-plane saturable absorption of graphene on a silicon slot waveguide; In-plane saturable absorption of graphene on a silicon slot waveguide,” in *21st Optoelectronics and Communications Conference (OECC)*, 2016.
- [23] P. Demongodin, H. El Dirani, J. Lhuillier, *et al.*, “Ultrafast saturable absorption dynamics in hybrid graphene/Si<sub>3</sub>N<sub>4</sub> waveguides,” *APL Photonics*, vol. 4, no. 7, Jul. 2019.
- [24] K. Alexander, Y. Hu, M. Pantouvakis, *et al.*, “Electrically Controllable Saturable Absorption in Hybrid Graphene-Silicon Waveguides,” in *Conference on Lasers and Electro-Optics (CLEO)*, 2015.
- [25] T. Reep, C. Wu, Z. Wang, *et al.*, “Saturable absorption of a double layer graphene modulator on a slot waveguide,” in *IPC IEEE*, 2022.

# Micro-Transfer-Printed III-V-on-Si Semiconductor Optical Amplifiers with High Saturation Power

Emadreza Soltanian,<sup>1,2</sup> Maximilien Billet,<sup>1,2</sup> Artur Hermans,<sup>1,2,3</sup> Bart Kuyken,<sup>1,2</sup> Jing Zhang,<sup>1,2</sup> and Gunther Roelkens<sup>1,2</sup>

<sup>1</sup> Photonics Research Group, INTEC, Ghent University - IMEC, Ghent, Belgium

<sup>2</sup> Center for Nano- and Biophotonics, Ghent University - IMEC, Ghent, Belgium

<sup>3</sup> Research Laboratory of Electronics, Massachusetts Institute of Technology (MIT), Cambridge, USA

## Abstract

*Integrated III-V-on-Si high saturation power semiconductor optical amplifiers (SOAs) with high output power are essential for silicon photonics (SiPh) as the leading candidate for high volume production of photonic integrated circuits (PICs) in a wide variety of applications and markets such as coherent optical communications, sensing and spectroscopy, and LiDAR. InP-based SOAs with high optical confinement can suffer from two-photon absorption and non-linear absorption associated with the generated carriers, while in this work, we used pre-fabricated InP SOAs, micro-transfer-printed ( $\mu$ TP) on a silicon waveguide within a silicon-on-insulator (SOI) PIC. The hybrid III-V/Si optical mode reduces confinement in the active region of the SOA, which results in an increased saturation power. The possibility of co-integration of high saturation power SOAs with the previously demonstrated  $\mu$ TP narrow linewidth widely tunable III-V-on-silicon lasers as optical output power boosters can lead to the required high output power of coherent optical communications. At the conference, we will present further details on the design, fabrication, and characterization results of the SOAs.*

## Introduction

SiPh realizes PICs on 200 mm or 300 mm SOI wafers with high uniformity and yield by taking advantage of the existing CMOS fabrication infrastructure. Since optical gain cannot be provided by Si, III-V semiconductors have been introduced to SiPh. The integration of III-V-on-Si high output saturation power SOAs is a must for SiPh to be the leading platform for high-volume applications such as optical communications, sensing and spectroscopy, LiDAR, etc.

In this work, the  $\mu$ TP method is used to integrate pre-fabricated InP SOAs [1] on a silicon waveguide within a SOI PIC. The SOA design relies on a hybrid III-V/Si optical mode [2], resulting in a reduced confinement in the active region, which has a narrow-to-wide tapered design, reducing power density towards the wide side of the SOA. This results in an increased output saturation power.

## Design and Fabrication

There are two main approaches to achieve an integrated high output saturation power SOA [2]: 1- having low confinement in the active region, and 2- having a large cross-section active region.

As illustrated in Fig. 1(a), From left to right, the SOA consists of 4 sections: 1- a taper for evanescent partial coupling from single-mode Si waveguide to III-V, 2- a narrower side, which results in a higher gain for a given injection current, 3- a wider side, which provides lower power density, resulting in higher output saturation power, and 4- an inverted taper for coupling the light from III-V to the single-mode Si waveguide. The

SOA design relies on not only a hybrid III-V/Si mode to lower the confinement factor, but also a large cross-section active region in the widest part of its tapered design. The Si waveguide width underneath the III-V is consistently  $2\ \mu\text{m}$  wider than multi-quantum well (MQW) layers to keep the confinement in the active region low over all the fourth parts. Fig. 1(b) shows a stitched microscope image of the fabricated III-V coupon, which is  $\mu\text{TP}$ -ed on a Si waveguide within a SOI PIC.

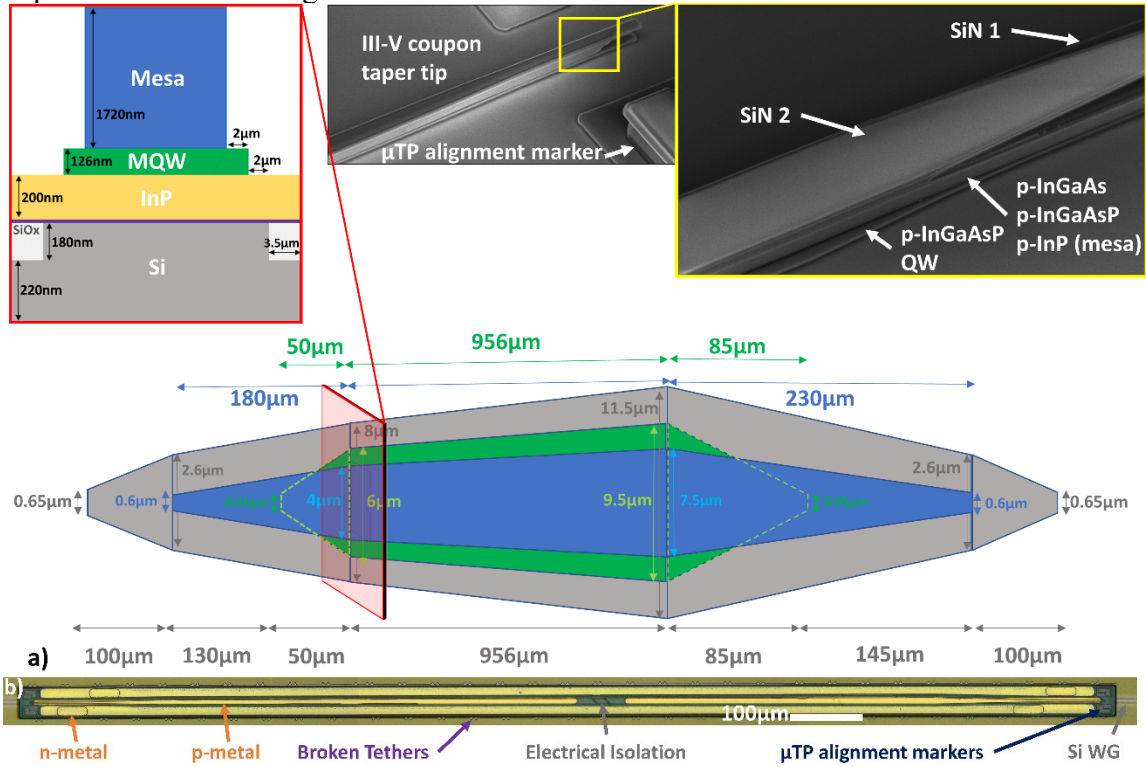


Figure 1: (a) Detailed schematic of the hybrid III-V-on-Si tapered SOA design (top view), indicating p-InP mesa, active area, and silicon waveguide underneath. A schematic cross-section and two SEM images of the III-V coupon are shown in the inset (not to scale), (b) Microscope image of a coupon  $\mu\text{TP}$ -ed on a Si waveguide.

In this work, we used a similar fabrication process flow and III-V epitaxial stack as the previously demonstrated  $\mu\text{TP}$  narrow linewidth widely tunable III-V-on-silicon lasers and transmitter [3, 4], which typically requires more quantum wells than high-output power amplifiers [5]. Here, there is just one additional step to create electrical isolation between the narrow and wide sides of the SOA by inductively coupled plasma (ICP) etching the  $200\ \text{nm}$  of cladding p-InP prior to p-metal deposition, in comparison to the described III-V fabrication process flow in [3]. The  $\mu\text{TP}$  process is based on the use of an elastomeric poly-dimethyl siloxane (PDMS) stamp to pick up the pre-fabricated InP-based SOA (which is undercut by selectively etching the release layer) from its native III-V source wafer and to print it on the target substrate, which contains  $400\ \text{nm}$  thick Si waveguides with an etch depth of  $180\ \text{nm}$ . A spin-coated DVS-BCB adhesive bonding layer of less than  $40\ \text{nm}$  enables a high-yield printing process.

## Characterization

To characterize the SOA, the sample was placed on a  $20^\circ\text{C}$  temperature-controlled stage. The device under test is optically probed using cleaved standard single-mode fibers (SMFs) on a fiber stage. To have better control over the narrow side and the wide side of

the SOA, which are electrically separated by the isolation island, separate probe needles are used to electrically drive each side of the amplifier, simultaneously. The left/right SOA section has a differential resistance of  $11/9 \Omega$ , while injecting 100 mA in each segment.

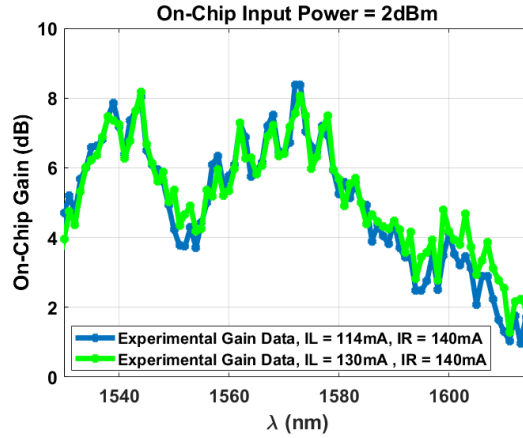


Figure 2: Gain as a function of wavelength, while the on-chip input power is +2.0 dBm and the pump current of the left and right sides are 114/130 mA and 140 mA, respectively.

The gain spectrum for 2 dBm optical input power is shown in Fig. 2, while the pump current on the left and right sides are 114/130 mA and 140 mA. The dip in the gain curves is attributed to the interference of two propagating modes in the SOA, which are excited by a slight misalignment of the transfer printed SOA. At the wavelength of 1544 nm and 1573 nm, which correspond to the wavelength of maximum optical gain for the left side pump current of 130 mA and 114 mA respectively, the small-signal gain of 8.4 dB and 9.4 dB and an output saturation power of 18.4 dBm and 15.4 dBm were extracted by fitting a curve to the experimental data according to (1), as shown in Fig. 3 and Fig. 4.

$$G(P_{in}) = G_0 \frac{1 + P_{in}/P_s}{1 + G_0 P_{in}/P_s} \quad (1)$$

Equation (1) relates the SOA gain factor  $G$  to the input power  $P_{in}$ , material gain saturation power  $P_s$ , and small-signal gain  $G_0$  [2].

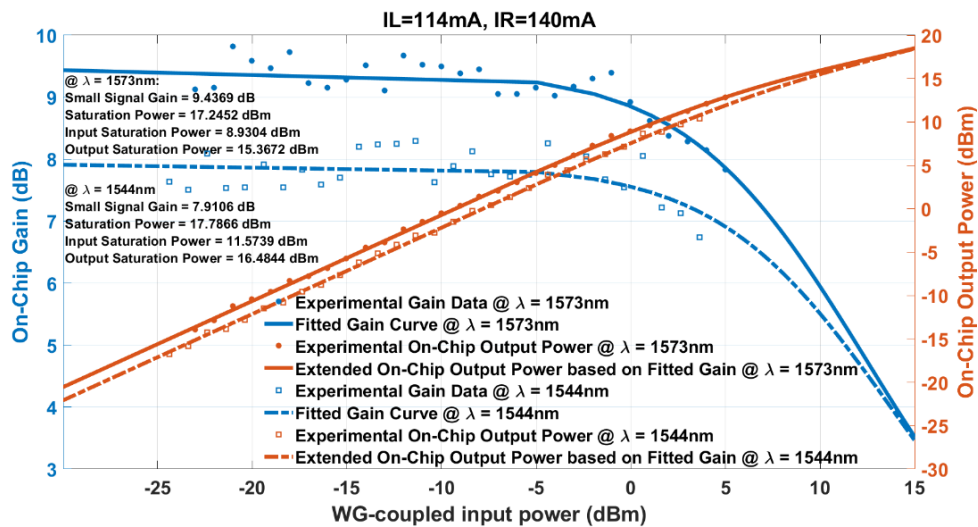


Figure 3: The gain as a function of on-chip optical input power (left side). The on-chip output power as a function of the input power (right side). The points are measured values and the lines are fitted curves at wavelengths of 1544 nm and 1573 nm. The pump current of the left and right sides are 114 mA and 140 mA, respectively.

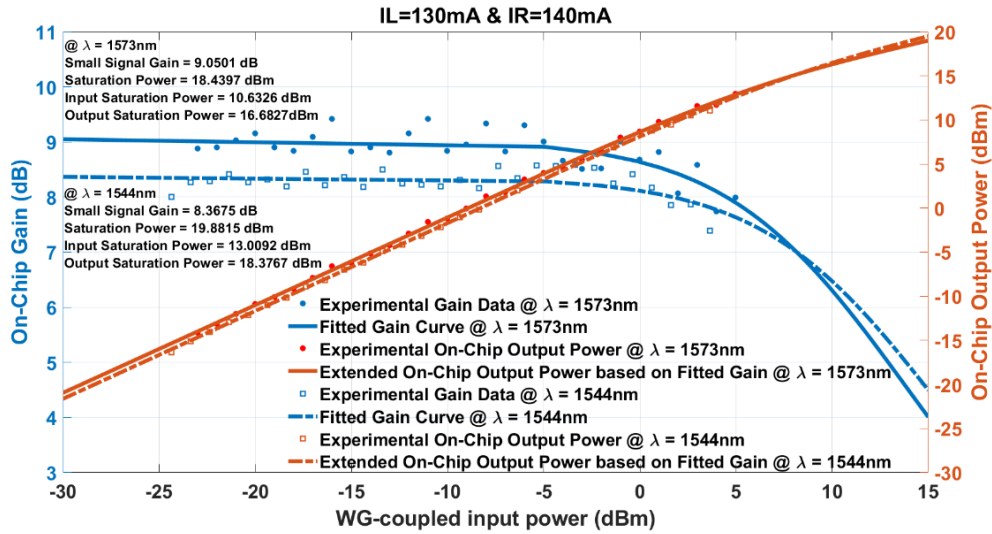


Figure 4: The gain as a function of on-chip optical input power (left side). The on-chip output power as a function of the input power (right side). The points are measured values and the lines are fitted curves at wavelengths of 1544 nm and 1573 nm. The pump current of the left and right sides are 130 mA and 140 mA, respectively.

## Conclusion

We demonstrated a tapered  $\mu$ TP-ed III-V-on-Si SOA with an on-chip output saturation power of 18.4 dBm and an 8.4 dB small-signal gain at the wavelength of 1544 nm.  $\mu$ TP not only requires no singulation and handling of individual III-V chips, but also allows for densely integrating different non-native components on a SiPh platform with minimal disruption to the SiPh process flow in a high-throughput manner. The possibility of co-integration of the presented SOAs with the recently demonstrated  $\mu$ TP narrow linewidth widely tunable III-V-on-silicon lasers [3] and transmitter [4] as an optical output power booster, can lead to the required high output power for e.g. coherent optical communications.

## Acknowledgments

This work was supported by the European Union's Horizon 2020, Marie Skłodowska-Curie grant agreement 814276. E. S. thanks Kasper Van Gasse for the helpful discussions.

## References

- [1] B. Haq, S. Kumari, K. Van Gasse, J. Zhang, A. Gocalinska, E. Pelucchi, B. Corbett, and G. Roelkens, "Micro-transfer-printed III-V-on-silicon C-band semiconductor optical amplifiers," *Laser & Photonics Rev.* 14, 1900364 (2020).
- [2] Kasper Van Gasse, Ruijun Wang, and Gunther Roelkens, "27 dB gain III-V-on-silicon semiconductor optical amplifier with > 17 dBm output power," *Opt. Express* 27, 293-302 (2019).
- [3] E. Soltanian, G. Muliuk, S. Uvin, D. Wang, G. Lepage, P. Verheyen, J. Van Campenhout, S. Ertl, J. Rimböck, N. Vaissiere, D. Néel, J. Ramirez, J. Decobert, B. Kuyken, J. Zhang, and G. Roelkens, "Micro-transfer-printed narrow-linewidth III-V-on-Si double laser structure with a combined 110 nm tuning range," *Opt. Express* 30, 39329-39339 (2022).
- [4] J. Zhang, E. Soltanian, B. Haq, S. Ertl, J. Rimböck, B. Matuskova, E. Pelucchi, A. Gocalinska, J. Van Campenhout, G. Lepage, P. Verheyen, W. Bogaerts, and G. Roelkens, "Integrated optical transmitter with micro-transfer-printed widely tunable III-V-on-Si laser," in *2022 Optical Fiber Communications Conference and Exhibition (OFC)*, (2022), pp. 1–3.
- [5] A. Abbasi, J. Verbist, J. Van Kerrebrouck, F. Lelarge, G. Duan, X. Yin, J. Bauwelinck, G. Roelkens, and G. Morthier, "28 Gb/s direct modulation heterogeneously integrated C-band InP/SOI DFB laser," *Opt. Express* 23, 26479-26485 (2015).

# Design of a Broadband Adiabatic Coupler for Interfacing PICs to Optical Redistribution Layers

J. Van Asch,<sup>1,2</sup> J. He,<sup>2</sup> J. Missinne,<sup>1</sup> G. Lepage,<sup>2</sup> J. Van Campenhout<sup>2</sup> and G. Van Steenberge<sup>1</sup>

<sup>1</sup> Centre for Microsystems Technology (CMST), imec and Ghent University, Gent, Belgium

<sup>2</sup> Imec, Leuven, Belgium

## Abstract

*The design of a broadband adiabatic coupler for interfacing PICs to ORDLS is presented, enabling optical interconnections between PICs, or providing an interface towards an optical fiber connector. As first proof-of-concept, the coupling between a SiN waveguide and a polymer waveguide ORDLS is investigated. A generic taper-layout model, implemented in Lumerical Mode, maximizes the SiN-to-ORDLS coupling efficiency for various integration techniques. We obtain polarization-tolerant coupling losses smaller than 1 dB across the O-band, while maintaining the SiN taper length below the 1-mm footprint limit. The 1-dB SiN-to-ORDLS lateral alignment tolerance is  $\pm 1.8 \mu\text{m}$ , within reach of our target integration/assembly tools.*

## Introduction

Efficient optical coupling between two Photonic Integrated Circuits (PICs) is crucial for the next generation of optoelectronic devices. Nowadays, the major challenges for the optical signals transfer are the stringent alignment tolerance between different waveguides, polarization sensitivity and wavelength dependency. Here we demonstrate that efficient coupling is possible between a SiN waveguide, located in a PIC, and a polymer Optical Redistribution Layer (ORDLS), addressing the mentioned problems. Soon, we will experimentally demonstrate this concept based on Back-End-Of-Line (BEOL) compatible processes with low-loss SiN waveguides [1].

## Adiabatic optical coupler

For optimal working conditions, the optical coupling between two waveguides needs to be adiabatic. This means there is very limited intensity loss due to reflection and/or radiation when coupling light from one waveguide to another. This calls for a dedicated taper design with small geometrical changes to minimize the energy transfer from any currently present (fundamental) modes to other (higher order) modes [2].

As shown in Figure 1, we consider a polymer ORDLS waveguide that remains constant in geometry along the propagation direction, while a second SiN waveguide in optical proximity has a gradually decreasing width. A dedicated light signal, initially coming from the PIC, is launched into this latter, SiN tapered waveguide. Due to the varying geometric shape of the taper, the light beam gets less confined and is expanded in diameter while propagating through the taper. From the moment the Mode Field Diameter (MFD) is large enough to optically experience the presence of the ORDLS waveguide, a part of the light and energy is coupled from the SiN waveguide to the ORDLS waveguide. The highest energy transition between the 2 waveguides occurs at phase-matching condition, when the propagation constants  $\beta_1$  and  $\beta_2$  of the 2 isolated (uncoupled) waveguides are identical. To quantitatively monitor the evolving difference in effective index  $n_{eff}$  of the individual waveguides, we define  $\delta = (\beta_2 - \beta_1)/2$ , with  $\beta_i =$

$2\pi n_{eff,i}/\lambda$  for each waveguide ( $i = 1$  or  $2$ ). As we investigate the adiabatic coupler in the O-band, we use  $\lambda = 1310$  nm as the central wavelength. Additionally, we also define  $2S = 2(\delta^2 + \kappa^2)^{1/2} = \beta_e - \beta_o$  as the difference between the propagation constants for the even and odd supermode, with  $\kappa$  being the coupling coefficient between the SiN and ORDL waveguide in the case of the coupled waveguides setup.

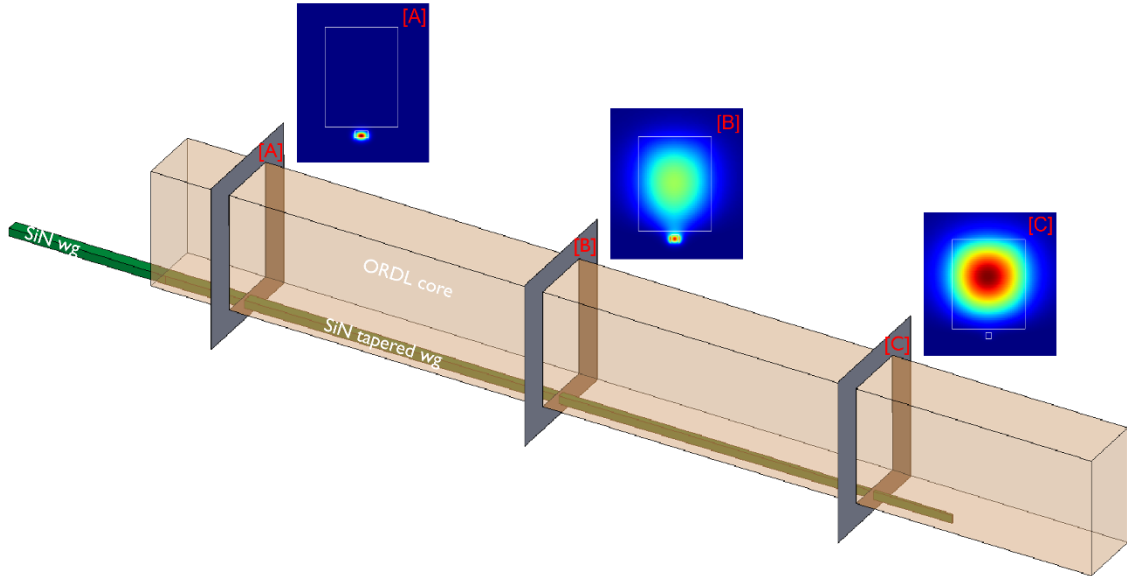


Figure 1: Illustration of the adiabatic coupling between a SiN (tapered) waveguide and an ORDL core. Light that is initially confined by the SiN waveguide, is gradually spreading out into both waveguides, forming the 2 fundamental supermodes. At the end of the adiabatic coupler, almost all light is confined by the ORDL waveguide. The inserted mode profiles are acquired by Lumerical Mode FDE simulations.

At phase-matching condition,  $\delta = 0$  and so  $\kappa = (\beta_e - \beta_o)/2$ . Finally, with  $\varepsilon$  the fraction of unwanted power coupling to other modes, the minimally required coupler length can be derived as  $L = \frac{1}{\kappa\sqrt{\varepsilon}}$ . This length  $L$  allows the initially launched mode to adiabatically transfer from the SiN to the ORDL waveguide [3].

## Cross-section configurations and taper shape

To support the theoretical concept of adiabatic coupling, we consider 3 implementation approaches (shown in Figure 2) for establishing the SiN-to-ORDL adiabatic coupling.

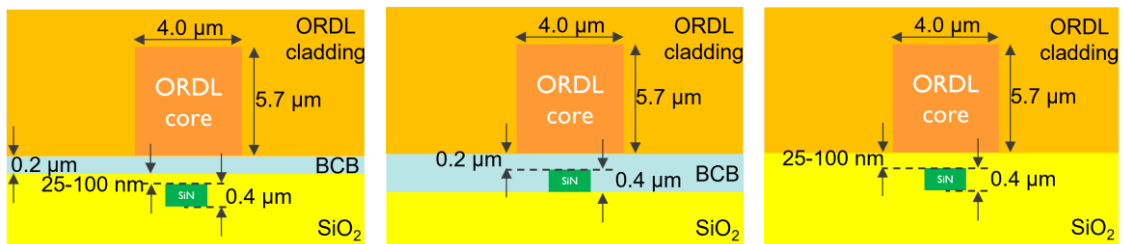


Figure 2: Schematic illustrating the cross-section for the 3 main setups in our simulations. Additionally, some dimensions are changed to overcome potential challenges on the PIC manufacturing.

For setup #1, the PIC part consists of a SiN tapered waveguide with constant height =  $0.4$   $\mu\text{m}$ , with variable width starting from  $710$  nm in the straight waveguide section. The SiN taper is surrounded by  $\text{SiO}_2$  acting as cladding material to ensure mode confinement. The polymer ORDL consists of core/cladding made from EpoCore/EpoClad material [4]. The ORDL dimensions are chosen to obtain a circular Gaussian beam profile. At  $\lambda = 1310$

nm, EpoCore has a refractive index of 1.579, while EpoClad’s refractive index is 1.571. To achieve optical coupling, both parts need to be brought in very close proximity to each other. In this case we assume the PIC and ORDL are bonded by using benzocyclobutene (BCB), acting as glue between both parts.

As shown in the middle graph of Figure 2, setup #2 is slightly different as the SiN taper is located on top of SiO<sub>2</sub> and additionally surrounded by BCB. As will be shown later, the higher refractive index of BCB (with respect to SiO<sub>2</sub>) has a beneficial influence on the coupling strength between SiN and ORDL.

In order to include multiple bonding techniques, we add a third cross-section to our analysis, to allow lithography as integration technique instead of adhesive bonding [5].

Each cross-section has its own specific coupling strength  $\kappa$  and required coupler length  $L = \frac{1}{\kappa\sqrt{\epsilon}}$ . Depending on the value for  $\epsilon$  that we allow to occur, the SiN taper length is fixed. The exact taper layout (as illustrated in Figure 3 for setup #2) is defined based on a semi-analytical method, by ensuring a large overlap (linked with  $\epsilon$ ) between consecutive sections in the taper. In the following section, we show the Lumerical EME simulation result for each setup, based on the best-matching taper layout in each situation. By sweeping the dedicated taper length, it is determined how resistant the coupling efficiency can be to fluctuations in taper length.

## Coupling efficiency and wavelength dependency

The right figure of Figure 3 displays the coupler loss behavior as a function of taper length at the central wavelength  $\lambda = 1310$  nm. Note that, except for 1 analyzed setup, the coupler loss is lower than 1 dB for a taper length around 750  $\mu\text{m}$ . Comparing the different graphs, setup #2 can be considered the most suitable cross-section since it shows the least coupler loss for both TE and TM polarization. For this reason, we stick to this setup for further analysis in the current publication.

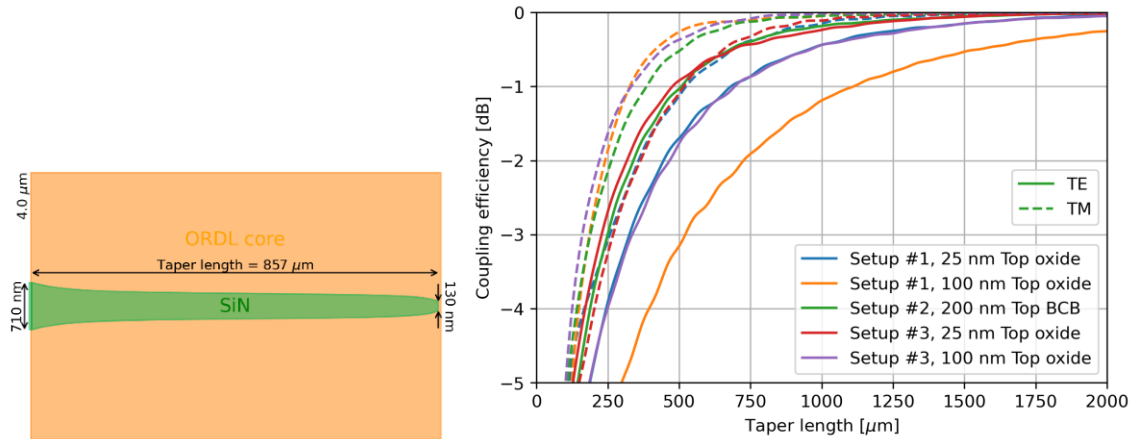


Figure 3: [Left] Exemplary taper layout, specifically designed for setup #2. Note that the taper’s width decreases fast at both ends, and slowly in the middle at round the phase-matching condition.

[Right] Comparison between the 3 setups in terms of coupler loss for  $\lambda = 1310$  nm. The graphs are the result of Lumerical Mode EME simulations making use of the dedicated taper layout for each setup.

Looking at the wavelength dependency in Figure 4, we can state that it is feasible to obtain an optical coupler length below 1 mm, while maintaining a coupler loss below 1 dB over the entire O-band spectrum. Besides this, the difference in coupling efficiency between both polarizations for a suitable coupler length value is always lower than 1 dB. Finally, when investigating the tolerance for aligning the ORDL with respect to the PIC, we find

the results depicted in Figure 5. When maintaining the same 1-dB threshold for additional coupler loss, the lateral alignment tolerance is  $\pm 1.8 \mu\text{m}$ .

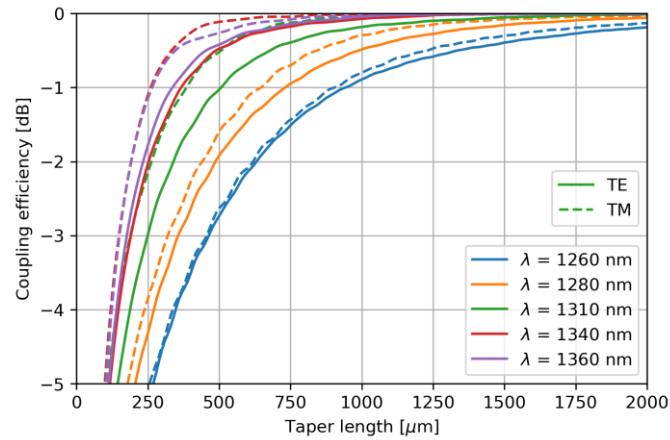


Figure 4: Broadband behavior of the coupler, for setup #2.

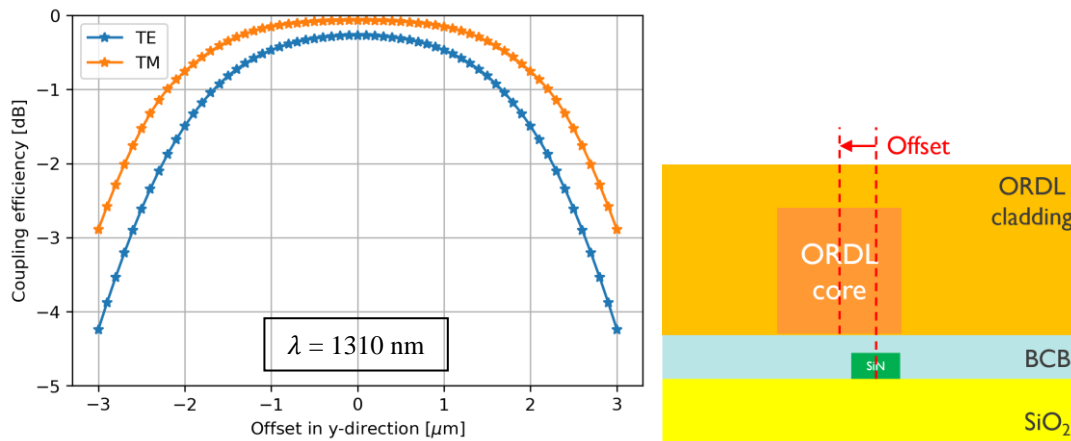


Figure 5: Alignment tolerance of ORDL with respect to the SiN (tapered) waveguide, for setup #2.

## Conclusion

It is demonstrated that an adiabatic coupling, with less than 1 dB coupler loss, can be achieved between a polymer ORDL and SiN tapered waveguide of shorter than 1 mm. Due to the broadband behavior, low polarization dependence and alignment tolerance, we show a compact device footprint on the PIC.

## Acknowledgement

Part of this work was supported by imec's industry-affiliation R&D Program on Optical I/O.

## References

- [1] N. Golshani et al., "Low-loss, low-temperature PVD SiN waveguides," in Proceedings of the IEEE 17<sup>th</sup> International Conference on Group IV Photonics (GFP), 2021.
- [2] R. Dangel et al., "Polymer Waveguides Enabling Scalable Low-Loss Adiabatic Optical Coupling for Silicon Photonics," IEEE Journal of selected topics in quantum electronics, vol. 24, No. 4, 2018.
- [3] X. Sun et al., "Adiabaticity criterion and the shortest adiabatic mode transformer in a coupled-waveguide system," Optics Letters, vol. 34, No. 3, 2009.
- [4] Micro Resist Technology GmbH, datasheet, <<http://www.microresist.de>>.
- [5] A. Elmogi et al., "Comparison of epoxy- and siloxane-based single-mode optical waveguides defined by direct-write lithography," Optical Materials, vol. 52, pp. 26-31, 2016.

# Application-Specific Optimization of Near-Infrared Spectral Sensors

D.M.J. van Elst,<sup>1</sup> A. van Klinken,<sup>1</sup> F. Ou,<sup>1,2</sup> C. Li,<sup>1</sup> M. Petruzzella,<sup>1,2</sup> P.J. van Veldhoven<sup>1</sup> and A. Fiore.<sup>1</sup>

<sup>1</sup> Department of Applied Physics, Eindhoven Hendrik Casimir Institute, Eindhoven University of Technology, PO Box 513, NL 5600 MB Eindhoven, The Netherlands.

<sup>2</sup> MantiSpectra B.V., Flux Building, Groene Loper 3, 5612 AE Eindhoven, The Netherlands.

*Spectral sensing is attracting increasing interest for the analysis of materials throughout a wide variety of applications. The use of light provides a fast and non-destructive way to investigate the chemical composition of materials. We have recently reported a fully-integrated, robust and low-cost near-infrared (900-1700nm) spectral sensor consisting of resonant-cavity-enhanced photodetectors. Here we report an approach to optimize its spectral response for specific applications. We use the transfer-matrix method to simulate the response of the sensor and predict the performance for known reflection or transmission spectra from a specific sensing problem. A particle swarm optimization is used to find a design providing optimized sensing accuracy, which can be a non-trivial combination of resonant wavelengths.*

## Introduction

There is substantial interest in spectral sensing for the analysis of materials in a wide variety of applications, as it allows for a fast and non-destructive method to measure the chemical composition of materials. Specifically, near-infrared (NIR) spectral sensing has seen increasing progress in past years. The NIR region contains first and second overtones of C-H, OH and N-H molecular bonds, as well as combinations of these vibrational modes. Due to the overlapping nature of these absorption bands, the features in NIR spectra are often broad and hard to interpret directly [1] and chemometric methods are used to build predictive models [2].

For most in-field and in-line applications, small, portable and affordable sensors are needed, which has motivated research in miniaturization and wafer-scale fabrication. There are a variety of ways to miniaturize spectral sensors [3]. While spectrometers based on waveguide circuits are compact and mass-manufacturable, their limited spectral range and very small input étendue (and thereby the impossibility to efficiently couple incoherent light from a large area) makes them unsuitable for most in-line and portable sensing applications. We have previously demonstrated an approach to spectral sensing based on an array of 16 resonant-cavity enhanced (RCE) detectors as a compact, robust and low-cost solution [4]. Fig. 1a provides an optical image of such a spectral sensor. By varying the thickness of a tuning layer inside the cavity, the resonance of each detector (pixel) can be shifted to different wavelengths. The spectral response of the multipixel array (Fig. 1b) displays peaks with full-width half-maximum  $\text{FWHM} \approx 60\text{nm}$  and high peak responsivity ( $R=0.3\text{A/W}$ ). While the sensor does not measure the full incident spectrum, the generated photocurrents allow us to retrieve information from the object [4]. The effectiveness of this approach has recently been demonstrated on a variety of real-life applications using a standard configuration of our sensor [5, 6].

While the present sensor has general applicability, we can ask the question what the best configuration of the sensor is for a given application. Indeed, for a given problem only certain spectral bands carry relevant information and the data from some pixels is

not used in the prediction models. Using less and larger pixels with response in the most relevant spectral bands would provide a higher signal-to-noise ratio (SNR) for a given total sensor area. It is therefore attractive to determine the minimum number of pixels required for a given problem and exploit the higher SNR to improve sensing performance. A similar optimization of sensor spectra has been reported previously in the context of filter arrays [7, 8]. Here we report an approach to find the optimal configuration of resonant-cavity detector structures for a specific sensing problem, with variable number of pixels and SNR.

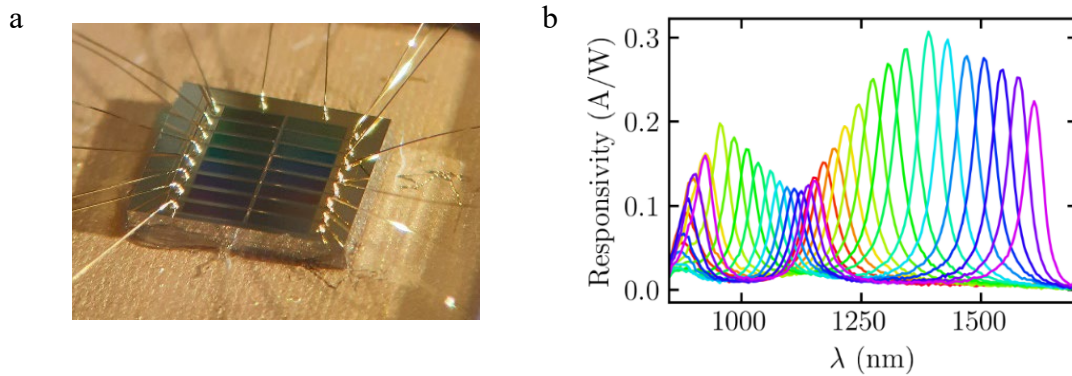


**Figure 1** a) Image of the multipixel array with 16 resonant-cavity enhanced detectors. b) Measured responsivity curves for each of the pixels in the array.

## Methods

A schematic of the optimization procedure is displayed in Fig. 2. In order to demonstrate the approach, a dataset with transmission spectra for varying concentrations of methanol in isopropanol was experimentally acquired. This problem was chosen because of the high reproducibility across multiple experiments. A specific application is characterized by a dataset of transmission spectra from the solution along with calibrated values (the concentration of methanol). The responsivity curves for an arbitrary configuration are calculated using the transfer-matrix method. The resulting expected photocurrents are then determined by multiplying the incident spectra with the responsivity curves. Variable Gaussian noise is added to these photocurrents, to simulate the read-out noise during an actual experiment. A part of the resulting dataset is used to train a model, whereas the rest is used to test how well this model is able to predict the calibrated values from the photocurrents. This results in a value for the ratio of performance to deviation, or RPD, which is the ratio between the standard deviation of the calibrated values and the root-mean-square error of prediction by the model. The RPD is used as the figure of merit (FOM) for the optimization.

The FOM is optimized using a particle swarm optimization (PSO). Here, the thicknesses of the tuning layers are the degrees of freedom. During the optimization the fabrication constraints, such as the range of thicknesses that are feasible to deposit and the combinations that are possible with the layout of available optical lithography masks, are taken into account. Each particle consists of a set of response curves and a resulting calculated RPD. During each iteration the particles move towards a new position based on the best positions within the group, their neighbors and their own memory. When the FOM no longer improves over multiple iterations, the optimization is finished.

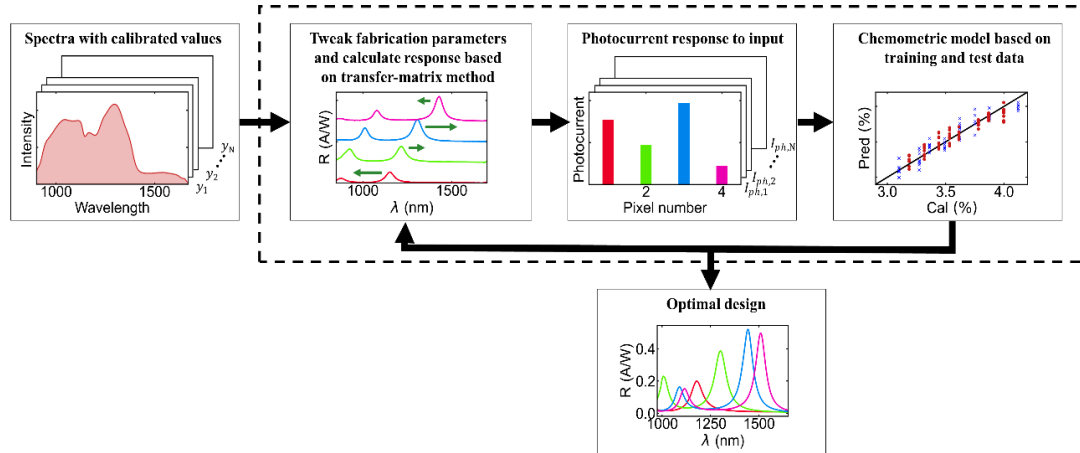


**Figure 2** Schematic of the application specific optimization procedure. The steps in the dashed lines are part of the particle swarm optimization, where each particle is a configuration of the sensor. When the figure of merit has not improved for many iterations anymore, the optimal design is taken from the memory of the particles.

## Results and discussion

Fig. 3 shows the results of the optimization procedure for this problem using a configuration with 4 pixels and a noise corresponding to an SNR of 19000 on average over all pixels. There were 500 particles in the swarm, which are initially distributed evenly over the design space. The RPD at iteration 0 is the best solution among these initial particles (therefore already higher than the average for a random configuration) and can then be seen to increase over 27 iterations (Fig 3a). The FOM shows plateaus and increases at specific steps. This is because the optimal solution does not improve by simply shifting the wavelength continuously. There might be specific wavelength ranges that are of importance and that need to be reached before the FOM improves. Fig 3b shows the final prediction on the dataset, where the calibration data was used to train the model and the test data used to calculate the prediction strength. Fig 3d shows the simulated responsivity curves for the optimal solution. During the optimization the FOM reaches RPD=15.8 and when testing the sensor on data that was not part of the optimization it has an RPD=12.8. This RPD indicates high sensing performance. A tolerance analysis to fabrication errors is shown in Fig 3c. The thicknesses of the optimized design are changed by randomly adding deviations with a normal distribution with standard deviation  $\sigma$ , after which the RPD is calculated again. This is done multiple times for each  $\sigma$  to get an average RPD. For increasing levels of deviation from the design, the RPD can be seen to always be less than the optimum. Sometimes a slight increase can be seen for higher values of  $\sigma$ , this is again due to the effect of specific wavelength ranges that can be of higher importance than others.

The optimal number of pixels heavily depends on the sensing problem and on the noise level of the read-out. If the read-out is not too noisy, increasing the number of pixels generally improves the performance. Also, a larger number of pixels improves the robustness to fabrication errors. For larger noise levels, the trade-off between number of pixels and the resulting decreasing SNR becomes more important and the optimization procedure can add more value. The main advantage of using an optimization procedure, as compared to handpicking the wavelengths, is that it takes all combinations of bands into account, while also including the influence of noise on the read-out.

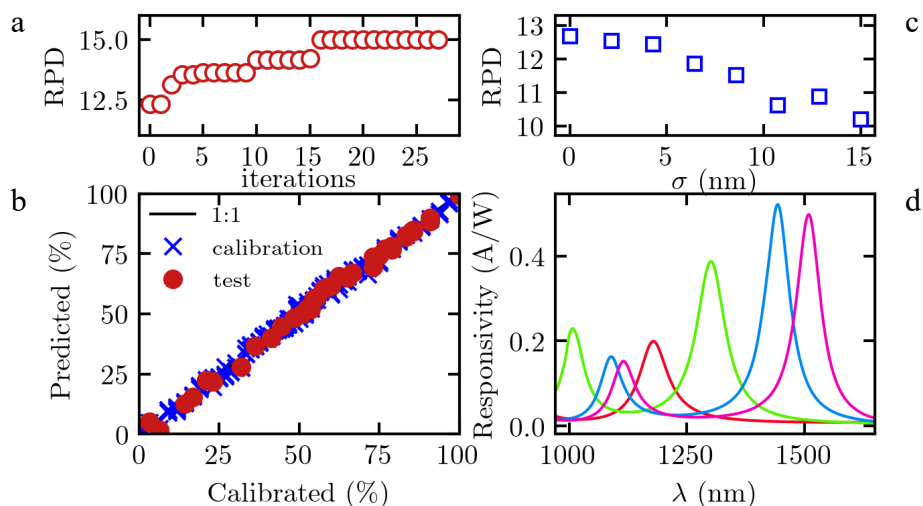


**Figure 3** Results of the particle swarm optimization for sensing the concentration of methanol in isopropanol for a 4 pixel configuration.. a) shows the evolution of the RPD corresponding to the best solutions found in the swarm throughout the iterations of the optimization. b) displays the final predictions strength corresponding to a particle with responsivity curves as shown in d). The tolerance to deviations in fabrication is shown in c), where random deviations are added to the thicknesses of the optimized design with a normal distribution with standard deviation  $\sigma$ .

## Conclusion

Miniaturized spectral sensors based on detector arrays are a powerful tool for real-time and in-field analysis of materials. Here, we described an approach to optimize the response of a spectral sensor for a specific application using a pre-calibrated spectral dataset. The resulting design can be a non-trivial combination of resonant wavelengths, taking into account the SNR of the read-out system. The procedure is applied to the case of determining the concentration of methanol in isopropanol and shows the potential for high performance, even using a small number of detectors.

## Acknowledgements

This research was funded under NWO - SYstem change for New Ecology-based and Resource efficient Growth with high tech In Agriculture (Synergia) n. 17626 (D.M.J.v.E.), NWO TTW project n. 16670 (A.v.K.) and Penta Call 2 project Environmental Sensors for AIR Quality (ESAIRQ) n. 16113 (M.P.).

## References

- [1] Ozaki, Y. et al. Near-Infrared Spectroscopy. *Springer*; 2021
- [2] Pasquini, C. et al. Near infrared spectroscopy: A mature analytical technique with new perspectives – A review. *Analytica Chimica Acta*; 2018
- [3] Zongyin, Y. et al. Miniaturization of optical spectrometers. *Science*; 2022
- [4] Hakkel K.D. et al. Integrated near-infrared spectral sensing. *Nat Communications*; 2022
- [5] Ou F. et al. Handheld NIR Spectral Sensor Module Based on a Fully-Integrated Detector Array. *Sensors*; 2022
- [6] Kranenburg R.F. et al. On-site illicit-drug detection with an integrated near-infrared spectral sensor: A proof of concept, *Talanta*; 2022
- [7] Soyemi, O. et al. Design and testing of a multivariate optical element: The first demonstration of multivariate optical computing for predictive spectroscopy. *Analytical Chemistry*; 2001
- [8] Tan, H. et al. Genetic optimization of mid-infrared filters for a machine learning chemical classifier. *Opt. Express*; 2022

# Optimizing LED Performance for LiFi: Bandwidth versus Efficiency

Diego Vargas Romero<sup>1</sup>, Thiago E. B. Cunha<sup>1</sup>, Jean-Paul M. G. Linnartz<sup>1,2</sup>

<sup>1</sup>Electrical Engineering, Eindhoven University of Technology, 5600 MB Eindhoven, The Netherlands

<sup>2</sup>Signify (Philips Lighting) Research, 5656 AE Eindhoven, The Netherlands

*Optical transmission is attractive for future wireless communication because signals can be confined in a specific coverage area. In designing a system based on LEDs, the trade-off between transmission bandwidth and optical power is important. As a common practice with micro-LEDs, one may drive the LED at a high current density, beyond the optimum efficiency point, to boost the bandwidth. Bit rates of multiple gigabit/s have been demonstrated, but coverage is small. However, using high current densities is discouraged by self-heating, as only a part of the electrical power is converted to optical power. A rising temperature reduces efficiency, causing a degradation of the SNR. We combine multiple models, not only the ABC photon generation and the LED dynamic responses subject to a rapidly varying current but also, the junction voltage method to estimate its temperature. We quantify the achieved throughput in a DCO-OFDM link at different temperatures. This leads to the insight that there is an optimal size of the active region and an optimal current density that maximizes the throughput of the wireless link at different temperatures. The work presented here builds upon work that we published earlier, and we place this in the perspective of a combined system model.*

## Introduction

The standardization of the new wireless generation (6G) is expected to start in the next years. 6G will provide higher data rates, lower latency, and more massive access compared to the last generation. Higher data rates require bigger amounts of free spectrum. Nevertheless, the RF spectrum is already very congested, thus a migration to higher frequencies, such as THz, is necessary. In this frequency range, we have ultra-violet, visible light, and infrared bands. Optical wireless communication (OWC) has the possibility to be a key technology in 6G. Therefore, it is necessary to understand and overcome some particular channel limitations in order to optimize throughput [1]. OWC uses LEDs as a light source due to their low cost. However, these devices suffer from a low 3dB bandwidth. Additionally, unlike RF, the signal power is concentrated in the line-of-sight (LoS) link, then it is highly affected by blockage. Different methods solved these limitations by using new circuit drivers, different modulation techniques, distributed MIMO, sectorization, and optimization methods among others.

Independently on the circuit driver, modulation scheme, or equalization technique, the LED 3dB bandwidth is a major limitation to achieve higher throughput. Commonly, conventional LEDs have a  $f_{3dB}$  between 10 ~ 20 MHz, making its time response slow when shorter bit times are required. In [2]- [3], the 3dB bandwidth is increased by reducing the size of the active area. A smaller active area increases the injection current density, accelerating the process of carrier generation or recombination inside the active region. The rise and fall time will be reduced, making this kind of LED, micro-LED, more suitable for high-speed data transmission. Nevertheless, as we will see from models developed in our earlier papers and as we confirm via new experiments, there

is a trade-off between efficiency and frequency response. Micro-LEDs have a poor efficiency response compared to conventional LEDs. We explore to what extent that hampers throughput if coverage is also a requirement.

### LED Communication Model

We consider a reference LED with specific recombination parameters ABC(D) and an active region size  $A_w$ . The current density plays an important role in the trade-off between the efficiency and the bandwidth of the LED. The  $f_{3dB}$  increases with higher current density, thus the response of the LED becomes faster and the OWC system can transmit in shorter bit times. Nevertheless, the efficiency will be reduced causing an SNR degradation in the wireless link. In our model, we fix the total current power of the OWC system, but we change the current density by scaling the active region of the LED to  $\zeta A_w$ , where  $\zeta$  is a scaling factor. While we optimize the throughput,  $\zeta$  is a degree of freedom. If  $\zeta < 1$ , the current density is higher than in the reference. For example, if  $\zeta > 1$ , the new LED has a  $\zeta$  times larger active region thus a  $\zeta$  times lower current density compared to the reference LED. The scaled carrier rate equation is

$$\frac{dN_{QW}(t)}{dt} = \frac{I(t)}{\zeta q} - \left( AN_{QW}(t) + BN_{QW}^2(t) + CN_{QW}^3(t) \right), \quad (1)$$

where  $N_{QW}$  is the total number of carriers per normalized unit of area. The LED current  $I(t)$  contains a DC component and a modulated signal:  $I(t) = I_{DC} + i(t)$ . The DC term may already be present for illumination. Similarly,  $N_{QW}(t)$  contains a bias component  $N_{QW}$  and a modulation signal  $n_{QW}(t)$ . According to [4], the rate equation for the small signal is

$$\frac{dn_{QW}(t)}{dt} = \frac{i(t)}{\zeta q} - \left( \tilde{A}n_{QW}(t) + \tilde{B}n_{QW}^2(t) + \tilde{C}n_{QW}^3(t) \right), \quad (2)$$

where the first term in the Taylor expansion ( $\tilde{A} = A + 2BN_{QW} + 3CN_{QW}^2$ ) is  $2\pi f_{3dB}$ . The second and third-order terms in equation (2) generate distortion according to [5]. We neglect third-order distortion and assume that the second-order term is invertible [6], thus we focus on the  $\tilde{A}$  term. At low modulation frequencies ( $f < f_{3dB}$ ), the optical output generated by the small signal is

$$\phi(t) = \text{LEE} \frac{f_R}{f_{3dB}} \frac{\eta}{q} i(t), \quad (3)$$

where LEE is the light extraction efficiency,  $\eta$  is the photon energy and we denote  $2\pi f_R = 2BN_{QW}$ . In previous works [4] and [7], we referred  $f_R/f_{3dB}$  as the (differential) dIQE, which applies for small signals. Fig. 1 plots the efficiency droop when a higher current density drives the LED. Additionally, the  $f_{3dB}$  increases at higher current densities. We show that the dIQE plays a bigger role in the optimization of a DCO-OFDM link than the IQE.

### Throughput of DCO-OFDM Link

DCO-OFDM can exploit the low-pass nature of the LED channel. It can maximize throughput by optimally assigning power and bit load per sub-carrier [8]- [9]. A detector with responsivity  $R_{PD}$  transforms the received optical power  $h\phi(t)$  into an electrical signal, the signal power is

$$\sigma^2 = h^2 \eta_{PD}^2 \text{LEE}^2 \text{dIQE}^2 \sigma_{IN}^2, \quad (4)$$

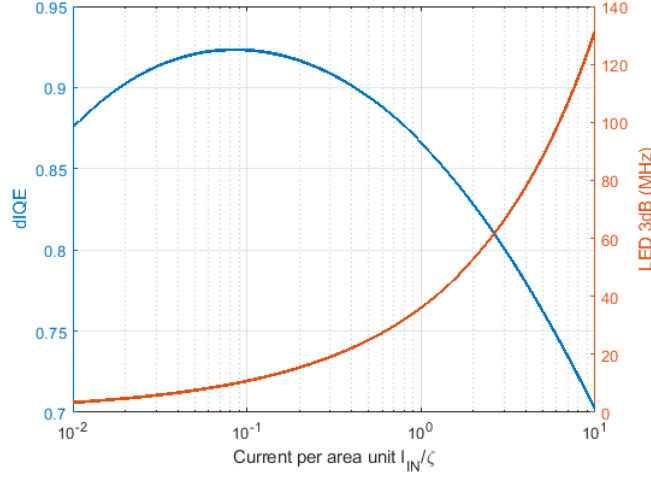


Fig. 1: Differential (small signal) efficiency dIQE and the  $f_{3dB}$  versus the current per unit area. Higher current density accelerates (higher  $f_{3dB}$ ), but reduces the efficiency.

where  $h$  is the path-loss between the transmitter and receiver,  $\eta_{PD} = \eta R_{PD}/q$  and  $\sigma_{IN}^2$  is the variance of  $i(t)$ . Based on the optimization algorithm from [8], the maximum total throughput of the DCO-OFDM over a first-order low-pass LED channel is [4]

$$R = \frac{2}{\ln 2} f_{3dB} \left( \sqrt[3]{\frac{3Q_R \text{dIQE}^2 \text{LEE}^2}{2\Gamma f_{3dB}}} \right) - \frac{2}{\ln 2} f_{3dB} \arctan \left( \sqrt[3]{\frac{3Q_R \text{dIQE}^2 \text{LEE}^2}{2\Gamma f_{3dB}}} \right), \quad (5)$$

where  $\Gamma$  describes the penalty to use QAM to reach a certain uncoded BER [9]. We defined  $Q_R$  as the Communication-Power-over-Noise-Power-Density

$$Q_R = h^2 \eta_{PD}^2 \frac{\sigma_{IN}^2}{N_0}, \quad (6)$$

$N_0$  is the noise density. Additionally,  $\sigma_{IN}^2$  must stay below the DC bias current by a factor of  $z^2$  to avoid clipping, so  $\sigma_{IN}^2 = I_{DC}^2/z^2$  [10]. We have not yet modeled the effects that temperature has on the efficiency and bandwidth of the LED. In the next section, we discuss this topic and the degradation of a DCO-OFDM throughput caused by an increment in temperature.

### Temperature Effects over the OWC Link

In the recombination process from (1), only a portion of the total number of carriers generates photons, the rest will generate heat. This heat causes a temperature increment in the junction affecting the physical characteristics of the LED such as the photon energy, and the radiative and non-radiative recombination parameters. The LED is a self-heating device when it is driven by a DC bias current, like in the case of a DCO-OFDM OWC link. Therefore, we cannot obviate its effects on the total throughput. In [11], we estimated the recombination parameters ABC at different temperatures. Fig. 2 plots the effects of the temperature over the total data rate of the OWC link. We notice not only a degradation of the total throughput but also a displacement of the optimum value  $\zeta$  that maximizes the data rate. The optimum  $\zeta$  value increases from 0.02 to 0.04, when the junction temperature raises from 20 °C to 60 °C.

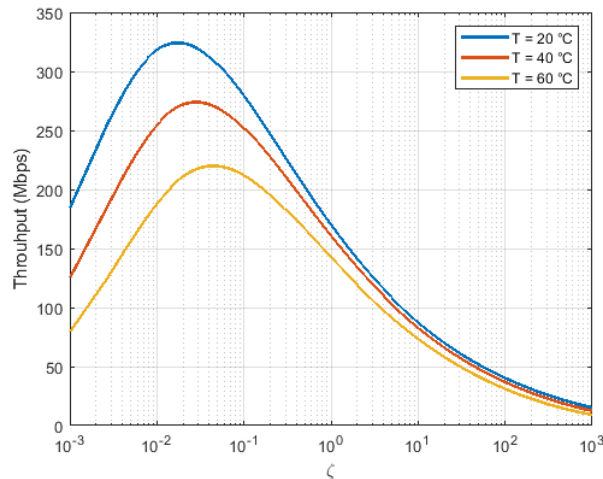


Fig. 2: Modelled effect of the junction temperature on the throughput of a DCO-OFDM link, using measured LED response.  $\zeta$  is a scaling factor for the active region size.

## Conclusions

Simulation of DCO-OFDM shows that the total throughput does not monotonously increase with the 3dB bandwidth. On the contrary, there is an optimum current density that maximizes the total throughput. The total throughput depends also on the efficiency of the LED. Unlike the 3dB bandwidth, there is an efficiency droop at higher current densities. This proves our statement that there is a trade-off between these two parameters. Additionally, an increment in the temperature will not only reduce the data rates of the system but modify the optimum current density.

## References

- [1] A. Tsiatmas, F. M. Willems, J. P. M. Linnartz, S. Baggen, and J. W. Bergmans, "Joint illumination and visible-light communication systems: Data rates and extra power consumption." Institute of Electrical and Electronics Engineers Inc., 9 2015, pp. 1380–1386.
- [2] R. X. G. Ferreira, E. Xie, J. J. D. Mckendry, S. Rajbhandari, H. Chun, G. Faulkner, S. Watson, A. E. Kelly, E. Gu, R. V. Penty, I. H. White, D. C. O'brien, and M. D. Dawson, "High bandwidth gan-based micro-leds for multi-gb/s visible light communications," *IEEE PHOTONICS TECHNOLOGY LETTERS*, vol. 28.
- [3] A. Rashidi, M. Nami, M. Monavarian, A. Aragon, K. Davico, F. Ayoub, S. Mishkat-Ul-Masabih, A. Rishinaramangalam, and D. Feezell, "Differential carrier lifetime and transport effects in electrically injected iii-nitride light-emitting diodes," *Journal of Applied Physics*, vol. 122, 7 2017.
- [4] J.-P. M. G. Linnartz, T. E. B. Cunha, D. V. Romero, and X. Deng, "Throughput optimization for ir-leds in an optical wireless link," *ICC 2022 - IEEE International Conference on Communications*, 2022.
- [5] J. P. M. Linnartz, X. Deng, and P. V. Voorthuisen, "Impact of dynamic led non-linearity on dco-ofdm optical wireless communication," *IEEE Communications Letters*, vol. 25, pp. 3335–3339, 10 2021.
- [6] S. Mardanikorani, X. Deng, J.-P. M. G. Linnartz, and A. Khalid, "Compensating Dynamic Nonlinearities in LED Photon Emission to Enhance Optical Wireless Communication," *IEEE Trans. Veh. Technol.*, vol. 70, no. 2, pp. 1317–1331, 2021.
- [7] J.-P. M. Linnartz, C. Hoelen, P. V. Voorthuisen, T. Elias, B. Cunha, H. Tao, J.-P. M. G. Linnartz, J.-P. Linnartz, and C. Hoelen1.
- [8] S. Mardani and J.-P. Linnartz, "Capacity of the first-order low-pass channel with power constraint," in *Proc. Symp. Inf. Theory Sig. Proc. in the Benelux*, Enschede, The Netherlands, 2018, pp. 149–153.
- [9] S. Mardanikorani, X. Deng, and J.-P. M. G. Linnartz, "Sub-Carrier Loading Strategies for DCO-OFDM LED Communication," *IEEE Trans. Commun.*, vol. 68, no. 2, pp. 1101–1117, 2020.
- [10] S. Mardanikorani, X. Deng, and J. P. M. G. Linnartz, "Optimization and Comparison of M-PAM and Optical OFDM Modulation for Optical Wireless Communication," *IEEE Open J. Commun. Soc.*, vol. 1, pp. 1721–1737, 2020.
- [11] D. Vargas Romero and J.-P. M. G. Linnartz, "Impact of the IR LED temperature on the throughput of optical wireless communication links," in *Proc. SPIE*, 2023, to be published.

# Robust Beam Width Estimation with Sub-Pixel Resolution in Uncontrolled Imaging Conditions

P. Verhulst,<sup>1,2</sup> R. Paesen,<sup>1</sup> and G. Verschaffelt<sup>2</sup>

<sup>1</sup> XenomatiX, Research Park Haasrode, Romeinse straat 6, 3001 Leuven, Belgium

<sup>2</sup> Vrije Universiteit Brussel, Applied Physics Research Group, Pleinlaan 2, 1050 Brussels, Belgium

## Abstract

*Estimating the laser beam widths from a single image of numerous laser beams, which have a spatial extent of only a few pixels on the sensor, is not straightforward. Various beam width estimation methods are described in literature but the presence of image noise or background signals can heavily distort their estimated beam width. In this paper, we examine the feasibility of an image analysis method, proposed in the field of laser eye safety, to determine a laser's beam width. Here, the estimated beam width corresponds to the size of the evaluation window for which the ratio, referred to as the MTH ratio, between the beam power encircled by the evaluation window and its diameter is maximal. Based on simulations and experimental data, we show that this method yields accurate beam width estimations for different transverse beam profiles. We also demonstrate that the method is robust to noisy imaging conditions or the presence of background illumination. Moreover, we expand this method to make precise and accurate sub-pixel resolution beam width estimations on an image of multiple beams which are only of a few pixels large each.*

## Introduction

Laser beam profiling is the process to measure and quantify the (transverse) irradiance profile of a laser source. Commonly, laser beam profiling techniques use a CCD or CMOS sensor to obtain a 2D image of the irradiance profile where the grey value of each pixel represents the local irradiance of the laser beam incident on the sensor [1]. The most critical property examined through beam profiling is the laser's beam width. Common beam width estimation methods are the  $D4\sigma$  or second order moment method corresponding to the ISO 11146 standard [2], the D86 method [3], and the knife-edge method [4]. However, these methods are sensitive to noise or background offset levels on the measurement data [1]. Since in an industrial setting the imaging conditions are typically not precisely controlled, the need for a laser beam width method that works well under poor imaging conditions arises. Additionally, it might be of interest to have a method which can estimate the beam widths of multiple laser beams from a single image while the laser beams have a spatial extent of only a few pixels on the sensor. For these purposes, we investigate the usefulness of the so-called maximal thermal hazard (MTH) method introduced by Schulmeister et al. (2006) in [5].

## Robustness of the MTH Method in Uncontrolled Imaging Conditions

In the MTH method, one searches for the most hazardous combination of power within an area of the irradiance profile and the diameter of that area. The MTH beam width is defined as the diameter of an evaluation window for which the ratio of the power within the window's area and the diameter of the window is maximal [5].

Let us consider circular top-hat irradiance profiles. A top-hat laser beam is defined by an irradiance profile  $I(x, y)$  which has a constant amplitude  $I_0$  within the profile's diameter.

A typical graph of the MTH method, employing a varying circular evaluation window, applied to a computer generated top-hat irradiance profile with a diameter of 100 pixels is shown in Fig. 1. In this figure, we plot the ratio of the power within the circular evaluation window and the diameter of that evaluation window, henceforth referred to as the MTH ratio, as a function of the diameter of the evaluation window. If the diameter of the evaluation window is smaller than the spatial extent of the irradiance profile, the MTH ratio increases with increasing size of the evaluation window. When the evaluation window becomes larger than the irradiance profile, the MTH ratio will decrease as the power in the evaluation window will no longer increase. The evaluation window diameter for which the MTH ratio is maximal, is regarded as the profile's beam width.

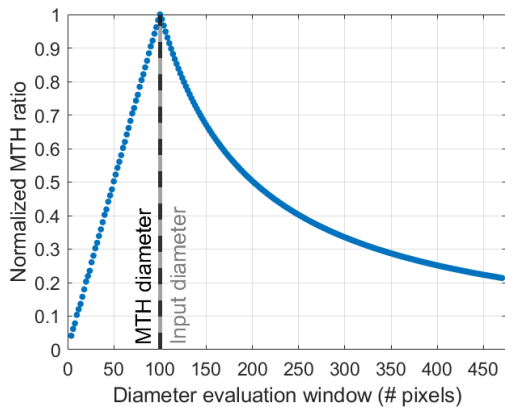


Fig. 1: Estimating the beam width of a circular top-hat irradiance profile as the diameter of a circular evaluation window for which the MTH ratio is maximal, indicated by the black dashed line. The input beam diameter of the top-hat irradiance profile is displayed by the grey line.

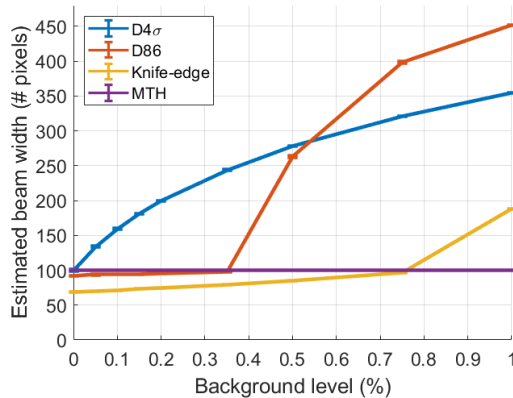


Fig. 2: The estimated beam diameters for all considered beam width methods in function of the added background offset level for computer generated top-hat irradiance profiles with a beam diameter of 100 pixels and with Poisson-Gaussian noise applied.

In order to assess the quality of the beam width estimation using the MTH method, we will compare its performance to the common beam width methods on images of computer generated top-hat irradiance profiles with varying strengths of background offset levels. The strength of the added background level is expressed as a percentage. For example, applying a background offset level of 1% on an image, the background offset level equals to 1% of the maximal pixel grey value of the image. For simplicity, a uniform background offset level across the entire image is considered and ranges from 0 to 1% in our simulation. Lastly, realistic image noise is added to the computer generated images using a Poisson-Gaussian noise model [6]. As the image noise will impact the results, we regenerate the noisy images and repeat the beam width estimations 100 times. The results on a top-hat irradiance profile with a beam diameter of 100 pixels are shown in Fig. 2 where we plot the mean value and the standard deviation of the estimated beam diameters in function of the applied background offset level. We observe that the  $D4\sigma$ , D86 and knife-edge beam width methods are highly susceptible to the presence of a background offset level in the image. Both the D86 and knife-edge method have a tipping point, i.e. a background offset level from which their estimated beam widths suddenly become extremely inaccurate. For the D86 method this tipping point is observed at a background offset level of about 0.35% and for the knife-edge method at about 0.75%. In contrast, the MTH method yields consistently accurate beam diameter estimations for each studied background offset level. In [7] we demonstrated the improved performance of the MTH

method in more detail, e.g. also using experimental data of Vertical-Cavity Surface-Emitting Lasers.

## Sub-Pixel Resolution Beam Width Estimations

A drawback of camera based beam profiling techniques is the limited resolution when the spatial extent of an irradiance profile on the sensor is small compared to the pixel size of the sensor. Therefore, it is generally recommended to fill the sensor's active area as much as possible with a single laser beam [1]. In this section, we will demonstrate that the MTH method can open the path to determine beam widths with a sub-pixel resolution of multiple irradiance profiles which extend only a few pixels on a single image.

In order to increase the resolution of the MTH beam width estimation, we assign weights to the pixels of the irradiance profile corresponding to the amount of overlap between the evaluation window and the pixels. If a pixel is entirely enclosed by the evaluation window, the pixel's signal value is fully added to the enclosed power. We can state that the pixel has a weight 1. Contrarily, the pixels located at the border of the evaluation window are typically only partially enclosed. For large beam diameters as the example in Fig. 1 and 2, these pixels are either completely added or disregarded depending on the amount of overlap when calculating the enclosed power. Now, these edge pixels are given a weight between 0 and 1, depending on the overlap of the evaluation window with that pixel. This overlap is determined through numerical integration using a Monte-Carlo technique. To calculate the enclosed power of an irradiance profile, the signal values of all evaluated pixels are weighted before summing them.

This pixel weighted MTH method is investigated on small top-hat irradiance profiles which are also generated using the Monte-Carlo integration technique. An example of the MTH ratio with a sub-pixel resolution of 0.04 pixels on a computer generated top-hat irradiance profile with a diameter of 3.6 pixels is given in Fig. 3. A good agreement between the input beam diameter and the estimated sub-pixel beam width is observed, illustrated by the grey solid line and black dashed line, respectively. The deviation of the estimated beam width with respect to the input beam diameter can be attributed to the fact that the pixel weighting technique assume that the irradiance across the pixel is uniformly distributed. This is not the case for pixels with a partial overlap of the irradiance profile. Nevertheless, if one would have used the non-pixel weighted MTH method with the resolution of only a pixel, the beam width would have been firmly underestimated as depicted by the red dashed line.

The goal is to accurately estimate the beam widths of small top-hat irradiance profiles with arbitrary diameter. We study the performance of the MTH method on noise-free images without a background offset level as well as on images with a background offset level of 0.1% and with Poisson-Gaussian noise applied. We repeat the beam width estimations 100 times and calculate the mean value and the standard deviation. We assess the quality of the beam width estimation of the pixel weighted MTH method by comparing the results with the non-pixel weighted MTH method. The beam diameter of the top-hat irradiance profiles is varied from 2 to 11 pixels in steps of 0.2 pixels. The sub-pixel resolution of the pixel weighted MTH method is set at 0.05 pixels. The results are shown in Fig. 4. While the non-pixel weighted MTH method nicely obtains the input beam diameter for integer input radii, it also returns integer values for non-integer input radii. While an error of the beam width estimation of 1 pixel can be acceptable for very large beam diameters, it yields poor beam width estimations for beam profiles only extending a few pixels. Displayed in red in Fig. 4, the pixel weighted MTH method

increases the accuracy of the beam width estimation and removes the step-like behavior. For input beam diameters larger than 3 pixels, the maximal deviation between the beam width and its estimation is improved from 1.6 to 0.6 pixels, illustrated by the dashed lines in the figure. When the background offset level and Poisson-Gaussian noise is present in the computer generated images, the pixel weighted MTH method maintains the improved accuracy with a high precision.

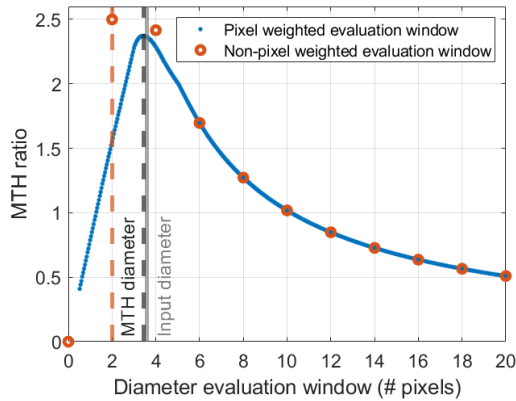


Fig. 3: The non-pixel weighted and pixel weighted MTH ratio of a top-hat irradiance profile with a diameter of 3.6 pixels.

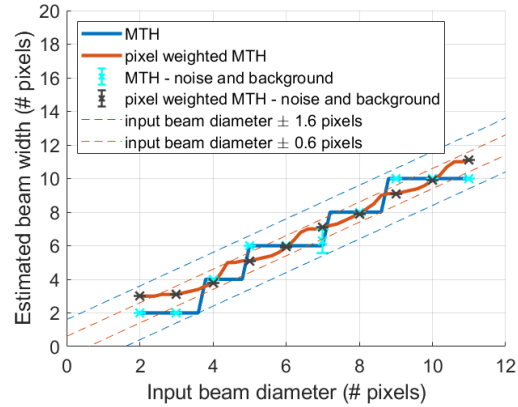


Fig. 4: The estimated beam widths for the pixel weighted and non-pixel weighted MTH method in function of the input beam diameter of computer generated top-hat irradiance profiles.

## Conclusion and Future Perspectives

We have demonstrated that the MTH methods is a suitable beam width estimation method for circular top-hat irradiance profiles in poor imaging conditions. Compared to the commonly used beam width methods, the MTH method yields more precise and accurate results. Furthermore, we expanded upon the MTH method through a pixel weighting technique to estimate beam widths of only a few pixels large with a sub-pixel resolution without losing its robustness in poor imaging conditions.

The residual error on the sub-pixel resolution seen in Fig. 4 can be improved upon by handling the weighting of the edge pixels in a more advanced manner. Expanding the method to take into account the non-uniform irradiance distributions across the edge pixels, the pixel's signal value added to the enclosed power can be more representative.

## References

- [1] C. B. Roundy and K. D. Kirkham, "Current Technology of Laser Beam Profile Measurements," in *Laser Beam Shaping*, CRC Press, 463-524, 2014.
- [2] ISO11146-1:2005(en), "Lasers and laser-related equipment — Test methods for laser beam widths, divergence angles and beam propagation ratios — Part 1: Stigmatic and simple astigmatic beams".
- [3] D. Wright, "Beamwidths of a diffracted laser using four proposed methods," *Optical and Quantum Electronics*, vol. 24, 1129-1135, 1992.
- [4] A. E. Siegman, M. W. Sasnett and T. F. Johnston, "Choice of Clip Levels for Beam Width Measurements Using Knife-Edge Techniques," *IEEE Journal of Quantum Electronics*, vol. 4, 1098-1104, 1991.
- [5] K. Schulmeister, et al., "Comparison of different beam diameter definitions to characterize thermal damage of the eye," in *Proceedings of SPIE, Laser Beam Control and Applications*, 61011A, 2006.
- [6] A. Foi, et al., "Practical Poissonian-Gaussian Noise Modelling and Fitting for Single-Image Raw-Data," *IEEE Transactions on Image Processing*, vol. 17, 1737-1754, 2008.
- [7] P. Verhulst, R. Paesen, and G. Verschaffelt, "Robust Beam Width Estimation with Sub-Pixel Resolution in Uncontrolled Imaging Conditions," *Applied Optics*, 2022. (*Under review*)

# Demonstration of low differential phase noise for optical phased arrays with optical amplification

B.S. Vikram<sup>1</sup>, Marco Gagino<sup>1</sup>, A. Millan-Mejia<sup>2</sup>, L. Augustin<sup>2</sup>, K.A. Williams<sup>1</sup>,  
V. Dolores Calzadilla<sup>1,3</sup>

<sup>1</sup> Technical University Eindhoven, Dept. of Electrical Engineering, Groene Loper 19, 5612 AP Eindhoven, The Netherlands

<sup>2</sup> SMART Photonics, High Tech Campus 29, AE Eindhoven, The Netherlands

<sup>3</sup> Photonic Integration Technology Center, Groene Loper 19, 5612 AP Eindhoven, The Netherlands

*Optical phased arrays (OPAs) are key enablers for light detection and ranging (LiDAR) in autonomous vehicles, free space optical communications, imaging and coherent beam combining. Active OPAs (with amplitude and phase control) allow the control of individual channel gains along with phases for enhanced control of far-field beam pattern. Path length variations and noise from amplifiers degrade the differential phase noise between the OPA channels, which is a key performance indicator that determines the far-field performance in terms of power in the main lobe, extinction of side lobes and pointing error. Conventionally, in fiber-based platforms, multiple phase locked loops are required to reduce the differential phase noise by locking the channels.*

*In this work, we investigate the differential phase noise in an InP active OPA and demonstrate less than 10 mrad differential phase noise corresponding to a stability better than  $\lambda/600$ . To the best of our knowledge, this is the first demonstration of low differential phase noise in an active OPA with amplification in a photonic integrated platform. This result enables on-chip OPA amplification in the InP platform without active locking, thus reducing the system complexity and power consumption.*

## Introduction

Optical phased arrays (OPAs) facilitate agile scanning of the optical beam while avoiding the moving parts that limit the speed and reliability. The beam steering capabilities of OPAs are utilized in light detection and ranging (LiDAR), free space optical communications (FSO), and for power scaling through coherent beam combining (CBC). In comparison to passive OPAs providing only phase control of each element, active OPAs (i.e., with optical amplifiers) allow amplitude and phase control of each element. The addition of amplitude control allows improved control of far-field beam pattern and aids in adaptive ranging. However, the noise added by the amplifiers and the path length fluctuations between the array elements deteriorates the phase noise, reducing the temporal correlation between the OPA elements. The deterioration, described by the differential phase noise between the OPA elements, degrades the side lobe suppression ratio of the far-field beam.

Conventionally, optical phase locked loops (OPLLs) [1], [2] are employed in aperture channels in fiber based OPAs to mitigate the degradation. As the number of elements in the OPA increase, multiple OPLLs[3] are required, significantly increasing the complexity and cost of the system. Integrated photonics has the potential for reducing the differential phase noise owing to reduced path length fluctuations between closely spaced elements in a photonic integrated circuit (PIC). OPAs can be implemented in various PIC platforms such as Silicon (Si) [4], Indium Phosphide (InP) [5], and Silicon Nitride (SiN) [6]. Among these, InP allows implementation of active OPAs with

semiconductor optical amplifiers (SOAs) in each channel. The additional phase noise generated from carrier density fluctuations and amplified spontaneous emission (ASE) from the SOAs along with the path length fluctuations on the chip will determine the far-field properties.

In this work, we report, to the best of our knowledge, the first measurements of differential phase noise in InP PICs. The measured differential phase noise ( $<10$  mrad) corresponds to a stability of better than  $\lambda/600$  between the OPA elements, and is achieved without the use of OPLLs. Analytical equations are used to evaluate the negligible deterioration of the far-field beam.

## Experimental Setup

The measurement setup including the driving sources, the PIC and the measurement equipment is shown in Figure 1. An external laser source (100 kHz, Keysight 81960A) drives the PIC whose temperature is maintained at 18° C. The edge-coupled signal, amplified by a booster SOA (driven at a current density of 5 kA/cm<sup>2</sup>), is subsequently distributed among the individual OPA elements by a star coupler. Each element consists of a phase modulator (PM) and a channel SOA (driven at 5 kA/cm<sup>2</sup>) which provide the phase and amplitude control respectively. An RF signal source (3 MHz) drives one of the PMs, frequency shifting the signal to obtain a heterodyne beat between two channels; no signal is applied on the other. A network of multi-mode interference (MMI) couplers is used to extract the beat signal between two adjacent channels, and is measured by an electrical spectrum analyzer (ESA) to extract the differential phase noise.

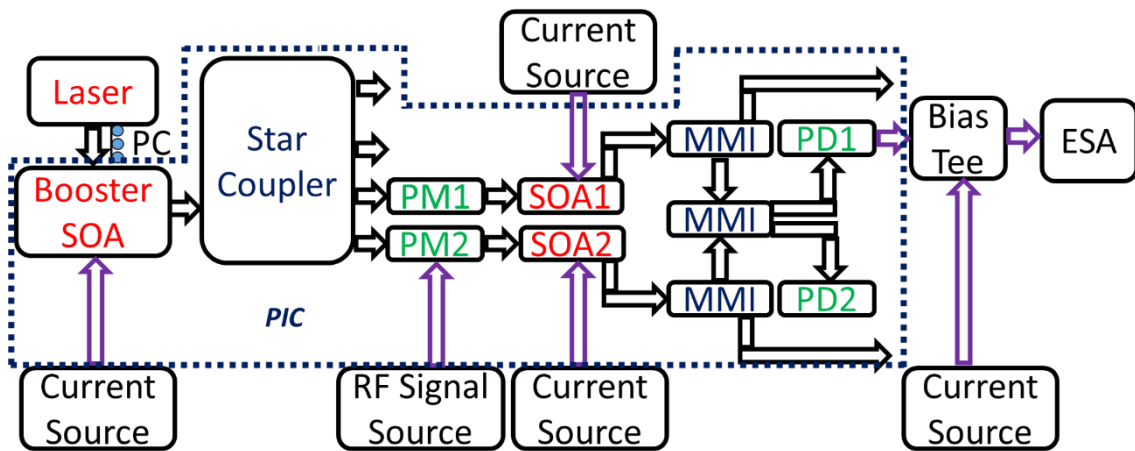


Figure 1 Schematic of the setup showing the sections of chip utilized for differential phase noise measurements. VOA-variable optical attenuator, SOA-Semiconductor optical amplifier, MMI-multimode interference coupler, PM-phase modulator, ESA- Electrical spectrum analyzer, PD-photodiode, PC- polarization controller.

## Results

The differential phase noise spectra measured with the laser operated at 1550 nm is shown in Figure 2. The differential phase noise rises at the rate of  $\sim 30$  dB/decade between 10 kHz to 100 kHz indicating that the temporal phase fluctuations between the two paths have reduced correlation. The rate falls to  $\sim 2$  dB/decade below 10 kHz indicating highly correlated temporal phase fluctuations between the two paths. The RMS differential phase noise (obtained from integrating the plot from 100 Hz to 1 MHz) is less than 10 mrad across the C-band which is equivalent to a stability better than  $\lambda/600$ .

Figure 3 shows the influence of differential phase noise on the far-field beam pattern that is evaluated using equations (1-2) [7] for the case of emitters (100 elements, 2.2  $\mu\text{m}$  spaced) with uncorrelated phase errors.

$$I_G^{unpert} = \frac{\sin^2(\pi N \theta d / \lambda)}{\sin^2(\pi \theta d / \lambda)} \quad (1)$$

$$I_G^{uncorr} = \exp(-\sigma_\phi^2) I_G^{unpert} + N(1 - \exp(-\sigma_\phi^2)) \quad (2)$$

Here,  $N$  is the number of channels in the array,  $\theta$  is the angular position,  $d$  is the channel spacing,  $\lambda$  is the wavelength,  $\sigma_\phi$  is the RMS phase noise,  $I_G^{unpert}$  is the unperturbed (ideal) far-field intensity,  $I_G^{uncorr}$  is the far-field intensity with uncorrelated phase errors. When the differential phase noise is 10 mrad, the influence on the far-field beam pattern is minimal. Significant deterioration is expected when the differential phase noise is in the range of several hundreds of milliradians.

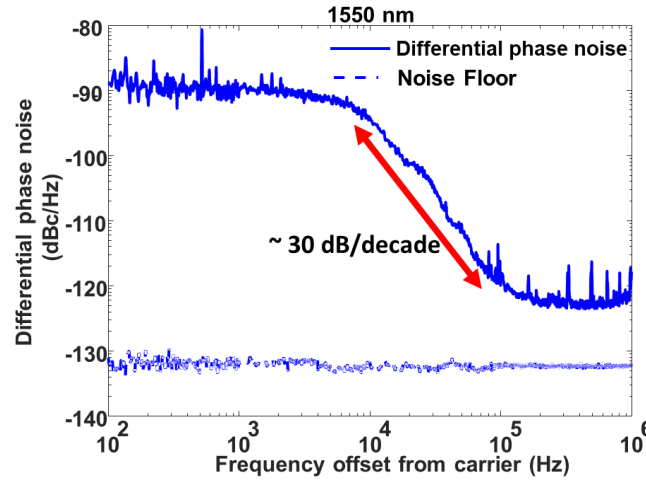


Figure 2 Differential phase noise spectrum with the source laser at 1550 nm along with measurement noise floor.

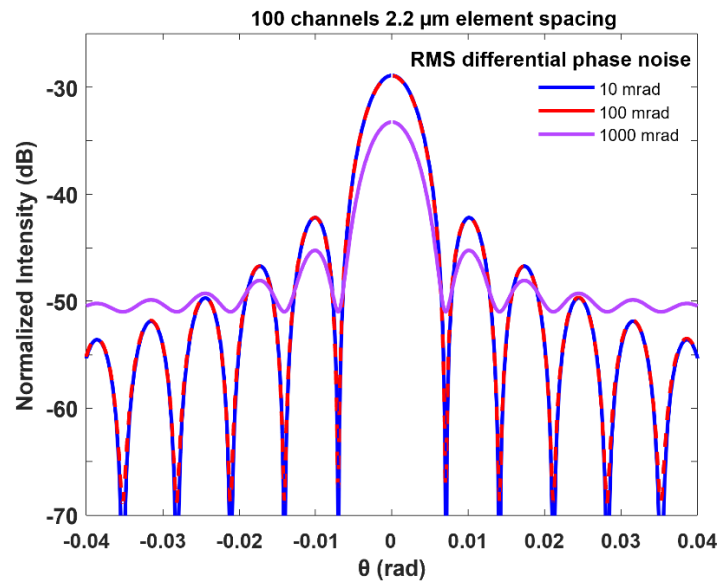


Figure 3 Impact of differential phase noise on far-field beam pattern for a 100 channel OPA with 2.2  $\mu\text{m}$  spacing.

## Conclusions

We report a low differential phase noise (<10 mrad) between active OPA channels in an InP PIC without any active locking. These initial results indicate the future potential of InP PICs for scalable active OPAs with reduced complexity and power consumption.

## Acknowledgment

*The authors would like to acknowledge Gilles Feugnet and Jerome Bourderionnet from Thales Research and Technology, for insightful technical discussions. This work has received funding support from the European Union Horizon 2020 program through the NewControl project under grant no 826653.*

## References

- [1] K. Balakier, M. J. Fice, L. Ponnampalam, A. J. Seeds, and C. C. Renaud, "Monolithically Integrated Optical Phase Lock Loop for Microwave Photonics," *Journal of Lightwave Technology*, vol. 32, no. 20, pp. 3893–3900, Oct. 2014, doi: 10.1109/JLT.2014.2317941.
- [2] Sasa Ristic, Ashish Bhardwaj, Mark J. Rodwell, Larry A. Coldren, and Leif A. Johansson, "An optical phase-locked loop photonic integrated circuit," *Journal of Lightwave Technology*, vol. 28, no. 4, pp. 526–538, 2009.
- [3] A. Yariv *et al.*, "Coherent beam combining with multilevel optical phase-locked loops," *JOSA B*, Vol. 24, Issue 12, pp. 2930–2939, vol. 24, no. 12, pp. 2930–2939, Dec. 2007, doi: 10.1364/JOSAB.24.002930.
- [4] K. van Acoleyen, W. Bogaerts, and R. Baets, "Two-dimensional dispersive off-chip beam scanner fabricated on silicon-on-insulator," *IEEE Photonics Technology Letters*, vol. 23, no. 17, pp. 1270–1272, 2011, doi: 10.1109/LPT.2011.2159785.
- [5] M. Gagino, M. B. J. van Rijn, E. A. J. M. Bente, M. K. Smit, and V. Dolores-Calzadilla, "Broadband Operation of an InP Optical Phased Array," *IEEE Photonics Technology Letters*, vol. 34, no. 10, pp. 541–544, May 2022, doi: 10.1109/LPT.2022.3171979.
- [6] B. Szlag *et al.*, "SiN integrated optical phased arrays for two-dimensional beam steering at a single near-infrared wavelength," *Optics Express*, Vol. 27, Issue 4, pp. 5851–5858, vol. 27, no. 4, pp. 5851–5858, Feb. 2019, doi: 10.1364/OE.27.005851.
- [7] C. D. Nabors, "Effects of phase errors on coherent emitter arrays," *Applied Optics*, Vol. 33, Issue 12, pp. 2284–2289, vol. 33, no. 12, pp. 2284–2289, Apr. 1994, doi: 10.1364/AO.33.002284.

# Design of a 785 nm/1850 nm wavelength (de)multiplexer based on multimode interference coupler

K. Wang, M. Dijkstra, C.E. Osornio Martinez, S.M. García-Blanco

Integrated Optical Systems Group, MESA+ Institute, University of Twente, 7500 AE Enschede, The Netherlands

## Abstract

*Aluminium oxide material ( $Al_2O_3$ ) is a promising material for integrated photonics with a very wide transparency window (200 – 5500 nm). Channel waveguides fabricated by RF reactive sputtering have shown losses lower than 0.1 dB/cm at 1550 nm[1]. Compared with other silicon-based photonic material platforms,  $Al_2O_3$  has higher trivalent rare earth solubility[2]. Amplification and lasing can be achieved by  $Tm^{3+}$  doped  $Al_2O_3$  in the wavelength range of  $\sim 1.8$ - $1.9 \mu m$ [3]. After being amplified, the pump laser ( $\sim 785$  nm) and the signal laser ( $\sim 1850$  nm) need to be demultiplexed.*

*In this work, a demultiplexer operating at 785 nm and 1850 nm wavelengths in a 550 nm thick  $Al_2O_3$  platform was designed based on the MMI principle. The optimized MMI demultiplexer has a multimode region with a size of  $14.65 \mu m * 3150 \mu m$ . For 785 nm and  $1.85 \mu m$  wavelengths, the simulated extinction ratio (ER) is 37.75 dB and 23.47 dB respectively, and the simulated insertion loss (IL) is lower than 0.1 dB in both wavelength.*

## Introduction

$Al_2O_3$  is a promising integrated optical material, which is reported in the previous literature as a very suitable rare earth doped host material[2]. Thulium-doped  $Al_2O_3$  can be used to make amplifiers work at 1850 nm wavelength[3]. For the on-chip amplifier, an optical wavelength splitter can be used to combine/separate the pump and signal laser before/after amplification.

Several approaches have been reported to implement (de)multiplexer in integrated photonics, including directional couplers[4], Mach-Zehnder interferometers[5] and multimode interferometers (MMI)[6]. Among them, MMI has as advantages of ease of fabrication, low excess loss, compact size, and large fabrication tolerance errors[6].

In this work, an MMI-based 785 nm/1850 nm wavelength (de)multiplexer is designed and simulated in a 550 nm thick  $Al_2O_3$  platform. An additional taper is added between the output taper and MMI region to achieve low insertion loss at dual wavelengths, which will be described in detail in the design section below. The results obtained by simulation show excellent optical characteristics, with insertion loss below 0.1 dB at both pump and signal wavelengths.

## Design

The cross section of the  $Al_2O_3$  platform is shown in Fig. 1 (a). It consists of a 550 nm thick  $Al_2O_3$  strip waveguide on  $8 \mu m$   $SiO_2$  layer and covered with  $6 \mu m$   $SiO_2$  cladding layer. Fig. 1 (b) shows the layout of a basic MMI-based 1x2 (de)multiplexer. According to the MMI principle[7], the input/output tapers are placed at the position corresponding to  $\pm W/6$  from the centerline of the MMI region, where  $W$  is the width of the MMI. In

order to achieve that both the 785 nm and 1850 nm light can be input from the same port of the MMI, but output from different output ports, the length of the MMI needs to satisfy the following equations[6], [7]:

$$L_{\pi,\lambda} = \frac{\pi}{\beta_0 - \beta_1} \cong \frac{4n_{eff}W^2}{3\lambda} \quad Eq. 1$$

$$L_{MMI} = n \times L_{\pi,785} = (n + m) \times L_{\pi,1850} \quad Eq. 2$$

where,  $L_{\pi,\lambda}$  is the beat length for the wavelength  $\lambda$ ,  $\beta_0$  and  $\beta_1$  are propagation constants of mode 0 and mode 1 of the multimode region respectively,  $n_{eff}$  is the effective index of the fundamental mode,  $W$  is the width of the MMI region,  $L_{MMI}$  is its length,  $L_{\pi,785}$  and  $L_{\pi,1850}$  are beat lengths for 785 nm and 1850 nm respectively,  $n$  is integer number and  $m$  is odd number.

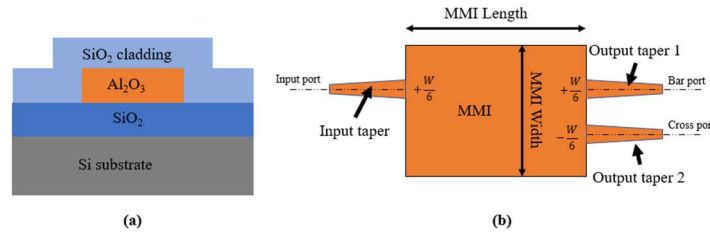


Fig. 1 (a) Cross section of the Al<sub>2</sub>O<sub>3</sub> platform. (b) The schematic of the MMI based 1x2 (de)multiplexer.

Fig. 2 (a) shows the simulated intensity near the input port of the MMI. The intensity of the field at the corner of input port is very low. Therefore, the corner area does not affect the working of the MMI[8]. The maximum angle of laser entering MMI from the input waveguide is [8]:

$$\theta_C = \cos^{-1} \frac{n_{cl}}{n_{co}} \quad Eq. 3$$

where  $n_{cl}$  and  $n_{co}$  are the effective refractive indices of cladding and core respectively at the wavelength of interest. The effective refractive indices of cladding and core used in this work are obtained via Lumerical Mode simulation.

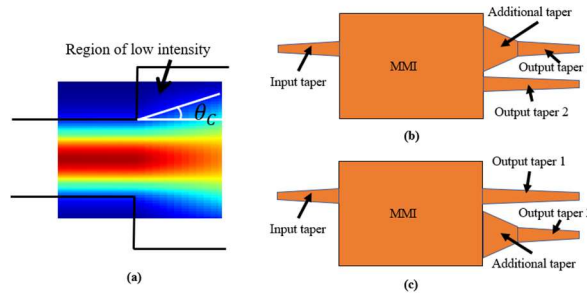


Fig. 2 (a) Field pattern near the input port of MMI chamber. (b) and (c) Optimized MMI shape. An additional taper is added before the output port 1 or output port 2.

Therefore, an additional taper added between the output taper and MMI chamber, like shown in Fig. 2 (b) and (c), will not intersect the outermost ray as long as the following condition is satisfied[8]:

$$\frac{L_{at}}{\frac{W_{at}}{2}} \leq \cot(\theta_c) \quad Eq. 4$$

where  $L_{at}$  is the length of the additional taper,  $W_{at}$  is the width of the additional taper at the interface with the MMI region.

### Optimized design

In this work, the FDE solver in Lumerical is used to simulate the MMI effective indices of different MMI widths. From the simulation, the beat length at 785 nm and 1850 nm for different MMI widths is calculated according to Eq. 1 and shown in Fig. 3 (a). And the beat length ratio between  $L_{\pi,785}/L_{\pi,1850}$  is shown in Fig 3 (b). In order to fulfill Eq. 2, one possible solution is  $n = 5$ ,  $m = 7$ , Which leads to a beat length ratio of 2.4. As seen in Fig. 3 (b), the corresponding MMI width is 14.65  $\mu\text{m}$ .

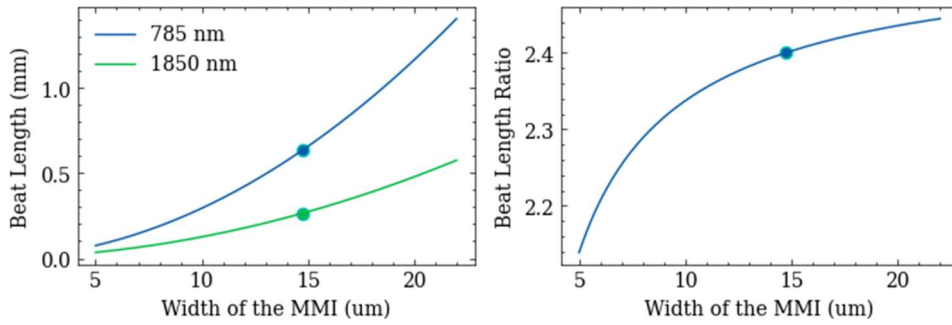


Fig. 3. (a) Beat length of different MMI widths. (b) Beat length ratio of different MMI widths.

Due to beat length from Eq. 1 is an approximation of the period of light change in the MMI[7]. In order to get the accurate MMI length, simulations of MMI length sweep are done in Lumerical EME solver. The results shows 3150  $\mu\text{m}$  and 3155  $\mu\text{m}$  are the length of MMI chamber to give the best insertion loss for 1850 nm and 785 nm respectively.

Therefore, the final design selected Fig. 2 (c), the MMI length is set to 3150  $\mu\text{m}$ . And an additional taper with 5  $\mu\text{m}$  length, 7.7  $\mu\text{m}$  width is added at the 785 nm output port.

### Results and discussion

The simulation was accomplished by the EME solver in Lumerical software.

Fig. 4 shows the simulated intensity pattern of the optimized (de)multiplexer when working at 785 nm (right) and 1850 nm (left). The 785 nm output power focus at the cross port, while the 1850 nm output power focus at the bar port.

The performances of the wavelength demultiplexer are characterized by the extinction ratio (ER) and the insertion loss (IL), which are defined as:

$$ER = 10 \log \left( \frac{P_d}{P_u} \right) \quad Eq. 5$$

$$IL = 10 \log \left( \frac{P_d}{P_i} \right) \quad Eq. 6$$

where,  $P_d$ , and  $P_u$  are the intensities in the desired and undesired output waveguides respectively, and  $P_i$  is the input optical power at input waveguide.

The simulated insertion loss are 0.094 dB and 0.095 dB for 785 nm and 1850 nm respectively. The extinction ratio are 37.75 dB and 23.47 dB respectively. Fig. 5 shows the additional insertion loss caused by MMI length variations and wavelength variations, which represent the fabrication tolerance error and bandwidth of MMI respectively. With a requirement of 1 dB insertion loss, the fabrication tolerance of the MMI length is about  $\pm 12 \mu\text{m}$ , the bandwidth of the MMI is 5.6 nm and 16.4 nm for pump and signal wavelength respectively.

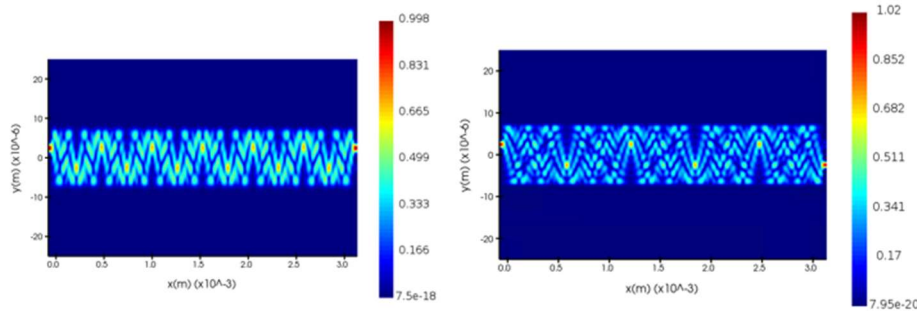


Fig. 4. Simulated intensity pattern of the demultiplexer at (a) 1850 nm wavelength (b) 785 nm wavelength.

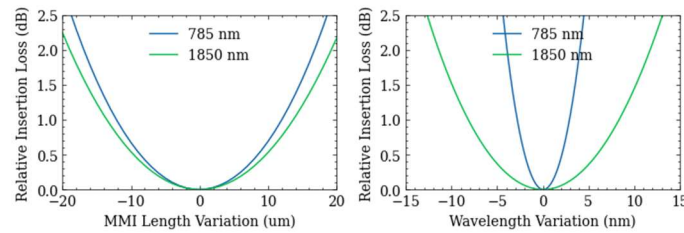


Fig. 5. Relative insertion loss caused by variation of (a) MMI length and (b) Wavelength.

## Conclusion

This paper proposes a (de)multiplexer operating at 785 nm and 1850 nm wavelengths in a 550 nm thick  $\text{Al}_2\text{O}_3$  platform. Simulation results showed that the insertion losses are below 0.1 dB for both wavelengths, extinction ratio is 37.75 dB for 785 nm and 23.47 dB for 1850 nm. The size of the demultiplexer MMI region is  $14.65 \mu\text{m} * 3150 \mu\text{m}$ .

## References

- [1] W. Hendriks *et al.*, "Poly-crystalline low-loss aluminium oxide waveguides," in *PROCEEDINGS OF SPIE*, Mar. 2021, p. 32. doi: 10.1117/12.2578141.
- [2] W. A. P. M. Hendriks *et al.*, "Rare-earth ion doped  $\text{Al}_2\text{O}_3$  for active integrated photonics," *Advances in Physics: X*, vol. 6, no. 1. Taylor and Francis Ltd., 2021. doi: 10.1080/23746149.2020.1833753.
- [3] N. Li *et al.*, "High-power thulium lasers on a silicon photonics platform," *Opt Lett*, vol. 42, no. 6, p. 1181, 2017, doi: 10.1364/ol.42.001181.
- [4] Y. Ding *et al.*, "On-chip two-mode division multiplexing using tapered directional coupler-based mode multiplexer and demultiplexer," *Optics Express*, Vol. 21, Issue 8, pp. 10376-10382, vol. 21, no. 8, pp. 10376–10382, Apr. 2013, doi: 10.1364/OE.21.010376.
- [5] M. Papadovasilakis *et al.*, "Fabrication tolerant and wavelength independent arbitrary power splitters on a monolithic silicon photonics platform," *Optics Express*, Vol. 30, Issue 19, pp. 33780-33791, vol. 30, no. 19, pp. 33780–33791, Sep. 2022, doi: 10.1364/OE.463721.
- [6] C. Yao *et al.*, "An ultracompact multimode interference wavelength splitter employing asymmetrical multi-section structures," *Optics Express*, Vol. 20, Issue 16, pp. 18248-18253, vol. 20, no. 16, pp. 18248–18253, Jul. 2012, doi: 10.1364/OE.20.018248.
- [7] L. B. Soldano and E. C. M. Pennings, "Optical Multi-Mode Interference Devices Based on Self-Imaging: Principles and Applications," *Journal of Lightwave Technology*, vol. 13, no. 4, pp. 615–627, 1995, doi: 10.1109/50.372474.
- [8] A. Bakhtazad *et al.*, "MMI Multiplexer for Dual-Channel Erbium-Doped Waveguide Amplifiers," *Optics Express*, Vol. 9, Issue 4, pp. 178-183, vol. 9, no. 4, pp. 178–183, Aug. 2001, doi: 10.1364/OE.9.000178.

# Large Scale optical controlled mm-wave beam steering system for non-terrestrial network

Shiyi Xia<sup>1,3,4\*</sup>, Mingyang Zhao<sup>5</sup>, Guotong Li<sup>3,4</sup>, Ad.C.F. Reniers<sup>2</sup> and Ton Koonen<sup>1</sup>

<sup>1</sup> Institute of Photonic Integration, Eindhoven University of Technology, NL 5600 MB Eindhoven, Netherlands

<sup>2</sup> Department of Electrical Engineering, Eindhoven University of Technology, NL 5600 MB Eindhoven, Netherlands

<sup>3</sup> University of Chinese Academy of Sciences, Beijing 100049, China

<sup>4</sup> Innovation Academy for Microsatellites of CAS, Shanghai 201203, China

<sup>5</sup> International Collaborative Laboratory of 2D Materials for Optoelectronics Science & Technology of Ministry of Education, Institute of Microscale Optoelectronics, Shenzhen University, Shenzhen 518060, China.

Correspond author: s.xia@tue.nl

## Abstract

*Non-terrestrial networks' primary benefits their ability to give worldwide coverage, completing and enhancing terrestrial networks in the air, sea, forest, and distant locations. Optical wireless communication is progressively taking the place of non-terrestrial inner network connectivity. Beamforming is necessary to concentrate the energy and lower power usage. The optical control mm-wave beam-steering system in this situation not only fixes the broadband beam squint issue, but also works well with optical wireless communication. Because of arrayed waveguide grating routers (AWGR), we suggest and verified a sizable optical controlled mm-wave phased array beam-steering system.*

## Introduction

Satellites are attractive to both developed and developing countries because of their wide coverage. Low earth orbit(LEO) satellite networks enable ubiquitous wireless coverage, which facilitates information access in non-urban areas of terrestrial networks. LEO satellites serve a wide range of audiences, including aircraft, ships, and automobiles, which in turn places a demand on beam flexibility. Beamforming is an essential technology in user-customized design. In the 3GPP next generation communication protocol [1], satellite Internet is defined as a complement to terrestrial Internet.

First, in 1995 Frigyes et al. used optical techniques to solve various approaches to the fundamental problem of broadband phased arrays, namely the most critical beam strabismus [2]. Xu et al. 1996 demonstrated a real-time delay-line phased array antenna feeding system based on a multi-channel optical outlier detection technique [3]. Corral et al. in 1997 proposed and demonstrated a new approach for real-time delay (TTD) optical feeding of phased array antennas [4]. Yegnanarayanan et al. proposed and demonstrated the extension to a two-dimensional (2-D) antenna array with independent control of azimuth and elevation angles by using an intermediate-stage optical wavelength conversion [5]. Lee et al. proposed an optical real-time delayed beamforming system using dispersion-compensating fiber and multi-wavelength lasers for phased-array antennas in 2011 [6]. However, the efficiency of the photovoltaic conversion and the high complexity of the system prevent the extensive use of delay lines to compensate for each antenna array in large scale arrays. And in satellite communications, a wide range of scans is necessary, especially for low orbiting satellites. We therefore propose a two-stage optical controlled phased array antenna. For large angle scans, the optical true-time-delay



$\Delta f$  is the half bandwidth of wide band signal, and  $f_0$  is the center frequency of the wide band signal. As normal, the maximum deflection angle  $\Delta\theta_{f_{\max}} \leq \Delta\theta_{1/2} / 4$ , where  $\Delta\theta_{1/2}$  is the half power beam width (HPBW), when  $\theta_B = 60^\circ$ . Assume  $\Delta\theta_{1/2} = 2^\circ$ , the  $\Delta f_{\max} / f_0$  was limited to 0.02. It narrows the bandwidth of signal. As insert an OTTD, length  $l$ , time delay  $\tau_A$ , the antenna crossing time can easily reduce as  $T_A' = T_A - \tau_A = L \sin \theta_B / c - l / c$ . The deflection angle could rewrite as

$$\Delta\theta'_{f} \approx -(\Delta f / f_0)(1 - \tau_A / T_A) \tan \theta_B . \quad (2)$$

If  $T_A = \tau_A$ ,  $\Delta\theta'_{f} = 0$ , there is no antenna across time. Cleverly reducing the complexity of the system by decomposing the subarray, as shown in Fig.1, to reduce the impact of the crossing time on the beam. In this architecture, the OTTD time delay in  $M^{\text{th}}$  subarray can be selected as  $\tau_M = m(M-1)d \sin \theta_B / c$ , which makes the signals of each sub-array located in the  $\theta_B$  direction of the beam will have no time difference. The phase shift value provided by the  $i^{\text{th}}$  digital phase shifter within each antenna sub-array is  $i\varphi_B$ . Although the internal subarray still receives the effect of transition time and aperture effect, each subarray beam will still squint. However, the aperture area of each subarray is reduced to  $1/M$  of the original, so the aperture crossing time will be reduced to  $T_A / M$  of the original. Therefore, the system limits on the instantaneous signal bandwidth can be relaxed by a factor of  $M$  by allowing a subarray beam offset angle of  $1/4$  the HPBW,  $\Delta f_{\max} / f_0 \leq M \cdot \Delta\theta_{1/2} / 2 \sin \theta_B$ .

## Experiment and Results

The key components of the experiment are a tunable laser source (TLS Santec MLS-2100) and two symmetrical AWGRs (Gemfire 80ch AWG DMX). TLS control the true-time-delay value via adjusting the wavelength. Tunable optical carriers generated by the TLSs is coupled and fed into an Mach-Zehnder modulator (MZM) via a polarization controller. The optical carrier is modulated by the RF signal generated by the vector network analyzer (VNA, Agilent Technologies PNA Network Analyzer E8361C). The VNA generates millimeter wave RF signals in the frequency range from 25 GHz to 36 GHz. Erbium-doped fiber amplifier (EDFA) is used to compensate for the loss of symmetrical AWGR to ensure that the optical power at the input PD (XPDV2120RA) is 0 dBm, which is in the linear area of photodiode (PD). The Variable gain amplifier (VGA) on the RF board is used to balance the amplitude of the two sub-arrays. The  $S_{21}$  phase response of each link is obtained experimentally by detecting the signals fed back from the different output points (e.g., Figure 2, orange monitoring point).

The experimental results are shown in Figure 3. Figure 3(a) is the optical domain spectrum after observing the modulation through the spectrometer. By appropriately adjusting  $V_\pi$ , the modulated signal lies in the linear region of the MZM. The phase response obtained at the detection point PD allows to analyze the delay generated by the different wavelengths of optical carriers passing through the AWGR. By fitting the data, we obtain different time delays: 0.058434 micro second, 0.71755 micro second, 0.91651 micro second, 2.736 micro second, 1.5178 micro second, 3.3476 micro second. Due to the instability of the PD, there are 20 Pico second errors in the delay-time.

In Fig 3(b), the digital phase shifter is given a different amount of phase shift by the beam pointing principle. The beam pointing of  $-16.56^\circ$  at 27 GHz is achieved. However,

without OTTD, the beam points at  $-14.76^\circ$  and  $-22^\circ$  at 26 GHz and 28 GHz, respectively. This has a large pointing error. Therefore, the  $S_{21}$  phase response of each path was remeasured using the experimental set-up as shown in Fig 2. The  $S_{21}$  phase response of each path was remeasured using the experimental equipment as in Figure 2. After recalculating each phase for beam synthesis, the beam is no longer shifted at 26 GHz, 27 GHz and 28 GHz.

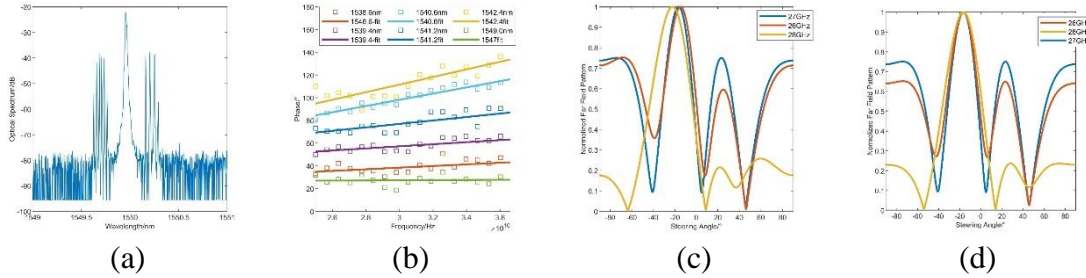


Figure 3. Experimental results: (a) Spectrograms; (b) Different wavelength delay time; (c) Phase response of AWGR; (d) Optical controlled phased-array far-field pattern

## Conclusion

In this paper, the results of the vector network analyzer test verified the compensation of the crossing time by using symmetric AWGR-based OTTD on the subarray. It reduces the beam pointing shift of the phased-array antenna in broadband wide-angle scanning. The advantage of using AWGR in the future lies more in the conversion of WDM to air-division multiplexing in all-optical satellite Internet, and the combination of optical multiplexing mode and RF multiplexing mode is realized to increase the throughput capacity of the satellite under the restricted frequency band. In the next step we will further use AWGR compensation for a wide range of angles and adjust the digital phase shifter for fine angle scanning experiments.

## References

- [1] Rinaldi F, Maattanen H L, Torsner J, et al. Non-terrestrial networks in 5G & beyond: A survey[J]. IEEE access, 2020, 8: 165178-165200.
- [2] Frigyes I, Seeds A J. Optically generated true-time delay in phased-array antennas[J]. IEEE Transactions on Microwave Theory and Techniques, 1995, 43(9): 2378-2386.
- [3] Xu L, Taylor R, Forrest S R. True time-delay phased-array antenna feed system based on optical heterodyne techniques[J]. IEEE Photonics Technology Letters, 1996, 8(1): 160-162.
- [4] Corral J L, Marti J, Fuster J M, et al. True time-delay scheme for feeding optically controlled phased-array antennas using chirped-fiber gratings[J]. IEEE Photonics Technology Letters, 1997, 9(11): 1529-1531.
- [5] Yegnanarayanan S, Jalali B. Wavelength-selective true time delay for optical control of phased-array antenna[J]. IEEE Photonics Technology Letters, 2000, 12(8): 1049-1051.
- [6] Lee H, Jeon H, Jung J. Optical true time-delay beam-forming for phased array antenna using a dispersion compensating fiber and a multi-wavelength laser[C]//2011 4th Annual Canopus Fly by Wireless Workshop. IEEE, 2011: 1-4.

# Inverse design of perfectly vertical apodized grating couplers with a gold reflector

M. Yang,<sup>1,2</sup> Y. Yan<sup>2</sup>, Z. Wu<sup>2</sup>, M. Zhao,<sup>2\*</sup> and G. Morthier<sup>1\*</sup>

<sup>1</sup> Ghent University - IMEC, Photonics Research Group, INTEC, Ghent, Belgium

<sup>2</sup> Dalian University of Technology, School of Optoelectronic Engineering and Instrumentation Science, Dalian, China

*Grating couplers (GCs) have been widely used for optical coupling between photonic chips and optical fibers. But they can also be used as transmitters and receivers for free-space optical (FSO) processing. In order to design high-performance perfectly vertical GCs, we combined the apodization of the grating, to enhance the directivity using inverse electromagnetic design techniques, with a gold reflector to reduce the downward transmission. For a Gaussian beam, vertically incident from free-space, the simulation results show that a coupling efficiency of about 80% is possible for C-band with these novel GCs.*

## Introduction

Silicon photonics is a promising scalable platform that integrates a massive number of devices on the same chip by heterogeneous integration or monolithic integration. It has been efficiently used for optical switching and networking for data centers [1]. Besides, another important application is free-space optical (FSO) processing, which has received more attention in recent years. The mixture of silicon photonics and FSO processing contributes to the miniaturization of FSO systems to the chip scale, which will reduce the size, weight, and power consumption (SWaP) of the optical systems [2]. The optical coupling to the chip is of critical importance, which commonly includes edge coupling and grating coupling. The edge coupler has excellent coupling efficiency due to the better optical mode match between the input optical beam and the edge coupler [3]. Unfortunately, the edge coupler lies on the edge of the chip that should be diced and is limited to linear dimensions. Conversely, due to the three-dimensional (3D) character of FSO, the grating couplers (GCs) that are much more flexible in terms of arbitrary coupling position on the chip are probably the most suitable method for the optical coupling of FSO-to-chip.

In 3D optical information processing, the direction of FSO is usually uncertain, but the most broadly used and typical direction is perfectly vertical to the surface. Even if it's not vertical, it can also be processed by using lens transformation. Therefore a high-efficiency GC designed for perfectly vertical coupling is particularly critical. Actually, the optical mode is generally Gaussian in most FSO systems. In order to design high coupling efficiency GCs, the optical mode of the grating must match the Gaussian [5]. In the case of typical partially-etched GCs, the available degrees of freedom are the period, duty cycle, etch depth, and grating film thickness, which limit the number of optimizable degrees of freedom to only a handful of parameters.

In this paper, we present the results using the inverse design from finite difference time domain (FDTD) numerical simulations and demonstrate an apodized GC with a gold reflector, which shows a high optical coupling efficiency from free space to silicon photonics chips. The apodized grating breaks the symmetry of the uniform grating [5], which leads to single-direction propagation of coupled light and the gold mirror reflects

almost all optical power upward to decrease the substrate loss. The rest of the paper is organized as follows. We first introduce basic working principles and theories for the GC. Next, we discuss numerical simulation results for the uniform GCs, GCs with a gold reflector, and apodized GCs with a gold reflector. We then compare and analyze the simulation results of the three types of GCs, leading to the optimal coupling efficiency of more than 80%. Finally, we present the conclusions.

## Device principle and methods

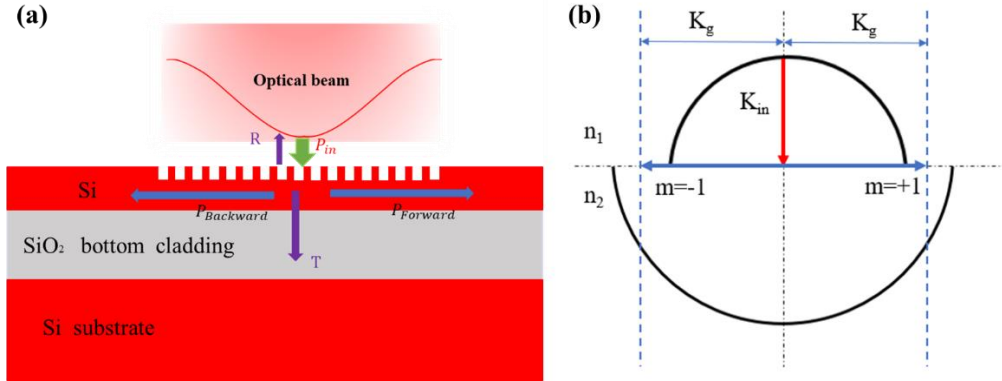


Figure 1. (a) Cross section of the uniform GC; (b) Wave-vector for a perfectly vertical receiving GC.

Considering a receptive GC, the optical beam above the chip along the grating waveguide will be diffracted forward and backward because of the effective index modulation by the etched grooves. Figure 1a shows the schematic cross-section of the standard uniform GC on SOI. The Bragg diffraction condition is the basic principle of GCs. The Bragg diffraction condition reveals the relationship between the input wavevector  $K_{in}$  of an FSO beam above the GC surface, the grating vector, and the waveguide vector  $K_{wg}$  of the waveguide mode. The Bragg diffraction condition is [6]:

$$K_{in} \sin \theta + mK_g = K_{wg} \quad (1)$$

where  $m$  is the grating diffraction order. For the perfectly vertical coupling,  $\theta = 0$ , the equation can be simplified, and is given by:

$$mK_g = K_{wg} \quad (2)$$

The Bragg diffraction can be better described by a wave-vector diagram. It is very obvious to predict the diffraction order from the wave-vector diagram. As shown in Figure 1b for a perfectly vertical coupling, the angle of the incident optical beam is 0 and then the forward and the backward propagating guided modes will meet the Bragg condition at the same wavelength due to the symmetry, for diffraction order  $m = -1$  and  $m = +1$ . It should be noticed that the wave-vector diagram can only be used to judge the actual diffraction light and the diffraction direction, but can not give the diffraction efficiency of the grating.

## Device design and simulation

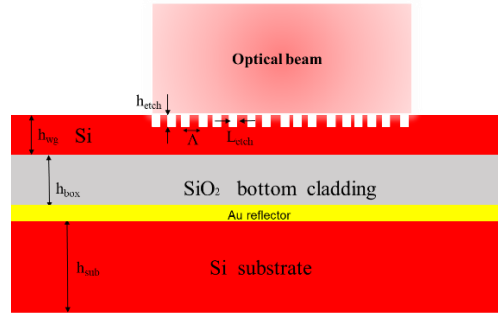


Figure 2. Sectional structure of apodized GC with a gold reflector.

The whole simulation was done using two-dimensional (2D) finite-difference time-domain (FDTD) simulations with the commercial software package Lumerical FDTD Solutions. We simulated the GCs performance for the SOI waveguide structure shown in Figure 2. In order to obtain high coupling efficiency, an apodized grating and bottom reflector were combined into the GCs. Specifically, the apodized grating disturbed the symmetry of a uniform grating to enhance the direction of coupling light to one side. Inserting a bottom reflector, such as a gold reflector with close to 100% reflectivity, redirected the optical power diffracted to the substrate to the grating layer, resulting in high coupling efficiency.

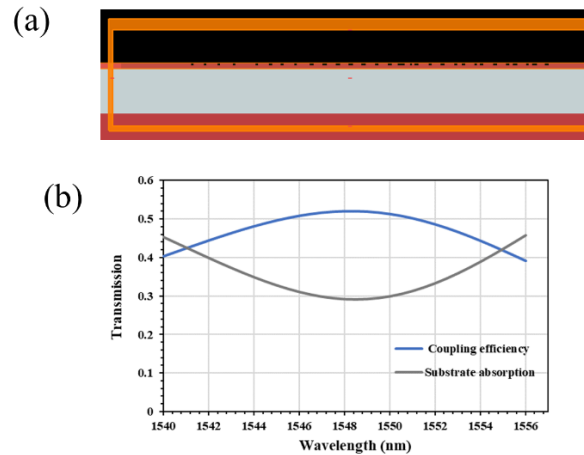


Figure 3. (a) Geometric structure simulated using 2D FDTD; (b) Calculated transmission spectra of perfectly vertical apodized GC

The apodized grating was designed using the gradient-based inverse design which breaks fundamental limits of previous intuition-based device methodology. The inverse design provided a far larger number of degrees of freedom for the grating. For every pitch, two geometric parameters, period and duty cycle, could be varied, with the result that the degrees of freedom depends on the number of pitches shown in Figure 3a. The apodized grating diffracted field was able to match the Gaussian field distribution, leading to a 52% coupling efficiency, as shown in Figure 3b. This is better than the uniform GCs. However, substrate absorption seriously affected the coupling efficiency. To the best of our knowledge, inserting a metallic bottom reflector was the best solution for substrate absorption.

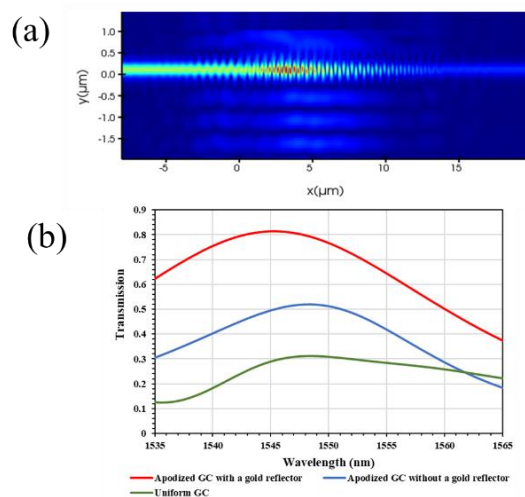


Figure 4. (a) Field intensity profiles radiated from the apodized GC with a gold reflector; (b) Coupling efficiency of the three types of GCs.

To further increase the efficiency of GCs, an 80nm thick gold layer was added under the buried layer to act as a backside metal reflector redirecting the optical power diffracted to the substrate in our design, as illustrated in Figure 2. And the thickness of the device layer and the buffer layer were 220nm and 4μm respectively. The 10μm diameter Gaussian beam was perfectly vertically incident on the GC. The frequency-domain electric field amplitude profile of the GC is given in Figure 4a. Obviously, the optical power was coupled onto the left waveguide directionally. As depicted in Figure 4b, the peak coupling efficiency of the apodized GC with a gold reflector of 81.3% was achieved at 1545nm. The GC had 25 periods and the minimum feature was 100nm, which could be achieved by electron beam lithography or deep ultra-violet photolithography.

## Conclusions

In conclusion, we presented efficient perfectly vertical apodized GCs with a gold reflector using inverse design. We designed and optimized a GC with a high coupling efficiency of 81.3% for C-band, taking advantage of the apodized grating and the gold reflector by improving the diffraction directionality of the grating. The perfectly vertical GCs were believed to be suitable for FSO processing.

**Funding:** This research was funded by the China Scholarship Council (CSC).

## References

- [1] Thomson D, Zilkie A, Bowers J E, et al. Roadmap on silicon photonics. *Journal of Optics*, 2016, 18(7): 073003.
- [2] Bütow J, Eismann J S, Milanizadeh M, et al. Spatially resolving amplitude and phase of light with a reconfigurable photonic integrated circuit arXiv preprint arXiv:2204.09284, 2022.
- [3] Van Laere F, Claes T, Schrauwen J, et al. Compact focusing grating couplers for silicon-on-insulator integrated circuits. *IEEE Photonics Technology Letters*, 2007, 19(23): 1919-1921.
- [4] Taillaert D, Bienstman P, Baets R. Compact efficient broadband grating coupler for silicon-on-insulator waveguides. *Optics letters*, 2004, 29(23): 2749-2751.
- [5] Mossberg T W, Greiner C, Iazikov D. Interferometric amplitude apodization of integrated gratings. *Optics Express*, 2005, 13(7): 2419-2426.
- [6] Eggleton B J, Kerbage C, Westbrook P S, et al. Microstructured optical fiber devices. *Optics Express*, 2001, 9(13): 698-713.

# Polarization dependent gold-coated multicore fiber interferometer for refractometry

T.-B. Zhu<sup>1</sup>, K. Chah<sup>1</sup>, Y.-G. Nan<sup>1</sup>, F. Chiavaioli<sup>2</sup>, J. Villatoro<sup>3,4</sup> and C. Caucheteur<sup>1</sup>

<sup>1</sup> University of Mons, Dept. Of Electromagnetism and Telecommunication, 31 Boulevard Dolez, 7000 Mons, Belgium

<sup>2</sup> National Research Council of Italy, Institute of Applied Physics “Nello Carrara”, 50019 Sesto Fiorentino, Italy

<sup>3</sup> Department of Communications Engineering, University of the Basque Country UPV/EHU, 48013 Bilbao, Spain

<sup>4</sup> IKERBASQUE, Basque foundation for Science, Bilbao, Spain

## ***Abstract***

*A single supermode interferometer fabricated with a segment of a seven-core fiber fusion-spliced to a standard single-mode fiber has the capability of monitoring temperature and refractive index simultaneously. In this work, we study the effect of a thin metal film deposited on the end face of the multicore fiber on the interferometer. We demonstrate that for a ~10 nm-thick gold layer on the multicore facet, the interferometer shows an important polarization dependency, which thereby influences the refractometric sensitivity.*

## **Introduction**

An optical fiber sensor that can measure refractive index requires easy fabrication and reproducible response for real-world applications. There are several kinds of optical fiber sensors that are capable of monitoring refractive index, for example, tilted Bragg gratings [1,2], Fabry-Perot interferometers [3] and multicore fiber (MCF) interferometers [4]. Among all the aforementioned optical sensors, a supermode interferometer which is composed of a centimeter-long segment of MCF spliced to a single mode fiber (SMF) is popped up with its advantages of dual-parameter (temperature and surrounding refractive index (SRI)) sensing, controllable supermodes and reproducibility. The capability of supermode MCF interferometer in sensing temperature and refractive index simultaneously has been experimentally and analytically investigated in [5-7].

In this work, we investigate the effect of a 10 nm-thick gold layer on the MCF's facet on the performance of the interferometer. We show that unlike the bare MCF interferometer, the interference amplitude sensitivity to SRI is polarization dependent with a maximum sensitivity of ~7.8 a.u./RIU. This effect provides a possibility of further surface modification to enhance the refractometric sensitivity. Furthermore, it has a potential in biosensing by functionalizing the facet of MCF.

## **MCF interferometer and statement of the work**

A sketch of the cross section of the multicore fiber used to fabricate the interferometer is shown in Fig. 1(a). The interferometer is assembled with the multicore fiber fused spliced to a conventional single mode fiber (SMF). The MCF is cleaved at a length  $L= 3.7$  cm and the cleaved end facet of the multicore fiber is coated with a 10 nm-thick gold layer

using a sputtering chamber from Leica (shown in Fig. (b)). Fig. 1(c) shows the interrogation set-up of the sensor, which is composed of a supercontinuum laser source from NKT, an optical polarizer set at the input of a circulator and an optical spectrum analyzer (OSA) connected to the output of a circulator. The OSA collects the reflected optical signal from the MCF interferometer. To study the polarization effect on the device, we changed the input polarization of the light within  $180^\circ$  by a step of  $30^\circ$ . The reflection spectra of the sensor were recorded and analyzed. Fig. 1(d) shows the microscope image of the gold-coated MCF facet.

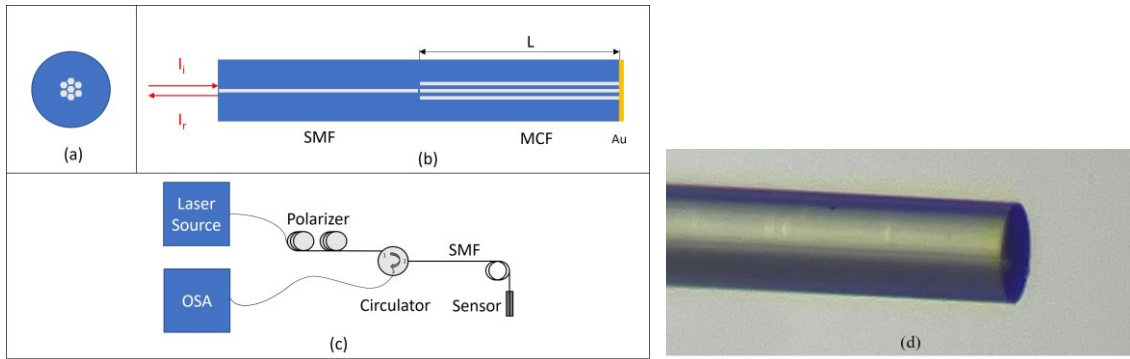


Fig. 1. (a) Cross-section of the multicore fiber. (b) Consistence of MCF interferometer. (c) Set-up of the refractometric experiment. (d) Microscopic image of 10nm gold-coated MCF facet

For each input polarization, the MCF interferometer is immersed into different LiCl solutions with RI ranging from 1.3333 to 1.3600. The evolution of the reflection spectra (amplitude of the peaks and their respective wavelength shift) were analyzed.

## Experimental results

Firstly, we checked the refractometric characteristic of a bare MCF supermode interferometer. The evolution of the interference pattern as a function of RI change is shown in Fig. 2(a).

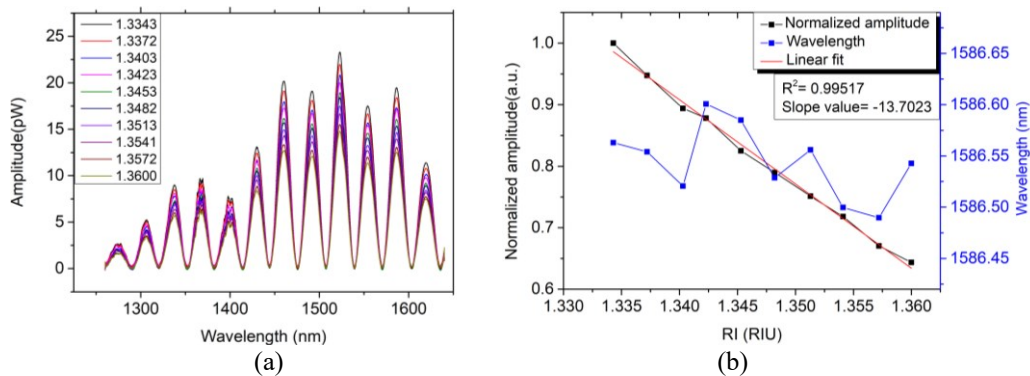


Fig. 2. Reflection spectra of a bare MCF with unpolarized light. (a) Evolution of the interference spectra as a function of RI change. (b) Normalized amplitude and wavelength shift of peak at 1586nm.

We considered the spectral range from 1460 nm to 1600 nm because the interference pattern shows good contrast and SNR ratio. We first analyzed all the peaks in terms of wavelength and amplitude changes versus SRI modification. Since, all the peaks show the same behavior, in the following, we focus and show only the evolution of one peak around 1586 nm as a function of SRI. The wavelength shift of this peak and the

normalized amplitude (peak amplitude divided by the initial value) evolution as a function of the RI change are shown in Fig. 2(b). The linear fit in terms of amplitude versus RI indicates that the refractometric sensitivity of the peak is  $\sim 13.7$  a.u./RIU. Besides, the wavelength of the peak is unchanged when the RI increases.

After studying the bare MCF in terms of RI sensing, we fabricated a sample with a 10 nm gold layer deposited on the MCF facet to evaluate its performances for RI measurements. Fig. 3(a) shows the evolution of the interference spectra of MCF versus RI change. When the RI of the solution increases from 1.3335 to 1.3600, the peak around 1580 nm shows a slight decrease in normalized amplitude but no wavelength evolution. The linear fit of the normalized amplitude (as shown in Fig. 3(b)) indicated that the refractometric sensitivity of the peak is relatively weak, about  $\sim 1.39$  a.u./RIU.

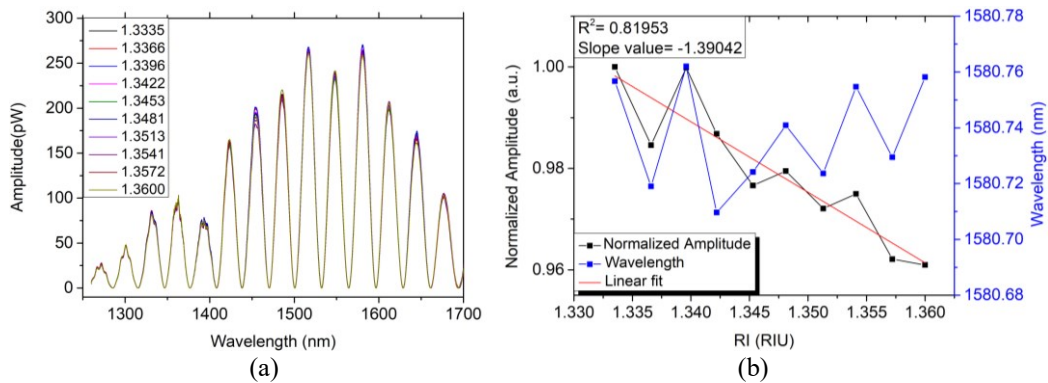


Fig. 3. Spectra of a 10 nm gold-coated MCF with unpolarized light. (a) Interference spectra as a function of RI change. (b) Normalized amplitude and wavelength evolution of a peak versus RI change.

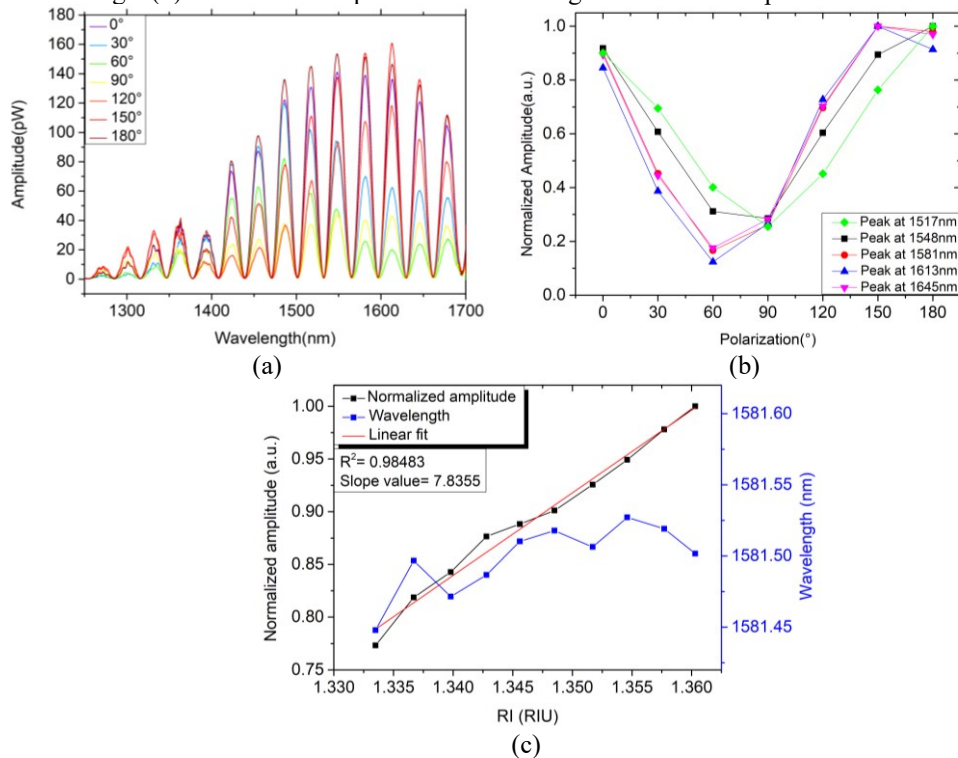


Fig. 4. Results with a 10nm gold-coated MCF with polarized light. (a) Interference spectra observed at different polarizations. (b) Peaks evolution as a function of polarization state. (c) Normalized amplitude and wavelength evolution of an interference maximum versus RI change.

To investigate the refractometric properties of the MCF interferometer under different polarization angles of light, we measured the spectral response to RI changes each  $30^\circ$  of

linearly polarized light up to  $180^\circ$ . Fig. 4 shows the experimental results of 10 nm gold-coated MCF to RI changes using polarized light. It is known that when polarized light propagates through an interface, its polarization state will change. At a flat surface, a greater proportion of the intensity component is polarized parallel to a surface (s-polarized) and is reflected compared with the component polarized perpendicular to that (p-polarized) [8]. So, when the reflected light reaches minimum amplitude, the polarization of the light will be left p-polarization. From Fig. 4(a), one can see that the interference spectra show strongly polarization dependency. Fig. 4(b) shows the evolution of 5 interference peaks as a function of polarization. When the polarization of the input light is around  $90^\circ$  (as indicated by the yellow curve), the amplitude of all interference patterns reaches minimum. The evolution of the peak located at 1581 nm as a function of RI change is shown in Fig. 4(c), with a sensitivity of  $\sim 7.8$  a.u./RIU. Here again, the wavelength position of the peak is unchanged with RI increases.

## Conclusions

The spectral characteristics of an MCF interferometer have been investigated to show the interesting perspectives of gold-coated MCF for refractive index sensing. The experimental results show that the bare MCF interferometer is sensitive to the surrounding environment. When the MCF facet is coated with a 10 nm-thick gold layer, the interferometer showed a strong polarization dependency. We observed a sensitivity to SRI only for polarized light with higher sensitivity under p-polarization. The observed behavior may be a result of plasma excitation in the thin gold layer by the polarized supermodes in the multicore fiber. Although, this requires further investigations. In any case, our results suggest the possibility for bio-sensing with a MCF interferometer if the gold layer is properly functionalized for binding a biological recognition element.

## Acknowledgements

The authors are grateful to E. Antonio-Lopez, A. Schülzgen, and R. Amezcua-Correa of CREOL, USA for providing the multicore fiber used in the experiments reported here.

## References

- [1] J. Albert, L. Y. Shao, and C. Caucheteur, "Tilted fiber Bragg grating sensors. *Laser & Photonics Reviews*," 7(1), 83-108(2013).
- [2] T. Zhu, M. Loyez, K. Chah, and C. Caucheteur, "Partially gold-coated tilted FBGs for enhanced surface biosensing. *Optics Express*," 30(10), 16518-16529(2022).
- [3] T. Yoshino, K. Kurosawa, K. Itoh, and T. Ose, "Fiber-optic Fabry-Perot interferometer and its sensor applications," *IEEE Transactions on Microwave Theory and Techniques*, 30(10), 1612-1621(1982).
- [4] L. Yuan, "Recent progress of multi-core fiber based integrated interferometers," In 2009 International Conference on Optical Instruments and Technology: Advanced Sensor Technologies and Applications (Vol. 7508, pp. 15-22). SPIE(2009).
- [5] J. A. Flores-Bravo, R. Fernández, E. A. Lopez, J. Zubia, A. Schülzgen, R. A. Correa, and J. Villatoro, "Simultaneous sensing of refractive index and temperature with supermode interference," *Journal of Lightwave Technology* 39.22 (2021).
- [6] J. A. Flores-Bravo, and J. Villatoro, "Dual-Parameter sensing with a single supermode Interferometer," *Sec. Physical Sensors* 820612 (2022).
- [7] J. Amorebieta, G. Durana, A. Ortega-Gomez, R. Fernandez, J. Velasco, I. S. Saez de Ocariz, ... and J. Villatoro, "Packaged Multi-Core Fiber Interferometer for High-Temperature Sensing," *J. Lightwave Technol.* 37, 2328–2334 (2019).
- [8] J. J. Foster, S. E. Temple, M. J. How, I. M. Daly, C. R. Sharkey, D. Wilby, and N. W. Roberts, "Polarisation vision: overcoming challenges of working with a property of light we barely see," *The Science of Nature*, 105(3), 1-26(2018).

# Design of InP membrane SOA with butt-joint active-passive interface

A. Zozulia<sup>1</sup>, V. Pogoretsky<sup>1</sup>, P. J. van Veldhoven<sup>1</sup>, J. Bolk<sup>1</sup>, K. A. Williams<sup>1</sup>, S. Rihani<sup>2</sup>, G. Berry<sup>2</sup>, M. Robertson<sup>2</sup>, J. Rawsthorne<sup>2</sup> and Y. Jiao<sup>1</sup>

<sup>1</sup>Photonics Integration group, Eindhoven University of Technology, PO Box 513, 5600 MB Eindhoven, The Netherlands

<sup>2</sup>Huawei Technologies Research & Development (UK) Ltd, IP5 3RE Ipswich, UK

*A butt-joint SOA design for InP on Si membrane (IMOS) platform is proposed. The new design features the butt-joint interface between the SOA and passive nanophotonic waveguide, which makes the interface a factor of 2 to 6 shorter than in the current twin-guide SOAs, with possibility to reduce it further to factor of 5-10. This makes the new SOA a promising candidate for high-speed directly modulated lasers (DML) applications, where extremely short SOAs (40-100  $\mu\text{m}$  long) and short distances between reflectors are usually required.*

## Introduction

Indium Phosphide membrane on Silicon (IMOS) is a membrane platform for the fabrication of photonic integrated circuits (PICs), which combines membrane SOAs with ultra-compact high confinement nanophotonic waveguides [1]. This platform is promising to enable a high density of optical components and a smaller footprint of optical transceivers of the future. One of the potential bottlenecks for high-density integration on IMOS is the 50- $\mu\text{m}$ -long 2-stage taper transition between the SOA building block of  $1.5 \times 2 \mu\text{m}$  in the cross-section and the passive waveguide of  $0.3 \times 0.4 \mu\text{m}$  in the cross-section [2]. Long active-passive interfaces can hinder the performance of lasers where an ultra-short cavity is desired, such as directly modulated lasers [3]. We propose a new SOA design, where a butt-joint regrowth of passive waveguides enables a 24- $\mu\text{m}$  long interface, with the potential to reduce it to  $<10 \mu\text{m}$ .

## Active-passive interface optimization

Integration of a high gain and low resistance SOA with a compact passive waveguide has always been a challenge for membrane photonics. In the previously developed twin-guide IMOS SOA, an InGaAsP optical waveguide containing 4 quantum wells (QW) is sandwiched between n- and p-doped InP contact layers [4]. The effective index of the fundamental optical mode inside the  $2 \mu\text{m}$  wide SOA  $n_{\text{eff soa}} = 3.23$ . The doped layers are removed from the passive waveguide to reduce optical losses, and the waveguide dimensions are reduced to enable high optical confinement and therefore high density integration. In the  $2 \mu\text{m}$  wide passive InGaAsP waveguide  $n_{\text{eff pas}} = 2.92$ . The shortest active-passive interface can be achieved when an SOA is directly connected to a passive waveguide of the same width via butt-joint, but in this case Fresnel reflections, caused by effective index mismatch, will create an undesirable Fabry-Perot cavity inside the SOA. To match effective indexes, a taper is made at the top and bottom of the passive waveguide.

An SOA epitaxial layer stack was optimized for the butt-joint interface. Compared to previously specified twin-guide SOA, the separate confinement heterostructure (SCH) thickness was reduced from 500 nm to 300 nm. The p-InP contact layer thickness was

reduced from 800 nm to 600 nm. The n-contact thickness was increased from 80 nm to 200 nm. This helps to reduce diode resistance, enable more symmetric optical field distribution in the SOA, and more fabrication-tolerant surface gratings made on the n-contact side. 60 nm layers of non-intentionally doped (n.i.d.) InP was added at the top and bottom of the SCH to reduce optical losses of the mode from highly doped layers.

We optimized the interface between the updated SOA stack, which has dimensions of  $1.3 \times 2 \mu\text{m}^2$ , and passive waveguide, which has dimensions of  $0.3 \times 2 \mu\text{m}^2$ . The cross-sections are shown on Figure 1. A commercial eigenmode expansion solver (EME) is used for the simulation. The simulation setup is shown on Figure 2. The taper consists of 2 sections, which are optimized separately. The optimization parameters are section length and width of the waist between 2 sections. The taper tip width is set to 200 nm during the optimization, because this tip width is readily achievable from the fabrication point of view. The main figures of merit of the optimization are the fundamental mode power reflection and transmission coefficients ( $|S_{11}|^2$  and  $|S_{21}|^2$ ).

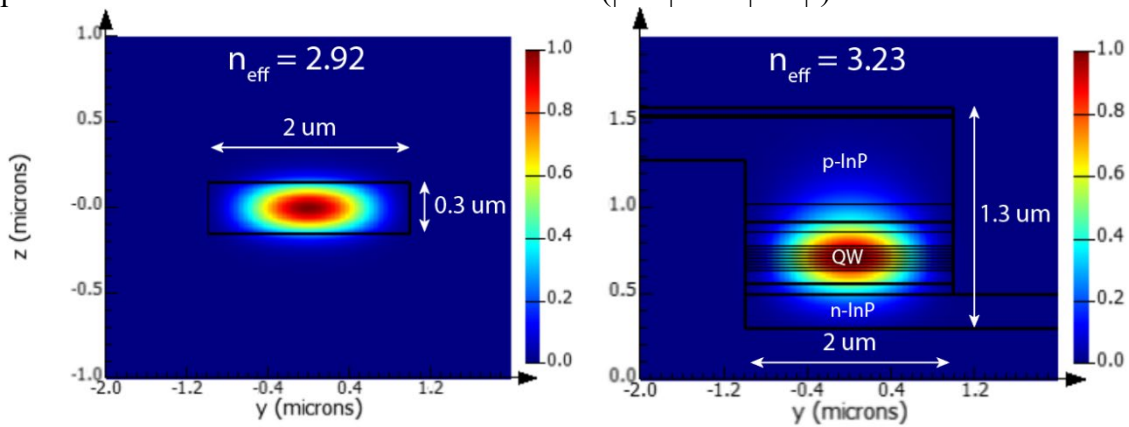


Figure 1. Left: Passive waveguide cross-section. Right: SOA building block cross-section

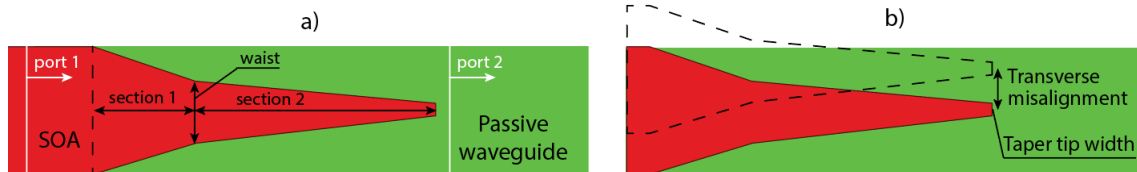


Figure 2. Schematic top view of the active-passive interface. a) Main simulation parameters. b) parameters of tolerance study

$|S_{21}|^2$  is highly dependent on the lengths of taper sections, because for some values of the length the fundamental mode power gets converted to higher order modes at the output of the interface. By sweeping over the section length, we can identify maxima of the  $|S_{21}|^2$

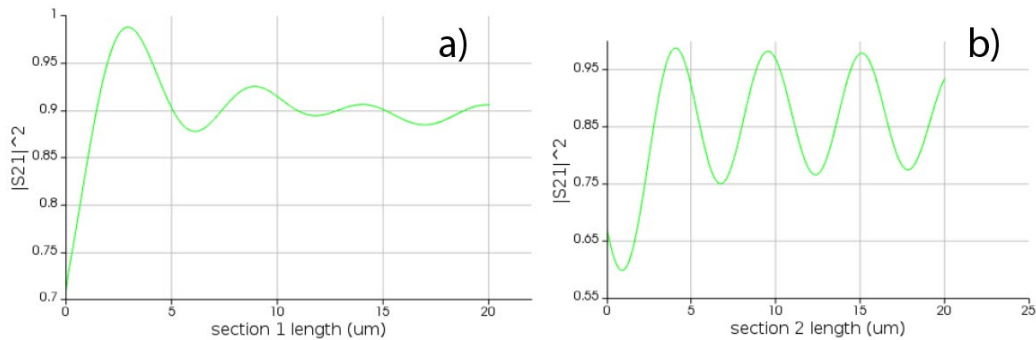


Figure 3. Interface transmission function vs a) section 1 length, b) section 2 length, when section 1 length is fixed at 3 um.

function (see Figure 3) and choose several structures with section lengths, corresponding to different maxima, to study their fabrication tolerances. We do it also for different waist widths and for taper tip widths of 200 and 300 nm.

After the optimization, 3 different designs with best performance are chosen to perform the tolerance study. The summary of parameters for selected designs is given in the Table 1. Taper 1 has a total length of 7.8  $\mu\text{m}$ , the length of both sections corresponds to the first maxima of the  $|S_{21}|^2$  function. Taper 2 has a total length of 12  $\mu\text{m}$  and the tip width of 0.3  $\mu\text{m}$ , which is more relaxed in terms of fabrication. Taper 3 has a total length of 24.25  $\mu\text{m}$ , and is a good compromise between length, performance and sensitivity to fabrication errors.

Table 1. Geometric parameters and simulated transmission and reflection of 3 selected taper designs

	Section 1, $\mu\text{m}$	Section 2, $\mu\text{m}$	Waist, $\mu\text{m}$	Tip, $\mu\text{m}$	$ S_{21} ^2$	$ S_{11} ^2$
Taper 1	3.5	4.3	0.7	0.2	0.989	3.7E-5
Taper 2	3.0	9.0	1.0	0.3	0.973	7.4E-5
Taper 3	9.25	15.0	0.7	0.2	0.976	3.3E-5

Figure 4 shows the change in taper performance due to deviations of the most important parameters: transverse misalignment and tip width. Taper 1 has the highest transmission in the optimal design point, however, it is less tolerant of misalignment error. A taper of 24.25  $\mu\text{m}$  has the most relaxed fabrication tolerances. The reflections are -37 to -45 dB and the transmission into the fundamental mode is 94-97% in the tolerance range that we expect from the fabrication tools.

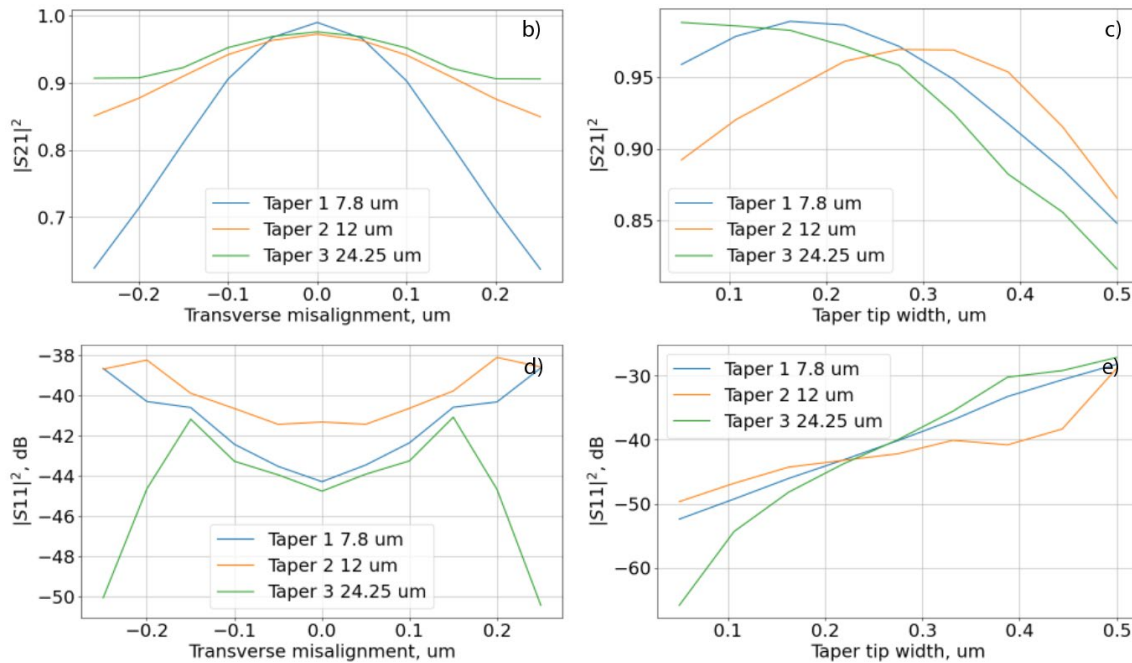


Figure 4. Tolerance comparison for 3 different taper designs. a) Tolerances in consideration. b), d): Transverse misalignment of the taper relative to the waveguide. c), e): change of the taper tip width

## Experimental results

After the optimization, a taper tip width of 300 nm in the semiconductor was achieved.

This taper is expected to give  $< -37$  dB of optical reflections. The optical performance of the taper can only be evaluated after the processing is completed. The IV curve of several fabricated diodes was measured. The series resistance of a 400  $\mu\text{m}$  long diode is 2.4  $\Omega$ , for the contact area of 10800  $\mu\text{m}^2$ . In previously demonstrated IMOS diodes the series resistance was 5-8  $\Omega$  for the contact area of 100000  $\mu\text{m}^2$  [4].

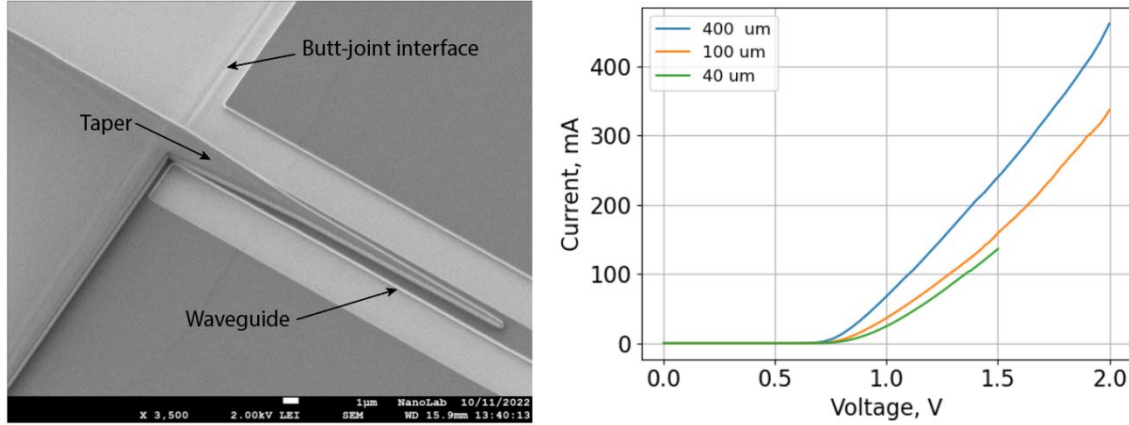


Figure 5. Left: Bird's eye view of the fabricated active-passive interface. Right: measured IV characteristics of diodes of different length.

## Conclusion

A new design of a membrane SOA was proposed. The butt-joint regrowth allowed us to reduce the length of the active-passive interface to 24.25  $\mu\text{m}$  with relaxed fabrication tolerances and to 7.8  $\mu\text{m}$  with tight tolerances. The layer stack and the fabrication process flow were optimized to enable butt-joint regrowth and usage of optical lithography. The fabricated SOAs show good diode behavior with low series resistance.

## Acknowledgements

This work was supported by the Huawei research grant HDMI. The authors thank Pim Voorthuijzen for fruitful discussion and Smart Photonics<sup>®</sup> for support with etching.

## References

- [1] Y. Jiao *et al.*, "InP membrane integrated photonics research," *Semicond. Sci. Technol.*, vol. 36, no. 1, p. 013001, Jan. 2020, doi: 10.1088/1361-6641/abcadd.
- [2] S. F. G. Reniers, "Integration of a polarization converter on the active-passive IMOS platform," Phd Thesis 1 (Research TU/e / Graduation TU/e), Eindhoven University of Technology, Eindhoven, 2022.
- [3] P. Bardella and I. Montrosset, "A New Design Procedure for DBR Lasers Exploiting the Photon-Photon Resonance to Achieve Extended Modulation Bandwidth," *IEEE J. Sel. Top. Quantum Electron.*, vol. 19, no. 4, pp. 1502408–1502408, Jul. 2013, doi: 10.1109/JSTQE.2013.2250260.
- [4] V. Pogoretskiy, "Nanophotonic membrane platform for integrated active devices and circuits," Phd Thesis 1 (Research TU/e / Graduation TU/e), Technische Universiteit Eindhoven, Eindhoven, 2019.

# Edge computing platforms for AI-driven services: from enhanced security to the semiconductor industry

M. Perea,<sup>1</sup> J.A. Álvarez-García,<sup>1</sup> O. Deniz,<sup>2</sup> P. Szanto,<sup>3</sup> L. Liss,<sup>4</sup> J.J. Vegas Olmos<sup>4</sup>,  
O. Bouchmal<sup>5</sup>, I. Tafur Monroy<sup>5</sup>

<sup>1</sup> Universidad de Sevilla, Dept. Lenguaje y Sistemas Informáticos, Sevilla, Spain

<sup>2</sup> University of Castilla-La Mancha, VISILAB, E.T.S.I.I, Ciudad Real, Spain

<sup>3</sup> Faculty of Electrical Engineering and Informatics, Budapest University, Budapest, Hungary

<sup>4</sup> Software Architecture NVIDIA Corporation, Yokneam, Israel

<sup>5</sup> Eindhoven University of Technology, Department of Electrical Engineering, Eindhoven, The Netherlands

*This paper presents user scenarios that benefit from edge computing platforms and the ability to offload artificial intelligence intense processes from the end user subsystems. Then, we briefly describe one of the main challenges in edge computing, the parametrization of the resources in terms of processing power and network capacity, to effectively execute services and applications.*

## I. Introduction

In the first decades of the 21st century, through developments in photonic technologies being integrated into transceivers and co-processors, linear processing capacity and transmission capacity have been finally balanced. This is leading to a massive introduction of artificial intelligence (AI), which will transform most aspects of the end-users ecosystems in a variety of verticals, from smart-cities, automobile, factory 4.0, healthcare to mobility. These developments are forcing networks to complete a full circle: as the initial internet was local-based with small-servers in-house, we migrated to cloud services massively over the last 20 years. However, requirements of AI processes in terms of processing and latency needs and ever-growing bandwidth increase in the communication systems are pushing back to local servers feeding the users. This is now called edge computing.

As a result, networks can be now split in three segments: cloud computing (for intensive processing or storage service), edge computing (light AI and services) and artificial-internet-of-things (AIoT) (decentralized communications). In particular, technology paradigms that require real-time processing and low reaction times (i.e. autonomous vehicles, electric grid control) are particularly interested in having processing power closer in terms of networking cycles. Hence, the effective deployment of AI services and applications should now be measured not only in terms of processing power available but also in terms of efficient networked access to such resources.

This paper provides an overview of some of the key use cases being developed in the contexts of European and national projects developing edge computing enabling AI. Then, it will elaborate on one of the main challenges facing the community at the crossroads between AI researchers and network researchers, namely the parametrization of needed resources to effectively execute the services and applications offered to the users.

## II. Architectural reference for Deep Learning Edge Computing

To meet the computational requirements of Deep Learning (DL), a common approach is to leverage cloud computing, but moving the data from the source to the cloud introduces several challenges that normally cannot satisfy real-time requirements: latency (queuing and propagation delays), scalability (network access can become a bottleneck) and privacy (sensitive data to the cloud) [1].

Edge computing [2] is becoming the standard computing paradigm for latency-sensitive real-time IoT workloads since it addresses the aforementioned limitations related to centralized cloud-computing models. Such a paradigm brings the service and utilities of cloud computing closer to the end user and is characterized by quick processing and fast application response time, solving cloud computing issues: latency is decreased given the proximity to data sources (enabling real-time services), and scalability bottlenecks are eliminated using a hierarchical architecture avoiding process thousands of devices data per node and privacy concerns are reduced passing the information to the local trusted edge server, thus avoiding traversal of the public Internet.

On the other hand, a new challenge appears: how to accommodate the high resource requirements of DL on less powerful edge compute resources, how to allocate and dimension the hierarchical architecture to serve an adequate number of edge devices to satisfy the client requirements (i.e. frames per second, real-time response, etc.), and what level of Edge intelligence [3] is needed, or how training and inference are shared between device, edge and cloud maintaining privacy.

Therefore, edge computing emerges as an attractive alternative to cloud computing, without hindering the possibility of edge and cloud co-existing: some works have combined edge computing with cloud computing, resulting in hybrid edge-cloud architectures. The main advantages of this are the backbone network relief, distributed edge computing nodes that can handle many computation tasks, the agile service response,

reducing the delay of data transmissions and improving the speed of response by edge-hosted services, and strong cloud backup, which provides powerful processing and massive storage capabilities when the edge cannot afford it.

## III. Use cases

This section describes use cases that are currently being evaluated in BRAINE [4] and ID2PPAC European Projects and VICTORY national project [5].

### A. Hyperconnected smart cities

The interactions between Internet of Things (IoT) devices and new smart sensors are growing exponentially [6], creating massive and continuous flows of events from the most diverse origins. Edge computing allows implementing a Smart city Edge infrastructure where various sensor data is processed, and services based on this data are offered by multiple tenants. By creating multi-tenant platforms for smart service providers costs can be saved on private single-tenant infrastructure, data can be shared among service providers to develop new services and most importantly privacy and data sovereignty can be safeguarded on the platform compliant. AI-assisted edge computing platforms are able to anticipate changes in the city (for example weather conditions, public events, emergencies, etc.) and in line with those changes redistribute instances or place new instances on the camera's infrastructure. This adds pressure on the edge

computing platforms, that need to be able to process large volumes of audio/video from HW resources with different constraints (QoS, Latency, resolution), from different services (logistics planning, city space planning, pollution, security and emergency response, crowd management, retail, infrastructure maintenance, etc.).

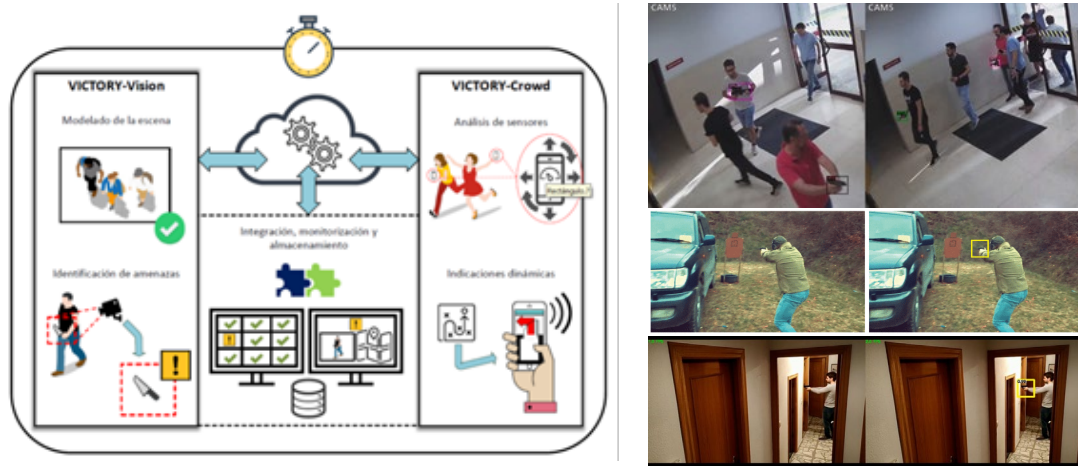


Figure 1. (Left) An edge computing platform conducts live processing for scene modelling, weapon and threats identification, crowd analysis in emergency situations and dynamic emergency signals and instructions to users. (Right) VICTORY results. Top: study and dataset related to CCTV handgun detection [7]. Middle [8] and bottom [9]: Combination of pose and object detection (left – only object detection, right – proposed in VICTORY).

A representative example of this paradigm is the surveillance system depicted in Figure 4, developed as part of a national project in Spain. The VICTORY system (VIsion and Crowdsensing Technology for an Optimal Response in physical-securityY) combines actionable data obtained from surveillance cameras and wearable sensors (smartphones, smartwatches, etc.) to provide rapid detection of dangerous situations inside public buildings. When smartphones are used, instructions can be sent so that people can evacuate through less risky routes. Such a system has developed advanced AI-based techniques for detecting the presence of handguns in the image. The technique is based not only on the appearance of the handgun but also on the pose of the individual, which may be more visible than the gun itself, see Figure 5.

## B. Semiconductor sector digitalization

The recent introduction of AIoT integrated circuit devices has led to an additional need to produce small series of specialized circuitry devices with a very short life cycle compared to past technologies. Therefore, the beyond state-of-the-art industry 4.0 digitization innovations for semiconductor manufacturing are associated to the electronic components and systems end markets which require cost reductions and in consequence:

- 1) Re-define Moore's law from spatial shrinking to novel 3D technology and materials,
- 2) The requirement for cycle time reduction and,
- 3) Improvement of the process and metrology equipment throughput, reproducibility, accuracy and efficiency.

Hence, the semiconductor sector is now transitioning from in-line metrology (fabricate, AI-process, discard) to real-life metrology (AI-process while fabricating, with zero production waste). This migration requires a move from cloud computing to almost

embedded edge computing, where data from integration equipment is feed life and processes in-line. ID2PPAC, led by ASML in Eindhoven is examining together with NVIDIA and TUE how to integrate AI-enabling technologies into the production lines for semiconductors.

#### **IV. Future work**

As it can be perceived, the calculus to dimension the number of processing units to deal with scalability is not a trivial problem and the literature shows the implementation of specific situations, frameworks or even use case systems, but normally this calculus is overestimated in order to avoid bottlenecks in computation process but, these bottlenecks can appear due to other reasons such as the DL model selected. Furthermore, there exist some techniques such as operators fusion, quantization or optimization stacks that can be included to improve the computation power for DL models. Is here where we would like to advance the state-of-the-art, generating an Edge DL computing formula to include all the possible variables and obtain the best fit for each problem and configuration.

#### **Acknowledgment**

This work was partly funded under the BRAINE project ('Edge computing and AI technology for big data processing'- Horizon 2020 framework Grant Agreement 876967), ID2PPAC ('Integration of processes and moDules for the 2 nm node meeting Power Performance Area and Cost requirements' - Horizon 2020 framework ECSEL Grant Agreement 101007254), MADEin4 ('Metrology Advances for Digitized ECS industry 4.0' – Horizon 2020 framework ECSEL Grant Agreement 826589) and DISARM project ('Automatic Detection of Armed Individuals' - Grant n. PDC2021-121197, funded by MCIN/AEI/ 10.13039/501100011033, IoTalentum project (EU Horizon 2020 Marie Skłodowska-Curie European Training Network on Internet of Things with grant number 953442) and by the "European Union NextGenerationEU/PRTR").

#### **References**

- [1] J. Chen et al., "Deep Learning With Edge Computing: A Review." Proceedings of the IEEE 1655-1674, 2019.
- [2] M. Satyanarayanan, "The emergence of edge computing." Computer 50.1 (2017): 30-39.
- [3] Z. Zhou et al., "Edge intelligence: Paving the last mile of artificial intelligence with edge computing". Proceedings of the IEE, 1738-1762, 2019.
- [4] F. Paolucci, et al. "Industrial Cyber Security at de Network Edge: The BRAINE Project Approach." Cybersecurity workshop by European Steel Technology Platform (2020): 119-131.
- [5] F. Enriquez, et al. "Vision and crowdsensing technology for an optimal response in physical-security." International Conference on Computational Science (2019): 15-26.
- [6] Y. Perwej, et al. "The internet of things (IoT) and its application domains." International Journal of Computer Applications 975.8887 (2019): 182.
- [7] J.L. Salazar, et al. "Real-time gun detection in CCTV: An open problem." Neural networks 132 (2020): 297-308.
- [8] J. Ruiz-Santaquiteria, et al. "Handgun detection using combined human pose and weapon appearance." IEEE Access 9 (2021): 123815-123826.
- [9] A. Velasco-Mata, et al. "Using human pose information for handgun detection." Neural Computing and Applications 33.24 (2021): 17273-17286.

# A QAOA-based solution for routing optimization for optical networks in 6G

O. Bouchmal,<sup>1</sup> B. Cimoli,<sup>1</sup> R. Stabile,<sup>1</sup> A. Sabbah,<sup>1</sup>

J.J. Vegas Olmos<sup>2</sup>, and I. Tafur Monroy<sup>1</sup>

<sup>1</sup> Eindhoven University of Technology, Department of Electrical Engineering, Eindhoven, The Netherlands

<sup>2</sup> Software Architecture NVIDIA Corporation, Yokneam, Israel

*Identifying an optimal packet route while fulfilling Quality of Service criteria is a prominent optimization problem belonging to the NP-Hard problem category. In addition, with the development of 6G and Beyond networks, packet routing will become more challenging. In this paper, we propose a Hybrid Quantum-Classical Algorithm-based solution for the pathfinding problem named Quantum Approximate Optimization Algorithm. We describe our approach to network modeling then we will explain how this algorithm can be applied to solve pathfinding problems, what is the equivalent implementation of a network model in quantum computing and what are the main advantages of using it compared to classical methods (i.e. Dijkstra and classical machine learning).*

## Introduction

Routing is a combinatorial optimization problem that falls under Non-deterministic Polynomial-time Hard (NP-Hard) problems. Moreover, in the 6G era, it is expected that the network topology's scale and complexity will increase, with extremely heavy computational applications such as VR/AR, V2X, and Massive-IoT [1]. Therefore, solving routing problems in 6G mobile networks will become more complex. Classical Machine Learning algorithms need a heavy learning process that requires huge computing capabilities [2]. Moreover, with the massive amount of data that is expected to be processed by 6G use cases (i.e. connectivity density for M-IoT is expected to reach  $10^7$   $d/km^2$  and a peak data rate  $> 1Tbps$ ), high computing power and computational time capabilities are required. In this case, the lack of these requirements may negate the benefits and advantages of having 6G (ultra-low latency, high throughput, high reliability...). Moreover, routing is considered one of the pillar functions in networking, and normally, the performance of a network is defined based on the quality and the accuracy of the routing decisions. Many techniques such as legacy routing protocols (i.e., OSPF, BGP...), Linear programming algorithms (i.e. Dijkstra...), and ML algorithms (i.e. Reinforcement Learning) were applied in order to optimize the routing decisions [3]. However, these techniques fail when the size of the network becomes larger and denser. In this regard, Quantum Computing (QC) can be used in order to accelerate ML algorithms. This combination between QC and ML is known as Quantum Machine Learning (QML) [4]. Since its appearance, QML proved that it can provide better performance regarding real-time and heavy computational applications. QML is considered a potential candidate that can reduce or even break the complexity of NP-Hard problems. In this context, we propose a QML-based algorithm for routing optimization entitled Quantum Approximate Optimization Algorithm (QAOA). In section II, we provide a general overview of QC and QML. In section III we explain our QAOA-based solution for routing optimization. Finally, section IV, reports the conclusions.

## Quantum Machine Learning and Approximate Optimization Algorithm

QC is a field of study that utilizes quantum physics to build powerful processors able to execute certain types of computations better than a conventional computer. QML is combining ML algorithms with QC techniques. The main idea behind QML is to translate the classical data and algorithms into a quantum-manageable language to exploit the quantum properties (superposition, entanglement, and parallelism) of quantum processors. Normally, known as Noisy-Intermediate Scale Quantum computers (NISQ) [5]. The number of qubits and quantum gates in NISQ is limited and these qubits are significantly sensitive to noise which makes them collapse in a relatively short time. In this regard, a new class of hybrid algorithms has been developed especially for the NISQ era, known as Variational Quantum Algorithms (VQA) [5]. The main idea behind the VQAs is to use the quantum computer for computing and measuring the result, while the classical computer is used in to correct some of the noise generated from using the NISQ processors and optimize the results. One of the well-known VQAs is Quantum Approximate Optimization Algorithm (QAOA).

QAOA is a variational quantum-heuristic algorithm that was proposed in 2014 by Edward Farhi [6], as a solution for combinatorial optimization problems. The problem is divided into two parts: one to be solved by a quantum computer, and the other by a classical one, as depicted in Fig 1. Therefore, it consists of: a Variational Quantum Circuit (VQC), containing a set of quantum gates: Hadamard, Cost, and mixing Hamiltonian gates, that are prepared and measured on a quantum computer/simulator. The main role of the Hadamard gates in the circuit is to set the qubits into an equal superposition. Followed by a layer of cost and mixing Hamiltonians, parametrized respectively by  $\gamma$  and  $\beta$ , which are defined according to the objective function. A Hamiltonian in quantum physics represents the total energy of the quantum system. Then the classical optimizer uses the outcome of the measurement to decide on the new set of parameters that may lead the quantum computer to produce a new optimized objective function. Those parameters are provided as a new input to the VQC and the process again is repeated until the cost function converges to its meaning (maximization or minimization).

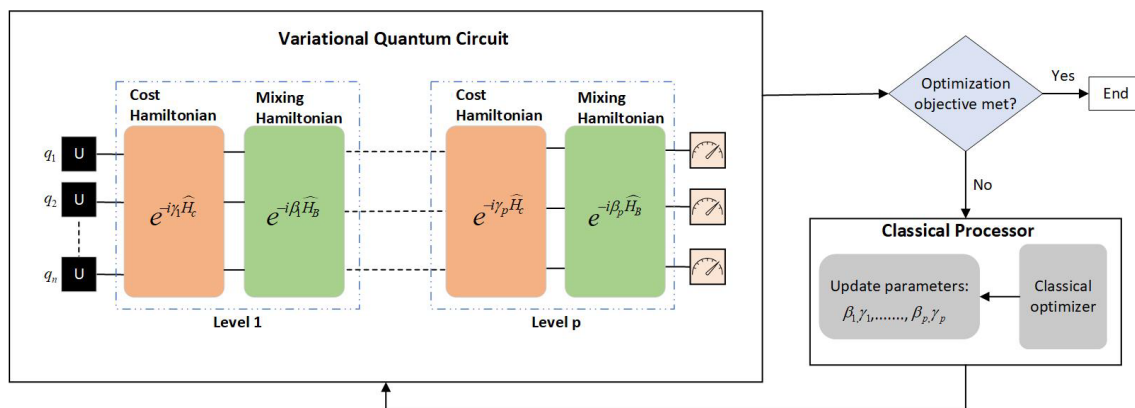


Figure 1: Quantum Classical loop of QAOA

In QC, the optimal solution to an optimization problem corresponds to the ground energy state of the system, therefore, in order to solve an optimization problem using quantum computers, we have to convert it into a problem of characterization of quantum Hamiltonian[7] [8].

## Quantum Approximate Optimization Algorithm for Routing

The first step that we did in the process of applying QAOA for routing optimization is to convert a simple undirected graph  $G = (V, E)$  into a quantum circuit, where  $V$  represents the vertices and  $E$  are the edges of the graph, Fig 2.

The qubits in our case will play the role of the vertices of the graph. The first layer in our circuit corresponds to the Hadamard gates we apply to put our qubits/vertices in an equal superposition.

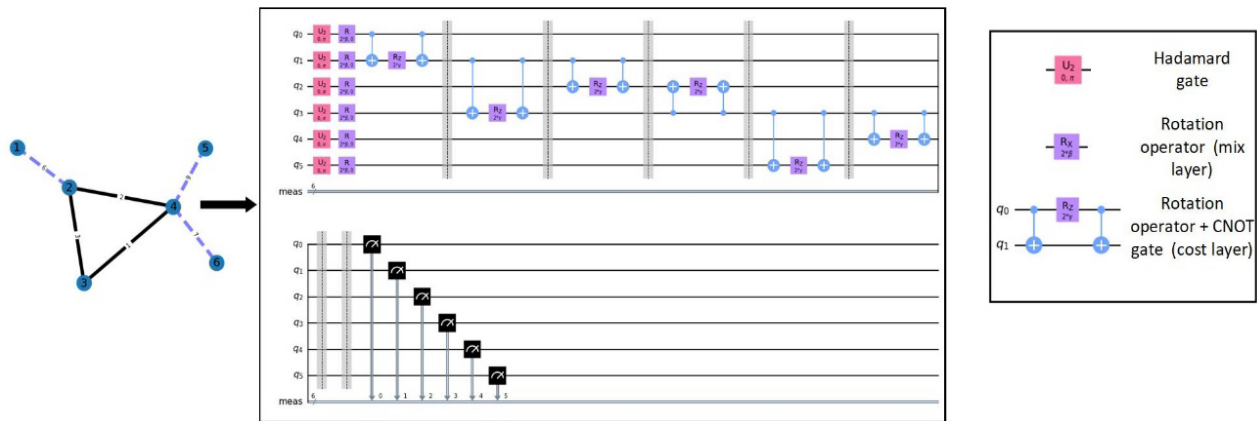


Figure 2: the equivalent VQC of a network

The second layer represents the mixing Hamiltonian characterized by the parameter  $\beta$  that we mentioned above. This layer consists of the rotation operator  $R_x$  which is a single qubit rotation around the x-axis through the angle of rotation  $\beta$ . Usually,  $\beta$  takes a value between  $[0, \pi]$  [6]. The third layer of the circuit represents the cost Hamiltonian and it consists of two types of quantum gates:  $R_z$  and the controlled-NOT (CNOT) gates.  $R_z$  is a single qubit rotation around the z-axis through the angle of rotation  $\gamma$ . Usually,  $\gamma$  takes a value between  $[0, 2\pi]$  [6]. The CNOTs are two-qubit operations, where the first qubit acts as the control and the other one as the target qubit. This gate creates an entanglement of two qubits if and only if the control qubit is in superposition (for that we implemented the Hadamard gates in the first place). A combination of one  $R_z$  and two CNOT gates, in our case, represents the edge between the vertices of the graph. In Fig 2, we separate each edge of the graph with a gray barrier to facilitate understanding of the circuit component. Finally, in the last layer, we measure in the computational basis to get a bitstring bitstrings samples  $x_i \in \{0, 1\}^n$  correspond to the optimal solutions of the routing problem.

The circuit in Fig 2 represents a QAOA circuit of depth  $p=1$ , we can adapt the depth of the circuit as we want, meaning that we cascade the mix and cost layers, and it will be just a repetition of the same circuit multiple times behind each other, and supposedly higher-depth QAOA will provide better performance regarding the accuracy compared to the low-depth implementations [7]. However, this is not always the case as this system is affected by the noise generated from the quantum gates, and at higher depth QAOA the noise becomes larger, which affects at the end the accuracy of the solution. Moreover, a level- $p$  QAOA has  $2p$  parameters that need to be optimized classically (for each mix/cost layer we add, we will have a different  $\beta$  and  $\gamma$ ), and as  $p$  increases, parameter optimization becomes passive due to the curse of dimensionality [9].

The second part of the hybrid loop of the QAOA is the classical optimizer (see Fig1, right side), the main role of this entity is to improve the guess of the VQC and correct some of the noise generated from the “noisy” quantum gates. Thus choosing a classical optimizer that fits the problem is very important for the success of the QAOA [10]. An example of the classical optimizers that is supported by the Qiskit framework are COBYLA, ADAM, and SPSA [11].

In future works, we need to integrate the weights of the graph into the quantum circuit. The weights are going to be the parameter multiplied by the angle of rotation of the cost Hamiltonian  $\gamma$ . Moreover, we need to develop a mathematical formulation of the routing optimization based on the QAOA that will help to solve the problem even faster than the current best-routing algorithms.

## Conclusion

Routing is considered one of the most important functionalities in networking and normally, it defines the performance of a network, thus ensuring the optimality of packet route while fulfilling QoS criteria is a very important task that needs to be addressed. In this regard, this paper proposed a hybrid quantum algorithm entitled QAOA for routing optimization. The proposed hybrid QC-based approach provides a high computational efficiency in terms of computation time and accuracy, by utilizing the unique features of both classical and quantum computers. We expect that the QAOA will be a well-suited solution for routing optimization in the NISQ era.

## Acknowledgment

This paper received support from the European Union Horizon 2020 research and innovation program within the framework of IoTalentum Marie Skłodowska-Curie Actions ITN-ETN with grant number 953442, the ECSEL-JU project BRAINE and the Dutch Ministry of Economic Affairs and Climate Policy (EZK), as part of the Quantum Delta NL program.

## References

- [1] Nawaz, Syed Junaid, et al. "Quantum machine learning for 6G communication networks: State-of-the-art and vision for the future." IEEE access 7 (2019): 46317-46350
- [2] Chen, Mingzhe, et al. "Artificial neural networks-based machine learning for wireless networks: A tutorial." IEEE Communications Surveys & Tutorials 21.4 (2019): 3039-3071.
- [3] Amin, Rashid, et al. "A survey on machine learning techniques for routing optimization in SDN." IEEE Access (2021).
- [4] O'Quinn, Wesley, and Shiwen Mao. "Quantum machine learning: Recent advances and outlook." IEEE Wireless Communications 27.3 (2020): 126-131.
- [5] Amin, Rashid, et al. "A survey on machine learning techniques for routing optimization in SDN." IEEE Access (2021).
- [6] Preskill, John. "Quantum computing in the NISQ era and beyond." Quantum 2 (2018): 79.
- [7] Farhi, Edward, Jeffrey Goldstone, and Sam Gutmann. "A quantum approximate optimization algorithm." arXiv preprint arXiv:1411.4028 (2014).
- [8] Khan, Tariq M., and Antonio Robles-Kelly. "Machine learning: Quantum vs classical." IEEE Access 8 (2020): 219275-219294.
- [9] Chen, Lei. "Curse of dimensionality." Encyclopedia of Database Systems. 2009.
- [10] Fernández-Pendás, Mario, et al. "A study of the performance of classical minimizers in the quantum approximate optimization algorithm." Journal of Computational and Applied Mathematics 404 (2022): 113388.
- [11] <https://qiskit.org/documentation/stubs/qiskit.algorithms.optimizers.html>

# Tailoring of electric dipoles for highly directional excitation in parity-time symmetric waveguides

A. De Corte<sup>1</sup>, and B. Maes<sup>1</sup>

<sup>1</sup> Micro- and Nanophotonic Materials Group, Research Institute for Materials Science and Engineering, University of Mons, 20 Place du Parc, B-7000 Mons, Belgium

*The flexibility of photonic structures offers an ideal platform for exploring parity-time (PT) symmetry phenomena. In these platforms, electric dipoles are often used as accurate models for electromagnetic sources, and elliptical dipoles were shown to provide for directional mode excitation. Here, we tailor the polarization of an electric dipole to cancel one of the modes of two coupled PT-symmetric waveguides. This creates a contrast between wave propagation on both sides of the dipole, which manifests differently depending on the unique features of the modes in the various PT regimes.*

## Context

Electric dipole sources have been used for several years in integrated photonics as compact electromagnetic sources, due to their efficient coupling to photonic guided modes [1,2]. The near-field directionality of circularly polarized electric dipoles has recently been demonstrated, by taking advantage of constructive or destructive interference of different evanescent waves. [3,4] Coupling waveguides to these dipoles can lead to directional excitation of the waveguide modes. However, the directionality is lost if the dipole is at the center of an inversion-symmetric photonic structure like coupled waveguides. In order to restore the contrasting properties between two sides, we exploit the unique characteristics of parity-time-symmetric coupled waveguides.

Parity-time (PT) symmetry can be realized in coupled waveguides by using a balanced profile of their imaginary refractive index, with one waveguide made of a gain material and the other with an equal amount of loss. [5] The uniqueness of these structures stems from the two regimes in which they can operate depending on the value of the gain-loss parameter  $\gamma$ , that defines the absolute imaginary part of the refractive index in the waveguides. The transition between these two regimes occurs at the exceptional point (EP), which is located at a certain value of  $\gamma$  dependent on the structure geometry. In the PT-symmetric regime ( $\gamma < \gamma_{EP}$ ), both modes of the structure propagate without any gain or loss, whereas in the PT-broken regime ( $\gamma > \gamma_{EP}$ ) one mode benefits from the gain and is amplified while the other experiences losses and decays.

In this work, we take advantage of the characteristics of such a PT-symmetric structure with tailored dipoles to create various types of left-right contrasted wave propagation.

## Structure

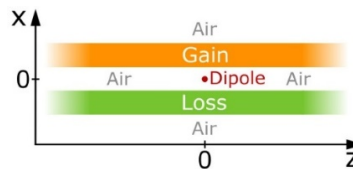


Figure 1 - Schema of the photonic structure used in the simulations. The dielectric gain and loss materials are represented in orange and green respectively and the air in white. The location of the dipole is marked by a red dot.

In our structure, the electric dipole is placed in the center of the air layer separating two PT-symmetric slab waveguides. The waveguide made of the gain material with refractive

index  $n = 2 + i\gamma$  is at the top, and the lossy guide with index  $n = 2 - i\gamma$  is at the bottom (fig. 1). The value of the gain-loss parameter  $\gamma$  at the EP for our structure is  $= 0.1231$ . We use the CAMFR (CAvity Modeling Framework, [6]) eigenmode expansion Maxwell equations' solver to numerically simulate our setup for values of  $\gamma$  ranging from 0 to 0.2.

## Dipole-mode coupling theory

To create the desired left-right contrasted propagation, we need to directionally excite a mode of the structure using the dipole source. Therefore, we first need to understand how a dipole couples to a photonic mode.

The excitation amplitude ( $A_m$ ) of a mode  $m$  by a source of dipole moment  $\vec{p}$  is given by

$$A_m \propto \vec{p} \cdot \vec{E}_m(\vec{r}_0) \quad (1)$$

where  $\vec{r}_0$  is the dipole position and  $\vec{E}_m$  is the electric field associated to mode  $m$ . [6]

According to the Maxwell equations, the longitudinal electric field component ( $E_z$ ) of two identical modes propagating in opposite directions need to have opposite signs. We define  $E_{mx}$  and  $E_{mz}$  as the field components of the right-side mode ( $z > 0$ ) at the dipole position  $\vec{r}_0$  and develop the scalar products of equations (1):

$$A_m \propto p_x E_{mx} \pm p_z E_{mz} \quad (2)$$

with the  $+$  sign corresponding to a mode propagating on the left ( $z < 0$ ) and the  $-$  sign to a mode on the right of the dipole ( $z > 0$ ).

By setting  $A_m$  to 0, equation 2 shows that the mode can be excited on one side while being canceled on the other side if

$$p_x E_{mx} = \mp p_z E_{mz}. \quad (3)$$

The mode will be canceled on the left side in the  $-$  case and on the right side in the  $+$  case. Since in our structure the modes electric field and the dipole moment can be complex, the condition with their polar expressions then becomes  $|p_x| e^{i\phi_{px}} |E_x| e^{i\phi_{Ex}} = \mp |p_z| e^{i\phi_{pz}} |E_z| e^{i\phi_{Ez}}$  which is fulfilled if

$$|p_x| |E_x| = |p_z| |E_z| \text{ and } \phi_{px} - \phi_{pz} = \phi_{Ez} - \phi_{Ex} (+\pi) \quad (4)$$

where  $\pi$  needs to be added if one cancels the mode on the left side.

## Mode analysis

As shown by the theory, the field of a mode at the dipole position is a crucial variable to directionally excite this mode. Therefore, we next study the evolution of the modal field in (0,0) as a function of the gain-loss parameter  $\gamma$ .

Depending on the value of  $\gamma$ , the electric field profile of the modes along  $x$  exhibits different symmetries: symmetric or antisymmetric in the PT-symmetric regime and asymmetric in the PT-broken regime. These result in different phases and moduli of the electric field of the modes at the dipole position, since an antisymmetric component will not contribute to the field at the dipole position ( $x = 0$ ). For both modes, in figure 2, we represent the quantities that intervene in the cancellation condition (eq. 4): the moduli of  $E_x$  and  $E_z$  as well as the phase difference between  $E_z$  and  $E_x$  as a function of  $\gamma$ .

In the PT-symmetric regime ( $\gamma < 0.1231$ ), figure 2(a) shows that the  $x$  and  $z$  field components have an equal complex phase, as  $\phi_{Ez} - \phi_{Ex} = 0$ . This is due to the peculiar symmetries of the modes in this regime: the symmetric parts of their  $x$  and  $z$  field components are both real for mode 1 and imaginary for mode 2. Figure 2(b) also shows that the relative intensities of  $E_x$  and  $E_z$  vary with  $\gamma$ , differently for modes 1 and 2. At the EP ( $\gamma = 0.1231$ ), the modes are defective, meaning that in addition to their eigenvalues

– propagation constants – being equal, their profiles are identical. Their fields are thus equal at the dipole position.

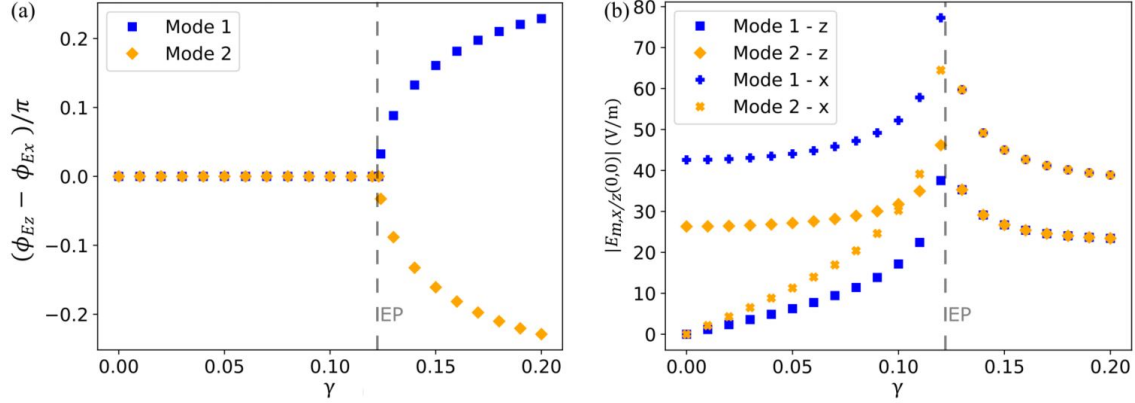


Figure 2 – (a) Phase difference and (b) moduli of the x and z electric field components of modes 1 (blue) and 2 (orange) at the dipole location for  $\gamma = 0$  to 0.20. The exceptional point is marked by a grey dashed line.

In the PT-broken regime ( $\gamma > 0.1231$ ), it can be seen on figure 2(b) that the field moduli of modes 1 and 2 are equal component by component (identical blue and orange results). This is once again explained by the symmetries of the modes. In this regime, the electric fields of the two modes are asymmetric, one mode being stronger in the gain guide while the other is more in the loss guide, but their profiles are mirrored with respect to  $x = 0$ . Modes 1 and 2 thus have equal values of  $|E|$  at the source. Their profiles are also complex conjugates in this regime, which explains the opposite phase differences in figure 2(a).

## Dipole tailoring and resulting contrasting behaviors

Considering the evolution of the phase and modulus of the modal field with  $\gamma$ , we can now calculate the dipole polarization required to cancel the desired mode on one side using equation (4). We choose to cancel mode 2 on the left side.

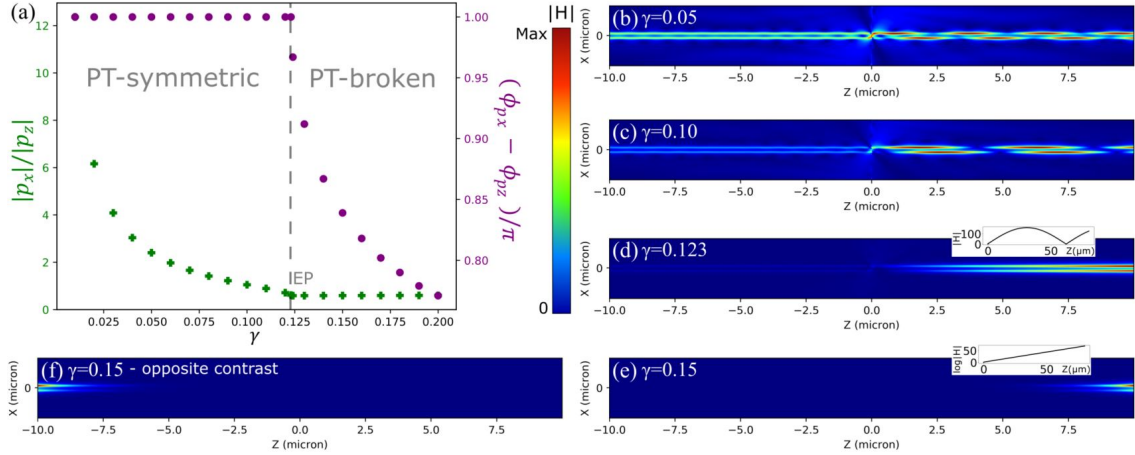


Figure 3 – (a) Characteristics of the dipole tailored for the desired contrast at each  $\gamma$ . (b-e) Magnetic field absolute value  $|H|$  in the structure. The dipole, tailored for each  $\gamma$ , is in  $(0,0)$ . The insets represent (d)  $|H|$  or (e)  $\log|H|$  at  $x=0$ . (f) The dipole tailored for  $\gamma = 0.15$  is used, with an added phase of  $\pi$  compared to image (e).

In the PT-symmetric regime, since it has been seen in Fig. 2(a) that  $\phi_{Ez} - \phi_{Ex} = 0$  for both modes, the phase difference of the adequate dipole (purple in fig. 3(a)) is  $\phi_{px} - \phi_{pz} = \pi$  for any value of  $\gamma$  below 0.1231. However, the ratio between  $|p_x|$  and  $|p_z|$  (green in fig. 3(a)) needs to be adjusted to account for the variation in  $|E_x|$  and  $|E_z|$ . In the PT-broken regime, the dipole phase difference needs to be adjusted for each  $\gamma$  as the mode

phase difference varies, but the x-to-z component ratio of the dipole moment remains almost constant as  $|E_x|$  and  $|E_z|$  evolve with similar tendencies as a function of  $\gamma$ .

Using the dipole tailored for each  $\gamma$  to excite the modes of the structure, we observe and compare the wave propagation on the left and right sides.

In the PT-symmetric regime (fig. 3(b,c)), mode 2 is one of the two propagating modes of the structure. Removing this mode on the left produces a uniform field profile, while exciting both modes on the right causes a beating, thus creating a contrast in the wave propagation between the two sides of the dipole. The beating pattern observed on the right also changes as  $\gamma$  varies since the propagation constants – the eigenvalues – vary with the PT conditions. Close to the EP, the modes become defective. As seen in figure 3(d), both modes are then canceled on the left, while the step of the beating pattern becomes almost infinite as the propagation constants are nearly equal. The system behaves as a single waveguide, which results in a near-complete directionality. In the PT-broken regime (fig. 3(e)), mode 2 is the gain mode. Removing it on the left makes the field considerably smaller than on the right side, as the gain mode remains on the right making the field explode. It is also important to note that for any  $\gamma$  the contrast can be reversed between the two sides by adding a phase of  $\pi$  to the phase difference between the components of the adequate dipole (fig. 3(f)). This feature could be used with the beating contrast in a directional coupler arrangement, as it would enable the selective excitation of any of the four ports. It could also lead to directional lasing if used with the directional amplification.

## Conclusion

By tailoring the polarization of a dipole to the properties of the modes of PT-symmetric coupled waveguides, a directional mode excitation is achieved in both PT regimes. This creates a left-right contrast in the wave propagation in the structure, with the presence of either beating in the PT-symmetric regime or field amplification on a chosen side of the dipole. Our results also highlight a feature of the EP: the defectiveness of the modes in this unique configuration enables a near-complete directional excitation.

In the end, these various types of contrasting phenomena may offer new possibilities for integrated photonics applications, routing setups, and lasing behavior.

## Acknowledgements

This work benefits from the support of the French Community of Belgium within the framework of the financing of a FNRS-FRIA grant.

## References

- [1] Aiello, A., P. Banzer, M. Neugebauer and G. Leuchs, “From transverse angular momentum to photonic wheels,” *Nat. Photonics*, Vol. 9, 789-795, 2015.
- [2] Espinosa-Soria A. and A. Martinez, “Transverse spin and spin-orbit coupling in silicon waveguides,” *IEEE Photonics Technol. Lett.*, 28, 1561-1564, 2016.
- [3] Rodríguez-Fortuño, F. J. et al., “Near-field interference for the unidirectional excitation of electromagnetic guided modes,” *Science*, Vol. 340, 328-330, 2013.
- [4] Picardi, M. F., A. V. Zayats and F. J. Rodríguez-Fortuño, “Janus and Huygens Dipoles: Near-Field Directionality Beyond Spin-Momentum Locking,” *Phys. Rev. Lett.*, Vol. 120, No. 117402, 2018.
- [5] Feng, L., R. El-Ganainy and L. Ge, “Non-Hermitian photonics based on parity-time symmetry,” *Nat. Photonics*, Vol. 11, 752-762, 2017.
- [6] P. Bienstman, “Rigorous and efficient modelling of wavelength scale photonic components,” Ph.D. thesis, Universiteit Gent, 2001.

# Design of dense InP based optical antenna array for 2D beam steering

Fathema Farjana, Yi Wang, and Yuqing Jiao

Eindhoven Hendrik Casimir Institute (EHCI), Eindhoven University of Technology, Eindhoven,  
5600MB, the Netherlands

*This paper presents an optical phased array (OPA) utilizing SiO<sub>2</sub> gratings on InP membrane on Silicon (IMOS) platform for large-angle optical beam steering. Width-engineered waveguides are leveraged for crosstalk suppression to achieve dense integration. In the simulation, < -20 dB channel crosstalk is achieved at 1550 nm wavelength for a 2 mm-long antenna array with 1 μm pitch. A large steering range of 73° × 13.6° is obtained with an SNR of -7.4 dB. Such a 2D steering OPA has great potential to realize full-solid LiDAR for its large FOV, small SNR, and monolithic compatibility with InP lasers and amplifiers.*

## Introduction:

Optical phased array (OPA) has become a crucial candidate for light detection and ranging (LiDAR) in autonomous driving cars for its potential of precise, ultrafast inertia-free beam steering of high reliability, high scalability, and mass manufacturability [1]. OPA in automotive cars needs to achieve a large FoV and high resolution. However, the desirable wide FoV is limited by the evanescent coupling in an antenna array, and the coupling strength is inversely proportional to the antenna spacing [1]. A sparse array with non-uniform emitter spacing provides an interesting alternative to reduce the crosstalk. Though this scheme keeps the side lobes suppressed during the beam-steering process while achieving 80° × 17° FoV, it sacrifices the energy concentration in the main lobe (≤ 40% [2]). For long-range applications like in LiDAR, it could be detrimental as it will result in the degradation of signal-to-noise ratio (SNR). Alternatively, an ultra-compact dense array with subwavelength pitch has been proposed with very low crosstalk (below < -18 dB) using thin waveguide strips [3] and also by using periodic nano-blocks [4]. However, in these designs, the width of nano blocks [4] and the minimum gap [3] of a few tens of nanometers, are challenging in fabrication. Song W. et al. has proposed a superlattice structure of waveguides at sub-wavelength-pitch, where the crosstalk between adjacent waveguides can be suppressed under -20 dB by changing the widths of the waveguides [5]. This superlattice concept is leveraged in this paper to suppress crosstalk.

For Si photonic-based LiDAR systems, it is still challenging to realize the monolithic integration of laser source and semiconductor optical amplifier (SOA) arrays which are important for a beam steerer [6]. In contrast, the InP membrane on silicon (IMOS) platform can provide monolithic integration of active and passive devices and the compactness of SOI platform [7]. In this paper, high-density integration of OPA is achieved on the IMOS platform using superlattice theory for crosstalk suppression. For the eye-safe wavelength range of 1500-1600 nm, the design resulted in a high lateral FoV for 2D beam steering with low SNR.

## Design:

The structure of the OPA on the IMOS platform is shown in Fig. 1. The gratings are on top of a 300 nm thick InP membrane waveguiding layer as shown in Fig 1(a). The buffer layer for IMOS platform

is composed of benzocyclobutene (BCB) and SiO<sub>2</sub> stacks [8], but in the design it is approximated with 2 μm layer of SiO<sub>2</sub>, since the BCB layer do not interact with the optical mode [6]. The low-index-contrast SiO<sub>2</sub> gratings are designed on the surface of the highly confined InP membrane waveguide as proposed in [6] to achieve weak coupling. A thickness of 200 nm is chosen for the gratings to ensure about 90% of the light is emitted from the grating antenna by 2 mm effective length. This 2 mm effective length is long enough to produce a beam of high resolution as proven in [6]. To overcome the crosstalk throughout the designed array the superlattice concept is used where the array is composed of subarrays of waveguides. In the subarray, the cross-talk is minimized between adjacent waveguides by introducing propagation constant mismatch using different waveguide widths. The subarrays are made sufficiently large to avoid crosstalk among same width waveguides. In the schematic of Fig. 1(b) the grating array superlattice is composed of N number of subarrays. Fig 1(c) shows that, each subarray of the design consists of two antennas of widths W1 = 550 nm and W2 = 580 nm, and grating periods of  $\Lambda_1$  and  $\Lambda_2$  of 50% duty cycle respectively. Here in the design for a pitch of 1 μm, a 30 nm width mismatch is used in the subarray that created an effective index mismatch of 0.04 to suppress the crosstalk between adjacent antennas. Fig. 1(d) depicted the 3D structure of the design. In our design, the longitudinal beam steering ( $\theta$ , along the antenna length) is done by wavelength tuning. Since in a subarray, two widths are used, the effective index ( $n_{eff}$ ) of each grating is also different. This leads to different periods of the antennas in the subarray in order to achieve a same emission angle. In the design the emission angle  $\theta$  is chosen 13° for 1550 nm central wavelength ( $\lambda_0$ ) to prevent the Bragg reflection. The grating periods ( $\Lambda$ ) are calculated for different widths based on their effective indices using the grating equation [6]:

Finally, we obtain  $\Lambda_1 = 726$  nm and  $\Lambda_2 = 713$  nm for 550 and 580 nm antenna widths, respectively.

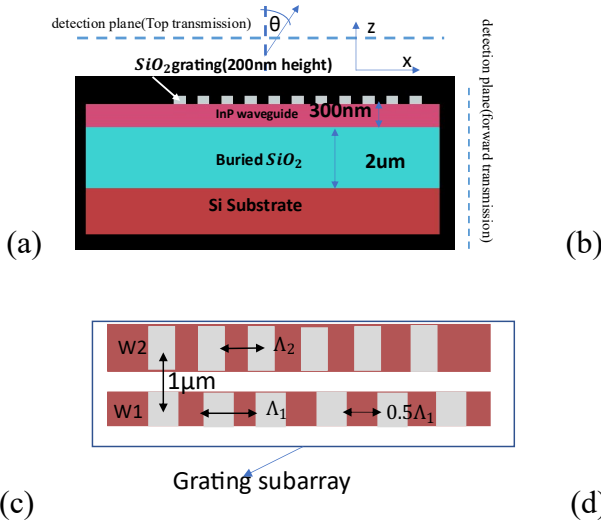


Figure 1. (a): Layer structure of grating antenna on IMOS platform, (b): Schematic of the grating sub-array, (c): Grating antenna subarray structure, (d): 3D illustration of grating based OPA.

## Simulation:

As 3D finite-difference time-domain (FDTD) algorithm is computationally heavy for large structures, the crosstalk of the design is verified using Lumerical's Eigen Mode Expansion (EME) solver. A 2 mm antenna length is calculated for a 0.05° target angular resolution [6]. A simplified model is shown in Fig. 2(a) to study the crosstalk of a superlattice array of two alternating widths, where three

waveguide is simulated (on which the gratings are made). The 1<sup>st</sup> (WG1) and 3<sup>rd</sup> (WG3) waveguides are of same width of 550 nm and 2<sup>nd</sup> (WG2) waveguide is of 580 nm. In the simulation, TE mode is chosen for the WGs. Fig. 2(b) shows that, the launched light in WG1 have minimal interaction with the adjacent waveguide resulting in crosstalk < -20 dB depicted in line graph of Fig. 2(c). To compare the result with equal-width WGs Fig. 2(b) illustrates the field profile where a strong coupling can be seen in neighboring WGs making it unsuitable for the array design.

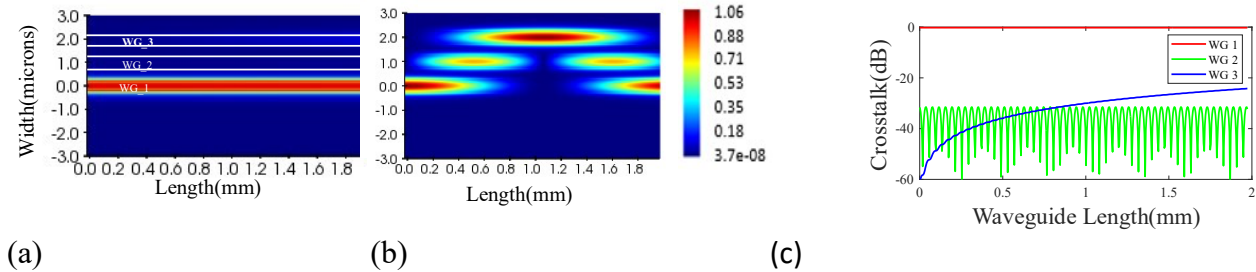


Figure 2. (a): Field profile for array of 3 WGs of 550 and 580 nm width. (b): Field profile for same width (550 nm) WG array showing strong field overlap. (c): Line-graph of crosstalk in WG2 and WG3 from source waveguide WG1.

The designed array is a 1D array consisting of 8 subarrays of two different widths antenna with extra one of 580 nm width to make the structure symmetric around the middle antenna. The steering angle and FWHM (full width at half maximum) of the beam in the far field are recorded for these two GA widths by changing the wavelength from 1500-1600 nm in 20 nm steps. Here, to reduce the simulation time, only 40 nm length is simulated. As scattering is a linear process, the FWHM of a full 2 mm long device can be obtained via extrapolation. In simulation, A total of 13.6° of steering angle is achieved for a wavelength tuning range of 100 nm with an average beam width of ~2.35° and ~2.41° for 550 and 580 nm GA, respectively. The steering angle and FWHM for both the GA are in good agreement, as shown in Fig 3(a). Fig. 3(b) depicts the longitudinal steering of 13.6° with beam intensity for the 1×17 channels array for the 100 nm wavelength range. For 40 um length of the antenna, the array achieved an average beam width of 2.351°. Here, the beam intensity decreases slightly with increasing steering wavelength.

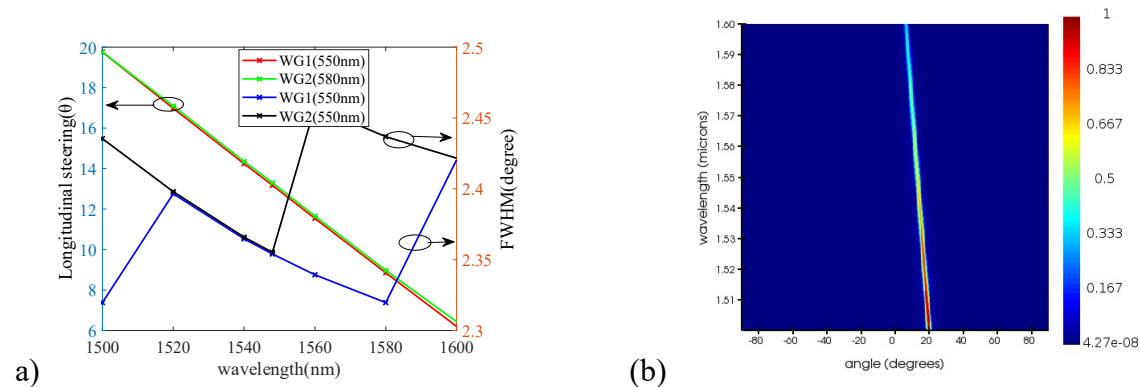


Figure 3: (a): Steering angle with wavelength and FWHM beam width of the steered beam of 550 and 580 nm GA. (b): Wavelength steered map for 100 nm wavelength range and steering intensity.

Now, to see the steering capability in the lateral direction ( $\psi$ , across the antenna array) of the 17 channels array, the beam is steered by changing the phase shift between adjacent antennas from -140° to +140° for the 1550 nm wavelength. In Fig. 4(a) the steering map is shown where a FoV of 73° is achieved in the lateral direction with side lobe suppression ratio (SLSR) of -7.4 dB. Here, the beam intensity is normalized to 1 and the pattern envelope is conserved. The beam width is limited by the diffraction from array size of 17 channels to 4.58°. It is also seen in the figure that the beam width of

main lobe has broadened to  $5.73^\circ$  when steered to the edge. By combing lateral steering with the wavelength tuning, 2D beam steering with  $1 \times 17$  channels GA array is achieved. Here for longitudinal steering, the wavelength is tuned from 1500-1600 nm, and lateral steering is done by changing the phase from  $-140^\circ$  to  $140^\circ$ . In Fig. 4(b), this 2D steering map is shown. The beam is steered along the perimeter of the entire field of view of  $73^\circ \times 13.6^\circ$  in  $\psi \times \theta$ . The normalized intensity of far-fields of these steered beams are shown overlaid upon each other, and the dotted rectangular area shows the entire FoV. In the figure, the respective steering values for beam positions are shown.

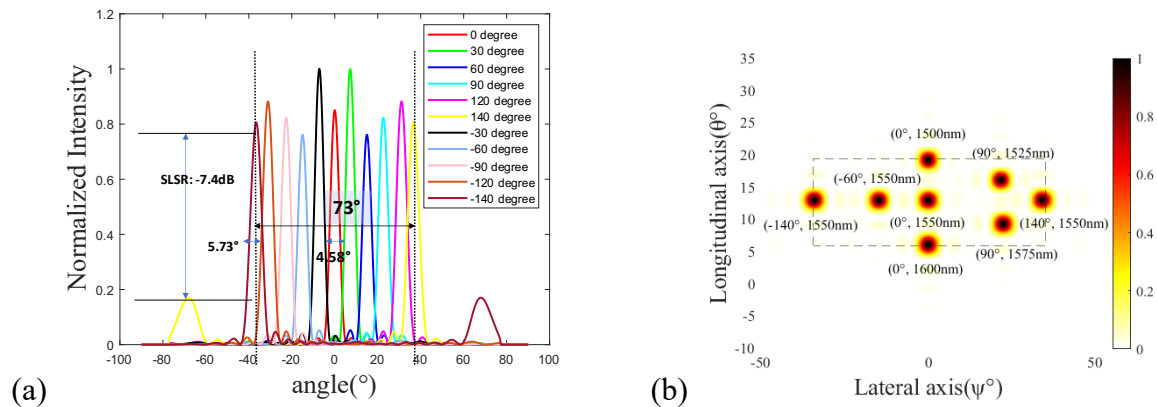


Figure 4. (a): Numerical results of beam steering of superlattice structure by using FDTD method with the phase shift -  $140^\circ$  to  $+140^\circ$ . (b): 2D beam steering around a  $73^\circ \times 13.6^\circ$  FoV.

## Conclusion:

The proposed design is a InP-based grating antenna array for 2D beam steering. Here, the superlattice concept is leveraged to achieve low crosstalk and large FoV in lateral steering. For the 17 channels GA array, a  $73^\circ$  of FoV is achieved numerically. This OPA structure on the IMOS platform can potentially achieve high integration density with monolithic active components, which will contribute to a fully-integrated solid-state automotive LiDAR.

## References:

- [1] C.-P. Hsu *et al.*, 'A Review and Perspective on Optical Phased Array for Automotive LiDAR', *IEEE J. Sel. Top. Quantum Electron.*, vol. 27, no. 1, pp. 1–16, Jan. 2021, doi: 10.1109/JSTQE.2020.3022948.
- [2] T. Komljenovic, R. Helkey, L. Coldren, and J. E. Bowers, 'Sparse aperiodic arrays for optical beam forming and LIDAR', *Opt. Express*, vol. 25, no. 3, p. 2511, Feb. 2017, doi: 10.1364/OE.25.002511.
- [3] L. Wang *et al.*, 'Design of a low-crosstalk half-wavelength pitch nano-structured silicon waveguide array', *Opt. Lett.*, vol. 44, no. 13, p. 3266, Jul. 2019, doi: 10.1364/OL.44.003266.
- [4] G. Zhou, S.-W. Qu, J. Wu, and S. Yang, 'Design of a Low-Crosstalk Sub-Wavelength-Pitch Silicon Waveguide Array for Optical Phased Array', *IEEE Photonics J.*, vol. 13, no. 4, pp. 1–8, Aug. 2021, doi: 10.1109/JPHOT.2021.3103392.
- [5] W. Song *et al.*, 'High-density waveguide superlattices with low crosstalk', *Nat. Commun.*, vol. 6, no. 1, p. 7027, Nov. 2015, doi: 10.1038/ncomms8027.
- [6] Y. Wang *et al.*, 'InP-Based Grating Antennas for High-Resolution Optical Beam Steering', *IEEE J. Sel. Top. Quantum Electron.*, vol. 27, no. 1, pp. 1–7, Jan. 2021, doi: 10.1109/JSTQE.2019.2958999.
- [7] Z. Wu, Q. Huang, J. Xia, and W. Jiang, 'Optical phased array antenna with wide steering range using grating array superlattices', in *Sixth International Conference on Optical and Photonic Engineering (icOPEN 2018)*, Shanghai, China, Jul. 2018, p. 96. doi: 10.1117/12.2500591.
- [8] Y. Jiao *et al.*, 'Indium Phosphide Membrane Nanophotonic Integrated Circuits on Silicon', *Phys. Status Solidi A*, vol. 217, no. 3, p. 1900606, Feb. 2020, doi: 10.1002/pssa.201900606.

# Characterization of a MZI based tunable filter using an optimization algorithm

T. Kabir,<sup>1</sup> S. Tondini,<sup>1</sup> J. Hazan,<sup>1</sup> D.M.H Abusada,<sup>1,2</sup> K.A Williams,<sup>1</sup> M. J. R. Heck<sup>1</sup>

<sup>1</sup> Eindhoven University of Technology, Eindhoven Hendrik Casimir Institute, Eindhoven, the Netherlands.

*We present the characterization of a Mach-Zehnder Interferometer (MZI) based tunable filter to achieve stepwise tuning over a free spectral range (FSR) of 10 nm, with a 3-dB bandwidth of 1 nm. The design is a wavelength-selective tunable filter that employs eight reversely biased voltage-driven electro-optic phase modulators (EOPM) to change the phase of the light in the eight arms of a MZI tree. A star coupler is used to achieve the splitting and combining of the light at the filter input and output. The simulated transmission profile is compared to experimental results when the arms are driven through an optimization algorithm. This allows for estimating the contribution of initial dephasing in each arm that can be attributed to phase errors. We show a tuning of 9 nm with 1 nm steps using a Nelder-Mead stochastic search algorithm for voltages. Filter's figures such as pass-band shape and full width half maximum (FWHM) are also estimated. The filter has been realized on the indium phosphide (InP) generic platform, on a multi-project wafer (MPW) run..*

## Introduction

Tunable lasers are crucial to many applications in datacom and sensing, particularly in dense wavelength division multiplexing (DWDM) [1], gas sensing [2], optical coherence tomography [3] and LIDAR [4]. The key requirements for tunable lasers in these fields are miniaturization, faster speed, large integration capacity and energy efficiency. For this, photonic integrated circuit or PIC-based tunable lasers are particularly interesting. A core component of an integrated widely tunable laser (tunability  $\gg 10$  nm) is a tunable mode selection filter. Several types of tunable filters have been demonstrated in monolithic PICs. The state of the art includes ring resonators [1], sampled grating distributed Bragg reflectors (SGDBR) [6] and Mach Zehnder interferometers (MZIs) [7] [8]. Sampled gratings and ring resonator based tunable lasers are promising in terms of wide tunability, with demonstrated tuning ranges above 40 nm [5]. However, for SGDBR structures, the fabrication of complex gratings requires high-resolution lithography techniques like electron beam lithography. In case of ring resonator based filters, the tuning is slow as it employs thermal effects. Furthermore, these types of filters suffer from frequency drift that is attributed to the injection current-based tuning. On the other hand, in the monolithic InP generic platform [9], filters using an MZI-based feed-forward structure employ electro-optic effect-based tuning. This mechanism helps to overcome the heat induced frequency drift problems, and is also potentially faster. Also, compared to DBR gratings, these structures are relatively simple to fabricate. These filters have also exhibited very wide tuning range such as 74 nm, measured by Latkowski *et al.* [10]. In this paper we describe the preliminary measurement results of a tunable filter based on MZI feed-forward structure that uses electro-optic phase modulators (EOPM) on each arm of the MZI. The filter is tuned by varying the phase on the EOPMs with reverse bias voltage.

In the first section we will describe the design of the filter and the theory of the tuning mechanism. In the second section we will elaborate on the measurement setup and the optimization algorithm called *Nelder-Mead stochastic search* [11] used to search for the voltage configuration. In the third section we will discuss the obtained results from the experiments in terms of filter performance.

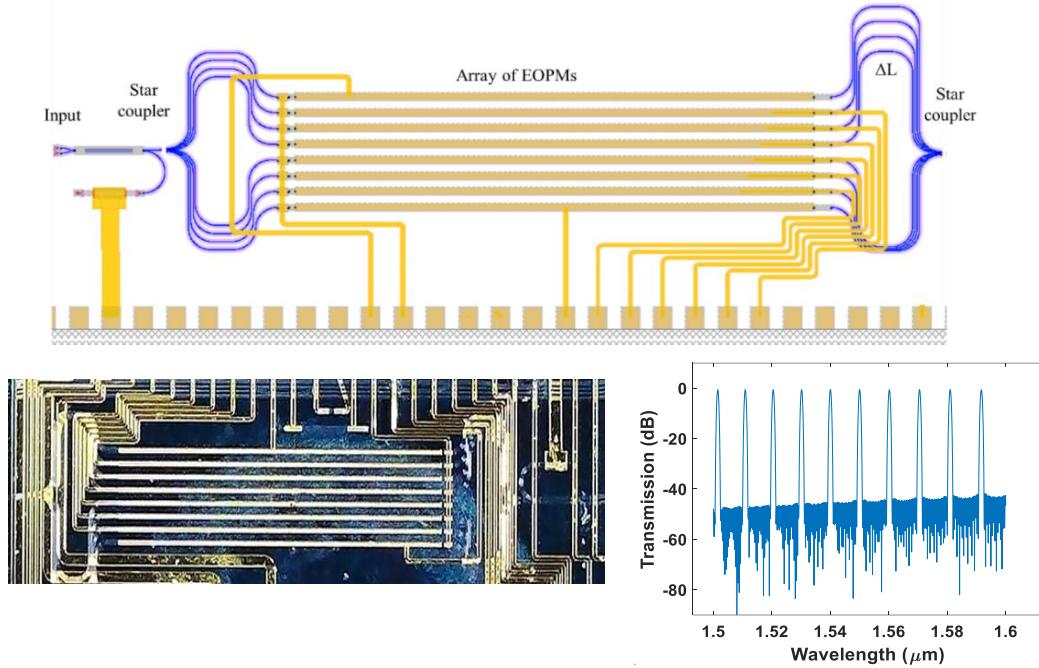


Figure 1: (a) GDS design of the realized filter. (b): Microscopic picture of realized chip. (c): Stimulated profile of filter structure resulting in a wavelength dependent sinc function

## PIC design and filter mechanism

Papers The GDS of the designed filter consists of 8 MZI arms as shown in Figure 1a. A star coupler of 1:8 configuration is used to couple and split the light. The pitch and waveguide width of the star coupler is chosen such that we have equal power distribution on the arms. Each arm has individual phase control through an EOPM with length of 2400  $\mu\text{m}$ . By design the EOPMs can have a phase shift of 12 to 15 degree/ V.mm. So the theoretical  $V_\pi$  value is 6.24 V.

The geometric length mismatch results in the sinc shape of the filter, and it also determines the free spectral range (FSR) of the filter. The designed FSR is 10 nm. The filter is tuned by varying the voltages on the EOPMs within the range of 0 to  $V_{2\pi}$ . The goal is to get constructive interference between the light from each arm for the target wavelength ( $\lambda_{\text{target}}$ ). Figure 1b shows the realized chip on the InP platform developed by Smart Photonics on a multi project wafer (MPW) run.

To tune the filter, different kinds of waveforms can be implemented for the voltage signals. A sawtooth or a sine waveform can be a viable option. The theory and mechanism of the sawtooth tuning is described in detail in a previous work [12]. Certain challenges are foreseen in tuning with preset waveforms. First of all, contrary to theory, the initial condition of the relative voltages on the filter arms are unknown to us. One way of finding the initial condition can be using a genetic algorithm [13]. Moreover, the number of combinations required for trial to find out the optimum combination for a target wavelength is too large. Even for 10 voltage steps, the number of combinations to try becomes  $10^8$ . In this paper we present a more time- efficient approach of using an optimization algorithm rather than using waveforms. The measurement setup and the algorithm is discussed in detail in the further sections.

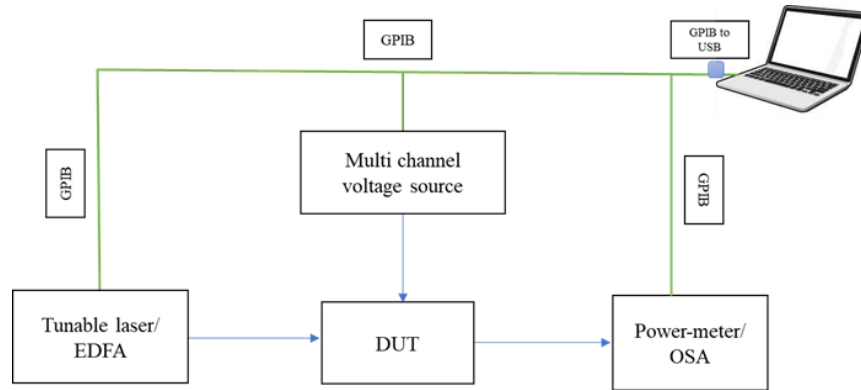


Figure 2 Experimental setup for filter measurement.

## Experimental setup and optimization loop

The measurement setup is illustrated in Figure 2. The setup is connected in two ways: a tunable laser source (TLS) coupled with power meter (PM) and erbium doped fiber amplifier (EDFA) coupled with optical spectrum analyzer (OSA). The EDFA works as an input broadband source and OSA to collect the optical spectrum. A multichannel voltage source is used to apply the voltages. The voltage source, PM and OSA are connected to the computer via a general-purpose interface bus (GPIB) to sweep the different voltage conditions automatically and for recording the data in an automated way. To achieve a tuning of 10 nm, the range 1548 to 1558 nm has been split into 10 steps where, at first, the TLS is kept fixed at  $\lambda_{\text{target-1}}$  and the output is recorded through the PM. Given this configuration, we ran the optimization algorithm, which outputs an array of voltages that gives maximum transmission for that target wavelength. After this, the full spectrum is collected, and the TLS takes a step forward in wavelength to  $\lambda_{\text{target-2}}$  and so on.

The optimization algorithm chosen for this specific task is the Nelder-Mead stochastic search. It is based on the convergence of the vertices of a simplex of  $N+1$  dimensions with respect to the degrees of freedom of the search domain (8 in our case) into a single point. Given a starting seed, the 9-dimensions polyhedron will shrink towards degeneration by following iterative evaluations of the target function (optical power in our case) in each vertex. At each step, all vertices but the one which has the best target function value will be then pushed in that direction.

## Results and discussion

In this section we present the first results of filter tuning. Figures 3a and b illustrates the tuning of the filter for a 9 nm range, with coarse steps of 1 nm. The contour plot in Figure 3a shows the 10 nm FSR of the filter. The optimizer is implemented for tuning the wavelength range of 1548-1557 nm. After obtaining the optimized voltages, we recorded the spectra to retain the filter shape.

Figure 3b shows the peak wavelengths obtained during tuning. We find that the optimizer works with a maximum error of 0.63 nm from the target wavelength. This is attributed to the error of calibration of the optimizer. The reliability of the filter is checked with two trials, and maximum error between two trials is 0.12 nm.

In Figure 4a we show the tuning waveforms that are retrieved from the search algorithm. The range of voltage is limited by the multi-channel voltage source that has a range of  $\pm 10V$ . In future measurements, we will implement a range that can cover the  $V_{2\pi}$  range.

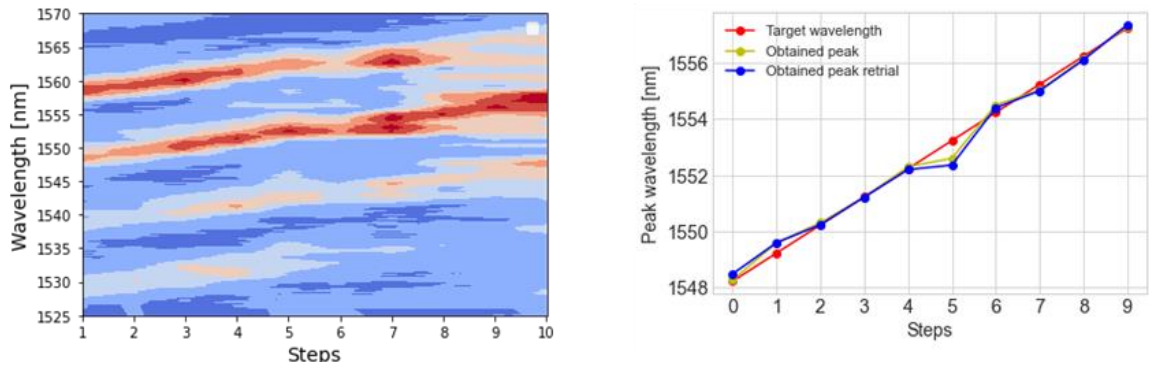


Figure 3: (a) Contour plot showing tuning of filter with 10 steps with each step of 1 nm. (b) Peak wavelength with target wavelength in red and retrials in green and blue

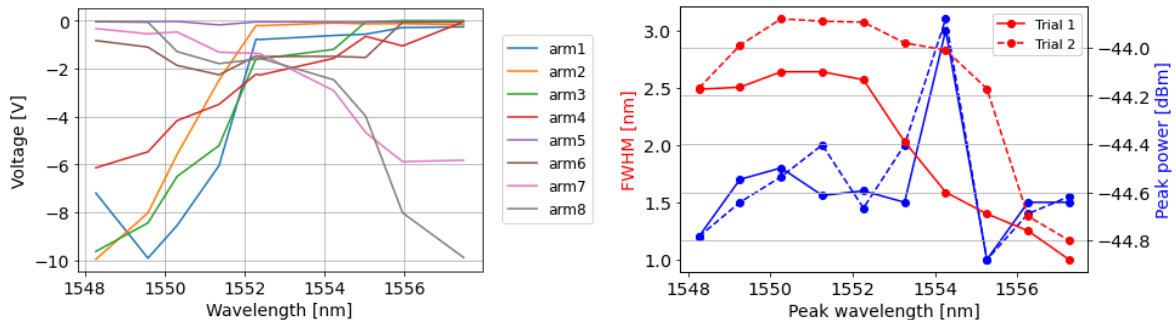


Figure 4: (a) The phases of 8 arms with tuning. (b) Evolution of filter parameters FWHM and peak power with tuning. The dashed and solid lines correspond to two trials of measurements respectively.

In Figure 4b, the evolution of FWHM and peak power is shown with tuning in wavelength. It is seen that the filter shape changes through the measurement, the FWHM varying from designed value of 1 nm, increasing up to 3.5 nm. This can be because of the limitation of the optimizer, as it optimizes on the peak power and does not yet take into account the shape of the filter. The peak power also varies, but that can be an effect of the setup or misalignment of fibers. These results can be further improved with increasing the number of steps to omit the outliers and improving the optimizer by scattering the starting seed.

## Conclusion

The first results of an 8 arm tunable filter with a stochastic search based optimization algorithm is presented. The filter is tuned for a 9 nm range, with results shown for different parameters such as peak wavelength, FWHM and peak power. The algorithm can be further improved by feeding the spectra results to converge to vertices that have the best peak power as well as side-mode-to-main-mode-ratio (SMTR) and FWHM. Further work involves improving the search algorithm and implementing it in measuring tunable lasers that contain this kind of filter.

## References

- [1] K. Tsuzuki et al., "Full C-Band Tunable DFB Laser Array Copackaged With InP Mach-Zehnder Modulator for DWDM Optical Communication Systems."
- [2] A. Hänsel and M. J. R. Heck, "Feasibility of telecom-wavelength Photonic integrated circuits for gas sensors," *Sensors*, vol. 18, no. 9, p. 2870, 2018, doi: 10.3390/s18092870.
- [3] J. Hazan, T. Couka, R. Pajkovic, K. Williams, and E. Bente, "Control strategy for a monolithically integrated widely tunable laser system on INP for optical coherence tomography," *Novel In-Plane Semiconductor Lasers XXI*, 2022.
- [4] B. Behroozpour, P. A. M. Sandborn, M. C. Wu and B. E. Boser, "Lidar System Architectures and Circuits," in *IEEE Communications Magazine*, vol. 55, no. 10, pp. 135-142, Oct. 2017, doi: 10.1109/MCOM.2017.1700030.
- [5] S. Matsuo and T. Segawa, "Microring-resonator-based widely tunable lasers," *IEEE Journal on Selected Topics in Quantum Electronics*, vol. 15, no. 3, pp. 545-554, May 2009, doi: 10.1109/JSTQE.2009.2014248.
- [6] Moon-Hyeok Lee, Francisco Soares, Moritz Baier, Martin Möhrle, Wolfgang Rehbein, Martin Schell, "53 nm sampled grating tunable lasers from an InP generic foundry platform," *Proc. SPIE 11356, Semiconductor Lasers and Laser Dynamics IX*, 1135605 (1 April 2020)

- [7] S. Latkowski *et al.*, "Novel Widely Tunable Monolithically Integrated Laser Source," in *IEEE Photonics Journal*, vol. 7, no. 6, pp. 1-9, Dec. 2015, Art no. 1503709, doi: 10.1109/JPHOT.2015.2493722.
- [8] Quanan Chen, Kuankuan Wang, Chun Jiang, Xiang Ma, Ye Liu, Qiaoyin Lu, and Weihua Guo, "Butterfly-packaged multi-channel interference widely tunable semiconductor laser with improved performance," *Opt. Express* 29, 6344-6355 (2021)
- [9] "An introduction to InP-based generic integration technology." [Online]. Available: <https://iopscience.iop.org/article/10.1088/0268-1242/29/8/083001>. [Accessed: 16-Nov-2022].
- [10] "Novel widely tunable monolithically integrated laser source," *IEEE Xplore*. [Online]. Available: <https://ieeexplore.ieee.org/document/7305755>. [Accessed: 16-Nov-2022].
- [11] <https://docs.scipy.org/doc/scipy/tutorial/optimize.html>
- [12] Kabir, T., de Graaf, J.P. and Heck, M.J. R (2021) "Novel tuning algorithm for continuous and widely tunable integrated lasers," *IEEE Benelux Chapter Annual Symposium 2021*.
- [13] B. W. Tilma, "Integrated tunable quantum-dot laser for optical coherence tomography in the 1.7 $\mu$ m wavelength region," *Eindhoven University of Technology research portal*, 18-Nov-2015. [Online]. Available: <https://research.tue.nl/en/publications/integrated-tunable-quantum-dot-laser-for-optical-coherence-tomogr>. [Accessed: 16-Nov-2022].

# Aluminum nitride low loss waveguides

S. Mardani, W.A.P.M. Hendriks, M. Dijkstra, S.M. Garcia-Blanco

Integrated Optical Systems Group, MESA+ Institute, University of Twente, P.O. Box 217, 7550 AE, Enschede, The Netherlands

*Integrated photonics based on thin film technology has created a revolution in application fields including quantum information processing, optical sensing/metrology, and bio/chemical sensing. Most materials and platforms commonly used in integrated photonics, such as silicon-on-insulator (SOI), silicon nitride ( $\text{Si}_3\text{N}_4$ ) and indium phosphide (InP) do not show transmission below  $\sim 450$  nm, hindering the development of PICs operating in the ultraviolet wavelength range. Furthermore, devices in this wavelength range also require modulation and switching in order to enable complex emerging applications.*

*Among the different materials, aluminum nitride (AlN) has a wide transparency window, from the ultraviolet to the mid-infrared. This feature helps photonic devices made with AlN to be active in this range of wavelengths. AlN also exhibits high electro-optic and piezoelectric coefficients. Unfortunately, prohibitively high losses have prevented PICs from benefiting from its excellent optical properties.*

*Here, we present our work on the sputter deposition and annealing of low-loss AlN slab waveguides. The optical performance of the films will be discussed. Preliminary slab propagation losses as low as 1.5 dB/cm at 633 nm of wavelength have been experimentally demonstrated.*

## Introduction

Many applications require photonic integrated circuits (PICs) operating in a broad spectrum down to the UV and visible (UV-vis). A PIC platform in this wavelength range requires broadband materials that are optically transparent and have low propagation losses. Aluminum nitride (AlN), with its wide bandwidth (6.2 eV) and unique optical properties, holds great promises in ultrabroadband PICs [1] [2].

Many studies have been done on wafer-scale AlN deposition technology. Different deposition methods can be used for producing this thin film, including metal-organic chemical vapor deposition (MOCVD), molecular beam epitaxy (MBE), electron cyclotron resonance dual-ion beam sputtering, and pulsed laser ablation. They are expensive and complicated processes. Among the available deposition techniques, radio frequency (RF) magnetron reactive sputtering is lower cost and recognized as the leading technology to achieve AlN films with excellent quality and surface morphology [3]. Provided that low optical propagation losses can be achieved, AlN layers deposited by this method are ideal candidates for integrated photonics.

In this work, we show our advancements towards low-loss high-confinement AlN waveguides for PICs. First, a 147 nm thick AlN layer is deposited by reactive sputter coating and its surface and optical properties are characterized. Next, different annealing temperatures are studied, again followed by surface, material and optical characterization. Slab losses  $\sim 1.5$  dB/cm at 633 nm have been experimentally demonstrated.

## Experimental details

The AlN layer is deposited using a RF reactive sputtering system on 10 cm diameter silicon wafers with 8  $\mu\text{m}$  thick thermal oxide. An Al target (99.99 % purity, 101.6 mm diameter) is powered with its own RF power source. The depositions are performed with a constant RF power of 500 W applied to the aluminum target. All parameters used for the deposition of the AlN layer with a thickness of 147 nm are given in Table 1.

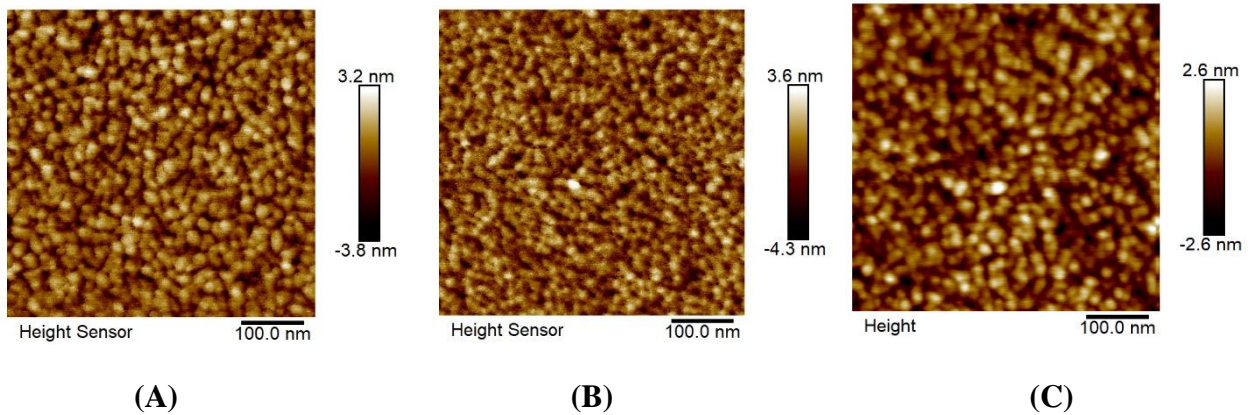
Table 1 Optimized Rf reactive sputtering process parameters

Parameter	Value	Unit
Argon flow	40	sccm
Nitrogen flow	4	sccm
Base pressure	7 E-7	mbar
Pressure	5 E-3	mbar
Substrate set temperature	400	$^{\circ}\text{C}$
Target-substrate distance	4.5	cm
Power	500	W

The deposited layer is annealed at 400  $^{\circ}\text{C}$ , 500  $^{\circ}\text{C}$ , 600  $^{\circ}\text{C}$ , and 700  $^{\circ}\text{C}$ . After the wafer is put into the annealing oven,  $\text{N}_2$  is delivered to the chamber at a flow rate of 2 slm. The standby temperature is 400 $^{\circ}\text{C}$  and then increases at a rate of 8 $^{\circ}\text{C}/\text{min}$ . We kept the wafer at the desired temperature for 3 hours each time.

Surface and optical analysis are performed before and after annealing. First, the thickness and refractive index are measured using an Woollam M-2000UI ellipsometer. Given the 8  $\mu\text{m}$  oxide layer a fitting range from 600 to 1600 nm is used to determine the layer properties with a Cauchy model of the layer. The surface roughness of the layers is measured using a Bruker Fast Scan AFM. The propagation loss of the layer is measured using a Metricon 2010/M prism coupler with a propagation loss module. The propagation loss is determined at 636 nm, 521 nm, 451 nm and 403nm of wavelength.

The surface morphologies of the AlN thin film before and after annealing for each temperature are presented in Figure 1. The scanned area was 500x500  $\text{nm}^2$ . The surface roughness before annealing was 0.57 nm RMS. After annealing, the determined RMS increase step by step with increasing temperature. We can therefore confidently conclude that the annealing significantly increases the surface roughness.



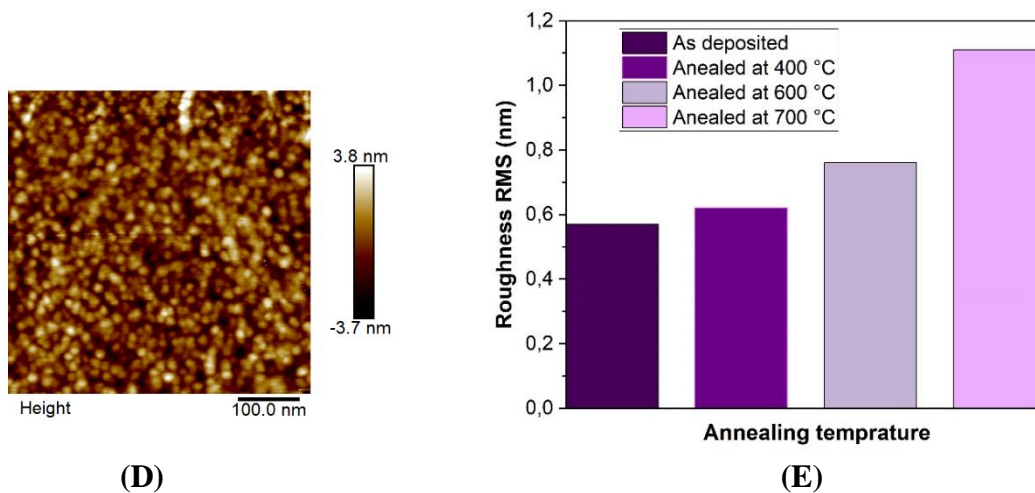


Figure 1 Surfaces of AlN thin films (A) As deposited, (B) annealed at 400°C, (C) annealed at 600°C, (D) annealed at 700°C. (E) RMS for all conditions.

The refractive index of the layers at the wavelength of 633 nm before and after the annealing process at temperatures 400°C, 500°C, 600°C, and 700°C is 2.01, 2.04, 2.02, 2.03 and 2.03, respectively. The results show that the refractive index of the layers did not change significantly.

Figures 2 (A), (B), (C) and (d) show the effect of the annealing process on the propagation losses as determined by the prism coupling measurements.

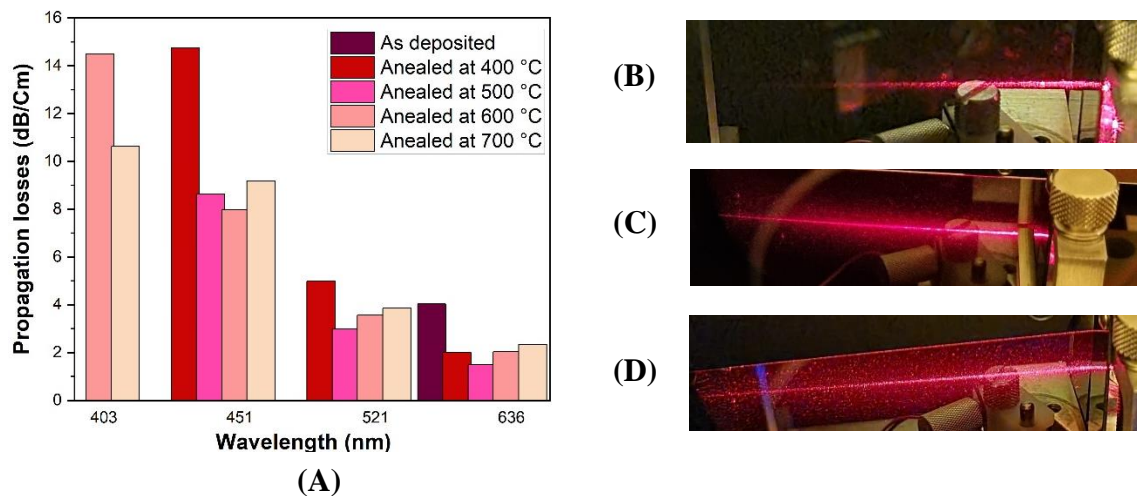


Figure 2 (A) Propagation losses at different wavelengths before and after annealing. Picture of the guided red light (636 nm) for (B) as deposited (4 dB/cm), (C) annealed at 400°C (2 dB/cm), and (D) annealed at 600°C (2.06 dB/cm).

Before the annealing process, the AlN layer was high losses and we just measured 4.03 dB/Cm at 636 nm wavelength. The annealing process helped reduce the layer's propagation losses and enabled optical propagation for shorter wavelengths. Recently, Dong et al. and Wu et al. showed that the annealing process could effectively reduce the propagation loss of AlN waveguides[4,5]. The absorption of materials due to hydrogen bonds formed during the deposition process is one of the reasons for the high propagation losses in the layer. The remaining H<sub>2</sub>O and O<sub>2</sub> in the deposition chamber cause these bonds to form[6]. High temperature annealing reduces propagation losses by removing some impurities.

As the temperature increases, the propagation losses increase. Losses are affected by various parameters such as impurities, roughness and crystalline morphology. During sputtering, atomic mismatches are created in the AlN film structure. Annealing, by reducing the stress in the layer and its effect on the crystal lattice, reduces threading dislocations and defects in the AlN layer and the crystalline morphology and impurities can be improved[7]. Also, we can see that the annealing process has increased the surface roughness, as a result of which the propagation losses increase[8]. In Figure 2(a), we can see that up to a temperature of 500°C, the impact of the reduction of threading dislocations and defects in the layer may be more obvious. Thus, the losses are significantly reduced. After that, as the annealing temperature increases, the losses due to scattering plays the main role and causes an increase in propagation losses.

Figure 2(B-D) shows a picture of the fundamental 636 nm mode propagating through the layer before and after annealing. This propagation qualitatively and visually corroborates the previously discussed quantitative measurements of low propagation loss in our polished AlN films. These experimental results confirm the ability of the AlN sputter deposition and annealing process to produce and develop a low-loss optical layer for waveguide fabrication.

## SUMMARY

In summary, we report the fabrication, annealing and characterization of AlN layers with low propagation losses in the 633 nm and visible wavelength range. Silicon wafers with 8 μm thick thermal oxide buffer were sputter coated with an AlN layer of thickness 147 nm. The measured propagation losses show that the annealing process can reduce the propagation losses for the AlN layer.

**Acknowledgements:** This project has received support from the European Research Council Proof-of-concept grant (project number 964006) and from TKI Holland High Tech under project name PICOSTAR.

## References

- [1] C. Xiong, W. H. P. Pernice, and H. X. Tang, "Low-Loss, Silicon Integrated, Aluminum Nitride Photonic Circuits and Their Use for Electro-Optic Signal Processing," *Nano Lett.*, vol. 12, no. 7, pp. 3562–3568, Jul. 2012, doi: 10.1021/nl3011885.
- [2] Y. Taniyasu, M. Kasu, and T. Makimoto, "An aluminium nitride light-emitting diode with a wavelength of 210 nanometres," *Nature*, vol. 441, no. 7091, Art. no. 7091, May 2006, doi: 10.1038/nature04760.
- [3] A. Iqbal and F. Mohd-Yasin, "Reactive Sputtering of Aluminum Nitride (002) Thin Films for Piezoelectric Applications: A Review," *Sensors (Basel)*, vol. 18, no. 6, p. 1797, Jun. 2018, doi: 10.3390/s18061797.
- [4] B. Dong *et al.*, "Thermal annealing study of the mid-infrared aluminum nitride on insulator (AlNOI) photonics platform," *Opt. Express, OE*, vol. 27, no. 14, pp. 19815–19826, Jul. 2019, doi: 10.1364/OE.27.019815.
- [5] X. Wu, J. Feng, X. Liu, and H. Zeng, "Effects of rapid thermal annealing on aluminum nitride waveguides," *Opt. Mater. Express*, vol. 10, no. 12, p. 3073, Dec. 2020, doi: 10.1364/OME.410129.
- [6] D. Cao *et al.*, "Effects of rapid thermal annealing on the properties of AlN films deposited by PEALD on AlGaIn/GaN heterostructures," *RSC Adv.*, vol. 5, no. 47, pp. 37881–37886, Apr. 2015, doi: 10.1039/C5RA04728E.
- [7] B. Liu, J. Gao, K. M. Wu, and C. Liu, "Preparation and rapid thermal annealing of AlN thin films grown by molecular beam epitaxy," *Solid State Communications*, vol. 149, no. 17, pp. 715–717, May 2009, doi: 10.1016/j.ssc.2009.02.008.
- [8] S. Mardani, M. Dijkstra, W.A.P.M. Hendriks, M.P. Nijhuis - Groen, S.M. Garcia-Blanco, "Low-loss chemical mechanically polished Al<sub>2</sub>O<sub>3</sub> thin films for UV integrated photonics," presented at the 23rd European Conference on Integrated Optics, ECIO 2022, May. 2022.

# Generation of optical frequency combs at sub-GHz repetition rates with a hybrid-integrated mode-locked diode laser

A. Memon\*, A. van Rees, J. Mak, Y. Fan, P. J. M. van der Slot, H. M. J. Bastiaens, K-J. Boller

Laser Physics and Nonlinear Optics, Mesa+ Institute of Nanotechnology, Faculty of Science and Technology, University of Twente, Enschede, the Netherlands

\*a.memon@utwente.nl

*Optical frequency combs based on broadband-gain bulk lasers offer low intrinsic linewidths and sub-GHz line-spacing. Nevertheless, susceptibility to mechanical and acoustic perturbations and the complexity of pumping of these lasers have motivated chip-integrated extended cavity diode lasers using low-loss and long  $\text{Si}_3\text{N}_4$  feedback circuits to extend the laser cavity for low repetition rates. Typically, saturable absorbers are used for mode-locking, however, the short upper-state carrier lifetime in semiconductor optical amplifiers requires repetition rates of a GHz or higher. We demonstrate absorber-free generation of optical frequency combs in a hybrid integrated InP- $\text{Si}_3\text{N}_4$  mode-locked diode laser, using a low-loss  $\text{Si}_3\text{N}_4$  feedback circuit that extends the on-chip optical roundtrip length up to 60 cm by three highly-selective ring resonators. This enables passive as well as hybrid mode-locking with a low repetition rate of around 484 MHz.*

## Introduction

Optical frequency combs (OFCs) are a special class of laser sources whose optical spectrum consists of a series of equidistant frequency lines. OFCs based on optically pumped bulk lasers, e.g., Ti:Sapphire lasers or rare earth doped fiber lasers, have provided an important path to applications such precision spectroscopy [1], dual-comb spectroscopy [2], distance measurements [3] or LIDAR [4]. Having available long resonator lengths and a long (up to millisecond) lifetime of laser inversion is the key for high resolution, because low (sub-GHz) repetition rates and narrow spectral linewidths can be realized. However, the intrinsic susceptibility of bulk lasers to mechanical and acoustic perturbation, their relatively large size, and the complexity of optical pumping poses limitations for wide-spread use and out-of-the-lab systems. Recently, much effort has been put into developing OFCs in integrated photonics offering chip-based, compact, solutions with low power consumption, such as diode-pumped Kerr frequency combs [5]. An interesting alternative to avoid optical pumping are diode lasers where mode-locking, and thus frequency comb generation, is achieved with intracavity saturable absorbers. To reduce the repetition rates toward the lower GHz range, heterogeneous [6] and hybrid integrated extended cavity lasers [7] have been mode-locked using extended cavities based on low-loss  $\text{Si}_3\text{N}_4$  feedback circuits. There, mode-locking is based on the generation of pulses with integrated saturable absorbers. However, even though much longer and low-loss waveguide cavities can be realized with  $\text{Si}_3\text{N}_4$ , a further lowering of the repetition rate into the sub-GHz range is difficult, because the relatively short upper state lifetime in semiconductor amplifiers of about 1 ns leads to instabilities that build-up between pulses from amplified spontaneous emission.

This limitation in the repetition rate motivated us to explore an alternative approach called Fourier domain mode-locking (FDML) [8], where no saturable absorber is present and mode-locking provides a quasi-continuous output. Recently, such FDML has been shown experimentally with diode lasers reaching very low repetition rates of 255 [9] and 360 [10] MHz, respectively, based on sharp spectral feedback filtering. However, these lasers were either based on bulk feedback (a Bragg fiber [9]) or the authors reported on possibly independently locked groups of modes [10]. Stable FDML with hybrid integrated lasers has been observed with sharp spectral filtering using two microring resonators [11, 12], but both repetition rates were well above the 1-GHz inverse upper state lifetime limit (around 5 and 2 GHz, respectively). A detailed physical explanation of the mode-locking dynamics, based on a resonance between relaxation oscillation and mode spacing was given recently [13]. We note that the described experimental and theoretical work is restricted to passive mode-locking, where the repetition rate is intrinsically less stable than with additional (active) external modulation, to cause hybrid mode-locking.

Here we present the generation of frequency combs with a repetition rate as low as 484 MHz using an extended cavity hybrid integrated InP-Si<sub>3</sub>N<sub>4</sub> laser for FDML. The free spectral range of the laser cavity is reduced compared to that reported in refs. [11] and [12] by using a triple microring Vernier filter as a feedback mirror. This introduces sharper spectral filtering and extends the optical cavity roundtrip length to approximately 60 cm. We also demonstrate hybrid mode-locking, which stabilizes the repetition rate to the ten-kHz level through diode current modulation with an external RF oscillator.

## Experimental results

The hybrid laser that is used for the experiments is presented in Fig. 1. The laser cavity comprises two components, an InP gain chip and a Si<sub>3</sub>N<sub>4</sub> feedback chip. The gain chip is equipped with a semiconductor optical amplifier (SOA), which at the left end is coated with a highly reflective (HR) mirror, and at the other end with an anti-reflective (AR) mirror. The Si<sub>3</sub>N<sub>4</sub> waveguide circuit

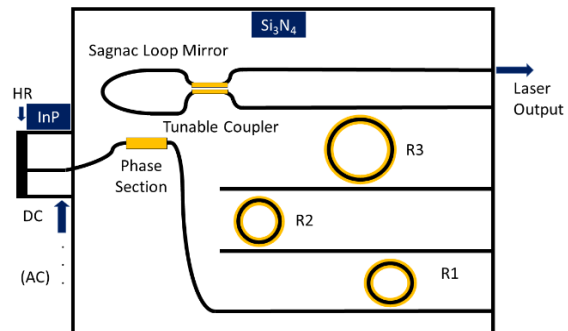


Figure 1: Schematic view of the hybrid integrated laser

comprises three microring resonators (MRR) of different radii, which form part of the feedback mirror and restricts the number of oscillating longitudinal modes of the laser. The feedback chip is equipped with thermoelectrical heaters (yellow in Fig. 1) to fine-tune the cavity length with the phase section, for adjusting the resonances of the microresonators and to adjust the output coupling. A spiral (not shown in Fig. 1) increases the cavity length of the laser and helps reduce the laser's free spectral range (FSR). Back reflections at the InP and Si<sub>3</sub>N<sub>4</sub> interface are reduced by both tilting the waveguides with regard to the facet normal and an anti-reflection coating on the InP facet.

To generate the frequency-modulated optical frequency combs, the laser is operated in two ways. First, passive mode-locking is realized using a low DC current (50 mA) for pumping. Secondly, hybrid mode-locking is performed by applying an additional AC current component with a signal generator, which modulates the gain of the laser and stabilizes the mode-locking operation. In the following, we present both mode-locking techniques and their effect on the RF and optical linewidths of the laser.

## Passive mode-locking

Firstly, we tune the laser as a single-frequency laser by adjusting the three micro-ring resonators to a common resonance, until single-frequency oscillation is achieved. Next, we detune the phase section which causes multimode oscillation. Further fine-tuning induces mode-locking which shows up as an optical comb spectrum as in Fig. 2a. To provide higher resolution, we recorded the RF spectrum with a photodiode and an electrical spectrum analyzer (ESA, Keysight N9000B CXA). The RF spectrum shows a single fundamental frequency and its harmonics, proving that the optical lines are equidistant, thereby confirming mode-locking. The RF spectrum shows a repetition rate of around 484 MHz. This is more than an order of magnitude lower than in the first demonstration with two microring resonators [11], about a factor of five lower than in [12], and it is a factor of two below the lifetime-limit of 1 GHz for standard mode-locking.

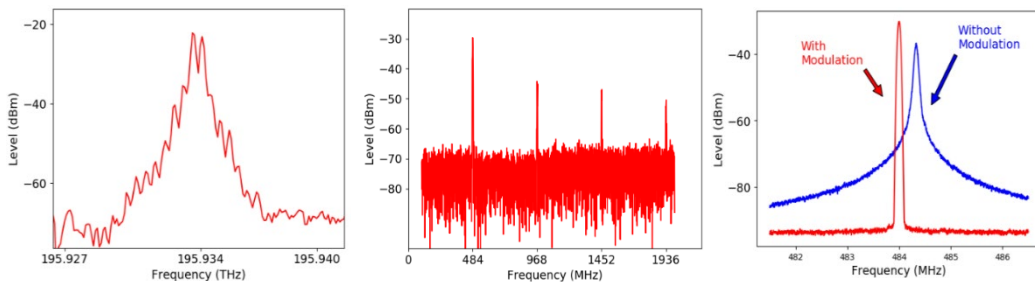


**Figure 2:** a) Resolution limited optical spectrum at 50 mA DC pump current, recorded with an optical spectrum analyzer (OSA, WaveAnalyzer). The spectrum displays 15 equidistant comb lines, b) the corresponding RF spectrum shows an FSR of 484 MHz and c) RF linewidth without and with modulation

## Hybrid mode-locking and linewidth comparison

Implementing passive mode-locking is simpler in terms of technological effort, as it does not require an external RF oscillator. However, it suffers from an intrinsic instability of the pulse repetition rate due to pulse jitter. In contrast, hybrid mode-locking using additional modulation with an external RF oscillator, synchronous with the passive mode-locking frequency, promises a stabilized repetition rate. We stabilize the pulse repetition rate with an external oscillator that modulates the laser gain with a weak AC signal (-5 dBm) at 484 MHz, superimposed to the 50 mA DC current (17 dBm power).

Figure 2c shows a comparison of the repetition rate linewidth obtained with passive and with hybrid mode-locking. With passive mode-locking (blue trace) the RF fundamental linewidth is rather broad. A Voigt fit yields a Gaussian linewidth component of 67 kHz (FWHM) and a relatively big Lorentzian component of 5.8 kHz seen as wide wings farther from the line center. With hybrid mode-locking, this changes clearly, as the free-running repetition rate becomes locked to the external modulation frequency. In Fig. 2c, the Gaussian component is reduced to 44 kHz, and the Lorentzian component is too small to be retrieved.

For characterization of the optical linewidth, we used delayed-self heterodyne detection [14] with an acousto-optic modulator at 80 MHz and a fiber delay line of approximately 2.5 km. The Voigt fit analysis yields a Gaussian linewidth component of 80 kHz (FWHM) and a Lorentzian component of 30 kHz with passive mode-locking. With active modulation, i.e., hybrid mode-locking, we obtain linewidth values of 103 kHz and 24 kHz for the Gaussian and Lorentzian components respectively.

## Locking range

Measuring the size of the locking range is important for judging the robustness of the repetition rate locking vs drifts of the resonator length. We have measured the locking range by stepwise tuning the external oscillator frequency around the passive repetition rate, while recording RF spectra as shown in Fig. 3. As soon as the oscillator frequency is brought into the locking range, the free-running (passive) repetition rate is extinguished and replaced by a single peak at the external frequency. Using these observations, we determined a relatively wide RF locking range of approximately 40 MHz.

## Conclusion

We have demonstrated the generation of on-chip optical frequency combs at a low repetition rate of 484 MHz via passive and hybrid mode-locking, using a long-cavity hybrid integrated InP-Si<sub>3</sub>N<sub>4</sub> diode laser. To explore the potential for a further lowering of the repetition rate, we have performed numerical simulations with a transmission line model based on [15]. The calculations show qualitative agreement with promise that lower repetition rates would become possible with further extended cavity lengths and steeper feedback filtering.

## References

- [1] T. Udem et al., *Nature* vol. 416, 233-237, 2002
- [2] I. Coddington et al., *Optica*, vol. 3, 414-426, 2016
- [3] J. Lee et al., *Scientific Reports*, vol. 4, 5134, 2014
- [4] W.C. Swann et al., *Optics Letters* vol. 31, 826-828, 2006
- [5] B. Stern et al., *Nature* vol. 562, 401-405, 2018
- [6] S. Cuyvers et al., *Laser & Photonics Reviews*, vol. 15, 2000485, 2021
- [7] H. M. J. Bastiaens et al., *SPIE OPTO* vol. 11705, 11705081, 2021
- [8] R. Huber et al., *Optics Express*, vol. 14, 3225-3237, 2006
- [9] M. Yuan et al., *Optics Letters*, vol. 46, 4855-4858, 2021
- [10] Y. Ibrahimi et al., *Journal of Lightwave Technology*, vol. 39, 7573-7580, 2021
- [11] J. Mak et al., *Optics Express*, vol. 27, 13307-13318, 2019
- [12] Y. Klaver et al., *Optics Letters* vol. 47, 198-201, 2022
- [13] C. Rimoldi et al., *IEEE Photonics Journal*, vol. 14, 1540707, 2022
- [14] M. Wada et al., *Measurement Science and Technology*, vol. 31, 125012, 2020
- [15] A. J. Lowery et al., *IEE Proceedings Journal (Optoelectronics)*, vol. 134, 281-289, 1987

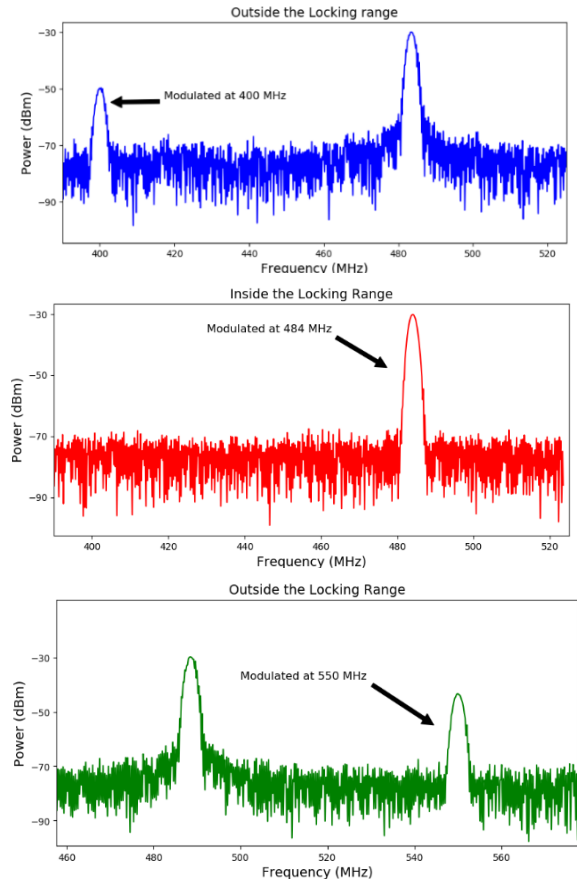


**Figure 3:** RF spectra from the passively mode-locked laser when tuning the additionally applied external modulation frequency. In (a) and (c) the laser is modulated outside the locking range. In (b) the laser is modulated at the frequency corresponding to the FSR, i.e. at 484 MHz.

# Hybrid mm-Wave and for High-Capacity Indoor Communication System

Carolina Amaral<sup>1</sup>, Ulf Johannsen<sup>2</sup>, and Eduward Tangdiongga<sup>1</sup>

<sup>1</sup> Department of Electrical Engineering, Electro-Optical Communication, Eindhoven University of Technology, 5600 MB Eindhoven, The Netherlands

<sup>2</sup> Department of Electrical Engineering, Electromagnetics, Eindhoven University of Technology, 5600 MB Eindhoven, The Netherlands

*This work presents the design of a hybrid communication system which combines the strengths of mm-wave and infrared optical wireless communication (IOWC) technologies. A flexible indoor wireless communication network can be achieved with IOWC and 60 GHz radio-over-fiber link, as an alternative to the current Wi-Fi system, to support more devices connected to each other via a wireless network to provide the Internet of Things services. The downstream is deployed with pencil radiation antennas to steer narrow infrared beams establishing wireless optical link between the access point and the user device (UD), thus a high-capacity optical link can be achieved by dedicating one wavelength per UD. The upstream is deployed with phased array antenna at 60 GHz band, beamforming techniques are explored to facilitate user mobility and to maximize system connectivity, counteracting the impact of possible wireless obstructions. Transmission rates of 10 Gbps and 1 Gbps are target for the downstream and upstream, respectively. Indoor optical networks require simple and low-cost systems with binary modulation formats; therefore, the intensity modulation and direct detection is deployed for the radio-optical conversion and on-off-keying for the modulation format.*

## I. Introduction

The expectation about the Internet of Things is that in the future many devices will be connected via the internet. This will make building and cities increasingly smarter. These developments place very high demand on the network in order to be able to transport large amounts of data efficiently and reliably. The radio frequency ISM spectrum for 2.4 and 5 GHz is already occupied with a large variety of services, introducing new services becomes increasingly impossible. Therefore, solutions are being investigated in order to complement the Wi-Fi network and to develop a high-capacity integrated system utilizing hybrid communication technologies that allow more spectra to be used.

This work investigates two technologies that are getting considerable attention: optical wireless communication (OWC) and millimeter wave (mm-wave) radio communication. The interest has been rising due to large available bandwidth. The optical spectrum is a key enabler for global internet connection. Extending the optical communication from optical fiber to include free-space optical wireless it is a significant step for future internet communication, making the OWC a promising alternative [1]. Beam-steered infrared light communication (BS-ILC) is one method for OWC that can be applied for indoor use cases, their short wavelength does not penetrate walls can provide high physical security [2]. The mm-wave band is referred in the frequency range from 30-300 GHz in the EM spectrum [3]. The unlicensed spectrum available for the 60 GHz band has gained interest in gigabit-per-second short-range wireless communication. An unlicensed band of 9 GHz around 57-66 GHz were assigned in Europe [4], encouraging commercial applications in the 60 GHz band.

OWC and mm-wave are promising alternatives for future wireless communication networks that relies on higher frequency bands. This work presents a flexible system that combines the strengths of both technologies. It feature the downstream high-capacity optical wireless link, the upstream mm-wave wireless link, and the user localization techniques for establishing the communication link in both directions.

## II. Optical Wireless Downstream

The OWC techniques for short range (indoor) communication are mainly: visible light communication (VLC) and beam-steered infrared light communication (BS-ILC) [5]. The BS-ILC technique operates independently from illumination, it is easy to implement since it relies on well-established S+C+L band technologies from fiber optics [6]. The narrow optical beams provided by BS-ILC serves one single user, achieving high security and high-capacity link. BS-ILC could be a complementary technology to support high-speed traffic demand, while Wi-Fi handles low-speed traffic. The implementation of an optical indoor wireless system, illustrated in Figure 1, consists of a residential gateway (RG) which interfaces the outdoor access network and indoor wireless network. The optical cross connect (OXC) is responsible for the dynamic routing of optical wireless signals that are steered to users' devices (UDs). Autonomic network protocols management are deployed at the central communication controller (CCC) [2].

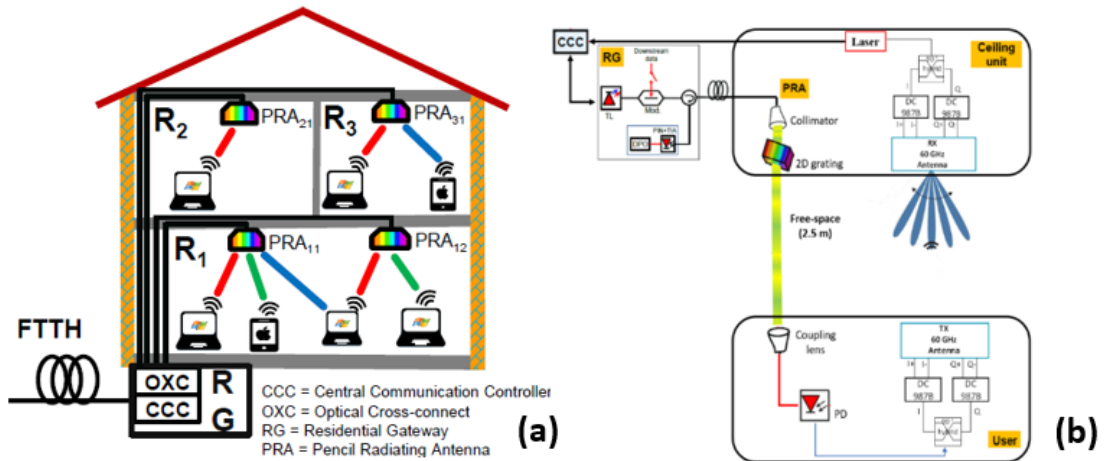


Fig. 1. (a) Indoor optical/radio network architecture [4], (b) Hybrid wireless system: mm-wave upstream at 60 GHz and optical downstream.

A key challenge for this system is to support user mobility. Figure 1(b) illustrate the hybrid wireless system. At the ceiling unit a pencil radiating antenna directs the beams to the users according with the wavelength selected at the RG, each wavelength corresponds to a location in the room. The phased-array antenna scans the room searching for the UD using beam steering, for a RSSI value above a certain threshold the user is localized. This localization information is shared with the optical network so the optical downstream can also be adjusted. At the user side the optical signal is coupled by lens to a photodetector (PD), which is converted to the radio domain to be transmitted by the mm-wave upstream in the 60 GHz carrier.

## III. mm-Wave Upstream

The mm-wave upstream system designed is based on the radio-over-fiber technology. To implement the wireless path operating at high frequency bands, phased-array antennas are considered. These antennas are able to perform beam steering for user localization. Figure 2(a) illustrates the EVK06002 from *Sivers* used as transmitter and receiver modules

with an antenna array optimized for operation in 57-71 GHz band, beamforming transceivers for radio beam-steering and compatible with IEEE 802.11ad standard. The module operates with baseband I/Q differential signals.

The mm-wave uplink will be integrated with an optical network. Figure 2 (b) illustrate the mm-wave upstream system design. At the user side the data stream comes from the photodiode PD as baseband OOK modulated signal. The *Interface 1* converts the NRZ signal to I/Q signals to be transmitted by the antenna module. The 90°-hybrid split the signal into I/Q. The DC987B-A differential amplifier boards convert the input into two differential outputs (180° out of phase) therefore *Interface 1* converts one single input into 4 differential I/Q outputs (I+, I-, Q+ and Q-). The baseband signal is upconverted to 60 GHz carrier by the antenna module to be transmitted. The signal is transmitted wirelessly to the access point (AP)/PRA at the ceiling.

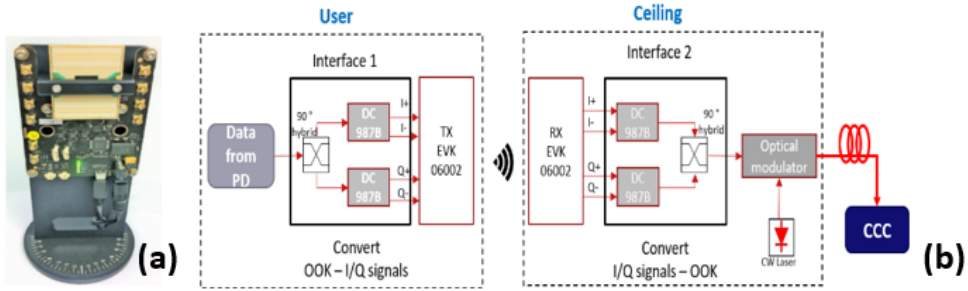


Fig. 2. (a) EVK06002 TX/RX antenna module for 60 GHz, (b) mm-Wave upstream schematic.

Then, the signal 60 GHz signal is down converted to baseband and in an analogous way the *Interface 2* converts 4 differential I/Q signals to one single output. Then, the baseband (radio) signal is modulated by an optical modulator to be transmitted over a short-length fiber to be processed at the CCC.

### a. User Localization

The quasi-optical nature of mm-wave results in sharp and narrow beamwidth radio signals. These narrow beams, generated by phased-array antennas, can gather accurate angle information such as angle of arrival (AoA), angle of departure (AoD) and the received signal strength information (RSSI) [7]. RSSI values are simpler to obtain in a wireless network. To estimate the UD location only from RSSI values, it's necessary to determine the dependence between RSSI values and the distance between AP and UD choosing a suitable propagation model. Eq. 1 describes the propagation model or path loss model. The signal attenuation between transmitter and receiver to be inversely proportional to the distance between them to the path loss factor [8].

$$P_R = \alpha - 10 \cdot n \cdot \log_{10}(d) + X \quad (1)$$

where  $d$  is the distance between AP and UD and the term  $X$  denotes Gaussian random variable with zero mean caused by shadowing. The term  $\alpha$  depends on the factors of fast and slow fading, antenna gains  $G_t$  and  $G_r$ , and transmitted power  $P_t$ , often this value is known [8].

### b. Antenna Module Analysis

To avoid the saturation of the received antenna module the transmitter module gain must be adjusted for a certain distance. Figure 3(a) shows the relation between the maximum transmitter module gain and distance between the antennas.

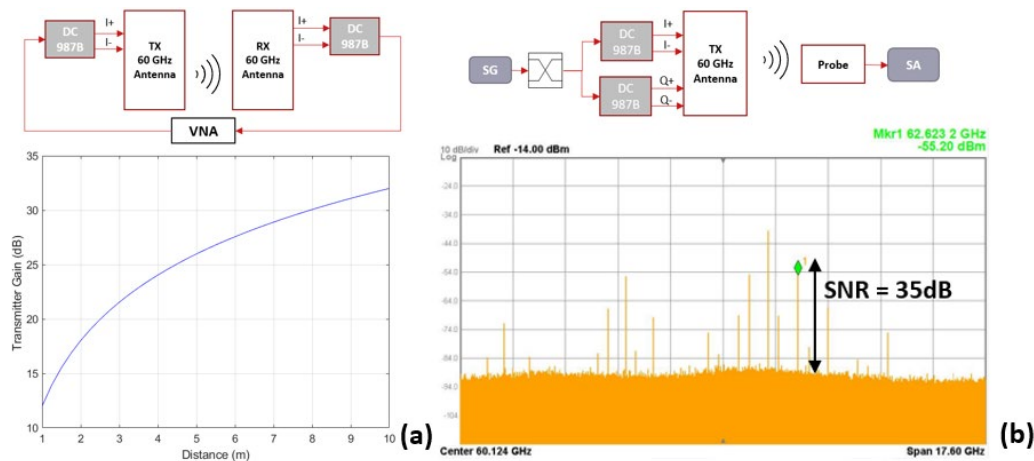


Fig. 3. (a) Gain of the transmitter over distance between transmitter and receiver, (b) Spectrum analysis of the received signal.

During the transmission the signal is affected by random noise, signal to noise ratio (SNR) indicates how strong the signal is compared to the channel noise. Figure 3(b) shows a SNR value above 20 dB, which is recommended for wireless data links.

## V. Conclusion

Due the growing demand for internet services and the rising number of connected devices, the demand for wireless bandwidth is getting beyond the current indoor wireless network capacity. A logical way to tackle this bandwidth crunch is to combine the best aspects optical/radio wireless technologies. This work proposes a flexible hybrid wireless network which combines mm-wave for upstream and infrared optical wireless for downstream for an indoor use case. The system dynamically routes one wavelength per user providing high-capacity and unshared link. The radio beam steering is used to scan the room and provide to the network user localization. Steered infrared optical beam and mm-wave radio beam are promising future solution to the increasing demand in indoor wireless services.

## References

- [1] H. Haas, J. Elmirghani, I. White, "Optical wireless communication", *Phil. Trans. R. Soc. A.*, 378, 2020.
- [2] K. A. Mekonnen, "Dynamic Ultrahigh-Capacity Indoor Wireless Communication Using Optical-Wireless and Millimeter-Wave Radio Techniques," PhD, Eindhoven University of Technology, 2018.
- [3] Z. Pi, F. Khan, "An introduction to millimeter-wave mobile broadband systems", *IEEE Communications Magazine*, pp. 101-107, 2011.
- [4] N. Guo, R. C. Qiu, S. S. Mo, K. Takahashi, "60-GHz millimeter-wave radio: principle, technology and new results", *EURASIP J Wireless Communication Networking*, 2007.
- [5] T. Koonen, "Indoor optical wireless systems: technology, trends and applications", *J. Light. Technol.*, vol. 36, no. 8, pp. 1459-1467, 2017.
- [6] T. Koonen, J. Oh, K. Mekonnen, Z. Cao, E. Tangdiongga, "Ultra-high-capacity indoor optical wireless communication using 2D-steered pencil beams", *Philos. Trans. R. Soc. Math. Phys. Eng. Sci.*, vol 378, no. 2169, 2020.
- [7] J. A. del Peral-Rosado, R. Raulefs, J. A. López-Salcedo, G. Seco-Granados, "Survey of Cellular Mobile Radio Localization Methods: From 1G to 5G," *IEEE Communications Surveys & Tutorials*, vol. 20, no. 2, pp. 1124-1148, 2018
- [8] S. Mazuelas, A. Bahillo, R. Lorenzo, P. Fernandez, F. Lago, E. Garcia, J. Blas, E. Abril, "Robust Indoor Positioning Provided by Real-Time RSSI values in Unmodified WLAN Networks," *IEEE Journal of Selected Topics in Signal Processing*, vol. 3, no. 5, pp. 821-830, 2009.

# A Deep Reinforcement Learning Approach for Computation Offloading at the 5G Network Edge

C. Stan,<sup>1</sup> J.J. Vegas Olmos,<sup>2</sup> I. Tafur Monroy,<sup>1</sup> and S. Rommel<sup>1</sup>

<sup>1</sup> Dept. of Electrical Engineering, Eindhoven University of Technology, 5600MB Eindhoven, The Netherlands

<sup>2</sup> NVIDIA Corporation, Ofer Industrial Park, Yokneam, Israel

*Multi-access edge computing (MEC) is envisioned as a key enabler for fifth generation (5G) networks, bringing new resources into the computing continuum spanning from user devices to the centralized cloud. The advantages introduced by MEC play an important role in achieving the targeted 5G key performance indicators (KPIs), but at the same time its introduction raises new questions in terms of how frequently data should be offloaded from the end user device to the edge for processing since the optical front-, mid- and backhaul are constantly employed in the data transfer and MEC capabilities are limited compared to cloud data centers. In this context, a deep reinforcement learning (DRL) computation offloading solution is proposed which aims to provide optimal binary offloading decisions (local or MEC task execution). The DRL agent is set to evaluate the trade-off between factors such as computation energy consumption, communication delay via time-varying wireless channels and optical connections between 5G base stations (gNodeBs) and multiple MEC nodes. In order to preserve user data privacy, we propose an alternative training method for the DRL algorithm, i.e., a federated learning framework, as opposed to the centralized method where training data is collected in a predefined storage location.*

## Introduction

Multi-access edge computing (MEC) [1] comes at a time when the requirements for quality of experience (QoE) are becoming more demanding with each generation of mobile networks. To cope with this, the advantages introduced by the traditional mobile cloud computing (MCC) are leveraged when deploying edge nodes into the network. This way, the computing, storage and networking resources are brought in the close proximity of the user equipment (UE), therefore the requests sent to the network receive a much faster response since they are processed at the edge. Moreover, emerging applications developed under the umbrella of 5G mobile networks benefit from low latency and enhanced computing power from MEC. Compared to MCC, MEC provides flexibility since the edge nodes are deployed in a distributed manner, but at the same time it also comes with limited computational power and storage capacity [2]. In this context, offloading every computational task to the edge node for processing is not feasible, therefore optimal decisions in terms of offloading to edge nodes have to be taken. There are multiple examples of applications that can benefit from computation offloading, augmented and virtual reality (AR/VR), face recognition and gaming being just a part of them. The decision of whether to offload or not tasks coming from such applications in a constantly changing network environment such as the 5G network, starting from the wireless domain up to the optical backhaul, can easily turn into a complex problem. In this case, artificial intelligence (AI) techniques such as reinforcement learning (RL) can

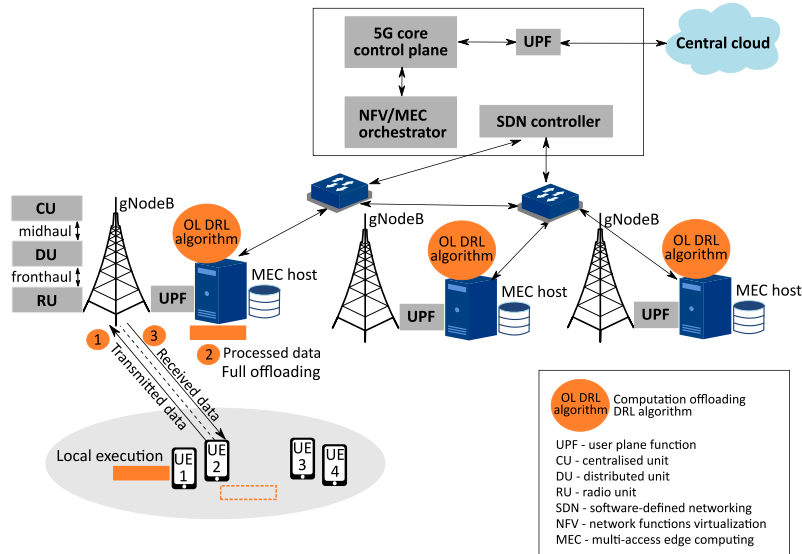


Fig. 1. 5G network architecture comprising MEC nodes with DRL agents and detailed offloading procedure (local or MEC execution).

be employed to take the optimal offloading decisions based on the always varying 5G environment and weight the trade-off between factors that influence offloading such as computational delay and energy consumption, to name but a few. Moreover, to deal with the computational complexity coming from the dynamic network states, deep reinforcement learning (DRL) can be adopted to approximate values or policies for RL problems with a large state space [3]. In respect to computation offloading decisions based on DRL, various research has been carried out for different types of networks. In [4] a two-time scale DRL approach was designed to minimize task execution time and computation, communication and storage usage in 5G ultra dense networks (UDN), also employing federated learning (FL) training. [5] uses DRL for computation offloading formulated as a binary optimization problem in a vehicular edge-cloud computing network to minimize the total energy and time cost of the system. DRL-based binary offloading decisions were also applied in [6] in an edge assisted Power Internet of Things (PIoT) network, aiming to maximize the average utility function, modeled as a weighted sum of reduction in latency and energy consumption. In [7], DRL-based online offloading was proposed to learn the binary offloading decisions from experience and deal with resource allocation, given the time-varying wireless channels.

In the following sections, we offer insights about computation offloading (factors that influence offloading, offloading types), propose a DRL framework where training is performed with centralized and distributed methods, and finally conclude the paper.

## Deep reinforcement learning for computation offloading

When it comes to computation offloading, several challenges have to be addressed in order to offer a high QoE to the users. One challenge is the offloading decision itself which aims to determine whether the offloading will bring benefit to the users or not by evaluating the computation and communication costs. Since 5G networks are the main focus of the paper, user mobility is considered another challenge in offloading since service continuity has to be ensured while offloading [2]. The main focus of the paper is the offloading decision challenge where different offloading factors are weighted in order to make the optimal decision. Therefore, the main factors that can influence an offloading

decision are: the communication cost, both in time-varying wireless channels and optical front-, mid- and backhaul and the energy consumption required for both communication and computation. Given these factors, one can define the offloading cost as follows:

$$O = w_1(T^{comm,DL} + T^{comm,UL}) + w_2T^{exec} + w_3(E^{comm,DL} + E^{comm,UL}) + w_4E^{exec} \quad (1)$$

where  $T^{comm,DL}$  and  $T^{comm,UL}$  represent the time required for uplink and downlink communication in the wireless and optical domains, and  $T^{exec}$  is the task execution time.  $E^{comm,DL}$ ,  $E^{comm,UL}$  and  $E^{exec}$  refer to the energy consumed to communicate on downlink, uplink and during task execution, respectively.  $w_{1,2,3,4}$  represent the weights with values in  $[0,1]$ , which are directly linked to the importance of each component specified in Eq. (1). In common offloading scenarios, the uplink channels are employed more often compared to the downlink channels and the reason is that the data volume transmitted by the UEs to gNodeB is higher compared to the response sent by MEC after processing. Moving on to offloading types, there are three common offloading decision that can be configured into the network: first is local execution – the computation is performed locally at the UE since the evaluation of the offloading cost did not show otherwise, second is full offloading at MEC – all the computation tasks are performed at MEC, and third is partial offloading – in this case, a fraction of the offloading tasks are performed at MEC, while the rest is executed locally on the UE. In Fig. 1., two such types of offloading decisions are represented in a 5G network architecture. First, for UE 1 the best decision is to proceed with local execution, while for UE 2, the optimal decision is to offload to MEC through 5G gNodeB. Steps 1 and 3 show the transmission on uplink and downlink, while step 2 is the actual processing.

Known for its ability to learn by interacting with the environment, DRL [3] is proposed for optimal decision-making in an offloading scenario. In order to do so, the first step is to model the DRL as a Markov Decision Process (MDP) with state, action and space. The state space can be represented by the user data rates in both uplink and downlink which are highly influenced by the large-scale fading (pathloss, shadowing) and small-scale fading (statistically modelled as Rice or Rayleigh distributions). Other components of the state space can be: the data size of the task, the number of CPU cycles required for processing or a delay constraint for low-latency applications. The action space is represented as the offloading decision which can be seen as a binary decision: 0 – local execution and 1 – offload to MEC. The reward function aims to minimize the offloading cost as exemplified in Eq. (1).

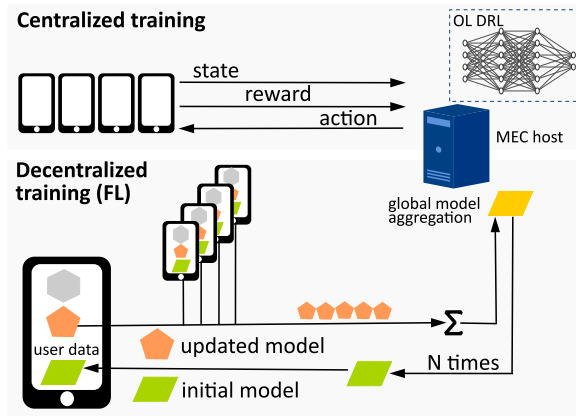


Fig. 2. Centralized and decentralized (FL) training methods for the offloading DRL.

In addition, apart from the traditional method of training an AI algorithm, i.e., the centralized method where the algorithm is running on a server where the training data is collected in a predefined storage location (Fig. 2. top), the DRL can also be trained in a decentralized manner using the FL framework. As depicted at the bottom of Fig. 2., the DRL model is sent from MEC to the selected UEs for on-device training and model update. The responses coming from the end devices are aggregated into a global model and after a specified number of rounds for model update, the final model is obtained. The benefit of such training is user privacy preservation since data necessary for DRL training coming from the UEs does not have to be sent and stored in a central database. In the FL framework, the update coming from the UEs contains much less information compared to the case where the entire raw data has to be centrally collected [8]. Such type of training also comes with drawbacks since the data coming from model update is transmitted through the wireless and optical domains, as it happens with offloading, therefore open questions still remain on how the two techniques interact with each other, how are the resources split in the network or what should be the priority queue between them.

## Conclusions and future work

In this work, computation offloading together with DRL and FL are introduced as methods to improve QoE and shift the computationally intensive tasks at the 5G network edge. First, benefits and challenges of computation offloading were introduced, and second, a DRL algorithm with two training methods is proposed which aims to make optimal offloading decisions in the always changing and expanding network environment. As future work, the proposed offloading DRL is planned to be implemented and evaluated, as well as compared to the current benchmark solutions.

## Acknowledgements

This work was supported by the EC H2020 MSCA ITN-ETN IoTalentum (grant no. 953442) and ECSEL JU BRAINE (grant no. 876967).

## References

- [1] ETSI GS MEC 003, "Multi-access Edge Computing (MEC); Framework and Reference Architecture," March 2022, v3.1.1.
- [2] P. Mach and Z. Becvar, "Mobile Edge Computing: A Survey on Architecture and Computation Offloading," in *IEEE Commun. Surv. Tutor.*, vol. 19, no. 3, pp. 1628-1656, thirdquarter 2017, doi: 10.1109/COMST.2017.2682318.
- [3] X. Wang et al., "Deep Reinforcement Learning: A Survey," in *IEEE Trans Neural Netw. Learn Syst.*, 2022, doi: 10.1109/TNNLS.2022.3207346.
- [4] S. Yu et al., "When Deep Reinforcement Learning Meets Federated Learning: Intelligent Multitimescale Resource Management for Multiaccess Edge Computing in 5G Ultradense Network," in *IEEE Internet Things J.*, vol. 8, no. 4, pp. 2238- 2251, 15 Feb.15, 2021, doi: 10.1109/JIOT.2020.3026589.
- [5] M. Khayyat et al., "Advanced Deep Learning-Based Computational Offloading for Multilevel Vehicular Edge-Cloud Computing Networks," in *IEEE Access*, vol. 8, pp. 137052-137062, 2020, doi: 10.1109/ACCESS.2020.3011705.
- [6] J. Hu et al., "Deep Reinforcement Learning for Task Offloading in Edge Computing Assisted Power IoT," in *IEEE Access*, vol. 9, pp. 93892-93901, 2021, doi: 10.1109/ACCESS.2021.3092381.
- [7] L. Huang et al., "Deep Reinforcement Learning for Online Computation Offloading in Wireless Powered Mobile-Edge Computing Networks," in *IEEE Trans. Mob. Comput.*, vol. 19, no. 11, pp. 2581-2593, 1 Nov. 2020, doi: 10.1109/TMC.2019.2928811.
- [8] K. Bonawitz et al., "Towards Federated Learning at Scale: System Design," 2019. [Online]. Available: <https://arxiv.org/abs/1902.01046>.

# Design of a Micro-Transfer-Printed III-V-on-Silicon-Nitride 100-GHz-class Modulator

Y. Wei, W. Yao, M.J.R. Heck and Y. Jiao

Eindhoven Hendrik Casimir Institute (EHCI), Eindhoven University of Technology, Eindhoven,  
5600MB, The Netherlands

*We report the design of a coplanar stripline (CPS) Mach-Zehnder modulator (MZM) with push-pull electrode configuration in a heterogeneous III-V-on-silicon-nitride platform, using micro-transfer printing technology. The electrical and optical properties, as varied parameters of the electrode, are investigated to achieve low microwave attenuation, matched impedance, and electro-optic velocity match. The optimized design gives a simulated high-speed performance with 109-GHz electrical bandwidth and 111-GHz electro-optical bandwidth. The compact footprint of 25  $\mu\text{m}$  in width and 1 mm in length allows massive integration on the target photonic circuits.*

## Introduction

Silicon nitride (SiN) is a promising technology platforms for photonic integrated circuits (PICs). Owing to several attractive features, including ultralow propagation loss (below 10 dB/m around 1550 nm) [1, 2], broad wavelength transparency [3], low thermal sensitivity [4] and CMOS compatibility, SiN photonics is ideal for a wide variety of PIC applications, such as coherent communications, sensing, Light Detection And Ranging (LIDAR), and microwave photonics. While SiN enables high-performance passive circuits, the fulfillment of such applications requires the combination with high-speed efficient modulators, which are not viable using SiN due to its insulating nature and the absence of Pockels effect [5]. Integrating modulators of other materials is therefore necessary. A III-V semiconductor, such as indium phosphide (InP), is a straightforward candidate considering its strong electro-optical effects, full capacity of active components, and mature wafer-scale manufacturing. Despite the large refractive index difference between SiN and common III-V materials, approaches to the heterogeneous III-V/SiN coupling interface have been proposed and verified for different integration technologies, such as adiabatic tapers using an intermediate amorphous silicon (a-Si) layer for micro-transfer printing [6], and spot size converters for flip-chip integration [7]. Following these solutions, promising III-V/SiN devices like mode-locked lasers [8] and frequency combs [9] have been demonstrated. However, so far the demonstrations of a high-speed III-V/SiN modulator remain elusive.

On the generic indium phosphide (InP) foundry platform, Mach-Zehnder modulator (MZM) utilizing Quantum-confined Stark effect (QCSE) based on the multiple quantum well (MQW) structures has been experimentally demonstrated with 1.4-dB electro-optic bandwidth of 67 GHz [10]. In this work, utilizing a similar design, we further explore the possibility of realizing such a high-performance modulator on a InP-on-SiN platform. The electrical and optical properties are studied for a heterogeneous configuration in terms of the waveguide and transmission line parameters, showing the potential of high-speed performance. The integration will be achieved by micro-transfer printing technology [11] after the pre-fabrication of both InP modulator elements and SiN circuits.

## Modulator architecture

Figure 1 shows the schematic of the designed InP on-SiN Mach-Zehnder modulator. The InP phase-shift function is implemented in deeply etched waveguides, through p-i-n doped epitaxial layers grown on InP substrates. Dedicated MQW structures are included in order to use more efficient QSCE for electro-optic modulation. Defined in the coupon configuration, a thin n-InP layer is needed for an efficient optical coupling between the InP waveguide and the underlying SiN waveguide. The design of the travelling-wave electrode is crucial to realize high-speed performance. Here, the coplanar strip-line (CPS) electrodes are used in push-pull configuration, placed in-plane at the same height on top of two waveguides. Since the capacitors in two MZM arms are in series, the overall capacitance is significantly reduced to half of that of one phase shifter. Apart from the ground-to-signal (GS) electrodes enabling the radio-frequency (RF) voltage swing, a close-by metal pad is also needed to apply a common positive potential to the n-InP layer for the direct-current (DC) reverse bias. As shown in Fig. 1(b), after propagating through the InP phase-shift section, the light will be coupled from an InP deeply-etched waveguide to the intermediate a-Si waveguide, and then finally to the SiN waveguide utilizing adiabatic tapers. At the end, both SiN waveguides are combined by a multimode interference coupler (MMI) and the interference of the two optical waves leads to intensity modulation depending on the phase difference between both arms of the MZM.

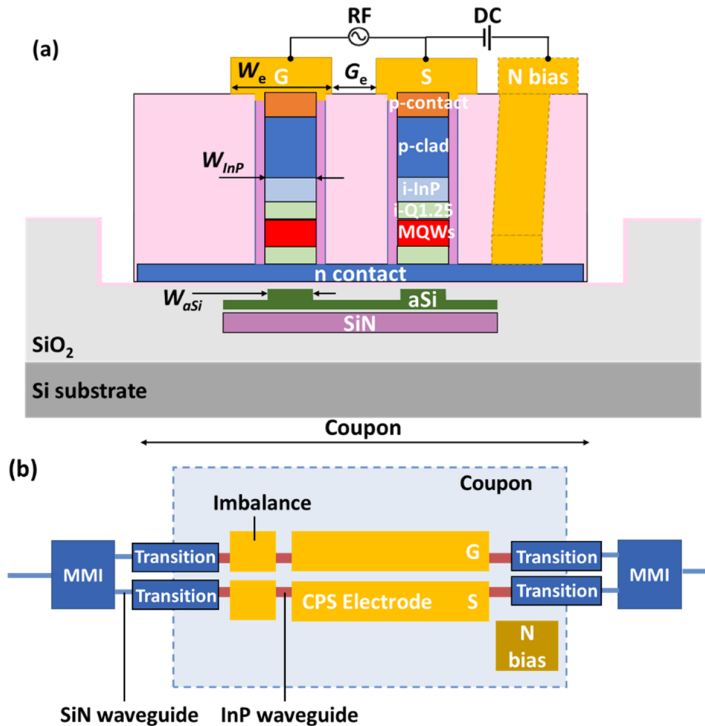


Figure 1. (a) The cross-section and (b) the top view of the designed III-V-on-SiN MZM.

## Electrical and electro-optical simulation

The electrical performance is investigated under the drive of DC or RF source in the commercial software COMSOL Multiphysics and CST Studio Suite, respectively. Fig. 2(a) shows the simulated conduction and valence band energies in such p-i-n junction, and a 1.2-V built-in potential can be obtained, indicating that the depletion area exists at 0-V bias voltage. The thickness of this depletion area increases as the bias voltage increases in reverse direction, as depicted in Fig. 2(b). The change in electrical field will affect the complex refractive index of the optical mode through multiple electro-optic effects, including linear electro-optic effect, QCSE, and carrier-induced effects. The combined effects offer a modulation efficiency  $V_{\pi}L$  of 7.5 Vmm, known from the

previous test of the CPS MZM utilizing the same MQW structures on the generic InP platform [10].

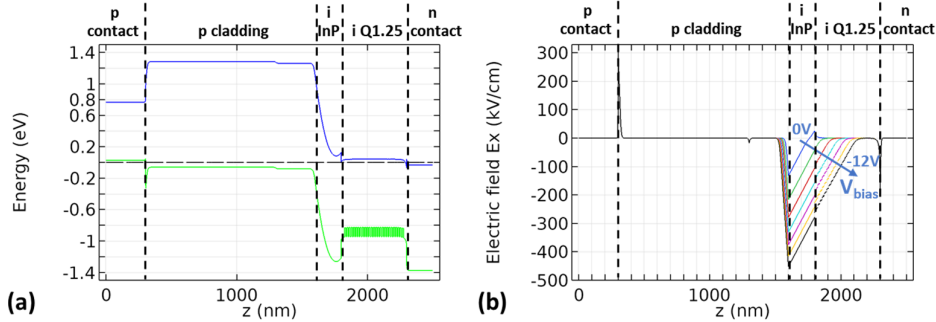


Figure 2. (a) Simulated conduction and valence band energies along the p-i-n junction at 0-V bias voltage. (b) Electric field distribution as bias voltage varies from 0 V to -12 V.

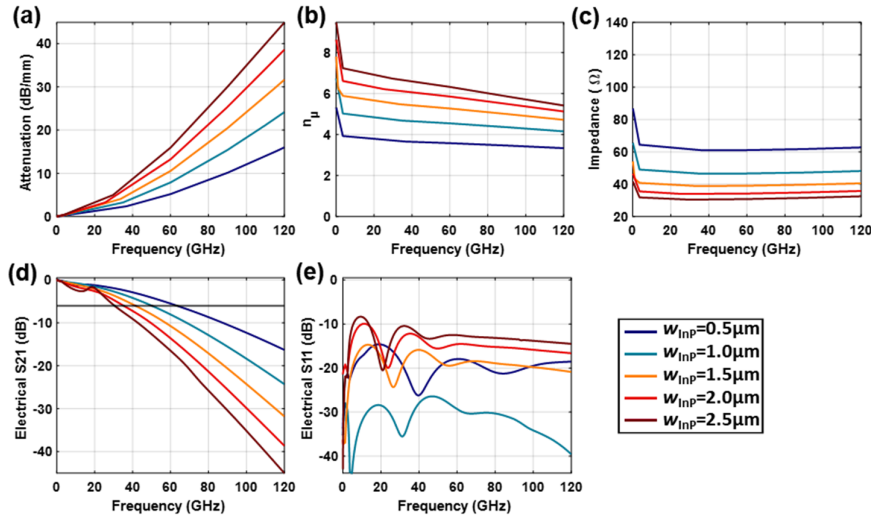


Figure 3. Simulated (a) attenuation, (b) microwave index, (c) line impedance, (d) electrical scattering parameters S21, and (e) S11 as varying waveguide widths for a 1-mm-long electrode at 0-V bias voltage.

The microwave behavior of the modulator with CPS electrodes is simulated by a 3D electro-magnetic full-wave solver where a physical model including exact geometry and material properties is set up. The influences of the waveguide width  $W_{\text{InP}}$ , the electrode width  $W_e$ , and the electrode gap  $W_g$  are investigated. It turns out that the waveguide width has the strongest impact on the electrical bandwidth. As shown in Figure 3, a narrower InP waveguide would reduce the microwave attenuation and index, while increasing the line impedance. Due to the reduction of loss, the electrical 6-dB bandwidth is improved significantly from 35 GHz for 2 $\mu\text{m}$ -wide waveguide to 62 GHz for 0.5 $\mu\text{m}$ -wide waveguide. Such narrow InP waveguide is enabled on our heterogenous platform thanks to the employment of scanner lithography. The microwave phase index can be tuned to be closer to the optical group index of around 3.5 for the minimum walk-off and optimum electro-optic interaction during traveling-wave operation. The line impedance, in an ideal case, should be adjusted to the standard of 50  $\Omega$  to avoid mismatch and reflection. Following these principles, the parameter set is chosen as  $W_{\text{InP}} = 0.5 \mu\text{m}$ ,  $W_e = 10 \mu\text{m}$ , and  $G_e = 5 \mu\text{m}$ , realizing an electrical bandwidth of 109 GHz at -8V bias voltage, as can be seen in Fig. 4(a).

Finally, the optical mode and electro-optical response are analyzed. To keep the fundamental transverse-electric (TE) mode well confined in the quaternary core of InP

waveguide, the underlying a-Si waveguide has to be narrower than 0.2  $\mu\text{m}$ . Simulated by the Ansys Lumerical mode solver, the group index of TE<sub>0</sub> mode is 3.6, close to the microwave index of 2.8 for the designed parameters. The electro-optical response is calculated using Giovanni's theory [12], predicting a 3-dB bandwidth of 111 GHz (Fig. 4(c)).

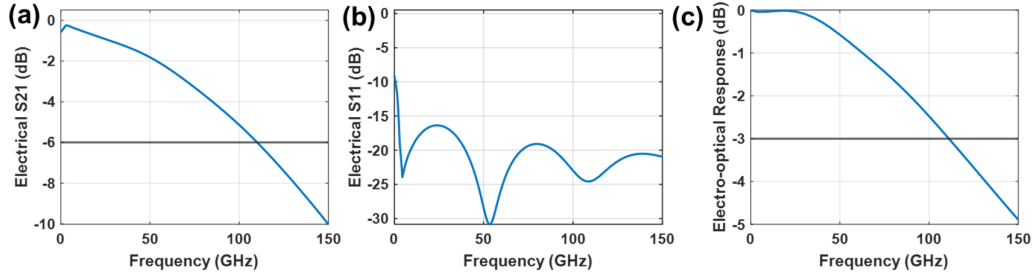


Figure 4. Simulated bandwidths of the optimized MZM design. (a) electrical scattering parameters S21, (b) S11, and (c) electro-optical frequency response of 1-mm-long electrode at -8-V bias voltage.

## Conclusion

To conclude, we design a 100 GHz-class MZM on a heterogenous InP-on-SiN platform. The smaller feature size of the InP waveguide and the intermediate a-Si layer give a larger freedom to optimize the design. The large bandwidth, compact footprint, and moderate efficiency of the designed modulator make it a promising candidate for the high-performance modulator on SiN.

## Acknowledgements

This work was supported by the European Union through the Horizon 2020 project INSPIRE (grant 101017088).

## References

- [1] Heck, Martijn JR, et al. "Ultra-low loss waveguide platform and its integration with silicon photonics." *Laser & Photonics Reviews* 8.5 (2014): 667-686.
- [2] Pfeiffer, Martin HP, et al. "Ultra-smooth silicon nitride waveguides based on the Damascene reflow process: fabrication and loss origins." *Optica* 5.7 (2018): 884-892.
- [3] Rahim, Abdul, et al. "Expanding the silicon photonics portfolio with silicon nitride photonic integrated circuits." *Journal of lightwave technology* 35.4 (2017): 639-649.
- [4] Arbabi, Amir, and Lynford L. Goddard. "Measurements of the refractive indices and thermo-optic coefficients of Si<sub>3</sub>N<sub>4</sub> and SiO<sub>x</sub> using microring resonances." *Optics letters* 38.19 (2013): 3878-3881.
- [5] Alexander, Koen, et al. "Nanophotonic Pockels modulators on a silicon nitride platform." *Nature communications* 9.1 (2018): 1-6.
- [6] de Beeck, Camiel Op, et al. "Heterogeneous III-V on silicon nitride amplifiers and lasers via microtransfer printing." *Optica* 7.5 (2020): 386-393.
- [7] Theurer, M., et al. "Actively aligned flip-chip integration of InP to SiN utilizing optical backscatter reflectometry." 45th European Conference on Optical Communication (ECOC 2019). IET, 2019.
- [8] Hermans, Artur, et al. "High-pulse-energy III-V-on-silicon-nitride mode-locked laser." *APL Photonics* 6.9 (2021): 096102.
- [9] Briles, Travis C., et al. "Hybrid InP and SiN integration of an octave-spanning frequency comb." *APL Photonics* 6.2 (2021): 026102.
- [10] Meighan, A., et al. "High-density 100 GHz-class Mach-Zehnder modulators integrated in a InP generic foundry platform." 2022 Conference on Lasers and Electro-Optics (CLEO). IEEE, 2022.
- [11] Corbett, Brian, et al. "Transfer printing for silicon photonics." *Semiconductors and Semimetals*. Vol. 99. Elsevier, 2018. 43-70.
- [12] Ghione, Giovanni. *Semiconductor devices for high-speed optoelectronics*. Vol. 116. Cambridge: Cambridge University Press, 2009.

# 637-nm Hybrid-Integrated Diode Laser

L. V. Winkler,<sup>1,2</sup> A. van Rees,<sup>1</sup> K. Gerritsma,<sup>1</sup> M. Hoekman,<sup>3</sup> P.P.J. Schrinner,<sup>3</sup>  
R. Dekker,<sup>3</sup> P.J.M. van der Slot,<sup>1</sup> C. Nölleke,<sup>2</sup> and K.-J. Boller<sup>1</sup>

<sup>1</sup> Laser Physics and Nonlinear Optics group, MESA+ Institute for Nanotechnology, Faculty of Science and Technology, University of Twente, Enschede, The Netherlands

<sup>2</sup> TOPTICA Photonics AG, Gräfelfing, Germany

<sup>3</sup> LioniX International BV, Enschede, The Netherlands

*We present the first hybrid integrated extended cavity diode laser (ECDL) tunable around 637 nm. This wavelength range is important for excitation of nitrogen vacancy centers (NV) in diamond, one of the leading platforms for quantum information processing. The laser comprises a custom designed Si<sub>3</sub>N<sub>4</sub> circuit using high-confinement, low-loss, double-stripe waveguides to provide frequency selective feedback to a semiconductor optical amplifier (SOA). The SOA, a tilted-waveguide GaAs double-pass amplifier, and the Si<sub>3</sub>N<sub>4</sub> feedback circuit are hybrid integrated using tapers for mode matching. Two microring resonators in the feedback circuit serve for single-wavelength operation and wide tuning. The laser shows a threshold pump current of 50 mA with 0.26 mW fiber-coupled output power. The laser can be tuned across the full gain bandwidth of 6 nm, including the NV-center target wavelength.*

## Introduction

Photonic quantum technologies, including applications such as chip-integrated optical clocks, quantum-key distribution systems and photonic quantum processors are being developed at a rapid speed [1]. Upscaling of such systems calls for chip-integrated lasers to be used as sources. While infrared integrated lasers at telecom wavelengths are already mature, many of the applications require integrated visible lasers that do not yet exist, e.g., for addressing particular atomic and ionic transitions, quantum dots or nitrogen vacancy centers. Chip integration and spectral control of such sources appears feasible by exploiting the wide transparency range and high index contrast of the Si<sub>3</sub>N<sub>4</sub> / SiO<sub>2</sub> platform, to provide low-loss waveguide circuits [2] for the visible range [3].

An important step was the first demonstration of a visible hybrid-integrated laser [4] in the silicon nitride platform. The laser operates around a center wavelength of 685 nm, such as to address transitions in strontium. As the basic approach, an extended cavity diode laser design was chosen because this can offer free tunability and wide spectral coverage, single-frequency operation, and ultranarrow linewidth. A subsequent approach for visible output was self-injection locking of Fabry-Perot (FP) diode lasers [5]. There, however, laser emission is bound to predefined FP modes and requires a proper feedback phase for temporally stable operation.

Here, we present the first hybrid integrated extended cavity diode laser (ECDL) operating at wavelengths around 637 nm, which is of interest for targeting nitrogen vacancy centers [6]. The laser is tunable over the entire gain bandwidth, using the Si<sub>3</sub>N<sub>4</sub> platform with a custom designed waveguide cross section for low-loss dual-ring Vernier filter feedback.

## Waveguide Design and Characterization

To realize a proper feedback circuit for the 637-nm range in the Si<sub>3</sub>N<sub>4</sub> waveguide platform, we designed a dedicated waveguide cross section as displayed in Fig. 1(a).

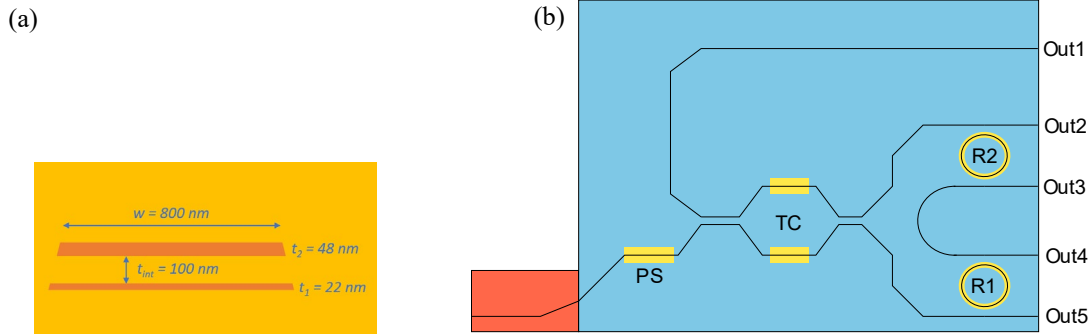


Figure 1. (a) Custom designed double-stripe waveguide cross-section to provide low propagation and bend loss in the visible (red: Si<sub>3</sub>N<sub>4</sub> core, yellow: SiO<sub>2</sub> cladding). (b) Schematic drawing of the extended cavity laser with a GaAs semiconductor optical amplifier on the left (in red) coupled to a Si<sub>3</sub>N<sub>4</sub> feedback circuit (in blue). Thermo-optic heaters are implemented for tuning of the overall cavity length with a phase section (PS), to tune the output coupling (TC) and to tune the laser wavelength via the optical length of the microring resonators (R1, R2). The first port is the main output port of the laser, while the other ports serve as monitor ports.

The design procedure aimed on enabling low propagation loss and low bend loss, to enable short microring resonators with a large free spectral range and high spectral selectivity. These properties are required for single-frequency oscillation with high side-mode suppression, and for expanding tunability across the full gain bandwidth of the diode amplifier. Losses expected from sidewall scattering were estimated via path integrals of the mode intensity along the waveguide. To avoid scattering into higher-order modes, we restricted the design to cross-sections that guide only a single transverse mode. Mode field distributions were calculated with a 2D finite difference mode solver [7] to optimize the core geometry parameters along the following guidelines: Increasing the aspect ratio of the SiN cores minimizes loss from sidewall scattering. Thicker cores and a double-stripe geometry (compared to a single stripe) provide tighter guiding for minimizing bend loss. During the optimization, we restricted the cross sections to negligible bend loss ( $\leq 0.01 \text{ dB/cm}$ ) for bend radii down to  $100 \mu\text{m}$ . 2D tapers were designed for mode matching to a semiconductor optical amplifier (SOA) and to output fibers. To provide high fabrication fidelity at small feature size, and to obtain smoother sidewall surfaces than with contact lithography, fabrication was carried out via DUV stepper lithography.

To verify the intended properties of the new cross section and circuit components, an experimental characterization is required before integration with a SOA. Of central interest is quantifying the propagation loss, specifically, in a single pass over longer propagation length. Directional couplers were characterized as well, as these determine, together with waveguide losses, the frequency selectivity of the laser feedback from the microring resonators. Fig. 2(a) shows the measured propagation loss vs wavelength, as measured using a 47 cm long waveguide spiral. For the target wavelength of 637 nm, the propagation loss is 0.33 dB/cm. Decreasing losses at longer wavelengths can be addressed to reduced scattering, while increasing loss (beyond 720 nm) is due to bend loss. Fig. 2(b)

shows the measured wavelength dependent coupling strengths (traces) compared to the target values (horizontal lines). We find satisfying agreement, with a somewhat higher coupling than the nominal target values.

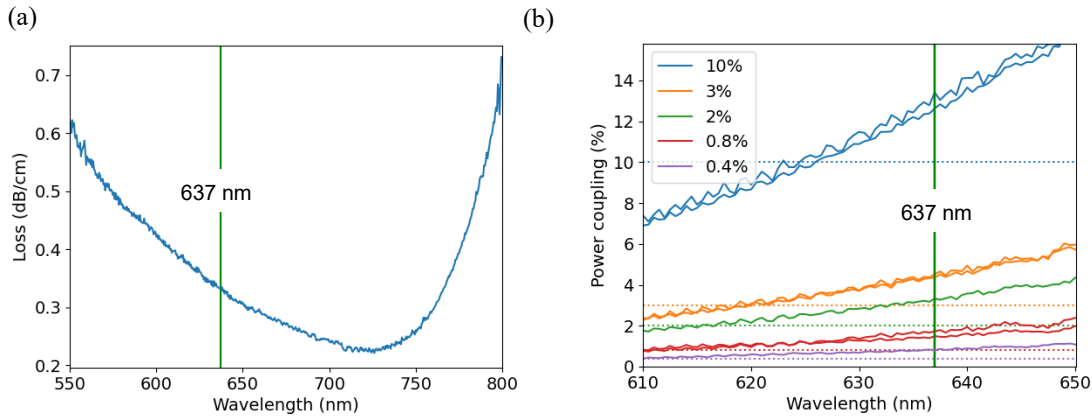


Figure 2: (a) Propagation loss measured in single-pass with a 47-cm long spiral. (b) Measured wavelength dependence of directional couplers (solid traces) compared with target values (horizontal dotted lines).

## Hybrid integrated laser design and fabrication

The overall design of the laser is depicted in Fig. 1(b). The waveguide circuit forms an ECDL comprising tunable microring resonators in Vernier configuration [8] and a double-pass GaAs semiconductor optical amplifier (SOA). The reflective back facet of the SOA acts as one mirror of the laser cavity, while the Vernier feedback circuit acts as the other cavity mirror. The SOA is a super-luminescent diode (SLED) with a center wavelength of 638 nm. For double-pass amplification, the back facet has a high-reflectivity coating ( $>95\%$ ). To reduce undesired feedback from the SOA output facet, the ridge waveguide of the SLED is curved to form an angle with the surface normal. Additionally, the output facet is anti-reflection coated ( $<0.1\%$ ).

On the feedback chip, two micro-ring resonators (R1 and R2) with respective radii of 100 and 103  $\mu\text{m}$  and nominal 0.8% couplers form a Vernier filter with high side-mode suppression over a 14 nm wide free spectral range. This aims on enabling single-wavelength operation over the entire gain bandwidth. Thin film electric heaters are implemented to tune the overall cavity length with a phase section (PS), tune the Vernier filter, and to provide tunable output coupling (TC) via the first port (Out1). The other ports can deliver additional output or serve as monitor ports. The SOA and feedback chips are hybrid-integrated on a thermo-electric cooler. The laser is packaged in a butterfly housing with electric wire bonding and a fiber array at the laser output ports.

## Laser operation and wavelength tuning

The laser is operated using a laser driver (Chilas TLC), a temperature controller (Thorlabs TED200) and a diode laser current source (ILX Lightwave LDX-3620). For simultaneous recording of the laser output power and spectra, the fiber-coupled laser output is sent via a calibrated fiber splitter to a power meter (Thorlabs PM100D) and an optical spectrum analyzer (OSA, ANDO AQ6317).

Figure 3(a) shows the laser output power vs. diode laser drive current, as recorded from the first port (Out1). In this recording, the laser wavelength is set to 638.6 nm. Upon increasing the pump current, with fixed heater powers at R1, R2, and the phase section, we find a laser threshold current of around 50 mA. At 72 mA pump current, the laser

output power is 0.26 mW. The variations of output power vs pump current can be addressed to longitudinal mode-hops caused by index changes in the diode amplifier.

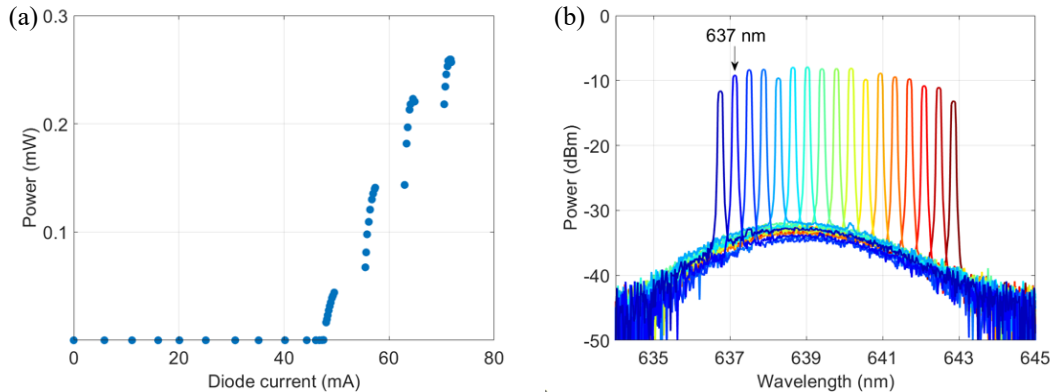


Figure 3: (a) Measured fiber-coupled output power at a laser wavelength of 638.6 nm. The output power is 0.26 mW at 72 mA pump current. (b) Laser output spectra measured with a constant pump current of 66.87 mA and the spectral resolution set to 0.1 nm. 17 traces, each showing single-wavelength emission, are recorded with stepwise tuning the heater power of microring R1 in the range between 58 and 231 mW (lower wavelengths correspond to higher power). The approximate wavelength of diamond NV centers is indicated with an arrow.

Figure 3(b) shows a superimposed series of output spectra from port Out2, recorded using the OSA with the resolution set to 0.1 nm. The experiment was carried out with a fixed pump current of 66.87 mA and stepwise varying the heater power at R1 in the range between 58 and 231 mW. Analogous tuning is expected when acting on the R2 heater. The recordings show a wavelength tuning range of more than 6 nm. The hybrid laser demonstrated here can be tuned across the wavelength range of NV color centers in diamond [6], which complements integration and upscaling for circuits with embedded NV single photon emitters [9].

## Acknowledgments

This project is funded by the Netherlands Enterprise Agency (project “Unlocking hybrid photonics for ultra-precise laser applications”).

## References

- [1] J. L. O’Brien, A. Furusawa, and J. Vučković, “Photonic quantum technologies,” *Nat. Photonics*, vol. 3, no. 12, pp. 687–695 (2009).
- [2] C. G. H. Roeloffzen, et al., “Low-Loss Si<sub>3</sub>N<sub>4</sub> TriPleX Optical Waveguides: Technology and Applications Overview,” *IEEE J. Sel. Top. Quantum Electron.*, vol. 24, no. 4, 4400321 (2018).
- [3] P. Muñoz, et al., “Silicon Nitride Photonic Integration Platforms for Visible, Near-Infrared and Mid-Infrared Applications,” *Sensors*, vol. 17, no. 9, 2088 (2017).
- [4] C. A. A. Franken, A. van Rees, et al., “Hybrid-integrated diode laser in the visible spectral range,” *Opt. Lett.*, vol. 46, no. 19, pp. 4904-4907 (2021).
- [5] M. Corato-Zanarella, et al., “Widely tunable and narrow linewidth chip-scale lasers from deep visible to near-IR,” arXiv:2109.08337 (2021).
- [6] M. W. Doherty, et al., “The nitrogen-vacancy colour centre in diamond,” *Phys. Rep.*, vol. 528, no. 1, pp. 1–45 (2013).
- [7] OptoDesigner 2021, <https://www.synopsys.com/photonic-solutions/optocompiler/optodesigner.html>
- [8] K.-J. Boller, et al., “Hybrid Integrated Semiconductor Lasers with Silicon Nitride Feedback Circuits,” *Photonics*, vol. 7, no. 1, 4 (2019).
- [9] P. P. J. Schrinner, et al., “Integration of Diamond-Based Quantum Emitters with Nanophotonic Circuits,” *Nano Lett.*, vol. 20, no. 11, pp. 8170–8177 (2020).

# Design of a Unidirectional Laser by using a Nd-doped $\text{Al}_2\text{O}_3$ Taiji Resonator for Sensing Purposes

D. J. M. Wojcik, C. E. Osornio-Martínez, B. Jongebloed, and S. M. García-Blanco

Integrated Optical Systems, MESA+ Institute for Nanotechnology, University of Twente, 7500 AE Enschede, The Netherlands

*In the health and medicine fields, continuously higher demands are set for the sensitivity and limit of detection (LOD) of sensors. Photonic Integrated Circuits (PICs) have the potential to achieve high performance. However, many sensors are being made with passive material, which leaves a lot of room to improve the LOD. In this work, a design of an active  $\text{Nd}^{3+}:\text{Al}_2\text{O}_3$  Taiji resonator is proposed. The design has the potential for both exceptional point sensing and unidirectional lasing. The power coupling of the coupling sections is optimised for a pump wavelength of 800 nm and a lasing wavelength of 1064 nm.*

## Introduction

In the health and medicine fields, biosensors are necessary to detect diseases, concentrations of solvents, or dangerous pollutants. Photonic Integrated Circuits (PICs) have a potential to improve the sensitivity and limit of detection of such sensors. However, they must be low-cost, easy to use, small, fast and accurate. Sensing on PICs can be done by immobilizing a layer of capture probes on the surface of a waveguide, so that biomarker molecules can be attached to the surface. The presence of these molecules then changes the effective refractive index of the waveguide, which translates to a change of optical path length that is detected by the sensor.

By using active resonators, the linewidth can be reduced [1] and it is expected that this will reduce the LOD. In previous work of the research group, ytterbium has been used for a laser at 1  $\mu\text{m}$  [2]. However, the slope efficiency of the laser is low ( $\sim 0.1\%$ ) and the laser threshold is high because the ytterbium has a simple two-level energy scheme. In this work, neodymium will be used to dope the  $\text{Al}_2\text{O}_3$  core material. Neodymium has a four-level system, with emission wavelength 1.06  $\mu\text{m}$ . A four-level gain medium does not have the problem of reabsorption of the lasing wavelength, while two- or three-level gain media do.

In this work, an active Taiji resonator (i.e., a Taiji laser) design is proposed. A Taiji resonator is a microring resonator (MRR) with an additional S-waveguide in the middle of the resonator cavity, as shown in Figure 1 [3]. This design permits a further increase of the sensitivity by working at the exceptional point [4]. At this point, the sensitivity exceeds the sensitivity that can be obtained in Hermitian systems.

Moreover, Taiji lasers have been shown to robustly lase unidirectionally [5, 6], since the clockwise (CW) mode in the ring can couple to the counterclockwise (CCW) mode, but not the other way around. Furthermore, the design of a Taiji laser has been theoretically investigated [7]. The results of this research will serve as the basis for design choices for the optimal coupling lengths of the S-waveguide.

The combination of  $\text{Al}_2\text{O}_3$  and Nd is novel, since so far, only one device has been made with the end goal of making an optical backplane [8]. There, amorphous  $\text{Nd}^{3+}:\text{Al}_2\text{O}_3$  was used to create amplifiers at wavelengths of 880 nm, 1064 nm and 1330 nm. The maximum gain that was achieved for 1064 nm was 6.3 dB/cm.

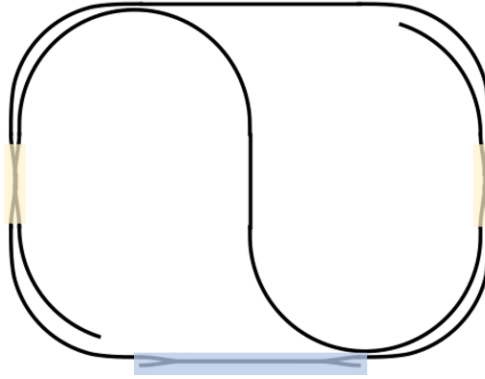


Figure 1: Schematic overview of the design of the Taiji resonator. The yellow areas indicate the S-waveguide coupling sections and the blue area indicates the coupling section with the bus waveguide. The ends of the S-waveguide are tapered and are terminated at an angle to prevent back reflections.

## Methods and Materials

RF reactive magnetron co-sputtering (AJA ATC 1500) is used to deposit an  $\text{Nd}^{3+}:\text{Al}_2\text{O}_3$  layer on a  $\text{SiO}_2$  wafer with a controlled oxygen flow. The loss of a  $\text{Nd}^{3+}:\text{Al}_2\text{O}_3$  slab waveguide without cladding was measured with a prism coupling setup (Metricron 2010/M) and the results are shown in Figure 2. At 521 nm, there is higher loss, due to an absorption peak of neodymium at this wavelength.

Poly-crystalline aluminium oxide will be used as the core material of the waveguides. As a laser sensor base, this material has many advantages such as its broad transparency range, its high solubility for rare-earth ions, and its high refractive index, which enables compact PIC design.

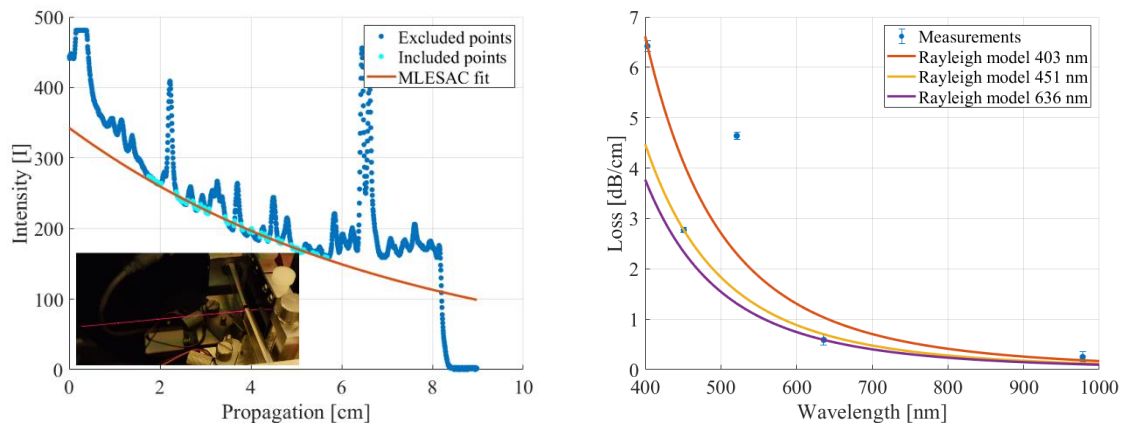


Figure 2: (a) The propagation of a  $\text{Nd}^{3+}:\text{Al}_2\text{O}_3$  slab waveguide for a wavelength of 636 nm with a loss of  $0.58 \pm 0.12$  dB/cm. Including a picture of the 636 nm guiding mode in the experimental prism coupling set up. (b) Propagation loss plotted as a function of wavelength. The loss at 521 nm is high, due to an absorption peak of Nd. Dots represent measured losses while the lines are fits based on a Rayleigh scattering model.

## Simulations and designs

For the design of the Taiji laser, several parameters must be simulated and optimised to achieve performance near optimal conditions. First, the modal field in the waveguides must be analysed and the dimensions must be chosen. A schematic overview of the waveguide cross section and materials is shown in Figure 3. For the cladding material, PMMA is used, which was shown to exhibit low propagation losses at the wavelength range of interest (i.e., around 1  $\mu\text{m}$ ).

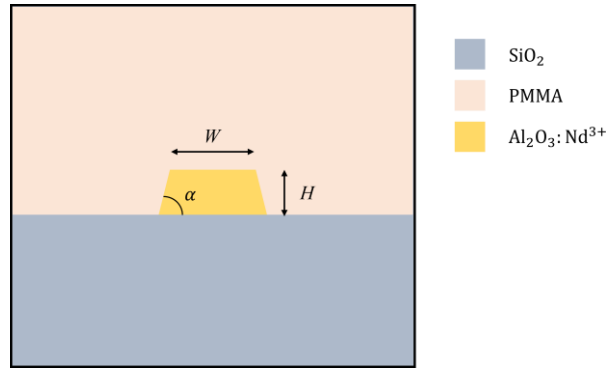


Figure 3: A schematic view of the waveguide cross section, with  $W$  as the width,  $H$  as the thickness and  $\alpha$  as the wall angle of the waveguide.

The waveguide cross section was simulated using Lumerical Mode Solutions software and three widths for the designs are chosen such that there is one monomodal waveguide, one bimodal waveguide and one geometry which is on the edge having one and two modes. The widths are  $1\ \mu\text{m}$ ,  $1.6\ \mu\text{m}$  and  $1.3\ \mu\text{m}$ , respectively. In principle, it is desirable to have a monomodal waveguide. However, a higher confinement of the mode is obtained as the waveguide dimensions increase. This leads to a higher overlap of the pump field with the gain material, which in turn results in a higher gain. The confinement of the pump field for the smallest cross section is 72.9% and for the largest cross section 78.1%. The thickness of the fabricated slab waveguide was used for the simulations, which was 376 nm.

The coupling section with the bus waveguide must be optimised such that the coupling power is minimised for the signal wavelength and is maximised for the pump wavelength. The optimisation is done by using supermode theory. The effective refractive index is simulated with the Finite-Difference Eigenmode solver for the odd and even modes in the coupling section. These effective refractive indices are then used to calculate the coupling coefficients of the coupling sections, using equations from [9]. The resulting simulation is shown in Figure 4a. In this figure, the power coupling is plotted as a function of coupling length for the pump and signal wavelength. Additionally, the optimal coupling length is indicated with a dashed and dotted vertical line. The gap width between the two waveguides was set to  $0.6\ \mu\text{m}$ .

The same principle is used to determine the optimal coupling for the S-waveguide couplers. However, in this case, the amount of coupling for the signal wavelength is restricted to the following rules of thumb:  $\sqrt{\gamma_S/\gamma_A} \geq 0.5$  and  $\gamma_S/\gamma_A \leq 1$  [7]. Where  $\gamma_A$  is the intrinsic loss of the ring and  $\gamma_S$  is the loss due to the coupling with the S-waveguide. The first rule of thumb is the minimal restriction for having robust unidirectional lasing, such that there is no spontaneous switching between the CW and CCW modes. The second rule of thumb is the upper limit for the coupling to the S-waveguide, such that the laser threshold is not too high.

$\gamma_A$  is estimated by using the loss measurements of similar designs in the group, which is 26.4 dB/m [4]. In Figure 4b, the power coupling is plotted. Moreover, the maximum and minimum coupling lengths are indicated with vertical lines. For these coupling sections, a larger gap width of  $1.2\ \mu\text{m}$  was chosen to make the lengths long enough for fabrication.

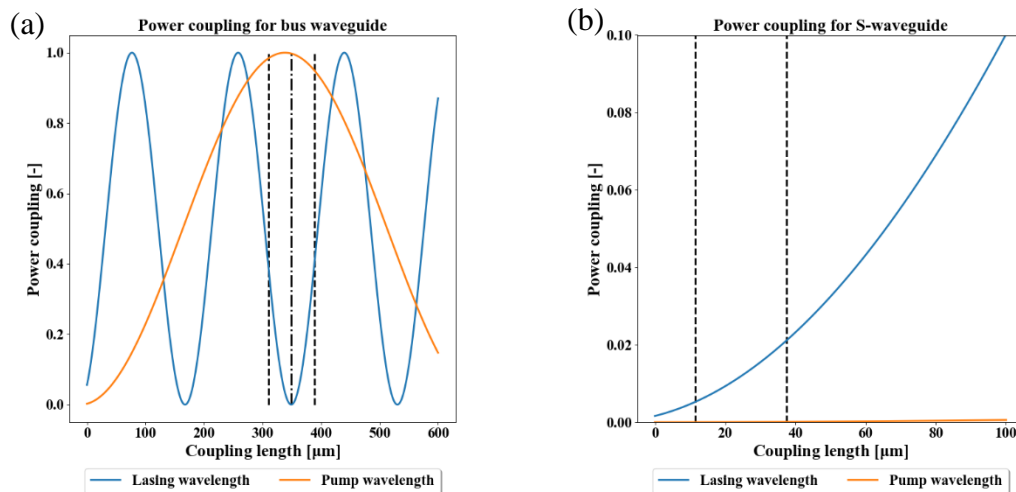


Figure 4: Power coupling simulation results for the coupling sections of the bus waveguide (a) and S-waveguide (b). Upper and lower limits of the optimal coupling are indicated with dashed lines. The width of the waveguides is 1  $\mu\text{m}$  and the gap width used for (a) is 0.6  $\mu\text{m}$  and for (b) is 1.2  $\mu\text{m}$ .

## Conclusion

The coupling sections of the Taiji laser were investigated by simulations. Ultimately, the optimal coupling lengths for lasing at 1.06  $\mu\text{m}$  are 348.9  $\mu\text{m}$  for the coupling to the bus waveguide and the coupling for the S-waveguide should be between 11.4  $\mu\text{m}$  and 37.4  $\mu\text{m}$ . The coupling lengths of all coupling sections should be varied around the simulated values, such that fabrication variations can be taken into account.

The next step in the project is to fabricate the design with E-beam lithography for multiple concentrations of neodymium doping. Afterwards, the devices will be characterised and further optimization will be carried on.

## References

- [1] L. He, S. , Ahin, K. Ozdemir, and L. Yang, “Whispering gallery microcavity lasers,” 2012, doi: 10.1002/lpor.201100032.
- [2] M. de Goede *et al.*, “Al<sub>2</sub>O<sub>3</sub>:Yb<sup>3+</sup> integrated microdisk laser label-free biosensor,” 2019, doi: 10.1364/OL.44.005937.
- [3] L. Pavesi *et al.*, “Unidirectional reflection from an integrated ‘taiji’ microresonator,” *Photonics Research*, Vol. 8, Issue 8, pp. 1333-1341, vol. 8, no. 8, pp. 1333–1341, Aug. 2020, doi: 10.1364/PRJ.393070.
- [4] B. Jongbloed, “Integrated Optical Self-Referenced Sensing at the Exceptional Point,” University of Twente, Enschede, 2022.
- [5] J. P. Hohimer and G. A. Vawter, “Unidirectional semiconductor ring lasers with racetrack cavities,” *Appl. Phys. Lett*, vol. 63, p. 2459, 1993, doi: 10.1063/1.110474.
- [6] S. Kharitonov and C. S. Brès, “Isolator-free unidirectional thulium-doped fiber laser,” *Light: Science & Applications* 2015 4:10, vol. 4, no. 10, pp. e340–e340, Oct. 2015, doi: 10.1038/lsa.2015.113.
- [7] A. Muñoz de las Heras and I. Carusotto, “Unidirectional lasing in nonlinear Taiji microring resonators,” *Phys Rev A (Coll Park)*, vol. 104, no. 4, p. 043501, Oct. 2021, doi: <https://doi.org/10.1103/PhysRevA.104.043501>.
- [8] J. Yang, “Neodymium-doped Waveguide Amplifiers and Lasers for Integrated Optical Applications,” University of Twente, Enschede, 2010.
- [9] M. Bahadori *et al.*, “Design Space Exploration of Microring Resonators in Silicon Photonic Interconnects: Impact of the Ring Curvature,” *Journal of Lightwave Technology*, vol. 36, no. 13, pp. 2767–2782, Jul. 2018, doi: 10.1109/JLT.2018.2821359.

# Fast switchable supercontinuum generation in strongly coupled waveguides

Lisi Xia,<sup>1</sup> Peter J.M. van der Slot,<sup>1</sup> Maximilian Timmerkamp,<sup>2</sup> H.M.J. Bastiaens,<sup>1</sup>  
Carsten Fallnich,<sup>2</sup> and Klaus-J. Boller<sup>1,2</sup>

<sup>1</sup> MESA+ Institute for Nanotechnology, University of Twente, Enschede 7500 AE, The Netherlands

<sup>2</sup> Institute of Applied Physics, University of Muenster, Corrensstrasse 2, 48149 Muenster, Germany

## **Abstract**

*We present a novel approach for fast switching of supercontinuum spectra in chip-integrated waveguides. Using the multimode generalized nonlinear Schrödinger equation, we calculate supercontinuum spectra for a system of two strongly coupled silicon nitride waveguides, excited with femtosecond pump laser pulses at a wavelength of 1.5  $\mu\text{m}$ . The cross section of the identical waveguide cores and their spacing is chosen to impose a strongly different dispersion for the two fundamental supermodes in the pump wavelength range. Specifically, the symmetric supermode is designed to attain normal dispersion while the anti-symmetric supermode shows anomalous dispersion. In this configuration, two vastly different supercontinuum spectra can be generated depending on which supermode is selected for pumping. To enable a fast selection or switching between the two supercontinuum spectra, i.e., within milliseconds to nanoseconds, we consider a tunable phase shifter implemented in one of the waveguides near the input facet. Such phase shifter can be based on the thermal-optic, stress-optic, or electro-optic effect. Compared to switching between supercontinuum spectra in a single waveguide, our method offers an increased freedom in dispersion design, and it can be fully integrated for compact and robust implementation.*

## **Introduction**

Supercontinuum generation (SCG) is the nonlinear optical generation of ultrawide optical spectra, by exploiting the interplay of self-phase modulation and dispersion. Coherent generation with record-wide bandwidth has been achieved in tightly confining  $\text{Si}_3\text{N}_4$  /  $\text{SiO}_2$  waveguides, pumped with low-energy femtosecond pulses<sup>[1,2]</sup>. To shape the output spectrum of supercontinuum generation and for optimizing pumping at a desired wavelength, the size and shape of the waveguide core can be designed to set a desired waveguide dispersion, such as normal or anomalous dispersion. However, switching or programming the output spectra after fabrication<sup>[3]</sup>, such as for frequency agile dual comb spectroscopy<sup>[4]</sup> is difficult because the waveguide dispersion of widely transparent waveguides is only weakly dependent on external parameters. Optically controlling the dispersion via the Kerr nonlinearity is attractive due to its ultrafast speed<sup>[5]</sup> but implementation requires additional, high-intensity control pulses. Temperature tuning of SCG using high-index liquids in hollow core fibers has been demonstrated<sup>[6]</sup> but spectral changes are slow in such bulk approach. Variation of input beam focusing to photonic crystal fibers was used to impose strong changes in supercontinuum spectra<sup>[7]</sup>. However, reliably reproducing the required high alignment precision appears challenging.

Here we present a method for fast switching the shape of supercontinuum generation via fast shifting between supermodes in a system of two strongly-coupled waveguides with identical core size, to avoid the named limitations.

## Approach

The fork-shaped waveguide circuit design for our approach is schematically depicted in Figure 1. A femtosecond pump pulse with a flat wavefront is incident to two adjacent waveguides. Inverse tapers are used to provide efficient input coupling, while the input power is equally distributed to the two input prongs. With further propagation, the spacing between the waveguide prongs is diminished toward a constant and small gap such that the two input modes become strongly coupled via their evanescent field and form a pair of supermodes. A phase shifter in one of the input prongs is used to let the pump radiation excite one of the two possible supermodes, either the symmetric supermode (SSM) when no phase shift is applied, as shown in Figure 1 a), or the antisymmetric supermode (ASM) shown in Figure 1 b), when a  $\pi$ -phase shift is applied. The picture on the right in Figure 1 shows the generated supercontinuum spectra in both supermodes (SSM in blue and ASM in red). It can be seen that applying a  $\pi$ -phase shift generates a greatly different supercontinuum spectrum.

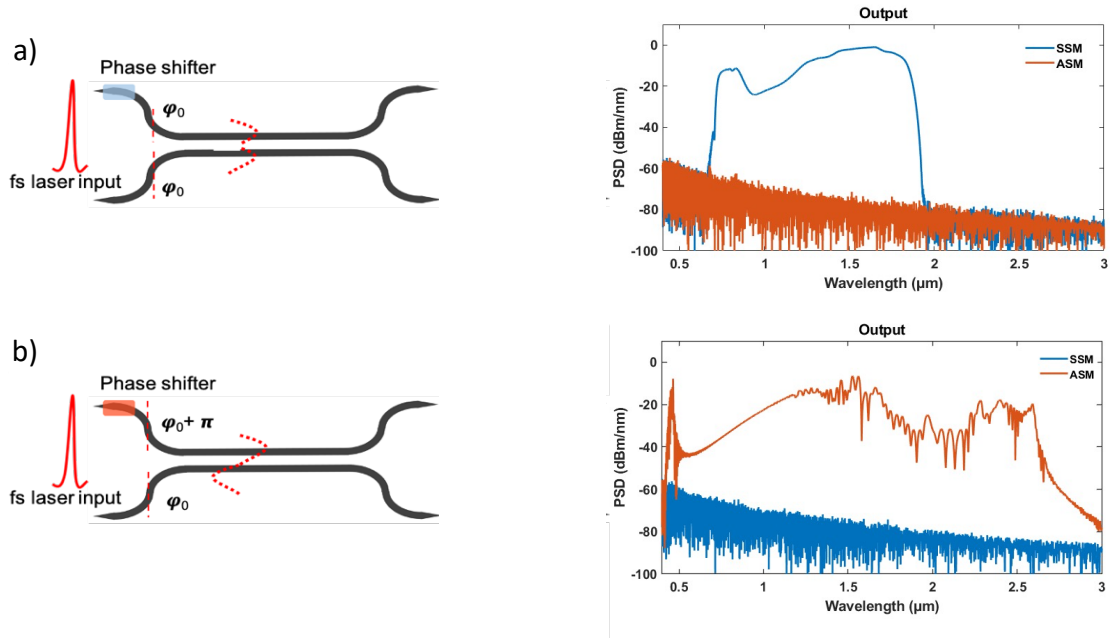


Figure 1. Waveguide circuit with two strongly coupled waveguides for switching the shape of supercontinuum spectra with a phase shifter in one of the input prongs. The applied phase determines which supermode of the waveguide pair is pumped. The calculated power spectral density (PSD) profiles of supercontinuum generation in the a) SSM and b) ASM, respectively are shown on the right. Applying a phase change of  $\pi$  yields a fully different supercontinuum spectrum.

## Modelling and Results

To calculate the shown spectra we used the multimode generalized nonlinear Schrödinger equation [8] which includes higher order dispersion, self-steepening, Raman scattering and mode-to-mode coupling. The dimensions of the two  $\text{Si}_3\text{N}_4$  waveguide cores, embedded in  $\text{SiO}_2$ , are chosen as  $1 \mu\text{m}$  (width) by  $800 \text{ nm}$  (height) and separated by a small horizontal gap of  $300 \text{ nm}$  to induce a strong coupling and thereby form a set of orthogonal and clearly distinct supermodes. The field distribution of the two fundamental supermodes and their dispersion are found with a 2D mode solver. Figures 2 a) and b) show the waveguide cross section geometry and field profiles for the two fundamental

SSM and ASM supermodes, respectively. The corresponding group velocity dispersion profiles are displayed in Figure 2 c). Figure 2 c) shows that the two supermodes possess distinctly different dispersion profiles, namely, the SSM offers normal dispersion (black curve under the zero dispersion line) while the ASM shows anomalous dispersion (red curve above the line).

The nonlinear coupling of the modes through intermodal cross phase modulation (XPM) and four-wave mixing (FWM) is accounted for with intermodal coupling constants calculated from mode field overlap integrals [8]. Spontaneous emission processes are implemented as white noise fields that simulate the vacuum field in both modes. The simulations are carried out assuming pumping with an Er-doped fiber laser system using as example a 1554-nm pump wavelength with a pump pulse duration of 165 fs. The simulations are carried out over a propagation length of 10 mm. This length is sufficient to bring the spectral broadening to its saturation, that is, the output spectra do not significantly broaden any more if increasing the input power.

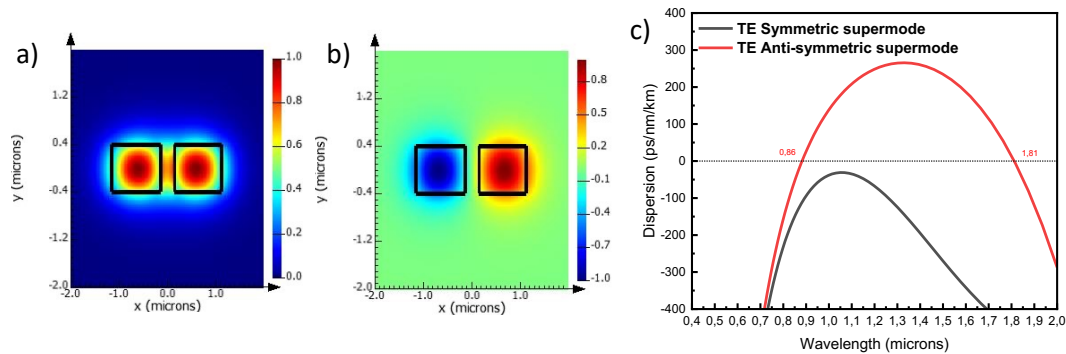


Figure 2. a) Fundamental SSM and b) ASM, provided by two adjacent waveguide cores of 1  $\mu\text{m}$  by 800 nm size, separated by 0.3  $\mu\text{m}$ . The color code indicates the field strength and phase distribution. The graph c) shows the normal and anomalous group velocity dispersion profiles of the two supermodes.

We investigated, particularly, two cases of supercontinuum generation (SCG) via injecting the pump in either one of the two supermodes, while leaving the other mode non-pumped. Our goal of such single-mode excitation is to avoid simultaneous but mutually independent SCG in two modes which would lead to spatially and spectrally complex field distributions at the output. For the same reason we intend that nonlinear energy transfer between the supermodes remains negligible. Such energy transfer could be caused by amplified noise, intermodal FWM and XPM, or by intermodal dispersive wave generation [9].

For the first case of pumping only the SSM, the spectral broadening reaches its saturation with a pulse energy of 3.7 nJ, corresponding to a peak power of 21 kW. The evolution of the supercontinuum in the SSM and ASM as a function of propagation distance is shown in Figure 3 a) and Figure 3 b), respectively. Figures 3 a) and b) show that a supercontinuum is generated in the pumped mode, while the non-pumped mode contains only spurious radiation (a fraction of  $1.6 \times 10^{-6}$  is calculated for the ASM after the 10 mm interaction length). A spectral bandwidth of around 1300 nm is achieved with a flat and smooth shape because generation is based on all-normal dispersion.

For the other case where pump radiation is injected only into the ASM saturation of spectral broadening is already reached a pulse energy of 0.4 nJ (2.3 kW). The evolution

profiles of the supercontinuum for the SSM and ASM for this case are shown in Figures 3 c) and d), respectively, and the spectrum is much wider (more than 2500 nm), as expected due to the stronger confinement of the mode to the waveguide cores and due the anomalous dispersion in that mode. Again, the supercontinuum is only generated in the pumped mode, and the energy in the other mode is negligible, with a calculated fraction of  $1.5 \times 10^{-5}$ .

By switching the pump light between the two fundamental supermodes, e.g., using a heater on one of the input waveguides, one may quickly switch between two different supercontinuum spectra.

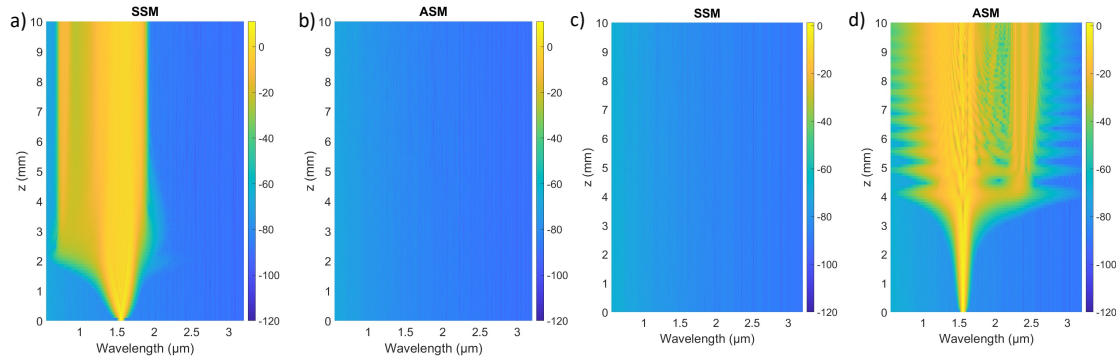


Figure 3. Spectral evolution vs propagation coordinate of the a) SSM and b) ASM if pump radiation is injected only into the SSM. The evolution for pumping only the ASM is shown in c) and d). In both cases supercontinuum is generated only in the pumped mode, though with largely different spectra.

## Conclusions

Our approach of supercontinuum generation in strongly coupled waveguides appears promising for fast switching between largely different output spectra, because rapid phase shifting can be achieved with various methods. These can be based on the thermo-optical, strain-optical, the acousto-optical or the electro-optical effect, depending on which switching speed is desired. Compared to switching and tuning supercontinuum spectra in a single waveguide, our approach allows for chip-integration and electrical control, which is attractive for implementation as compact and robust photonic building block. Although we have discussed only the case of pure single-mode excitation of supercontinuum spectra, the underlying switching between different dispersion profiles may also be useful for a rapid control of the gain profile of waveguide based parametric oscillators and amplifiers<sup>[10]</sup> to modify or extend their tuning range.

## References

- [1] J. P. Epping et al., *Opt. Express* **23**, 19569 (2015),
- [2] M. A. G. Porcel et al., *Opt. Express* **25**, 1542 (2017)
- [3] M. Song et al., *Sci. Rep.* **12**, 18036 (2022)
- [4] G. Milot et al., *Nat. Photon.* **10**, 27 (2016)
- [5] O. Melchert et al., doi: 10.1109/CLEO/Europe-EQEC52157.2021.9541569F
- [6] C. Wang et al., *IEEE Photon. J.* **10**, 1400211 (2018)
- [7] M.-L. Hu, et al., *Opt. Express* **14**, 1942 (2006)
- [8] Poletti et al., *J. Opt. Soc. Am. B* **25**, 1645 (2008)
- [9] N.M. Lüpken et al., *Laser & Photonics Rev.* **15**, 2100125 (2021)
- [10] N.M. Lüpken et al., *Opt. Express* **29**, 10424 (2021)

# Analysis of frequency modulation non-linearity and its impact on range resolution and accuracy of FMCW LiDAR

L. Zhang<sup>1</sup>, K.A. Williams<sup>1</sup>, V. Dolores Calzadilla<sup>1,2</sup>

<sup>1</sup> Technical University Eindhoven, Dept. of Electrical Engineering, Groene Loper 19, 5612 AP Eindhoven, The Netherlands

<sup>2</sup> Photonic Integration Technology Center, Groene Loper 19, 5612 AP Eindhoven, the Netherlands

## Abstract

FMCW LiDAR has attracted huge attention in recent years due to its ability to detect distance and velocity simultaneously, as well as its the ability for improving detection sensitivity. LiDAR accuracy and resolution highly depend on the frequency modulation linearity of the laser source. This paper provides a detailed theoretical analysis of the frequency modulation residual nonlinearity and its impact on both the range resolution and accuracy. The impact of root mean square (RMS) residual nonlinearity and the shape of residual nonlinearity are studied. This analysis aims at providing depth in the understanding of LiDAR systems.

## Introduction

With the rapid emerging of autonomous driving and robotic vehicles, the LiDAR market will have a multi-fold increase in the coming years [1]. Currently, the commercially mature LiDAR solutions are based on the time-of-flight (ToF) detection method, where cost effective pulsed lasers are used. However, the maximum range is limited by the output power and the peak power also has eye safety concerns. More recently, a coherent frequency modulated continuous wave (FMCW) LiDAR has been proposed for better sensitivity and higher resolution.

In FMCW LiDAR, a laser transmitter emits a linear frequency-modulated signal to the target object. Then, the reflected signal mixes with the emitted signal in a balanced photodetector to generate a beating signal. Both the distance and velocity information can be extracted through the beat note. Based on the principle of the FMCW, the linearity of the laser frequency sweeping is of crucial importance for the detection performance. Due to the typical nonlinearity of lasing frequency change with injection current, it is not straightforward to realize linear frequency modulation through direct current-based modulation. Some effort has been dedicated to calibrate the lasing frequency by utilizing a frequency tracker [2] or a pre-distortion algorithm [3]. However such approaches need many optical and electrical components to build the feedback loop or generate a dedicated modulation signal, which will dramatically increase the complexity and also the cost of the whole system. FMCW signal could also be generated through external modulator based on linear electro-optical effects [4], but a complicated IQ modulator and bias-driven circuits are needed to realized single-side-band modulation.

## Simulation principle and the resolution of linear signal

Based on the principle of FMCW LiDAR, the initial laser electric field can be expressed as equation (1),

$$E_i = |\widetilde{E}_{i0}| \exp(i2\pi(f_0 + kt + f(t))t + \varphi_0) \quad (1)$$

Where  $|\widetilde{E}_{i0}|$  is the amplitude of the electric field,  $f_0$  is the initial frequency,  $k$  is the modulation frequency slope,  $t$  is the time,  $f(t)$  is the nonlinear part of frequency modulation and  $\varphi_0$  is the initial phase. The echo signal of a target object with a time delay of  $\tau$  can be expressed in equation (2) as,

$$E_b = |\widetilde{E}_{b0}| \exp(i2\pi(f_0 + k(t - \tau) + f((t - \tau)))(t - \tau) + \varphi_0) \quad (2)$$

Where  $|\widetilde{E}_{b0}|$  is the amplitude of the returned electric field. The emission and return signal will combine in a photodetector to generate a beating note through square-law detection. The detection resolution and accuracy can be extracted from a Fourier transform of the beating waveform. The whole processes are carried out in MATLAB to analyse the impact of the nonlinearity.

Firstly, we study the condition of perfect linear signal by set  $f(t) = 0$ . The delay time is set as 10 ns in the whole simulation for easy calibration with the experiments. The launch and return frequency-modulated signals are shown in Fig 1(a) under a triangular modulation. The residual nonlinearity is also shown in the right axis and it keeps zero in the whole time span for an perfect linear signal. The residual error is calculated through the difference of the launch signal and its linear fitting. Fig 1(b) shows the generated beating signal waveform in time domain.

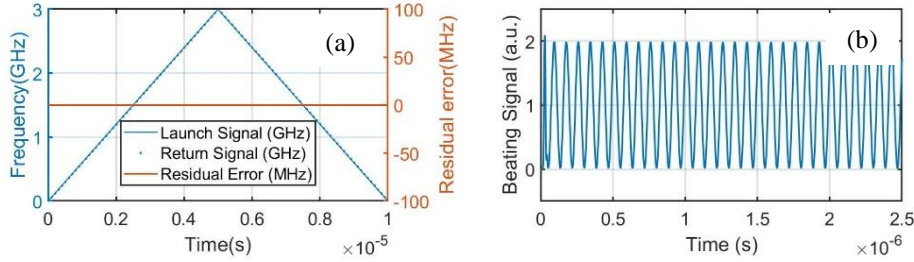


Fig 1(a) Launch and return frequency-modulated signals and residual nonlinearity of the signal. (b) Generated beating signal waveform in time domain.

Through a Fourier transform of the beating waveform, we can get the frequency domain beating signal, where we can easily extract the detection resolution and accuracy. Since there is a one-to-one correspondence between beating frequency and delay time, we simply transform the beating frequency as the delay time in the x-axis. Fig 2(a) shows the Fourier transformed signal of the perfect linear launch signal in Fig 1(a), where a resolution of 0.048m is achieved after applying a Lorentz fitting and extracting its full width half maximum (FWHM). As can be seen, the peak of the signal is perfectly aligned with the delay time of 10 ns, which means a perfect detection accuracy. Regarding the principle of FMCW discussed above, the best achievable distance resolution ( $\Delta d$ ) depends on the chirp bandwidth ( $B$ ) with a relationship given in equation (3),

$$\Delta d = \frac{c}{2nB} \quad (3)$$

Where  $c$  is the speed of light and  $n$  is the refractive index of the transmission medium. To calibrate our simulation, we extract the resolution under different chirp bandwidth as shown in Fig 2(b). The theoretical curve is also shown, which matches well with our simulation.

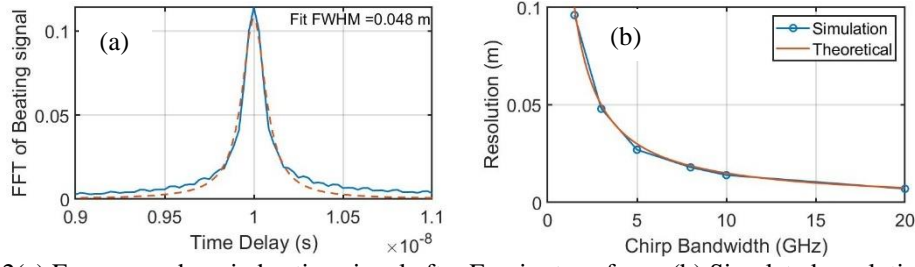


Fig 2(a) Frequency domain beating signal after Fourier transform. (b) Simulated resolution under different chirp bandwidth.

## Analysis of nonlinearity and its impact on range sensing

Then, a second-order nonlinearity ( $f(t) = At^2$ , where  $A$  is a parameter to calibrate the amplitude) is added in the launch signal with different RMS residual nonlinearity. Fig. 3 (a) shows the launch/return frequency modulated triangle signal as well as the residual nonlinearity curve. The RMS residual nonlinearity of this signal is 3.02 MHz, which is calculated using equation (4).

$$RMS = \sqrt{\frac{\sum_1^N (f_{laser} - f_{linear-fit})^2}{N}} \quad (4)$$

, where  $f_{laser}$  is the instantaneous lasing frequency,  $f_{linear-fit}$  is the linear fit to  $f_{laser}$ , and  $N$  is the sample number.

The Fourier transform of the beating signal shows a resolution of 0.086 m as shown in Fig. 3(b), where the nonlinear induced deterioration results in almost twice the detection resolution compared with the linear case. In addition, the detection peak is also shifted from 10 ns, which means a deterioration of the detection accuracy. Fig. 4 (a) and (b) show the resolution and peak position shift under different RMS error induced by second-order nonlinearity. As can be seen, both the resolution and accuracy would deteriorate severely with the increase of residual nonlinearity.

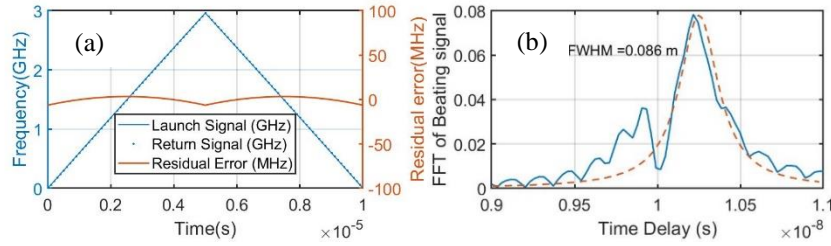


Fig 3 (a) launch and return frequency-modulated signals with 3 MHz RMS nonlinearity, as well as the residual nonlinearity of the signal. (b) Fourier transform of the beating signal.

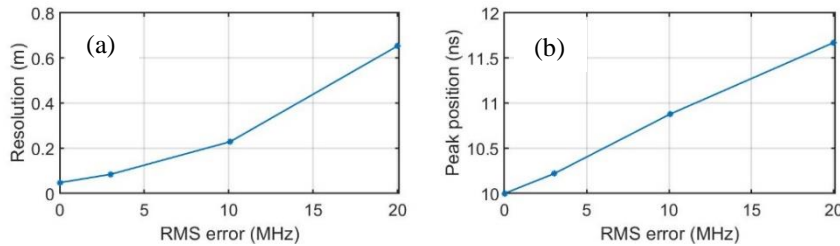


Fig 4 (a) resolution and (b) peak position under different RMS error induced by second-order nonlinearity

Since the second-order nonlinearity would have both positive and negative signs, we also simulate the condition with different sign and keep the same RMS nonlinearity. As

shown in Fig. 5 (a) and (b), different sign will not change the detection resolution but the peak position is shifted from positive side to the negative side. The peak shift originates from the adiabatic shift of the beating frequency caused by the nonlinearity.

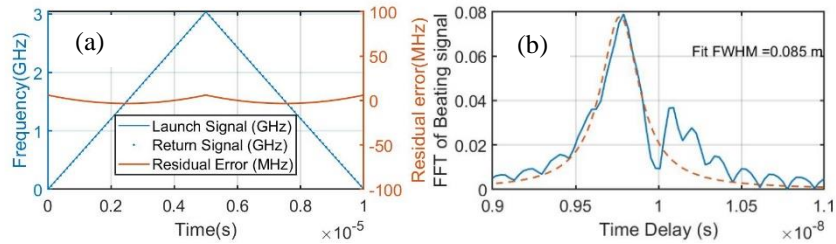


Fig 5 (a) launch and return frequency-modulated signals with 3 MHz RMS nonlinearity and the negative second-order residual nonlinearity. (b) Fourier transform of the beating signal

To further investigate the impact of the shape of the residual nonlinearity, we add a sine-type of nonlinearity ( $f(t) = A\sin(2\pi t/T)$ , where  $A$  is a parameter to calibrate the amplitude and  $T$  is the ramp time of the triangle waveform) with the same RMS error of 3 MHz. Fig 6 (a) and (b) shows the launch signal and the Fourier transform of the beating signal. As can be seen, several peaks appear at both the positive side and negative side around the delay time. This peak distribution lead to an even worse resolution ( $\sim 0.44$  m) compared with the second-order nonlinearity with the same RMS error.

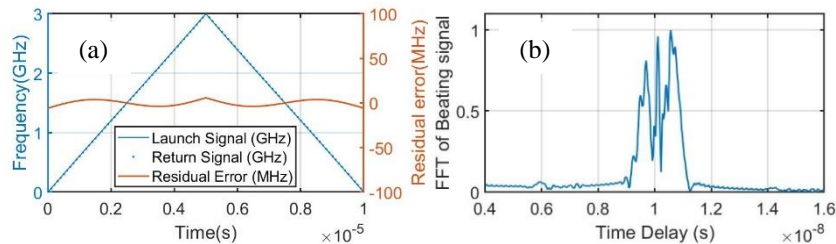


Fig 6 (a) launch and return frequency-modulated signals with 3 MHz RMS nonlinearity and the sine-type residual nonlinearity. (b) Fourier transform of the beating signal.

## Conclusion

In this paper, a detailed theoretical analysis of the frequency modulation nonlinearity and its impact to the range resolution and the accuracy is provided. The impact of root mean square (RMS) residual nonlinearity and the shape of residual nonlinearity are studied. This analysis gives in-depth understanding of LiDAR system performance and their dependence on FMCW linearity.

## Acknowledgments

This work has received funding support from the European Union's Horizon 2020 program through the NewControl project under grant no. 826653.

## References

- [1] <https://www.edge-ai-vision.com/2021/09/lidar-adoption-technology-choices-and-supply-chain-management-are-the-key-enablers/>
- [2] A. Martin et al., "Photonic Integrated Circuit-Based FMCW Coherent LiDAR," in *Journal of Lightwave Technology*, vol. 36, no. 19, pp. 4640-4645, Oct.1, 2018.
- [3] X. Zhang, J. Pouls, and M. C. Wu, "Laser frequency sweep linearization by iterative learning pre-distortion for FMCW LiDAR," *Opt. Express* vol. 27, pp. 9965-9974, 2019.
- [4] M. Kamata, Y. Hinakura and T. Baba, "Carrier-Suppressed Single Sideband Signal for FMCW LiDAR Using a Si Photonic-Crystal Optical Modulators," *Journal of Lightwave Technology*, vol. 38, no. 8, pp. 2315-2321, 2020.

# Non-reciprocal transmission in ring resonators with saturable absorption

I. Luntadila Lufungula,<sup>1</sup> B. Kuyken<sup>1</sup>

<sup>1</sup> Photonics Research Group, Department of information technology (INTEC),  
Ghent University-imec, Belgium

## Abstract

*On-chip non-reciprocal devices are useful building blocks for all-optical signal processing but are hard to integrate on-chip. Magneto-optic or nonlinear devices can be used but these require strong magnetic fields and high optical powers respectively.*

*We use a non-linear add-drop ring resonator to enable nonreciprocal behavior at reasonable powers ( $\sim 10$  dBm). The ring has different power coupling coefficients  $\kappa_1 > \kappa_2$  to the bottom and top bus waveguides which results in different powers in the ring when going from the add to the drop port and vice versa.*

*By adding a saturable absorber in the ring we turn this difference in power into a difference in transmission since in one direction the loss will be saturated while the other direction will have significant extra loss, breaking the reciprocity in the system. In this work we simulate the theoretical properties and discuss the experimental feasibility of an on-chip implementation of this device. With a simple saturable absorber model we simulate 34 dB extinction ratio between the different propagation directions with only 2.3 dB of insertion loss in the forward direction.*

## Introduction

All optical signal processing could accelerate real-time tasks with optical inputs such as in-line denoising and machine learning by staying in the optical domain and avoiding slow analog-to-digital converters. Nonreciprocal devices are a basic building block to realize these optical systems but they remain hard to integrate. These devices require either strong magnetic fields combined with exotic magneto-optic materials or high optical power to use optical nonlinearities efficiently [1] [2]. This last requirement can be relaxed by using a resonator to build up power. We use an add-drop ring resonator augmented with a saturable absorber (SA) to enable low power nonreciprocal behavior.

## Design

Importantly our ring has different power coupling coefficients  $\kappa_1 > \kappa_2$  to the bottom and top waveguides. This results in different powers in the ring when going from the add to the drop port (Fig. 1a) and vice versa (Fig. 1b). We first analyze the ring without the SA and using the formulas described in [3] we find:

$$\frac{P_{ring}^{(a)}}{P_{ring}^{(b)}} = \frac{\kappa_1}{\kappa_2}$$

Since the SA is not included in this calculation, it is a linear system and the power in the ring scales linearly with the power inserted from the bus waveguide.

This inserted power only depends on the coupling gap and the input power. Assuming equal input power it is the asymmetry in coupling gaps which results in an asymmetry of power in the ring. By adding a saturable absorber this difference in power in the ring results in a difference in transmission when going forward from the add to the drop port or backward (Fig 1c).

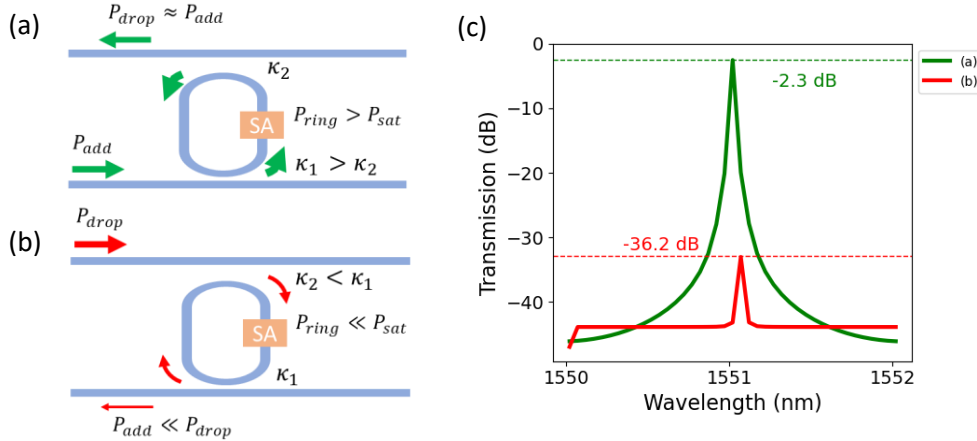


Fig.1 (a) Schematic optical transmission from the add to the drop port, the power coupling to the ring  $\kappa_1 = 0.03$  is strong enough to partly saturate the saturable absorber (SA), have a buildup of power in the ring and transmit power to the drop port, (b) In the other direction, the coupling to the ring  $\kappa_2 = 0.01$  is weaker which results in considerable absorption in the SA, little power buildup in the ring and a low transmission from the drop to the add port (c) Simulated power transmission for (a) and (b)

## Nonreciprocal response

For simulating the device shown in Fig.1 we assume a simple equation for the saturable absorber loss :

$$\alpha_{SA} = \frac{\alpha_0}{1 + \frac{P_{ring}}{P_{sat}}}$$

We assume the following values for the SA :

$$P_{sat} = -2 \text{ dBm}, \kappa_1 = 0.03, \kappa_2 = 0.01, \alpha_0 = 10 \text{ dB}$$

The saturation power is quite realistic but the high extinction of 10 dB will be challenging to achieve in a practical system.

Because the loss in the ring is directly determined by the power in the ring it is important to take into account the dynamics of the buildup of power in the ring as there is no guarantee that the power will reach the steady state described above.

We use Lumerical Interconnect time domain simulation in parallel with an iterative matrix method in Python to simulate the system. The matrix method works by determining the loss in the ring at every time step by the power in the ring at that moment. This technique takes into account the transient buildup.

For nonreciprocal device we want to optimize both the rejection of the backward propagation and the forward insertion loss. Fig. 2(a) shows their values for different coupling coefficients. We choose  $\kappa_1=0.03$ ,  $\kappa_2=0.01$  as optimum because there is a

good tradeoff between only 2.4 dB insertion loss in the forward direction but 41 dB loss in the backward direction.

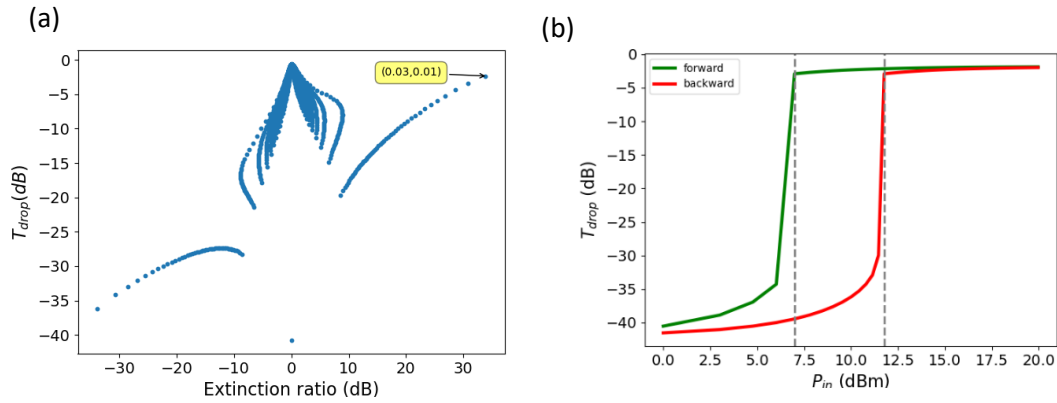


Fig.2 (a) Plotting the two figure of merits for nonreciprocal devices against each other, each point is a different combination of coupling coefficients  $\kappa_1, \kappa_2$   
 (b) Forward and backward transmission to drop port in function of the input power, the nonreciprocal range is from 7 to 12 dBm

Both Lumerical and the matrix method show that the system does not always end up in one of the steady-state solutions without SA described above. Fig. 2b shows that if the input power is low the losses in the SA will be too high preventing power buildup even in the forward direction. The non-reciprocal response persists from 7 to 12 dBm input power, making sure that the system is robust to power fluctuations.

However the nonreciprocal behavior disappears if there are simultaneous beams going forwards and backwards. This is a problem for using it as an optical isolator but can be of use in all-optical signal processing.

## Dynamic behavior

Aside from the nonreciprocal response, this system also displays some interesting nonlinear dynamic properties. By giving our models initial conditions where at  $t=0$  there is high power in the ring the system evolves to a high transmission state even for the backwards propagation ( see Figure 3) . This is because the initial high power bleached the SA making the power buildup possible and once the power is built up the losses remain

low. It is the reservoir of photons built up in the beginning which keep partly saturating the SA.

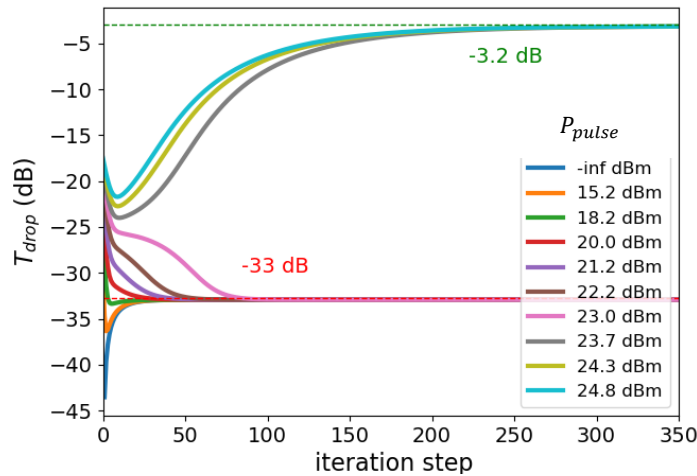


Fig.3 A strong pulse can saturate the absorption allowing for transient power buildup resulting in low loss transmission even in the backwards directions

This theoretical concept of an initial high power can be experimentally achieved by sending in a pulse of light after which the CW light will now have a low loss path to the drop port even after the pulse has passed. This behavior can be useful as an all optical memory [4] or as a spiking neuron in machine learning networks. The pulse threshold could be set by tuning the coupling gaps and the system could be reset by turning of the CW light or tuning the SA bandgap.

## Conclusion

We show nonreciprocal behavior in a simple asymmetric add-drop ring by adding a saturable absorber. Although this system cannot isolate simultaneous beams it's dynamic properties could be used in all-optical signal processing applications such as denoising and machine learning.

Future work will focus on including realistic values for the extinction ratio and residual loss of the saturable absorber in simulation. These results can then be used to fabricate a real device by transfer printing a saturable absorber on a ring resonator.

## References

- [1] L. Bi., et al. "Magneto-optical thin films for on-chip monolithic integration of non-reciprocal photonic devices." *Materials* 6.11 (2013): 5094-5117.
- [2] S. Hua, et al. "Demonstration of a chip-based optical isolator with parametric amplification." *Nature communications* 7.1 (2016): 1-6.
- [3] W. Bogaerts et al. "Silicon microring resonators." *Laser & Photonics Reviews* 6.1 (2012): 47-73.
- [4] A. Theoni, G. T. Kanellos, and N. Pleros. "Optical RAM and integrated optical memories: a survey." *Light: Science & Applications* 9.1 (2020): 1-16.

# Material optimization via optical and spectroscopic parameters of $\text{Al}_2\text{O}_3:\text{Er}^{3+}$ for the development of amplifiers and lasers

D. B. Bonneville, C. E. Osornio-Martinez, M. Dijkstra and S. M. García-Blanco

Integrated Optical Systems, MESA+ Institute for Nanotechnology, University of Twente, 7500 AE Enschede, The Netherlands.

*In this work, we report on the optical and spectroscopic optimization of  $\text{Al}_2\text{O}_3:\text{Er}^{3+}$  for the development of amplifiers and lasers by providing details on optical processes in the material such as luminescent lifetimes, signal enhancement, and propagation and absorption losses. In this manner we intend to optimize the host material for favourable  $\text{Er}^{3+}$  transitions to maximize the available net gain at 1550 nm, when pumped at 1480 nm. By measuring and tracking a variety of parameters across fabrication and treatment steps, ideal methods are discovered for maximizing optical gain in  $\text{Al}_2\text{O}_3:\text{Er}^{3+}$  waveguides.*

## Introduction

Photonic integrated circuits (PICs) are becoming widespread in their research and application to alleviate a variety of limitations in fields such as sensing, telecommunications, quantum information and LIDAR (light-detection and ranging). Monolithic (integrated on one chip) photonic devices however still require high power, stable-linewidth emission sources to enable key components in a variety of applications. To address this, new materials are required to provide optical gain that can be integrated on to the silicon platform. Although III-V materials provide direct bandgap transitions and electrical pumping, they suffer from drawbacks such as power and noise limitations, as well as complicated and costly processing like epitaxy and wafer-bonding. Rare-earth ions can be integrated into materials several ways including ion implantation [1], gas precursors via atomic layer deposition (ALD) [2], and solid targets during sputtering [3]. Reactive magnetron sputtering is a readily scalable technique which provides wafer processing and relatively fast deposition rates on a variety of substrates.  $\text{Al}_2\text{O}_3$  has been demonstrated to be a suitable host for rare-earth ions, including  $\text{Er}^{3+}$  and  $\text{Yb}^{3+}$  [3–5] leading to on-chip amplifier and lasers. In this work we demonstrate  $\text{Al}_2\text{O}_3:\text{Er}^{3+}$  waveguide amplifiers fabricated via reactive magnetron sputtering and electron-beam lithography (EBL). Annealing is demonstrated to decrease the background propagation losses of fabricated samples. The refractive index and photoluminescent lifetimes (PL) for a variety of films are shown, before and after annealing at multiple temperatures for two different concentrations. Pumping at 1480 nm was used to produce on-chip gain, which is shown for the small signal regime, and for high signal powers at 1532 and 1550 nm. It is revealed through lifetime, signal enhancement (SE) and loss measurements that annealing enables gain for fabricated samples up to a limit, which is  $\text{Er}^{3+}$  concentration dependent. Pathways and prospects for improvement are discussed.

## Fabrication

Films were deposited in the MESA+ clean-room facilities using reactive magnetron sputtering following procedures outlined in [6]. Films reported in this work vary in  $\text{O}_2$  flow from approximately 2.8–3.2 sccm with deposition rates of  $\sim 4$  nm/min and stage temperatures up to  $760^\circ\text{C}$ . Erbium concentrations are approximately known using calibrated sputtering powers based on Rutherford backscattering measurements (RBS). Samples were stored in  $\text{N}_2$  ambient in between fabrication steps to avoid  $\text{OH}^-$  contamination. Electron-beam lithography (EBL) was used to pattern negative resist at a dose of  $1000 \mu\text{C}/\text{cm}^2$  to be used as an etch mask for the definition of spirals, ring

resonators and straight waveguides for signal enhancement and loss characterization. Nanotapers with widths and lengths of 0.15 and 2000  $\mu\text{m}$  were designed and optimized for 1480 nm coupling which were included to increase on-chip pump power. Reactive ion-etching (RIE) was performed to define the waveguides with 25 and 10 sccm of  $\text{BCl}_3$  and  $\text{HBr}$  gas flows respectively at a chamber pressure of 3 mTorr and 25 W RF power. Plasma-enhanced chemical vapour deposition (PECVD) was used to deposit a  $\text{SiO}_2$  cladding at a deposition rate of 37 nm/min using 200 and 710 sccm of  $\text{SiH}_4/\text{N}_2$  and  $\text{N}_2\text{O}$  respectively, with a chamber pressure of 650 mTorr at 300  $^\circ\text{C}$  stage temperature and 60 W of power. Chips were diced and measured before and after annealing in a tube furnace in  $\text{N}_2$  ambient. Film thicknesses of  $\sim 800$  nm and waveguide widths of 1.6  $\mu\text{m}$  were used for the majority of the work demonstrated.

## Characterization

Waveguides and films were characterized as fabricated and after annealing in order to track the optimal parameters for gain as they develop for a variety of temperatures. Films were measured with prism coupling before patterning revealing losses from  $\sim 0.9$ –1.6 dB/cm at 636 nm for the samples presented here. Ring resonator samples were measured at  $>1600$  nm in order to track the background propagation losses in between annealing steps, as shown in Fig. 1 a) for the starred sample with an  $\text{Er}^{3+}$  ion concentration of  $2.9 \times 10^{20}/\text{cm}^3$ , which was annealed at 500  $^\circ\text{C}$ . Figure 1b) demonstrates increasing refractive index and lifetime measured in films with variable angle spectroscopic ellipsometry (VASE) and 976 nm pumping respectively as deposition set stage temperature rises. Shown in the inset is a sample PL measurement as well as lifetime for two different concentrations across annealing temperatures. Figure 1c) shows the lifetime setup, which was measured using a 976 nm pump diode and a 10 Hz modulation source with back reflected ASE signal. Powers were kept low to ensure that reabsorption and reemission of the signal or unwanted excitation was not occurring following methods described in [7]. Methods from [1] were used to assess and fit the data.

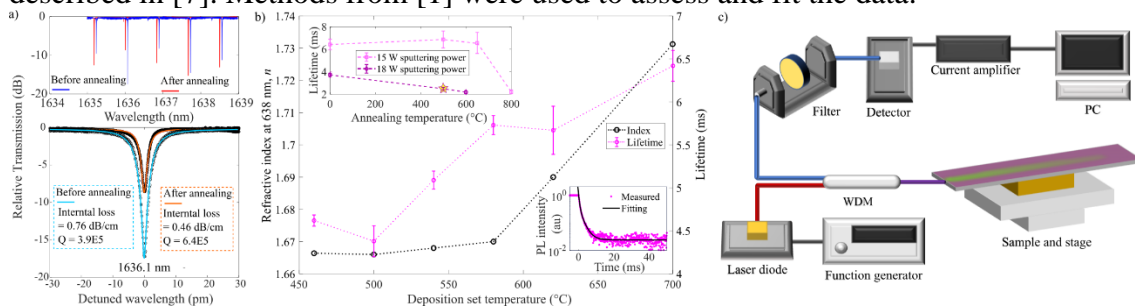


Figure 1. a) Ring resonator measurements for a 1.3  $\mu\text{m}$  wide, 786 nm thick waveguide with a gap of 1.3  $\mu\text{m}$  and radii of 300  $\mu\text{m}$ , with 18 W sputtering power before and after annealing at 500  $^\circ\text{C}$ . b) Refractive index and lifetime for a variety of deposition temperatures with inset sample PL measurement (bottom right) and lifetime vs annealing temperature for films with 15 and 18 W sputtering power (top left). c) PL lifetime measurement setup including a 976 nm laser diode,  $<1100$  nm blocking filter and 980/1550 WDM.

A decrease of 0.3 dB/cm is observed after annealing at 550  $^\circ\text{C}$  shown in Fig. 1a). As demonstrated in Fig. 1b), the deposition temperature has an impact on the lifetime and index of the alumina. Films shown in the inset were deposited at 760  $^\circ\text{C}$  to get the  $\text{Er}^{3+}$  lifetime closer to its intrinsic value  $\sim 7$ –8 ms. As shown in the inset, (top left) samples with higher  $\text{Er}^{3+}$  concentrations ( $1.6$  vs.  $2.9 \times 10^{20}/\text{cm}^3$ ) have lower lifetimes, likely due to clustering in the host and fast quenching of the luminescent decay. It is anticipated annealing the samples provides additional energy for the ions to redistribute in the host, allowing clusters to form, which would happen at lower thermal thresholds for higher

concentrations. The decrease of propagation losses due to the alumina host enables low-loss waveguides and potential for high gain amplifiers. Tracking the lifetime across annealing temperatures, as well as the propagation losses reveals ideal parameters to optimize the gain.

In order to quantify the on-chip gain for the devices, waveguide losses were measured as well as signal enhancement (SE). The starred sample from the inset (top left) in Fig. 1b) was used to characterize the gain. Figure 2a) demonstrates the setup used to pump and measure the samples for SE at high and low powers for 1532 and 1550 nm. Butterfly mounted 1480 nm diodes were used to pump the waveguides, and an erbium-doped fiber amplifier (EDFA) as well as a 1550 nm laser diode were used to measure high signal power gain for 1532 and 1550 nm respectively. For small signal gain the tunable laser was used without the EDFA in the setup. An optical spectrum analyzer (OSA) was used to detect signals and distinguish and correct for the amplified spontaneous emission (ASE) after passing through a low-pass filter. Polarization maintaining fibers were used with motor-controlled stages for alignment. Waveguide losses were measured using cut-back and an IR camera at 1532 and 1550 nm to avoid the ground-state excitation that can occur due to signal power build up during ring resonator measurements.

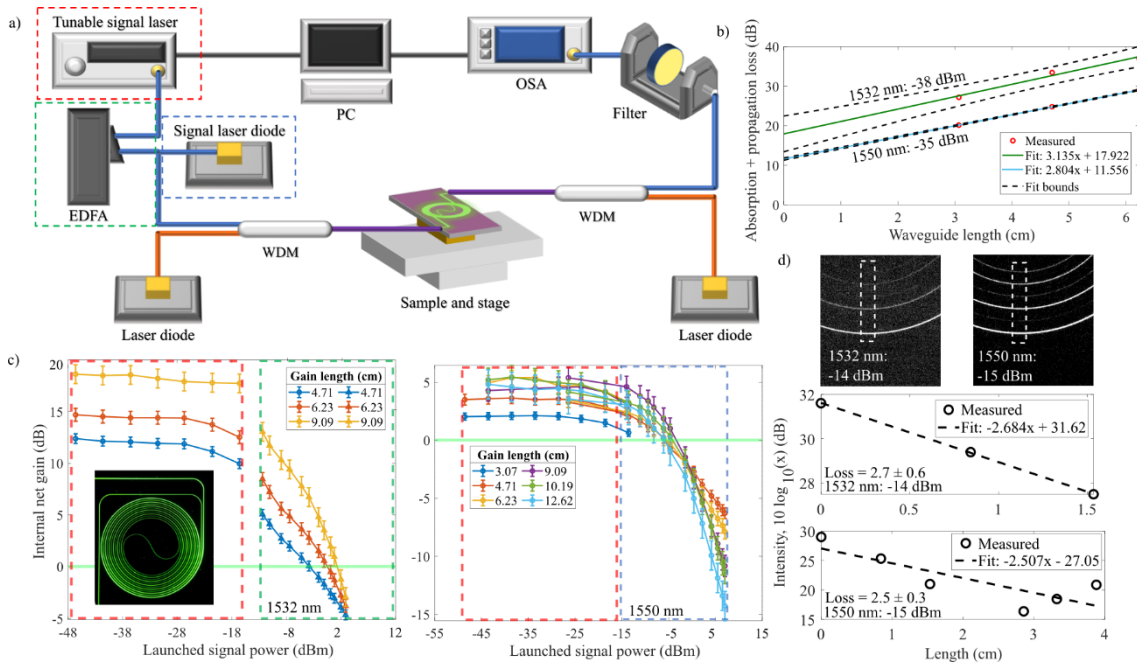


Figure 2. a) Pumping setup for measuring gain with three different source options including a tunable laser source, an EDFA and a high-power signal diode for small signal, and high power 1532 and 1550 nm measurements respectively. b) Cut-back loss measurements in varying spiral lengths. c) Internal net gain measurements for waveguide of varying length with 502 mW launched 1480 nm pump power for 1532 and 1550 nm varying signal powers. Inset included of sample during test. d) IR images of waveguide with 1532 and 1550 nm guided modes and obtained fits for loss verification.

Figure 2b) demonstrates the fits obtained from varying spiral lengths used for cutback loss estimations revealing total losses (absorption plus propagation) of  $\sim 3.1$  and  $2.8$  dB/cm for 1532 and 1550 nm respectively. On-chip peak (internal) gain of  $18.7$  dB for a  $9.09$  cm waveguide as well as  $2.6$  dB/cm for a  $4.71$  cm waveguide is shown in Fig. 2c) at  $1532$  nm. This is achieved with bi-directional pumping at  $1480$  nm ( $\sim 500$  mW launched pump power) to ensure large amounts of on-chip pump power and high signal power gain thresholds in comparison to enhanced energy-transfer up conversion (ETU)

with 980 nm pumping. To verify the losses used for gain calculations, IR camera images were used to measure the scattering while coupled in a spiral and used to extract the intensity as a function of length, shown in Fig 2d). The upper-bounded error result was used in both cases to calculate the gain, resulting in total loss subtractions of 3.2 and  $2.8 \pm 0.1$  dB/cm at 1532 and 1550 nm respectively from the SE measurements.

Future work aims at realizing new samples with varying concentrations and annealing steps to optimize the gain, similar to the study shown here. In parallel designs will be altered to measure devices without nano-tapers to study the influence of coupling loss at 1532 nm, which was considerably higher here than 1550 nm as seen in Fig. 2b). It is anticipated lower concentration samples will provide higher possible annealing temperatures before clustering and therefore lower achievable losses. After optimizing the gain material, the process will be applied to multi-layer waveguide systems for the realization of integrated amplifiers on laser cavity architectures.

## Conclusion

Waveguide losses, lifetime and on-chip gain was demonstrated on reactively sputtered  $\text{Al}_2\text{O}_3:\text{Er}^{3+}$  waveguides fabricated with EBL and RIE. Lifetime was shown to be deposition stage temperature dependent, while decreasing with annealing after a certain temperature depending on the concentration. Annealing was demonstrated to reduce propagation losses by 0.3 dB/cm for a sample with an ion concentration of  $2.9 \times 10^{20}/\text{cm}^3$ , which was subsequently measured for gain with 1480 nm pumping. Losses were measured via cutback and IR imaging, resulting in total losses of 3.2 and  $2.8 \pm 0.1$  dB/cm, which were subtracted from the SE data obtained by pumping. On-chip gain of 18.7 dB was achieved in a 9.09 cm long waveguide, as well as 2.64 dB/cm in a 4.71 cm long waveguide at 1532 nm for 502 mW launched pump power. Annealing and measuring lower concentration samples is promising to further reduce the losses and optimize the amplifier performance.

## Funding

This project has received funding from the European Union's Horizon 2020 research and innovation program under grant agreement No 101017136. This result reflects only the author's view and the European Commission is not responsible for any use that may be made of the information it contains.

## References

- [1] Y. Liu, et al., "A photonic integrated circuit-based erbium-doped amplifier," *Science*, vol. 376, 2022.
- [2] J. Rönn, et al., "Ultra-high on-chip optical gain in erbium-based hybrid slot waveguides," *Nature Communications*, vol. 10, no. 1, 2019.
- [3] W. A. P. M. Hendriks et al., "Rare-earth ion doped  $\text{Al}_2\text{O}_3$  for active integrated photonics," *Advances in Physics X*, vol. 6, no. 1, 2021.
- [4] S. A. Vázquez-Córdova et al., "Erbium-doped spiral amplifiers with 20 dB of net gain on silicon," *Optics Express*, vol. 22, no. 21, 2014.
- [5] J. D. B. Bradley et al., "Monolithic erbium- and ytterbium-doped microring lasers on silicon chips," *Optics Express*, vol. 22, no. 10, 2014.
- [6] C. I. Emmerik et al., "Relative oxidation state of the target as guide line for depositing optical quality RF reactive magnetron sputtered  $\text{Al}_2\text{O}_3$  layers," *Optical Materials Express*, vol. 10, no. 6, (2020).
- [7] R. Wang et al., "Erbium-ytterbium co-doped aluminum oxide thin films: Co-sputtering deposition, photoluminescence, luminescent lifetime, energy transfer and quenching fraction," *Optical Materials*, vol. 111, (2021).

# Study of polarization effects on distributed vibration sensing based on FBGs array

Fourier Sandah<sup>1,2</sup>, Michel Dossou<sup>2</sup>, Marc Wuilpart<sup>1</sup>

<sup>1</sup>Electromagnetism and Telecommunications Department, University of Mons, Mons, Belgium

<sup>2</sup>University of Abomey-Calavi, URPHORAN, Polytech School of Abomey-Calavi, LETIA, Cotonou, Benin

Structural health monitoring has recently attracted much attention in research and development thanks to distributed optical fibre sensors. Among distributed optical fibre sensors, phase-sensitive optical time-domain reflectometry ( $\varphi$ -OTDR) allows distributed vibration sensing by analysing the interference properties of the backscattered/reflected signal when an optical pulse is launched into the sensing fibre[1]. As the Rayleigh backscattered light is relatively weak, fibre Bragg grating (FBG) arrays can be inscribed in the sensing fibre to increase the signal-to-noise ratio. The interference of the signals reflected by two consecutive FBGs (containing information about the local applied vibration) is subject to a polarization fading effect when the polarization states of the two reflected signals are not aligned. The present work first aims to evaluate by simulation the polarization fading effect in the case of a direct detection phase-OTDR scheme using a standard single mode fibre as the sensing fibre. Then, the simulation tool was extended to estimate the improvement resulting from the use of a spun fibre. Spun fibres can indeed strongly reduce the polarization fading effect in  $\varphi$ -OTDR systems. The next lines present the principle of FBG-assisted Phase-OTDR, followed by a description of the simulation method and a presentation of the results, i.e. the obtained polarization sensitivity for unspun and spun fibres.

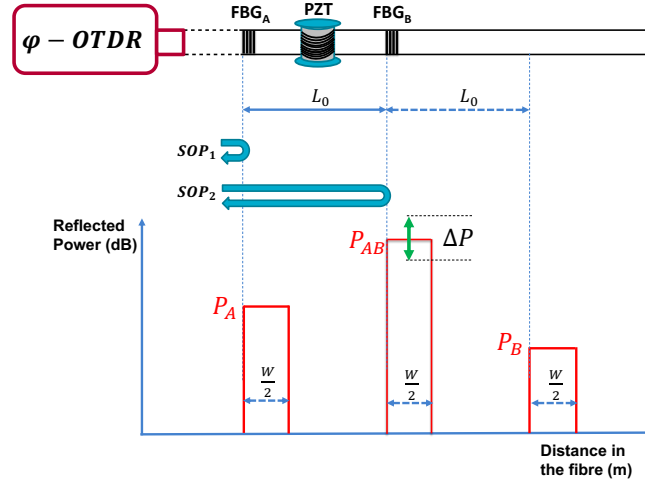


**Figure 1:** Principle of FBG-assisted Phase-OTDR interrogated by a double pulse signal. For a pair of successive FBGs, the Phase-OTDR trace presents a 3-level feature that includes an interference zone sensitive to the applied vibration.

The principle of FBG-assisted phase-OTDR interrogated with a double pulse is described in figure 1 where two successive weak reflectivity FBGs ( $FBG_A$  and  $FBG_B$ ) are written along the sensing fibre. The distance between the FBGs is denoted by  $L$ . The coherent laser embedded in the phase-OTDR setup launches two pulses of width  $W$  with a delay corresponding in the spatial domain to twice the distance between the FBGs [2]. The phase-OTDR detects the power level  $P_A$  ( $P_B$ ) reflected by  $FBG_A$  ( $FBG_B$ ), and  $P_{AB}$ , the interference resulting from the addition of the electric field reflected by  $FBG_A$  and  $FBG_B$  as [3]:

$$E_{AB} = E_A + E_B \quad (1)$$

$$= E_{in} T^2(t) r_A(t) + E_{in} [T(t)]^2 [t_A(t)]^2 r_B(t) e^{j\Delta\phi(t)} \quad (1)$$

$$P_{AB} = |E_{AB}|^2 = E_{AB}E_{AB}^* = |E_{in}|^2|T(t)|^4|r_A(t)|^2 + |E_{in}|^2|T(t)|^4|t_A(t)|^4|r_B(t)|^2 + 2|E_{in}|^2|T(t)|^4|t_A(t)|^2|r_A(t)||r_B(t)|\cos(\Delta\phi(t) + \theta(t)) \quad (3)$$

with  $E_{in}$  the complex electric field at the FBG array input,  $r_A(r_B)$  the complex reflection coefficient of  $FBG_A(FBG_B)$ ,  $t_A$  the complex transmission coefficient of  $FBG_A$ ,  $E_A(E_B)$  the electric fields reflected by  $FBG_A(FBG_B)$ ,  $\theta(t) = \arg[r_B/r_A]$ , and  $\Delta\phi(t)$  is twice the phase difference induced between  $FBG_A$  and  $FBG_B$ .  $\Delta\phi(t)$  varies with time if a vibration is applied thanks to the piezo transducer (PZT). In fact, the PZT, by stretching the fibre between FBGs, allows the variation of optical path difference (OPD)  $\Delta L(t)$  and create a phase change of the interference signal [4]. The resulting phase shift  $\Delta\phi(t)$  is given by  $\Delta\phi(t) = \frac{4\pi}{\lambda} n \Delta L(t)$ . Therefore, when a vibration is applied between  $FBG_A$  and  $FBG_B$ ,  $P_{AB}$  will vary with time over a  $\Delta P$  power variation (see figure 1).  $\Delta P$  depends on the  $\beta z$  product ( $\beta$  is the propagation constant and  $z$  the length) integrated over the distance between the successive FBGs. As the Rayleigh backscattering is much smaller than the reflected powers, it can be neglected.

Equation (3) presents the ideal case where the fibre birefringence is not considered. Therefore, the state of polarization  $SOP_1$  and  $SOP_2$  (of the gratings reflected waves) were considered aligned and the  $\Delta P$  power variation reaches its maximum possible value. When birefringence cannot be neglected, the waves reflected by gratings will be characterized by two different SOPs resulting in a polarization fading coefficient in the  $P_{AB}$  expression. When the two SOPs are orthogonal (worst case), the two reflected waves no longer interfere and  $P_{AB}$  becomes insensitive to the external perturbation and  $\Delta P = 0$ . Clearly this situation should be avoided to ensure a good operation of the sensor. The present study analyses the sensitivity of FBG-assisted phase-OTDR systems to polarization fading effect considering unspun and spun fibres. The sensitivity to polarization effects of the sensor can be quantified as the polarization fading sensitivity (PFS) parameter as:

$$PFS = 10 \log_{10} \left( \frac{\Delta P_{max}}{\Delta P_{min}} \right) [dB] \quad (4)$$

where  $\Delta P_{max(min)}$  is the maximum (minimum)  $\Delta P$  observed when sweeping all the possible input SOP (azimuth angle  $\varphi \in [0, 2\pi]$  and ellipticity angle  $\chi \in [-\frac{\pi}{4}, \frac{\pi}{4}]$ ). When SOPs reflected by FBGs are aligned whatever is the input SOP, the PFS is equal to 0 dB ( $\Delta P_{max} = \Delta P_{min}$ ). When the SOPs are orthogonal for at least one of the input SOP,  $\Delta P_{min} = 0$  and  $PFS$  reaches the infinity.  $\Delta P$  depends on the input SOP and on the fibre birefringence properties. These two features are therefore taken into account in our modeling. The input SOP (at the input of the first FBG) can be expressed by a Jones vector as given in equation (5):

$$V_n = \begin{pmatrix} v_{nx} \\ v_{ny} \end{pmatrix} = \begin{pmatrix} \cos \varphi \cos \chi - j \sin \varphi \sin \chi \\ j \sin \varphi \sin \chi + \cos \varphi \sin \chi \end{pmatrix} \quad (5)$$

The birefringence effect of the fibre section between the FBGs is described by the Laming matrix (based on Jones formalism) that relates the input and output SOPs of the fibre section. The Laming matrix allows to model the birefringence effects of both unspun and spun fibres. A spun fibre is a specialty fibre in which the linear birefringence axes (polarization eigenmodes) rotates with a (constant in our case) spin rate  $\xi$  (in rad/m).

along the fibre axis in order to reduce the effective global linear birefringence [5]. The specific features of a spun fibre is its spun period  $S_P = 2\pi / \xi$  [m] and the local beat length  $L_B$ . An unspun fibre corresponds to the case of a linear birefringence medium without polarization mode coupling (the polarization eigenmode are constant along the fibre).

In this work the birefringence of a spun fibre of length  $z$  can be described by two lumped birefringent matrix elements: a retarder [Jones matrix  $R$ ] with principal axis orientation  $\varphi(z)$  followed by a rotator matrix  $\Omega(z)$ . R.I. Laming et al. [5] have presented the Jones matrix describing the fibre by the matrix  $M$ . as:  $[M] = [\Omega][R]$  with:

$$[R] = \begin{pmatrix} \cos \frac{R(z)}{2} + j \sin \frac{R(z)}{2} \cos 2\phi(z) & j \sin \frac{R(z)}{2} \sin 2\phi(z) \\ j \sin \frac{R(z)}{2} \sin 2\phi(z) & \cos \frac{R(z)}{2} - j \sin \frac{R(z)}{2} \cos 2\phi(z) \end{pmatrix} \quad (6)$$

and

$$[\Omega] = \begin{pmatrix} \cos \Omega(z) & -\sin \Omega(z) \\ \sin \Omega(z) & \cos \Omega(z) \end{pmatrix} \text{ where } \phi(z) = \frac{\xi z - \Omega(z)}{2} + \frac{m\pi}{2} + \theta_{1s}, \quad (7)$$

$$R(z) = 2 \sin^{-1} \left( \frac{1}{(1+q^2)^{1/2}} \cdot \sin \gamma z \right) \text{ and } \Omega(z) = \xi z + \tan^{-1} \left( \frac{-q_L}{(1+q_L^2)^{1/2}} \tan \gamma z \right) \quad (8)$$

with  $z = L_0 + \Delta L(t)$ ,  $\Delta L(t)$  is a sinusoidal length variation induced by the vibration frequency and  $L_0$  the initial length of fibre wounded around the PZT.  $m_L$  and  $n_L$  are integers and  $\theta_{1s}$  is the initial orientation (at  $z = 0$ ) of the local slow axis (the angle between the coordinate system  $x$  axis and the slow axis). The parameters  $q_L$  and  $\gamma_L$  are defined as followed:

$$q_L = \frac{2(\xi(L_0 + \Delta L(t)) + f)}{\Delta\beta} \text{ and } \gamma_L = \frac{1}{2} \sqrt{\Delta\beta^2 + 4(\xi + f)^2} \quad (9)$$

where  $\Delta\beta$  represents the local linear birefringence (is equal to  $2\pi/L_B$ ).  $f$  is the Faraday-induced rotation angle per unit length.  $f$  differs from zero when the fibre is subject to a longitudinal magnetic field which is not the case in this work ( $f = 0$ ). For a Laming matrix  $M$  in the forward direction, the corresponding Jones matrix in the backward direction is equal to the transpose of  $M$ . Therefore, the back and forth propagation in the same fibre is described by the following matrix product:  $M_{bf} = M^T M$ . The interference power  $P_{AB}$  can therefore be recalculated based on the new complex electric field reflected by the gratings:

$$E_A = \begin{pmatrix} E_{Ax} \\ E_{Ay} \end{pmatrix} = r \begin{pmatrix} V_{nx} \\ V_{ny} \end{pmatrix} \quad (10)$$

$$E_B = \begin{pmatrix} E_{Bx} \\ E_{By} \end{pmatrix} = t_A M^t r_B M t_A \begin{pmatrix} V_{nx} \\ V_{ny} \end{pmatrix} e^{j\frac{4\pi}{\lambda} n(L_0 + \Delta L(t))} \quad (11)$$

$$P_{AB} = |E_{Ax} + E_{Bx}|^2 + |E_{Ay} + E_{By}|^2 \quad (12)$$

where  $n$  is the mean refractive index. Figure 2(a) presents the evolution of  $\Delta P$  while varying in all possible case of input SOPs when  $L_B = 4L_0$  (worst case) using an unspun fibre. For some SOP,  $\Delta P$  is closed to zero so that the PFS reaches 85.24 dB. To mitigate the polarization effect, an example of spun fibre is used with a spun period  $S_P = 5$  m (0.03 m) for a distance between gratings of 40 m and a beat length  $L_B$  of 1m. The resulting PFS give 2.21 dB (0.02dB) clearly showing that the use of a spun fibre reduces the PFS and is therefore beneficial for a good operation of the sensor.

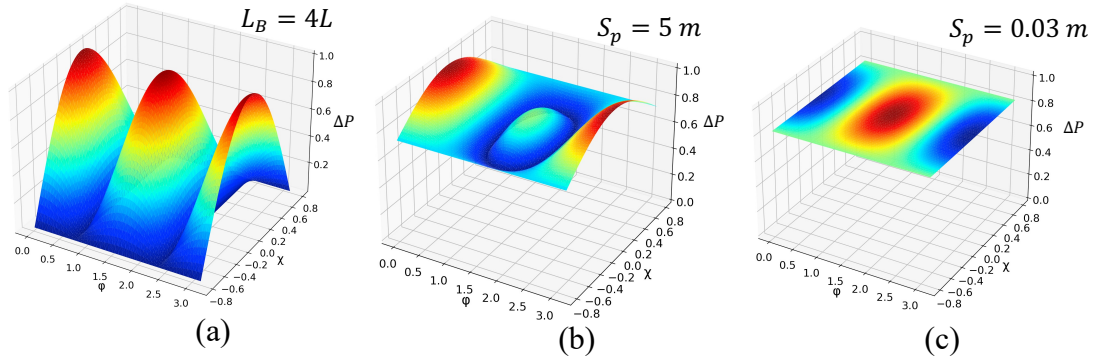


**Figure 2:** a)  $\Delta P(\varphi, \xi)$  for a unspun fibre with  $L_B = 4L_0$ , PFS = 85.24 dB, b) a spun fibre with  $S_p = 5m$ , PFS = 2.21 dB and c) a spun fibre with  $S_p = 0.03m$ , PFS = 0.02 dB.

Figure 3(a) presents the evolution of PFS as function of  $L_B/L_0$  using an unspun fibre. The high PFS peaks are obtained when  $L_B = \frac{4L}{2m+1}$ , with  $m$  a positive integer. In these case, at least on input SOP results into two nearly orthogonal reflected SOPs. Figure 3(b) presents the PFS evolution as function of  $L_B/L$  for different spun period values. The efficiency of spun fibres to mitigate polarisation effect clearly appears (specifically for  $S_p < 2m$ ).

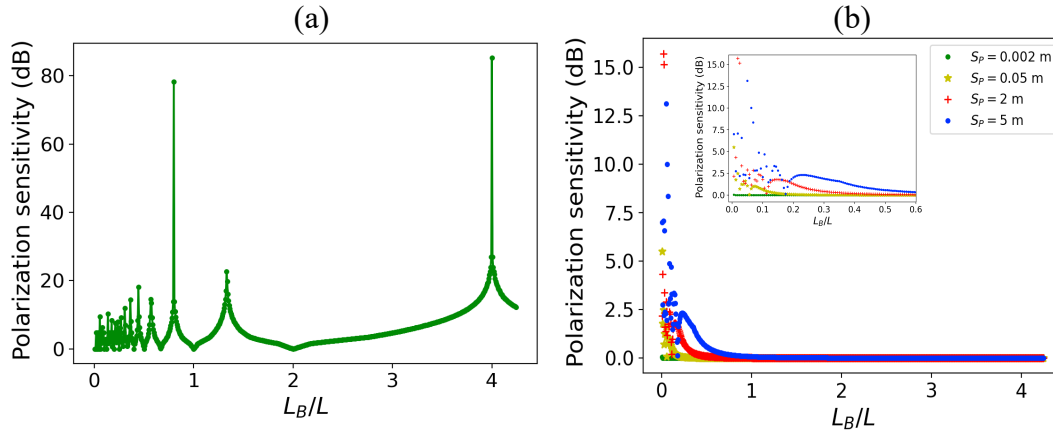


**Figure 3:** PFS as a function of  $\frac{L_B}{L}$  (between 0.25 and 4.25) for  $\theta_{1s} = 0$ ,  $\Lambda = 536.42$  nm,  $L_0 = 40m$   $n_0 = 1.4471$ ,  $\delta n = 1.610 \times 10^{-5}$ ,  $L_{FBG} = 4$  mm,  $\nu = 1$ , and  $\Delta n = 2$ .

In conclusion, the present study presented a simulation tool that enables to analyse the effect of polarization on a FBG assisted phase-OTDR for both unspun and spun fibres. The spun fibre enables to mitigate the polarisation effects on the system.

- [1] M. F. Bado and J. R. Casas, "A Review of Recent Distributed Optical Fiber Sensors Applications for Civil Engineering Structural Health Monitoring," *Sensors*, vol. 21, no. 5, Art. no. 5, Jan. 2021.
- [2] F. Sandah, M. Dossou, and M. Wuilpart, "Spectral Shadowing Compensation in Double-pulse FBG-assisted  $\varphi$ -OTDR," in *PIERS 2022*, pp. 530–535, 2022.
- [3] V. de Miguel Soto et al, "Spectral shadowing suppression technique in phase-OTDR sensing based on weak fiber Bragg grating array," *Opt. Lett.*, vol. 44, no. 3, p. 526, Feb. 2019.
- [4] X. Zhang et al., "A high performance distributed optical fiber sensor based on  $\Phi$ -OTDR for dynamic strain measurement," *IEEE Photonics J.*, pp. 1–1, 2017.
- [5] R. I. Laming and D. N. Payne, "Electric current sensors employing spun highly birefringent optical fibers," *J. Light. Technol.*, vol. 7, no. 12, pp. 2084–2094, 1989.

# Novel-Graphene-Nanoelectrodes-Based Terahertz Photomixers

A. J. Jumaah,<sup>1</sup> J. M. B. P. Sosa,<sup>1</sup> I. T. Monroy,<sup>1</sup> J. Gómez Rivas Rivas,<sup>2</sup> H. G. Roskos,<sup>3</sup> and S. Al-Daffaie<sup>1</sup>

<sup>1</sup> Department of Electrical Engineering, Eindhoven University of Technology

<sup>2</sup> Department of Applied Physics and Science Education, Eindhoven University of Technology

<sup>3</sup> Physikalisches Institut, Goethe-Universität Frankfurt am Main

## Abstract

*Novel Terahertz (THz) photomixers fabricated on low-temperature-grown (LTG) GaAs are demonstrated using multi-layer-graphene (MLG) as transparent nanoelectrodes instead of conventional opaque metal electrodes. MLG improves sensitivity and responsivity by more than one order of magnitude. The higher responsivity of the new interdigitated graphene device leads to an enormously enhanced dynamic range. Also the bandwidth of the new THz MLG-based photodetector is increased twice as compared with the metallic interdigitated THz photodetector devices. The main enhancements of graphene finger nanoelectrodes are due to the transparency of the graphene. That was approved by simulations, where more than 97% of the light beam allows propagating through graphene for excitation. The area under the graphene fingers is fully exposed to light added to the edges, whereas only the edges are covered by light in conventional devices. Therefore, the graphene electrodes result in higher photocarriers that are modulated by the incoming THz wave and enhance the responsivity of the device. The functionality of the MLG does not depend on the incident laser wavelength and the active photoconductive materials. There is no reason to assume that this benefit of graphene nanoelectrodes is limited to LTG-GaAs-based photomixer devices. We expect similar responsivity enhancements for other photomixing materials, as they are used, e.g., in the 1.3-1.55  $\mu\text{m}$  wavelength regime of fiber-based telecommunication.*

## Introduction

Graphene, consisting of a 2D monolayer of carbon atoms arranged in a hexagonal lattice, is one of the most attractive materials being investigated due to its unique optical and electrical properties. Graphene absorbs only 2.3% of visible light [1]. The gapless electronic band structure and high intrinsic mobility of graphene make it a highly desirable material to substitute metals as electrical conductors, provided the Fermi level is high. The combination of high transparency and conductivity makes the graphene a very attractive material as transparent conductive electrode for optoelectronic devices [2]. This pertains also to THz photoconductor devices (THz photomixers). Photoconductor devices are of particular interest in the THz research field, since they can act as THz emitters and detectors, especially if a wide range of tunability of terahertz devices is required. For the generation of the continuous-wave (CW) THz signals, two single-frequency, but frequency-tunable optical waves are mixed in a high-speed photoconductive material. The waves are in-coupled through metallic electrodes of an electrically biased broadband antenna [3]. The generated photocurrent depends on the incident optical power and oscillates with a frequency corresponding to the frequency difference of the two optical waves, which is chosen to be in the THz region. The higher the optical power, which reaches the photoconductive materials, the higher the generated

photocurrent which can be obtained, and the higher the THz output power will become [4]. The oscillation frequency of the generated photocurrent can easily be adjusted over the full bandwidth of the photoconductive antenna by tuning the frequency difference of the two optical waves [5]. It has recently been shown that THz interdigitated graphene photoconductor devices are far superior to standard ones with metallic electrodes. In Refs. [6-9], it has been shown that the charge carriers excited directly under the transparent graphene nanoelectrodes contribute enormously to the generated photocurrent which leads to a substantial increase in the THz output power [10, 11].

A significant advantage of photoconductor devices is that they can also be used as THz detectors [12, 13]. In this detector approach, the device operates without an external bias field. The incoming optical beatnote modulates the carrier density and thus the conductance of the semiconductor between the antenna leaves (which together represent a photoconductive antenna). The electric radiation field of the THz wave will act as a bias field and accelerate the photogenerated carriers. The product of the optical beat signal and the THz field results in a photocurrent that is dependent on the amplitude of the incident THz wave and the phase difference between that wave and the optical beatnote. In CW homodyne measurement systems, as shown schematically in Figure 1, two photoconductor devices are implemented. The first photoconductor (emitter) is used to generate THz waves. The second photoconductor (receiver) is used to detect the generated THz waves. In these CW homodyne measurement systems, the optical beat signal is split into two paths. The first path is used for the THz source, where the device needs a bias field to generate THz waves. Optical components, such as lenses and parabolic mirrors, are used to align and focus the THz beam onto the photoconductor receiver. The second path is used for the THz detector.

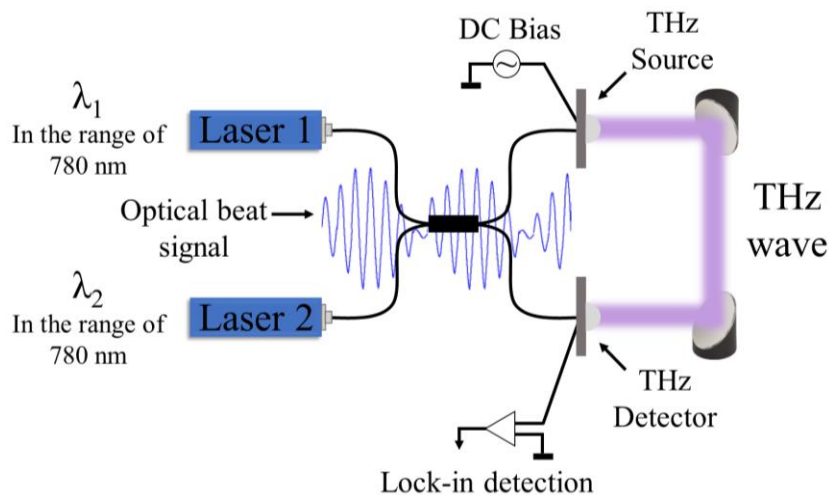


Figure 1: Coherent detection with a CW THz measurement system

## Graphene Transparency

When an incident optical beat signal is projected onto the active area of a photoconductor device, free carriers are generated inside the photoconductive material [13]. The THz wave is usually injected through the substrate and hits the photoconductive antenna from the opposite side. The electric field of the incoming THz wave acts as a bias field that generates a voltage drop  $V_{THz}$  between the antenna contacts. Combined with the modulation of the conductivity by the optical beat signal, the detected photocurrent is

$$I_{det} = V_{THz}G = e\mu_c n_c V_{THz} \frac{A}{l} \quad (1)$$

where  $G$  is the device conductance,  $e$  the electron charge,  $\mu_c$  the carrier mobility,  $n_c$  the carrier concentration,  $A$  the electrodes area, and  $l$  the length of the propagation path which the generated photocarriers follow to reach the electrode. The higher the optical power which reaches the photoconductive material, the higher the generated density of photocarriers, and the higher the measured photocurrent which determines the detector sensitivity. In conventional photomixers with metallic finger electrodes, these will reflect the light beam. The light will excite charge carriers only in the gap between the electrode fingers. Of these carriers, only those generated close to the edges of the electrodes finally contribute to the photocurrent because of the ultrashort lifetime of the charge carriers in the semiconductor. In contrast, graphene electrodes allow the optical beat signal to excite also the area under the electrodes. Many more charge carriers then contribute to the measured photocurrent [14], which leads to a pronounced increase in the sensitivity of the THz photoconductor detector [14, 15, 16].

## Device Fabrication

The new interdigitated graphene detector was fabricated by transferring 6-8 layers of CVD-grown graphene onto the top of a low-temperature growth (LTG) GaAs substrate. The LTG-GaAs layer (wafer thickness  $\sim 1.5 \mu\text{m}$ ) was grown on top of a GaAs substrate. A broadband spiral antenna with  $10 \mu\text{m}$  separation between the antenna contacts was fabricated on the graphene sheet using a standard optical lithography process. A second optical lithography process and an etching of the MLG in an oxygen plasma were performed to form the interdigitated configuration of the MLG. The interdigitated configuration was performed with a finger width of  $0.5 \mu\text{m}$ , a spacing gap between the fingers of  $1.5 \mu\text{m}$ , and the finger length of  $9 \mu\text{m}$ , as shown in Figure 2a. A layer of SiNx of  $150 \text{ nm}$  coats the device to isolate the graphene nanoelectrodes from environmental contamination. In addition, detectors with interdigitated gold fingers were fabricated in a single photolithographic lift-off process including a  $150 \text{ nm}$  thick Au layer on LTG-GaAs. The same fingers configuration was performed for the metallic electrodes of the detectors, as shown in Figure 2b.

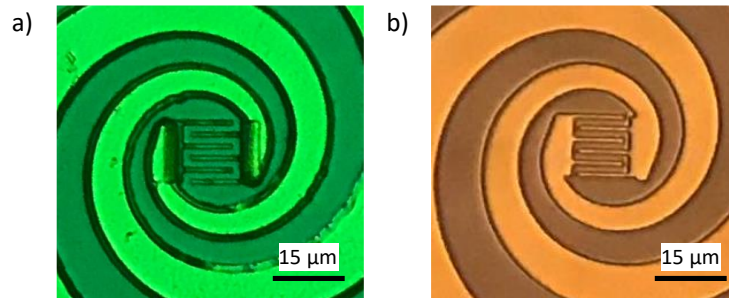


Figure 2: CW THz detectors with: a) interdigitated MLG electrodes, and b) interdigitated gold electrodes.

## THz Measurements

The sensitivity of the new THz interdigitated graphene photoconductor detector was compared experimentally with the performance of a standard photoconductor detector

using a commercial THz source. For this purpose, the commercial THz source was set in a homodyne coherent detection configuration. The interdigitated graphene photoconductor detector had the same geometrical dimensions of the interdigitated graphene electrodes as the standard metal-finger-based photoconductor device. Two detuned distributed feedback diode lasers (DFB-LDs) ( $\lambda = 780$  nm) were used to characterize the two detectors in a homodyne detection system. Total optical powers of 31 mW and 30.5 mW were used to illuminate the active areas of the emitter and the detector photoconductor, respectively. The frequency difference between the two detuned DFB-LDs was controlled by temperature and current controllers. The frequency of the THz radiation from the THz emitter was tuned by varying the frequency difference between the two DFB-LDs. A scanning range of the THz radiation from 50 GHz to 1.9 THz was obtained, allowing us to measure the frequency-dependent photocurrent for both photoconductor devices over a large frequency range.

## Results and Discussion

A frequency step of 50 MHz was chosen to scan the THz radiation from 50 GHz to 1.9 THz. Figure 3 shows the detected THz photocurrent for the interdigitated graphene photoconductor device. This photocurrent is compared with the reference data obtained using the conventional metal-electrodes-based photoconductor device. For both devices, the photocurrent exhibits a peak in the 100-GHz range, followed by a gradual roll-off to the noise floor. The roll-off is mainly determined by the frequency characteristics of the emitter and detector antennas together with the lifetime of the charge carriers. The most important feature of the measurements is, however, that the graphene photoconductor exhibits a more than one order of magnitude (20 times) larger photocurrent than the standard metal-finger-based device, and this over the whole frequency range with a measureable photocurrent. Furthermore, the interdigitated graphene photoconductor device was able to detect the THz beam up to 1.25 THz, which is twice the bandwidth of the standard metal-finger-based device. This enhancement in the device performance is attributed to the high conductivity and high transparency of graphene, which allows almost all of the light beam to penetrate the nanoelectrode material and increase the number of carriers which contribute to the photocurrent.

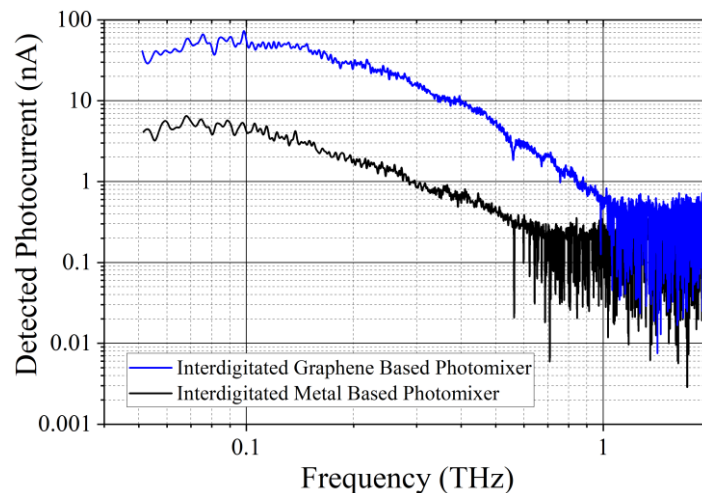


Figure 3: Comparison of the detected THz photocurrent of the detector with interdigitated graphene electrodes with that of the detector with metal electrodes.

## Conclusions

The work presented here demonstrates room-temperature coherent detection of CW THz radiation using a new type of THz photoconductor device based on interdigitated graphene nanoelectrodes on LTG-GaAs photoconductive material. The device was compared with a standard metal-finger-based photoconductor device. The high optical transparency of graphene allows most of the optical light beam to penetrate the graphene nanoelectrodes of the fingers. The higher the transmitted light intensity, the higher the photo-generated carrier density, and the higher the detected photocurrent. The measurements show a more than one order of magnitude increase of the detected photocurrent compared to the standard metal-finger-based photoconductor device. Additionally, the interdigitated graphene detector exhibits a bandwidth twice as large as that of the standard metal-finger-based detector. This performance of the graphene nanoelectrodes offers a new path to provide highly responsive devices for THz applications.

## References

- [1] P. Li, C. Chen, J. Zhang, S. Li, B. Sun, and Q. Bao, "Graphene-based transparent electrodes for hybrid solar cells," *Front. materials* vol. 1, 26, 2014.
- [2] Y. Jiang, L. Gao, X. Wang, W. Dai, J. Wu, X. Dai, and G. Zou, "Laser tailored multilayer graphene grids for transparent conductive electrodes," *Nanoscale research letters*, vol. 14, 1–6, 2019.
- [3] K.A. McIntosh, E. R. Brown, K. B. Nichols, O. B. McMahon, W. F. DiNatale, and T. M. Lyszczarz, "Terahertz photomixing with diode lasers in low-temperature-grown GaAs," *Applied Physics Letters* vol. 67, no. 26, 3844-3846, 1995.
- [4] S. Al-Daffaie, O. Yilmazoglu, F. Küppers, and H. L. Hartnagel. "1-D and 2-D nanocontacts for reliable and efficient terahertz photomixers," *IEEE Transactions on Terahertz Science and Technology* vol. 5, no. 3, 398-405, 2015.
- [5] R. Mendis, C. Sydlo, J. Sigmund, M. Feiginov, P. Meissner, and H.L. Hartnagel, "Tunable CW-THz system with a log-periodic photoconductive emitter," *Solid-State Electronics*, vol. 48, no. 10-11, 2041-2045, 2004.
- [6] A. Jumaah, S. Al-Daffaie, O. Yilmazoglu, and F. Küppers, "Graphene–nanowire hybrid photomixer for continuous-wave terahertz generation," in *42nd International Conference on Infrared, Millimeter, and Terahertz Waves (IRMMW-THz)*. IEEE, 1-2, 2017.
- [7] A. Jumaah, S. Al-Daffaie, O. Yilmazoglu, F. Küppers, and T. Kusserow, "Interdigital multilayer-graphene nanoelectrodes for continuous wave terahertz photomixers," in *European Microwave Conference in Central Europe (EuMCE)*, IEEE, 265-267, 2019.
- [8] A. Jumaah, S. Al-Daffaie, O. Yilmazoglu, F. Küppers, and T. Kusserow, "Experimental investigation of graphene layers as 2d nanoelectrodes for continuous wave terahertz generation," in *44th International Conference on Infrared, Millimeter, and Terahertz Waves (IRMMW-THz)*, IEEE, 1-2, 2019.
- [9] A. J. Jumaah, S. Al-Daffaie, T. Kusserow, I.T. Monroy, "Highly transparent graphene electrodes for cw thz applications, In 45th International Conference on Infrared, Millimeter, and Terahertz Waves (IRMMW-THz), IEEE 1–2, 2020.
- [10] A. J. Jumaah, S. Al-Daffaie, O. Yilmazoglu, and T. Kusserow, "Continuous-wave terahertz emitter with hybrid nanoelectrodes based on graphene and nanowire," *OSA continuum* vol. 3, no. 7, 1826-1833, 2020.
- [11] A. Jumaah, S. Al-Daffaie, O. Yilmazoglu, and F. Küppers, "Graphene enhanced 2-D nanoelectrode for continuous wave terahertz photomixers," In *43rd International Conference on Infrared, Millimeter, and Terahertz Waves (IRMMW-THz)*, IEEE, 1-2, 2018.
- [12] F. Sizov, and A. Rogalski, "THz detectors", *Progress in Quantum Electronics*, vol. 34, no. 5, 278-347, 2010.
- [13] A. J. Jumaah, S. Al-Daffaie, T. Kusserow, and I.T. Monroy. "High performance graphene-based CW THz photoconductive detector," In *45th International Conference on Infrared, Millimeter, and Terahertz Waves (IRMMW-THz)*, IEEE, 01-02, 2020.
- [14] A. J. Jumaah, H. G. Roskos, and S. Al-Daffaie, "Novel-coupled graphene nanoelectrodes enhanced terahertz photodetector," *APL Photonics*, [Under review].

- [15] A. Rogalski, "Terahertz detectors and focal plane arrays," *Elektronika: konstrukcje, technologie, zastosowania*, vol. 51, no. 4, 93-108, 2010.
- [16] E. Moreno, Z. Hemmat, J. B. Roldán, M. F. Pantoja, A. R. Bretones, and S. G. García, "Time-domain numerical modeling of terahertz receivers based on photoconductive antennas," *JOSA B*, vol. 32, no. 10, 2034-2041, 2015.

# Implementation of an optimization model and interface for an optimized operation of Semiconductor Optical Amplifier cascades in Optical Switches

Desalegn Wolde Feyisa, Salim Abdi, Zhaowei Chen, Yuqing Jiao, Nicola Calabretta and Ripalta Stabile

Institute for Photonic Integration, Eindhoven University of Technology, PO Box 513, 5600MB Eindhoven, the Netherlands.

## **Abstract**

*Optical switches are becoming crucial in optical communication networks to scale switching capacity to meet continuously growing traffic demand. Semiconductor optical amplifier (SOA)-based switches could play such roles as they can meet current optical network capacity and speed scaling requirements. To scale up an SOA-based switch, we need to cascade several SOAs in a multistage configuration, which increases noise figures and hinders scalability, exacerbated by the difficulty in setting the optimal parameters to mitigate the noise building up. Therefore, we develop a technique for optimizing parameters in SOA cascades, specifically bias current for each SOA, depending on SOA length, the losses between consecutive SOAs, and the input optical power, which is imperative. To this end, we experimentally measure the parameters of a single SOA and create its model, including gain dynamics and noise figures in the VPI photonics modeling tool, to build an SOA cascade circuit model. Then we develop an optimization algorithm that can automatically find the optimum operating condition for each SOA in SOA cascades. Our approach is based on carefully mapping the input power and bias currents to the path performance. We then validate the method experimentally with a chain of integrated SOA devices.*

## **1. Introduction**

Optical signals are known for their fast signal transportation, high bandwidth capacity, agnostic to transmission format, and consumption of less energy per transmitted bit [1]. While this feature has already been widely used in signal transportation, switching in the optical domain is crucial to take full advantage of these desirable features of communication in the domain. Large port count optical switches needed to cope with a growing global network and the number of nodes that need to be interconnected require complex control layer implementation. Specifically, when SOAs are cascaded in a multistage configuration [2], controlling the switch becomes more challenging. Switch modeling and control layer automation are necessary for the design and circuit operation phase due to the following reasons: -

1. The design and design validation stages are crucial in improving the performance of complex optical circuits. Implementing robust and hierarchical modular modeling of the circuit in advance is vital for a fast design cycle and parameter optimization. For instance, important SOA design parameters such as waveguide width and SOA length impact signal integrity differently in a standalone SOA and SOAs in a chain. The gain, extinction ratio, OSNR, and gain saturation depend

not only on the performance of the individual SOA but also on the signal quality and level from the preceding SOA.

2. The control layer development and testing are relatively more manageable, accessible, flexible, and cheap in the model than working on the actual circuit. It also allows the development of the switch control algorithm and testing at the design stage than waiting for fabrication. The development of the control layer on an actual circuit is sometimes costly as some devices are pricy. For instance, measuring eight paths simultaneously for an  $8 \times 8$  switch requires eight laser arrays and 8 BERT, which is expensive. However, this can be done on a software basis quickly and in parallel, cutting a lot of time. It allows one to evaluate the component parameter effect on the circuit level.
3. In blocking or rearrangeable non-blocking switch configuration, path scheduling and control are complex. Scheduling concepts are easy to develop on models and then deploy into the circuit

This paper will show strategies to model a switch module that emulates a realistic switch and develop a switch control method and user interface for switch design and control automation. We will discuss a process for selecting the optimal currents that give the best performance for a path.

## 2. Modular optical switch modeling

VPI photonics component maker tools allow component models based on measured data or transfer functions from other design tools. In this work, we model each switch component and emulate the optical switch in the VPI photonics design tool. After making the component model based on our design, we validate whether it works as intended and use it for control layer implementation, automation, and optimization.

Fig 1 shows the modular switch modeling. Fig 1a contains the elementary building blocks customized according to our design. We model the waveguide, waveguide crossing, waveguide bends, multimode interference splitter/combiner, and SOA and transfer the

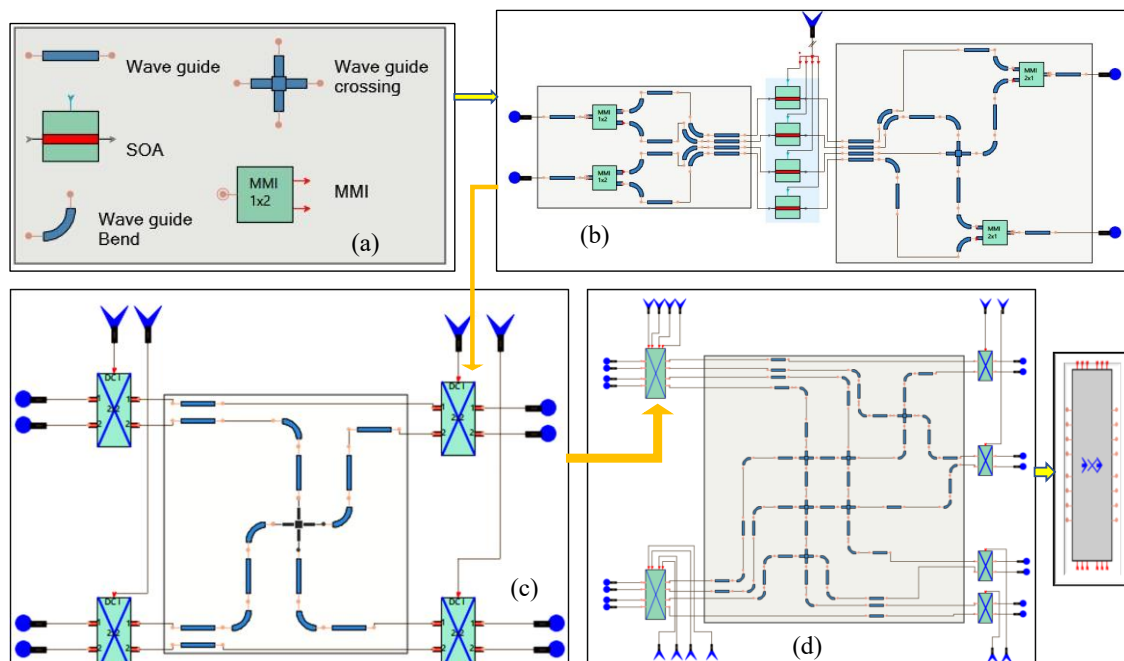


Figure 1: Modular optical switch modeling for development of design and control automation methods

model to VPI to build the smallest switch-building block module as in Fig 1b. Then the compact model of the  $2 \times 2$  switch is used to construct  $4 \times 4$  and  $8 \times 8$ , as shown in figs 1b and 1c, respectively. The switch control and optimization layers are then applied to the compact  $8 \times 8$ . This modular approach is crucial both in design and actual implementation. It enables validation of the design process on a small scale and scales it quickly by simplifying the design process and localizing error diagnosis.

### 3. Switch control layer implementation for control automation

The schematic of a switch is created in the VPI photonics design tool, as in Fig 1, and connected to MATLAB. The switch parameters to be controlled and the switch output are monitored by programs developed in MATLAB. The software provides suitable currents to the switch depending on optimization rules. Several files are created to facilitate the control and convey the circuit information to the software. The SOA correspondence file stores mapping information between SOAs in the circuit and associated drivers; the SOA id file contains the ids of SOAs. Additionally, the flag files, such as the SOA flag file, contain if an SOA is working or inactive, a path flag has status information about the path, and the port flag indicates the status of ports.

The algorithm for implementing the control layer is shown in figure 2. It starts by reading the flag and SOA information files and assigning them to global variables declared within MATLAB. It then displays the current status of the circuit on the graphical user interface created in MATLAB for user information. The control layer continuously probes if there is a path connection request from a user. If a connection request is detected for a path, the software checks if all flags are clear and the path can be established. If the path is free, the control layer will set the current to the optimal value found from the current tuning algorithm, updates the related flag status, and updates the displays accordingly. If the path is currently connected, the request is counted as a path clear request, the path is disconnected, and the associated flags are cleared. If the two conditions are not fulfilled, the path is busy, and the busy flag is updated. In this case, either one/more SOAs in the path are occupied by other connections, or the input/output port is busy.

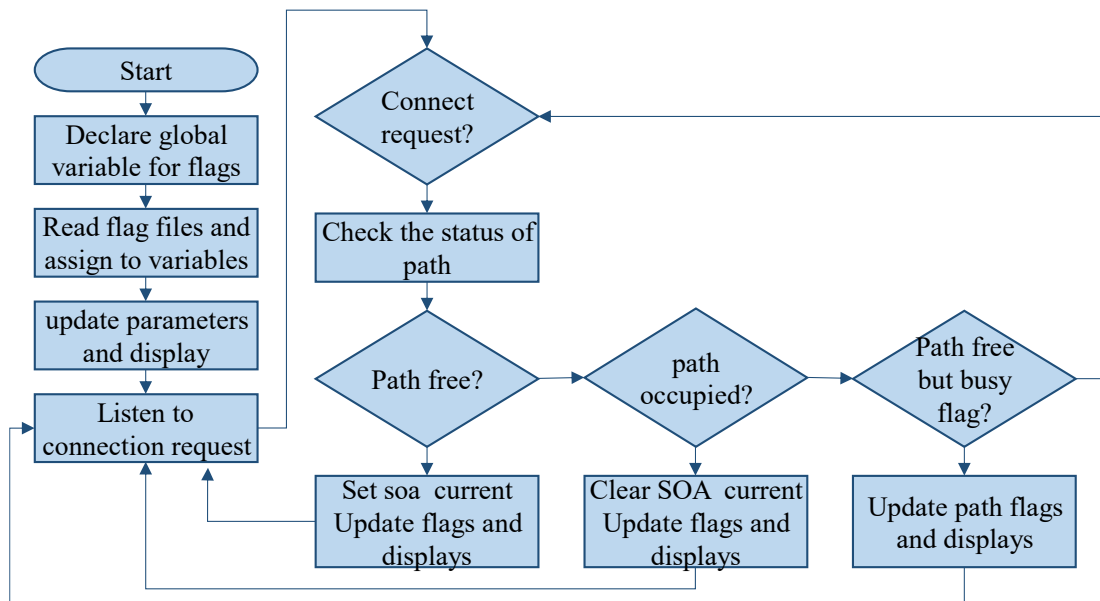


Figure 2: Algorithm for automated switch control implementation

#### 4. Automatic optimal current selection implementation

The optimal current selection is time-consuming and challenging to achieve if done manually. However, it is possible to mathematically establish the relation between optimal currents at a particular input power and the optimal signal integrity from sample data sets generated from the circuit. This can be done in two separate approaches, shown in fig 3. The first is by creating a parametric equation relating input power and currents to the BER and then applying optimization algorithms to find currents that give minimal BER. The second approach uses a black box approach where data sets are used to train the system and generate a look-up table that shows the optimal BER at a given input power. The former method is suitable when the relationship among the parameters follows a pattern and can be described by equations, while the former can describe complex relations

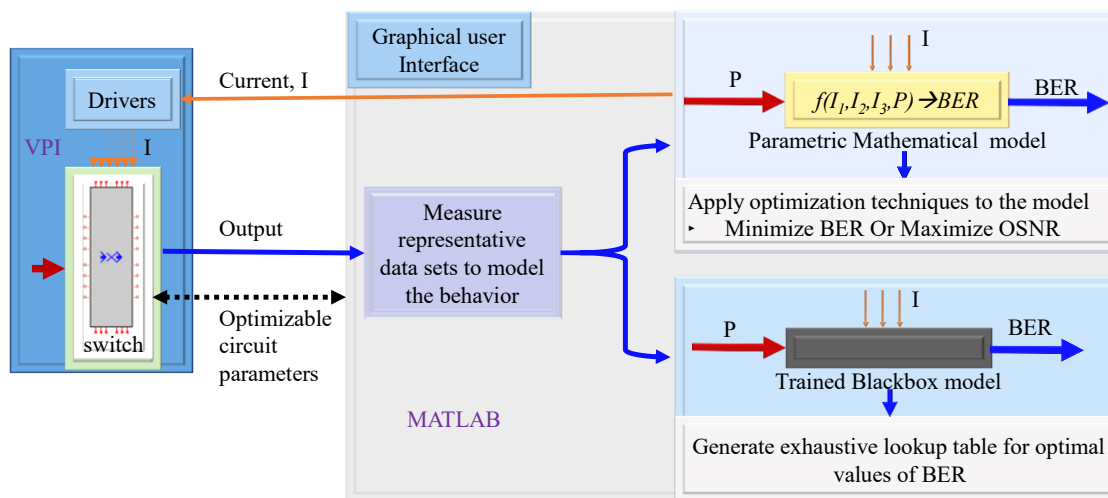


Figure 3: schematic indicating optimal switch drive current selection techniques

#### 5. Conclusion and future outlook

We show a model of an optical switch. We implement a control layer that controls the switch without knowing how the switch is designed by using files that convey information about the on-chip parameters to the control layer software. We discussed the method to find the currents that give the optimal values for the signal integrity. We will apply Both forms of selecting optimal currents to the model in the future to make a performance comparison analysis.

#### Acknowledgment

This work was supported by the H2020 ICT TWILIGHT Project (contract No. 781471) under the Photonics PPP

#### References

- [1] J. Strand and A. Chiu, "Realizing the Advantages of Optical Reconfigurability and Restoration with Integrated Optical Cross-Connects," *J. Light. Technol.*, vol. 21, no. 11, pp. 2871–2882, 2003, doi: 10.1109/JLT.2003.819539.
- [2] R. Stabile, A. Albores-Mejia, and K. A. Williams, "Monolithic active-passive 16 × 16 optoelectronic switch," *Opt. Lett.*, vol. 37, no. 22, p. 4666, 2012, doi: 10.1364/ol.37.004666.

## References

- [1] X Leijtens. Jeppix: the platform for indium phosphide-based photonics. IET optoelectronics , 5(5):202, 2011.
- [2] Meint Smit, JJGM Van der Tol, and Martin Hill. Moore's law in photonics, 2012.
- [3] Ardavan F Oskooi, David Roundy, Mihai Ibanescu, Peter Bermel, John D Joannopoulos, and Steven G Johnson. Meep: A flexible free-software package for electromagnetic simulations by the fdtd method. Computer Physics Communications , 181(3):687702, 2010.
- [4] wgms3d - Full-vectorial waveguide mode solver. [www.soundtracker.org/raw/wgms3d/](http://www.soundtracker.org/raw/wgms3d/)
- [5] Lumerical: High-Performance Photonic Simulation Software. [www.lumerical.com](http://www.lumerical.com)
- [6] Nazca-Design™ photonic IC design framework <https://nazca-design.org>
- [7] Alyona Ivanova, Remco Stoffer, and Manfred Hammer. A variational mode solver for optical waveguides based on quasi-analytical vectorial slab mode expansion. arXiv preprint arXiv:1307.1315 , 2013.
- [8] Jens Buus. The effective index method and its application to semiconductor lasers. IEEE Journal of Quantum Electronics , 18(7):10831089, 1982.

# Equivalent circuit modelling of coplanar waveguide InP electro-optic phase modulators.

J. A. Hillier,<sup>1</sup> W. Yao,<sup>1</sup> M. J. Wale,<sup>1</sup> and K. A. Williams.<sup>1</sup>

<sup>1</sup> Eindhoven University of Technology, Dept. of Elec. Eng., De Zaale, 5600 MB, Eindhoven, Netherlands.

*Wider bandwidth, energy-efficient Mach-Zehnder modulators are required to meet ever-increasing performance requirements in fibre-optic communications. To push beyond the state-of-the-art device performance, better tools for design optimisation are highly warranted. Currently, the most accurate simulation tools are either formed empirically or are computationally intensive, limiting opportunities for extended design space exploration. In this work, we investigate utilising a parametric and analytical traveling-wave model for the design of Mach-Zehnder modulators in coplanar waveguide geometry. Vivaly, the model incorporates both optical and electrical mechanisms and emerges from physical parameters such as layer thicknesses, materials properties, mask feature dimensions, and bias voltage. Evaluating the design from such parameters allows for holistic analyses of the design, elucidating the key tuneable parameters for improved performance. This is demonstrated utilising a factor of 3000 less computational time than traditional, finite element method, techniques to investigate the small-signal modulation bandwidth of the Mach-Zehnder modulators for an indicative set of 25 distinct parameters with varied mask design feature, epitaxy growth control, and load impedance.*

## Introduction

Due to advancements in design and fabrication capabilities, state of the art InP-based Mach-Zehnder modulators (MZM) provide bandwidths of 80 GHz [1], with high-order modulation formats enabling increased spectral efficiency and data rates [2]. Ultimately, however, the potential data capacity is dictated by the electrical frequency response of the transmitter circuit [3]. While further advancements in fabrication capabilities (smaller pitch, higher tolerances [4]) alongside material improvements (higher-k dielectrics and lower metal losses [5]) will push the frequency response to larger bandwidths, there are still opportunities for design optimisation to enable > 100 GHz bandwidth MZMs. The most accurate methods for optimisation of circuit design (semi-analytical method of lines [6], and finite difference methods [7]) are computationally intensive, limiting opportunities for more wide-ranging, holistic design space exploration. Alternative methods, with lower computational overhead, generally rely on empirical methods to fit the lumped components of common transmission line theory to measured results [8]. While such methods provide a means for local optimisation [9], the range of validity is limited to the measurement used for fitting. They also fail to provide a deeper understanding of the underlying physical phenomena that govern and limit the operation of the MZM. Gaining such an understanding may be key to discovering new pathways for further design optimisation not revealed by brute force parameter sweeping techniques. This work investigates the use of a computationally efficient, non-iterative, and spatially resolved equivalent-circuit model for traveling-wave electrode MZMs. The electronic propagation across the electrode is resolved purely from the bulk material and dimensional parameters of the modulator building block and both the electronic and electro-optic phenomena are incorporated into the analytical procedure. To ensure adherence to physical reality, we expand upon previous iterations of the equivalent circuit

methodology [10], to consider a plethora of physical effects that influence device behaviour such as the effect of the device design on the microwave velocity (directly fed into calculating the velocity matching between electronic and photonic signals), the effect of a bias voltage on the depletion width, and the change in the intrinsic layer conductivity with temperature. This work aims to demonstrate the potential of the low computational overhead offered by the outlined model through preliminary investigations into wide-range parameter exploration and its impact on the potential MZM bandwidth.

### Equivalent circuit model

The model uses the Keysight Advanced Design System (ADS) environment to facilitate simulations for the propagation of small-signal electronic waves along the modulator arm. Vivally, we also incorporate the electro-optic analysis into the ADS environment so that the electro-optic effect and the resultant optical phase and intensity modulation can be used as optimisable parameters from the foundational material and device design properties. The model incorporates velocity matching, electrical reflections, and the influence of bias-voltage and temperature. Figure 1 presents a schematic diagram for the cross section of the design. The phase modulator of length  $l_{ps}$  follows the co-planar waveguide (CPW) design comprising a central “signal” track of width  $w_p$  with two “ground” tracks of width  $w_n$  on either side separated by a distance  $w_g$ .

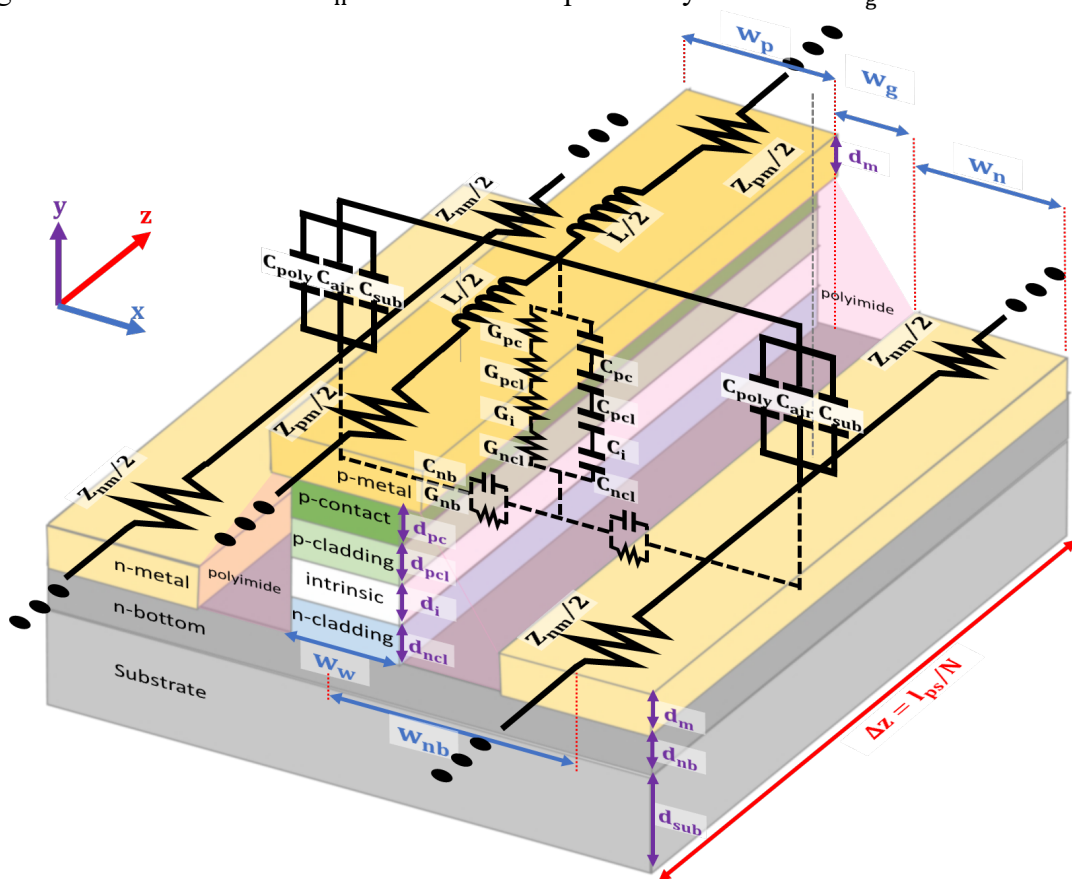


**Figure 1.** Schematic diagram of one ‘segment’ of the electrical equivalent circuit used in the analytical simulations (black lines). The circuit diagram is overlaid onto an (not-to-scale) illustration of the phase modulator element showing the material type and thickness (purple arrows) for each layer, the design dimensions (blue and red arrows), and the corresponding lumped component parameters (black labels).

An unintentionally doped “intrinsic” InP waveguide layer (white-shaded layer in Figure 1) is sandwiched between “p-cladding” and “n-cladding” layers (light green and light blue, respectively), of width  $w_w$ . A thin layer of InGaAs (dark green) is utilised as a “p-contact” layer between the p-cladding and signal track. The ground tracks lie on top of an “n-bottom” layer (dark grey) to facilitate an n-type contact. A polyimide passivation layer exists between the signal and ground metal tracks (pink layer). Each layer is described by a complex refractive index,  $\tilde{n} = n + j\kappa$ , conductivity,  $\sigma$ , and a thickness,  $d$ . The input parameters were taken from [4]. A single segment of the circuit model for the electrode is overlaid onto the schematic cross-section in Figure 1. The circuit is divided into  $N$  sections of length  $\Delta z$  and the non-negligible mechanisms for electronic transfer are represented by discrete lumped components within the cross-sectional element. The frequency,  $\omega$ , dependent values of conductance,  $G$ , capacitance,  $C$ , impedance,  $L$ , and inductance,  $\tilde{Z}$ , for each lumped component in Figure 1 are derived using a suite of relationships previously collated by A. Meighan [10]. The p-i-n stack capacitance and conductance are calculated from the permittivity and conductivity, respectively, multiplied by the ratio of the cross-sectional area to the current path length [3]. The complex impedance per unit length for the signal and ground tracks are defined as the ratio of the metal resistivity (scaled by the frequency-dependent skin depth) to the electrode width [11]. The CPW inductance alongside the polyimide, air, and substrate capacitances are calculated using the conformal mapping [12], with varied geometric moduli found by considering the relevant geometry [13]. To ensure that the model more accurately reflects physical reality, we expand upon previous iterations of the model by including the considering the influence of the changing depletion layer thickness with an applied bias voltage [14] and a temperature-dependent intrinsic layer conductivity [3]. The temperature dependence of these properties could have profound implications for device performance in practice, when temperatures significantly change during operation. We then calculate the microwave velocity,  $v_\mu = \text{Re}(L_{\text{eff}}, C_{\text{eff}})^{-1/2}$ , where the effective values of inductance of capacitance are required to account for the inductive and capacitive components of the metal track ‘resistor’ and the p-i-n stack ‘conductor’. These are given by the imaginary part of the metal track and p-i-n stack impedance over the frequency. The calculation of  $v_\mu$  is performed within ADS, improving upon previous iterations of the model that didn’t factor in a changing microwave index with design. We simulate the S-parameters for a two-port configuration with a source impedance,  $Z_S$ , and load impedance,  $Z_L$ , of  $50 \Omega$ . The  $-6$  dB electrical bandwidth is automatically extracted from the electronic transmission. The source termination was subsequently removed to simulate the propagation of the small-signal sinusoidal AC voltage with magnitude  $|V_{\text{AC}}| = -5$  dBm. The simulation accounts for multiple partial reflections at impedance mismatches within the circuit [3] to output the complex, frequency-dependent voltage across the intrinsic layer,  $\tilde{V}_{i,s}(\omega)$ , for each segment ‘s’. The difference in group velocity for the electronic and optical waves is accounted for by a phase offset in the microwave resulting in an effective voltage across the intrinsic layer,  $\tilde{V}_{i,s}^* = \tilde{V}_{i,s} \exp(j\omega(v_{\text{opt}}^{-1} - v_\mu^{-1})z)$ , where  $v_{\text{opt}}$  is the optical wave velocity [4]. The cumulative phase modulation is then  $\Delta\phi = (\pi/V_\pi)\bar{V}_1$ , where  $\bar{V}_1$  is the average voltage across the intrinsic layer across the phase shifter [3] and  $V_\pi = \lambda_0 d_i / n_g^3 r_{\text{Pockl}} l_{\text{ps}}$ , where  $\lambda_0 = 1550$  nm is the optical wavelength and  $r_{\text{Pockl}} = 1.4 \times 10^{-12} \text{ mV}^{-1}$  is the Pockels coefficient for bulk InP [15]. Finally, the modulation index,  $m(\omega) = |P_{\text{out}}(\omega)|/|P_{\text{in}}(\omega)|$  is calculated as a function of modulation frequency to give the small-signal response [3]:

## Design space exploration

The semi-analytical model outlined here is complete within seconds for each design variable combination.  $\sim 5$  s was used for the computation of each of the 25 parameters, a 3000 times improvement on computational time compared to finite element methods using similar equipment [10]. This enables assessment of more variables using smaller increments and/or larger ranges than has been previously realistic to do. Indeed, the present limiting factor is the user's ability to modify, output and plot relevant data, steps which could be automated to allow for multi-dimensional optimisation on a previously unattainable scale. To demonstrate this concept, Figure 2 presents the (a,b,c) Electrical  $-6$  dB and (d,e,f) electro-optic  $-3$  dB bandwidths as a function of an indicative set of design parameters. Specifically, we present the results while varying the (a,d) source/load impedance, (b,e) intrinsic layer thickness (at  $V_{DC} = 0$ ), and (c,f) waveguide width.

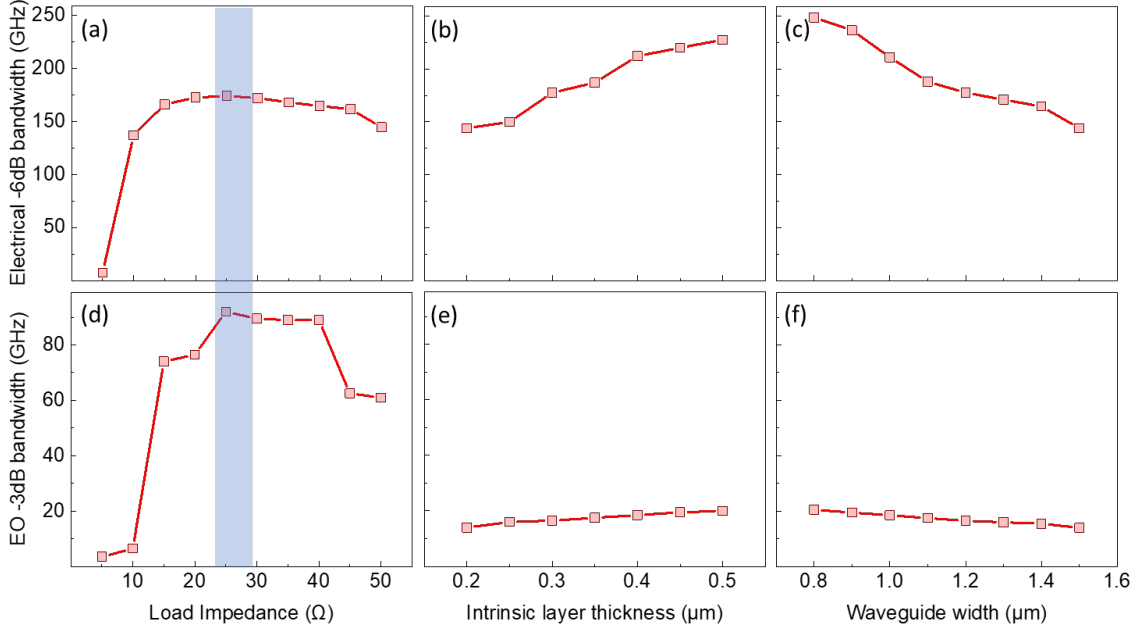


**Figure 2.** (a,b,c) Electrical  $-6$  dB and (d,e,f) electro-optic  $-3$  dB bandwidths as a function of a source/load impedance (5-50  $\Omega$  in steps of 5  $\Omega$ ), intrinsic layer thickness ( $\mu\text{m}$ ; 0.2-0.5  $\mu\text{m}$  in steps of 0.05  $\mu\text{m}$ ), and waveguide width (0.8-1.5  $\mu\text{m}$  in steps of 0.1  $\mu\text{m}$ ), respectively. The shaded blue area in (a) and (d) show the characteristic impedance of the modulator, across the range of simulated frequency.

It is seen in Figure 2a,d that the decrease of the source and load impedances significantly increases the electrical and electro-optic bandwidth down to 23.8 – 29.0  $\Omega$  (blue shaded region in Figure 2a,d), the characteristic impedance,  $Z_C$ , of the modulator design from 1 – 255 GHz. The bandwidth modulation is due to the reduction of back-reflections from the load especially at frequencies close to the bandwidth. Further reduction of the source and load impedance produces increased back-reflections, significantly reducing the bandwidths. This posits two possibilities to significantly enhance the electro-optic bandwidth of the CPW MZMs. Firstly, to increase the modulators characteristic impedance (while not significantly diminished performance), or to utilise a custom electronic driver design with lower source and load impedance. The 2<sup>nd</sup> option is clearly preferable (so as to not sacrifice device performance) but may not be trivial to practically achieve. In Figure 2b,e it is observed that an increase in the intrinsic layer thickness can also enhance both the electrical and electro-optic bandwidths. It must be noted, however,

that as  $V_{\pi} \propto d_i$  (Eq. 23), the 40% increase in the  $-3$  dB electro-optic bandwidth,  $BW_{EO}$ , corresponds to a 73% increase in  $V_{\pi}$ . Therefore,  $BW_{EO}/V_{\pi}$ , a potential ‘figure of merit’ for MZMs [10], is reduced from 0.84 – 0.69 GHz/V. This highlights how this, or other top-level figures of merit [4], would be better candidates to optimise for than just the bandwidth. Figure 2b,e shows that bandwidth gains can also be made by reducing the waveguide width. Such gains don’t affect  $V_{\pi}$  and so are more desirable than increasing the intrinsic layer thickness. It should be noted that, there are limitations for reducing the waveguide width, largely due to technological challenges for circuit fabrication [4].

## Conclusions

An analytical, non-iterative, and spatially resolved equivalent circuit model is presented. The model uses only geometrical and material parameter values as inputs, offering a much deeper understanding of the physical mechanisms behind device optimisation than both finite-difference and empirical circuit models. The formulation is grounded in the material science by considering how intrinsic material properties (doping density, permittivity) lead directly into the device characteristics when accounting for their geometry (thickness, widths) and effects of bias voltage and temperature. The low intensity of the computation was demonstrated to offer a wide-range, holistic, design space exploration on scales that were practically unattainable before.

## Acknowledgments

The authors acknowledge the work of A. Meighan in collating the relevant formulation and demonstrating the model validity through comparison with numerical simulation techniques and measurement [10].

## References

- [1] Y. Ogiso *et al.*, "80-GHz Bandwidth and 1.5-V  $V_{\pi}$  InP-Based IQ Modulator," *Journal of Lightwave Technology* 38(2), 249–255 (2020).
- [2] R. A. Griffin *et al.*, "InP coherent optical modulator with integrated amplification for high capacity transmission," in *Opt. Fiber Comm. Conference, OFC 2015 (OSA - The Optical Society, 2015)*.
- [3] G. Ghione, "*Semiconductor Devices for High-Speed Optoelectronics*" (Cambridge University Press, 2009).
- [4] W. Yao, "Towards a High-Capacity Multi-Channel Transmitter in Generic Photonic Integration Technology," *Doctoral Thesis, Eindhoven University of Technology* (2016).
- [5] L. Thylén and L. Wosinski, "Integrated photonics in the 21st century," *Photonics Res* 2(2), 75 (2014).
- [6] U. Rogge and R. Pregla, "Method of Lines for the Analysis of Strip-Loaded Optical Waveguides" (1991), 8(2).
- [7] J. Witzens *et al.*, "Design of transmission line driven slot waveguide Mach-Zehnder interferometers and application to analog optical links," *Opt Express* 18(16), 16902 (2010).
- [8] M. U. Sadiq *et al.*, "Efficient Modelling Approach for an InP Based Mach-Zehnder Modulator", *ISSC 2014/CICT 2014*, 2014, pp. 123-128 (2014).
- [9] W. Yao *et al.*, "Equivalent circuit modelling of integrated traveling-wave optical modulator in InP foundry platform," in *18th European Conference on Integrated Optics (ECIO 2016)* (2016), pp. 1–2.
- [10] A. Meighan, "Co-design of the high-speed photonic and electronic integrated circuits", *Doctoral Thesis, Eindhoven University of Technology* (2021).
- [11] K. S. Giboney, "Travelling-Wave Photodetectors," *Doctoral Thesis, University of California* (1995).
- [12] Y. R. Kwon *et al.*, "Quasi-TEM Analysis of "Slow-Wave" Mode Propagation on Coplanar Microstructure Mis Transmission Lines," *IEEE Trans Microw Theory Tech* 35(6), 545–551 (1987).
- [13] E. Chen and S. Y. Chou, "Characteristics of Coplanar Transmission Lines on Multilayer Substrates: Modeling and Experiments" *IEEE Transactions on Microwave Theory and Techniques* (1997), 45(6).
- [14] S. M. Sze and K. K. Ng, "*Physics of Semiconductor Devices*" (John Wiley & Sons, Inc., 2006).
- [15] S. Adachi, "*Properties of Group-IV, III-V and II-VI Semiconductors*" (John Wiley & Sons, Ltd, 2005).

# A Cross-Section Module To Bridge PIC Layout and Simulation Methods

L. Rossi,<sup>1</sup> M. Passoni,<sup>1</sup> and R. G. Broeke<sup>1</sup>

<sup>1</sup> Bright Photonic B.V., Horsten 1, 5612AX Eindhoven, the Netherlands

*This paper presents a versatile cross-section module and control layer in Nazca Design to interface between mask design and simulation tools, e.g. to find effective indices, and create and compare compact models. The module provides a standardized way to define a 2D cross-section geometry and material information, and subsequently port it to one or more simulation tools. 3D structures are created by combining cross-sections with mask layout. After running a simulation the module extracts and converts the simulation result into a standard data format for building compact models and/or comparisons in the analysis tool of choice, e.g. Matplotlib, Pandas or other.*

## Introduction

Integrated photonics has matured quickly in the past few years, and many technology platforms are now available, for example via multi-project wafer runs. As the number of components in photonic integrated circuits increases, the design flow reaches deeper into the circuit level, which is based on compact models of components, such as S-matrices in case of linear models.

Since photonics is an analog discipline, a different wavelength, polarization, or slight variations in the device geometry quickly requires new simulations for the generation of reliable models. Fortunately, there are many simulation tools and methods available, both free and/or open source, such as Meep [3] and wgms3d [4], as well as commercial, such as Lumerical Solutions [5]. However, each tool comes with its own interface and syntax. Therefore, generating the same geometry across multiple solvers for simulation input can become cumbersome and error-prone. At the output side (commercial) tools typically come with some internal result analysis for items like indices and mode characteristics. However, analysis definitions and grid handling may differ per tool, and with data still inside the different tools direct comparisons between tools at data level are difficult. Thus, a designer is often faced with a plethora of waveguide structures and materials, as well as multiple tools having different input and output interfaces and data formats.

To address these bottlenecks, this paper presents a waveguide cross-section geometry module (XSG) embedded within the Nazca Design framework [6]. The module interfaces between mask design (waveguide and compact model design) and simulation tools. The module provides a versatile and easy way to define a generic cross-section in Nazca, and ports it to the desired tool with a standardized syntax. It can make use of Nazca's mask layout information to create 3D structures. Simulations can be launched from the Nazca API using standardized commands; results are collected from the simulation tool(s) and converted in a common data format for further analysis by the designer.

## Methods

Most integrated optical components consist of a uniform cross-section across the wafer. Such devices can be decomposed into a two-dimensional cross-section and a one-dimensional polyline with locally varying width, as shown in Figure 1.

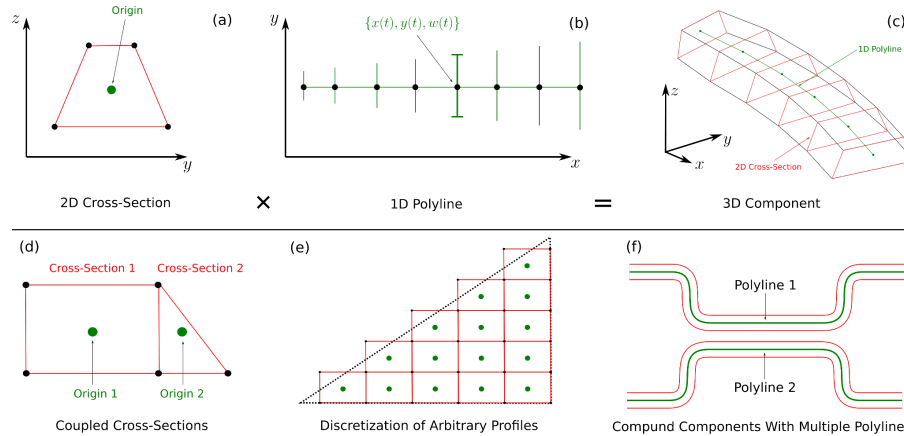


Figure 1: XSG module working principle. Decomposition of a 3D component (c) into a 2D cross-section (a) and a 1D polyline (b). The former (highlighted in red) describes the cross-sectional geometry and the materials therein employed (here left blank for simplicity); the polyline (highlighted in green) contains the path of the cross section and possible parameterized parameters of the cross section, such as a local width. Composite shapes can be used for more complex cross-sections and/or to simplify/enable interfacing with some tools. Examples are combining cross-sections having different polylines (d), discretization of arbitrary profiles with rectangular shapes (e), and a compound component (top-view/directional coupler) drawn with two separate polylines (f).

The cross-section contains information on the materials and the cross-sectional geometry and is defined with the XSG module; the one-dimensional polyline describes the  $(x, y)$  coordinates of the central points of the polygons on the mask and the local width  $w$  associated with them as  $\{x(t), y(t), w(t)\}$ , that is, a function of a normalized parameter  $t \in [0, 1]$ . This reuses the same concepts and methods as other mask elements, such as interconnects in Nazca. The XSG module contains two-dimensional shapes characterized by the vertices and the refractive index, which are defined by the user with three geometrical objects without an intrinsic orientation and a first-in-last-out masking property: trapezoids with variable sidewall angle, circles, and polygons with custom vertices.

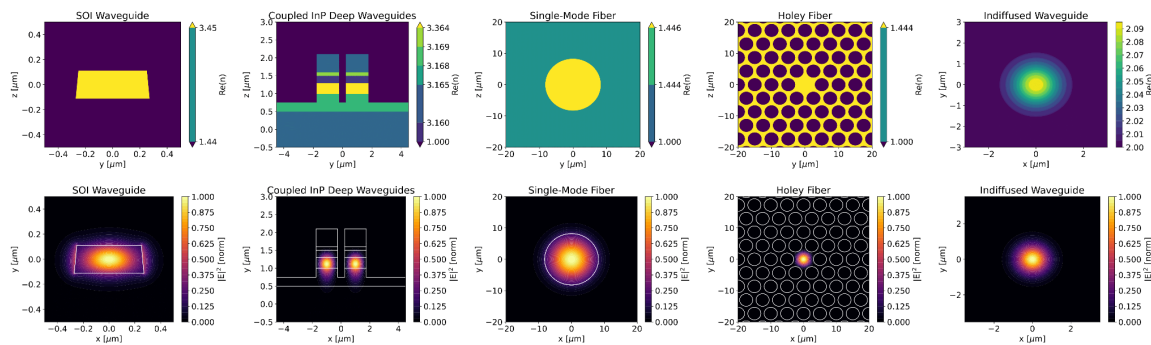


Figure 2: Example geometries that can be handled with the cross-section module and the associated fundamental mode electric field intensity at 1550 nm calculated with Lumerical MODE in these examples. Left to right: box waveguide, coupled waveguides, single-mode fiber, holey fiber, and in-diffused waveguide with Gaussian profile.

Figure 2 shows non-exhaustive examples that can be generated with the cross-section module. Rectangular geometries and circular geometries can be handled with trapezoids and circles, respectively; any other profiles can be directly defined from the vertices or can be imported from a function of position (e.g. diffusion profiles) by sampling its contour lines. Figure 1 shows how 3D components can be generated unifying the top- and side-view by extruding two-dimensional cross-sections into a set of three-dimensional vertices that describe polyhedra with a position-dependent width defined by the polyline.

The simulation flow with the XSG module is shown schematically in Figure 3. Overall, one design associated with one cross-section can be simulated with one standard command across multiple solvers to acquire a set of results represented in a common data format.

Firstly, the layout, the cross-section, and the index models of the materials are instantiated in Nazca. Then, the XSG module generates the vertices of the cross-sectional shapes and associates to them the material indices, which are extracted by evaluating the index models at the desired simulation settings. Combining the cross-sectional vertices, the refractive indices and the top-view polylines generates a unified, tool-independent geometry description. Furthermore, cross-sections can be parametrized with functions to easily perform sweeps by feeding different input settings into the module. Generating 3D simulations from the framework without exporting the layout to file and subsequently loading it in a tool allows one to retain valuable information such as the coordinates of Nazca pins, useful to place sources and monitors.

After the unified geometry with vertices and indices is defined in Nazca, it is translated into the desired tool description with and the simulation is then run by translating the desired settings, such as wavelength and polarization, into a set of standardized commands. Each tool requires a dedicated interface for the translation of the geometry and the commands: if a Python API is available, it is used directly; if a program is executed as a binary from the command line, the geometry is saved into a file and then run from Python as a shell command. Tools that do not offer an accessible interface cannot be used. When the interface communicates to the tool interface that the simulation is finished, the module extracts the results from the tool by querying the API or by reading the output files generated by the solvers. Eventually, Nazca converts the data into a common format including metadata for further analysis.

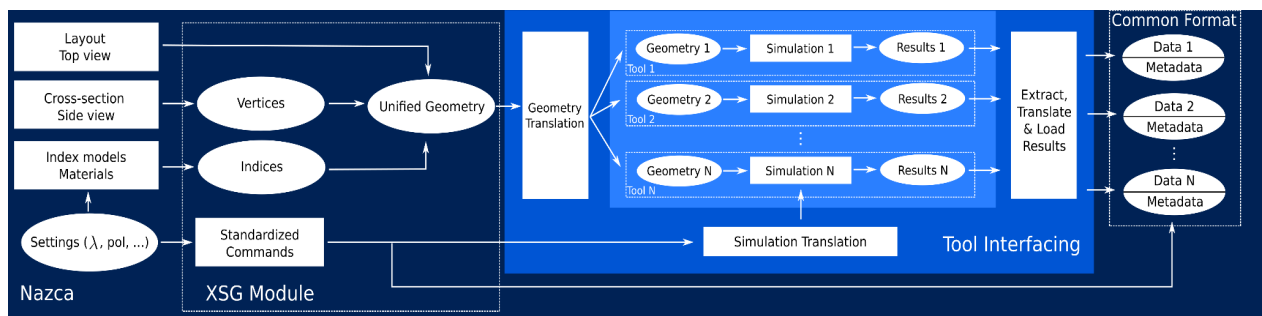


Figure 3: Simulation flow with the cross-section module. Vertices and indices are generated from Nazca from the side-view and material models and are joined to the layout into a unified, tool-independent geometry. Such geometry is exported to tools through a translation, and simulations are run through translated standardized commands. Results are extracted, translated and loaded into Nazca in a common format for further comparison with simulation metadata generated by the standardized command within the XSG module.

## Examples

This section presents two application examples to demonstrate a 2D and 3D problem handled by the XSG module. They show how from a single geometry and layout definition a comparison between results across tools and simulation methods is made. As a first example we report on the calculation of the modality of a silicon nitride asymmetric double stripe.

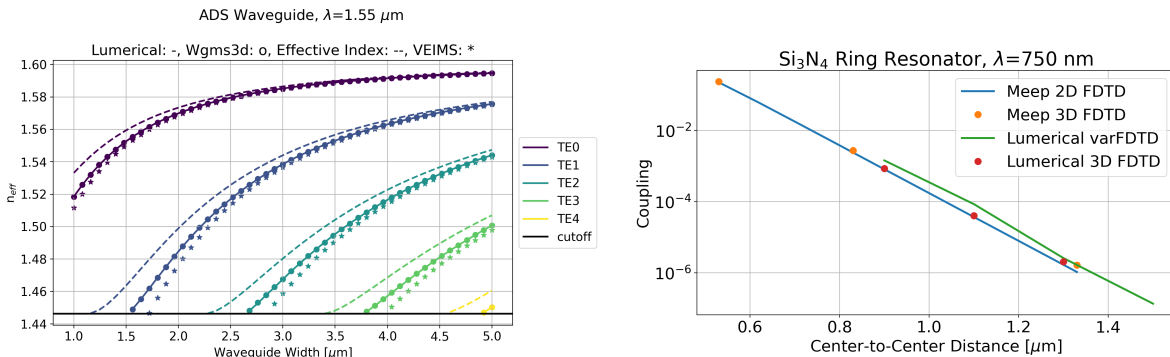


Figure 5: Modality calculation of a silicon nitride asymmetric double stripe waveguide performed with Lumerical (solid), wgms3d (circles), a variational mode solver (stars), and the effective index method (dashed) (a) and TE0 to TE0 transmission in a ring resonator as a function of ring-to-bus distance with Meep 2D (solid blue) and 3D (orange circles) FDTD, as well as Lumerical varFDTD (solid green) and 3D FDTD (red circles) (b).

waveguide, as shown in Figure 5a. This only requires a 2D geometry provided as a parametrized cross-section. The geometry from the cross-section module was fed into Lumerical, wgms3d, a variational eigenmode solver [7], and a multilayer solver performing the effective index method. As a second example we simulate a 3D silicon nitride ring resonator coupled to a straight bus waveguide with slanted sidewalls, where the power coupling from bus to ring as a function of the center-to-center distance is depicted in Figure 5b. The same geometry was sent to Meep 2D- and 3D-FDTD through “prisms”, as well as Lumerical varFDTD and 3D FDTD.

## Conclusion

We presented a cross-section geometry (XSG) module within Nazca-Design to interface between mask design and 2D and 3D simulations tools. A single cross-section geometry is exported to multiple tools. Simulations are run from Nazca and results can be retrieved in a standardized data format for further comparison and analysis by the designer.

## Acknowledgments

This work was supported by the European Commission within the project InPulse, grant number 824980. We would like to thank Thjis van den Brink for implementing a Python version of the variational eigenmode solver.

## References

- [1] Ardavan F Oskooi, *et al.* Meep: A flexible free-software package for electromagnetic simulations by the fdfd method. *Computer Physics Communications*, 181(3):687702, 2010.
- [2] wgms3d - Full-vectorial waveguide mode solver. [www.soundtracker.org/raw/wgms3d/](http://www.soundtracker.org/raw/wgms3d/)
- [3] Lumerical: High-Performance Photonic Simulation Software. [www.lumerical.com](http://www.lumerical.com)
- [4] Nazca-Design™ photonic IC design framework <https://nazca-design.org>
- [5] Alyona Ivanova, *et al.* A variational mode solver for optical waveguides based on quasi-analytical vectorial slab mode expansion. *arXiv preprint arXiv:1307.1315*, 2013.

# A 20-mode quantum photonic processor based on Silicon Nitride waveguides

C. Taballione<sup>1</sup>, M. Correa Anguita<sup>2</sup>, M. de Goede<sup>1</sup>, P. Venderbosch<sup>1</sup>,  
B. Kassenberg<sup>1</sup>, H. Snijders<sup>1</sup>, N. Kannan<sup>1</sup>, D. Smith<sup>1</sup>, J. P. Epping<sup>1</sup>,  
R. van der Meer<sup>2</sup>, P. W. H. Pinkse<sup>2</sup>, H. van den Vlekkert<sup>1</sup>, and J. J. Renema<sup>1,2</sup>

<sup>1</sup>QuiX Quantum B.V., 7521 AN Enschede, The Netherlands

<sup>2</sup>MESA+ Institute for Nanotechnology, University of Twente, 7522 NB Enschede, The Netherlands

## Abstract

*Photonics is one of the most attractive approaches to quantum computing, having gained momentum thanks to recent experimental results demonstrating a quantum advantage in photonics [1,2]. The strengths of photonics as quantum computing platform are as follows: first, quantum states of light are characterized by inherently low decoherence due to their weak interaction with the surrounding environment; second, photonic quantum states maintain their coherence at room temperature; third, photonic quantum computing can exploit the high maturity of existing classical integrated photonics technologies. These factors together mean that integrated photonics represents a scalable approach to large-scale quantum computing.*

*Integrated photonics is an essential technology for optical quantum computing. Universal, phase-stable, reconfigurable multimode interferometers (quantum photonic processors) enable manipulation of photonic quantum states and are one of the main components of photonic quantum computers in various architectures. In this paper, we report the realization of the largest quantum photonic processor to date. The processor enables arbitrary unitary transformations on its 20 input modes with a fidelity of  $F_{\text{Haar}} = 97.4\%$  and  $F_{\text{Perm}} = 99.5\%$ , an optical loss of 2.9 dB averaged over all modes, and high-visibility quantum interference  $V_{\text{HOM}} = 98\%$ . The processor is realized in  $\text{Si}_3\text{N}_4$  waveguides and operates at telecom wavelength.*

[1] Han-Sen Zhong et al. “Quantum computational advantage using photons”. In: *Science* 370.6523 (2020). *eprint*: <https://www.science.org/doi/pdf/10.1126/science.abe8770>, pp. 1460–1463.

[2] Hailong Zhou et al. “Self-Configuring and Reconfigurable Silicon Photonic Signal Processor”. In: *ACS Photonics* 7.3 (Mar. 2020). Publisher: American Chemical Society, pp. 792–799.

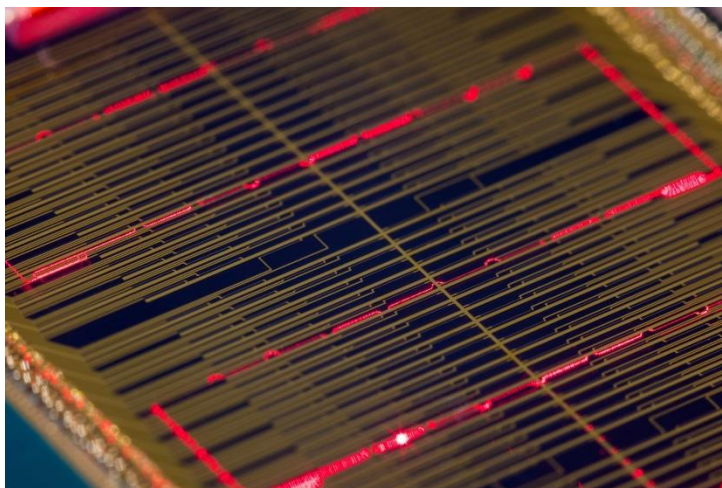


Figure 1 Photograph (zoom in) of the 20-mode quantum photonic processor when illuminated with visible red light. One of the waveguide paths is illuminated showing detailed features such as small spirals and directional couplers.